REPORT DOCUMENTATION PAGE

AFRL-SR-BL-TR-98-

0791

Public reporting burden for this collection of information is estimated to average 1 hour per response, including tl
and maintaining the data needed, and completing and reviewing the collection of information. Send commen
information, including suggestions for reducing this burden, to Washington Headquarters Services, Directorate fc
1204, Arlington, VA 22202-4302, and to the Office of management and Budget, Paperwork Reduction Project (07(

1. AGENCY USE ONLY (Leave Blank)	2. REPORT DATE	3. REPOR[illegible]
	December, 1994	Final

4. TITLE AND SUBTITLE	5. FUNDING NUMBERS
USAF Summer Research Program - 1994 Graduate Student Research Program Final Reports, Volume 10, Wright Laboratory	
6. AUTHORS Gary Moore	
7. PERFORMING ORGANIZATION NAME(S) AND ADDRESS(ES) Research and Development Labs, Culver City, CA	8. PERFORMING ORGANIZATION REPORT NUMBER
9. SPONSORING/MONITORING AGENCY NAME(S) AND ADDRESS(ES) AFOSR/NI 4040 Fairfax Dr, Suite 500 Arlington, VA 22203-1613	10. SPONSORING/MONITORING AGENCY REPORT NUMBER
11. SUPPLEMENTARY NOTES Contract Number: F49620-93-C-0063	
12a. DISTRIBUTION AVAILABILITY STATEMENT Approved for Public Release	12b. DISTRIBUTION CODE

13. ABSTRACT *(Maximum 200 words)*

The United States Air Force Graduate Student Research Program (USAF- GSRP) is designed to introduce university, college, and technical institute graduate students to Air Force research. This is accomplished by the graduate students being selected on a nationally advertised competitive basis during the summer intersession period to perform research at Air Force Research Laboratory Technical Directorates and Air Force Air Logistics Centers. Each participant provided a report of their research, and these reports are consolidated into this annual report.

14. SUBJECT TERMS	15. NUMBER OF PAGES
AIR FORCE RESEARCH, AIR FORCE, ENGINEERING, LABORATORIES, REPORTS, SUMMER, UNIVERSITIES	16. PRICE CODE

17. SECURITY CLASSIFICATION OF REPORT	18. SECURITY CLASSIFICATION OF THIS PAGE	19. SECURITY CLASSIFICATION OF ABSTRACT	20. LIMITATION OF ABSTRACT
Unclassified	Unclassified	Unclassified	UL

UNITED STATES AIR FORCE

SUMMER RESEARCH PROGRAM -- 1994

GRADUATE STUDENT RESEARCH PROGRAM FINAL REPORTS

VOLUME 10

WRIGHT LABORATORY

RESEARCH & DEVELOPMENT LABORATORIES

5800 Uplander Way

Culver City, CA 90230-6608

19981204 035

Program Director, RDL
Gary Moore

Program Manager, AFOSR
Major David Hart

Program Manager, RDL
Scott Licoscos

Program Administrator, RDL
Gwendolyn Smith

Program Administrator, RDL
Johnetta Thompson

Submitted to:

AIR FORCE OFFICE OF SCIENTIFIC RESEARCH

Bolling Air Force Base

Washington, D.C.

December 1994

DTIC QUALITY INSPECTED 4

GSRP FINAL REPORT TABLE OF CONTENTS i-xiv

1. INTRODUCTION 1

2. PARTICIPATION IN THE SUMMER RESEARCH PROGRAM 2

3. RECRUITING AND SELECTION 3

4. SITE VISITS 4

5. HBCU/MI PARTICIPATION 4

6. SRP FUNDING SOURCES 5

7. COMPENSATION FOR PARTICIPANTS 5

8. CONTENTS OF THE 1994 REPORT 6

APPENDICIES:

A. PROGRAM STATISTICAL SUMMARY A-1

B. SRP EVALUATION RESPONSES B-1

GSRP FINAL REPORTS

PREFACE

Reports in this volume are numbered consecutively beginning with number 1. Each report is paginated with the report number followed by consecutive page numbers, e.g., 1-1, 1-2, 1-3; 2-1, 2-2, 2-3.

This document is one of a set of 16 volumes describing the 1994 AFOSR Summer Research Program. The following volumes comprise the set:

VOLUME	TITLE
1	Program Management Report
	Summer Faculty Research Program (SFRP) Reports
2A & 2B	Armstrong Laboratory
3A & 3B	Phillips Laboratory
4	Rome Laboratory
5A & 5B	Wright Laboratory
6	Arnold Engineering Development Center, Frank J. Seiler Research Laboratory, and Wilford Hall Medical Center
	Graduate Student Research Program (GSRP) Reports
7	Armstrong Laboratory
8	Phillips Laboratory
9	Rome Laboratory
10	Wright Laboratory
11	Arnold Engineering Development Center, Frank J. Seiler Research Laboratory, and Wilford Hall Medical Center
	High School Apprenticeship Program (HSAP) Reports
12A & 12B	Armstrong Laboratory
13	Phillips Laboratory
14	Rome Laboratory
15A&15B	Wright Laboratory
16	Arnold Engineering Development Center

SRP Final Report Table of Contents

Author	University/Institution Report Title	Armstrong Laboratory Directorate	Vol-Page
MS Jennifer M Ball	Wright State University , Dayton, , OH Relation Between Detection and Intelligibility in	AL/CFBA	7- 1
MR. Richard G Best	Southwest Missouri State Univ. , Springfield, , MO The Effects of Socialization on Vocational Aspirat	AL/HRMJ	7- 2
MR. Daniel A Brown	Grand Canyon University , Phoenix, , AZ Toward Modeling Higher Level Control Systems: Inc	AL/HRAU	7- 3
MS. Susan T Chitwood	Bowling Green State University , Bowling Green, , OH Further Explorations in Epistemological Space	AL/CFHP	7- 4
John E Cisneros	California State University , Los Angeles , CA Aurally Directed Search: A Comparison Between Syn	AL/CFBA	7- 5
Candace E Clary	Duke University , Durham , NC Intra-Ocular Laser Surgical Probe (ILSP) for Vitre	AL/OEO	7- 6
Robert M Colbert	Villanova University , Villanova , PA Finite Element Modeling of Manikin Necks for the A	AL/CFBV	7- 7
MR. Mark C Delgado	University of Georgia , Athens, , GA Determination of the Oxidative Redox Capacity of A	AL/EQC	7- 8
MR. Steven J Essler	North Dakota State University , Fargo, , ND Estimation of Four Arterial Vascular Parameters fo	AL/AOCIY	7- 9
Lawrence R Gottlob	Arizona State University , Tempe , AZ Accuracy Curves in a Location-Cuing Paradigm for V	AL/HRAT	7- 10
MS. Jennifer L Greenis	Michigan State University , East Lansing, , MI ITS Evaluation: A Review of the Past and Recommen	AL/HRTE	7- 11

Author	University/Institution Report Title	Armstrong Laboratory Directorate	Vol-Page
MS. Patricia M Harn	University of Washington , Seattle , WA Testing R-Wise: Reading and Writing in a Supporti	AL/HRTI	7- 12
Jason E Hill	University of Scranton , Scranton , PA Rapid Bacterial DNA Fingerprintiing by the Polymer	AL/AOEL	7- 13
Mr. Rod J Hughes	Oregon Health Sciences University , Portland , OR Melatonin, Body Temperature and Sleep in Humans:	AL/CFTO	7- 14
Mr Roman G Longoria	Rice University , Houston , TX The Measurement of Work Experience: Issues and Im	AL/HRTE	7- 15
Uyen A Luong	Trinity University , San Antonio, , TX Millimeter Wave-Induced Hypertension Does Not Invo	AL/OER	7- 16
MR. Scott A Macbeth	University of Dayton , Dayton, , OH Using Electronic Brainstroming Tools to Visually	AL/HRG	7- 17
MR. Nicholas F Muto	University of Scranton , Scranton, , PA Rapid Bacterial DNA Fingerprinting by the Polymera	AL/AOEL	7- 18
Kevin P Nau	Kent State University , Kent , OH Proposal for the Establishment of a Comprehensive	AL/CFTF	7- 19
MR. Eric O Riise	Cal State Univ/Chico , Chico, , CA A Study of Interaction in Distance Learning	ALL/HRT	7- 20
Ms Heather E Roberts	Virginia Tech , Blacksburg , VA Gender and RAcial Equity of the Air Force Officer	AL/HRMM	7- 21
MR. Dale F Rucker	West Virginia University , Morgantown, , WV Improved Numerical Modeling of Groundwater Flow an	AL\EQC	7- 23

Author	University/Institution Report Title	Armstrong Laboratory Directorate	Vol-Page
Arthur M Ryan	Wright State University , Dayton , OH The Workload Assessment Monitor: Progress Towards	AL/CFHP	7- 24
Mark J Schroeder	North Dakota State University , Fargo , ND Arterial Elastance in the Maximization of External	AL/AOCIY	7- 25
MS. Katherine M Specht	Ohio State University , Columbus, , OH Tactile Perception in a Virtual Environment	AL/CFBA	7- 26
MR. Joseph M Stauffer	University of Iowa , Iowa City , IA Predicting Pilot Training Success with Logistic or	AL/HRMA	7- 27
DR. Scott G Stavrou	University of Central Arkansas , Conway, , AR Analysis of the Absorption and Metabolism of Trich	AL/OET	7- 28
MS. Virginia K Stromquist	Michigan Technological Inst. , Houghton, , MI Solid Phase Microextraction as a Method for Quanti	AL/EQC	7- 29
MR. Eric S Wieser	Trinity University , San Antonio, , TX Millimeter Wave-Induced Hypotension Does Not Invol	AL/OER	7- 30
MR. Gregory S Zinkel	Georgia Institute Technology , Atlanta, , GA A Study of the Use Predictive Modeling for Dynamic	AL/AO	7- 31

Author	University/Institution Report Title	Phillips Laboratory Directorate	Vol-Page
MR. William W Brocklehurst	University of Cincinnati , Cincinnati , OH Effect of Dissolved Gases on the Discharge Coeffic	PL/RKFA	8- 1
MR. Stephen E Clarke	Utah State University , Logan , UT REPORT NOT AVAILABLE AT PRESS TIME	PL/VTRP	8- 2
Peyman Ensaf	University of Denver , Denver , CO Influence of Model Complexity and Aeroelastic Cont	PL/WSA	8- 3
MR. Frank S Gulczinski	University of Michigan , Ann Arbor, , MI Interior Spectroscopic Investigation of Plasma Com	PL/RKCO	8- 4
MR. Derik C Herpfer	University of Cincinnati , Cincinnati , OH Drop Sizing of a Like-Impinging Element Injector I	PL/RKFA	8- 5
MR. Phillip N Hutton	Old Dominion University , Norfolk, , VA Effectiveness of Thermionic Heat Pipe Module	PL/VTPN	8- 6
MR. Robert J Leiweke	Ohio State University , Columbus , OH A Single Temperature/Material Ablation Algorithm f	PL/WSP	8- 7
MR. John I Lipp	Michigan Technological Univ , Houghton , MI Estimation of Tilts Extended Images in the Presenc	PL/LIAE	8- 8
MR. Stephen A Luker	University of Alabama , Tuscaloosa , AL Determining Cloud Coverages for Input to Thermal C	PL/GPAA	8- 9
MR. Daniel T Moriarty	MIT , Cambridge , MA Laboratory Experiments with the Versatile Toroidal	PL/GPSG	8- 10
MR. Tim C Newell	University of North Texas , Denton , TX Synchronization Using Control Chaotic Diode Resona	PL/LIDN	8- 11

SRP Final Report Table of Contents

Author	University/Institution Report Title	Phillips Laboratory Directorate	Vol-Page
Jeffrey W Nicholson	University of New Mexico , Albuquerque , NM Relaxation Processes in Gain Switched Iodine Laser	PL/LIDB	8- 12
MR. Sean R Olin	Boston University , Boston, , MA An Investigation of Flight Characteristics of the	PL/SX	8- 13
MS. Janet M Petroski	Cal State Univ/Northridge , Northridge , CA Thermoluminescence of Simple Species in Solod Mole	PL/RKFE	8- 14
MR. Aaron J Ridley	University of Michigan , Ann Arbor, , MI The Dynamic Convection Reversal Boundary	PL/GPIA	8- 15
MR. Richard M Salasovich	University of Cincinnati , Cincinnati , OH Fabrication and Mechanical Testing of Mixed-Matrix	PL/VTSC	8- 16
MR. Kevin L Scales	University of New Mexico , Albuquerque , NM A Study of Numeical Methods in Atomosperic Light P	PL/LIMI	8- 17
Greg T Sharp	University of New Mexico , Albuquerque , NM Further Studies of High Temperature Cs-Ba Tacitron	PL/WSP	8- 18
MR. Joseph M Sorci	Massachusetts Inst. Technology , Cambridge, , MA A Study of Low Frequency Weak Turbulence in a Holl	PL/GPID	8- 19
Jonathan Stohs	University of New Mexico , Albuquerque , NM Radiation Exposure of Photonic Devices	PL/VTET	8- 20
MR. Jose Suarez	Florida Inst. of Technology , Patrick AFB, , FL Meteoriod & Orbital Debris Collision Hazard Analys	PL/WSC	8- 21
MR. Tony F von Sadovszky	University of Nevada, Ren , Reno, , nv PICLL: A Portable Parallel 3D PIC Code Impleme	PL/WSP	8- 22

Author	University/Institution Report Title	Rome Laboratory Directorate	Vol-Page
MR. John C Bertot	Syracuse University , Syracuse, , NY Transferring Technology Via the Internet	RL/XPP	9- 1
MR. Jerry M Couretas	University of Arizona , Tucson, , AZ Analysis of Extraction and Aggregation Techniques	RL/IRDO	9- 2
MR. Frederick L Crabbe	Univ California/Los Angeles , Los Angeles, , CA Using Self-Organization to Develop Vector Represen	RL/IRDO	9- 3
MS. Julie Hsu	Louisiana State University , Baton Rouge, , LA An Assignment Based Approach to Parallel-Machine S	RL/C3CA	9- 4
Andrew J Laffely	Univ. of Maine , Orono , ME Automatic Extraction of Drainage Network from Di	RL/IRRP	9- 5
MR. Daniel K Lee	Southern Illinois University , Carbondale , IL Mutual Coupling Effect of Square Microstrip Patch	RL/ERA	9- 6
Slawomir J Marcinkowski	Syracuse University , Syracuse , NY Transferring Technology Via the Internet	RL/XPP	9- 7
MR. Sean S O'Keefe	Cornell University , Ithaca, , NY Integration of Optoelectronic Devices with Microwa	RL/OCBP	9- 8
MR Robert L Popp	University of Connecticut , Storrs , CT Multisensor-Multitarget Data Fusion Using an S-Dim	RL/OCTM	9- 9
MR. Steven J Pratt	Syracuse University , Syracuse, , NY Analysis and Comparison of the Performance/Life Co	RL/C3AB	9- 10
Francis X Reichmeyer	Syracuse University , Syracuse , NY Local Area ATM Network Interfaces	RL/C3AB	9- 11

Author	University/Institution Report Title	Rome Laboratory Directorate	Vol-Page
MR. David H Sackett	Rochester Institute of Technol , Rochestter , NY Self-Sustained Pulsation and High Speed Optical Ne	RL/OCPA	9- 12
ME. Paul E Shames	Univiersity of Cal/San Diego , San Diego, , CA A Study of High Speed Polarization Rotators for Us	RL/IRAP	9- 13
Terrence W Towe	Univ of Arkansas-Fayetteville , Fayetteville , AR REPORT NOT AVAILABLE AT PRESS TIME	RL/ERX	9- 14
Okechukwu C Ugweje	Florida Atlantic University , Boca Raton, , FL A Program Plan for Transmitting High-Data-Rate ATM	RL/C3BA	9- 15
MR. Martin A Villarica	Syracuse University , Syracuse, , NY A Study of the Application of Fractuals and Kineti	RL/ERDR	9- 16
Stanley J Wenndt	Colorado State University , Fort Collins , CO An Investigation of Cepstrum Based Speaker Identif	RL/IRAA	9- 17

SRP Final Report Table of Contents

Author	University/Institution Report Title	Wright Laboratory Directorate	Vol-Page
MS. Terri L Alexander	University of Central Florida , Orlando, , FL Design of Spectroscopic Material-Characterization	WL/MNGS	10- 1
MR. Joseph L Binford, III	University of Dayton , Dayton, , OH Thermal Stability Apparatus Design and Error Analy	WL/MLPO	10- 2
MR Jonathan A Bishop	University of Oklahoma , Norman, , OK Influence of Model Complexity and Aeroelastic Cons	WL/FIBR	10- 3
MR. Steven P Burns	Purdue University , West Lafayette, , IN The Use of Pressure Sensitive Paints on Rotating M	WL/POTF	10- 4
MR. Lance H Carter	University of Texas/Austin , Austin , TX Gain-Scheduled Bank-to-Turn Autopilot Design Using	WL/MNAG	10- 5
MR. Peng Chen	University of North Texas , Denton , TX Synthesis & Characterization of Lanthanum Phosphat	WL/MLLM	10- 6
MS. Lora A Cintavey	University of Cincinnati , Cincinnati , OH Processing and Characterization of Nonlinear Optic	WL/MLBP	10- 7
MR. William K Cope	University of Illinois/Urbana , Urbana, , IL Assessment of Gasp for the Simulation of Scramjet	WL/POPT	10- 8
Mike J Cutbirth	Oklahoma State University , Stillwater , OK A Study of the Heat Transfer for the High Flux Hea	WL/POOS	10- 9
Craig M Files	University of Idaho , Moscow , ID Using a Search Heuristic in an NP-Complete Problem	WL/AART-	10- 10
MR Edward M Friel	University of Dayton , Dayton , OH Direction Finding in the Presence of a Near Field	WL/AARM	10- 11

Author	University/Institution Report Title	Wright Laboratory Directorate	Vol-Page
MR. Keith D Grinstead	Purdue University , West Lafayette, , IN Obtaininng the Correction Factors for Two-Photon I	WL/POSF	10- 12
MR. Jason J Hugenroth	Louisiana State University , Baton Rouge, , LA A Research Plan for Evaluating Wave Gun as a Low-L	WL/MNAA	10- 13
MR. Andrew Kager	University of Central Florida , Orlando, , FL A Numerical Study of the Effect of Base and Collec	WL/ELRA	10- 14
MR. John C Lewis	University of Kentucky , Lexington , KY A Theory for the Testing of Materials Under Combin	WL/MNM	10- 15
MR. Kenneth P Luke	Wright State University , Dayton, , OH Three-Dimensional Modeling Using a Calibrated Came	WL/AARF-	10- 16
John D Mai	Univ of Calif-Los Angeles , Los Angeles , CA Preliminary Characterization and Calibration of Mi	WL/FIME	10- 17
MR Mark A Manzardo	Univ of Alabama-Huntsville , Huntsville , AL High Speed Imaging Infrared Polarimetry	WL/MNGS	10- 18
MR. David B Maring	University of FloridaFL , Gainesville, , FL Fabrication and White-Light Characterization of An	WL/MNG	10- 19
MR. Joseph R Miramonti	University of Missouri/Columbi , Columbia, a , MO Scanning Image Alegbra Networks for Vehicle Identi	WL/MNGA	10- 20
MS. Jennifer S Naylor	Auburn University , Auburn, , AL Automation Control Issues in the Development of an	WL/MNAG	10- 21
MR. Ned F O'Brien	University of Dayton , Dayton, , OH A Study of RF Fiber Optic Communication Link Techn	WL/AAAI-	10- 22

Author	University/Institution Report Title	Wright Laboratory Directorate	Vol-Page
MR. Tae W Park	Univ of Illinois/Chicago , Chicago, , IL A Numerical Study of DropleVortx Interactions in a	WL/POSF	10- 23
MS Margaret F Pinnell	University of Dayton , Dayton , OH A Parametric Study of the Factors Affecting the Op	WL/MLBM	10- 24
MR. Seth M Pinsky	Oregon Grad Inst. Sci & Tech , Portland, , OR S-Parameter Measurements on a GaAsFET Variable-Gai	WL/ELM	10- 25
MR. David A Ress	Tennessee Technological Univ , Cookeville, , TN Modifications To The Thinker Discovery System	WL/MLIM	10- 26
Mohammed A Samad	University of New Orleans , New Orleans , LA A Study of Delamination Damage and Energy Exchange	WL/FIVS	10- 27
MR. Robert W Slater III	University of Cincinnati , Cincinnati , OH Low-Velocity Impact of Moisture-Conditioned Lamina	WL/FIBE	10- 28
Ed P Socci	University of Virginia , Charlottesville , VA X-ray Diffraction Study of Siloxane/Cholestrol Bas	WL/MLPO	10- 29
MR. Edward A Thompson	University of Cincinnati , Cincinnati, , OH Annealed Fuzzy Control for a Self-Tuning Piezolect	WL/FIBG	10- 30
MR. Brent A Veltkamp	Michigan State University , East Lansing, , MI Pixel Plane Design for SIMD Graphic Processor	WL/ELED	10- 31
MR. Christopher C Vogt	University of Cal San Diego , San Diego, , CA The Combinatorics of Function Decomposition and Ap	WL/AART-	10- 32
MR. Ralph J Volino	University of Minnesota , Minneapolis, , MN Documentation of Boundary Layer Characteristics fo	WL/POTT	10- 33

Author	University/Institution Report Title	Wright Laboratory Directorate	Vol-Page
MR. Jeffrey A Walrath	University of Cincinnati , Cincinnati, , OH Integration of Champ Firm Macro Library with DSS	WL/AAAT-	10- 34

Author	University/Institution Report Title	Arnold Engineering Development Center Directorate	Vol-Page
MR. William A Alford	Univ. Tennessee Space Inst. , Tullahoma, , TN Design of Testing and Debugging Software for C31 N	Sverdrup	11- 1
MR. Brian C DeAngelis	University of Illinois/Urbana- , Urbana , IL Performance and Validation Studies of the Kiva-II	SVERDRU	11- 2
MR. Harold D Helsley	Univ Tennessee Space Inst , Tullahoma, , TN Development of a Monitor for a Multi-Processor Net	Sverdrup	11- 3
MR. Christopher W Humphres	University of Alabama , Tuscaloosa, , AL Parallelization of Chimera Utilizing PVM	Calspan	11- 4
MR. Curtis S Mashburn	Universtity of Tennessee Space , Tullahoma, , TN Prediction of the Performance of a 7-Stage Axial-F	Sverdrup	11- 5
MR. William S Meredith	Univ of Tennesse Sp. Inst. , Tullhoma, , TN REPORT NOT AVAILABLE AT PRESS TIME	Calspan	11- 6
MR. Michael S Moore	Vanderbilt University , Nashville , TN A Model Based Real Time Image Processing System	SVERDRU	11- 7
MR David T Pratt	Univ of Tennessee Space Inst , Tullahoma , TN Analysis and Comparison of the Performance/Life Co	Sverdrup	11- 8
MR. David B Underhill	Univ of Tenn Space Inst , Tullahoma , TN Application of Vorticity Confinement to a Delta Wi	Calspan	11- 9

Author	University/Institution Report Title	Frank J Seiler Research Laboratory Directorate	Vol-Page
MR. Christian S Bahn	Colorado School of Mines , Golden, , CO A Theoretical Study of Lithium and Molten Salt Gra	FJSRL/NC	11- 10
MR. Antonio M Ferreira	Memphis State University , Memphis, , TN Theoretical Investigations of the NLO Properties o	FJSRL/NC	11- 11
MS Joan Fuller	University of Alabama , Tuscaloosa , AL Investigations of Carbon Materials in Alkali Metal	FJSRL/CD	11- 12

Author	University/Institution Report Title	Wilford Hall Medical Center Directorate	Vol-Page
MR Ramachandra P Tummala	University of Miami , Coral Gables , FL Effects of Temperature on Various Hematological P	WHMC/RD	11- 13

1. INTRODUCTION

The Summer Research Program (SRP), sponsored by the Air Force Office of Scientific Research (AFOSR), offers paid opportunities for university faculty, graduate students, and high school students to conduct research in U.S. Air Force research laboratories nationwide during the summer.

Introduced by AFOSR in 1978, this innovative program is based on the concept of teaming academic researchers with Air Force scientists in the same disciplines using laboratory facilities and equipment not often available at associates' institutions.

AFOSR also offers its research associates an opportunity, under the Summer Research Extension Program (SREP), to continue their AFOSR-sponsored research at their home institutions through the award of research grants. In 1994 the maximum amount of each grant was increased from $20,000 to $25,000, and the number of AFOSR-sponsored grants decreased from 75 to 60. A separate annual report is compiled on the SREP.

The Summer Faculty Research Program (SFRP) is open annually to approximately 150 faculty members with at least two years of teaching and/or research experience in accredited U.S. colleges, universities, or technical institutions. SFRP associates must be either U.S. citizens or permanent residents.

The Graduate Student Research Program (GSRP) is open annually to approximately 100 graduate students holding a bachelor's or a master's degree; GSRP associates must be U.S. citizens enrolled full time at an accredited institution.

The High School Apprentice Program (HSAP) annually selects about 125 high school students located within a twenty mile commuting distance of participating Air Force laboratories.

The numbers of projected summer research participants in each of the three categories are usually increased through direct sponsorship by participating laboratories.

AFOSR's SRP has well served its objectives of building critical links between Air Force research laboratories and the academic community, opening avenues of communications and forging new research relationships between Air Force and academic technical experts in areas of national interest; and strengthening the nation's efforts to sustain careers in science and engineering. The success of the SRP can be gauged from its growth from inception (see Table 1) and from the favorable responses the 1994 participants expressed in end-of-tour SRP evaluations (Appendix B).

AFOSR contracts for administration of the SRP by civilian contractors. The contract was first awarded to Research & Development Laboratories (RDL) in September 1990. After completion of the 1990 contract, RDL won the recompetition for the basic year and four 1-year options.

2. PARTICIPATION IN THE SUMMER RESEARCH PROGRAM

The SRP began with faculty associates in 1979; graduate students were added in 1982 and high school students in 1986. The following table shows the number of associates in the program each year.

Table 1: SRP Participation, by Year

YEAR	Number of Participants			TOTAL
	SFRP	GSRP	HSAP	
1979	70			70
1980	87			87
1981	87			87
1982	91	17		108
1983	101	53		154
1984	152	84		236
1985	154	92		246
1986	158	100	42	300
1987	159	101	73	333
1988	153	107	101	361
1989	168	102	103	373
1990	165	121	132	418
1991	170	142	132	444
1992	185	121	159	464
1993	187	117	136	440
1994	192	117	133	442

Beginning in 1993, due to budget cuts, some of the laboratories weren't able to afford to fund as many associates as in previous years; in one case a laboratory did not fund any additional associates. However, the table shows that, overall, the number of participating associates increased this year because two laboratories funded more associates than they had in previous years.

3. RECRUITING AND SELECTION

The SRP is conducted on a nationally advertised and competitive-selection basis. The advertising for faculty and graduate students consisted primarily of the mailing of 8,000 44-page SRP brochures to chairpersons of departments relevant to AFOSR research and to administrators of grants in accredited universities, colleges, and technical institutions. Historically Black Colleges and Universities (HBCUs) and Minority Institutions (MIs) were included. Brochures also went to all participating USAF laboratories, the previous year's participants, and numerous (over 600 annually) individual requesters.

Due to a delay in awarding the new contract, RDL was not able to place advertisements in any of the following publications in which the SRP is normally advertised: *Black Issues in Higher Education, Chemical & Engineering News, IEEE Spectrum* and *Physics Today*.

High school applicants can participate only in laboratories located no more than 20 miles from their residence. Tailored brochures on the HSAP were sent to the head counselors of 180 high schools in the vicinity of participating laboratories, with instructions for publicizing the program in their schools. High school students selected to serve at Wright Laboratory's Armament Directorate (Eglin Air Force Base, Florida) serve eleven weeks as opposed to the eight weeks normally worked by high school students at all other participating laboratories.

Each SFRP or GSRP applicant is given a first, second, and third choice of laboratory. High school students who have more than one laboratory or directorate near their homes are also given first, second, and third choices.

Laboratories make their selections and prioritize their nominees. AFOSR then determines the number to be funded at each laboratory and approves laboratories' selections.

Subsequently, laboratories use their own funds to sponsor additional candidates. Some selectees do not accept the appointment, so alternate candidates are chosen. This multi-step selection procedure results in some candidates being notified of their acceptance after scheduled deadlines. The total applicants and participants for 1994 are shown in this table.

Table 2: 1994 Applicants and Participants

PARTICIPANT CATEGORY	TOTAL APPLICANTS	SELECTEES	DECLINING SELECTEES
SFRP	600	192	30
(HBCU/MI)	(90)	(16)	(7)
GSRP	322	117	11
(HBCU/MI)	(11)	(6)	(0)
HSAP	562	133	14
TOTAL	1484	442	55

4. SITE VISITS

During June and July of 1994, representatives of both AFOSR/NI and RDL visited each participating laboratory to provide briefings, answer questions, and resolve problems for both laboratory personnel and participants. The objective was to ensure that the SRP would be as constructive as possible for all participants. Both SRP participants and RDL representatives found these visits beneficial. At many of the laboratories, this was the only opportunity for all participants to meet at one time to share their experiences and exchange ideas.

5. HISTORICALLY BLACK COLLEGES AND UNIVERSITIES AND MINORITY INSTITUTIONS (HBCU/MIs)

In previous years, an RDL program representative visited from seven to ten different HBCU/MIs to promote interest in the SRP among the faculty and graduate students. Due to the late contract award date (January 1994) no time was available to visit HBCU/MIs this past year.

In addition to RDL's special recruiting efforts, AFOSR attempts each year to obtain additional funding or use leftover funding from cancellations the past year to fund HBCU/MI associates. This year, seven HBCU/MI SFRPs declined after they were selected. The following table records HBCU/MI participation in this program.

Table 3: SRP HBCU/MI Participation, by Year

YEAR	SFRP		GSRP	
	Applicants	Participants	Applicants	Participants
1985	76	23	15	11
1986	70	18	20	10
1987	82	32	32	10
1988	53	17	23	14
1989	39	15	13	4
1990	43	14	17	3
1991	42	13	8	5
1992	70	13	9	5
1993	60	13	6	2
1994	90	16	11	6

6. SRP FUNDING SOURCES

Funding sources for the 1994 SRP were the AFOSR-provided slots for the basic contract and laboratory funds. Funding sources by category for the 1994 SRP selected participants are shown here.

Table 4: 1994 SRP Associate Funding

FUNDING CATEGORY	SFRP	GSRP	HSAP
AFOSR Basic Allocation Funds	150	98*1	121*2
USAF Laboratory Funds	37	19	12
HBCU/MI By AFOSR (Using Procured Addn'l Funds)	5	0	0
TOTAL	192	117	133

*1 - 100 were selected, but two canceled too late to be replaced.
*2 - 125 were selected, but four canceled too late to be replaced.

7. COMPENSATION FOR PARTICIPANTS

Compensation for SRP participants, per five-day work week, is shown in this table.

Table 5: 1994 SRP Associate Compensation

PARTICIPANT CATEGORY	1991	1992	1993	1994
Faculty Members	$690	$718	$740	$740
Graduate Student (Master's Degree)	$425	$442	$455	$455
Graduate Student (Bachelor's Degree)	$365	$380	$391	$391
High School Student (First Year)	$200	$200	$200	$200
High School Student (Subsequent Years)	$240	$240	$240	$240

The program also offered associates whose homes were more than 50 miles from the laboratory an expense allowance (seven days per week) of $50/day for faculty and $37/day for graduate students.

Transportation to the laboratory at the beginning of their tour and back to their home destinations at the end was also reimbursed for these participants. Of the combined SFRP and GSRP associates, 58% (178 out of 309) claimed travel reimbursements at an average round-trip cost of $860.

Faculty members were encouraged to visit their laboratories before their summer tour began. All costs of these orientation visits were reimbursed. Forty-one percent (78 out of 192) of faculty associates took orientation trips at an average cost of $498. Many faculty associates noted on their evaluation forms that due to the late notice of acceptance into the 1994 SRP (caused by the late award in January 1994 of the contract) there wasn't enough time to attend an orientation visit prior to their tour start date. In 1993, 58 % of SFRP associates took orientation visits at an average cost of $685.

Program participants submitted biweekly vouchers countersigned by their laboratory research focal point, and RDL issued paychecks so as to arrive in associates' hands two weeks later.

HSAP program participants were considered actual RDL employees, and their respective state and federal income tax and Social Security were withheld from their paychecks. By the nature of their independent research, SFRP and GSRP program participants were considered to be consultants or independent contractors. As such, SFRP and GSRP associates were responsible for their own income taxes, Social Security, and insurance.

8. CONTENTS OF THE 1994 REPORT

The complete set of reports for the 1994 SRP includes this program management report augmented by fifteen volumes of final research reports by the 1994 associates as indicated below:

Table 6: 1994 SRP Final Report Volume Assignments

	VOLUME		
LABORATORY	SFRP	GSRP	HSAP
Armstrong	2	7	12
Phillips	3	8	13
Rome	4	9	14
Wright	5A, 5B	10	15
AEDC, FJSRL, WHMC	6	11	16

AEDC = Arnold Engineering Development Center
FJSRL = Frank J. Seiler Research Laboratory
WHMC = Wilford Hall Medical Center

APPENDIX A – PROGRAM STATISTICAL SUMMARY

A. Colleges/Universities Represented

Selected SFRP and GSRP associates represent 158 different colleges, universities, and institutions.

B. States Represented

SFRP -Applicants came from 46 states plus Washington D.C. and Puerto Rico. Selectees represent 40 states.

GSRP - Applicants came from 46 states and Puerto Rico. Selectees represent 34 states.

HSAP - Applicants came from fifteen states. Selectees represent ten states.

C. Academic Disciplines Represented

The academic disciplines of the combined 192 SFRP associates are as follows:

Electrical Engineering	22.4%
Mechanical Engineering	14.0%
Physics: General, Nuclear & Plasma	12.2%
Chemistry & Chemical Engineering	11.2%
Mathematics & Statistics	8.1%
Psychology	7.0%
Computer Science	6.4%
Aerospace & Aeronautical Engineering	4.8%
Engineering Science	2.7%
Biology & Inorganic Chemistry	2.2%
Physics: Electro-Optics & Photonics	2.2%
Communication	1.6%
Industrial & Civil Engineering	1.6%
Physiology	1.1%
Polymer Science	1.1%
Education	0.5%
Pharmaceutics	0.5%
Veterinary Medicine	0.5%
TOTAL	100%

Table A-1. Total Participants

Number of Participants	
SFRP	192
GSRP	117
HSAP	133
TOTAL	442

Table A-2. Degrees Represented

Degrees Represented			
	SFRP	GSRP	TOTAL
Doctoral	189	0	189
Master's	3	47	50
Bachelor's	0	70	70
TOTAL	192	117	309

Table A-3. SFRP Academic Titles

Academic Titles	
Assistant Professor	74
Associate Professor	63
Professor	44
Instructor	5
Chairman	1
Visiting Professor	1
Visiting Assoc. Prof.	1
Research Associate	3
TOTAL	192

Table A-4. Source of Learning About SRP

SOURCE	SFRP		GSRP	
	Applicants	Selectees	Applicants	Selectees
Applied/participated in prior years	26%	37%	10%	13%
Colleague familiar with SRP	19%	17%	12%	12%
Brochure mailed to institution	32%	18%	19%	12%
Contact with Air Force laboratory	15%	24%	9%	12%
Faculty Advisor (GSRPs Only)	--	--	39%	43%
Other source	8%	4%	11%	8%
TOTAL	100%	100%	100%	100%

Table A-5. Ethnic Background of Applicants and Selectees

	SFRP		GSRP		HSAP	
	Applicants	Selectees	Applicants	Selectees	Applicants	Selectees
American Indian or Native Alaskan	0.2%	0%	1%	0%	0.4%	0%
Asian/Pacific Islander	30%	20%	6%	8%	7%	10%
Black	4%	1.5%	3%	3%	7%	2%
Hispanic	3%	1.9%	4%	4.5%	11%	8%
Caucasian	51%	63%	77%	77%	70%	75%
Preferred not to answer	12%	14%	9%	7%	4%	5%
TOTAL	100%	100%	100%	100%	99%	100%

Table A-6. Percentages of Selectees receiving their 1st, 2nd, or 3rd Choices of Directorate

	1st Choice	2nd Choice	3rd Choice	Other Than Their Choice
SFRP	70%	7%	3%	20%
GSRP	76%	2%	2%	20%

APPENDIX B – SRP EVALUATION RESPONSES

1. OVERVIEW

Evaluations were completed and returned to RDL by four groups at the completion of the SRP. The number of respondents in each group is shown below.

Table B-1. Total SRP Evaluations Received

Evaluation Group	Responses
SFRP & GSRPs	275
HSAPs	116
USAF Laboratory Focal Points	109
USAF Laboratory HSAP Mentors	54

All groups indicate near-unanimous enthusiasm for the SRP experience.

Typical comments from 1994 SRP associates are:

> "[The SRP was an] excellent opportunity to work in state-of-the-art facility with top-notch people."
>
> "[The SRP experience] enabled exposure to interesting scientific application problems; enhancement of knowledge and insight into 'real-world' problems."
>
> "[The SRP] was a great opportunity for resourceful and independent faculty [members] from small colleges to obtain research credentials."
>
> "The laboratory personnel I worked with are tremendous, both personally and scientifically. I cannot emphasize how wonderful they are."
>
> "The one-on-one relationship with my mentor and the hands on research experience improved [my] understanding of physics in addition to improving my library research skills. Very valuable for [both] college and career!"

Typical comments from laboratory focal points and mentors are:

> "This program [AFOSR - SFRP] has been a 'God Send' for us. Ties established with summer faculty have proven invaluable."
>
> "Program was excellent from our perspective. So much was accomplished that new options became viable "
>
> "This program managed to get around most of the red tape and 'BS' associated with most Air Force programs. Good Job!"
>
> "Great program for high school students to be introduced to the research environment. Highly educational for others [at laboratory]."
>
> "This is an excellent program to introduce students to technology and give them a feel for [science/engineering] career fields. I view any return benefit to the government to be 'icing on the cake' and have usually benefitted."

The summarized recommendations for program improvement from both associates and laboratory personnel are listed below (Note: basically the same as in previous years.)

A. Better preparation on the labs' part prior to associates' arrival (i.e., office space, computer assets, clearly defined scope of work).

B. Laboratory sponsor seminar presentations of work conducted by associates, and/or organized social functions for associates to collectively meet and share SRP experiences.

C. Laboratory focal points collectively suggest more AFOSR allocated associate positions, so that more people may share in the experience.

D. Associates collectively suggest higher stipends for SRP associates.

E. Both HSAP Air Force laboratory mentors and associates would like the summer tour extended from the current 8 weeks to either 10 or 11 weeks; the groups state it takes 4-6 weeks just to get high school students up-to-speed on what's going on at laboratory. (Note: this same arguement was used to raise the faculty and graduate student participation time a few years ago.)

2. 1994 USAF LABORATORY FOCAL POINT (LFP) EVALUATION RESPONSES

The summarized results listed below are from the 109 LFP evaluations received.

1. LFP evaluations received and associate preferences:

Table B-2. Air Force LFP Evaluation Responses (By Type)

		How Many Associates Would You Prefer To Get ? (% Response)											
		SFRP				GSRP (w/Univ Professor)				GSRP (w/o Univ Professor)			
Lab	Evals Recv'd	0	1	2	3+	0	1	2	3+	0	1	2	3+
AEDC	10	30	50	0	20	50	40	0	10	40	60	0	0
AL	44	34	50	6	9	54	34	12	0	56	31	12	0
FJSRL	3	33	33	33	0	67	33	0	0	33	67	0	0
PL	14	28	43	28	0	57	21	21	0	71	28	0	0
RL	3	33	67	0	0	67	0	33	0	100	0	0	0
WHMC	1	0	0	100	0	0	100	0	0	0	100	0	0
WL	46	15	61	24	0	56	30	13	0	76	17	6	0
Total	121	25%	43%	27%	4%	50%	37%	11%	1%	54%	43%	3%	0%

LFP Evaluation Summary. The summarized repsonses, by laboratory, are listed on the following page. LFPs were asked to rate the following questions on a scale from 1 (below average) to 5 (above average).

2. LFPs involved in SRP associate application evaluation process:
    a. Time available for evaluation of applications:
    b. Adequacy of applications for selection process:
3. Value of orientation trips:
4. Length of research tour:
5. a. Benefits of associate's work to laboratory:
    b. Benefits of associate's work to Air Force:
6. a. Enhancement of research qualifications for LFP and staff:
    b. Enhancement of research qualifications for SFRP associate:
    c. Enhancement of research qualifications for GSRP associate:
7. a. Enhancement of knowledge for LFP and staff:
    b. Enhancement of knowledge for SFRP associate:
    c. Enhancement of knowledge for GSRP associate:
8. Value of Air Force and university links:
9. Potential for future collaboration:
10. a. Your working relationship with SFRP:
    b. Your working relationship with GSRP:
11. Expenditure of your time worthwhile:

(Continued on next page)

12. Quality of program literature for associate:
13. a. Quality of RDL's communications with you:
    b. Quality of RDL's communications with associates:
14. Overall assessment of SRP:

Laboratory Focal Point Reponses to above questions

	AEDC	*AL*	*FJSRL*	*PL*	*RL*	*WHMC*	*WL*
# Evals Recv'd	10	32	3	14	3	1	46
Question #							
2	90 %	62 %	100 %	64 %	100 %	100 %	83 %
2a	**3.5**	**3.5**	4.7	4.4	4.0	4.0	**3.7**
2b	4.0	3.8	4.0	4.3	4.3	4.0	3.9
3	4.2	3.6	4.3	3.8	4.7	4.0	4.0
4	3.8	3.9	4.0	4.2	4.3	NO ENTRY	4.0
5a	4.1	4.4	4.7	4.9	4.3	3.0	4.6
5b	4.0	4.2	4.7	4.7	4.3	3.0	4.5
6a	**3.6**	4.1	**3.7**	4.5	4.3	**3.0**	4.1
6b	3.6	4.0	4.0	4.4	4.7	3.0	4.2
6c	3.3	4.2	4.0	4.5	4.5	3.0	4.2
7a	3.9	4.3	4.0	4.6	4.0	3.0	4.2
7b	4.1	4.3	4.3	4.6	4.7	3.0	4.3
7c	3.3	4.1	4.5	4.5	4.5	5.0	4.3
8	4.2	4.3	5.0	4.9	4.3	5.0	4.7
9	3.8	4.1	4.7	5.0	4.7	5.0	4.6
10a	4.6	4.5	5.0	4.9	4.7	5.0	4.7
10b	4.3	4.2	5.0	4.3	5.0	5.0	4.5
11	4.1	4.5	4.3	4.9	4.7	4.0	4.4
12	4.1	3.9	4.0	4.4	4.7	3.0	4.1
13a	**3.8**	**2.9**	4.0	4.0	4.7	**3.0**	**3.6**
13b	**3.8**	**2.9**	4.0	4.3	4.7	**3.0**	**3.8**
14	4.5	4.4	5.0	4.9	4.7	4.0	4.5

3. 1994 SFRP & GSRP EVALUATION RESPONSES

The summarized results listed below are from the 275 SFRP/GSRP evaluations received.

Associates were asked to rate the following questions on a scale from 1 (below average) to 5 (above average)

1.	The match between the laboratories research and your field:	4.6
2.	Your working relationship with your LFP:	4.8
3.	Enhancement of your academic qualifications:	4.4
4.	Enhancement of your research qualifications:	4.5
5.	Lab readiness for you: LFP, task, plan:	4.3
6.	Lab readiness for you: equipment, supplies, facilities:	4.1
7.	Lab resources:	4.3
8.	Lab research and administrative support:	4.5
9.	Adequacy of brochure and associate handbook:	4.3
10.	RDL communications with you:	4.3
11.	Overall payment procedures:	**3.8**
12.	Overall assessment of the SRP:	4.7
13.	a. Would you apply again?	Yes: 85%
	b. Will you continue this or related research?	Yes: 95%
14.	Was length of your tour satisfactory?	Yes: 86%
15.	Percentage of associates who engaged in:	
	a. Seminar presentation:	52%
	b. Technical meetings:	32%
	c. Social functions:	03%
	d. Other	01%

16. Percentage of associates who experienced difficulties in:

a. Finding housing:	12%
b. Check Cashing:	03%

17. Where did you stay during your SRP tour?

a. At Home:	20%
b. With Friend:	06%
c. On Local Economy:	47%
d. Base Quarters:	10%

THIS SECTION FACULTY ONLY:

18. Were graduate students working with you?	Yes:	23%
19. Would you bring graduate students next year?	Yes:	56%

20. Value of orientation visit:

Essential:	29%
Convenient:	20%
Not Worth Cost:	01%
Not Used:	34%

THIS SECTION GRADUATE STUDENTS ONLY:

21. Who did you work with:

University Professor:	18%
Laboratory Scientist:	54%

4. 1994 USAF LABORATORY HSAP MENTOR EVALUATION RESPONSES

The summarized results listed below are from the 54 mentor evaluations received.

1. Mentor apprentice preferences:

Table B-3. Air Force Mentor Responses

		How Many Apprentices Would You Prefer To Get ?			
		HSAP Apprentices Preferred			
Laboratory	*# Evals Recv'd*	*0*	1	2	3+
AEDC	6	0	100	0	0
AL	17	29	47	6	18
PL	9	22	78	0	0
RL	4	25	75	0	0
WL	18	22	55	17	6
Total	**54**	**20%**	**71%**	**5%**	**5%**

Mentors were asked to rate the following questions on a scale from 1 (below average) to 5 (above average)

2. Mentors involved in SRP apprentice application evaluation process:
   a. Time available for evaluation of applications:
   b. Adequacy of applications for selection process:
3. Laboratory's preparation for apprentice:
4. Mentor's preparation for apprentice:
5. Length of research tour:
6. Benefits of apprentice's work to U.S. Air force:
7. Enhancement of academic qualifications for apprentice:
8. Enhancement of research skills for apprentice:
9. Value of U.S. Air Force/high school links:
10. Mentor's working relationship with apprentice:
11. Expenditure of mentor's time worthwhile:
12. Quality of program literature for apprentice:
13. a. Quality of RDL's communications with mentors:
    b. Quality of RDL's communication with apprentices:
14. Overall assessment of SRP:

	AEDC	*AL*	*PL*	*RL*	*WL*
# Evals Recv'd	**6**	**17**	**9**	**4**	**18**
Question #					
2	100 %	76 %	56 %	75 %	61 %
2a	4.2	4.0	**3.1**	**3.7**	**3.5**
2b	4.0	4.5	4.0	4.0	3.8
3	4.3	**3.8**	**3.9**	**3.8**	**3.8**
4	4.5	**3.7**	**3.4**	4.2	**3.9**
5	**3.5**	4.1	**3.1**	**3.7**	**3.6**
6	4.3	3.9	4.0	4.0	4.2
7	4.0	4.4	4.3	4.2	3.9
8	4.7	4.4	4.4	4.2	4.0
9	4.7	4.2	3.7	4.5	4.0
10	4.7	4.5	4.4	4.5	4.2
11	4.8	4.3	4.0	4.5	4.1
12	4.2	4.1	4.1	4.8	3.4
13a	**3.5**	**3.9**	**3.7**	4.0	**3.1**
13b	4.0	4.1	3.4	4.0	3.5
14	4.3	4.5	3.8	4.5	4.1

5. 1994 HSAP EVALUATION RESPONSES

The summarized results listed below are from the 116 HSAP evaluations received.

HSAP apprentices were asked to rate the following questions on a scale from 1 (below average) to 5 (above average)

1. Match of lab research to you interest:		3.9
2. Apprentices working relationship with their mentor and other lab scientists:		4.6
3. Enhancement of your academic qualifications:		4.4
4. Enhancement of your research qualifications:		4.1
5. Lab readiness for you: mentor, task, work plan		**3.7**
6. Lab readiness for you: equipment supplies facilities		4.3
7. Lab resources: availability		4.3
8. Lab research and administrative support:		4.4
9. Adequacy of RDL's apprentice handbook and administrative materials:		4.0
10. Responsiveness of RDL's communications:		**3.5**
11. Overall payment procedures:		**3.3**
12. Overall assessment of SRP value to you:		4.5
13. Would you apply again next year?	Yes:	88%
14. Was length of SRP tour satisfactory?	Yes:	78%
15. Percentages of apprentices who engaged in:		
a. Seminar presentation:		48%
b. Technical meetings:		23%
c. Social functions:		18%

DESIGN OF SPECTROSCOPIC MATERIAL-CHARACTERIZATION EXPERIMENTS FOR THE DEVELOPMENT OF EYESAFE SOLID-STATE LASERS

Terri L. Alexander
Graduate Research Associate
Center for Research in Electro-Optics & Lasers (CREOL)

University of Central Florida
Orlando, Florida 32816

Final Report for:
AFOSR Summer Research Program
Sensor Technology Branch
Wright Laboratories Armament Directorate

Sponsored by:
Air Force Office of Scientific Research
Eglin Air Force Base, Florida 32542

August 1994

DESIGN OF SPECTROSCOPIC MATERIAL-CHARACTERIZATION EXPERIMENTS FOR THE DEVELOPMENT OF EYESAFE SOLID-STATE LASERS

Terri L. Alexander
Graduate Research Associate
Center for Research in Electro-Optics & Lasers (CREOL)
University of Central Florida

Abstract

The Laser Radar Research Facility in the Sensor Technology Branch of Wright Laboratories Armament Directorate, Eglin Air Force Base, is researching the development of eyesafe solid-state lasers for use in many military and commercial applications. A fundamental part of this research is the investigation of energy transfer between various rare earth elements (i.e. Thulium and Holmium) in laser hosts. This paper reports on basic laser principles and the early design stages of these experiments.

DESIGN OF SPECTROSCOPIC MATERIAL-CHARACTERIZATION EXPERIMENTS FOR THE DEVELOPMENT OF EYESAFE SOLID-STATE LASERS

Terri L. Alexander

I INTRODUCTION

The Laser Radar Research Facility in the Sensor Technology Branch of Wright Laboratories Armament Directorate, Eglin Air Force Base, is researching the development of eyesafe solid-state lasers for use in many military and commercial applications. Applications which dictate eye safety include such things as atmospheric sensing where the potential hazards for human exposure exist.

A great deal of effort is currently being devoted to the development of a practical laser capable of generating coherent 2μm radiation. Eloquently explained by Dinndorf:

> Lasers which operate in the mid-to-far infrared spectral region are of great interest to the technical community as the human eye is not transmissive to electromagnetic radiation of wavelengths longer than ~1.5μm. The eye is no more sensitive to these wavelengths than any other portion of the human body; therefore these lasers which operate in this spectral region are considered "eyesafe". The 2μm wavelength is desirable because there is a local minimum in the water vapor absorption in this region and atmospheric transmission of the light is possible. [1]

II THEORY

Principles of Laser Amplification

The laser, by definition, is a device that amplifies light by means of stimulated emission of radiation. In practice, a laser is generally used as a source or generator of radiation. The generator is constructed by adding a

feedback mechanism in the form of mirrors to the light amplifier. The basic physical problem is the creation of a material with a sufficient degree of negative absorption for some frequency, so that adequate amplification is available to overcome incidental losses and deliver useful power.

Absorption, Emission, and Energy Levels

Lasers amplify light by absorbing and emitting energy. The means of absorption can be either electronic on the atomic level or rotational/vibrational on the molecular level. The emitted energy is a high-intensity beam of laser light. To understand the mechanics of amplification in this study, we must look to the transitions that occur between energy levels of the atom (atomic level).

Atoms consist of a positive charged nucleus surrounded by a cloud of negatively charged electrons orbiting the nucleus (Figure 1). Each electron travels in its own unique orbit at a diameter corresponding to the excitation state (energy level) of the electron. The energy that is absorbed by an atom goes to the electrons, either increasing the speed of the electrons travel or enlarging the diameter of the electrons' orbit. When energy is subsequently emitted by an atom, the electron returns to either a slower speed or a smaller diameter orbit. We will focus on the energy transitions which occur with increasing and decreasing electron orbits.

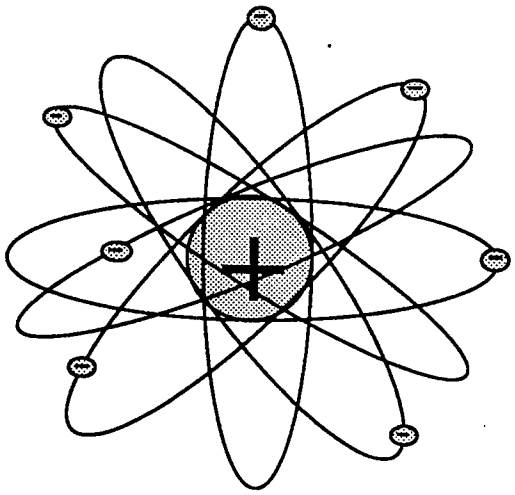


Figure 1. Positive nucleus surrounded by cloud of negatively charged electrons.

An interesting property of atoms is that only energy of specific amounts can be absorbed and emitted. The electron orbits can only increase and decrease to specific levels (diameters). In other words, the energy potential for any given atom is *quantified*. For example, an atom may absorb energy at 1.5 electron-volts but it will not absorb 1.45 or 1.55 electron-volts. After the energy is absorbed, the energy is also lost only in certain amounts because the electrons may only return to allowed orbits.

The energy levels for a specific atom can be shown with an energy level schematic (Figure 2). Here, the allowed energy levels for the atom are represented by different levels on the diagram. An atom in the ground state has energy level E^0 while an atom in the first excited state has energy level E^1, etc.

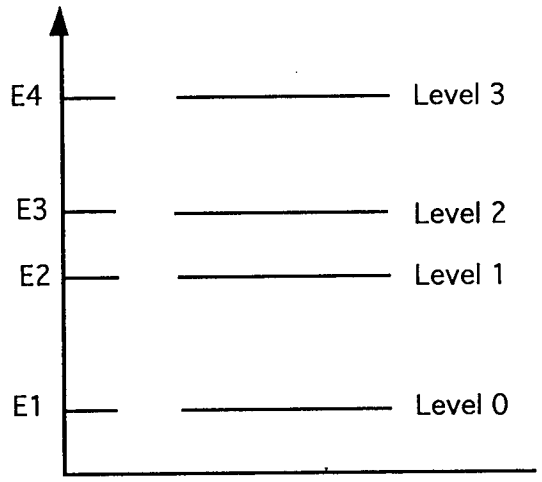


Figure 2. Energy level schematic with multiple energy levels.

As an atom absorbs energy, the absorbed energy must be equal to the difference between the allowed energy levels. An atom may absorb energy equal to the difference between E^0 and E^1 and move to the first excited state (level 1) but it cannot absorb energy less than $E^0 - E^1$. It can also absorb energy equal to $E^0 - E^2$ and move to the second excited state (level 2). However, it cannot absorb energy equal to $E^2 - E^1$. Correspondingly, when an atom loses energy, it must also lose energy in amounts equal to the difference between levels.

Photon Absorption

One method in which an atom may gain energy is to absorb a photon of light. To be absorbed, the photon must contain energy equal to the difference between two of the allowed energy levels of the atom. Because a photon's energy determines its wavelength, the atom will only absorb light of specific wavelengths which are equal to the allowed energy levels.

Spontaneous Emission

There are two ways in which an atom can subsequently lose energy: by transfer to another atom or by emitting a photon of light. When emitted as light, the emitted photons wavelength will correspond to the energy lost by the atom as it moves from a high energy level back to a lower level. The light emitted by an atom must correlate with the allowable energy levels for the atom.

Normally an atom will absorb energy, raising it to a higher energy level, and will remain in that energy state for some period of time (nanoseconds or milliseconds). This period is the *'spontaneous'* or *'upper-level'* lifetime of the atom. Eventually the atom will spontaneously emit a photon of light in a random direction and return to the ground state. This is *spontaneous emission* (Figure 3).

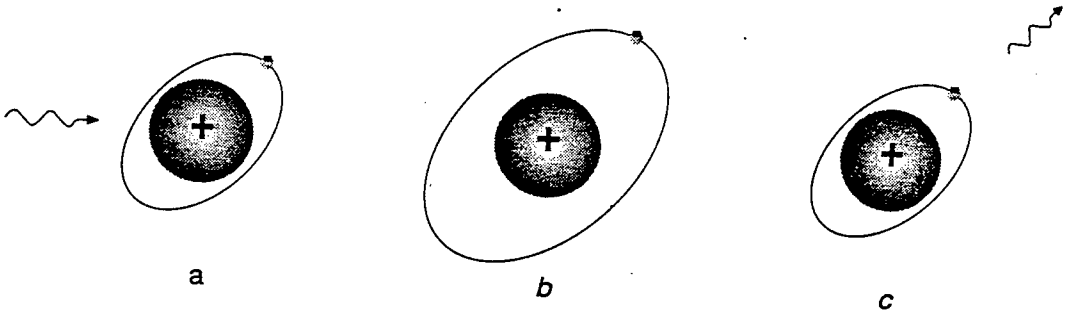


Figure 3. (a) An atom absorbs a photon, (b) remains in an energized state for a period of time, and (c) decays emitting a photon of light.

Stimulated Emission

Another mechanism by which an atom can emit light is by *stimulated emission* (Figure 4). During the spontaneous lifetime while the atom is in an upper level state and before spontaneous emission can occur, the atom can be stimulated to release its photon of light by interacting with another passing photon. The passing photons' wavelength must be equal to the difference of the electron's upper and lower energy levels to stimulate the atom to emit a photon. Because the emitted photon's wavelength is determined by the difference between the same energy levels, the passing and emitted photons will be the same wavelength. In addition, both photons will travel in the original direction of the passing photon and will be in phase. With equal properties of wavelength, direction, and phase, the photons constitute *coherent light.* This stimulated emission of coherent light is crucial to the operation of a laser.

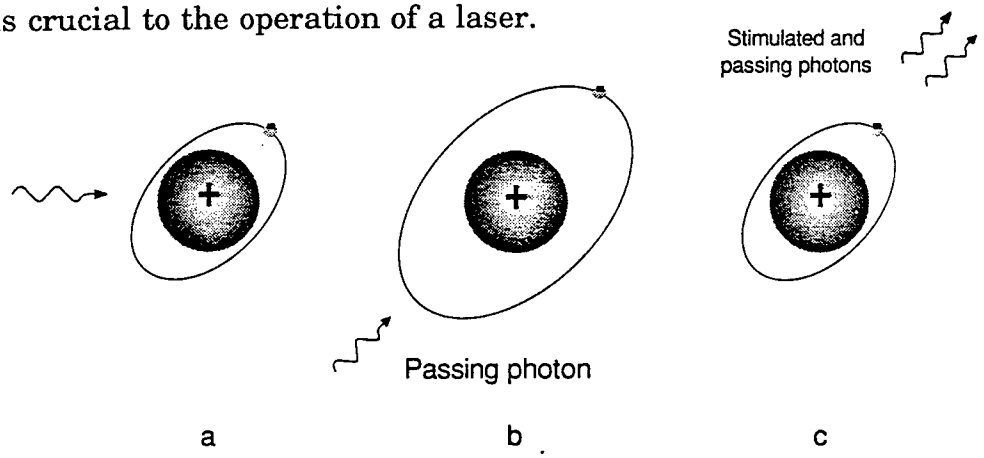


Figure 4. (a) An atom absorbs a photon, (b) is stimulated by a second passing photon, and (c) emits its photon.

Population Inversion

We have considered the energy transitions of a single atom. Now we must address the energy distribution of a large population of atoms. In any substantial population of atoms, the majority of the atoms will be in the ground state. The remaining atoms will be distributed among the higher energy levels in decreasing quantities. The population at each level is dictated by *Boltzmann's law*, one of the fundamental laws of thermal

dynamics. In Figure 5, each energy level for a specified atom is represented on the vertical axis of the diagram while the population for each level is represented by the length of the corresponding horizontal lines. As described by Boltzmann's law, each ascending level will have fewer atoms than the preceding level. The population of atoms is in a *thermal equilibrium distribution*. Applying heat to the population to increase the energy will subsequently increase the number of atoms above the ground state but will not change the overall distribution (i.e. a higher level will not contain more atoms than a lower level).

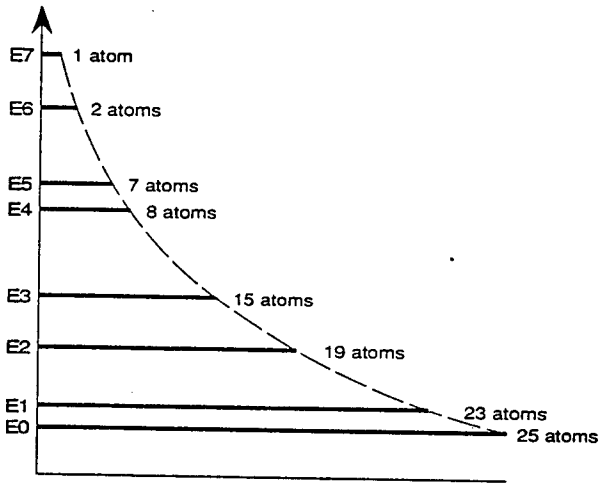


Figure 5. Energy distribution as defined by Boltzmann's law.

It is possible to force an energy distribution out of equilibrium (Figure 6). If some of the atoms in the ground state (E0) are forced to an upper level (E1) before any of the existing upper level atoms can spontaneously decay back down, a *population inversion* is created in which there are more atoms in the upper level state than the lower. The population inversion is a non equilibrium distribution and will not last very long. Ground state atoms must be continuously forced into the upper level to maintain the inversion. A sustained population inversion is crucial to maintaining stimulated emission.

Light Amplification

How does the laser amplify light? At the heart of all lasers is the *lasing medium,* which contains atoms that can be stimulated to spontaneously emit light. The medium may be a gas mixture ($C0_2$, helium-neon, etc.), a

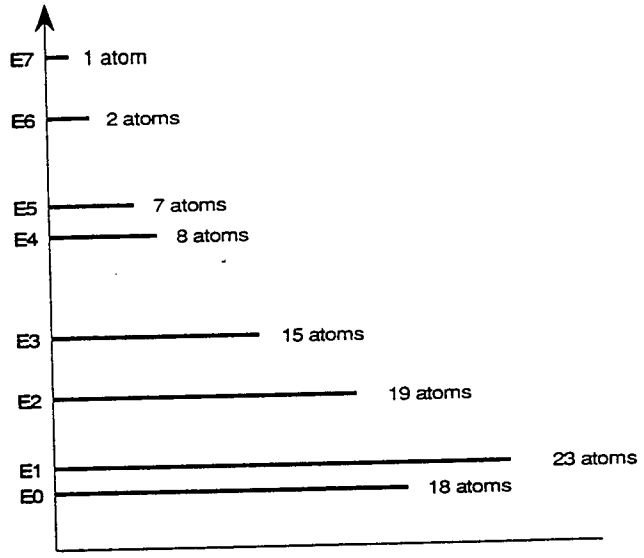


Figure 6. Population inversion between levels E0 and E1.

semiconductor substrate (laser diodes), a liquid (dye lasers), or a solid crystal (Nd:YAG, Nd:YLF, Ruby, etc.). The laser will also have an energy source to excite (pump) the atoms of the media. The pump source will usually be either an electric discharge, light from a hi-intensity light source, or another laser.

As the pump source excites the lasing media, sufficient energy is applied to create a population inversion and initiate spontaneous emission. The spontaneous light emitted by the media travel in random directions (Figure 7).

Optical feedback is created by placing a mirror at each end of the media to reflect those photons traveling along the longitudinal axis back into the media. The reflected photons cause other upper level atoms to emit their

photons by stimulated emission. As this process continues, on photon becomes two, two become four, four become sixteen, etc., thus - light amplification. All of the photons will be the same wavelength, will be in phase and will travel the same direction along the path of reflection. The population inversion assures that there is always a sufficient quantity of atoms in the upper level state to sustain the lasing process.

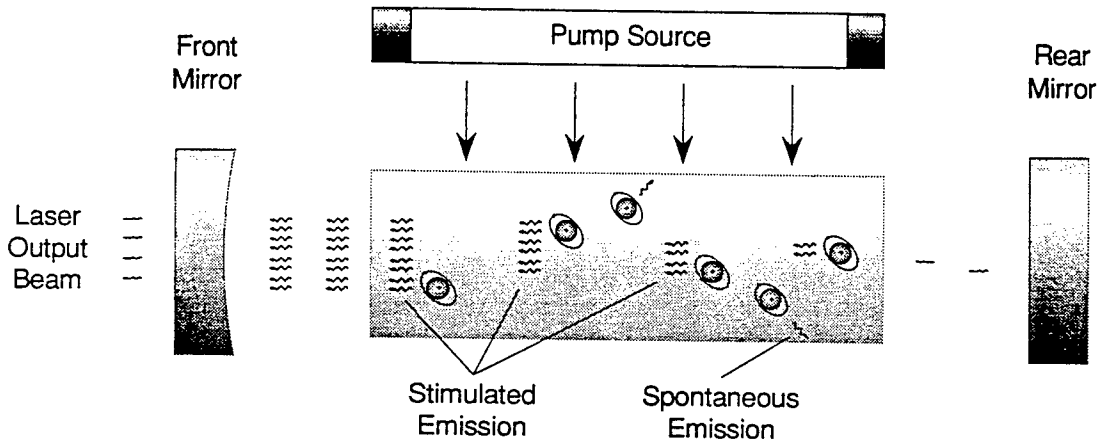


Figure 7. Spontaneous emission, stimulated emission, and the optical feedback.

One of the mirrors of the optical feedback is coated to 'leak' a small percentage (typically 10% or less) of the amplified light reflecting between the mirrors. This leakage is the laser output beam. [2-4]

III EXPERIMENTAL DESIGN

This section gives a complete description of the instrumentation and the experimental configuration in development at the Laser Radar Research Facility for spectroscopic fluorescence measurements.

Figure 8 shows a schematic diagram of the optical set-up. A Schwartz Electro-Optics Ti:Sapphire pulsed laser is used as the pumping source. The Titan-P laser generates a specified energy of 100 mJ at 800 nm in a nominal 10 nsec pulse and has a tuning range from 680 nm to 940 nm.

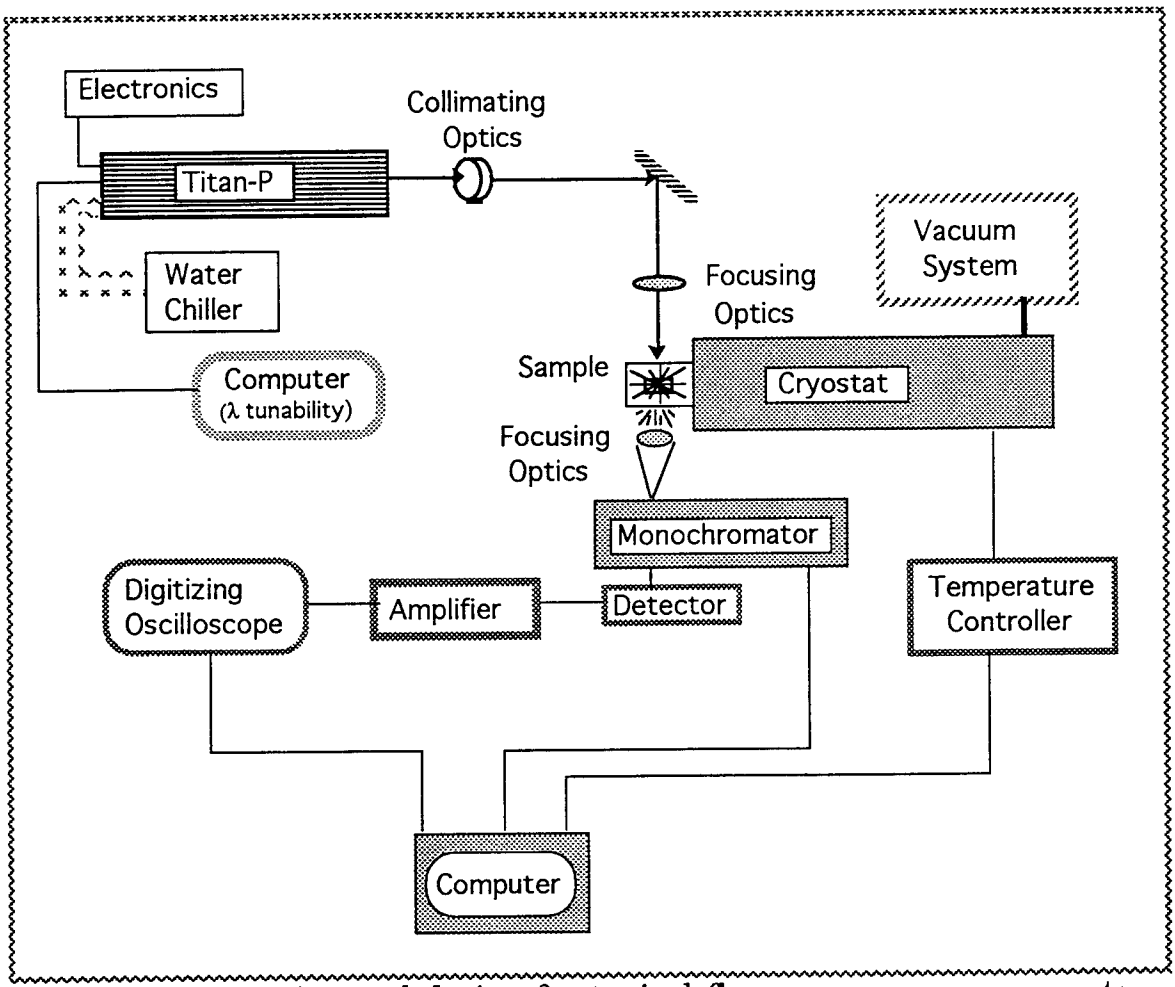


Figure 8. Experimental design for typical fluorescence measurements.

The sample temperature is controlled by a Janis Research SuperVariTemp (SVT) System. The Janis SVT System is a research cryostat that can be used to perform a wide variety of experiments in the temperature range form 1.5 K to 300 K. A diagram of the SVT system is shown in Figure 9. The Janis cryostat uses flowing helium gas, obtained by vaporizing LHe, to cool or warm the sample within the operating temperature range. LHe exits a main reservoir through a needle valve, and enters a vaporizer at the bottom of the sample tube. The vaporizer temperature is usually regulated by an automatic temperature controller, using a control heater and optional thermometer installed on the vaporizer. LHe enters the vaporizer, evaporates, warms up to the desired

temperature, and enters the sample tube. The helium vapor flows past the sample mount, warms or cools the sample, then exits through a vent port at the top of the cryostat. The actual temperature of the sample at any time can be monitored using a thermometer located on the sample mount. [5]

The sample fluorescence can be focused into a Monochromator for narrow band filtering. A Digitizing Oscilloscope is used for data collection.

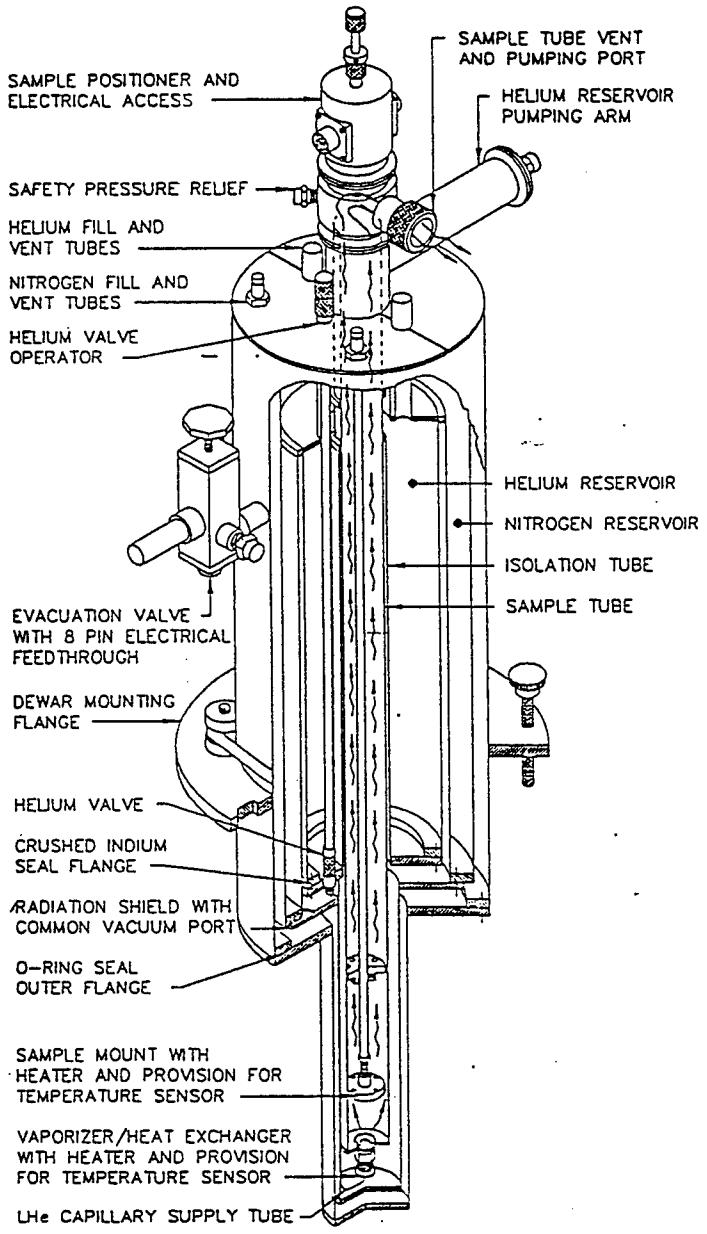


Figure 9. Typical SuperVariTemp System.

Figure 10 shows the vacuum system design support the Janis cryostat.

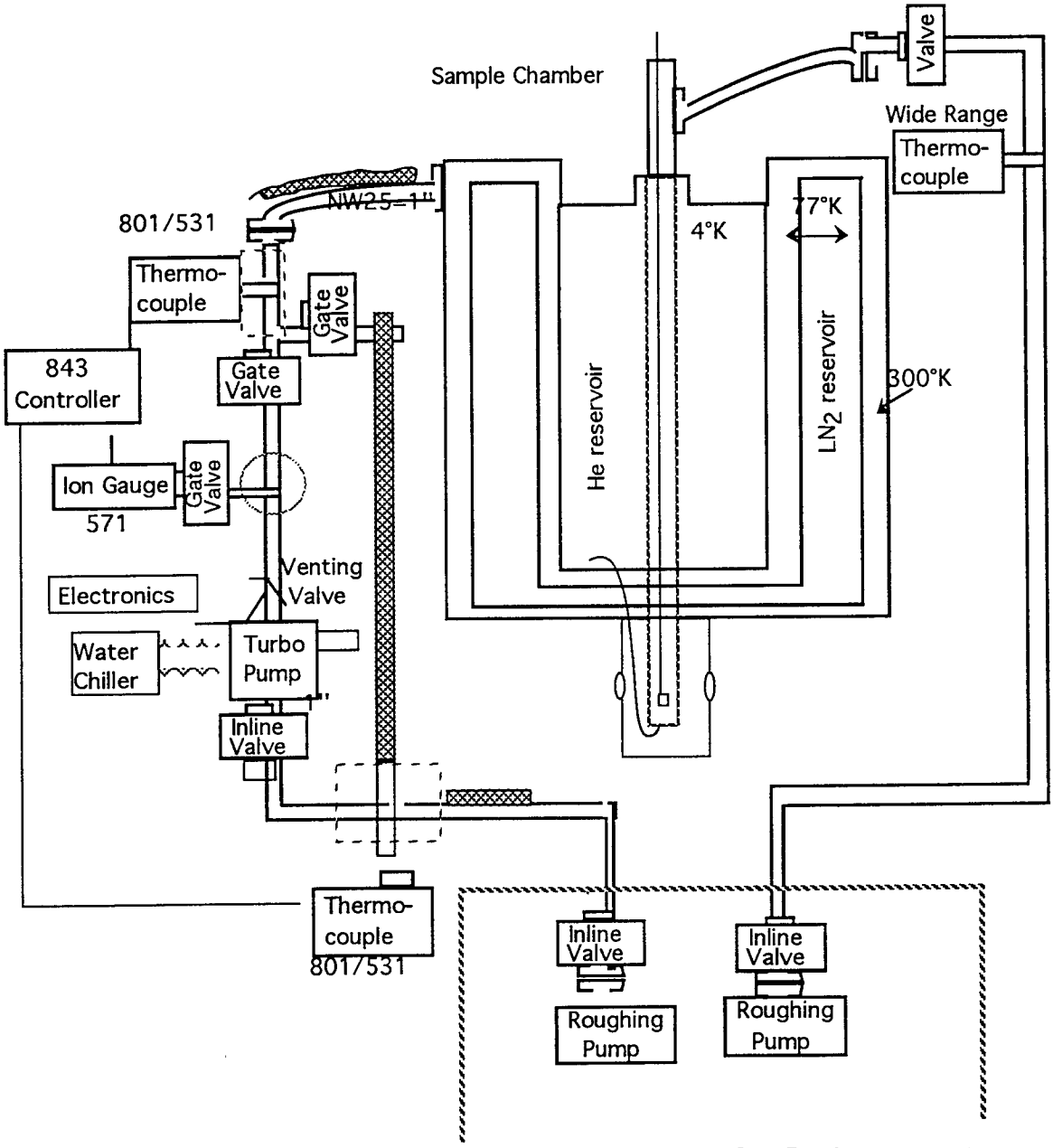


Figure 10. Vacuum system design to support the Janis cryostat.

IV ACKNOWLEDGMENTS

I would like to express my sincerest thanks and appreciation to the Laser Radar Research Facility for a very educational experience and a very enjoyable summer. Especially thanks to Lt. Ken Dinndorf for his leadership guidance and direction, and to Dave Hayden and Capt. Jody Madeville for their knowledge, experience and support in the lab.

V REFERENCES

[1] K. M. Dinndorf, *Energy Transfer Between Thulium and Holmium in Laser Hosts*, Doctoral Dissertation, Massachusetts Institute of Technology, September 1993.

[2] R. L. Stevenson, *Industrial Strength Laser Marking: Turning Photons into Dollars*, Control Laser Document, 1992.

[3] O. Svelto, D. C. Hanna, *Principles of Lasers*, Plennum Press, New York, 1989.

[4] F. L. Pedrotti, S. J., L. S. Pedrotti, *Introduction to Optics*, Prentice-Hall, Inc., New Jersey, 1987.

[5] Janis Research SuperVariTemp System User's Manual.

THERMAL STABILITY APPARATUS DESIGN AND ERROR ANALYSIS FOR MEASUREMENTS OF ELECTRO-OPTIC POLED POLYMERS

Joseph L. Binford, III
Graduate Student
Electro-Optics Program

Center for Electro-Optics
University of Dayton
300 College Park
Dayton, OH 45469-0245

Final Report for:
Graduate Student Research Program
Wright Laboratory

Sponsored by:
Air Force Office of Scientific Research
Bolling Air Force Base
Washington, D.C.

and

Wright Laboratory

August 1994

THERMAL STABILITY APPARATUS DESIGN AND ERROR ANALYSIS FOR MEASUREMENTS OF ELECTRO-OPTIC POLED POLYMERS

Joseph L. Binford, III
Graduate Student
Electro-Optics Program
University of Dayton

Abstract

We designed and built a temperature-controlled environment for studying the thermal stability of poled electro-optic polymers. Our temperature-controlled chamber allows easy optical access to the sample and will maintain a constant temperature (±5 °C) up to 300 °C. In addition to monitoring the decay of the nonlinearity at various temperatures in this apparatus, we may also use it to pole polymers that must be aligned and cured at the same time. We give preliminary results showing the decay of the electro-optic signal at 150°C for a Dow Corp. poled-polymer sample. We also completed an error analysis that shows how small deviations from the ideal experimental setup can alter the measured electro-optic signal and thus the coefficient r_{33}. The standard method for studying the electro-optic coefficients of poled-polymer samples is the reflection technique originally discussed by Teng and Man.[1] We studied errors in the determination of r_{33} that result from deviations from their ideal setup. We found that uncertainties in the incident angle contribute the greatest error (−3.87% error per degree of deviation). This analysis will help improve the accuracy in measuring the electro-optic coefficients of poled-polymer films.

THERMAL STABILITY APPARATUS DESIGN AND ERROR ANALYSIS FOR MEASUREMENTS OF ELECTRO-OPTIC POLED POLYMERS

Joseph L. Binford, III

Introduction

Poled-polymers are quite promising materials for applications requiring high-speed electro-optic switching or modulation. Unfortunately, nature seems to impose a trade-off between the strength and the thermal stability of the nonlinearity in poled polymer systems. Strict Air Force requirements for thermal stability of electro-optic materials imply that researchers must strive to accurately characterize the lifetime of the response of these materials at various temperatures. For this reason, we designed a temperature-controlled environment for determining thermal stability. We used this apparatus for an initial test of the electro-optic signal decay at elevated temperatures and found that our setup is adequate for measuring poled-polymer thermal stability. We also performed a theoretical study of how slight imperfections in the experimental setup of Teng and Man[1] will affect the measured electro-optic coefficient. This analysis determines experimental tolerances for accurate characterizations of the electro-optic material.

Discussion of Problem

The design of a temperature-controlled chamber was constrained by the following considerations: (1) the chamber must maintain a constant temperature, deviating by no more than say ±5-10 °C; (2) the chamber must reach temperatures of up to 300 °C; (3) the sample holder must be electrically insulated (in order to safely apply a strong electric field to the polymer); (4) the chamber base must be thermally insulated (to prevent heating the supporting table); (5) the chamber must allow a laser beam to pass through the chamber hull and leave again after either reflection or transmission by the sample; and (6) the chamber must allow electrical feedthrough to connect components within the chamber from the outside (e.g., heater wires, thermocouple wire, applied voltage wires, etc.). We wanted to keep the design simple and the cost of the materials within reason. Although modifications to this setup are still being made at the time of this report, an apparatus was constructed which satisfies these criteria. Figure 1 shows the temperature controlled environment in detail.

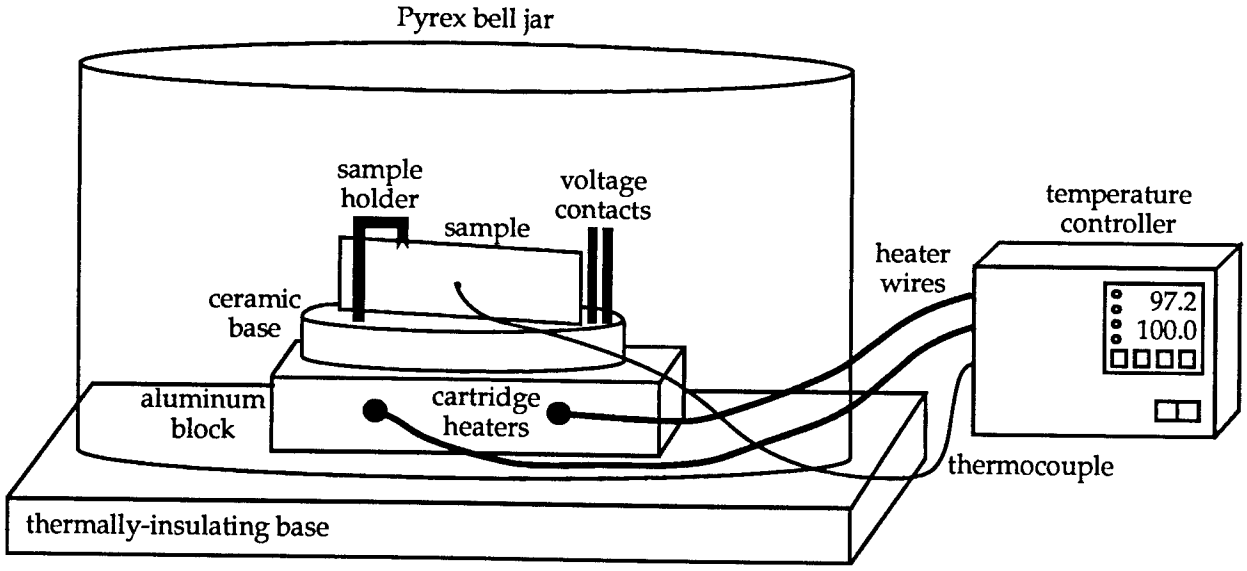


Figure 1. Temperature-controlled environment design. Within this apparatus we can monitor the decay of the electro-optic signal at a specific temperature or we can measure the strength of the nonlinearity as the polymer sample is poled.

This apparatus will be used in various setups for determining the electro-optic coefficient of the poled-polymer samples. One well-known and widely-used technique[1] examines the polarization state of a beam reflected at 45° from a polymer film subjected to an applied electric field. The electro-optic effect induces a change in the polarization state of the reflected beam and this change determines the sample's electro-optic coefficient. In our error analysis of experimental imperfections, we kept things simple so that we could find equations which show the relationship between the errors in the electro-optic coefficient and deviations in the setup. Further study with computer analysis could be readily performed for more accurate estimates. The experimental setup using the reflection technique, shown in Fig. 2, consists of a linear polarizer at -45°, an electro-optic poled-polymer sample whose normal is angled at +45° relative to an incoming polarized beam, a Babinet-Soleil retarder normal to the reflected beam (adjusted such that circularly-polarized light is produced), and an analyzer at +45°. The sample itself consists of a glass substrate coated with a patterned indium tin oxide (ITO - an electrically-conducting transparent electrode) layer. The polymer/chromophore mixture is spin coated on top of the ITO and cured. After curing a gold stripe is placed on top of the polymer to serve both as an electrode and a mirror. The alignment of the chromophore via contact poling gives a ∞mm point group structure whose crystalline axis is normal to the plate surface. The ITO and gold serve as the electrical contacts during both poling and electro-optic characterization. Ideally, in the absence of an applied voltage, the observed intensity beyond the analyzer will be 1/2 of the incident intensity. Small modulations in this bias intensity due to the applied electric field determine the electro-optic coefficient of the sample. However, problems with components in the system give errors in the measured electro-optic coefficient. Seven

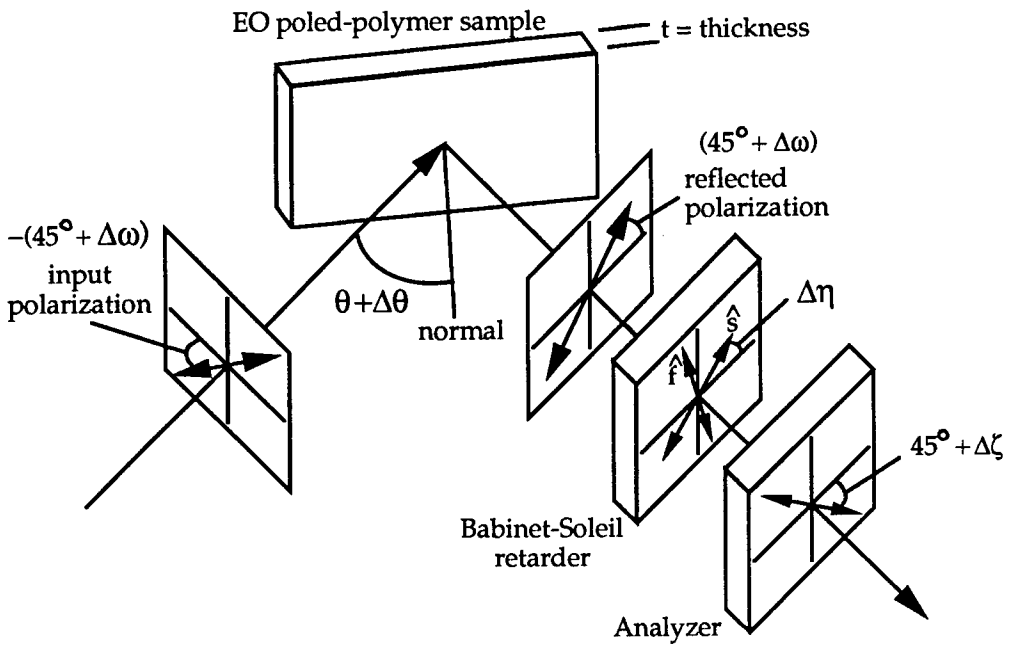


Figure 2. Experimental arrangement for measuring the electro-optic coefficient of a poled-polymer sample. The incident light beam travels through the polymer layer and reflects off of the gold electrode. After reflection, the Babinet-Soleil changes the beam polarization to circular (in the absence of an electro-optic effect). The application of an electric field produces small changes in the polarization and therefore the intensity of the light passing through the analyzer is modulated

errors in the system were considered: (1) thickness variation of the sample due to the piezoelectric and electrostrictive effects (both caused by the applied electric field); (2) input polarization angle deviation; (3) incidence angle deviation (or sample tilt in the horizontal plane); (4) sample plate tilt from the vertical; (5) the Babinet-Soleil rotation angle deviation; (6) the Babinet-Soleil phase shift deviation; and (7) analyzer polarization angle deviation. The following assumptions were also made: (1) All errors are considered individually in relation to the electro-optic effect; (2) all seven errors are small; (3) the ordinary and extraordinary rays refract through the electro-optic polymer at approximately the same angles; (4) the ordinary and extraordinary rays experience nearly the same refractive index; and (5) that $r_{13} = 1/3\ r_{33}$ (which implies that only one electro-optic coefficient is needed - r_{42} doesn't enter the problem because there is no applied field along the x or y directions). In addition, the following numerical values were assumed: (1) all deviation angles are at most 5°; (2) the wavelength is 850 nm; (3) the refractive index is 1.665; (4) the birefringence is 0.1; (5) the polymer thickness is one micron; (6) the polymer thickness variation is one angstrom; (7) the Babinet-Soleil phase shift can increase to five degrees; and (8) the relative intensity modulation is 2.5×10^{-4}. All of these considerations were taken into account in deriving the electro-optic coefficient error due to each of the seven deviations from the ideal experimental setup.

Methodology

The design of a temperature-controlled chamber was based mainly on the availability of materials. We first considered a standard oven with a glass door along with two mirrors to reflect the beam back out through the door. The advantages in this design were that the oven was already constructed (complete with a temperature controller) and that it was thermally insulated. Disadvantages included the questionable reliability of the controller (which hadn't been tested) and the difficulty of transporting the apparatus from place to place. Next, a box-like chamber was considered, having Pyrex glass covered ends and using cartridge heaters. The geometry seemed awkward, however, since easy access to the sample plate was desirable. Finally, we found a 7.25" dia., 3.75" high Pyrex bell jar, and decided that, upon finding a suitable thermally-insulating base material, a simple yet effective chamber could be built with symmetrical geometry and ease of access. A large 12" x 12" x 0.5" piece of insulating ceramic material serves as the base (withstanding up to 250° C), and a 0.5" thick thermally-conducting ceramic material holds the sample. The sample is heated via two 1/4" dia., 3" long cartridge heaters, rated at 120 V and 300 W each, inserted within a 3.5" x 2 5/8" x 0.5" aluminum base. The temperature controller consists of an Omega proportional controller (model CN76000) unit that pulses the voltage applied to the a solid-state relay, which in turn switches the line voltage applied to the cartridge heaters. An illustration of this experimental apparatus is shown in Fig. 1.

The derivation of the error in r_{33} due to each of the seven deviations in the experimental setup was determined after finding r_{33} for the ideal case, as derived in the Appendix. The result is shown below:

$$r_{33} = -\frac{3\lambda\sqrt{n^2-\sin^2\theta}}{4\pi n^2 \sin^2\theta\, V_{applied}}\,\frac{\Delta I}{I_{bias}} \qquad (1)$$

where λ is the wavelength, n is the refractive index, θ is the incident angle, $V_{applied}$ is the applied voltage, ΔI is the intensity modulation, and I_{bias} is the bias intensity. Notice that this result is different than the original expression in the paper of Teng and Man.[1] Their derivation omitted the pathlength difference external to the poled-polymer sample itself. See Fig. 3 for a clear depiction of the paths traveled by the ordinary and extraordinary rays.

For each of the experimental deviations discussed above, we derived the effect of that deviation on the measured parameter, r_{33}. To find the % change in r_{33} ($\%\delta r_{33}$), we track the progress of the polarization state of the light beam as it propagates through each element of the system by representing the polarization with its Jones vector.[2] After finding the polarization of the light following the Babinet-Soleil retarder, the relative intensity of the light after the analyzer determines the change in r_{33}.

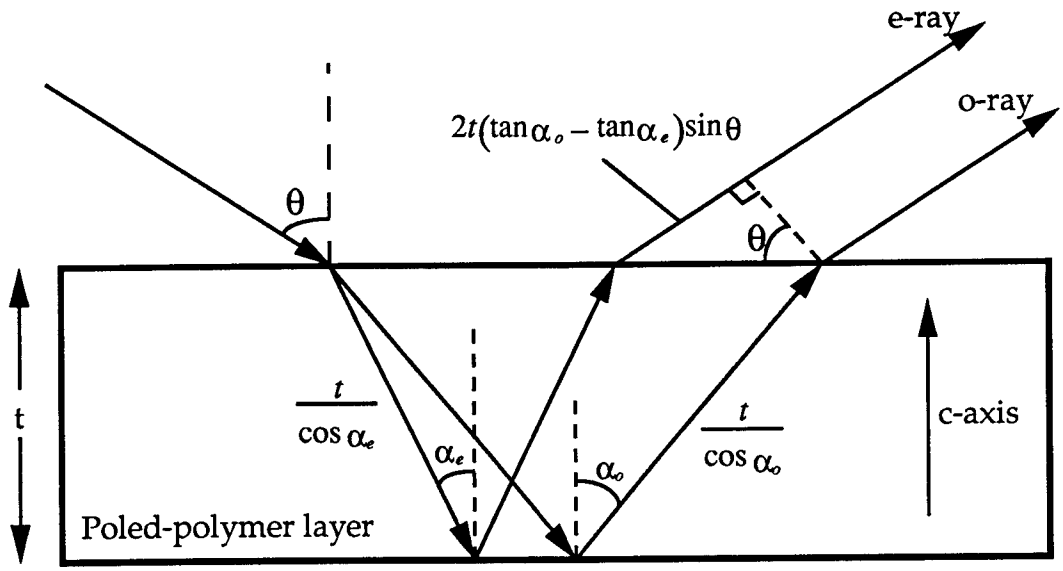


Figure 3. Ray paths for the extraordinary and ordinary components of the polarization. The total pathlength difference between the two rays includes a portion that lies external to the polymer layer itself.

Results:

The current design for the temperature-controlled chamber seemed quite suitable for future determination of electro-optic material stability. It is simple in design, yet fulfills the requirements of the experiment. The controller unit has various capabilities in "learning" how to maintain constant temperatures within certain tolerances. Tests show that the tolerance is about five degrees C, but that large, fast increases in the desired setpoint lead to significant overshoot of the intended temperature (as much as 20°C). This is due to the large thermal mass of our system. Future designs will eliminate much of this thermal inertia by thinning the sample-holder ceramic baseplate.

We used our temperature-controlled chamber for an initial test of the thermal stability of a sample that was loaned by Dow Chemical Corp. This poled-polymer sample has an initial electro-optic coefficient of r_{33} = 7 pm/V and a glass-transition temperature of T_g = 173 °C. Dow refers to this particular system as TP31D and this sample was poled at 100 V/μm and the polymer layer is 2.11 μm. We monitored the electro-optic signal (using the technique of Teng & Man[1]) with the sample mounted inside the "bell jar" apparatus shown in Fig. 1. We slowly increased the temperature of the sample until the electro-optic signal started to fall. When the temperature reached ≈150°C we noticed a rapid decay in the signal. We monitored the signal for 30 minutes at this temperature and found that the exponential decay rate was 11.2 minutes. This data is shown in Fig. 4. In the future this experimental setup may be used to monitor the long-term decay of any promising poled-polymer system.

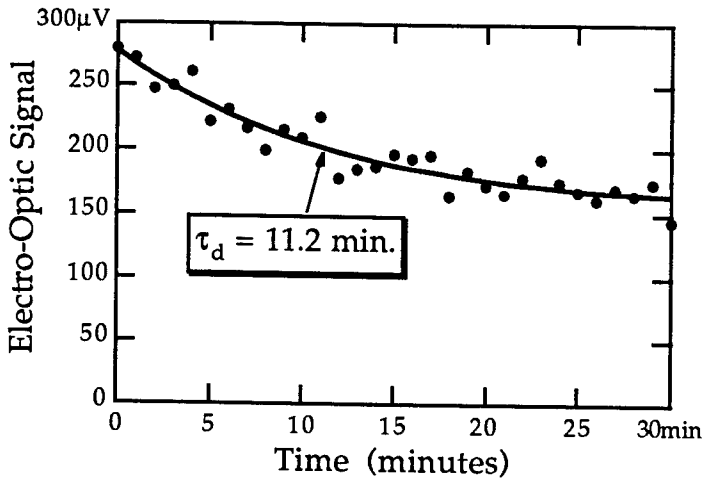


Figure 4. Temporal decay of the electro-optic signal for a Dow TP31D sample with a glass transition temperature of 173°C. The sample is held at ≈150°C. and the decay time at this temperature is ≈11 minutes.

The error analysis of r_{33} for the seven experimental deviations was derived using Jones calculus,[2] as mentioned previously. The percent change in r_{33} ($\%\delta r_{33}$) for these cases are shown below:

Case 1 Polymer thickness deviation Δt:

$$\%\delta r_{33} = \frac{400\pi\,\Delta t\,\delta n \sin^2\theta}{\lambda\, n\sqrt{n^2-\sin^2\theta}}\,\frac{I_{bias}}{\Delta I} \tag{2}$$

where $\delta n = n_e - n_o$ is the birefringence.

Case 2 Input polarization angle deviation $\Delta\omega$:

$$\%\delta r_{33} = \frac{200\,\Delta\omega^2}{1-\Delta\omega^2} \tag{3}$$

Case 3 Incidence angle deviation $\Delta\theta$ (sample rotation in the horizontal plane):

$$\%\delta r_{33} = \frac{100\left(2n^2-\sin^2\theta\right)\cos\theta}{\left(n^2-\sin^2\theta\right)\sin\theta}\,\Delta\theta \tag{4}$$

Case 4 Sample tilt from the vertical $\Delta\beta$:

$$\%\delta r_{33} = 200\left(\frac{1}{\sin^2\theta} - \frac{4\pi\, t\,\delta n}{\lambda\, n\sqrt{n^2-\sin^2\theta}}\right)\Delta\beta^2 \tag{5}$$

Case 5 Babinet-Soleil retarder orientation angle deviation $\Delta\eta$:

$$\%\delta r_{33} = 200\left(\frac{4\pi\, t\, \delta n \sin^2\theta}{\lambda\, n\sqrt{n^2-\sin^2\theta}} - 1\right)\Delta\eta^2 \tag{6}$$

Case 6 Babinet-Soleil retarder phase deviation $\Delta\Gamma$:

$$\%\delta r_{33} = 100\,\Delta\Gamma \tag{7}$$

Case 7 Analyzer polarization angle deviation $\Delta\zeta$:

$$\%\delta r_{33} = \frac{200\,\Delta\zeta^2}{1-\Delta\zeta^2} \tag{8}$$

Graphs for these seven cases are shown in Fig. 5, using the numerical values listed previously. As seen from the graphs, the incidence angle deviation gives the largest error in r_{33}, with –3.87 % error per degree of deviation. These results show that accuracy in the incidence angle is very critical, whereas the accuracy of the input polarization angle is not. Also, it is apparent that three of the errors are linear with respect to the change in r_{33} (thickness deviation, incidence angle deviation, and Babinet-Soleil phase deviation) whereas the other four are quadratic. This indicates that these other four errors are less critical.

Conclusion:

The design of our temperature-controlled chamber adequately satisfies the requirements of the electro-optic thermal stability experiment. The design was simple and material costs were minimal. The apparatus is easily operated and maintains a constant temperature to within ±5-10 °C, all the way up to 300 °C.

The error analysis of r_{33} from deviations in the experimental setup has shown that, although all deviations have some effect on r_{33}, the incidence angle deviation has the largest effect (–3.87 % error per degree of deviation), followed by the thickness deviation and the Babinet-Soleil phase deviation. All three of these deviations have a linear effect on the error. The other four deviations are quadratic in relation to the error and are thus less critical.

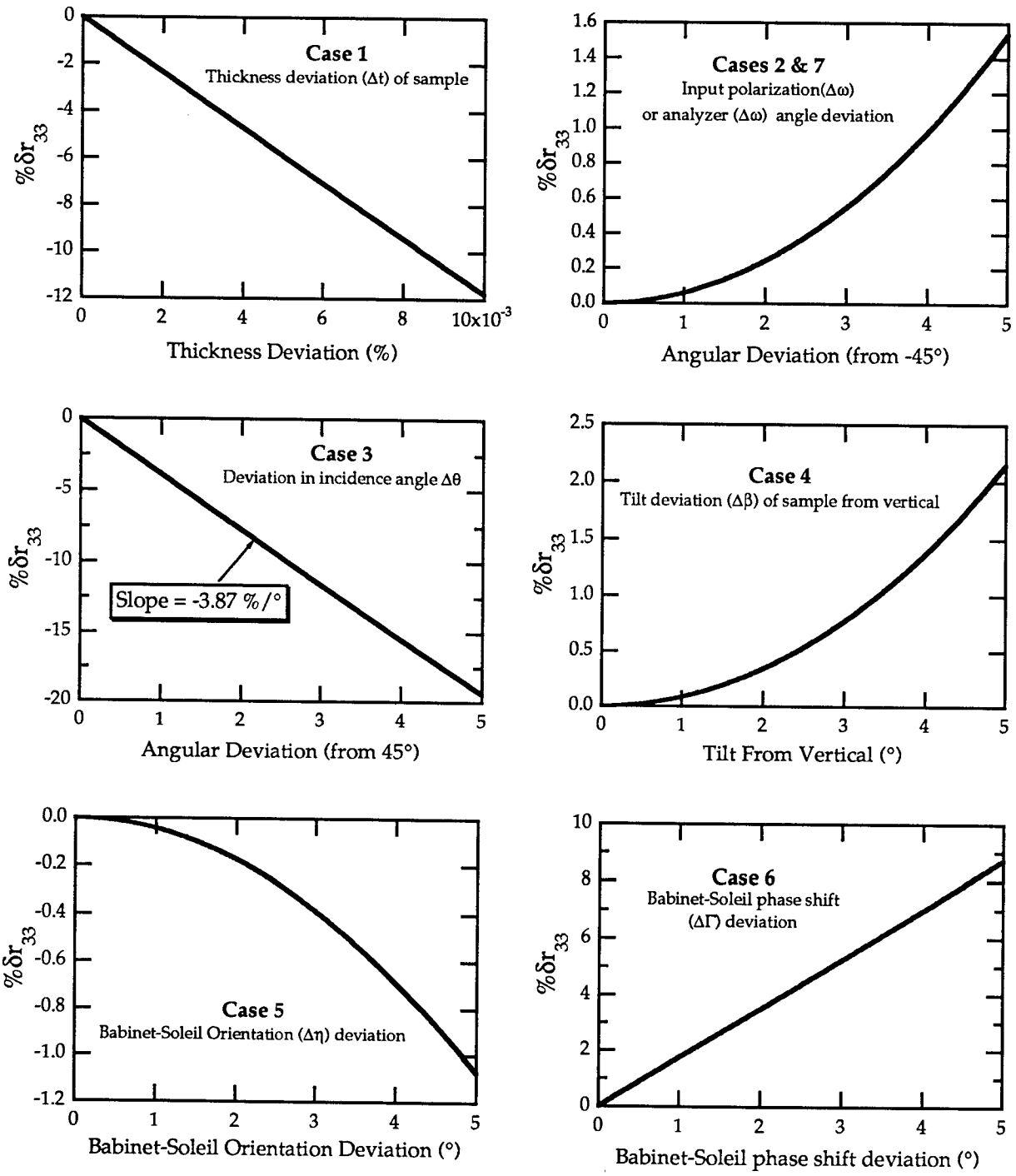


Figure 5. The effect of seven experimental errors on the measured electro-optic coefficient r_{33}. The individual cases are described in the text and case 2 & 7 give identical results. Here we plot the percent change in r_{33} ($\%\delta r_{33}$).

Acknowledgments:

We thank Paul von Richter for assisting in the design of the temperature-controlled environment and for diligently machining the requisite parts.

References:

1. Teng, C. C. and H. I. Man, "Simple Reflection Technique for Measuring the Electro-Optic Coefficient of Poled Polymers," Appl. Phys. Lett. **56** (18), 1734-1736 (1990).

2. Yariv, Amnon and Pochi Yeh, Optical Waves in Crystals: Propagation and Control of Laser Radiation. John Wiley & Sons (New York: 1984), 220-270.

Appendix: Derivation of r_{33} in the Ideal Experimental Setup.

First, find the phase shift Γ_{poly} due to the sample polymer:

$$\Gamma_{poly} = \frac{2\pi}{\lambda}\{n_e(\alpha_e)\, s_e(\alpha_e) - n_o\, s_o(\alpha_o)\} \tag{i}$$

where n_o and n_e are the ordinary and extraordinary refractive indices, s_o and s_e are the ordinary and extraordinary ray physical path lengths, and α_o & α_e are the ray angles within the polymer. The extraordinary index n_e is a function of α_e:

$$\frac{1}{n_e(\alpha_e)^2} = \frac{\cos^2\alpha_e}{n_o} + \frac{\sin^2\alpha_e}{n_e} \tag{ii}$$

The applied electric field is oriented along the c-axis of the ∞mm polymer structure and the 45° incident polarization implies that both the ordinary and extraordinary indices are modulated. The modified refractive indices are given by:

$$\begin{aligned} n_o' &= n_o + \Delta n_o \\ &\cong n_o - \tfrac{1}{2} n_o^3\, r_{13}\, E_z \end{aligned} \tag{iii}$$

and

$$\begin{aligned} n_e' &= n_e + \Delta n_e \\ &\cong n_e - \tfrac{1}{2} n_e^3\, r_{33}\, E_z \end{aligned} \tag{iv}$$

Using Snell's law for both rays:

$$\sin\theta = (n_o + \Delta n_o)\sin\alpha_o \tag{v}$$

and

$$\sin\theta = \left\{\frac{\cos^2\alpha_e}{n_o + \Delta n_o} + \frac{\sin^2\alpha_e}{n_e + \Delta n_e}\right\}^{-\frac{1}{2}} \sin\alpha_e \tag{vi}$$

In addition to the phase difference within the polymer, one must consider the phase difference due to the difference in physical path outside of the polymer. Within the polymer:

$$s_o(\alpha_o) = \frac{2t}{\cos\alpha_o} \text{ and } s_e(\alpha_e) = \frac{2t}{\cos\alpha_e} \tag{vii}$$

Outside of the polymer, the physical increase in the path of one of the rays is:

$$s_{out} = 2\,t\,(\tan\alpha_o - \tan\alpha_e)\sin\theta \tag{viii}$$

To complete the derivation we need the following quantities:

$$\frac{1}{\cos\alpha_o} = \frac{n_o + \Delta n_o}{\sqrt{(n_o + \Delta n_o)^2 - \sin^2\theta}} \tag{ix}$$

$$\tan\alpha_o = \frac{\sin\theta}{\sqrt{(n_o + \Delta n_o)^2 - \sin^2\theta}} \tag{x}$$

$$\frac{1}{\cos\alpha_e} = \frac{\sqrt{(n_e + \Delta n_e)^2 \sin^2\theta - (n_o + \Delta n_o)^2 \sin^2\theta + (n_o + \Delta n_o)^2 (n_e + \Delta n_e)^2}}{(n_o + \Delta n_o)\sqrt{(n_e + \Delta n_e)^2 - \sin^2\theta}} \tag{xi}$$

and

$$\tan\alpha_e = \frac{(n_e + \Delta n_e)\sin\theta}{(n_o + \Delta n_o)\sqrt{(n_e + \Delta n_e)^2 - \sin^2\theta}}. \tag{xii}$$

The total phase difference is given by:

$$\begin{aligned}\Gamma_{total} &= \frac{2\pi}{\lambda}\{n_e(\alpha_e)\,s_e(\alpha_e) - n_o\,s_o(\alpha_o) + s_{out}\} \\ &= \frac{2\pi}{\lambda}2t\left\{\left[\frac{n_o + \Delta n_o}{n_e + \Delta n_e}\right]\sqrt{(n_e + \Delta n_e)^2 - \sin^2\theta} - \sqrt{(n_o + \Delta n_o)^2 - \sin^2\theta}\right\}\end{aligned} \tag{xiii}$$

Using first-order binomial expansions, the birefringence $\delta n = n_e - n_o$ and the change in the birefringence $\Delta\delta n = \Delta n_e - \Delta n_o$:

$$\Gamma_{total} = \frac{2\pi}{\lambda}\frac{2t}{n_o\sqrt{n_o^2 - \sin^2\theta}}\left\{\begin{aligned}&\delta n\sin^2\theta - \frac{n_o\,\Delta n_o\,\delta n\sin^2\theta}{\{n_o^2 - \sin^2\theta\}} - \frac{\Delta n_o}{n_o}\delta n\sin^2\theta \\ &+ \Delta\delta n\sin^2\theta - 2\,n_o\,\delta n\,\Delta\delta n\end{aligned}\right\} \tag{xiv}$$

Assuming that $n \approx n_e \approx n_o$ and $r_{33} = 3r_{13}$:

$$\Gamma_{total} = \frac{2\pi}{\lambda}\frac{2t\sin^2\theta}{n\sqrt{n^2 - \sin^2\theta}}\left\{\delta n - \frac{1}{3}n^3\,r_{33}\,E_z\right\}. \tag{xv}$$

The phase difference caused by the birefringence is compensated by the Babinet-Soleil to give circularly polarized light and is not directly modulated by the applied electric field. The second term in Eq. (xv) gives the measured modulation in intensity following the analyzer, which leads to the electro-optic coefficient via:

$$r_{33} = \frac{3\lambda\sqrt{n^2 - \sin^2\theta}}{4\pi n^2 \sin^2\theta V_{applied}} \frac{\Delta I}{I_{bias}}, \qquad \text{(xvi)}$$

where λ is the wavelength, n is the refractive index, θ is the incident angle, $V_{applied}$ is the applied voltage, ΔI is the intensity modulation, and I_{bias} is the bias intensity.

Joseph Binford III
Report
Unavailable

INFLUENCE OF MODEL COMPLEXITY AND AEROELASTIC CONSTRAINTS ON THE MULTIDISCIPLINARY OPTIMIZATION OF FLIGHT VEHICLE STRUCTURES

Franklin E. Eastep
Professor
Department of Mechanical and Aerospace Engineering

The University of Dayton
103 College Park Dr.
Dayton, OH 45469-0227

Jonathan A. Bishop
NSF Graduate Research Fellow
School of Aerospace and Mechanical Engineering

The University of Oklahoma
865 Asp Avenue, FH 206
Norman, OK 73019-0601

Final Report for:
Summer Faculty Research Program
Summer Graduate Research Program
Wright Laboratory

Sponsored by:
Air Force Office of Scientific Research
Bolling Air Force Base, DC

and

Wright Laboratory

August 1994

INFLUENCE OF MODEL COMPLEXITY AND AEROELASTIC CONSTRAINTS ON THE MULTIDISCIPLINARY OPTIMIZATION OF FLIGHT VEHICLE STRUCTURES

Franklin E. Eastep
Professor
Department of Mechanical and Aerospace Engineering
The University of Dayton

Jonathan A. Bishop
NSF Graduate Research Fellow
School of Aerospace and Mechanical Engineering
University of Oklahoma

Abstract

This investigation focused upon the structural weight optimized design of two finite element models of a fighter-type wing of low aspect ratio using ASTROS. The optimal redesign of a fighter wing with the wing structure represented by a coarse and a complex finite element model is obtained with constraints imposed on strength, control reversal, and flutter using both subsonic and supersonic aerodynamic theories. The results from the two wings are comparable for flutter analysis; however, the results differ somewhat for control reversal. The reasons for this difference are investigated. Further study of both wings using different design variable schemes is also conducted.

INFLUENCE OF MODEL COMPLEXITY AND AEROELASTIC CONSTRAINTS ON THE MULTIDISCIPLINARY OPTIMIZATION OF FLIGHT VEHICLE STRUCTURES

Franklin E. Eastep
Jonathan A. Bishop

Introduction

An aircraft structural designer must consider aeroelastic instabilities (i.e. flutter, divergence, and control reversal) in addition to the strength requirements for the structural design of a high performance aircraft. In particular, he must design a structure such that the critical aeroelastic instability velocity is at least 15% above the maximum operational flight velocity while still insuring satisfactory strength at the velocity of the critical aeroelastic instability. The critical aeroelastic instability is defined to be the lowest velocity of the flutter, divergence, or control reversal velocities. At the same time, the structural designer desires to adjust the structural sizes to minimize the structural weight.

In recent years, structural optimization as needed and used by the aerospace industry has expanded in scope to include such additional disciplines as static and dynamic aeroelasticity, composite materials, aeroelastic tailoring, etc. One of the more promising multidisciplinary codes presently under development is the Automated Structural Optimization System (ASTROS)[1-3]. In this computer code, static, dynamic, and frequency response finite element structural modules, subsonic and supersonic steady and unsteady aerodynamic modules, and an optimization module are combined and allow for either analysis or optimized design of given aircraft configurations. Interfering surface aerodynamics are incorporated to handle the aerodynamic modeling of combinations of wigs, tails, canards, fuselages, and stores. Structures are represented by fully built-up finite element models, constructed from rod, membrane, shear, plate and other elements. Static and dynamic aeroelastic capabilities include trim, lift effectiveness, aileron effectiveness, gust response, and flutter analysis. The optimization and aeroelasticity modules of this code were used as a tool for the structural optimization of fully built-up finite element wing mdels in subsonic and supersonic flow with strength as well as static and dynamic aeroelastic constraints.

This project draws heavily on a previous study by Striz, Eastep, and Venkayya[4], which studied the behavior of a coarse finite element fighter wing model under strength, flutter, and aileron effectiveness constraints. The model used in that study is shown in Figure 1a.

For this study, a geometrically similar but more detailed fighter wing model with 550 nodal points was investigated to test the design capabilities of ASTROS when applied to complex structural representations (Figure 1b). This

model was a major modification of a previous finite element model by Love[5]. The same aeroelastic properties were determined as for the coarse model using the same number of design variables to allow for direct comparison of the results. Finally, the complex model was optimized using a larger number of design variables for a few sample cases.

Background and Objectives

The importance of this investigation can be stated as follows: in a modal-type flutter analysis of fully built-up finite element wing models as used in ASTROS, the structural behavior, which depends on the sizes of the structural members, influences the flutter behavior, i.e., the flutter speed and the flutter mode shapes, as asserted by Striz and Venkayya[6]. Also, optimization is very sensitive to the types of analyses used and their assumptions. Sometimes, even minor deviations can be compounded and exaggerated in the results as pointed out by Stria and Venkayya[7]. As the wing model is optimized, the thicknesses of the structural members are adjusted in each iteration, changing the normal modes and flutter behavior. The same essentially holds for such constraints as roll effectiveness, aileron effectiveness, and strength. Therefore, an understanding of the behavior of the optimization under the action of these imposed constraints will help determine such factors as move limits, upper and lower constraint bounds, etc. Furthermore, the comparison between the two models will illustrate the effects of model complexity on behavior. This will be of value in determining whether a simplified model is sufficient for a given task, or whether a more time consuming complex model is necessary.

Numerical Results and Discussion

The two fighter-type wing structural models were selected to be representative of a wing of low aspect ratio. Here, the theory is based on an idealized wing planform with an aileron located near the wing tip. The underlying structure of each wing is represented using finite elements, which is typical of built-up structures. These models were selected for weight optimization under strength as well as static and dynamic aeroelastic constraints; the first (Figure 1a), created for the previous study, was reasonably sized to allow for parametric investigations as performed in conceptual design. The more complex second model (Figure 1b), used in this project, would likely be used in the later phases of the preliminary structural design process. The geometry and the dimensions of the models are given in Figure 2. This figure shows the coarse structural model and the aerodynamic model used for flutter analysis. The complex model has identical exterior dimensions. The aerodynamic model used for steady aeroelastic analysis, i.e. the 9g pullup and roll cases, is similar to the flutter model except that it extends to the aircraft centerline.

In Reference 4, the sizes and locations of the structural elements of the 10-spar, 4-rib coarse model were selected and used as a nominal structural model. The structural mass of this wing was 497 lbs. Additionally, concentrated

weights were placed at the structural nodal points to simulate non-modelled structural and non-structural masses representing fuel, actuators, and stores. The aerodynamic modeling for the nominal and optimized structure was selected to be 36 aerodynamic boxes with 6 chordwise divisions and 6 spanwise division.

The 20-spar, 18-rib complex model was extensively modified from the original model by Love so that a valid comparison between it and the coarse model could be made. The wing box thickness profile was changed to that of the coarse model, and cross bracing at hard-point locations was removed. Each type of element was sized to obtain the same mass as in the coarse design, e.g., the total mass of the ribs in the complex model is equal to the total mass of the ribs in the coarse model, etc. Within this limitation, the thicknesses of the members were tapered from root to tip, as with the coarse model. Due to rounding error in the ASTROS weight generator, which was used to find the weight of each structural group, the final structural mass of the complex wing was slightly lower than that of the coarse wing at 488 lbs. The deflection of each wing when subjected to a concentrated tip load was then found to insure that the two wings were comparable. Finally, the non-structural masses were placed on the complex wing in a p!t4ern similar to that on the coarse wing and then moved to "tune" the complex wing so that its first few natural frequencies and mode shapes were reasonably close to those of the coarse wing.

Nominal Wing Structures

During the previous project, ASTROS was used to determine the individual stresses in the structural elements resulting from a 9-g pull-up at a Mach number of M = 0.85 at sea level. Additionally, using the same input Mach number, a flutter speed of approximately 30,100 in/sec for the nominal coarse model was found.

Finally, the roll effectiveness for a roll control system was determined for the nominal wing structure at a dynamic pressure near the control reversal dynamic pressure. The variation of aileron effectiveness of the nominal structure is displayed in Figure 3. As indicated there, the reversal dynamic pressure for the nominal coarse model at an input Mach number of M = 0.85 was approximately 45 psi.

The previous analysis was conducted in the subsonic Mach number regime (M = 0.85) using USSAERO for the steady flow and the Double Lattice aerodynamic formulation for the unsteady flow as incorporated in ASTROS. The application of these subsonic aerodynamic theories resulted in the prediction of aeroelastic instability velocities in the supersonic regime. To remove this inconsistency in problem formulation, USSAERO for the steady flow and one of the supersonic aerodynamic formulations in ASTROS, the Constant Pressure Method, were utilized in the continuation of this study. The Mach number was selected to be M = 1.2. When the nominal model was analyzed at this supersonic Mach number, a slightly lower flutter speed of 29,600 in/sec and a slightly lower reversal pressure

of 41 psi were found.

The splining method used to transfer aerodynamic loads to structural grid points which was used in this section for roll reversal analysis is considered suspect. It is believed that too many structural grid points were selected. Therefore, this portion of the project is currently being repeated with a more appropriate set of splining points. This revised set of splining points, which is similar to that used in Reference 5, has performed well in analysis of the nominal wing, but has not yet been included in the optimization runs. The new data will not all be available until after the deadline for this final report. The current data does illustrate the basic trends of the optimization.

Results for the nominal complex wing model differed, but agreed within expected limits. The flutter speed of 32,400 in/sec was 7.5% higher, indicating that the dynamic bending characteristics of the two wings are comparable.

However, the roll reversal dynamic pressure for the complex model was considerably lower than for the coarse model, at 31 psi. Since control reversal is caused by torsion due to an increased pitching moment when a control surface is deflected, it appears that the coarse wing has different torsional characteristics than the complex wing. Determining the cause of this difference occupied much of the summer research period. The conclusions are summarized later in this paper. Using the revised spline set, the roll reversal pressure was found to be 37 psi, which agrees much more closely with the coarse model results.

When the nominal complex model was analyzed at M = 1.2, two effects were observed: first, the reversal pressure decreased to 21 psi. This indicates that, unlike for the coarse wing, the pressure obtained using subsonic analysis seems to be greatly in error, since it was 50% higher than that obtained using supersonic analysis. Second, the flutter speed actually increased to 37,700 in/sec for the subsonic analysis. This does not necessarily represent an increase in the actual flutter speed of the wing; rather, it is an effect of the aerodynamic model used to calculate the aerodynamic matrices for the flutter model. Whether the flutter speed goes down or up when the formulation is changed from subsonic to supersonic cannot be predicted in advance of running the analysis. To determine the actual flutter speed of the win`, a matched-point iteration would need to be conducted.

Optimized Wing Structures

Coarse Wing

The fighter wing structural model was resized and optimized using ASTROS with both single and multiple constraints active at any given time as shown in Table 2a. These optimizations were originally performed in the

previous study, but different design variable minima were used for the strength optimization. Since the strength optimization results are used as constraints for all subsequent optimizations, the results are in most cases slightly different. Five design variables were used: one each for the ribs, spar webs, spar caps, quadrilateral skins, and triangular skins. The initial optimal structural model was obtained for a 9-g symmetric pull-up maneuver at M = 0.85 with a Von Mises stress constraint and prescribed stress yield values. The resulting optimum structure weighs 102 lbs, has a flutter speed of 17,900 in/sec, and a roll reversal pressure of 11 psi. The following optimization studies were conducted using this optimum as minimum allowable sizes for the individual structural members.

First, at M = 0.85, the structural model was resized and optimized using a constraint of an improvement of the reversal dynamic pressure from 45 psi to 52 psi. The increase in the reversal dynamic pressure was accomplished while the structural weight of the optimized wing was reduced from a nominal weight of 497 lbs to 480 lbs, as shown in Table 2a. As a by-product, the flutter speed increased to 29,500 in/sec.

As a comparison problem, with the reversal velocity used as a constraint, the structure was resized to yield the same reversal dynamic pressure as the nominal structure. This reduced the flutter velocity which, with the constraint on reversal dynamic pressure, dropped to 29,500 in/sec, as also indicated in Table 2a.

Using an increased flutter speed of 32,500 in/sec as a constraint resulted in a structure which was both lighter than the nominal wing and had a higher control reversal pressure (51 psi). This optimized wing had a weight of 440 lbs.

Increasing the flutter speed still further, to 33,000 in/sec, and requiring that the reversal dynamic pressure be at least that of the nominal model resulted in a wing which, paradoxically, is lighter than that of the previous case (424 lbs), while having a higher flutter speed. Obviously, the design ASTROS produced for the previous case is not a global optimum. This illustrates that adding constraints, even though they may not be active, can change the course of the optimization. It also reinforces the fact that numerical optimization schemes can only find local optima. The user must check these results, usually by using different initial conditions.

Finally, the structural model was resized and optimized using multiple constraints. In this case, it was required that the reversal dynamic pressure be the same as that for reversal of the nominal structure and that the flutter speed be increased to 31,000 in/sec. This increase of flutter speed is beyond that obtained when only a single constraint on reversal pressure was imposed. In this manner, the structural designer has the added advantage of precisely placing the velocity of certain aeroelastic instabilities relative to other aeroelastic instability velocities. Here, it was desired to make improvements in 4he flutter velocity while the structure is being weight optimized. In this particular case, the weight of the optimized structure was obtained as 382 lbs.

As with the analysis of the nominal coarse wing, the subsonic formulation used in the initial optimization predicted aeroelastic instabilities in the supersonic regime. Therefore, the optimizations were also evaluated for a supersonic input Mach number. The selected constraints for M = 1.2 were similar to those for M = 0.85. The respective reversal pressures, flutter speeds, and weight reductions for the optimized structure are again shown in Table 2a. They essentially confirm the trends found for M = 0.85 except that the minimum weights tended to be higher than for the subsonic cases. The exception to this was the optimization for nominal reversal pressure and increased flutter speed. Here, the stricter flutter constraint was the active constraint for both M = 0.85 and M = 1.2. Since the only effect of the supersonic aerodynamics is to shift the center of pressure from the quarter-chord line to the half-chord line, the flutter behavior of the wing should be nearly identical in both cases, causing the optimized designs to be essentially equal in weight.

Complex Wing

In order to provide a good comparison, the complex wing was optimized with the same types of constraints as the coarse wing. First of all, since the nominal performances of the wings were different, equivalent constraints were developed based on the percentage increases. Alternatively, the constraints from the coarse wing were applied directly to the complex wing. Both of these methods were used in this optimization study.

As with the analysis results, the spline set used for roll reversal analysis is suspect. Thus, the roll reversal results should be considered tentative.

When optimized for a 9-g pullup, the optimal complex wing weighed 151 lbs vs. 102 lbs for the coarse wing. The same number of design variables and the same linking scheme were used for both cases. The weight difference is probably due to the large element sizes in the coarse model, which "smear" the stresses and do not capture localized concentrations. The complex model, which does capture these concentrations, requires thicker elements to keep the stresses below material limits. Despite weighing more than the coarse wing, the flutter speed is slightly lower (17,500 in/sec). The roll reversal pressure for this case was 11 psi.

Next, the wing was optimized for an increase in reversal pressure to 36 psi. This is an increase of 15.5% over the reversal pressure for the nominal complex wing, the same percentage increase that was used for the coarse wing. The weight of this optimized wing was 392 lbs.

During this optimization, and all subsequent optimizations for control effectiveness, ASTROS had difficulty converging to the optimum. It often oscillated between a feasible and an infeasible design on successive iterations

rather than smoothly converging. To minimize this effect, the design variable move limits were manually restricted. Also, the program never actually identified the optimum; it simply oscillated between two nearly identical weights.

The complex wing was then optimized for the same (rather high) absolute reversal pressure as the coarse wing (52 psi). For this case, the structural weight increased greatly, to 950 lbs. As a by-product of the stiffer structure, the flutter speed increased to 54,700 in/sec. The high final weight seems to indicate that ASTROS was not able to converge to a reasonable minimum.

When the complex wing was optimized for a reversal pressure of 31 psi (the reversal pressure for the nominal wing), the optimized structure had a weight of 325 lbs. This is slightly better than the 349 lbs optimum for the coarse wing. At the same time, this optimization raised the flutter speed to 32,900 in/sec, whereas, for the coarse wing, the flutter speed dropped to 29,700 in/sec. Optimizing the complex wing for the same reversal pressure as the coarse wing, 45 psi, resulted in a design weighing 590 lbs with a flutter speed of 43,800 in/sec.

The complex wing was then optimized for a flutter speed of 34,900 in/sec, corresponding to an 8% increase, the same as for the coarse model. This optimization reduced the structural weight of the wing to 378 lbs, better than the 414 lbs optimum for the coarse design. Optimizing the complex wing for the same flutter speed as the coarse wing, 32,500 in/sec, produced a design with a weight of 334 lbs and a reversal pressure of 31.6 psi.

When the complex wing was optimized for a 9.6% increase in flutter speed with the same control reversal pressure as for the nominal wing, an optimal structural weight of 369 lbs was obtained. Flutter was the driving constraint in this design.

A different result was obtained when the complex model was optimized for a reversal pressure of 45 psi (nominal for the coarse wing) and an increased flutter speed of 33,000 in/sec. For this case, roll reversal was the driving constraint. The resulting design weighed 668 lbs and had a flutter speed of 43,300 in/sec, which is not consistent with the earlier case where a reversal pressure constraint of 45 psi was used without a flutter speed constraint, resulting in a structural weight of 590 lbs.

As with the corresponding coarse wing case, the inclusion of the flutter speed constraint (although not active) directs the optimization to a different optimum. This phenomenon also highlights the fact that numerical optimization cannot guarantee that the absolute minimum structural weight will be found; it only finds local minima. The designer must check the results, usually by optimizing beginning with different initial designs.

Finally, the wing was optimized for a 3% increase in flutter speed and for the nominal reversal speed. The optimum structure had a weight of 331 lbs. This represents substantial weight savings over the 466 lbs optimum for the coarse wing. When optimized for the same reversal pressure and flutter speed as the coarse wing (45 psi and 31,000 in/sec), the optimum structural weight was 614 lbs. For this case, the flutter constraint was not active, so the increase in weight seems to be due to the increased reversal pressure.

As with the coarse wing, the complex wing was also optimized using a supersonic aerodynamic formulation. The results of these analyses are given in Table 2b. In general, the weights were similar to those for the subsonic case when flutter was the driving constraint and higher than those for the subsonic case when roll reversal dominated. The exception to this was the case where a reversal pressure of 45 psi was used with no flutter constraint. The supersonic design weighed 306 lbs, while the subsonic design weighed 590 lbs.

A major deviation from the general trend was observed for the last case in Table 2b. For this case, ASTROS was not able to converge to a reasonable structural minimum weight but asked for ever-increasing member sizes to satisfy the constraints. The flutter constraint was not active, but, again, an inactive constraint influenced the optimization.

Further Study

To this point, all results for the coarse and complex wings have the simple, five-design variable linking scheme. A few additional cases, using both wings, were tested to determine the effects of using a slightly more complex scheme. For the coarse wing, the substructure (ribs and spars) was not designed; the optimum thicknesses from the corresponding heavily linked results are used. For the skins, each top element was linked with its corresponding bottom element. Thus, there are 31 skin design variables.

When optimized for strength during a 9g pullup, the optimum structural weight was found to be 101 lbs. This is a trivial overall weight savings over the heavy linking scheme. However, the actual structure of this design is different; some skin panels are thicker than those in the heavily linked optimum, and some are thinner.

Optimizing for a flutter speed of 32,500 in/sec at M=0.85, a design with a weight of only 303 lbs was found. The corresponding heavily linked design weighs 440 lbs. Thus, there is a definite benefit to allowing each skin panel to be optimized separately. With the heavy linking scheme, all skin panels are sized based on the most critical element; here, each element is sized based only on local conditions. At M=1.2, the optimum design weighs 400 lbs; again, this is substantially lighter than that obtained with heavy linking.

For the complex model, optimizing every skin panel would result in an excessively large number of design variables. Therefore, more extensive linking was used, and the substructure was also designed. As with the simple scheme, the linking was along structural function lines, i.e., ribs, spars, spar caps, and skins. Unlike with the previous scheme, not all elements of a specific type were linked to one variable. Rather, elements were linked to variables in three-bay increments. Since there are 18 bays on the wing, there are 6 design variables of each type, for a total of 24 design variables (quadrilateral skins and triangular skins were not separated).

It would be expected that this scheme would result in lighter optimum structures than the five-variable scheme, which forces overdesign of all elements linked to a particular variable if the most critical element is inadequate in the nominal model. The more complex linking scheme limits this tendency toward overdesign to only the particular bay containing the critical element.

When the 24-variable scheme was used to optimize the complex wing for a 9-g pull-up maneuver at M = 0.85, an optimum structural weight of 126 lbs was obtained. This weight was 16.6% lighter than the previous optimum design. However, as might be expected, the performance in flutter and roll reversal was worse than for the five-variable scheme. The control reversal pressure was slightly lower, at 10 psi. The flutter speed is 16,800 in/sec, which is also slightly less than the flutter speed for the wing optimized with five design variables.

Finally, the 24-variable wing was optimized for its flutter behavior. A flutter speed of 34,900 in/sec was chosen as the constraint. The resulting wing weighed 307 lbs (vs. 377 lbs for the five-variable wing), with a control reversal pressure of 30 psi (compared to 35 psi).

From these basic results, it can be seen that using a more complex design variable scheme seems to result in lighter optimum structures. However, the performance of these structures in areas other than those for which they were optimized may be poor. Therefore, all aeroelastic constraints should be included to ensure that none violate safety limits. For the given cases, the number of design variables used did not have a great effect on the computational expense of an analysis. Therefore, it may often be worthwhile to use more design variables. On the other hand, the variables should be linked along physical lines so that the resulting design can actually be manufactured.

Conclusions and Recommendations

The examples presented in thisinvestigation demonstrate that the optimization capabilities of the ASTROS procedure are well suited for the preliminary design environment. Any number of constraints of strength, divergence, control reversal, and flutter can be imposed on general finite element structural models of flight vehicles. The ability to

simultaneously consider many constraints from each of several disciplines allows the structural designer to develop non-intuitive solutions to the complex design problem placed on modern flight vehicle structures.

This investigation focused upon the structural weight optimal design of two models of a fighter-type wing of low aspect ratio. The optimal weight redesign of the wing structure was obtained with imposed constraints on strength, control reversal, and flutter, using both subsonic and supersonic aerodynamic theories. In general, the weight savings (at least for strength and flutter) were greater for the complex model than for the coarse model, when both used five design variables, and greatest for the complex wing using 24 design variables.

REFERENCES

1. Neill, D.J., and Herendeen, D.L., "ASTROS Enhancements, Volume I -- ASTROS User's Manual", **WL-TR-93-3025**, Flight Dynamics Directorate, Wright Laboratory, March 1993.

2. Johnson, E.H., and Venkayya, V.B., "Automated Structural Optimization System (ASTROS), Volume I - Theoretical Manual", **AFWAL-TR-88-3028/I**, Air Force Wright Aeronautical Laboratories, December 1988.

3. Neill, D.J., Johnson, E.H., and Herendeen, D.L., "Automated Structural Optimization System (ASTROS), Volume II - User's Manual", **AFWAL-TR-88-3028/III**, Air Force Wright Aeronautical Laboratories, December 1988.

4. Striz, A.G., Eastep, F.E., and Venkayya, V.B., "Influence of Static and Dynamic Aeroelastic Constraints on the Optimal Structural Design of Flight Vehicle Structures", **Proceedings, 32nd AIAA/ASME/ASCE/AHS/ASC Structures, Structural Dynamics and Materials Conference**, Baltimore, Maryland, 1991, pp. 470-476.

5. Love, M.H., Barker, D.K., and Bohlmann, J.D., "An Aircraft Design Application Using ASTROS", **WL-TR-93-3037**, Flight Dynamics Directorate, Wright Laboratory, June 1993.

6. Striz, A.G. and Venkayya, V.B., "Influence of Structural and Aerodynamic Modelling on Flutter Analysis", **Proceedings, 31st AIAA/ASME/ASCE/AHS/ASC Structures, Structural Dynamics and Materials Conference**, Long Beach, California, 1990, pp. 110-118.

7. Striz, A.G. and Venkayya, V.B., "Influence of Structural and Aerodynamic Modelling on Optimization with Flutter Constraint", **Proceedings, 3rd USAF/NASA Symposium on Recent Advances in Multidisciplinary Analysis and Optimization**, San Francisco, California, 1990.

TABLE 1a. Geometrical, Material, and Environmental Property Model Data

	COARSE DESIGN LOW ASPECT RATIO WING M = 0.85 and M = 1.2, Sea Level	
Constraints:	Strength (Von Mises), Reversal, Flutter	
Input:	Shear panel thickness:	0.08" in ribs 0.075" to 0.03" in spars
	Membrane thickness:	0.25" to 0.04" in skins
	Spar cap cross-sectional area:	1.0 to 0.5 in^2
	Spar stiffener cross-sectional area	0.05 in^2 (not designed)
	All values decreasing from root to tip	
Material:	E = 1.0*E7 lb/in^2, $\nu = 0.33$, $\rho = 0.1$ lb/in^3	
	Allowable stresses: 60.0*E3 lb/in^2 (tension and compression), 40.0*E3 lb/in^2 (shear)	

TABLE 1b. Geometrical, Material, and Environmental Property Model Data

	COMPLEX DESIGN LOW ASPECT RATIO WING M = 0.85 and M = 1.2, Sea Level	
Constraints:	Strength (Von Mises), Reversal, Flutter	
Input:	Shear panel thickness:	0.015" in ribs 0.062" to 0.005" in spars
	Membrane thickness:	0.25" to 0.046" in skins
	Spar cap cross-sectional area:	1.6 to 0.92 in^2
	Spar stiffener cross-sectional area	0.006 in^2 (not designed)
	All values decreasing from root to tip	
Material:	E = 1.0*E7 lb/in^2, $\nu = 0.33$, $\rho = 0.1$ lb/in^3	
	Allowable stresses: 60.0*E3 lb/in^2 (tension and compression), 40.0*E3 lb/in^2 (shear)	

TABLE 2a. WEIGHT OPTIMIZED WING WITH VARIOUS CONSTRAINTS
Coarse Wing, M = 0.85 and M = 1.2, Sea Level

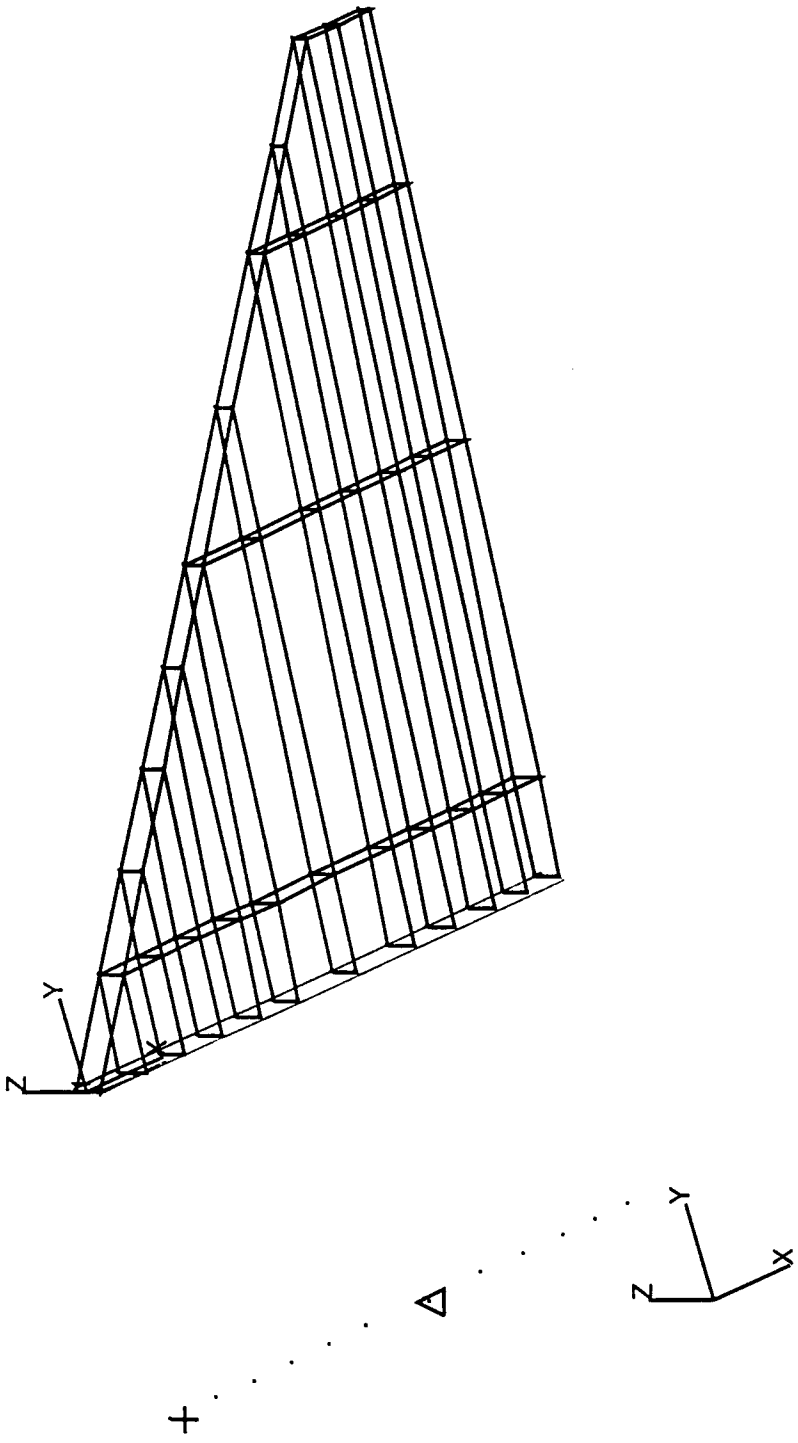
MODEL	MACH NUMBER	REVERSAL-q (#/in^2)	FLUTTER SPEED (in/sec)	STRUCTURAL WEIGHT (#)
Nominal	M = 0.85	45	30,100	497
	M = 1.2	41	29,600	497
Optimized (Strength)	M = 0.85	11	17,900	102
	M = 1.2	11	30,400	102
Optimized	M = 0.85	52*	32,400	480
	M = 1.2	52*	27,300	381
Optimized	M = 0.85	45*	29,500	398
	M = 1.2	41*	25,600	323
Optmized	M = 0.85	51	32,500*	440
	M = 1.2	53	32,500*	510
Optimized	M = 0.85	45*†	33,000*	424
	M = 1.2	41*†	33,000*	493
Optimized	M = 0.85	45*†	31,000*	382
	M = 1.2	41*†	31,000*	453

* indicates quantity was a constraint
† indicates constraint was not active in the optimized design

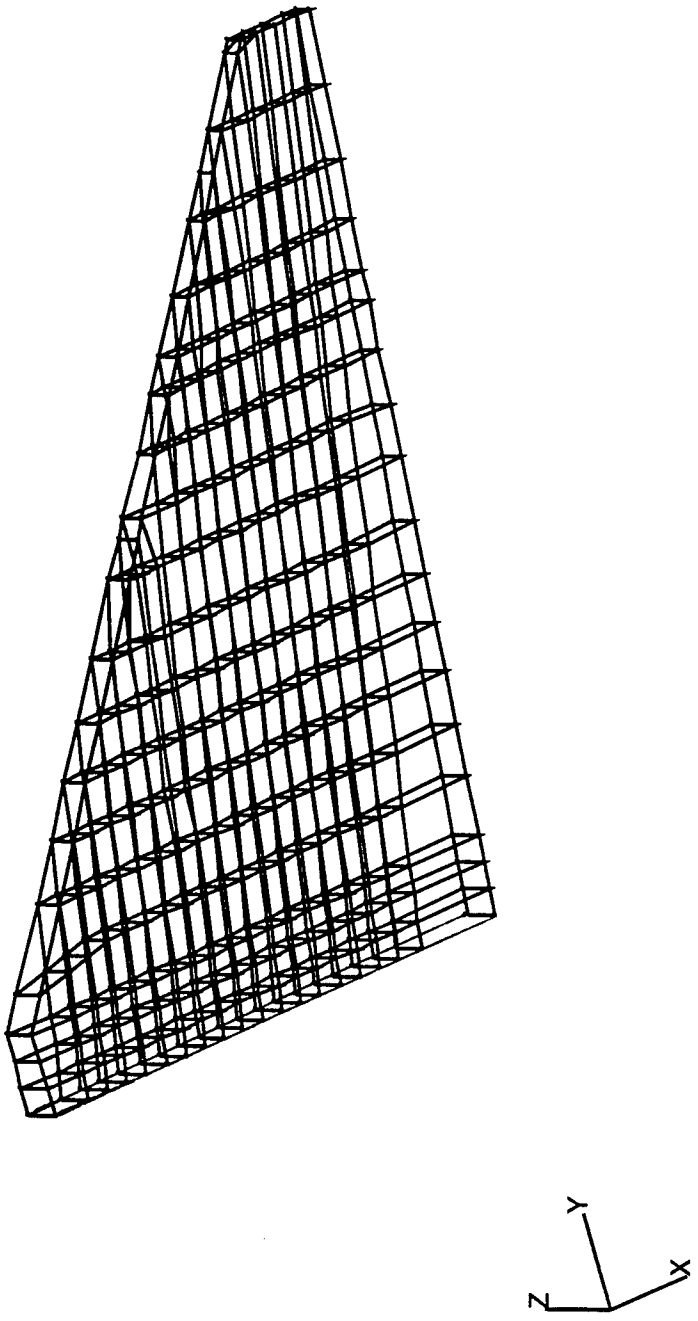
TABLE 2b. WEIGHT OPTIMIZED WING WITH VARIOUS CONSTRAINTS
Complex Wing, M = 0.85 and M = 1.2, Sea Level

MODEL	FLIGHT CONDITION	REVERSAL-q (#/in^2)	FLUTTER SPEED (in/sec)	STRUCTURAL WEIGHT (#)
Nominal	M = 0.85	31	32,400	488
	M = 1.2	21	37,700	488
Optimized (Strength)	M = 0.85	11	17,500	151
	M = 1.2	9	23,200	151
Optimized	M = 0.85	36*	36,700	392
	M = 0.85	52*	47,700	950
Optimized	M = 0.85	31*	32,900	325
	M = 1.2	31*	53,000	799
	M = 0.85	45*	43,800	590
	M = 1.2	45*	47,900	306
Optimized	M = 0.85	35	34,900*	377
	M = 1.2	16	34,900*	377
	M = 0.85	32	32,500*	334
	M = 1.2	14	32,500*	321
Optimized	M = 0.85, M = 1.2	31*†	35,500*	369
	M = 0.85	45*	33,000*†	668
Optimized	M = 0.85	31*†	33,300*	331
	M = 1.2	21*	33,300*†	304
	M = 0.85	45*	31,000*†	614
	M = 1.2	45*	31,000*†	(see text)

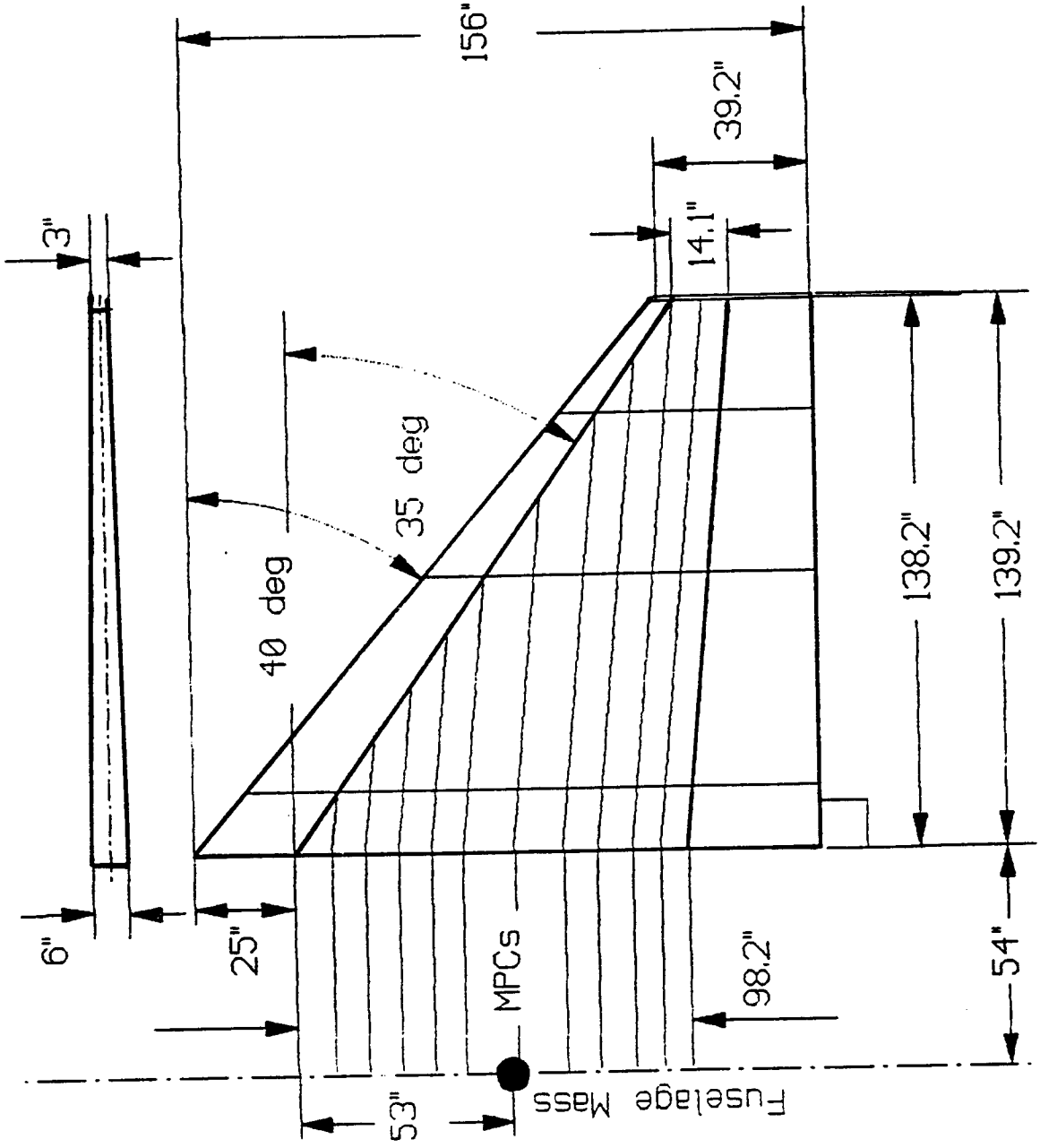
* indicated quantity was a constraint
† indicates constraint was not active in the optimized design



Coarse Model
Figure 1a



Fine Model
Figure 1b



Aerodynamic and Structural Geometry
Figure 2
(From Ref. 4)

THE USE OF PRESSURE SENSITIVE PAINTS ON ROTATING MACHINERY

Steven P. Burns
Graduate Student
Department of Aeronautics and Astronautics

Purdue University
Grissom Hall
West Lafayette, IN 47907

Final Report for:
Graduate Student Research Program
Wright Laboratory

Sponsored by:
Air Force Office of Scientific Research
Bolling Air Force Base, DC

and

Wright Laboratory

August 1994

THE USE OF PRESSURE SENSITIVE PAINTS ON ROTATING MACHINERY

Steven P. Burns
Graduate Student
Department of Aeronautics and Astronautics
Purdue University

Abstract

The current work involves measuring the surface pressure on a rotating blade with a laser scanning pressure paint system. The pressure paint consists of a fluorescent molecule which is mixed with a polymer than painted on the surface of interest. The laser is scanned across the model surface which excites the fluorescent molecule. The intensity with which the molecule emits light is dependent on the amount of oxygen quenching. If the pressure is low the molecule will emit a more intense light then if the pressure were higher. As more oxygen molecules are present they absorb the energy that would have been emitted as light. The system can be calibrated in two ways. The first would be to take an intensity reading with the known pressure and then take a reading at the condition of interest. Then the Stern-Volmer relationship of intensities can be used to calculate the pressure. A second way is to measure the decay time of the emitted intensity and calibrate that versus pressure. The purpose of the experiment is to get a complete surface map of the pressure on the rotating blade.

THE USE OF PRESSURE SENSITIVE PAINTS ON ROTATING MACHINERY

Steven P. Burns

Introduction

A surface pressure map of a compressor rotor blade is a very important analytical tool. The surface pressure map can be integrated to calculate the lift and drag on the body. Adverse pressure gradients can show regions that are prone to separate.

The conventional way to obtain surface pressure measurements is with the use of pressure taps and transducers. This method gives surface pressures at a discrete amount of points. In a rotating environment it can be quite difficult to get the pressure signal out of the engine and to the data collection equipment. Also the pressure taps weaken the structure of the rotating blade which limits the amount of taps. The use of pressure sensitive paints will result in a complete surface pressure map of the blade.

Pressure sensitive paints will emit a fluorescence proportional to the surface pressure when excited by a certain wavelength of light. The intensity of this emitted light ,as well as the decay time, can be calibrated with pressure. This paper will explain the physical process involved when using the paint. Then describe the two different types of data acquisition systems and mention the pressure paints use in previous experiments. Then mention the areas of application to rotating machinery. Finally the current work in progress will be described.

Background

Pressure sensitive paints consist of two parts: the fluorophore molecule, and the polymer within which the fluorophore is imbedded. The first part of this section will concern the fluorophore. The fluorescent molecule is excited to a higher energy level by the incoming photons of a light source. This light source could be a xenon flash lamp, ultra-violet light, or a laser source. When the molecule returns back to the ground state a photon of a longer wavelength is emitted.

While the molecule is in its excited state it can react with oxygen through a collisional process. The energy of the fluorescent molecule is transferred to the oxygen molecule. When the fluorescent molecule returns to the ground state it does not emit a photon. This whole process is known as oxygen quenching. The intensity of the fluorescent light will decrease with an increase in the presence of oxygen.

The local air pressure will cause a similar response since air is made up of 20 percent oxygen . The intensity of the fluorescent light will decrease with an increase in the local air pressure.

The oxygen quenching process can be described with the Stern Volmer equation

$$\frac{I_0}{I} = A + B\left(\frac{P}{P_0}\right)$$

This equation relates the fluorescent intensity ratio to the pressure ratio. The reference condition (I_0 , P_0) is usually taken at atmospheric pressure. Then intensity data taken at an unknown condition can be used to determine the pressure. The intensity ratio can also eliminate problems due to a non uniform paint job or non uniform illumination source. If the paint contains more fluorescent molecules in some areas than others, the resulting fluorescent pattern will be brighter in some areas. This non uniformity will be eliminated by taking the ratio of the flow on and flow off intensities. Some problems can arise with this method due to model deformation. If a rotor blade untwists at a high revolution speed its flow on image would not align with its flow off image. This problem can be overcome if the position of several points on the blade can be determined in the flow on and flow off image. A spatial transformation can then be developed to align the two images.

The phase sensitive detection method can be used to eliminate the need for a flow on and flow of image. This method relies on the fact that the fluorescent decay time will decrease with increasing oxygen concentration. An amplitude modulated laser source is used to excite the fluorescent molecule. Then a photo multiplier tube is used to pick up the emitted fluorescence. The modulation signal and photo multiplier signal are input to a lock in amplifier. The output of the lock in amplifier is the phase difference between the two signals. The emitted light has a phase shift due to the finite lifetime of the fluorescent decay. This phase difference will increase with decreasing oxygen concentration. A calibration curve can be developed which relates pressure to phase angle. The decay time is not sensitive to the amount of fluorescent molecule present or the power of the exciting light source. Therefore only a flow on measurement is needed.

A polymer matrix is needed to hold the fluorescent molecule to the surface of the model. The polymer matrix can effect the fluorescent output in two different ways. The oxygen molecules have to diffuse through the polymer layer in order to react with the fluorescent molecule. So the time response of the paint is directly related to the diffusion properties of the polymer. The second effect is to change the absorption and emission spectrum of the fluorescent molecule. This will effect the power required to excite the molecule and the intensity of the emitted fluorescence.

The many different combinations of fluorophores and binders which are currently used are shown in Table 1. This table can be used to compare the different formulations based on sensitivity and quantum yield. The sensitivity is defined as the ratio of intensity for a pure nitrogen environment to the intensity at atmospheric pressure. The fluorescent intensity will be the greatest in the nitrogen environment because their is no oxygen available to quench the fluorescence. The higher this ratio the more sensitive the paint will be to changes in pressure. The second criteria is quantum yield. The quantum yield is defined as the ratio of emitted photons to incident photons. A high quantum yield will result in a bright fluorescent light. This will increase the signal strength to the photo detection device.

Methods of Paint Application

There are several different methods of paint application. These include spray coating, dip coating with the sol gel process, and spin coating. The spray coating method uses an artist's airbrush to spray the paint mixture on the model surface. The fluorescent molecule is dissolved in the binder solution then sprayed on the model in overlapping coats. The process is repeated until a uniform coating is present on the model surface. The spray coating method has to be used for binders such as GP-197 which do not adhere well to the model surface in bulk quantities. The air brush atomizes the paint mixture which allows the small particles to adhere to the surface.

The second coating process that is being investigated is dip coating with the sol gel process. This process involves mixing several chemicals in solution which will gel over time and become a solid silica layer on the blade surface. The sol gel process is described in a paper by (Brinker [1]). The following chemicals are combined: 100 ml ethanol, 100 ml $Si(OC_2H_5)_4$, 8.2 ml water. The commercial name of the silica compound is silicon tetraethoxide (TEOS). The ethanol is used as a mutual solvent for the water and TEOS to mix together in. The water hydrolyzes the TEOS mixture to form silicon (SiO_2) particles. An acid can be used as a catalyst to speed up the process. Once the solution is mixed a fluorescent molecule can be added. The blade can be dip coated after the solution has started to gel. The thickness of the film can be controlled by the speed at which the blade is withdrawn from the solution. The fluid dynamics in the process are explained in a paper by (Scriven [2]). The film layer will be thin if the withdrawal speed is slow. The resulting coating is a silica network with nanometer size pores within which the fluorescent molecules rest. The paper by (MacCraith [3]) describes a sol gel process for depositing fluorescein on a fiber optic pH sensor.

Paint Calibration

The paint can be calibrated for pressure with two separate methods. The first method is to calibrate pressure ratio versus intensity ratio. The second method is to calibrate pressure versus phase angle.

The calibration setup for the intensity ratio is shown Figure 1. A calibration sample is painted and placed inside a vacuum chamber with an optical access window. The pressure inside the chamber can be controlled and measured from vacuum to atmospheric. A laser light source passes into the chamber and excites the fluorescent paint. The emitted fluorescence is collected with a lens and focused onto a photo multiplier tube. A 600 nm long pass filter is placed in front of the photo multiplier tube to reject the laser light and pass the fluorescence. The photo multiplier current is converted to voltage with a 1 k ohm resistor. Then the signal is amplified, filtered, and digitized. The pressure in the chamber is varied and the corresponding intensities are collected. The dark current is subtracted from the intensity values and the ratio is calculated.

The second calibration method works with the phase angle. The calibration setup is similar to the intensity method except the laser is amplitude modulated. The laser modulation signal and the photo multiplier tube signal are input to a lock in amplifier. The output phase angle is digitized with a computer.

Laser Scanning System

Once the calibration curves are calculated, actual pressure data can be obtained from the blade surface. There are two separate types of data acquisition systems. They are the laser scanning system and the CCD flash lamp system.

The laser scanning system will acquire pressure data in chordwise lines across the blade. Figure 2 shows the laser scanning system. The laser beam is split with one part sent to a photo diode and a second part sent to a computer controlled scanning mirror. The photo diode is used to measure the laser power output fluctuations. The scanning mirror will scan the blade in the radial direction, while the rotation of the blade causes a scan in the chordwise direction. The fluorescence is collected with a photo multiplier tube and the signal digitized. The flow off data is acquired with the blade rotating at 1 rpm. Then the flow on data is acquired at the desired rpm rate. Ensemble averaging can be used to reduced the noise in the signal. This noise can come from external lights or electrical noise in the equipment. The signals from 40 or more blade passes are added together then averaged.

Figure 3 shows the laser scanning system for use with the phase sensitive detection method. The laser is amplitude modulated at a frequency determined by equation 2.

$$\omega\tau = 1 \qquad (2)$$

τ = fluorescent decay time of a particular paint

This results in the maximum sensitivity for the lock in amplifier. The output signal has less noise than the intensity signal from the photo multiplier tube. This is a result of internal filters in the lock in amplifier.

CCD Flash Lamp System

A CCD camera with a flash lamp light source can be used to collect complete surface pressure maps of the blade. This is a full surface technique where as the laser scanning system is a point technique. Figure 4 shows the data collection set up. A flash lamp is set to strobe at the rotational frequency of the blade in order to stop the motion. A band pass optical filter is placed in front of the light to allow the correct excitation wavelength to pass through. The emitted fluorescent light passes through an optical filter and is collected with a CCD camera. The camera signal is then digitized with a frame grabber board. An 8 bit board can assign 256 gray scale levels to the picture. The gray scale picture can be false colored to enhance the pressure contours. Again a flow on and flow off image are acquired, the dark pixel count is subtracted, and the ratio is calculated.

Comparison of Systems

The two different measurement systems can be compared in three different areas: pressure resolution, spatial resolution, and optical access. The pressure resolution is determined by the noise of the measuring system and the resolution of the actual measuring instrument. If the system produces a signal with a lot of noise the actual pressure value may not be discernible. In the case of the laser scanning system the light signal is amplified with a photo multiplier tube which is a very low noise instrument. The resolution is set in the A/D board. A 12 bit A/D board would enable 1 part out 4096 to be resolved. In the case of the camera system the light signal is collected by a CCD chip. This has more noise than the photo multiplier tube. Changes in temperature can induce thermal noise into the signal. With an 8 bit frame grabber board 1 part out of 256 can be resolved. The noise can be reduced and the resolution increased with the use of a cooled digital CCD camera. The digital cameras can be cooled to between -40 degrees C and -100 degrees C. This will eliminate some of the thermal induced noise. The digital cameras can be

made with 16 bit resolution. The digital cameras are very expensive and the read out rate is slow compared to the analog cameras.

The spatial resolution of the laser scanning systems is set by the laser spot size. However small the laser beam can be focused determines the smallest distance between pressure measurements. The spatial resolution of the CCD camera is limited by the pixel size and magnification. A typical CCD camera has 512 by 512 pixel arrays. With the proper lenses the area of interest can be magnified to fill the 512 by 512 pixel array.

Optical access inside of a gas turbine engine can be a difficult task. A laser beam can reach a compressor blade surface or a turbine blade surface through the use of an optical access window. Figure 5 shows the laser beam path. A small hole would be cut out between the rotor and stator rows and a glass window would be mounted in the whole. An optical mirror probe could be used for access to even tighter spots as shown in figure 6. This probe would give you an increase in the angle at which the laser beam strikes the blade. This is necessary if the neighboring blade is very close and would block the beam otherwise. A third option would be to use a fiber optic probe. The laser would be focused onto the inner core of the fiber optic bundle and be transmitted inside the gas turbine engine. The fluorescent output would be picked up by the outer diameter of the fiber optic bundled and be transmitted back out of the engine to a photo multiplier tube.

Optical access inside the engine is difficult with a flash lamp and CCD camera. The camera would be ideal for taking the pressure distribution of the entire front fan face. However, getting to a blade deep inside the compressor or turbine is much more difficult. The light or the camera would have to be strobed at the same rotation rate of the engine in order to freeze the image.

Previous Work

To this date all of the previous work with pressure sensitive paint has been done on stationary models. This paper will mention three of the many different experiments that have used pressure sensitive paints. They will include the work done at TSAGI in Moscow, Russia, McDonnell Douglas, and Purdue University.

The work done at TSAGI is described in the paper written by (Phonov et al [4]). Phonov used the pressure sensitive paints on several different wind tunnel models. These include a model of the Buran space shuttle, the GAW-1 wing, and a canard with an internal balance. In these tests a laser was split of into illuminators which gave a broad distribution of light across the model surface. The fluorescent image is

picked up by a CCD camera. Figure 7 shows a comparison of the pressure sensitive paint data and internal balance data for the canard model. The pressures obtained from the fluorescent images were integrated in order to calculate the normal force on the canard. The force coefficients from the paint method agree with those from the internal balance.

McDonnel Douglass has developed a complete pressure paint data acquisition and reduction system which is described in the papers by (Donovan et al [5]) and (Morris et al [6]). The paints were used on three different wind tunnel models: an advanced fighter wing, a transport wing, and shock wave / boundary layer interaction. These tests used an argon ion laser which passes through a trifurcated fiber bundle and diffuses through ground glass. The fluorescence is picked up with a 12 bit CCD camera. The software package will ratio the flow on and flow off images and correct for any model displacement.

The work done at Purdue University uses the laser scanning system and is described in the paper by (Hamner et al [7]). A flat plate with pressure taps was painted with a Ruthenium based pressure sensitive paint. An axisymetric jet set at 1, 2, and 3 psi impinged on the flat plate. Figure 8 shows the pressures collected from the laser scanning system and the pressure taps. The pressure paint data agrees well with the pressure taps.

Application to Gas Turbine Engines

The pressure sensitive paints can be used in three regions of the gas turbine engine: the fan, the low pressure compressor, and a cold turbine. Figure 9 shows the typical temperatures and pressures encountered inside a gas turbine engine. The temperatures in the fan and the low pressure compressor are well within the limits of the pressure sensitive paints. However the temperature in the high pressure compressor and hot turbine are too high. Above 300 degrees F the fluorescence of the paint turns off. If the turbine were driven externally without the combuster being used the paints could be used on the cold turbine.

Current Work

The first step in the pressure paint process was calibration of two different paint formulations. The first paint used PTOEP as the active fluorescent molecule. The calibration setup as shown in Figure 1 was used. The resulting calibration plot is shown in Figure 10. As you can see this paint mixture is very sensitive below pressures of 9 psi, however the sensitivity begins to decline above 9 psi. This trend is typical of all pressure sensitive paints. When this plot is inverted it can be fit with the Stern Volmer equation. The Stern Volmer plot is shown in Figure 11. A linear curve fit is used to determine the

constants in the Stern Volmer equation. The intercept, A, is equal to 0.1178, and the slope, B, is equal to 0.9438. The same calibration procedure was tried with Ru(bpy) as the active fluorescent molecule. The calibration curve is shown in Figure 12 and the Stern Volmer Curve in Figure 13. As you can see the paint appears to loose its pressure sensitivity above 7 psi. I believe this is a result of the exciting light source and not the paint itself. Figure 14 , from a paper by (Carraway et al [8]), shows the absorption spectrum for a similar ruthenium molecule. The main absorption peaks are at 280 nm and 450 nm. The exciting laser source was at 543.5 nm. The Ru(BPY) molecule did not absorb enough energy at the higher wavelength provided by the green helium neon laser. This can be corrected if an argon ion laser is used. The laser can be tuned to emit in the blue region at 457 nm which would allow the Ru(BPY) molecule to absorb much more energy.

The current work involves a J-79 single stage compressor which is located at the propulsion directorate of Wright Patterson Airforce Base. This compressor has 22 rotor blades which have a chordwise length of 2.5 inches and a radial length of 8 inches. The blades were painted with a base coat of white paint. Then a PTOEP mixture was sprayed on top of the white base coat. The white primer layer enhances reflection of the fluorescence. The PTOEP absorption and emission spectrum ,from the paper by (Kavandi et al. [9]), are shown in Figure 15. A five miliwatt helium neon laser, which emits at 543.5 nm, was used to excite the fluorescent molecule. A long pass filter with a cut off wavelength of 600 nm was used to pass the fluorescent emission. The photo multiplier tube output was amplified by a factor of 200. The signal was low passed filtered at 25 KHz to eliminate any high frequency noise. Then the analog signal was sampled at 20 KHz and converted to digital form with a 12 bit A/D board.

A total of 5 rotor blades were painted with three different paint formulations. Figure 16 shows the intensity signal from the photo multiplier tube for the five different blades. The first two blades were painted one week earlier with a PTOEP mixture. The third blade was painted with a H_2TFFP mixture, the fourth with a one day old PTOEP mixture, and the fifth with a Ru(BPY) based paint. The first noticeable difference is the effect of photo bleaching. The signal from the newly painted PTOEP blade is much stronger than that from the two blades painted one week earlier. This is a result of ultra violet radiation, present in normal exposure to room lights, photo degrading the fluorescent molecule. This shows that data should be taken within one day of when the blade is painted and the mixture was calibrated. As you can see from looking at the fourth blade, the intensity did decrease between the slow rotation rate (105 rpm) and the fast rotation rate (1271 rpm). The ratio of these two signals was computed and the Stern Volmer equation applied. However, the resulting pressures were not significantly different from atmospheric pressure. This is because the paints are not very sensitive to small changes near atmospheric pressure. The tip mach number of the rotor was only 0.16, which would result in small pressure changes from atmospheric pressure. I think the pressure paints would be much more effective on a higher speed rotor.

Conclusions

The pressure sensitive paint technique has several advantages and disadvantages when compared to conventional pressure taps. Pressure paints are non intrusive and do not require holes to be drilled in the actual model for pressure taps. Model preparation is much less expensive and less time consuming then conventional pressure taps. Pressure paints offer a complete surface pressure map instead of discrete points. One disadvantage is that pressure paints have to be calibrated for the change in intensity due to temperature changes. Also optical access is always a concern.

Future work is planned to test the pressure paints on a faster compressor setup. The compressor will have a tip mach number of 1.6. This will give large changes in surface pressure which should be detectable by the pressure paints.

References

(1) Brinker, C. J. "Sol-Gel Derived Antireflective Coatings for Silicon", Solar Energy Materials 5 (1981), 159-172.

(2) Scriven, L. E. "Physics and Applications of Dip Coating and Spin Coating", Mat. Res. Soc. Symp. Proc., Vol. 121, 1988, 717-728.

(3) MacCraith, B. D., Ruddy, V., Potter, C., O'Kelly, B., and McGilp, J. F. "Optical Waveguide Sensor Using Evanescent Wave Excitation of Fluorescent Dye in Sol-Gel Glass", Electronic Letters, 4 July 1991, Vol. 27, No. 14, 1247-1248.

(4) Phonov, S. "Set of Luminescence Pressure Sensors for Aerospace Research", Sensors and Actuators, B: Chemical v B11 n 1-3 Mar 1 1993. p201-206.

(5) Donovan, J. F., Morris, M. J., Pal, A., Benne, M. E., and Crites, R. C. "Data Analysis Techniques for Pressure and Temperature Sensitive Paint", AIAA Paper 93-0176, 1993.

(6) Morris, M. J., Benne, M. E., Crites, R. C., and Donovan, J. F. "Aerodynamic Measurements Based On Photoluminescence", AIAA Paper 93-0175, 1993.

(7) Hamner, M., Campbell, B., Liu, T., and Sullivan, J. "A Scanning Laser System for Temperature and Pressure Sensitive Paint", AIAA Paper 94-0728, 1994.

(8) Carraway, E. R. and Demas, J. N. "Photophysics and Oxygen Quenching of Transition-Metal Complexes on Fumed Silica", Langmuir, 1991, Vol. 7, No. 12, 2991-2998.

(9) Kavandi, J., Callis, J., Gouterman, M., Khalil, G., Wright, D., and Green, E. "Luminescent Barometry in Wind Tunnels", Rev. Sci. Instrum. 61 (11), Nov. 1990, 3340-3347.

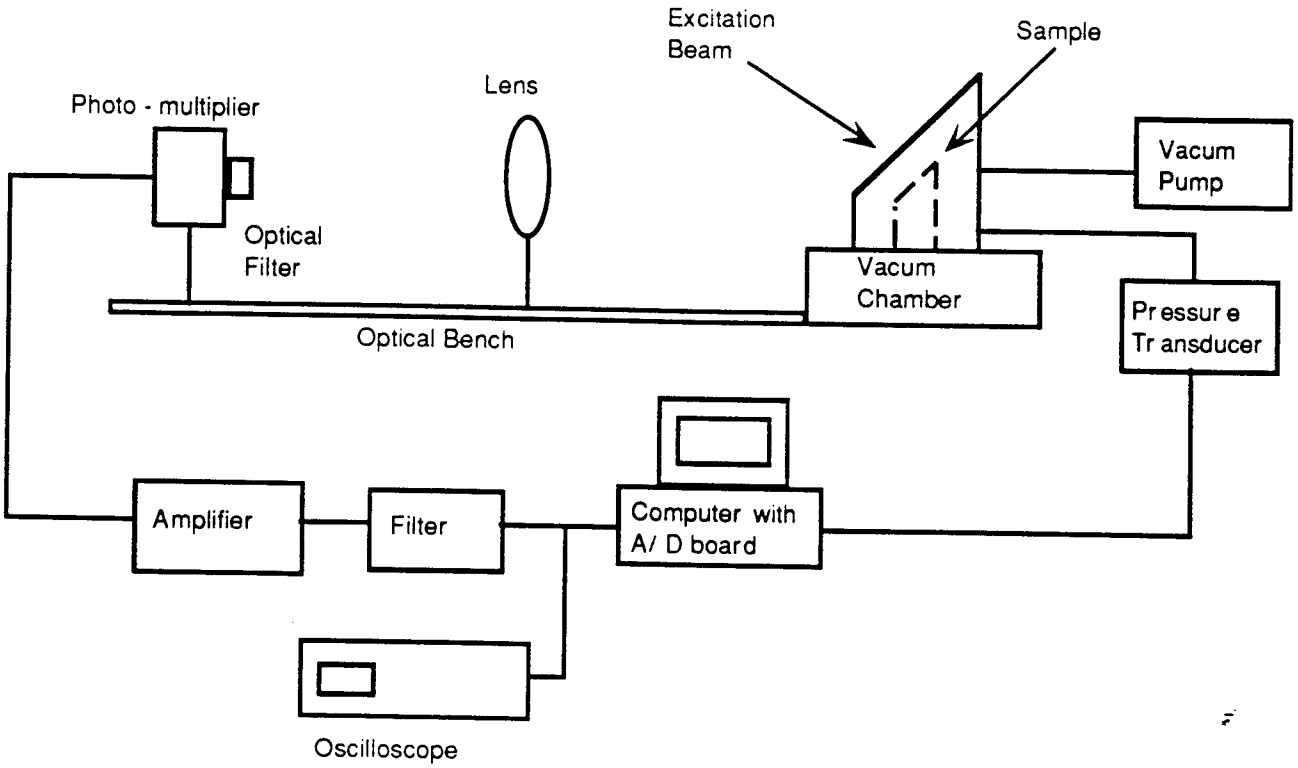


Figure 1: The calibration set up for the intensity method.

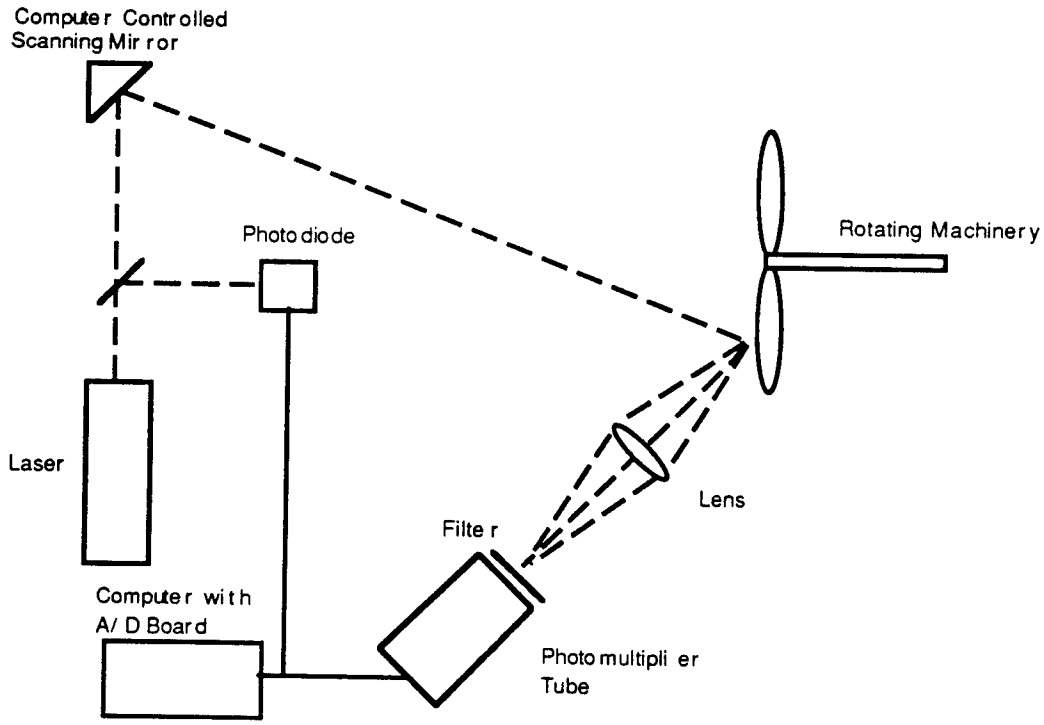


Figure 2: The laser scanning system using the intensity method

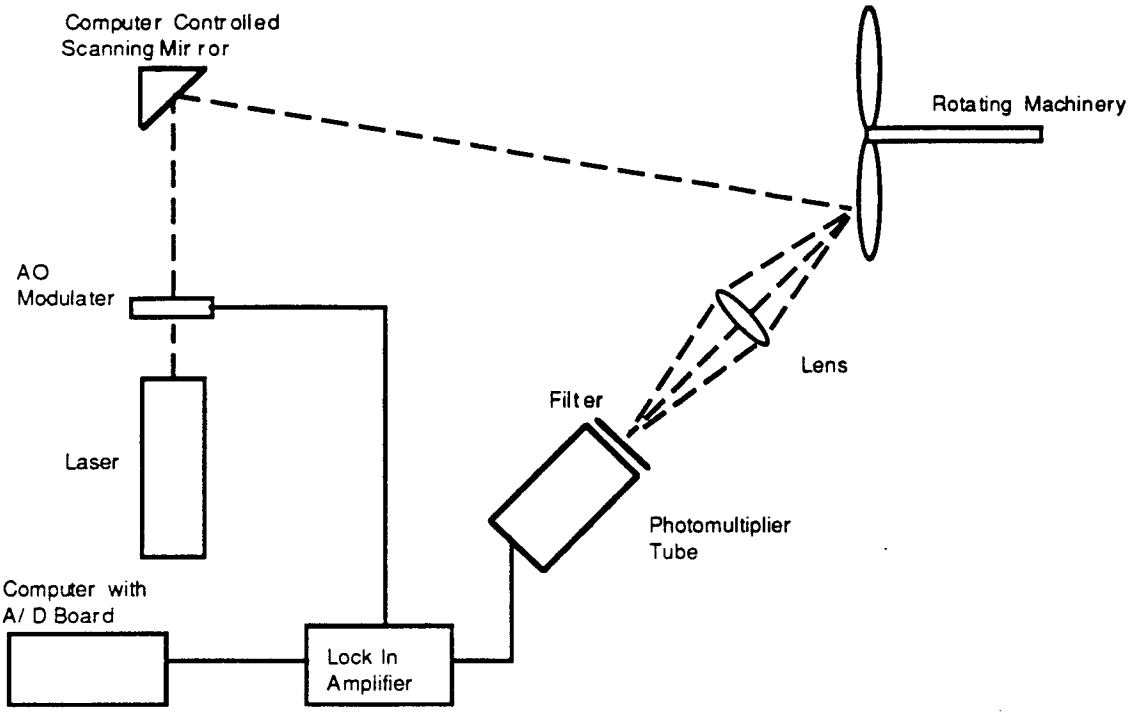


Figure 3: The laser scanning system using the phase method

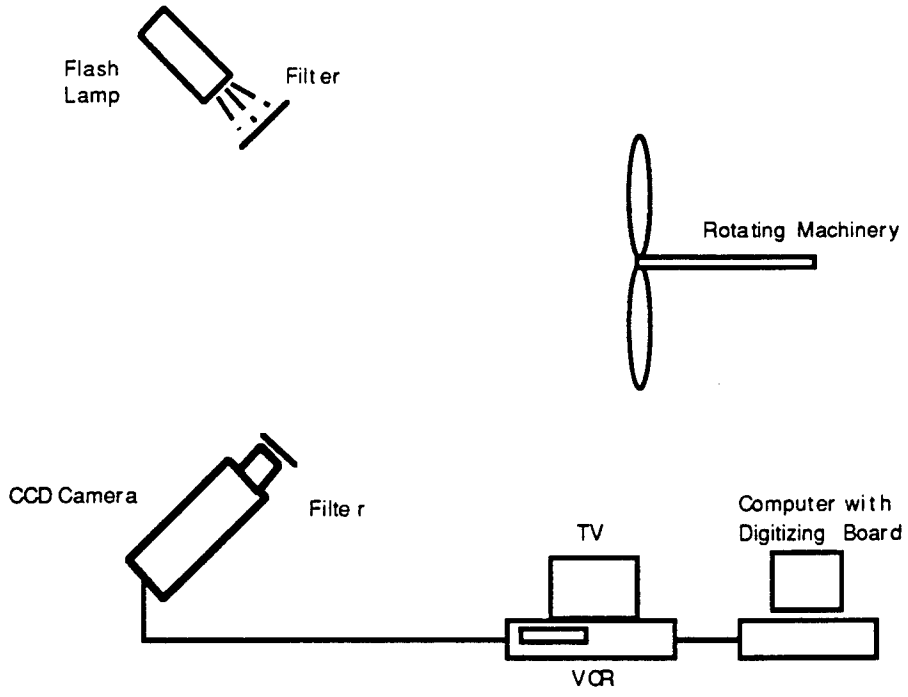


Figure 4: The CCD flash lamp system

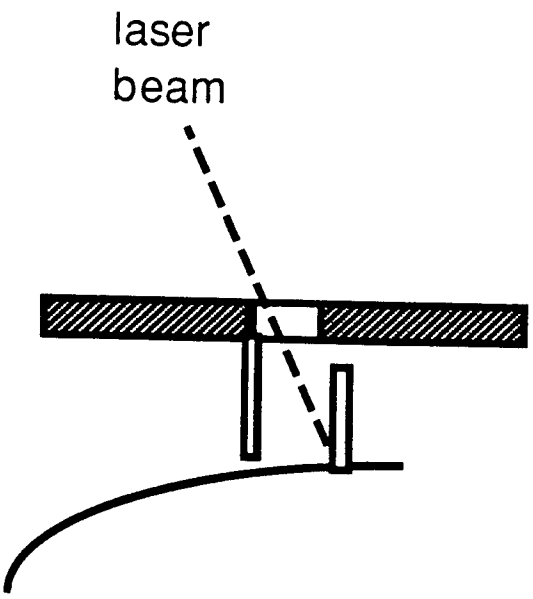


Figure 5: The laser optical access window

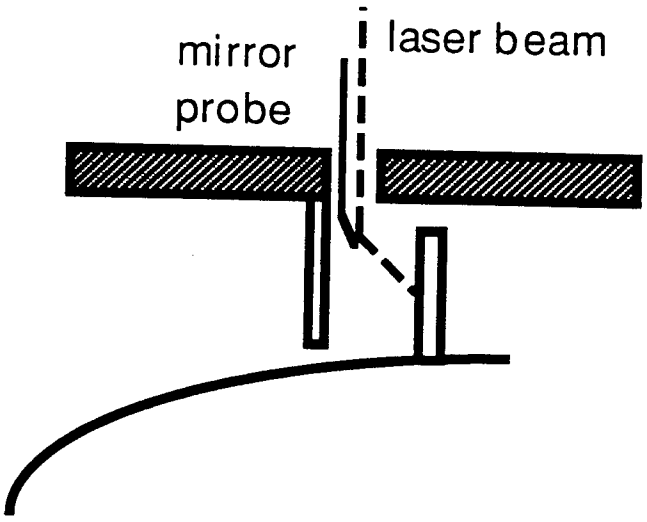
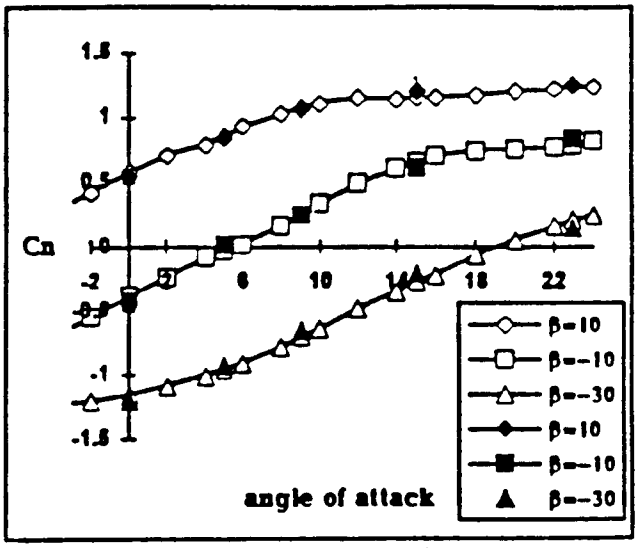


Figure 6: Optical access with a mirror probe



Comparison of $C_{n'}$ obtained with OPM (black markers) and internal balance system, on canard at different deflection angles β.

Figure 7: A comparison of pressure sensitive paint and internal balance data

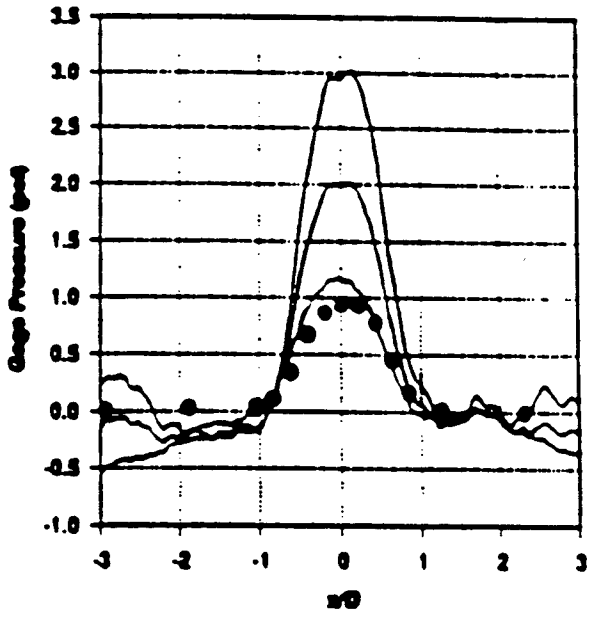


Figure 8: Pressure data from a jet impinging on a flat plate

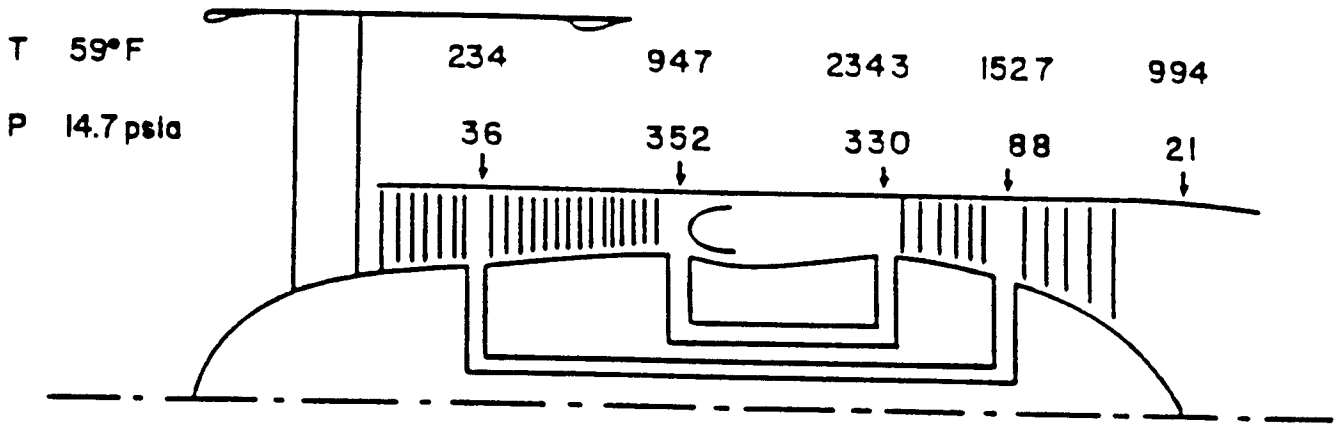


Figure 9: Temperature and pressure ranges in a gas turbine engine

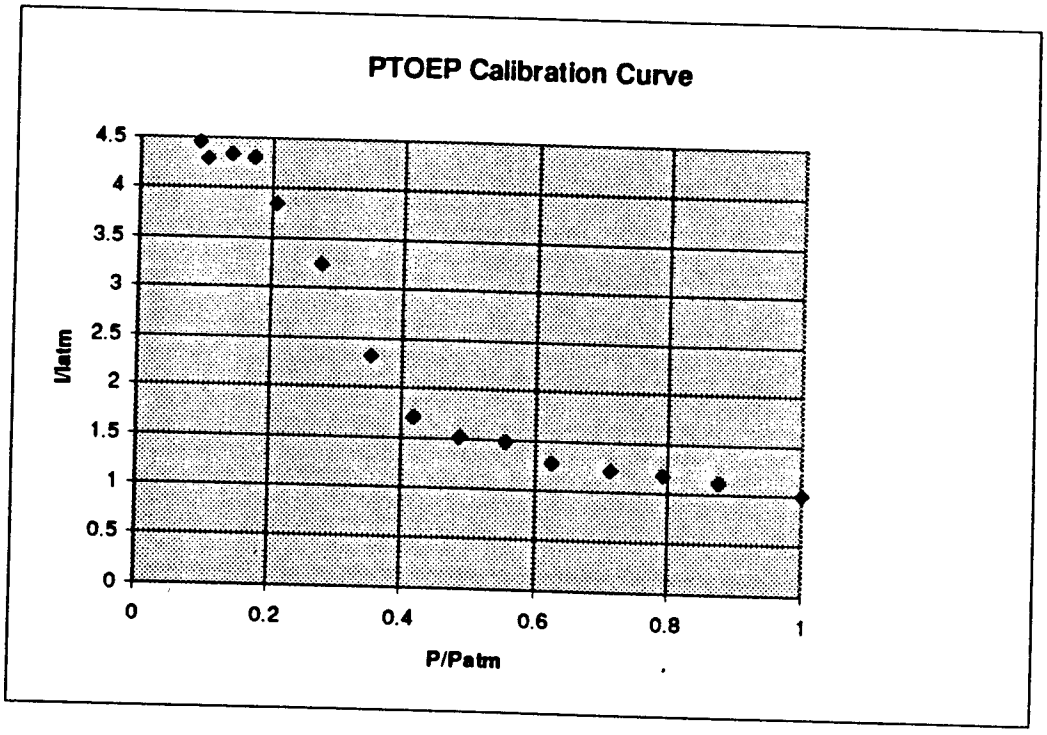


Figure 10: The PTOEP calibration curve

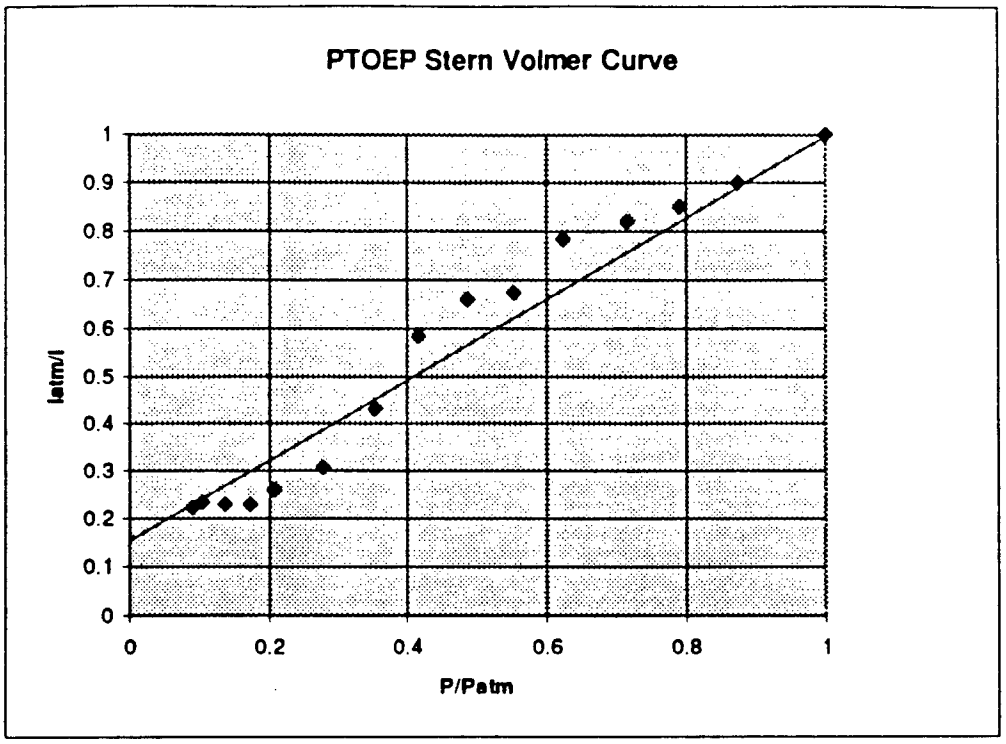


Figure 11: The Stern Volmer curve for PTOEP

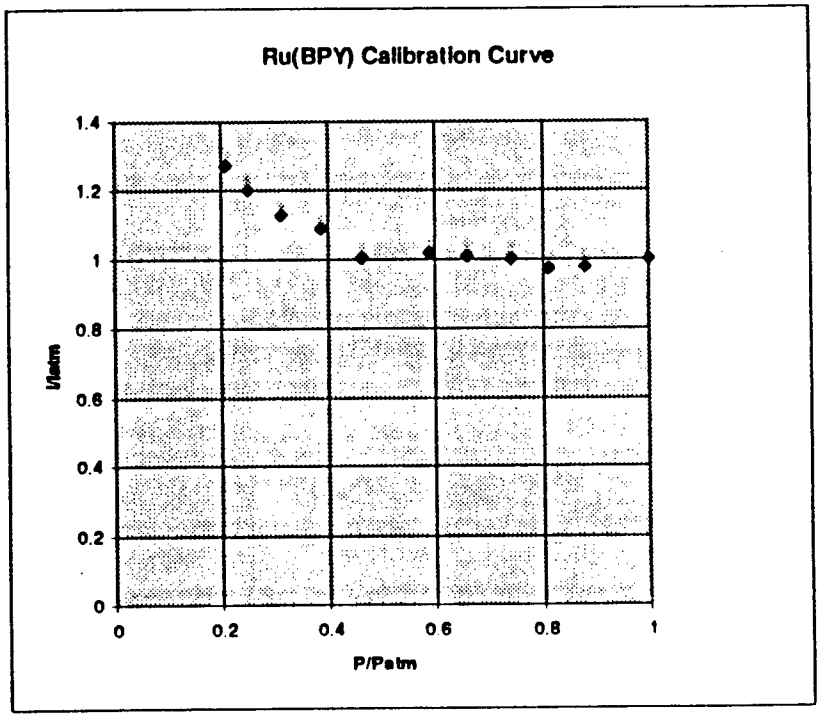


Figure 12: The Ru(BPY) calibration curve

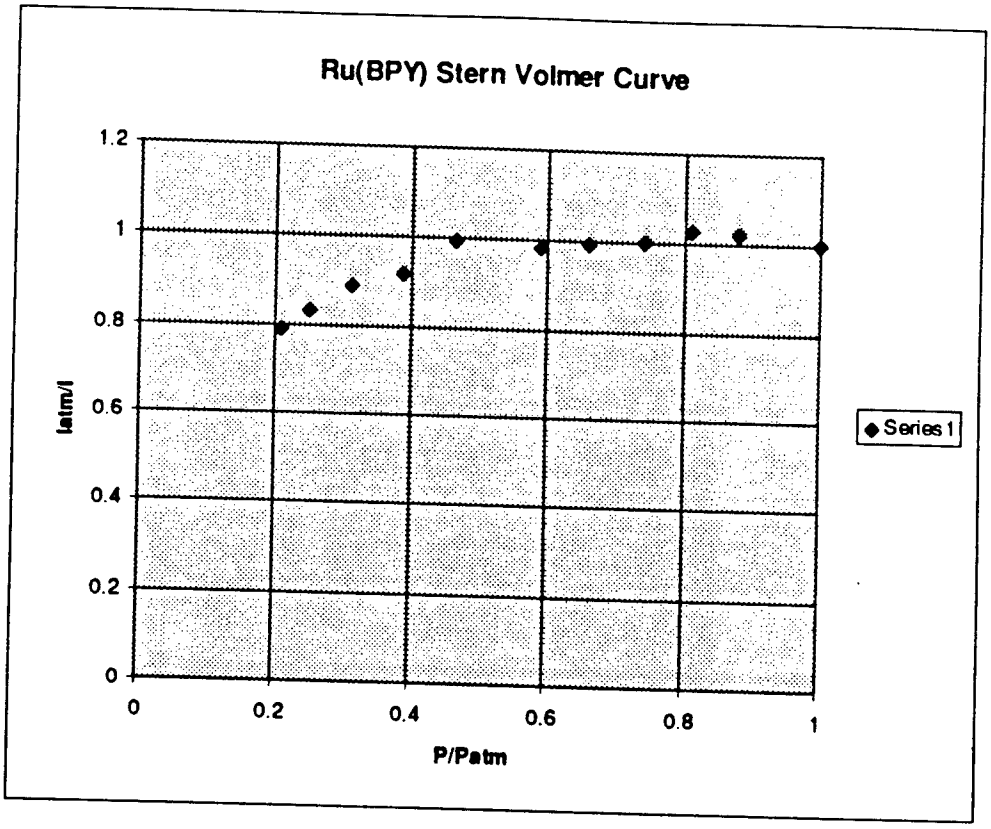


Figure 13: The Stern Volmer curve for Ru(BPY)

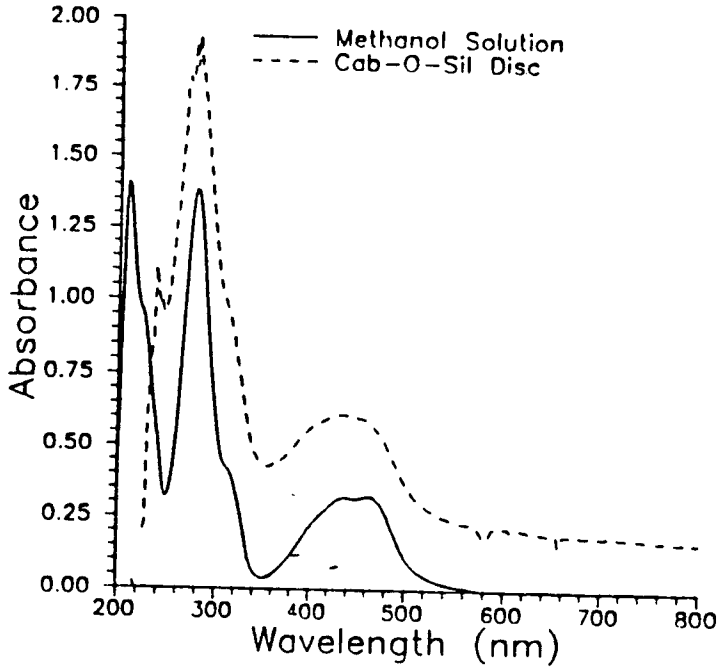


Figure 14: The absorption spectrum of Ru(Ph2phen) in methanol and on a Cab-O-Sil disk

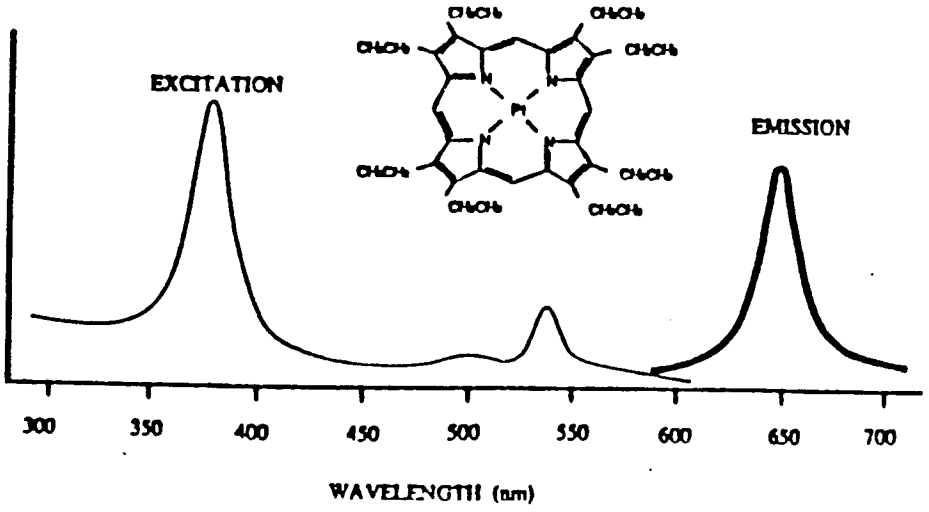


Figure 15: The PTOEP absorption spectrum

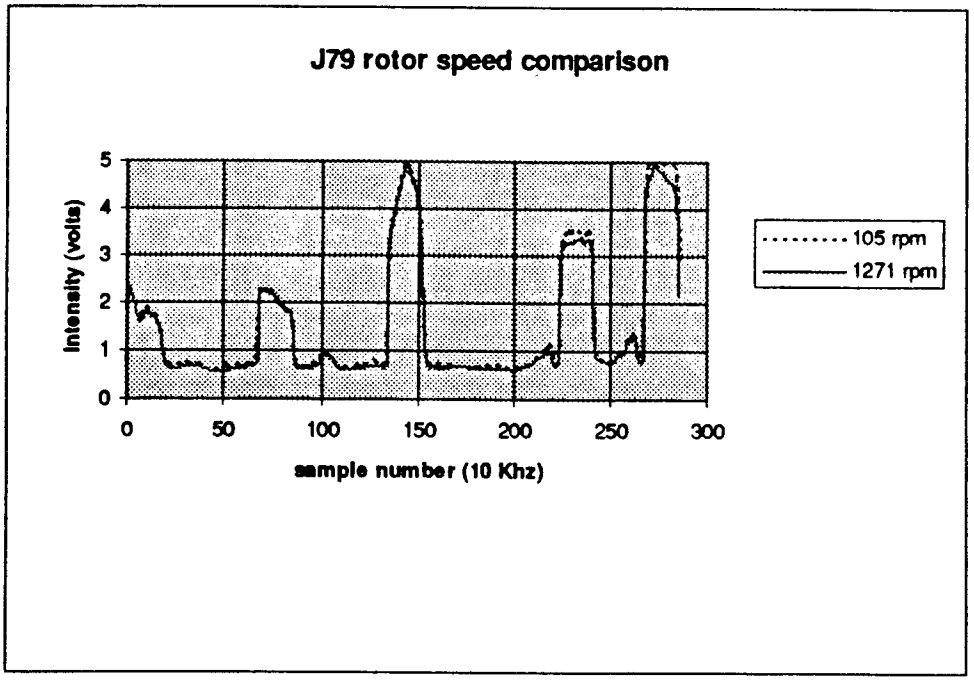


Figure 16: The Pressure paint intensity output from five painted blades

Active Ingredient	Binder	Sensitivity I_{N2}/I_{air}	Mechanical Properties	Emission Efficiency @ 1 atm	λ_{ex} (nm)	λ_{emit} (nm)
AC-1	B1	8.5	WEAK FLEXIBLE	GOOD,(0.6)		
AC-1 or AC-2	B2	6	TOUGH FLEXIBLE	GOOD,(0.9)		
AC-1 or AC-2	B2A	9	TOUGH FLEXIBLE	FAIR,(0.3)		
AC-1 or AC-2	B2B	14	TOUGH FLEXIBLE	FAIR,(0.3)		
AC-1	B3	25	TOUGH HARD	POOR,(0.04)		
PtOEP	B2, B2A	45	TOUGH FLEXIBLE	POOR,(0.01)		
INTECO		5.4				
LPS L2/L2T		4			320-350	425-550
LPS R1/R1T					400-500	500-700
LPS F1/F1T		2.5			320-350	425-550
PSP VB					320-350	350-550
PSP VR					400-500	500-700
PtOEP	Silica Gel	14.29		POOR,(0.086)	366, 543	
PtOEP	GP-197	3.5	BRITTLE HARD	GOOD,(1.0)	366, 543	640
PtOEP	Mod2 GP-197	3.33		POOR,(0.022)	366, 543	640
PtOEP	PMMA	1.63		GOOD,(0.57)	366, 543	640
Ru(BPY)	Silica Gel	4.0	BRITTLE		337, 457	600
Ru(ph_2-phen)						
H_2TFFP	Silica Gel				366, 543	640
Rose Bengal	Silica Gel	1.46		POOR,(0.176)	488	590
Pyrene	Silica Gel	1.52		FAIR,(0.41)	366	490
Perylene	Silica Gel	1.2		FAIR,(0.342)	366	570
Erythrosin B	Silica Gel	1.68		POOR,(0.182)	488	575

Table 1: The many different pressure sensitive paint formulations

GAIN-SCHEDULED BANK-TO-TURN MISSILE AUTOPILOT DESIGN USING LINEAR PARAMETER VARYING TRANSFORMATIONS

Lance H. Carter
Department of Aerospace Engineering and Engineering Mechanics

The University of Texas at Austin
2400 Inner Campus Drive
Austin, TX 78712

Final Report for:
Graduate Student Research Program
Wright Laboratory

Sponsored by:
Air Force Office of Scientific Research
Bolling Air Force Base, DC

September 1994

GAIN-SCHEDULED BANK-TO-TURN AUTOPILOT DESIGN USING LINEAR PARAMETER VARYING TRANSFORMATIONS

Lance H. Carter
Department of Aerospace Engineering and Engineering Mechanics
The University of Texas at Austin

Abstract

This paper presents a gain-scheduled autopilot design for a bank-to-turn (BTT) missile. The approach follows a recent design for a longitudinal missile autopilot. The method is novel in that the gain-scheduled design does not involve linearizations about operating points. Instead, the missile dynamics are brought to a linear parameter varying (LPV) form via a state transformation. An LPV system is defined as a linear system whose dynamics depend upon an a priori unknown but measurable exogenous parameter. This framework is applied to the design of a coupled longitudinal/lateral BTT missile autopilot. The pitch and yaw/roll dynamics are separately transformed to LPV form, where the cross axis states are treated as "exogenous" parameters. These are actually endogenous variables, so such a plant is called "quasi-LPV." Once in quasi-LPV form, a family of robust controllers using $\mathcal{H}^\infty$ optimal control is designed for both the pitch and yaw/roll channels. In both cases the scheduling variables are angle-of-attack and roll rate. The closed-loop response to step commands are simulated with the original nonlinear model.

1 Introduction

Bank-to-turn (BTT) tactical missiles present a particular challenge to autopilot design. BTT maneuvering is characterized by orienting the maximum aerodynamic normal force with the plane of the commanded direction. This is accomplished by rolling and pitching the missile while maintaining a zero sideslip angle. By contrast, skid-to-turn (STT) missiles develop a sideslip angle to change attitude, while the roll rate is minimized or left uncontrolled. Especially in the endgame phase of flight, BTT missiles may develop a large roll rate and angle-of-attack. This causes severe coupling in the system dynamics, which are also very nonlinear. Compared with STT missiles, it is difficult to uncouple the dynamical equations usable for linear classical SISO design techniques.

In [4], a survey of design methods for BTT autopilots is presented. The classical approach, typified by [5], uses linearized models about operating points. The initial design is performed by ignoring the pitch/yaw/roll plane interaction and treating each axis separately. A state-space approach is found in [6]. These largely decouple the model by assuming an axisymmetric geometry and simplified aerodynamic modeling. Most of these methods then schedule gains over the flight envelope designed from the linearized dynamics.

A novel approach to gain-scheduled missile autopilot design is presented in [1]. Rather than linearizing the dynamics via a truncated Taylor series, a family of linear plants is derived from a state transformation of the original dynamics. Since there is no linearization involved, it is not limited to the local operating point. In [1], this method is applied to a longitudinal missile autopilot, where angle-of-attack is the scheduling variable. Such families of linear plants indexed by a scheduling variable are referred to as linear parameter varying (LPV). These differ from linear time-varying plants in that the parameter variations are unknown *a priori,* but may be estimated upon system operation.

This paper closely follows the gain-scheduling approach of [1], but applies it to a fully coupled BTT missile model. A control design is considered during the endgame, when the missile encounters a large and rapidly varying angle-of-attack and roll rate. The key features of the present approach are summarized as follows. First, LPV systems are defined, and are shown to be expressible by certain nonlinear systems. Then the missile mathematical model is developed including (most) kinematic and inertial coupling. Next the dynamics are brought into LPV form by considering separate pitch and yaw/roll dynamics, and applying a suitable transformation. $\mathcal{H}^\infty$ optimal controllers are designed at fixed parameter values. Finally, the

closed-loop response to step commands are simulated with the original nonlinear system.

2 Nonlinear Systems as LPV Plants

LPV systems [1]-[3] are defined as linear systems whose dynamics depend on exogenous time-varying parameters. A state-space description of an LPV system can be represented as

$$\dot{x} = A(\theta)x + B(\theta)u(t) \tag{1}$$

$$y = C(\theta) \tag{2}$$

where θ is a vector of parameters unknown *a priori,* but may be estimated upon operation of the system. Typically, bounds on the parameter magnitude and rate are known. LPV systems therefore differ from LTV systems in that the time variations of the state-space realization matrices in the latter are known beforehand.

A family of controllers, K_θ, can be designed at each frozen parameter θ value, and well known linear design techniques can be used, utilizing convenient computer aided software tools. A gain-scheduling scheme may then consist of interpolating or switching between the linear controllers along the system trajectory.

Although these fixed parameter designs may exhibit good stability and robustness margins for fixed parameter values, it was shown in [2]-[3] that fast variations can be destabilizing. Therefore, only extensive simulations with the nonlinear model can verify control system performance for a particular design.

Certain nonlinear systems can also be represented as LPV plants. The nonlinear system is brought into LPV form using a suitable (nonlinear) transformation. In this case the "exogenous" parameters are actually endogenous to the state dynamics, hence the name "quasi-LPV". An example of this was shown in [1]-[2], for the following nonlinear plant:

$$\frac{d}{dt}\begin{pmatrix} z \\ w \end{pmatrix} = f(z) + A(z)\begin{pmatrix} z \\ w \end{pmatrix} + B(z)u \tag{3}$$

where u is the controller input, and z is the controlled output. References [1]-[2] call these systems "output-nonlinear" since the nonlinearities only depend on the measured output, z. To transform the system to quasi-LPV form, assume that there exist continuously differentiable functions $w_{eq}(z)$ and $u_{eq}(z)$ such that

$$0 = f(z) + A(z)\begin{bmatrix} z \\ w_{eq}(z) \end{bmatrix} + B(z)u_{eq}(z). \tag{4}$$

Then $A(z)$ and $B(z)$ are partitioned to conform with $(z \;\; w)^T$ as

$$A(z) = \begin{bmatrix} A_{11}(z) & A_{12}(z) \\ A_{21}(z) & A_{22}(z) \end{bmatrix}, B(z) = \begin{bmatrix} B_1(z) \\ B_2(z) \end{bmatrix} \tag{5}$$

After some manipulation, the state dynamics can be written as

$$\frac{d}{dt}\begin{bmatrix} z \\ w - w_{eq}(z) \end{bmatrix} = \begin{bmatrix} 0 & A_{12}(z) \\ 0 & A_{22}(z) - Dw_{eq}(z)A_{12}(z) \end{bmatrix}\begin{bmatrix} z \\ w - w_{eq}(z) \end{bmatrix} + \begin{bmatrix} B_1(z) \\ B_2(z) - Dw_{eq}(z)B_1(z) \end{bmatrix}[u - u_{eq}(z)] \tag{6}$$

where $w - w_{eq}(z)$ is the deviation away from the instantaneous equilibrium state parameterized by the output nonlinearity. Equation (6) is a quasi-LPV representation of the original nonlinear plant. Note that the "linearization" is due to a state transformation, rather than to a truncated Taylor series expansion about equilibrium values.

Next, integrators are augmented at the plant input to get the final design plant. As shown in [1], this is desirable in order to avoid updating the applied control signal by the equilibrium term $u_{eq}(z)$, and also to reduce steady-state tracking errors. Letting

$$u = \int \nu$$

the state dynamics become

$$\frac{d}{dt}\begin{bmatrix} z \\ w - w_{eq}(z) \\ u - u_{eq}(z) \end{bmatrix} = \begin{bmatrix} 0 & A_{12}(z) & B_1(z) \\ 0 & A_{22}(z) - Dw_{eq}(z)A_{12}(z) & B_2(z) - Dw_{eq}(z)B_1(z) \\ 0 & -Du_{eq}(z)A_{12}(z) & -Dueq(z)B1(z) \end{bmatrix}\begin{bmatrix} z \\ w - w_{eq}(z) \\ u - u_{eq}(z) \end{bmatrix} + \begin{bmatrix} 0 \\ 0 \\ 1 \end{bmatrix}\nu. \tag{7}$$

A series of controllers can be designed at fixed z values using the above design plant, and a gain-scheduling scheme is implemented. Note that although the controllers are linear designs, the control law is nonetheless nonlinear due to the feedback of the $w_{eq}(z)$ and $u_{eq}(z)$ equilibrium conditions. The following sections illustrate this more clearly, where the above framework is applied to a BTT missile autopilot design.

3 Missile Dynamics

The differential equations used to describe the missile dynamics were derived in a manner similar to that in [7]. They are representative of a BTT airframe traveling at Mach 2.75 and an altitude of 40,000 ft. The missile is considered in the end-game phase of flight, so the total translational velocity magnitude and mass are assumed constant. Furthermore, gravity terms are neglected, but may later be added into the guidance command as a bias. Since a BTT missile is nearly symmetrical in the pitch plane, two of the three cross products of inertia (I_{xy}, I_{yz}) are assumed to be zero. With these assumptions, the missile dynamics are as follows:

$$\dot{\alpha} = K_Q \left[-C_x \sin\alpha + C_z \cos\alpha\right] - \tan\beta(p\cos\alpha - r\sin\alpha) + q \tag{8}$$

$$\dot{\beta} = K_Q \left[C_y \cos\beta - C_x \cos\alpha \sin\beta - C_z \sin\alpha \sin\beta\right] - r\cos\alpha - p\sin\alpha \tag{9}$$

$$\dot{p} = I_1 pq + I_2 QSdC_l + I_3 QSdC_n \tag{10}$$

$$\dot{q} = \frac{1}{I_{yy}}\left[I_{xz}(r^2 - p^2) + (I_{zz} - I_{xx})pr + QSdC_m\right] \tag{11}$$

$$\dot{r} = I_4 pq + I_3 QSdC_l + I_5 QSdC_n \tag{12}$$

where

α = angle of attack

β = angle of sideslip

p = roll rate

q = pitch rate

r = yaw rate

Q = dynamic pressure

S = reference area

d = reference diameter

C_x, C_y, C_z = aerodynamic force coefficients along body x, y, and z axes

C_l, C_m, C_n = aerodynamic moment coefficients about body x, y, and z axes

I_{xx}, I_{yy}, I_{zz}, I_{xz} = moments of inertia

$I_1 - I_5$ = constants dependent upon moments of inertia

K_Q = constant dependent upon flight condition.

The missile mass property and flight condition data are given in the appendix. Note the above equations exhibit significant explicit kinematic and inertial coupling, and implicit coupling through the aero coefficients. Specifically, a BTT missile will develop a large roll rate and angle of attack while maintaining a small sideslip angle. Therefore, the roll rate will induce a large yaw rate through Equation (9). These roll/yaw rates will then be coupled into the pitch plane dynamics via Equation (11). The pitch dynamics also appear in the yaw/roll equations.

The controls appear in the aerodynamic force and moment coefficients, which, in general, are complicated nonlinear functions of both the states and the controls. These are in the form of tabular data, and so functional approximations were created by curve-fitting. The resulting aerodynamic model is as follows:

$$C_x(\alpha) = C_{x_o} + C_{x_\alpha}\alpha \tag{13}$$

$$C_y(\beta, \delta_r) = C_{y_\beta}\beta + C_{y_{\delta_r}}\delta_r \tag{14}$$

$$C_z(\alpha, \delta_q) = C_{z_o} + C_{z_\alpha}\alpha + C_{z_{\delta_q}}\delta_q \tag{15}$$

$$C_l(\alpha, \beta, \delta_p, \delta_r) = (a_1 + a_2\alpha)\beta + C_{l_{\delta_p}}\delta_p + a_3\alpha\delta_r \tag{16}$$

$$C_m(\alpha, \delta_q) = C_{m_o} + C_{m_\alpha}\alpha + C_{m_{\delta_q}}\delta_q \tag{17}$$

$$C_n(\delta_r) = C_{n_{\delta_r}}\delta_r \tag{18}$$

$$\tag{19}$$

where

δ_p = idealized roll control deflection

δ_q = idealized pitch control deflection

δ_r = idealized yaw control deflection.

A real missile airframe produces these idealized control deflections through fin mixing logic, not modeled here. All other terms in Equations (13-18) are constant stability derivatives, which are given in the appendix. These functions were chosen to approximate the tabular data to within $\pm 20\%$ over a range of $\alpha = [-10, 20]$ degrees and $\beta = \pm 5$ degrees.

4 Missile Autopilot Design

The following sections present the missile autopilot design. The above quasi-LPV method is applied to the BTT missile airframe dynamics to yield a pitch/yaw/roll gain-scheduled controller. The full states are assumed available for feedback, but in practice some must be estimated. First, in Section 4.1 the general design goals and methodology are discussed. The control law is designed in two separate channels, referred to as the "pitch channel" and the "yaw/roll channel." These controllers, described in Sections 4.2 and 4.3 respectively, are designed using $\mathcal{H}^\infty$ control theory. Section 5 shows the gain-scheduling scheme and the closed-loop simulation results with the original nonlinear equations.

4.1 Design Methodology

The guidance commands for a BTT airframe may require a large angle of attack and roll rate, while minimizing the sideslip angle, which results in a coordinated turn. Therefore, the control system design goals are to follow a simultaneous 20 degree step command in angle of attack, α_c, and a 300 deg/sec roll rate command, p_c. The sideslip angle, β, is commanded to zero, with the objective of maintaining $|\beta| \leq 5^o$. In practice, α is not commanded directly, but indirectly via normal acceleration commands. It is also desired to maintain a "reasonable" closed-loop performance in the presence of uncertainties in model parameters and unmodeled (flexible) dynamics. For the purposes of this preliminary study, specific time response performance objectives (percent overshoot, rise time, etc.) are not given.

As previously noted, the missile dynamics are highly coupled and nonlinear. A high roll rate and angle of attack induce a high yaw rate and pitch/yaw/roll kinematic coupling. The design challenge is to devise linear design models conducive to gain-scheduling techniques, while capturing the nonlinear structure of the system. The present approach uses the quasi-LPV framework to yield linear design plants not the result of Taylor series truncations. In [1], this was done for a longitudinal missile autopilot.

Towards this end, we seek a partition of the nonlinear missile dynamics, Equations (8-12), in the form of $[z \;\; w]^T$, such that the dynamics can be written as in Equation (3). In others words, all nonlinearities must be contained in the z states, or as products with the w states. Then a set of algebraic nonlinear equations must be solved (Equation (4)) for the equilibrium functions $w_{eq}(z)$ and $u_{eq}(z)$. For the missile problem, no such analytical solution can be found without greatly simplifying the dynamics.

To solve this problem, the control design is separated into a "pitch channel" and a "yaw/roll" channel. That is, the pitch channel uses only the $\dot{\alpha}$ and $\dot{q}$ equations. A pitch control law is designed for the pitch control deflection δ_q, to achieve the commanded angle-of-attack α_c. The yaw/roll states are considered as exogenous varying parameters.

Similarly, the yaw/roll channel uses only the $\dot{\beta}$, $\dot{p}$, and $\dot{r}$ equations. A yaw/roll control law is designed for the yaw control deflection δ_r, and the roll control deflection δ_p, to achieve the commanded roll rate p_c and zero sideslip. The pitch states are considered as exogenous varying parameters.

Another reason for this approach is the physical intuition that the pitch deflection primarily effects the angle-of-attack and pitch rate, while the yaw/roll deflections primarily effect the sideslip angle, yaw, and roll rates.

Finally, robust controllers using $\mathcal{H}^\infty$ optimal control are designed at various frozen parameter values for both the pitch and yaw/roll channels. Then a switching gain-schedule logic is implemented to achieve a global controller.

4.2 Pitch Channel Autopilot

For the purpose of design, the only addition assumption to be made is that the sideslip angle β is small. Then the pitch dynamics (Equations (8), (11)) can be written as

$$\begin{pmatrix} \dot{\alpha} \\ \dot{q} \end{pmatrix} = f(\alpha, p, r) + \begin{bmatrix} 0 & 1 \\ 0 & 0 \end{bmatrix} \begin{pmatrix} \alpha \\ q \end{pmatrix} + B(\alpha)\delta_q \tag{20}$$

where

$$f(\alpha, p, r) = \begin{pmatrix} K_Q \left[-(C_{x_o} + C_{x_\alpha}\alpha)\sin\alpha + (C_{z_o} + C_{z_\alpha}\alpha)\cos\alpha \right] \\ \left[I_{xz}(r^2 - p^2) + (I_{zz} - I_{xx})pr + QSd(C_{m_o} + C_{m_\alpha}\alpha) \right] / I_{yy} \end{pmatrix} \tag{21}$$

$$B(\alpha) = \begin{pmatrix} C_{z_{\delta_q}} \cos\alpha \\ \\ QSdC_{m_{\delta_q}} / I_{yy} \end{pmatrix}. \tag{22}$$

These equations are in the form of Equation (3), where $z = \alpha$ and $w = q$. The yaw/roll states (p, r) are

considered exogenous parameters. Next, Equation (4) is solved for the equilibrium functions $u_{eq}(z)$, $w_{eq}(z)$ resulting in

$$u_{eq}(z) = \delta_{q_{eq}}(\alpha, p, r) = -(C_{m_o} + C_{m_\alpha}\alpha)/C_{m_{\delta_q}} + \left[I_{xz}(r^2 - p^2) + (I_{zz} - I_{xx})pr\right]/QSdC_{m_{\delta_q}} \tag{23}$$

$$w_{eq}(z) = q_{eq}(\alpha, p, r) = -K_Q\left[-(C_{x_o} + C_{x_\alpha}\alpha)\sin\alpha + (C_{z_o} + C_{z_\alpha}\alpha + C_{z_{\delta_q}}\delta_{q_{eq}})\cos\alpha\right]. \tag{24}$$

Thus, the pitch dynamics can be written in the form of Equation (7), leading to the pitch channel design plant

$$\frac{d}{dt}\begin{bmatrix} \alpha \\ q - q_{eq}(\alpha) \end{bmatrix} = \tilde{A}(\alpha, p, r)\begin{bmatrix} \alpha \\ q - q_{eq}(\alpha) \end{bmatrix} + \tilde{B}(\alpha)\left[\delta_q - \delta_{q_{eq}}(\alpha, p, r)\right] \tag{25}$$

where $\tilde{A}(\alpha, p, r)$, $\tilde{B}(\alpha)$ are the transformed state-space matrices.

$\mathcal{H}^\infty$ controller designs were performed at fixed (α, p, r) values. See [9] for a complete discussion of $\mathcal{H}^\infty$ control theory. Briefly, the performance and robustness objectives are expressed as weighted perturbations on the design plant. Following the notation of [8], Figure 1 shows a generalized plant, controller, and perturbation block. Then generalized plant contains the design plant, plus weighting functions which normalize the perturbation such that $\|\Delta\|_\infty \leq 1$. The signal w contains all external inputs, x is an error signal, y is the measurements, and u is the control input. Let T_{xw} denote the closed-loop transfer function from w to x. Then a numerical iterative procedure was performed that finds a controller K such that $\|T_{xw}\|_\infty < \gamma$ if one exists. It is well known that $\|T_{xw}\|_\infty$ is an (arbitrarily conservative) upper-bound on a necessary and sufficiency condition for robust performance under structured uncertainty. Nevertheless, $\|T_{xw}\|_\infty < 1 \Rightarrow$ robust performance achieved. The interconnection structure for the pitch channel analogous to Figure 1 is shown in Figure 2, where

$$w = \begin{pmatrix} \alpha_c \\ d_r \\ n_1 \\ n_2 \end{pmatrix} \tag{26}$$

$$x = \begin{pmatrix} x_p \\ x_r \\ x_p \end{pmatrix} \tag{27}$$

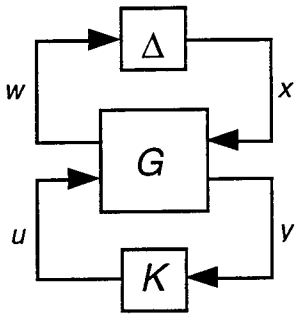


Figure 1: Generalized Plant Interconnection Structure

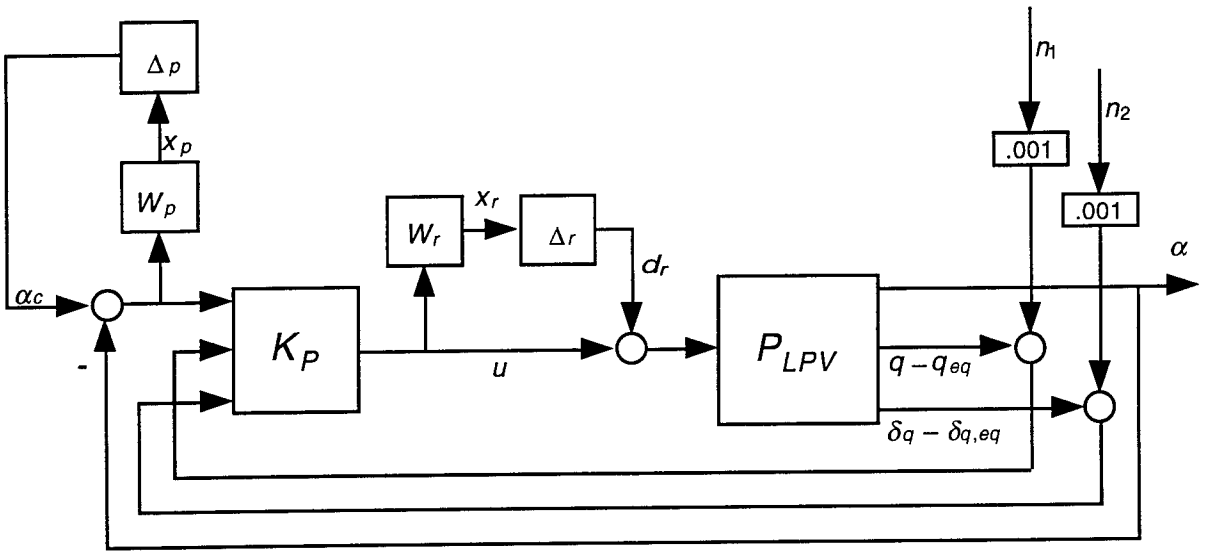


Figure 2: Pitch Channel Interconnection Structure

$$y = \begin{pmatrix} \alpha_c - \alpha \\ q - q_{eq} + n_1 \\ \delta_q - \delta_{q_{eq}} + n_2 \end{pmatrix}. \tag{28}$$

The W_r and W_p blocks are the robustness and performance weighting functions, respectively. These are taken directly from [1]. W_r reflects unmodeled flexible mode dynamics given by

$$W_r(s) = 2\frac{(s+100)(s+200)}{(s+1000)(s+2000)} \tag{29}$$

and the performance weighting, W_p is given by

$$W_p(s) = \frac{7(s+40)}{40(s+0.0001)}. \tag{30}$$

The signals n_1 and n_2 are small artificial noises necessary to satisfy rank conditions in the generalized plant.

Finally, four pitch channel controllers were designed at the following set points of α and p. The design yaw rate r was held fixed at zero. The units are in degrees and deg/sec.

K_{P11}, for $\alpha = 0$, $p = 0$

K_{P12}, for $\alpha = 0$, $p = 300$

K_{P21}, for $\alpha = 20$, $p = 0$

K_{P22}, for $\alpha = 20$, $p = 300$

All four controllers achieved robust performance for fixed α and p in $\tilde{A}(\alpha, p, r)$, $\tilde{B}(\alpha)$.

4.3 Yaw/Roll Channel Autopilot

The yaw/roll channel autopilot is developed in a manner very similar to that of the pitch channel. For the design plant, the sideslip angle β is again assumed to be small. Then the yaw/roll dynamics (Equations (9), (10), (12)) can be written as

$$\begin{pmatrix} \dot{\beta} \\ \dot{p} \\ \dot{r} \end{pmatrix} = f(\beta, p, \alpha, q) + \begin{bmatrix} K_Q C_{y_\beta} & 0 & -\cos\alpha \\ 0 & 0 & 0 \\ 0 & 0 & 0 \end{bmatrix} \begin{pmatrix} \beta \\ p \\ r \end{pmatrix} + B(\beta, p, \alpha, q) \begin{pmatrix} \delta_p \\ \delta_r \end{pmatrix} \tag{31}$$

where

$$f(\beta, p, \alpha, q) = \begin{pmatrix} -p\sin\alpha \\ I_1 pq \\ I_4 pq \end{pmatrix} \tag{32}$$

$$B(\alpha) = \begin{pmatrix} 0 & C_{y_{\delta_r}} \\ I_2 QSdC_{l_{\delta_p}} & QSd(I_2 a_3 \alpha + I_3 C_{n_{\delta_r}}) \\ I_3 QSdC_{l_{\delta_p}} & QSd(I_3 a_3 \alpha + I_5 C_{n_{\delta_r}}) \end{pmatrix}. \tag{33}$$

Again, these equations are in the form of Equation (3), where $z = [\beta \;\; p]^T$ and $w = r$. The pitch states (α, q) are treated as exogenous parameters. Equation (4) is again solved for the equilibrium functions $u_{eq}(z)$ and $w_{eq}(z)$, where $u_{eq}(z)$ now has two components corresponding to the yaw control deflection and the roll control deflection. The result is

$$u_{eq,1}(z) = \delta_{p_{eq}}(\beta, p, \alpha, q) = -(I_3 a_3 \alpha + I_5 C_{n_{\delta_r}})\delta_{r_{eq}} / I_3 C_{l_{\delta_p}} - I_4 pq / I_3 QSdC_{l_{\delta_p}} \tag{34}$$

$$u_{eq,2}(z) = \delta_{r_{eq}}(\beta, p, \alpha, q) = pq(I_2 I_4 - I_1 I_3) / QSdC_{n_{\delta_r}}(I_3^2 - I_2 I_5) \tag{35}$$

$$w_{eq}(z) = r_{eq}(\beta, p, \alpha, q) = K_Q \left[C_{y_\beta} \beta + C_{y_{\delta_r}} \delta_{r_{eq}} \right] / \cos\alpha - p \tan\alpha. \tag{36}$$

Now the yaw/roll dynamics can be written in the form of Equation (7), leading to the yaw/roll channel design plant

$$\frac{d}{dt} \begin{bmatrix} \beta \\ p \\ r - r_{eq}(\beta, p, \alpha, q) \end{bmatrix} = \tilde{A}(\beta, p, \alpha, q) \begin{bmatrix} \beta \\ p \\ r - r_{eq}(\beta, p, \alpha, q) \end{bmatrix} + \tilde{B}(\beta, p, \alpha, q) \begin{bmatrix} \delta_p - \delta_{p_{eq}}(\beta, p, \alpha, q) \\ \delta_r - \delta_{r_{eq}}(\beta, p, \alpha, q) \end{bmatrix} \tag{37}$$

where $\tilde{A}(\beta, p, \alpha, q)$, $\tilde{B}(\beta, p, \alpha, q)$ are the transformed state-space matrices.

As in the pitch channel, $\mathcal{H}^\infty$ controller designs were performed at fixed (α, p) values. The interconnection structure for the yaw/roll channel is shown in Figure 3, where

$$w = \begin{pmatrix} \beta_c \\ p_c \\ d_r(2) \\ n_1 \\ n_2 \\ n_3 \end{pmatrix} \tag{38}$$

$$x = \begin{pmatrix} x_p(2) \\ x_r(2) \\ x_p(2) \end{pmatrix} \tag{39}$$

$$y = \begin{pmatrix} \beta_c - \beta \\ p_c - p \\ r - r_{eq} + n_1 \\ \delta_p - \delta_{p_{eq}} + n_2 \\ \delta_r - \delta_{r_{eq}} + n_3 \end{pmatrix}. \tag{40}$$

The W_r and W_p weighting functions are the same as in the pitch channel, except that they are now $2x2$ blocks.

Four yaw/roll channel controllers were designed at the following set points of α and p, where β and q were held fixed at zero. The units are in degrees and deg/sec.

K_{Y11}, for $\alpha = 0$, $p = 0$

K_{Y12}, for $\alpha = 0$, $p = 300$

K_{Y21}, for $\alpha = 20$, $p = 0$

K_{Y22}, for $\alpha = 20$, $p = 300$

Again, all four controllers achieved robust performance for fixed α and p in $\tilde{A}(\beta, p, \alpha, q)$, $\tilde{B}(\beta, p, \alpha, q)$.

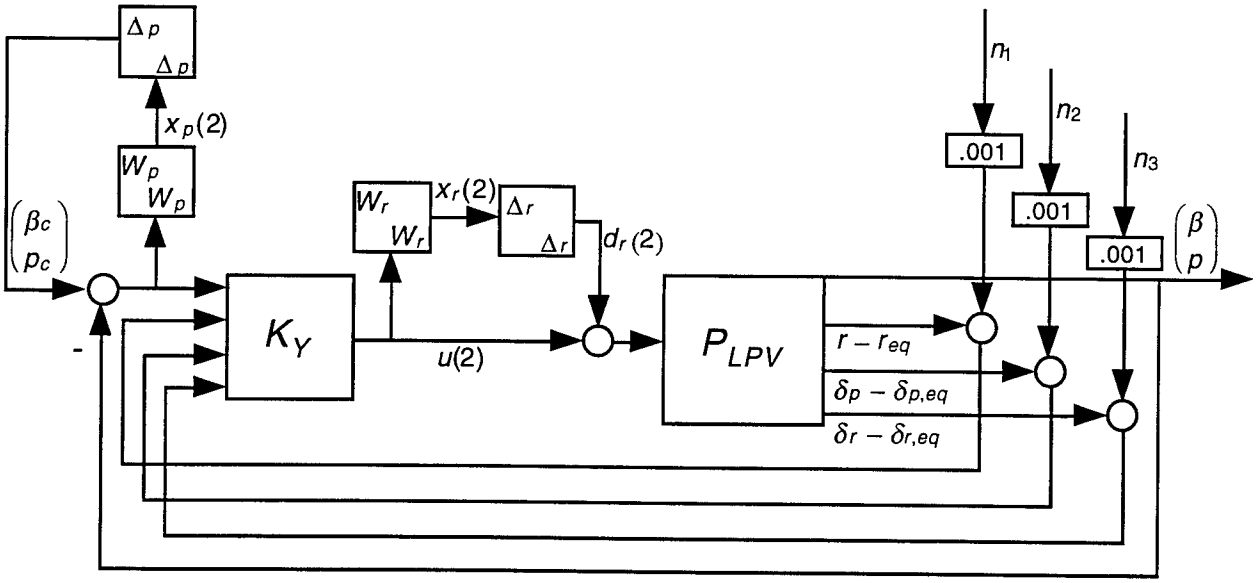


Figure 3: Yaw/Roll Channel Interconnection Structure

5 Simulation Results

Although the controllers achieved robust performance for fixed parameter values, there is no guarantee of even stability for fast parameter variations. This is not a result of poor stability margins in the fixed-point designs, but of the fact that for fast parameter variations the true dynamics are no longer being accurately represented. Furthermore, for this problem the controller feeds back updated equilibrium functions of the states, which is a kind of feedback linearization. Therefore, simulations with the nonlinear plant are required to verify stability and performance.

Figure 4 shows the actual implementation of the pitch/yaw/roll global controller with the nonlinear missile model. The block T represents the transformation to the deviation from equilibrium conditions form of the states. Note that although the control designs were linear, the control law is nonlinear because of this transformation (and the gain-scheduling).

The gain-scheduling scheme is of the "switching" type dependent on the instantaneous values of (α, p) as follows:

$$K_{P,Y} = \begin{cases} K_{11} & \text{for} \quad \alpha \leq 10^o \quad p \leq 150 \text{ deg/sec} \\ K_{12} & \text{for} \quad \alpha \leq 10^o \quad p > 150 \text{ deg/sec} \\ K_{21} & \text{for} \quad \alpha > 10^o \quad p \leq 150 \text{ deg/sec} \\ K_{22} & \text{for} \quad \alpha > 10^o \quad p > 150 \text{ deg/sec.} \end{cases} \tag{41}$$

Both the pitch and yaw/roll controllers were scheduled in this manner.

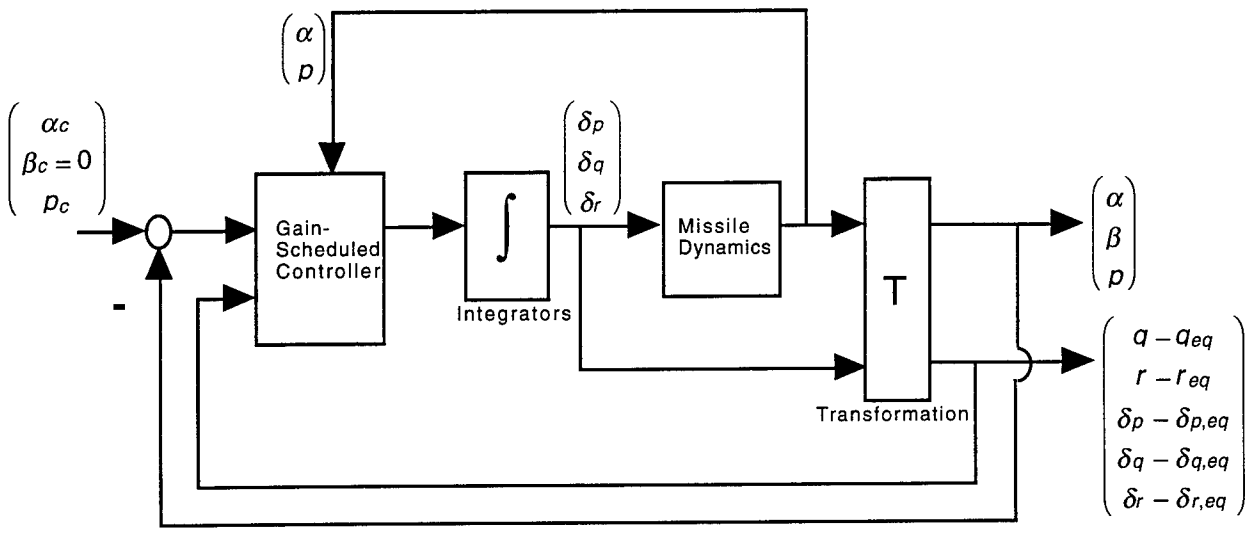


Figure 4: Angle-of-Attack Response to Step Command

The missile was trimmed at $\alpha = 0$ degrees and $p = 0$ deg/sec and the response was simulated to a simultaneous step command of $\alpha = 20$ degrees and $p = 300$ deg/sec. These results were found to be unstable, believed due to the fast variations of the pitch and roll body rates in the equilibrium functions $\delta_{p_{eq}}(\alpha, p, q)$ and $\delta_{r_{eq}}(\alpha, p, q)$. When (p, q) were frozen at a design point in these functions, the response stabilized. Figures 5, 6, and 7 show the resulting step response for the angle-of-attack, sideslip, and roll rate. Figure 8 shows the pitch, yaw, and roll control deflections.

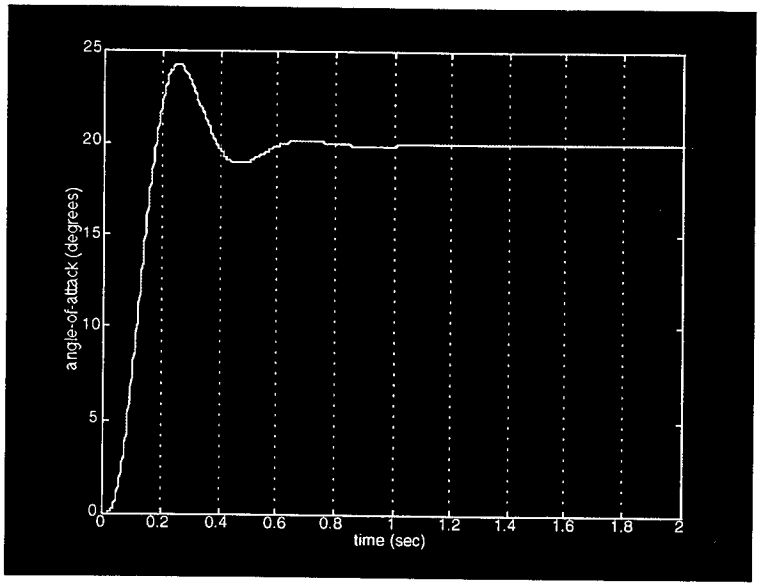


Figure 5: Angle-of-Attack Response to Step Command

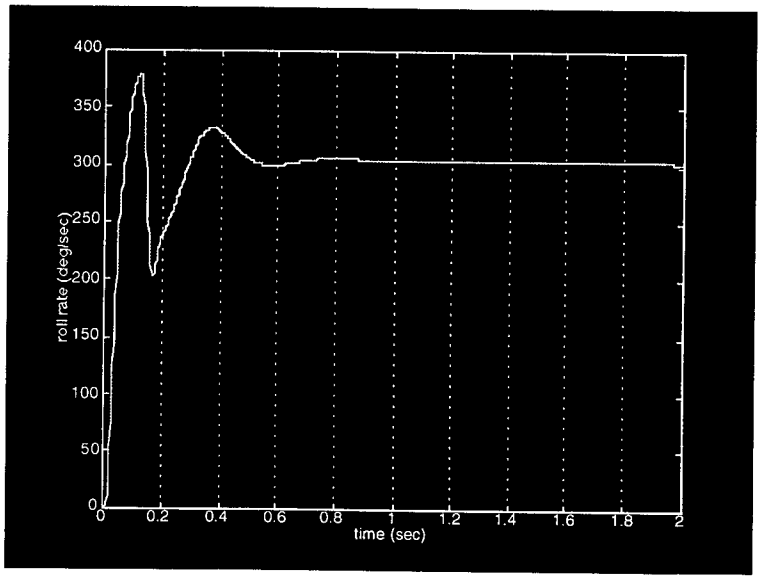


Figure 6: Roll Rate Response to Step Command

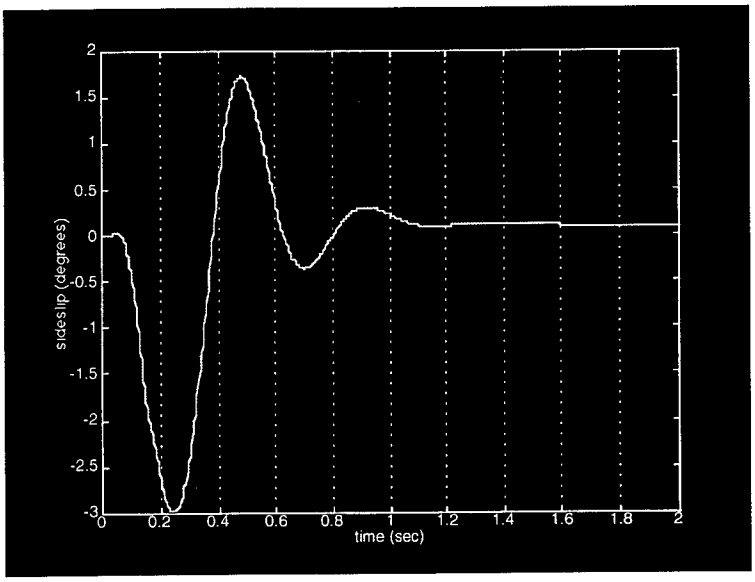


Figure 7: Sideslip Angle Response to Step Command

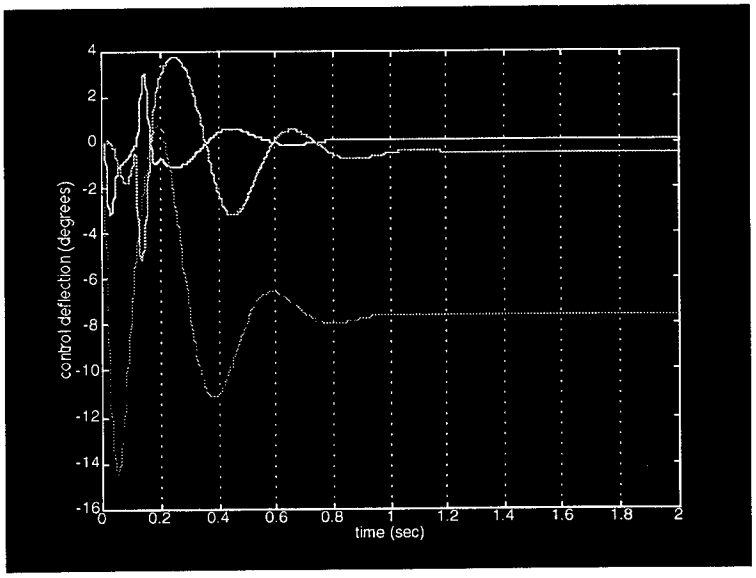


Figure 8: Control Deflections Response to Step Command

6 Conclusions and Future Work

This paper presented a gain-scheduled autopilot design for a BTT missile. The approach followed that of [1], in which the missile dynamics were brought into LPV form via a state transformation rather than a local linearization. The highly coupled and nonlinear dynamics necessitated the use of separate pitch and yaw/roll channels, where the cross channel states were treated as "exogenous" parameters. $\mathcal{H}^\infty$ optimal controllers were designed at fixed points, and a switching gain-scheduler was simulated for step commands in angle-of-attack and roll rate.

Future work could include the following. The controller design can be refined, such as by tuning the weighting functions and using μ-synthesis. Actuator dynamics and gravity terms can be added to the missile model. An observer can be designed to estimate unmeasurable states. Finally, a full 6 DOF simulation can be run including a guidance law and target model, to compute miss distances for a comparison to other BTT autopilot designs.

Appendix: Missile Data

Flight Condition

Mach	=	2.75
alt.	=	40,000 ft
Q	=	2073.7 lbs/ft^2
K_Q	=	0.0339 sec^{-1}

Missile Mass Properties and Geometry

All mass moment of inertias are in slug-ft^2.

I_{xx}	=	1.0798
I_{yy}	=	70.131
I_{zz}	=	70.6609
I_{xz}	=	-0.7043
I_1	=	-0.0150
I_2	=	0.9322
I_3	=	-0.0093
I_4	=	-0.9771
I_5	=	0.0142

Weight	=	227 lbs
S	=	0.3068 ft^2
d	=	7.5 inches

Aerodynamic Model Coefficients

C_{x_o} = -0.4962
C_{x_α} = 0.1699

C_{y_β} = -11.1180
$C_{y_{\delta_r}}$ = 4.6346

C_{z_o} = -0.1006
C_{z_α} = -27.2417
$C_{z_{\delta_q}}$ = -5.4832

a_1 = 1.4008
a_2 = -25.7771
a_3 = -4.4423
$C_{l_{\delta_p}}$ = -7.2605

C_{m_o} = -1.4785
C_{m_α} = -5.6355
$C_{m_{\delta_q}}$ = -38.7896

$C_{n_{\delta_r}}$ = -33.6611

Acknowledgments

This research was supported by an Air Force Office of Scientific Research (AFOSR) Summer Graduate Student Fellowship at the U.S. Air Force Armament Directorate, Eglin Air Force Base, FL. The author thanks Jim Cloutier, Chris D'Souza, and Darren Schumacher for invaluable technical support and guidance. The author also thanks Kristen Kichline for generating the figures.

References

[1] J.S. Shamma and J.R. Cloutier, "Gain-Scheduled Autopilot Design using Linear Parameter Varying Transformations," *J. Guidance, Control, and Dynamics,* Vol.16, No.2, pp. 256-263, March-April 1993.

[2] J.S. Shamma and M. Athans, "Gain Scheduling: Potential Hazards and Possible Remedies," *IEEE Control Systems Magazine,* pp.101-107, June 1992.

[3] J.S. Shamma and M. Athans, "Guaranteed Properties of Gain Scheduled Control for Linear Parameter-varying Plants," *Automatica,* Vol. 27, No.3. pp. 559-564, 1991.

[4] J.R. Cloutier, J.H. Evers, and J.J. Feeley, "An Assessment of Air-to-Air Missile Guidance and Control Technology," *Proc. of the American Control Conference,* June 1988.

[5] M.J. Kovach, T.R. Stevens, and A. Arrow, "A Bank-to-Turn Autopilot Design for an Advanced Air-to-Air Interceptor," *Proc. AIAA GNC Conf.*, pp.1346-1353, Monterey, Aug 1987.

[6] J.A. Bossi and M.A. Langehough, "Multivariable Autopilot Designs for a Bank-to-Turn Missile," presented at the 1988 American Control Conference, Atlanta, June 1988.

[7] C.N. D'Souza and D.A. Schumacher, "Derivation of the Full Nonlinear Equations of Motion for a Rigid Airframe," to be published.

[8] G. Balas, J.C. Doyle, K. Glover, A. Packard, and R. Smith, "μ-Analysis ans Synthesis Toolbox: μ-Tools," MUSYN, Inc., and The Mathworks, Inc., December 1990.

[9] J.C. Doyle, K. Glover, P.P. Khargonekar, and B.A. Francis, "State Space Solutions to Standard H_2 and H_∞ Control Problems," *IEEE Trans. Automat. Contr.*, Vol.34, pp.831-846, 1989.

SYNTHESIS & CHARACTERIZATION OF LANTHANUM PHOSPHATE SOL FOR FIBER COATING

PENG CHEN
Graduate Student
Department of Chemistry

University of North Texas
P.O.Box 6169
Denton, TX 76203

Final Report for:
Graduate Student Research Program
Wright Laboratory

Sponsored by:
Air Force Office of Scientific Research
Bolling Air Force Base, DC

and

Wright Laboratory

August 1994

SYNTHESIS & CHARACTERIZATION OF LANTHANUM PHOSPHATE SOL FOR FIBER COATING

PENG CHEN
Graduate Student
Department of Chemistry
University of North Texas

Abstract

Varies routes to synthesize lanthanum phosphate sol have been explored. Thus powdered lanthanum phosphate sol were characterized using powder x-ray diffraction (XRD) and differential thermal analysis/thermogravimetric analysis (DTA/TGA). Appreciable crystallization of lanthanum phosphate ($LaPO_4$) was observed above 400 °C and the average crystallite sizes were calculated as 150 Å, and 460 Å after heat treatment at 700 °C and 1100 °C respectively. Dip coatings of $LaPO_4$ onto sapphire fibers were carried out. The coated fibers were calcined at 1100 °C and examined using scanning electron microscope. The thickness of the coating ranged 60 to 150 nm depending upon the sol concentration and number of dip-coating. XRD of coated fibers revealed the formation of $LaPO_4$ after heat treatment above 700 °C.

TABLE OF CONTENTS

Figure 1.	XRD pattern of La_2O_3 after 700 °C	page 6-12
Figure 2.	XRD pattern of $La(OH)_3$	page 6-12
Figure 3.	XRD pattern of $LaPO_4$ after 700 °C	page 6-13
Figure 4.	XRD pattern of LaP_3O_9 after 700 °C	page 6-13
Figure 5.	XRD pattern of $LaPO_4$ sol after 1100 °C	page 6-14
Figure 6.	XRD pattern of $LaPO_4$ sol after 1200 °C	page 6-14
Figure 7.	XRD pattern of uncoated sapphire fibers	page 6-15
Figure 8.	XRD pattern of coated sapphire fibers	page 6-15
Figure 9.	$LaPO_4$ sol DTA/TGA room temperature to 1200 °C	page 6-16
Figure 10.	SEM RSD image of sol dip coated sapphire fiber	page 6-17
Figure 11.	SEM Micro graph of coated (0.01M sol)fiber cross section	page 6-17
Figure 12.	SEM Micro graph of coated (0.05M sol)fiber cross section	page 6-18
Figure 13.	SEM Micro graph of coated (0.05M sol)fiber cross section	page 6-18

SYNTHESIS & CHARACTERIZATION OF LANTHANUM PHOSPHATE SOL FOR FIBER COATING

Peng Chen

INTRODUCTION

A sol is a colloidal suspension of solid particles in a liquid. A colloid is a suspension in which the dispersed phase is so small that gravitational force can be ignored and interactions between particles are dominated by van der Waals force and surface charges. Virtually, any kinds of solid particles can be presence in terms of sol. A gel is a semisolid two-component system, rich in liquid. The sol is not necessarily amorphous, but is always a liquid. A gel is usually noncrystalline material and has a whole skeleton structure. It is clearly not a liquid. The formation and stability of sol are strongly depending on particle's size, concentration, temperature, reaction type, pH of system, and salt effect [Zakharova, 1992].

It is widely used to generate a thin film on surface since chemical concentration in the sol is low. Such a thin film can dramatically affect the properties of a material. For example, if a few monolayers of diamonds were coated on steel surface, one can expect weariness increased many folds due to the toughness of micro diamonds on surface. Currently, some advanced ceramics composites have demonstrated unique properties for potential practical applications, such as high temperature tolerance, high strength as well as escape radar detection. A ceramic is usually any metal oxide, nitrides and carbides in non crystalline & crystalline. Advanced ceramics materials are sintered compound based on carbides, nitride and oxides, or combinations of these compounds, and are characterized by rigid & highly directional atomic bonding that provides them with great hardness and high temperature stability. They are different from conventional ceramics. Mainly in the way they are made and formed by hot pressing or sintering fine powders.

As composite materials, they consist of at least two components. This gives them properties different and in many cases superior to those of the individual phases. If stronger fiber compatible with their surrounding matrices, that means the matrices must be compatible and have good bonding with fibers it supports. A tougher fiber can be relatively easy to obtain, but for a good matrix it is not true.

For instance, first generation glass fibers are easy to make, then Kevlar fiber, carbon fiber, silica carbides to boron nitrite fiber are all commercialized.

The harmony between reinforced fiber and matrix plays crucial role. For instance, carbon fiber with Young's modules 41000 MN/m^{-2}, but only half of strength left in composite with a matrix 20000 MN/m^{-2}. BN is very strong fiber, but it is difficult to find suitable matrix to turn into the practically useful advanced composite materials.

Integrity between matrix and fiber plays an another key role in any advanced composites. Matrix can be easy to crack but is not true for fiber because of its strength. Interfacial properties are one of most important factor of the integrity of composites.

Interfacial properties between fiber and matrix are obvious requirements for some specific applications. Morgan and Novinson have introduced functional interface for composite materials [Novinson, 1990, Morgan, 1993]. It is indicated that $LaPO_4$ [monazite type, Carron, 1958] may play a role between fibers and matrix to make whole composites useful. As reported earlier, $LaPO_4$ crystal can be used to improve the high temperature strength of alumina refractory concrete and motor [Novinson, 1990]. Such a role must be strong enough for chemical compatibility and weak enough to allow debonding [Kizilyalli, 1977, 1975].

More than 20 different phases of lanthanum phosphate are all possible products. As a typical rare earth chemical, lanthanum phosphate is not very difficult to prepare. It displayed many unique physical and chemical properties such as high temperature stability and so on.

EXPERIMENTS

Synthesis & Characterization of Lanthanum Phosphate Sol

There are many practical methods to obtain pure lanthanum phosphate (Monazite type $LaPO_4$) crystals by different reactions and/or their combinations [Inoue, 1993, Dhas, 1993, Tselebroskaya, 1991]. Other preparations can be found in literature [Kizilyalli, 1975, 1977, Tananaev, 1971]. Base on current available chemicals in the lab, the following chemical experiments have been designed and tested to yield pure lanthanum phosphate crystals as well as sol [Orlovskii, 1971, Mooney, 1950, Yu, 1989].

Method A

The most common chemical reagent of lanthanum is lanthanum chloride [Ivanov, 1969]. It is easy to mix with phosphoric acid to make precipitates as reaction 1. However, pH effect can not be ignored for this reaction. pH less than 4 is not recommended. Approximately 20 % phosphoric acid 1.05 g [5 mmole, diluted by 4 fold water] reacted with lanthanum chloride 1.227 g (5 mmole) which was dissolved in 5 ml water. White precipitates were immediately formed. Water washed three times of the precipitates, then dried in the room temperature. This is one of an equal molar ratio chemical reaction has been tested.

$$LaCl_3 + H_3PO_4 \longrightarrow LaPO_4 + 3\ HCl \quad \cdots\cdots [1]$$

Method B

Another routine to prepare lanthanum phosphate precipitates is by neutral reaction of lanthanum nitrite with ammonium phosphate (reaction 2). Lager size of $LaPO_4$ crystals can be obtained with high purity [Jarosewich, 1991]. Disadvantage of this experiment is that the complicated procedures and by products. First, ammonium phosphate was prepared by measured 5 ml [technical grade, ~30%] ammonium hydroxide solution, added 5 ml water, then gradually adding 85% phosphoric acid to reach the final pH around 7~8, cools down to crystallize, recrystallize again, vacuum filtering to get rid of mother solution, air dry and ready for use.

$$H_3PO_4 + NH_3{\cdot}H_2O \longrightarrow NH_4H_2PO_4 + H_2O \quad \cdots\cdots [2]$$

Second, prepare lanthanum nitrite. The procedure is: mixing 10 ml water with 2 g lanthanum oxide (reaction 3) or lanthanum hydroxide (reaction 4) in a baker. Then gradually adding concentrated nitric acid with care until all solids disappeared under hood with magnetic stirrer. Measure the pH, and it should reach 6~7. Solutions then were allowed to cool down inside refrigerator for a period of time to let it crystallize. Separating crystals by vacuum filtering, recrystallize again to get purified lanthanum nitrite, air dry and ready for use. It is extremely difficult to crystallize due to its high solubility in water [Bunzli, 1978].

$La_2O_3 + 6\ HNO_3 \longrightarrow 2\ La(NO_3)_3 + 3\ H_2O$ .....[3]

$2\ La(OH)_3 + 6\ HNO_3 \longrightarrow 2\ La(NO_3)_3 + 3\ H_2O$ .....[4]

$La(NO_3)_3 + 3\ NH_4H_2PO_4 \longrightarrow LaPO_4 + 3\ NH_4NO_3 + 2\ H_3PO_4$ .....[5]

$La(NO_3)_3 + NH_4H_2PO_4 \longrightarrow LaPO_4 + NH_4NO_3 + 2\ HNO_3$ .....[6]

Finally, weigh equal number of moles of both lanthanum nitrite and ammonium phosphate (reaction 6). Let them dissolved into the water to make 0.1 M solutions. When mixing these solutions under stirring, disperesive white insoluble precipitates will be formed. At last, centrifuge separated those precipitates. Water washed three times and air dried these powders. The equal numbers of moles of starting materials make the reaction 5 was impossible to happen.

Method C

Direct reaction between lanthanum oxide and phosphoric acid is an excellent choice. The reaction 7 itself is a very clean reaction; in addition, there is no any by product except water. The reaction is quite vigorous as indicated by releasing much heat. The large precipitates have been formed at the reaction site immediately, then gradually disappeared becoming sol. Such sol is extremely thick. The stability of this type sol is exceedingly good. It will not separate after a long time. It did separate overnight if the solution is too dilute. Further experiments have been conducted. The stability versus concentration factor has been determined at this stage. That is the concentration of the very stable sol can not be lowered than 0.1 M.

$La_2O_3 + 2\ H_3PO_4 \longrightarrow 2\ LaPO_4 + 3\ H_2O$ .....[7]

Collect 1.05 g or 0.72 ml of H_3PO_4 [5.35 mmole, 85% by weight, specific gravity d = 2*454/500 = 1.725] in a baker, then gradually add 0.218 g La_2O_3 [0.669 mmole, *f*w = 325.81] powders {prepared by reaction 8, dehydrated at 700 °C [Felsch, 1969, Kropiwnicka, 1988]}.

Allow stirring for 30 minutes and then separated by centrifuge. Water washed three times to get rid of excess acid Then dried on the hot plate to vaporize water. Finally calcined in furnace at 700°C for 2 hours. White lanthanum phosphate crystals were obtained. Figure 3 is XRD patterns for lanthanum phosphate crystals. It perfectly matched the standard JCPDS database file.

$$2\ La(OH)_3 \text{ ----------> } La_2O_3 + 3\ H_2O \cdots\cdots\cdots\cdots [8]$$

To prepare lanthanum oxide as reaction 8, weigh lanthanum hydroxide. Then dehydrate it in the programmable furnace at 700 °C for 120 minutes {Thermolyne Type 46200 High Temperature Furnace, 10 °C/Minutes temperature increase rate. }. Cool down to room temperature under the discooler. Almost 100% of water were removed at this temperature. After dried in furnace at 700 °C, La_2O_3 was quickly mounted on the micro slide for immediate XRD. Fundamentally, XRD patterns are not lanthanum hydroxide anymore. Figure 2 is XRD patterns for lanthanum hydroxide. At room temperature, atmosphere, lanthanum oxide was completely transformed into lanthanum hydroxide [Roy, 1953]. Such XRD patterns were compared with the JCPDS CD ROM PDP files. Patterns were all matched with standard lanthanum oxide La_2O_3, JCPDS file 05-0602. Therefore, it is confirmed that lanthanum hydroxide was transformed into lanthanum oxide very easily after calcination at 700 °C for 2 hours.

Method D

This one is extensively studied and can be reproducible in any scale in a lab. Lanthanum hydroxide directly reacts with phosphoric acid. This reaction is exothermic. Less than 10 % of phosphoric acid in reaction system would not be able to obtain good products. 20% phosphoric acid in reaction system needs more than few hours to complete but it is an excellent choice. The most important thing is that the sol is well formed at the slow reaction and there is no by product was created (reaction 9).

$$La(OH)_3 + H_3PO_4 \text{ ----------> } LaPO_4 + 3\ H_2O \cdots\cdots\cdots\cdots [9]$$

Approximately 20 % H_3PO_4 (diluted by distilled water 4 fold of 85% acid d=1.725) will be used to prepare lanthanum phosphate sol. 1.05 g or 0.72 ml of H_3PO_4 [5.35 mmole, 85% by weight] diluted by 4.0 ml water in a baker, then gradually adding 0.254 g $La(OH)_3$ [1.3375 mmole, fw = 189.93] powders. Allow stirring for 10 hours. Centrifuge separates the solid and water washes three times. Then dilute to any concentration required by coating experiments.

Method E

The reaction 10 is same as the method D. The only difference is that the phosphor to lanthanum ratio is 2 to 1 rather than 4 o 1. The results are not the same, however.

$$La(OH)_3 + 3\,H_3PO_4 \text{ ----------> } \mathbf{LaP_3O_9} + 6\,H_2O \cdots\cdots\cdots\cdots [10]$$

Approximately 15 % H_3PO_4 (diluted by distilled water 5 fold of 85% acid d=1.725) will be used to prepare lanthanum phosphate sol. 0.525g or 0.36 ml of H_3PO_4 [2.675 mmole, 85%] diluted by 2.0 ml water in a baker, then gradually adding 0.218 g La_2O_3 [0.669 mmole, fw = 325.81, kept inside dessicator] powders. Allow stirring for 10 hours. The sol could be formed and its concentration was 0.2792M. The molar ratio of La:P is 1:2. The completion of reaction is unclear at this ratio, but is clear for 1: 4 ratio. After overnight, the reaction is very good, the sol is very uniform and its viscosity is high. Such sol was put on the high temperature furnace for 120 minutes at 700 °C. White crystals were obtained. XRD patterns clearly showed that it was not a $LaPO_4$. It is orthombic lanthanum phosphate crystal in chemical formula LaP_3O_9. JCPDS file is 33-717 as match up standard [Botto, 1979, Chudiniva, 1979].

Fiber Dip-Coating Procedures:

The coating testing fiber is Alumina fiber (Sapphire) from Advanced Crystal Products Corporation, Woburn, MA 01801. Fiber segment 3 with begins orientation 38 degree, begins diameter 5.2 mils, end orientation 2 degree, end diameter 5.3 mils, was used throughout the experiment [Makishima, 1986, Mukherjee, 1984, Okada, 1990]. First, cut fiber into 3 inches long pieces; then cleaned by 85% H_3PO_4, water flushed out acids on surface of the fiber.

Four different concentrations of sol were prepared. They were 0.1, 0.05, 0.01, and 0.001 M $LaPO_4$. Dip coated 20 times; each time dried by infrared lamp before next coating (30 seconds were needed). The thin coating film can be observed immediately under the optical microscope. The coated fiber then calcined at 1100 °C for 120 minutes. Polarized reflected optical microscopy shown that the coating is real for concentrations of 0.01 and 0.05 M, but not for 0.1 M and 0.001 M, both of them were either too concentrated or too diluted for obvious reasons.

RESULTS AND CONCLUSION

The molar ratio between phosphors and lanthanum is the key role in reaction 9. Excess phosphoric acid has to be washed out in order to get lanthanum phosphate ($LaPO_4$) coating in final stage. If the excess phosphoric acid was not washed out, after dip-coating to sapphire fiber and calcined at 1100 °C, the coating layer would not be lanthanum phosphate in chemical formula $LaPO_4$, it was a mixture of many possible products. Also, quite strong interaction has been observed between fiber and coatings if excess acid remained in sol.

The reaction 10 has more understanding. If the excess phosphoric acid was washed out, then coated to the sapphire fiber, calcined at 1100 °C for two hours, the coating layer is lanthanum phosphate in terms of $LaPO_4$, same as product of reaction 9. However, if everything was remained in the coating sol, directly dip-coated on sapphire fibers, and then calcined at 1100 °C, the coating layer would be lanthanum phosphate in chemical formula of LaP_3O_9. In which the strong bonding is possible according to the fracture observation from SEM.

Any trace of sodium will interact with $LaPO_4$ at high temperature [Chuvlina, 1989]. Potassium is also interact with $LaPO_4$ in some degree [Jungowska, 1991, 1993].

Overall, lanthanum phosphate is a very complicated system. Not only it heavily depends on the initial molar ratio of starting materials, also calcination temperature. Below 400 °C, there is no pure lanthanum phosphate ($LaPO_4$) formed. Its crystal growth at 400~1100 °C. XRD data supports the results [Hikichi, 1993], refer figure 3, figure 5 and figure 6.

The crystal size was calculated according to **Scherrer formula**, $t = 0.9\,\lambda/\{B \cos \theta_B\}$, where t is particle size, λ is wavelength of x-ray used, B is the measured width to half the maximum intensity, in radians, and θ_B is a half of 2θ in degree. Virtually, B is essentially zero when the particle size excess about 0.1 micron.

Particle size is larger and the x-ray diffraction pattern is sharper when lanthanum phosphate was calcined at 1100 °C. Here is the details for calculations. File z00911.raw is XRD of lanthanum phosphate after 700°C calcination. B= 28.96 - 28.40 = 0.56 degrees = 0.009768 radians, λ = 1.54 Å for copper x-rays, B = 14.09 degrees, hence, particle size t equals 146 Å.

File z00012.raw is XRD of lanthanum phosphate after 1100°C calcination. B= 28.72 - 28.54 = 0.18 degrees = 0.00314 radians, λ = 1.54 Å for copper x-rays, B = 14.31 degrees, hence, particle size t equals 455 Å, or above three times larger than at 700 °C.

Sol formation depends on concentration of starting chemicals and aging period. Too high and too low were both not good for sol formation. 15~25% phosphoric acid will be a good choice. The aging process and period are necessary steps and overnight aging are strongly recommended.

0.1, 0.05, 0.01, 0.001 molar $LaPO_4$ sol have been tested by dip coating technique onto sapphire fiber. 0.1 and 0.001 molar concentration sol could not be used to get a good coating layer at this time. For 0.05 M $LaPO_4$ sol, the thickness of coating layer is approximately 150 nm in average by 20 times dip coatings as indicated by figure 12. The thickness of layer is approximately 60 nm for 0.01 M sol at 20 times dip coatings as shown on figure 11.

Figure 10 is a backscattering image taken from Leica 360 FE; it showed a clear $LaPO_4$ coating around the fiber. The coating layer was confirmed by XRD later, see figure 8. Figure 7 is the uncoated sapphire fibers XRD patterns [Foster, 1959]. The coating layers were somehow uniform and strongly depend on coating techniques.

Solving x-ray diffraction patterns, the conclusion is clear. The ratio between phosphoric and lanthanum determining the product if excess acid was not removed. Further it denoted that the lanthanum phosphate system is one of the extremely complicated system in nature, specially at high temperature. The chemistry behind the behavior of lanthanum phosphate depends upon the ratio of La to P and the temperature in a word.

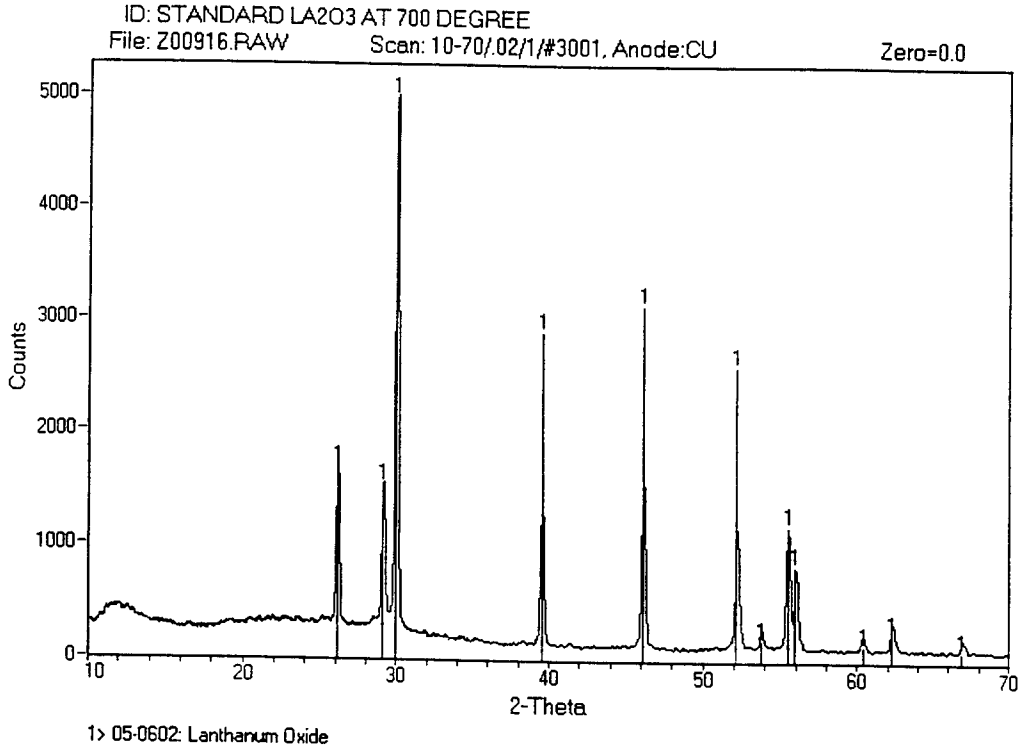


Figure 1. XRD pattern of La_2O_3 after 700 °C calcination, below is comparison with JCPDS file.

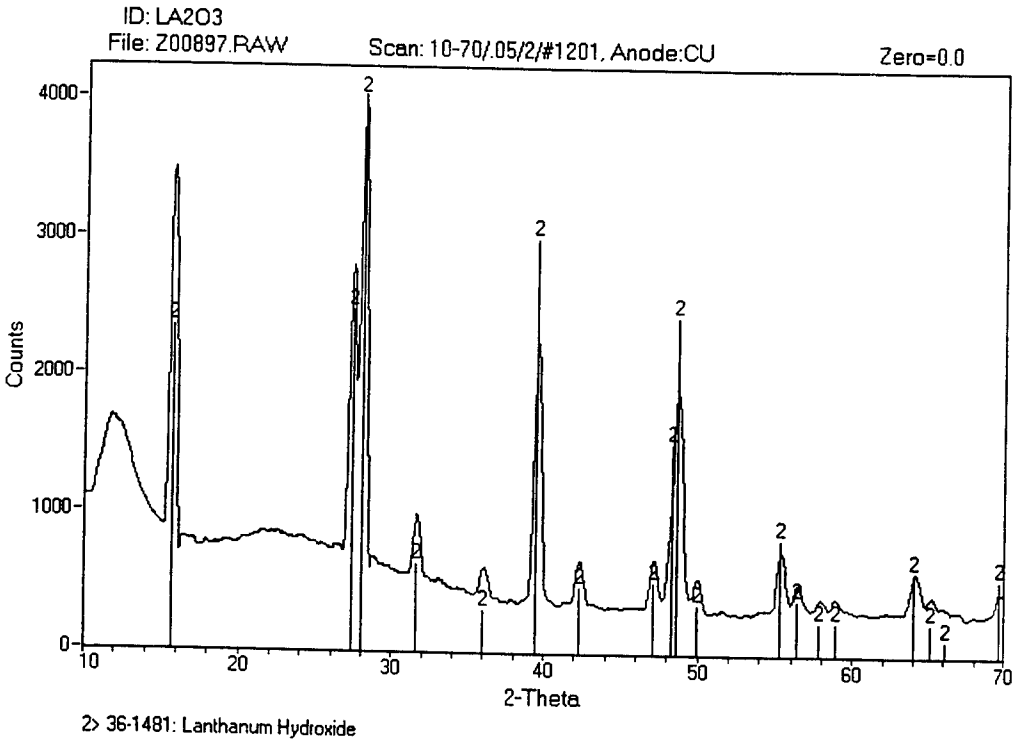


Figure 2. XRD pattern of $La(OH)_3$, below is comparison with JCPDS database file.

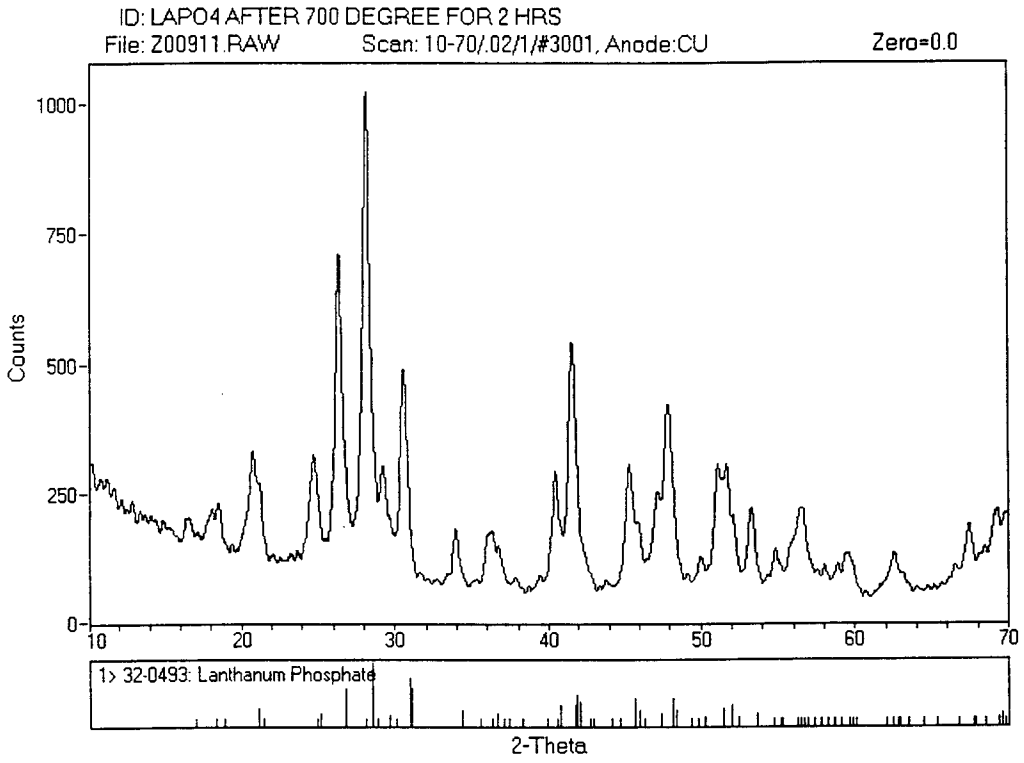


Figure 3. XRD pattern of $LaPO_4$ after 700 °C calcination, below is JCPDS file.

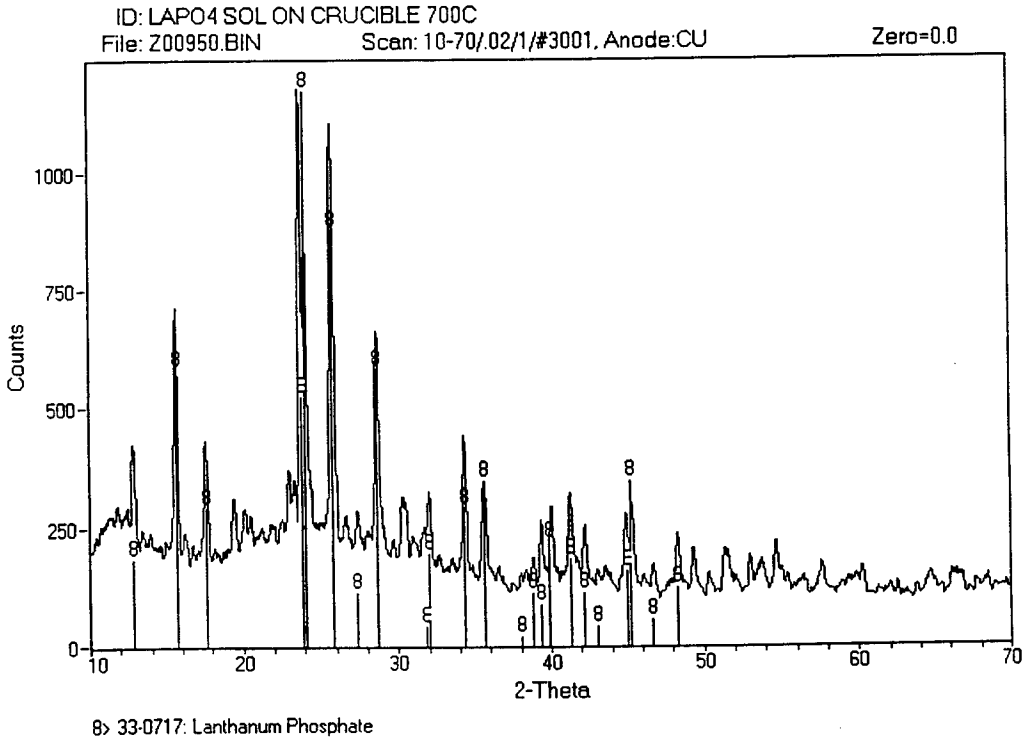


Figure 4. XRD pattern of LaP_3O_9 after 700 °C.

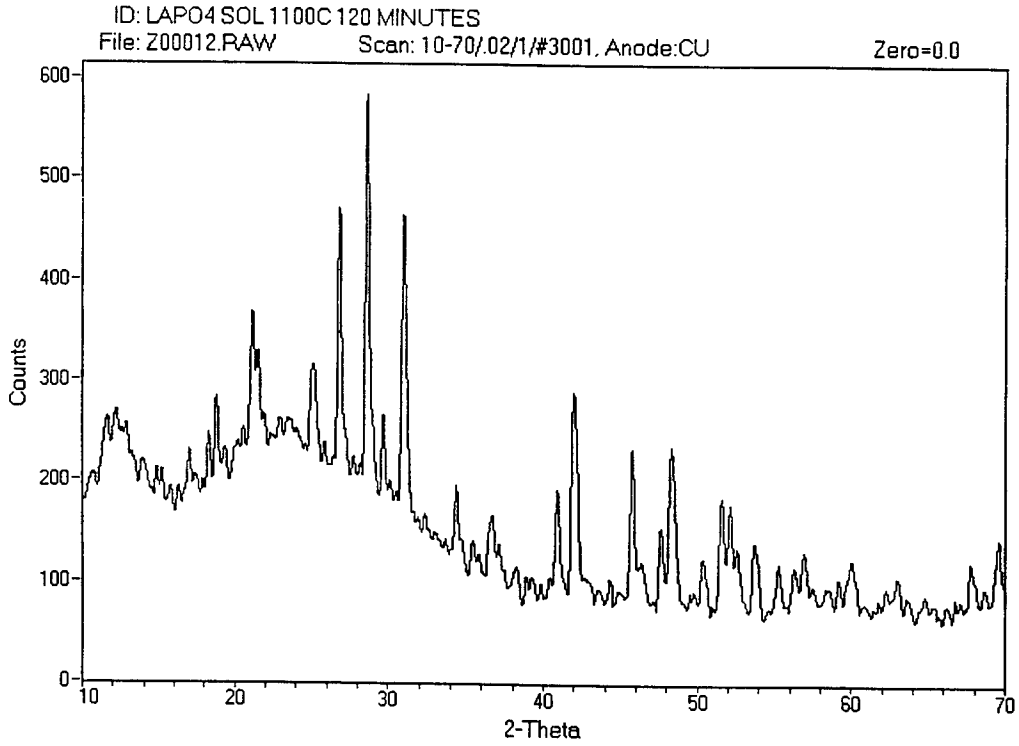


Figure 5. XRD pattern of $LaPO_4$ sol after 1100 °C.

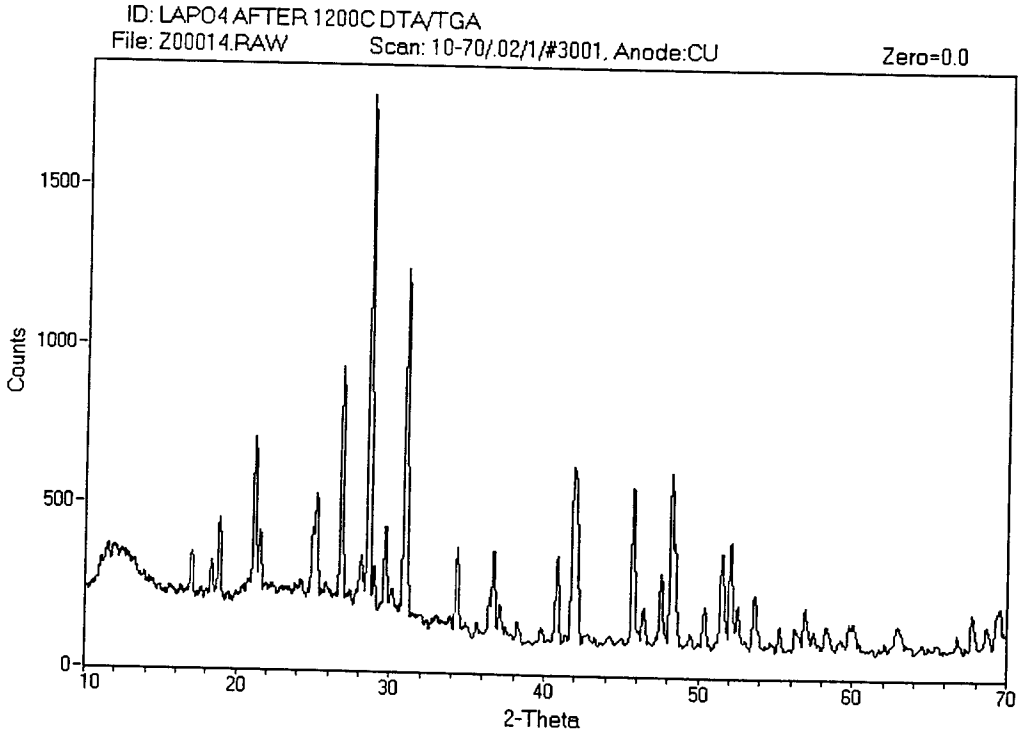


Figure 6. XRD pattern of $LaPO_4$ sol after 1200 °C.

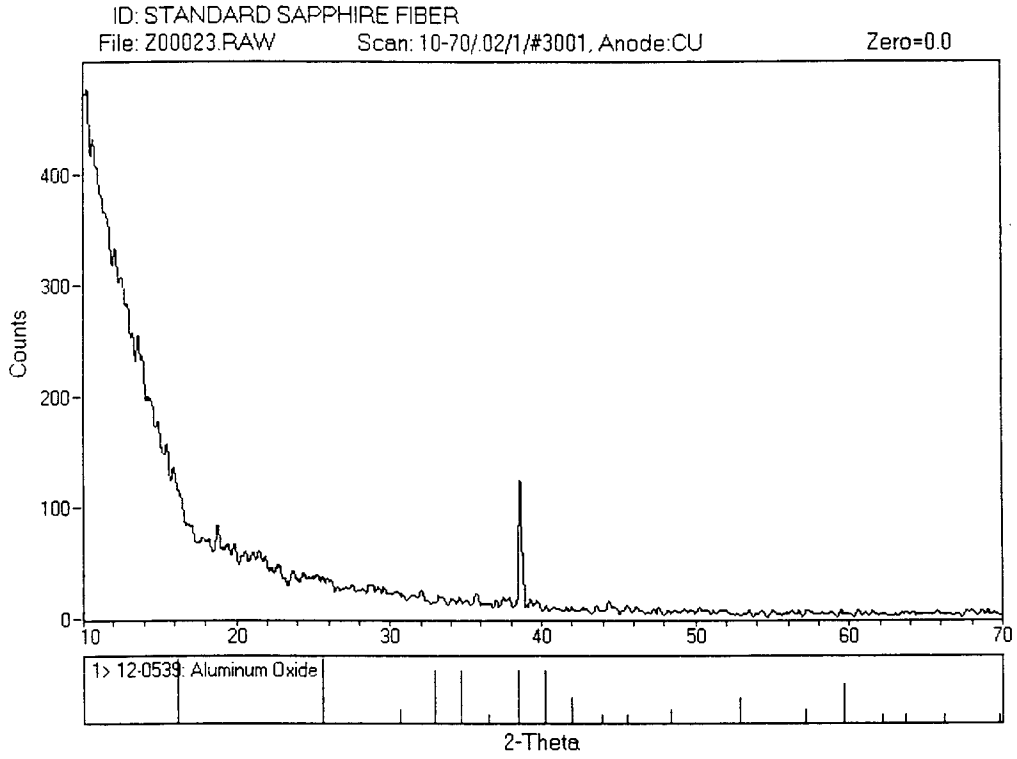


Figure 7. XRD pattern of uncoated sapphire fibers.

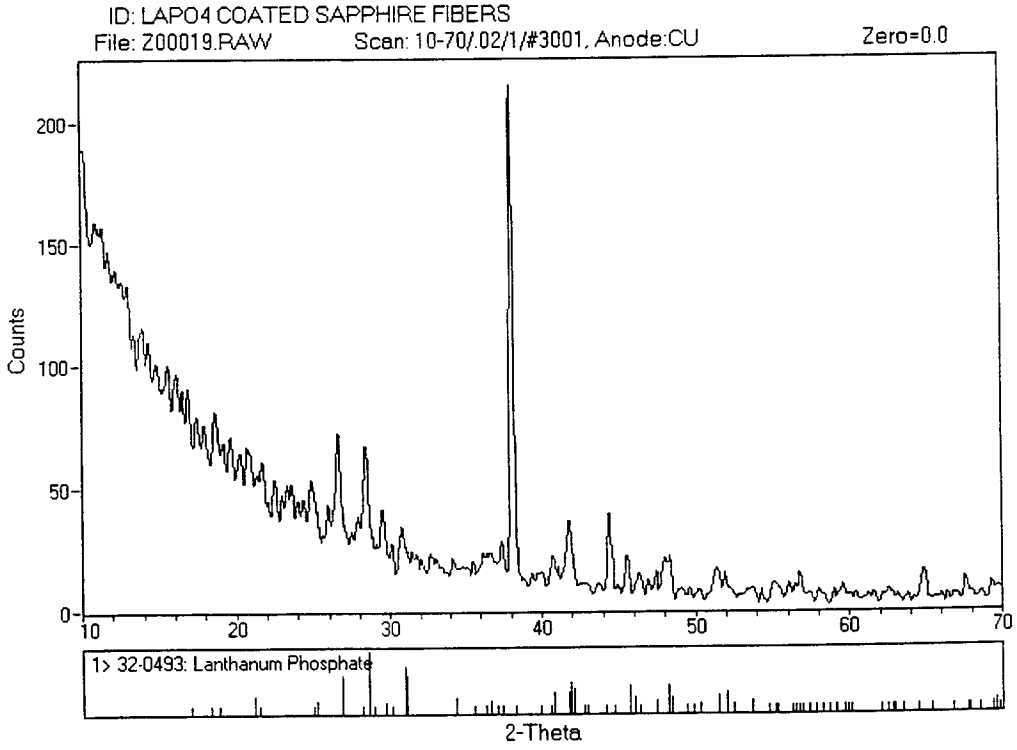


Figure 8. XRD pattern of $LaPO_4$ sol coated sapphire fibers after 1100 °C

NETZSCH THERMAL ANALYSIS

OPERATOR:	MMC	DATE:	25 Jul 1994
RUN No.	7	SAMPLE No.	4
SAMPLE NAME:	LAPO4	REFERENCE:	Alumina
CRUCIBLE:	Alumina	FILE NAME:	0:lapo2
LOT No.	1	ATMOSPHERE	air
FLOW RATE,cc/min:	0	HEAT RATE,deg C/min:	5
SAMPLE Wt.,mg:	52.9	REFERENCE Wt.,mg:	51.2
DTA RANGE mv. FS	.3	TG RANGE mg. FS	50
THERMOCOUPLE TYPE	S		

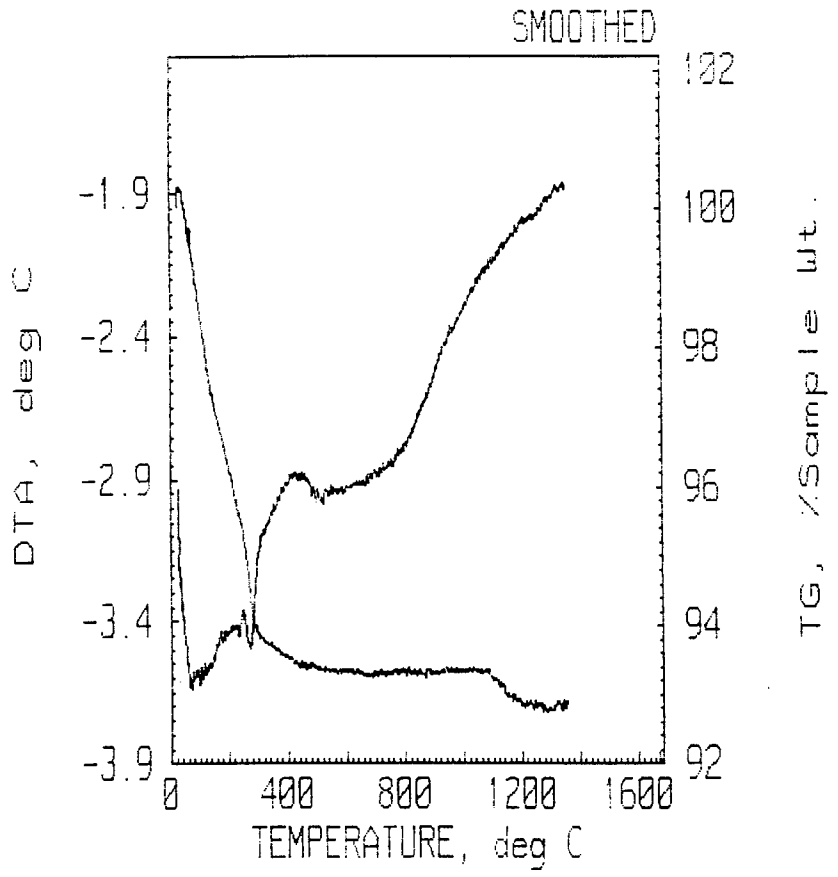


Figure 9. $LaPO_4$ sol DTA/TGA room temperature to 1200 °C.

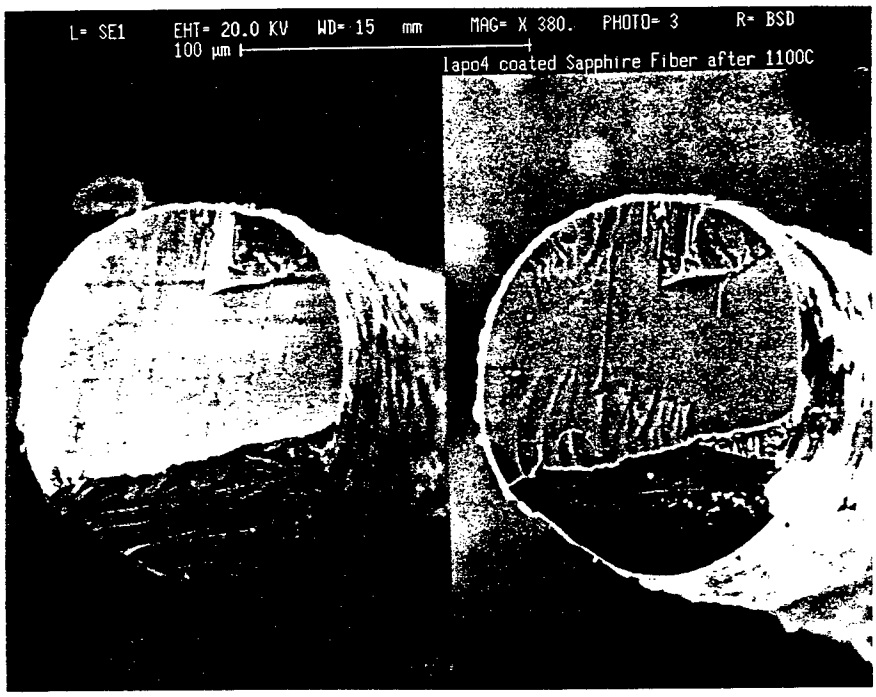


Figure 10. SEM RSD image of sol dip coated sapphire fiber.

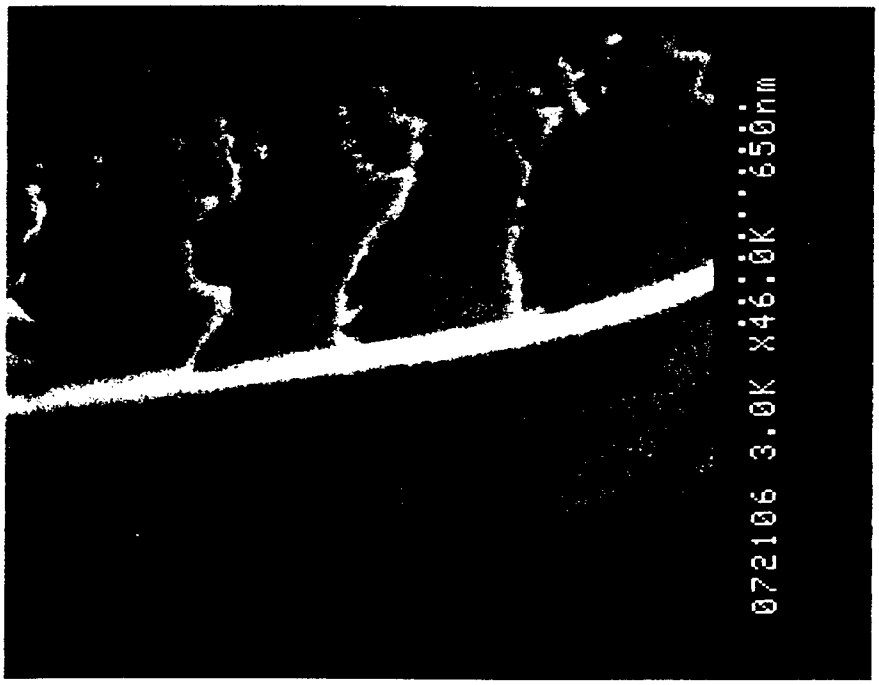


Figure 11. SEM Micro graph of coated (0.01M sol)fiber cross section.

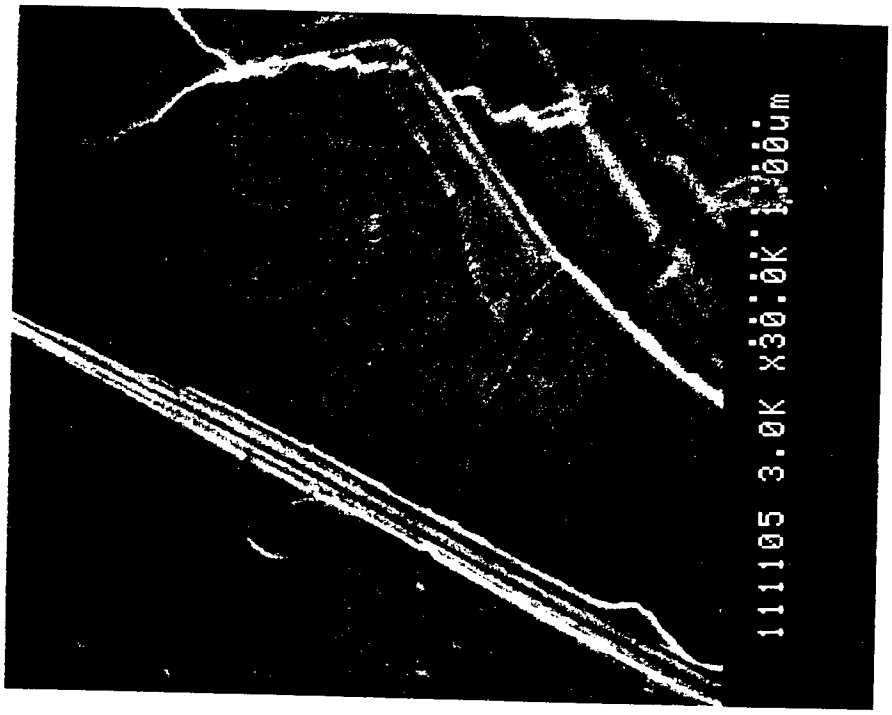


Figure 12. SEM Micro graph of coated (0.05M sol)fiber cross section.

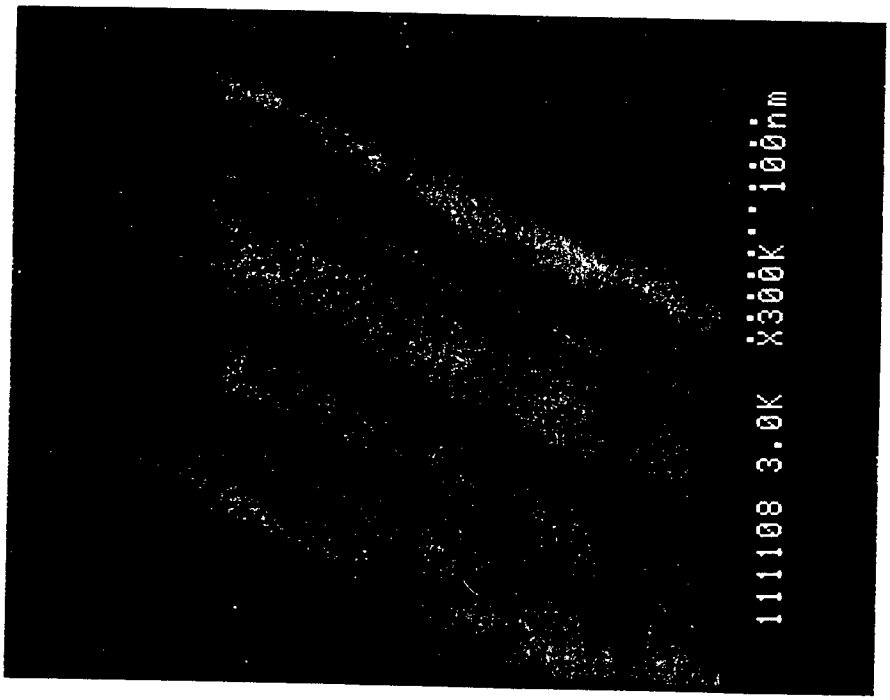


Figure 13. SEM Micro graph of coated (0.05M sol)fiber cross section.

ACKNOWLEDGEMENTS

I especially appreciate Dr. R. Kerans and Dr. T. Mah for their genuine suggestions and kindly help. Also, Dr. John Woodhouse will be appreciated for his techniques support of Hitachi 900 high resolution SEM and JOEL 840 Microanalyser. Dr. Peter Brown for his time and his kindly help of Leica 360FE and backsacttering images will be sincerely appreciated.

REFERENCES

Botto, I. *J. Appl. Crystallogr.*, 12 257 (1979).

Bunzli, Jean-Claude G., Etienne Moret, and Jean-Robert Yersin, *Helv. Chim. Acta* Vol. 61, Fasc. 2 (1978), 762-771.

Carron, M. *Geol. Surv. Bull. (U.S.)*, 1036 253 (1958).

Chudinova, N. N. *Inorg. Chem.* 15,654-658 (1979).

Chuvilina, E. L.; Poletaev, I. F.; Zimina, G. V. Zh. *Neorg. Khim.*, 34(5), 1274-80 (1989).

Chuvilina, E. L.; Poletaev, I. F.; Zimina, G. V. *Zh. Neorg. Khim.*, 34(5), 1274-80 (1989).

Dhas, Arul N.; Patil, K. C. *J. Alloys Compd.*, 202(1-2), 137-41 (1993).

Felsche, J. *Naturwissenschaften*, 56 212 (1969).

Foster, P. *J. Electrochem. Soc.*, 106 971 (1959).

Hikichi, Y. and Yu, C. F. et al. *J. Alloy Compd.*, 192 (1-2), 102-4 (1993).

Inoue, Masashi; Nakamura, Tomohiro; Otsu, Hiroyuki; Kominami, Hiroshi; Inui, Tomoyuki *Nippon Kagaku Kaishi*, (5), 612-16 (1993).

Ishida, Masanobu *Jpn. Kokai Tokkyo Koho*, 5 pp. Kyocera Corp. (1992).

Ivanov, M. *Sov. Phys. Crystallogr.* (Engl. Transl.), 13 786 (1969).

Jarosewich, Eugene; Boatner, L. A. *Geostand. Newsl.*, 15(2), 397-9 (1991).

Jungowska, W.; Znamierowska, T. *J. Therm. Anal.*, 39(6), 715-20 (1993).

Jungowska, Wanda; Znamierowska, Teresa *J. Solid State Chem.*, 95(2), 265-9 (1991).

Kizilyalli, M.; Welch, A. J. E. Rare Earths Mod. Sci. Technol., [Rare Earth Res. Conf.], 13th, Meeting Date 1977, 209-17. Edited by: McCarthy, Gregory J.; Rhyne, J. J. Plenum: New York, N. Y.

Kizilyalli, Meral *J. Pure Appl. Sci.*, 8(2), 179-86 (1975).

Kropiwnicka, Jolanta; Znamierowska, Teresa, Industrial Inorganic Chemicals, 49-5 (1988), 73-76.

Makishima, A., H.Kubo, K. Wada, Y. Kitami, and T. Shimohira, . *Amer. Cera. Soc.*, Vol. 69, No. 6, 127-129 (1986).

Mooney, R. C. *Acta Cryst.*, 3 (1950), 337-340.

Mukherjee, S. P. "Deposition of Transparent Noncrystalline Metal Oxide Coatings by the Sol-Gel Process," Ultrastructure Processing of Ceramics, Glass, and Composites, pp.178-188, Eds. L. L. Hench, and D. R. Ulrich, John Wiley & Sons. New York, 1984.

Novinson, Thomas U.S., 6 pp. Cont.-in-part of U.S. Ser. No. 161,503, abandoned. (1990). US 4961786 A 901009 US 89-345874 890501

Okada, Kiyoshi and Nozomu Otsuka, Ceramic Transactions, Vol.6, 425-434, Mullite and Mullite composites edited by S. Somiya, R.F. Davis, & J. A. Pask, American Ceramics Society, Westville, OH, 1990.

Orlovskii, V. P., H. Schafer, V. P. Repko, G. M. Safronov, and I. V. Tananaev, *Inorg. Chem.* 7 860-866 (1971).

Popolitov, Vyacheslav I.; Yaroslavskij, Igor M.; Dimitrova, Olga V.; Strelkova, Elena E. *Izobreteniya* 1992, (41), 95.

Roy, Rustum and H. A. McKinstry, *Acta Cryst.* 6, 365 (1953).

Tananaev, I. V.; Repko, V. P.; Orlovskii, V. P.; Safronov, G. M.; Kurbanov, Kh. M.; Khaimova, A. G. Akad. Nauk SSSR, *Neorg. Mater.*, 7(10), 1769-72 (1971).

Tselebrovskaya, E. G.; Dzhurinskii, B. F.; Lysanova, G. V.; Komova, M. G. *Neorg. Khim.*, 36(10), 2467-9 (1991).

Yu, Yaqin; Li, Mei; Hu, Ninghai *Wuji Cailiao Xuebao*, 4(1), 25-32 (1989).

Zakharova, B. S.; Komissarova, L. N.; Naumov, S. V.; Traskin, V. Yu. *Neorg. Khim. im. Kurnakova Neorg. Mater.*, 28(8), 1738-43 (1992).

Zakharova, B. S.; Komissarova, L. N.; Naumov, S. V.; Traskin, V. Yu. *Neorg. Mater.*, 28(8), 1731-7 (1992).

PROCESSING AND CHARACTERIZATION OF NONLINEAR OPTICAL PBZT FILMS

Lora A. Cintavey
Graduate Assistant
Department of Materials Science and Engineering

University of Cincinnati
Department of Materials Science and Engineering
ML #12
Cincinnati, OH 45221

Final Report for:
Summer Graduate Research Program
Wright-Patterson Air Force Base Laboratory

Sponsored by:
Air Force Office of Scientific Research

and

Wright Laboratory Materials Directorate
Wright-Patterson Air Force Base, OH 45433

September 1994

PROCESSING AND CHARACTERIZATION OF NONLINEAR OPTICAL PBZT FILMS

Lora A. Cintavey
Graduate Assistant
Department of Materials Science
University of Cincinnati

Abstract

Solutions of poly (p-phenylene benzobisthiazole) (PBZT) in methane sulfonic acid (MSA) were prepared. Viscosities of the less concentrated solutions were measured by dilute solution viscometry. Viscosities of the more concentrated solutions were determined with a Rheometrics Dynamic Spectrometer (RDS) model 7700 cone and plate rheometer. The dependence of viscosity on strain rates was also recorded. A plot of viscosity versus concentration was constructed for the entire range of concentrations. Thin films of PBZT were spun on glass slides and silicon wafers using a spin coater for purposes of wave guiding. Since the thickness of the film is a controlling factor in wave guiding, the thicknesses were probed using a profilometer. Studies are still in progress to correlate the thickness of the films directly to the concentrations of the PBZT solutions.

PROCESSING AND CHARACTERIZATION OF NONLINEAR OPTICAL PBZT FILMS

Lora A. Cintavey

Introduction

In recent years, the interest in developing materials for nonlinear optical (NLO) applications has grown. Currently, electronic devices dominate the world's technology. The concept of controlling light beams (photons) in a similar manner as electrons offers possibilities of greatly increased speed and memory capacity over electrical devices. Optical controlling and switching devices are two possible applications for NLO materials of interest to the Air Force. Avionics systems can be advanced significantly with the implementation of "photonics" technology.

Methodology

The development of PBZT has been accompanied by processing difficulties. PBZT is a rigid rod polymer and exists in a solid form as feathery gold flakes. Due to the structure of the polymer, solubility is possible only in aggressive solvents. In this case, methane sulfonic acid (MSA) was used to make solutions of concentrations ranging from 2.5% PBZT by weight down to less than 0.01% PBZT by weight.

Dilute Solution Viscometry:

Viscosities of concentrations less than 0.05% PBZT by weight were measured by dilute solution viscometry. The equipment used included a Ubbelohde 100ml viscometer in a temperature bath regulated at 30°C. The relationship between concentration in g/dl and concentration in weight percent is shown below.

Concentration (g/dl)	Concentration (weight %)
0.01	0.0068
0.0125	0.0084
0.0167	0.0113
0.025	0.0169
0.05	0.0337

Figure 1 shows the results of the solution viscometry study.

Viscosities obtained from dilute solution viscometry are intrinsic viscosities. The use of a silicone standard and the equations given below allow the viscosity unit conversion from g/dl into stokes.

$$\eta = Ct\rho - E\rho/t^2$$
$$\eta_o = Ct_o\rho_o - E\rho_o/t_o^2$$

where:
η - viscosity
ρ - density
t - efflux time of solution
t_o - efflux time of solvent
C and E - constants for particular viscometer

The viscosity in stokes is described as kinematic viscosity or η/ρ.

The second term in each of these equations is negligible because the efflux time for the silicone standard was greater than 100 seconds. The C constant was calculated first using the silicone efflux time, the density of silicone, and it's known viscosity. That constant was then used along with the efflux times of the PBZT/MSA solutions and the density of MSA to calculate the unknown viscosity of the solutions.

Rheometrics (cone and plate viscometer):

Viscosities of the more concentrated solutions (0.5, 1.0, 1.5, 2.0, and 2.5% PBZT by weight) were studied with a Rheometrics Dynamic Spectrometer Model 7700 cone and plate rheometer. Dynamic strain sweeps were conducted on each concentration at 30°C to determine the strain below which the viscosity was independent of strain (linear viscoelastic region). The percent strain (for each concentration) used in running the dynamic rate sweep is shown below.

Concentration	**% strain (used in the rate sweep)**
0.5% by weight	150%-200%
1.0% " "	70%
1.5% " "	70%
2.0% " "	70%
2.5% " "	20%

Dynamic rate sweeps of each concentration at 0°C, 30°C, and 70°C are shown in Figures 2-4. A common trend observed for all solutions (at every temperature) was a decrease in viscosity with increasing strain rate.

By combining data from the dilute solution viscometer and the cone and plate rheometer, a master plot of viscosity versus concentration was constructed (Figure 5). The cone and plate rheometer measures

dynamic viscosity in units of poise. Since these values are dynamic viscosities, a viscosity at zero shear rate was unattainable for the more concentrated solutions. The viscosity values at a shear rate of 1 rad/sec were used as a reference value. This shear rate was the lowest shear rate that registered reliable viscosity and torque values.

Spin coating:

Initial attempts at spin coating were conducted on glass slides. A solution of 0.1 weight % PBZT was spun in two stages. The first stage is called the spread stage and used a relatively slow rate of rotation (usually from 200-300 rpm) to coat the substrate thoroughly with the dope. The second stage is called the spin stage and used a faster rate of rotation to create a uniform thin film. The 0.1 weight % PBZT solution was spun using spread cycle rates from 200 to 300 rpm for times of 5 to 15 seconds. Spin cycle rates ranged from 500 to 700 rpm for times of 20 to 30 seconds. Since the solvent used for PBZT was an acid, the films had to be soaked in distilled water after spinning to remove the acid and coagulate the film. The films were soaked anywhere from 1 to 3 days before being put in an oven at 150°C to dry, again for several days. Problems occurred during coagulation of the film in water. Water is a non solvent for the PBZT films; therefore, the films shrunk when submerged in the water. Due to the rectangular geometry of the glass slides, many of the films delaminated in the water before the acid was completely removed, making it impossible to test their thickness. This effect became increasingly worse with the more concentrated solutions. However, the delamination was less severe when the films were spun on circular (2" diameter) oxidized silicon wafers. This is believed to be due to the circular geometry and the presence of the oxide layer on the wafer.

Thicknesses of the 0.1% PBZT by weight films varied with different spin rates, yet, all of the films ranged from 100 to 300 angstroms in thickness. The profilometer was set at 2500 angstroms full scale, the most sensitive setting. Due to the very thin nature of the films, no correlation between spin rates or spin times and the thickness could be accurately made. One film was spun from the 0.5% PBZT by weight solution at a spread rate of 200 rpm for 5 seconds and a spin rate of 700 rpm for 30 seconds. Its thickness was found to be approximately 1250 angstroms.

Films must be on the order of a micron for wave guiding purposes. The films spun with the 0.1 and 0.5% PBZT by weight solutions were thus too thin to use as wave guides. Higher concentrations, 1.0 and 1.5% PBZT by weight, solutions were examined next. Since their viscosities are much higher, the solutions were heated to 100°C before spinning, to increase their ability to spread. These two concentrations were spun using one and two stage processes. The first batch of films was spun in a one step process at 300 rpm for

30 seconds. A second batch was spun using the two step process previously mentioned. In this case, a spread cycle of 300 rpm for 15 seconds and a spin cycle of 500 rpm for 10 seconds was used. These films were coagulated (soaked in distilled water for 3 days) and are currently being dried for profilometry studies.

Future work

Near term research:

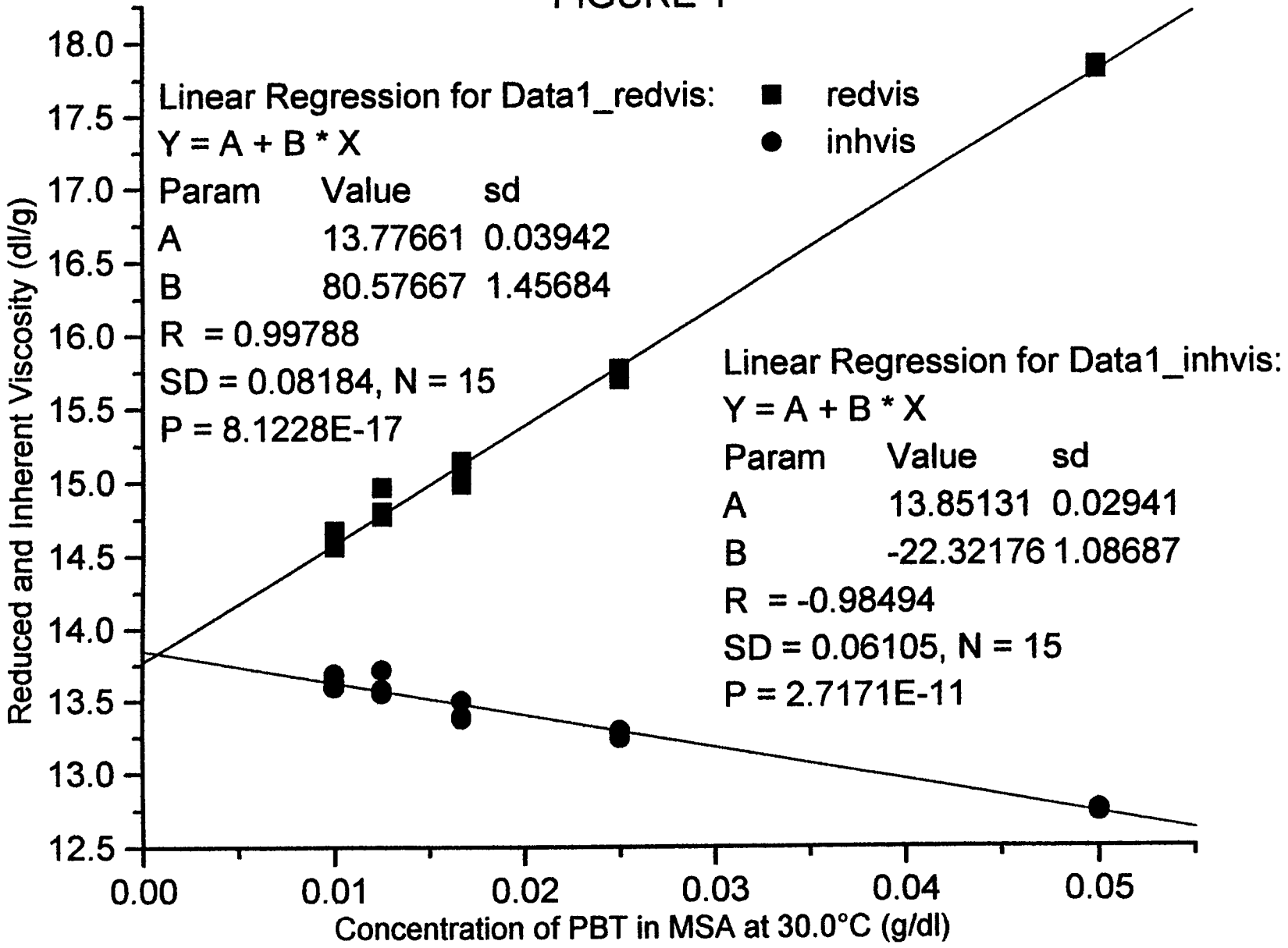
Thicknesses will be studied on the films spun from 1.0 and 1.5% PBZT by weight solutions. Adjustments to the spread and spin conditions will be made to tailor the thickness of the films for wave guiding. The films will be further prepared for wave guiding and the actual guiding done on the films by methods yet to be determined.

Long term research:

- Nonlinear optical measurements
- Control of coagulation rate to optimize the optical clarity
- Assessment of film morphology and mechanical properties
- Final table correlating concentration, spread and spin rates, and times

I want to express special thanks to Lisa Denny, Bill Click, Dr. Mark Husband, Dr. Chyi-Shan Wang, and my advisor Dr. Steve Clarson for all their help and support in this work.

FIGURE 1


Linear Regression for Data1_redvis:
Y = A + B * X
Param Value sd
A 13.77661 0.03942
B 80.57667 1.45684
R = 0.99788
SD = 0.08184, N = 15
P = 8.1228E-17
redvis
inhvis
Linear Regression for Data1_inhvis:
Y = A + B * X
Param Value sd
A 13.85131 0.02941
B -22.32176 1.08687
R = -0.98494
SD = 0.06105, N = 15
P = 2.7171E-11
Reduced and Inherent Viscosity (dl/g)
18.0
17.5
17.0
16.5
16.0
15.5
15.0
14.5
14.0
13.5
13.0
12.5
0.00
0.01
0.02
0.03
0.04
0.05
Concentration of PBT in MSA at 30.0°C (g/dl)

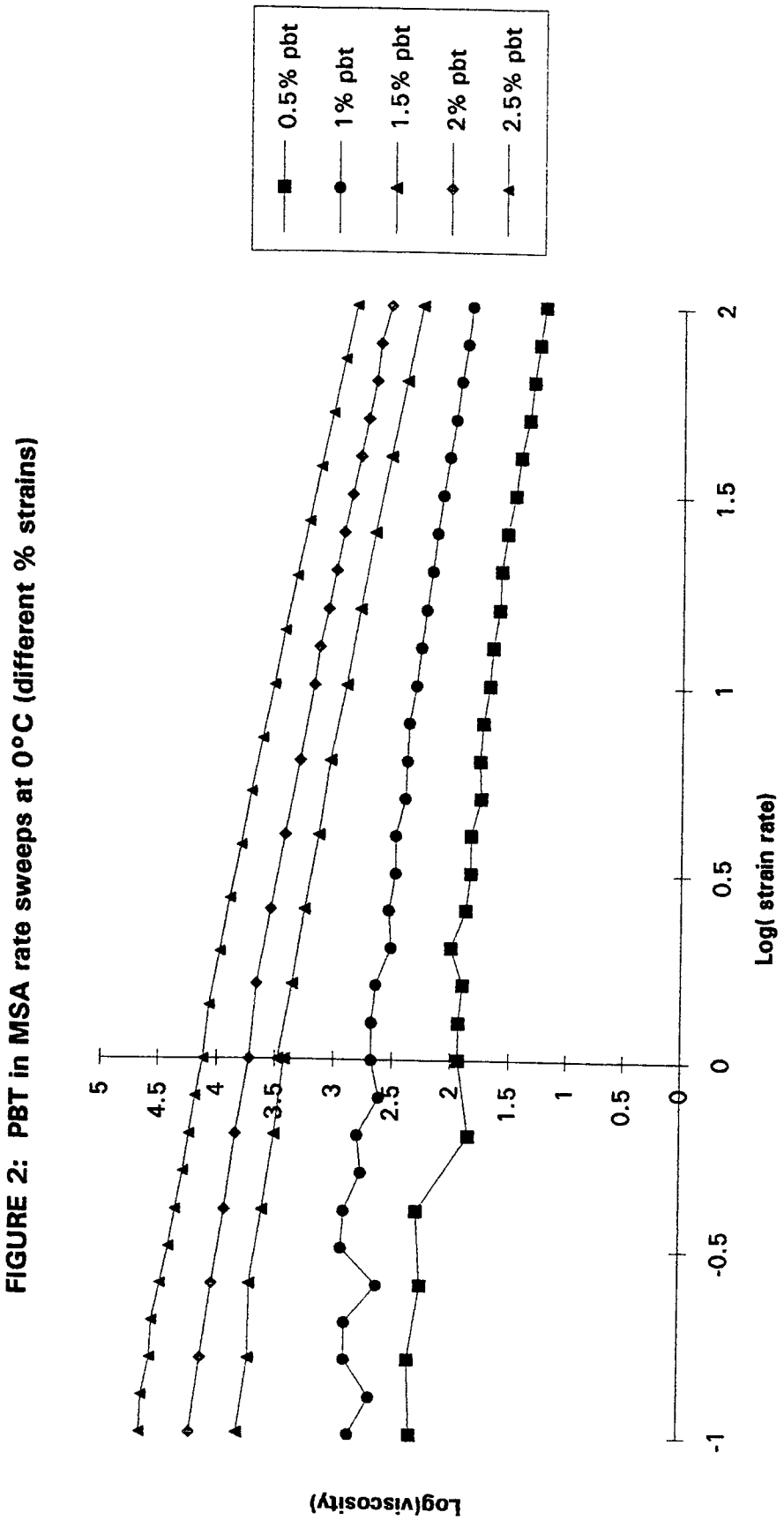


FIGURE 2: PBT in MSA rate sweeps at 0°C (different % strains)

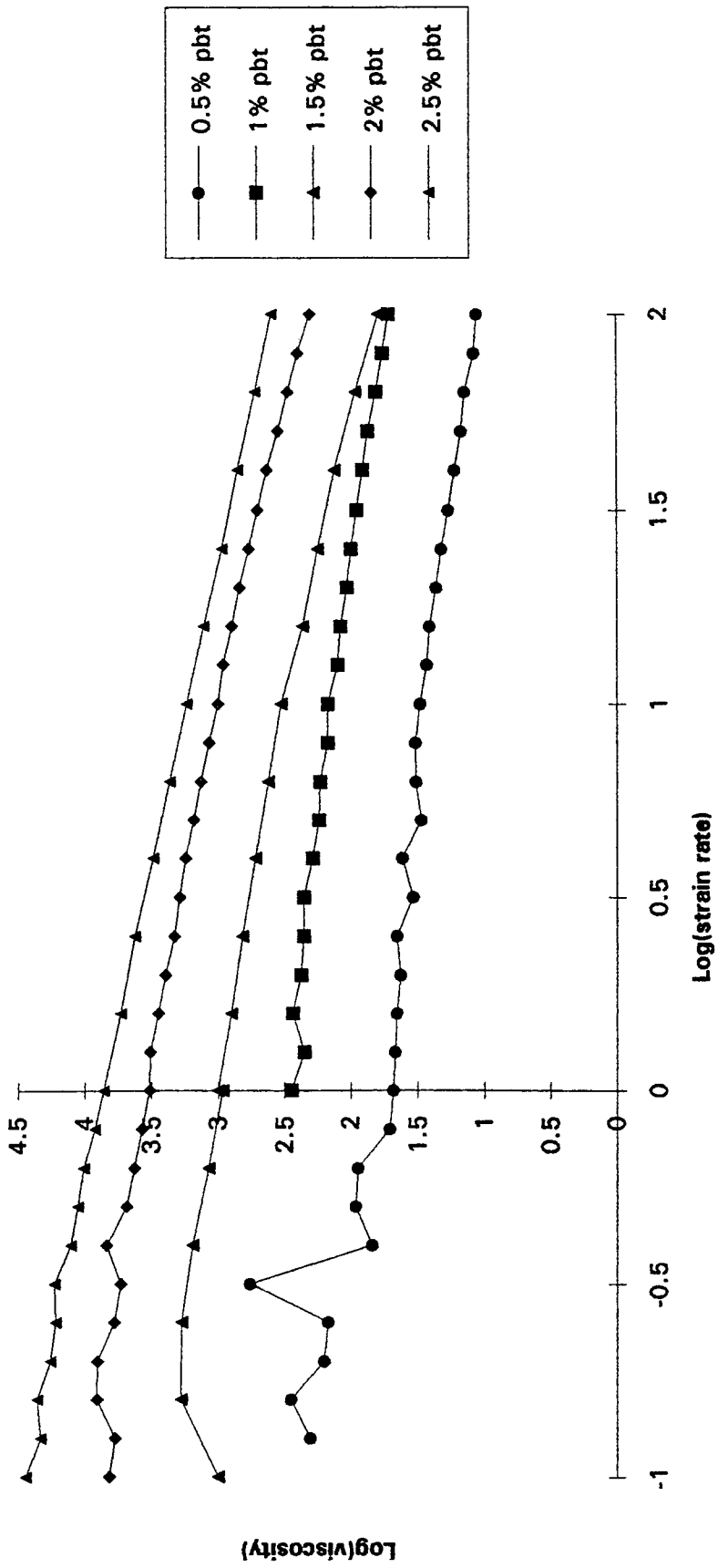
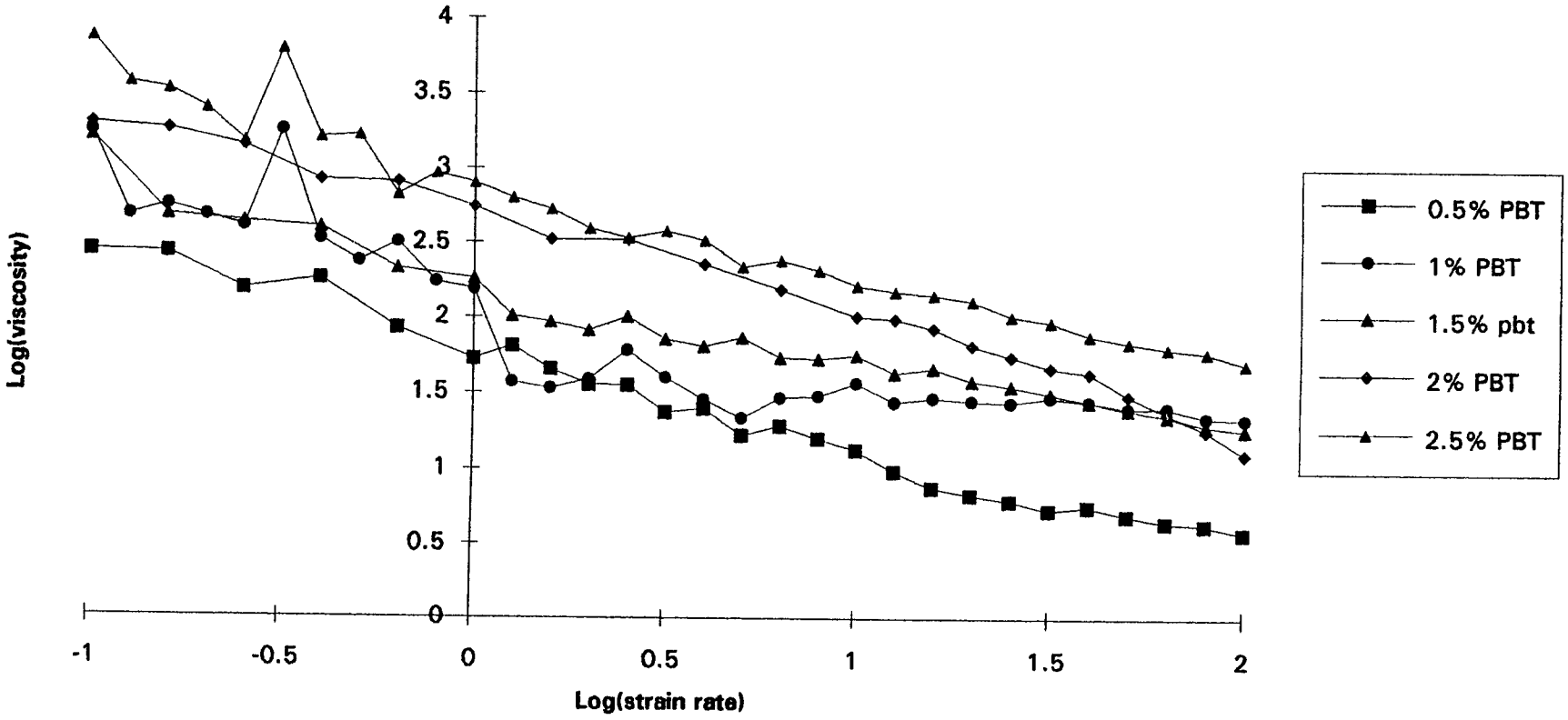
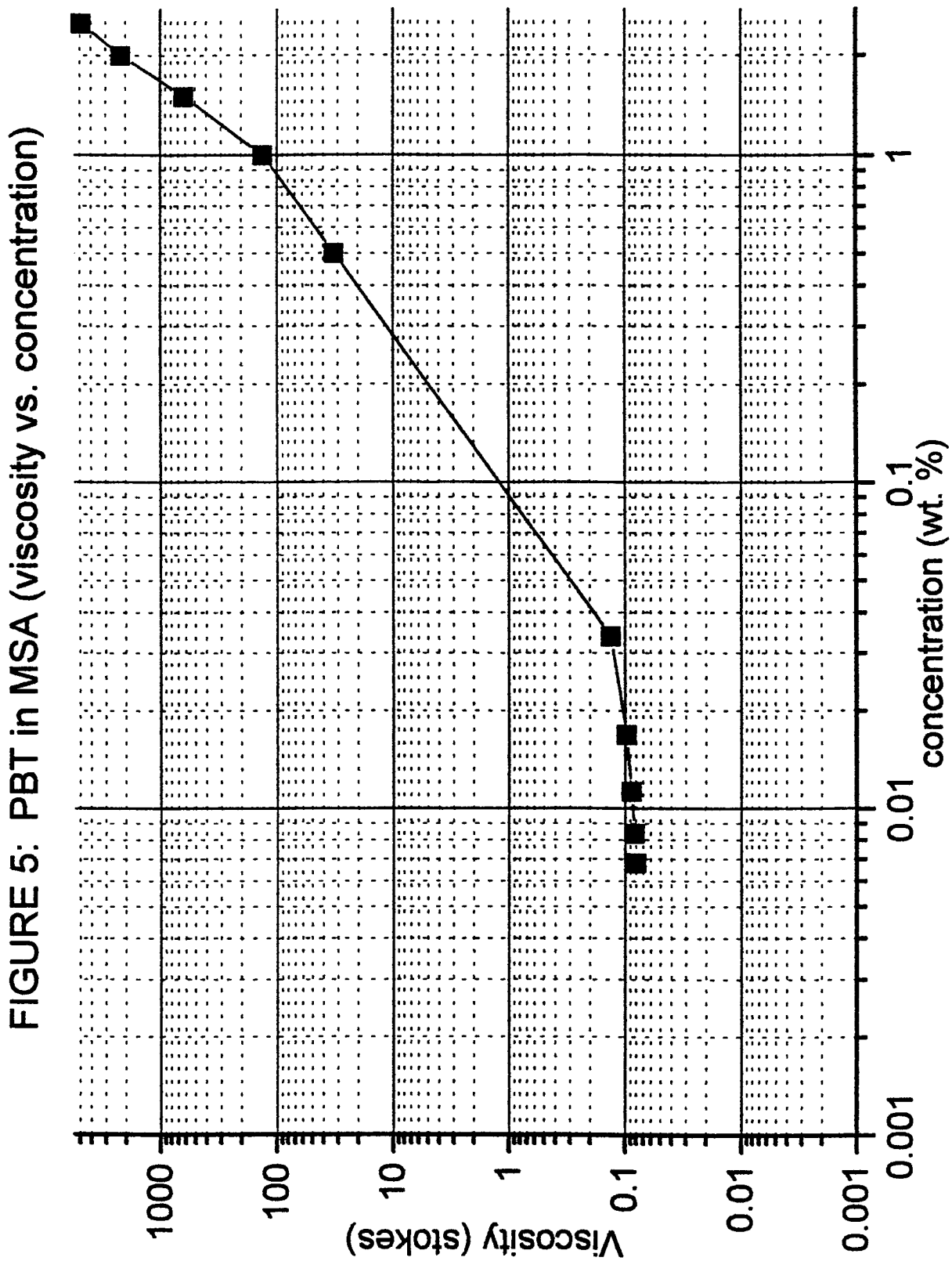


FIGURE 3: PBT in MSA rate sweeps at 30°C (different % strains)

FGURE 4: PBT in MSA rate sweeps at 70°C (different % strains)




FIGURE 5: PBT in MSA (viscosity vs. concentration)
Viscosity (stokes)
1000
100
10
1
0.1
0.01
0.001
0.001
0.01
0.1
1
concentration (wt. %)

ASSESSMENT OF GASP FOR THE SIMULATION OF SCRAMJET COMBUSTOR FLOW FIELDS

Wm. Kevin Cope
PhD Candidate
Department of Mechanical and Industrial Engineering

University of Illinois at Urbana-Champaign
140 Mechanical Engineering Building
1206 West Green Street
Urbana, IL 61801

Final Report for:
Graduate Student Research Program
Aero Propulsion and Power Directorate

Sponsored by:
Air Force Office of Scientific Research
Bolling Air Force Base, DC

and

Aero Propulsion and Power Directorate

August 1994

ASSESSMENT OF GASP FOR THE SIMULATION OF SCRAMJET COMBUSTOR FLOW FIELDS

Wm. Kevin Cope
PhD Candidate
Department of Mechanical and Industrial Engineering
University of Illinois at Urbana-Champaign

ABSTRACT

An assessment of GASP for predicting SCRAMJET combustor flow fields has been completed. The program was evaluated by comparing numerical solutions with experimental data obtained for supersonic turbulent flow over a blunt base. The turbulence models available in GASP are: Baldwin-Lomax, Lam-Bremhorst low Re number k-ε model, and Chien's low Re number k-ε model. The results revealed that the Lam-Bremhorst low Re number k-ε model provided the most accurate predictions. The Lam-Bremhorst model predicted the wake closure to within 29% and the base pressure to within 36%. The solutions for u, v, and p have also been compared to experiment. A preliminary study of helium injection into a Mach 2 airstream has also been completed. The grid structure, boundary conditions, and problem formulation have been developed. An approximate solution on a coarse grid (≈ 102,000 cells) was obtained to a residual of $4.5(10^{-2})$. The solution on the coarse grid was observed to then diverge. Recommendations for proceeding with the investigation of helium injection into a Mach 2 airstream using GASP are given.

ASSESSMENT OF GASP FOR THE SIMULATION OF SCRAMJET COMBUSTOR FLOW FIELDS

Wm. Kevin Cope

INTRODUCTION

The objective of the investigation was to assess the ability of GASP to predict SCRAMJET combustor flow fields. The *G*eneral *A*erodynamic *S*imulation *P*rogram (GASP) is a computer program which approximately solves the Favre averaged equations of turbulent fluid motion. The program is based on a finite volume discretization of the governing equations and is capable of performing either explicit or implicit time integration. The program is appropriate for either two-dimensional or three-dimensional geometries and can solve either the full equation set or the thin-layer form of the governing equations.

The flow field of primary interest is depicted in Figure 1. A strut is mounted parallel to a $M_\infty = 2$ airstream. Fuel is injected from the blunt base of the strut in a direction parallel to the airstream. The configuration is of interest in the development of supersonic combustion ramjet engines. The primary goal in the study of such flows is to obtain the greatest mixing between fuel and air while at the same time incurring minimal losses (i.e. low drag and pressure drop). The ability to simulate such flow fields by numerical solution of the equations of motion is important for two reasons. First, if the simulations are capable of making accurate predictions (as evidenced by agreement with experimental observation), the numerical method may be used to perform parametric tests of various mixing enhancement devices, thus minimizing the cost of fabricating and experimentally testing components which may not improve mixing. Lastly, numerical simulation can be used in conjunction with experimental studies for the purpose of describing qualitatively and quantitatively the structures present in such flow fields.

The assessment of GASP's predictive capability was accomplished by simulating the supersonic, turbulent flow over a two-dimensional blunt base. The 2-D baseflow was chosen because of the fact that such a flow is a primary component of the flow depicted in Figure 1. A baseflow exists between the fuel and air streams as well as between the air streams above and below the strut. If the program is incapable of predicting this more basic flow field, predicting a baseflow compounded by three-dimensional effects due to injection from a circular orifice would not be possible.

Supersonic turbulent baseflow is a current topic of research interest. The prediction of base pressure for such flow has been performed using multi-component models (Korst, 1956) for many years. With the development of both high speed computers and techniques for solving the equations of fluid motion, many researchers are attempting to make such predictions by solving the Favre averaged Navier-Stokes equations. The methods employed thusfar have solved primarily the thin-layer Navier-Stokes equations with a Baldwin-Lomax type turbulence model (Diewert, 1987). The use of two equation models such as the k-ε model of Launder and Spalding, 1974 has been explored by Childs and Caruso, 1987. Childs and Caruso have proposed modifications to the basic k-ε model for both compressibility and curvature effects (Childs and Caruso, 1989). Recently, Sahu has compared two algebraic models (Baldwin-Lomax and Chow) and the low Re number k-ε model of Chien with experimental data for supersonic, turbulent flow over an axisymmetric blunt base (Sahu, 1994). The results obtained by these investigators seem to indicate that prediction of turbulent baseflow remains a very difficult task. No one turbulence model has been shown to be superior to all others.

In the present report, the results of a turbulence model assessment are given. The results of a grid dependence study using the Baldwin-Lomax turbulence model to predict two-dimensional baseflow are given first. The mesh refinement in the study ranged from 10,720 cells to 96,480 cells. The actual assessment of turbulence models available with GASP subsequently follows. Results obtained using the Baldwin-Lomax model, Lam-Bremhorst low Re number k-ε model, and Chien's low Re number k-ε model are compared with experimental data. Finally, some initial results of the simulation of the three-dimensional injector flow are presented.

TWO-DIMENSIONAL BASEFLOW

The assessment of GASP for simulating SCRAMJET combustor flows was accomplished by considering the flow over a two dimensional base. The problem considered is depicted in Figure 2. Air at mach number of 2.56 approaches the base from above while air at mach number of 2.05 approaches the base from below. The low mach number stream has a pressure 2.14 times that of the upper stream (PR=2.14). The flow has been experimentally investigated by Amatucci, Dutton, et al., 1992. The results of numerical simulation using GASP are compared with the experimental results in the following evaluation.

a. Flow field approximation

The computational domain used to describe the baseflow is depicted in Figure 3. A total of five (5) zones were used to describe the geometry. The grid used was a Cartesian grid with the distribution given by a hyperbolic tangent distribution (see Thompson, et al., 1985). In this study, grid adaptation was not used due to the fact that an adaptive grid procedure was not available. A program entitled "basegrid.f" was written to specify the cell distribution for the two-dimensional baseflow.

The inlet profiles of u and k for the upper and lower streams were specified from the experimental data. The inlet boundary layers were experimentally measured at a location 4 mm upstream of the base. The inlet of the computational domain was chosen to coincide with the measurement location. The compressible turbulent boundary layer profile of Maise and McDonald (Warsi, 1993) was used to describe the velocity profile. In particular, the friction velocity was chosen that gave the lowest root-mean-square difference between experiment and boundary layer profile. The expression for the freestream velocity is given below:

$$\left(u_e^* - u^*\right)/u_\tau = -2.5\ln\left(\frac{y}{\delta}\right) + 1.25\left[2 - w\left(\frac{y}{\delta}\right)\right] \tag{1}$$

$$\bar{u} = \frac{u_e}{2A^2}\left[\sqrt{B^2+4A^2}\sin\left\{\frac{u^* A}{u_e} - \sin^{-1}\left(\frac{B}{\sqrt{B^2+4A^2}}\right)\right\} + B\right] \tag{2}$$

$$A = \sqrt{\frac{\gamma-1}{2}M_e^2\frac{T_e}{T_{aw}}} \tag{3}$$

$$B = \frac{T_e}{T_w}\left(1 + r\frac{\gamma-1}{2}M_e^2\right) - 1 \tag{4}$$

where $u_{\tau,lower\,BL} = 26.05$ m/s and $u_{\tau,upper\,BL} = 26.76$ m/s. The simulations using both Lam-Bremhorst k-ε and Chien's k-ε model required specification of k and ε at the inflow. The turbulence intensity was experimentally determined and from this quantity the turbulent kinetic energy was obtained:

$$k = \frac{3}{2}\left(\sigma|\vec{V}|\right)^2 \tag{5}$$

where σ is the turbulence intensity. These values of turbulent kinetic energy at the inflow were curve fit by using 9th order polynomial expressions for k_{upper} and k_{lower}. The turbulent dissipation rate, ε was then specified by using an expression given by Rotta:

$$\varepsilon = \frac{ck^{3/2}}{l} \tag{6}$$

where c=0.164 (see pg. 533; Warsi, 1993). The mixing length, l was specified by van Driest's damping function:

$$l = \kappa y\left\{1 - \exp\left(-y^+ / 26\right)\right\} \tag{7}$$

where κ=0.4.

The upper and lower walls of the wind tunnel were specified as free slip walls. To the extent that the dynamics of the boundary layers present on these two surfaces do not affect the baseflow, this is an accurate approximation. The base itself was specified to be a no-slip, no-penetration, adiabatic wall. The outflow plane was specified by first order extrapolation of primitive variables which is valid only for supersonic flow.

The discrete approximation of the integral form of the governing equations was accomplished by using Roe/Harten flux difference splitting (Hirsch, 1990). A third order accurate expression in conjunction with the minmod limiter (Chakravarthy, 1985) was used for obtaining the "left" and "right" states of the Riemann problem. Time integration was accomplished by using approximate factorization. All viscous terms were treated by using second order central differencing. In all simulations of the 2-D baseflow, the *full* Navier-Stokes equations are treated. The governing equations have not been reduced to the thin-layer equations in the present study.

In obtaining converged solutions for the 2-D baseflow, computations were started by using first order van Leer flux vector splitting. By the nature of the splitting, van Leer FVS is more "diffusive" than the Roe/Harten FDS. It was deemed useful to start with a potentially more diffusive flux function so as to aid in converging a high speed flow simulation in which the initial condition was the freestream flow at M=2.56. In general, the calculation was started with first order van Leer FVS and then first order Roe/Harten

FDS was used. The final converged solution was then obtained using third order accurate Roe/Harten FDS with minmod limiter.

The solution of 2-D baseflow on fine grids (>300x300) was obtained by use of mesh sequencing. GASP has the capability of starting a calculation on a coarse grid, iterating to a specified residual, and then interpolating to the next finest grid. The process is referred to as mesh sequencing and is also known as nested iteration when used in the context of multigrid methods (Briggs, 1987). Mesh sequencing allows one to obtain a reasonable initial estimate of the flow variables on the finest grid instead of simply specifying the freestream quantities as the initial estimate. The mesh sequencing feature of GASP was used extensively during the investigation. It is important to note however that when using a low Re k-ε model, the coarsest grid in the mesh sequence MUST be within $y^+ \cong 5$. If the first cell on the *coarsest* sequence does not satisfy this criteria, divergence may result. The solution of the low Re number k-ε model is best obtained by restarting with a Baldwin-Lomax solution with k and ε specified by freestream turbulence intensity and length scale. Therefore, when a solution with Lam-Bremhorst's or Chien's model is desired, one should start the calculation using Baldwin-Lomax on a coarse grid (with mesh sequencing to $y^+ \cong 5$) with a diffusive flux function, work up to the finest grid and obtain a reasonable solution with the Baldwin-Lomax turbulence model and third order Roe/Harten with minmod limiter. Subsequently, the k-ε solution on the finest grid may be obtained by starting with a converged Baldwin-Lomax solution.

b. Grid dependence study

A grid dependence study has been performed for the simulation of 2-D baseflow. In any simulation of turbulent flow by solution of the Favre averaged Navier-Stokes equations, truncation error will be present. If conclusions are to be made as regards the turbulence models, truncation error must not be allowed to corrupt the solution. Therefore, simulations using the Baldwin-Lomax turbulence model have been performed on grids comprised of 10,720 cells (>100x100), 42,880 cells (>200x200), and 96,480 cells (>300x300).

The prediction of wake closure (X_R) and base pressure (P_B) was observed to improve slightly with grid refinement. Table 1 gives the values obtained for X_R and P_B on each grid. The experimentally observed values for these parameters were 1.4H (H=Base height) and 13.8 kPa respectively. The wake closure on both the coarse and fine grids was equal

to 0.72H. The base pressure prediction improved from 3.8 kPa on the coarse grid to 5.34 kPa on the fine grid.

The streamwise variation of static pressure at the mid-line of the base (y = -0.5H) exhibits significant difference on all grids considered (Figure 4). The pressure level is actually seen to rise with grid refinement. The Baldwin-Lomax model prediction becomes less accurate with grid refinement implying that coarse grid solutions with this model may be deceptively close to experiment.

The profiles of u and v at x=5 mm and 30 mm from the base are given in Figures 5-8. The x=5 mm profile was selected for comparison because it was the closest measurement to the base and the x=30 mm profile was selected because it is located at a position just ahead of the wake closure. These profiles reveal that the 96,480 cell grid provides some improvement in the prediction of these variables when compared to the coarse grid solution. It is also apparent that a monotonic variation in these profiles with grid refinement was not observed for this flow field.

The grid dependence study revealed that the best solution was obtained on the 96,480 cell grid. It cannot be rigorously stated that the solution on this grid is "grid independent". The solution on a 400x400 grid (or finer) would be required in order to establish the grid dependence more rigorously. A solution adapted grid using the 96,480 cell mesh could also be used to more completely determine the grid dependence. Time constraints did not facilitate further inquiry into grid dependence. For the purposes of model assessment, the 96,480 cell mesh was used.

c. Turbulence model assessment

The three turbulence models available in GASP are: Baldwin-Lomax algebraic model, Lam-Bremhorst's low Re number k-ε model, and Chien's low Re number k-ε model. The solutions obtained using these models have been compared with experimental results.

The prediction of the streamwise velocity (u) near the base region is accomplished reasonably well by all models (Figure 9). The maximum value of u is accurately calculated. The transverse velocity (v) predictions reveal the expansions which occur from the top and bottom of the base (Figure 10). The counter rotating vortices which form behind the base are indicated by the change from negative to positive v at y=-0.5H.

The u and v profiles at x=30 mm from the base reveal the differences in the various predictions. The Lam-Bremhorst model is observed to give the best agreement with experimental data. The algebraic model of Baldwin-Lomax gave the least accurate

prediction. The solution obtained from Chien's low Re number k-ε model is almost identical to the Lam-Bremhorst solution. The low Re number models seem to differ only quantitatively and then only by a marginal amount. The qualitative nature of these two model predictions are the same. None of the models accurately predicts the minimum in the u profile at x=30 mm or the extreme values in the profile of v.

The streamwise variation of the static pressure is more accurately predicted by the Lam-Bremhorst low Re number k-ε model (Figure 13). All models overpredict the rise in static pressure with distance from the base, with the Baldwin-Lomax model giving the least accurate prediction. Also, all of the turbulence models predicted a decrease and then increase in the static pressure immediately behind the base. The experimental result indicates that the pressure is uniform in this region.

The prediction of both wake closure and base pressure was more accurately obtained by the Lam-Bremhorst low Re number k-ε model. The wake closure was predicted to within 29% and the base pressure within 36%. Chien's low Re number k-ε model provided a similar result but was slightly less accurate. The Baldwin-Lomax algebraic model gave the worst prediction and in general should not be used for making predictions of base pressure (see Table 2).

The basic flow structure as obtained by the three different models was essentially the same. Figures 14 and 15 compare the solutions obtained by the Baldwin-Lomax and Lam-Bremhorst models respectively. The Lam-Bremhorst and Chien solutions were nearly identical as regards mach contour, therefore only one solution is presented. The wake closure is the most obvious difference between the model predictions. Also, the outflow boundary from the Lam-Bremhorst solution is entirely supersonic, while the Baldwin-Lomax solution contains a subsonic region. The mixed sub/supersonic outflow boundary cannot be treated accurately with GASP. The outflow boundary should be moved further downstream to where M>1 or else a mixed boundary condition should be included in GASP.

THREE-DIMENSIONAL INJECTOR

The efficient mixing of a fuel jet in a supersonic air stream is essential to the development of a supersonic combustion ramjet engine. Research being conducted by the experimental research branch, advanced propulsion division, aero propulsion and power directorate is aimed at understanding the structure present in such mixing flows. Research is also being conducted into various means of enhancing the fuel/air mixing in SCRAMJET

combustors. It is desirable to be able to simulate such flow fields so as to help in the process of understanding such flows and in performing parametric investigations of mixing enhancement techniques. A preliminary numerical study of the strut mounted injector flow has thus been performed.

The geometry considered is shown in Figure 1. Air at freestream mach number equal to 1.906 approaches the strut base from above and below. Helium is injected from a circular orifice in the strut base in a direction parallel to the freestream flow. The helium jet exits at M=1 with a pressure equal to that of the air in the freestream (51.59 kPa). The momentum ratio of jet to freestream $\left((\rho V)_j/(\rho V)_\infty \right)$ was equal to 0.187.

The grid used to describe the geometry is shown in Figures 16 and 17. The grid was generated by using the GRIDGEN software developed for Wright-Patterson Air Force Base. Figure 16 depicts the inflow, sidewall, strut surface, and symmetry boundary of the grid. Figure 17 shows a close-up of the grid in the vicinity of the injector.

The left most plane (i=0) shown in figure 16 is the inlet plane. The streamwise velocity profile at the inlet plane was specified by curve fitting experimental data obtained by researchers in the experimental research branch. The Maise and McDonald curve fit given by equations 1-4 was used for this purpose. The friction velocity was determined to be approximately 23.63 m/s. The static temperature was obained from the Crocco-Busemann relation. The freestream static pressure was assumed to be uniform at the inlet and equal to 51.59 kPa. The back surface (k=0) was specified as a free slip wall. This surface was placed at the location of the boundary layer edge. Likewise the top most boundary (j=jdim; not shown) was specified as a free slip wall at a location equal to the boundary layer edge. The strut was treated as a no slip, no penetration, adiabatic wall.

The grid was comprised of three zones. The first zone, located above the strut, was set up to solve the thin-layer equations in a space marching manner using a second order upwind combined with Roe/Harten FDS and the Baldwin-Lomax turbulence model. The second and third zones, placed behind the strut were global iteration zones in which the full Navier-Stokes equations were solved using the first order Roe/Harten flux function and the Baldwin-Lomax turbulence model. The first zone contained 24 cells in the streamwise direction (x), 56 cells in the wall normal direction (y), and 68 cells in the spanwise direction (z). The first cell above the strut was located at $y^+ = 3$. Zones two and three were each comprised of 96 cells in the streamwise direction, 56 cells in the wall normal direction, and 68 cells in the spanwise direction. The total grid structure consisted of 822,528 cells.

The problem statement, grid structure, and boundary conditions for simulating the 3-D injector have been completed. However, the complete solution of the flow on the finest grid was not obtained during the study. Calculations of the 3-D injector flow were made using a two level mesh sequence arrangement. The solution on the "coarse" grid (approx. 102,000 cells) was obtained to an overall residual of 4.5 (10^{-2}) after approximately 480 cycles. The program then halted due to a math library error in computation. The program attempted to take the square root of a negative number. The most likely cause of the problem is overexpansion. At the edge of the strut and at the edge of the injector, strong expansions exist. Past work in simulating baseflows (Diewert, 1987) has revealed that numerical undershoots may cause the predicted pressure to become negative. The solution subsequently halts due to a floating point exception or math library error. In order to solve this problem, a lower CFL number should be used. Also, the grid structure near the strut surface should be compressed so that the cells in the vicinity of the expansions are smaller. The grid will then more accurately resolve the sharp gradients that exist in those regions.

CONCLUSIONS

An assessment of GASP for predicting SCRAMJET combustor flow fields has been completed. The program was evaluated by comparing numerical solutions with experimental data obtained for supersonic turbulent flow over a blunt base. The results revealed that the Lam-Bremhorst low Re number k-ε model provided the most accurate predictions. The Lam-Bremhorst model predicted the wake closure to within 29% and the base pressure to within 36%. In using GASP to perform parametric studies or in answering questions regarding flow structure, this fact must be kept in mind. The program should not be used to address questions in which a tolerance below $\approx$30% is desired.

A preliminary study of helium injection into a Mach 2 airstream has been completed. The grid structure, boundary conditions, and problem formulation have been completed. An approximate solution on the coarse grid ($\approx$ 102,000 cells) was obtained to a residual of 4.5(10^{-2}). The solution on the coarse grid was observed to then diverge. The calculation of helium injection into a Mach 2 airstream should be continued, albeit with a lower CFL number. The current results were obtained by starting the calculation at CFL=0.1. The use of a lower CFL number is not unreasonable for *starting* a calculation. The CFL number can be started at a low value and subsequently increased to values on the order of one. The grid used in the vicinity of the flow separation should also be refined. By using a finer grid

in this region, the sharp gradients will be better predicted. The potential for observing numerical undershoots in the flow variables will thus be minimized.

REFERENCES

Amatucci, V. A., Dutton, J. C., Kuntz, D. W., and Addy, A. L. (1992). "Two-Stream, Supersonic, Wake Flowfield Behind a Thick Base, Part I: General Features". AIAA Journal. vol. 30. no. 8. August 1992. pp. 2039-2046.

Briggs, William L. (1987). A Multigrid Tutorial. Society for Industrial and Applied Mathematics. Philadelphia, PA. 1987.

Chakravarthy, S. R. and Osher, S. (1985). "A New Class of High Accuracy TVD Schemes for Hyperbolic Conservation Laws". AIAA-85-0363. January 14-17, 1985. Reno, NV.

Childs, Robert E. and Caruso, Steven C. (1987). "On the Accuracy of Turbulent Base Flow Predictions". AIAA-87-1439. January 1987. Reno, NV.

Childs, R. E. and Caruso, S. C. (1989). "Assessment of Modeling and Discretization Accuracy for High Speed Afterbody Flows". AIAA-89-0531. January 9-12, 1989. Reno, NV.

Diewert, George S., Andrews, Alison E., and Nakahashi, Kazuhiro. (1987). "Theoretical Analysis of Aircraft Afterbody Flow". Journal of Spacecraft and Rockets. vol. 24. no. 6. pp. 496-503.

Hirsch, C. (1990). Numerical Computation of Internal and External Flows. vol. 2. Computational Methods for Inviscid and Viscous Flows. John Wiley and Sons.

Korst, H. H. (1956). "A Theory for Base Pressures in Transonic and Supersonic Flow". Journal of Applied Mechanics. vol. 23. no. 4. 1956. pp. 593-600.

Launder, B. E. and Spalding, D. B. (1974). "The Numerical Computation of Turbulent Flows". Computer Methods in Applied Mechanics and Engineering. vol. 3. pp. 269-289.

Sahu, Jubaraj. (1994). "Numerical Computations of Supersonic Base Flow with Special Emphasis on Turbulence Modeling". AIAA Journal. vol. 32. no. 7. July 1994. pp. 1547-1549.

Thompson, Joe F., Warsi, Z. U. A., and Mastin, C. Wayne. (1985). Numerical Grid Generation. Foundations and Applications. Elsevier Science Publishing Co.

Warsi, Z. U. A. (1993). Fluid Dynamics. Theoretical and Computational Approaches. CRC Press.

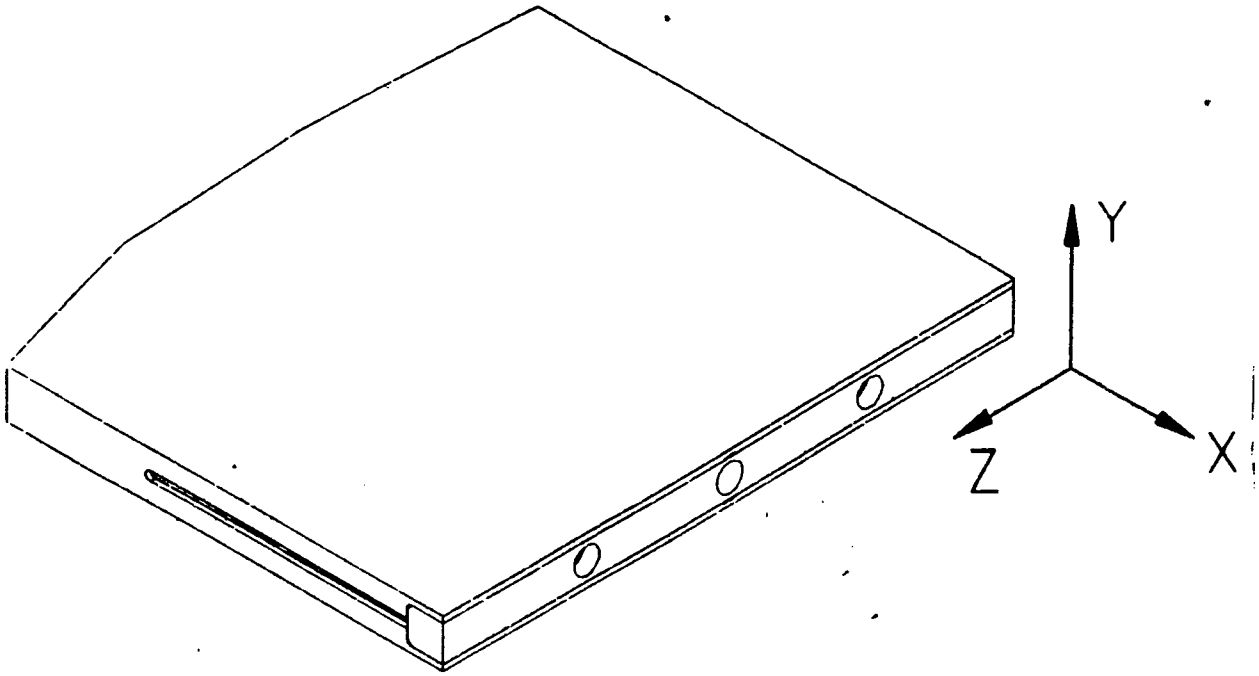


Figure 1: Schematic of strut mounted injector. The helium is injected from the base of the strut in a direction parallel to the airstream.

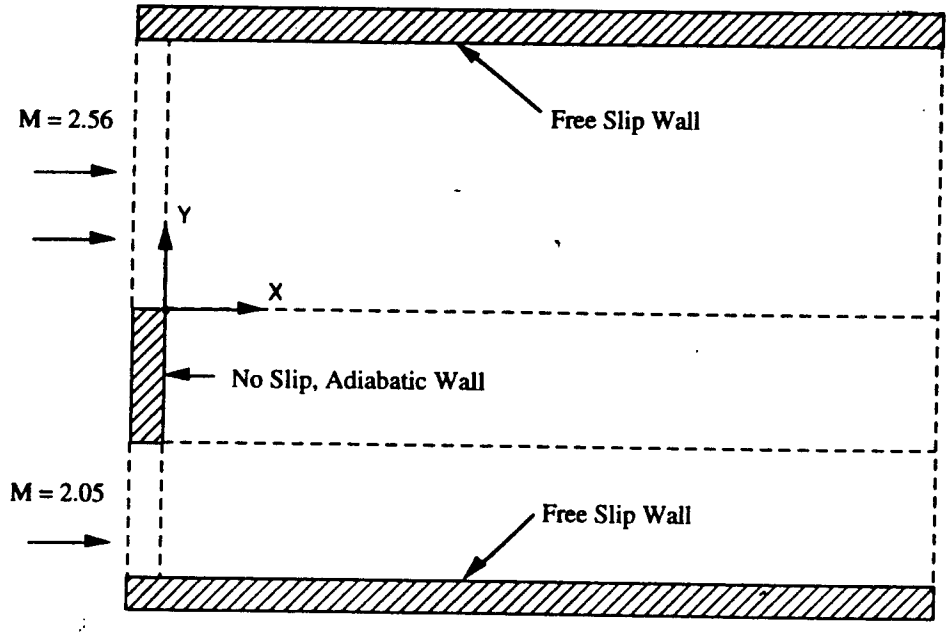


Figure 2: Schematic of two-dimensional base flow studied by Amatucci, Dutton, et al., 1992. The 2-D base flow was used in the assessment of turbulence models available in GASP.

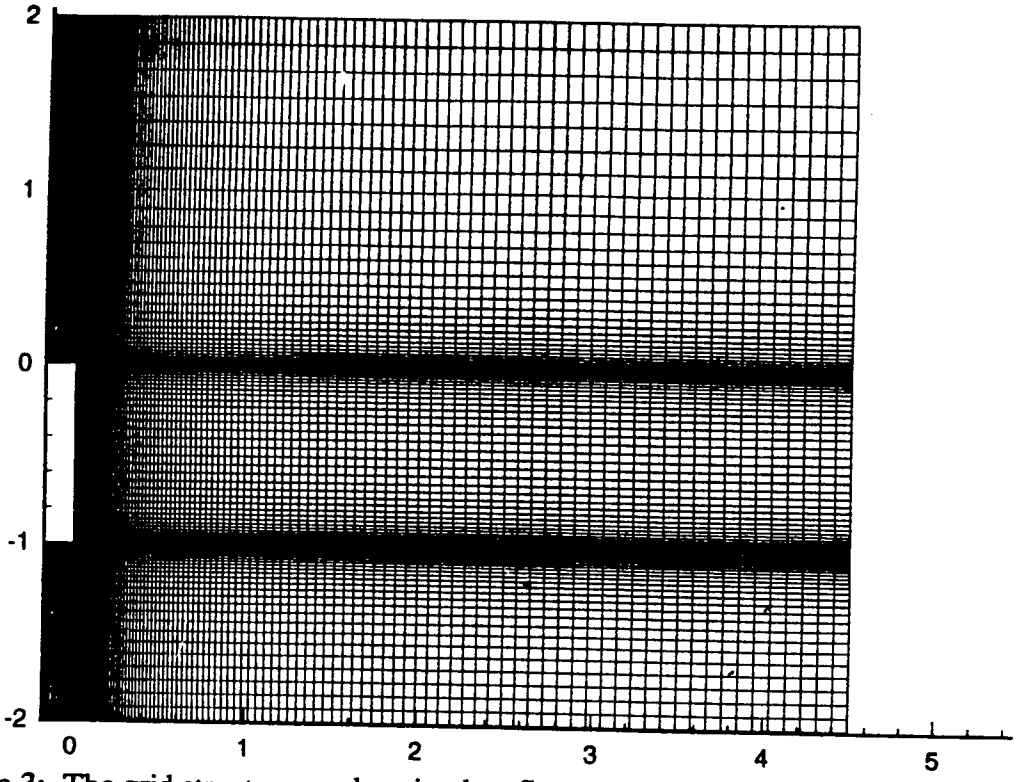


Figure 3: The grid structure used to simulate flow over the two-dimensional base. A total of five (5) zones were used in describing the geometry. The 10,720 cell grid is shown.

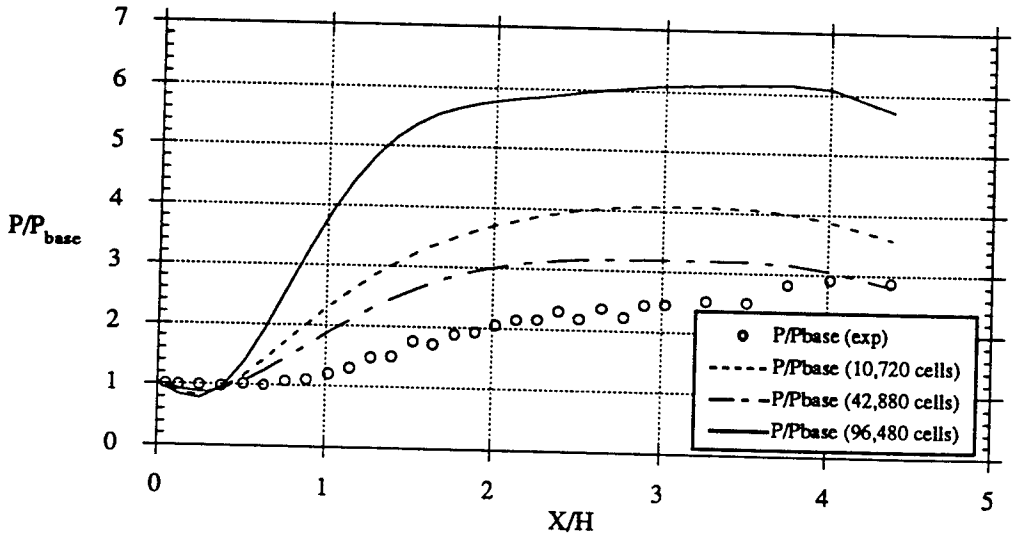


Figure 4: Streamwise variation of static pressure on different grid densities. y=-0.5 H.

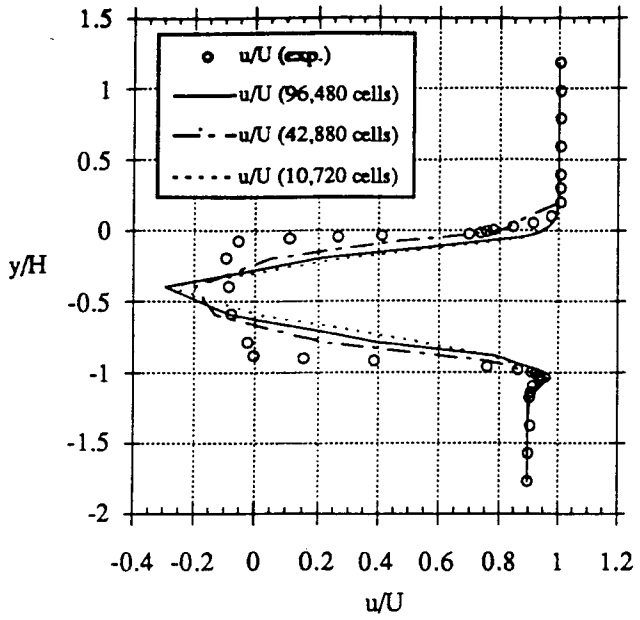


Figure 5: Streamwise velocity profiles for different grid densities at x=5 mm from base.

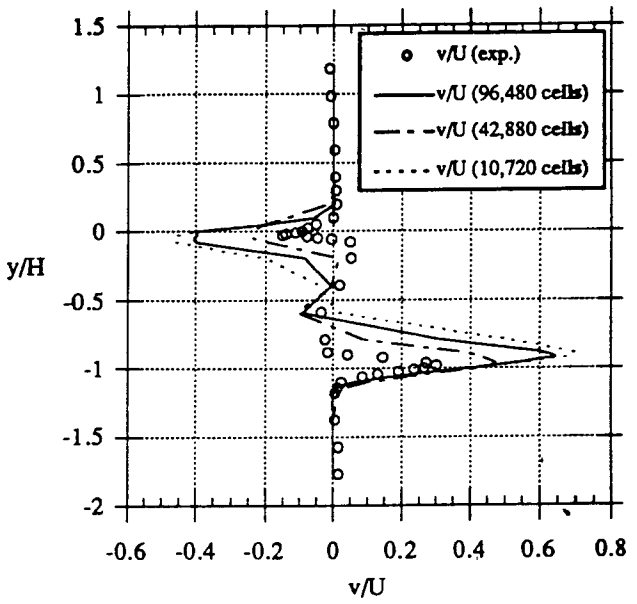


Figure 6: Transverse velocity profiles for different grid densities at x=5 mm from the base.

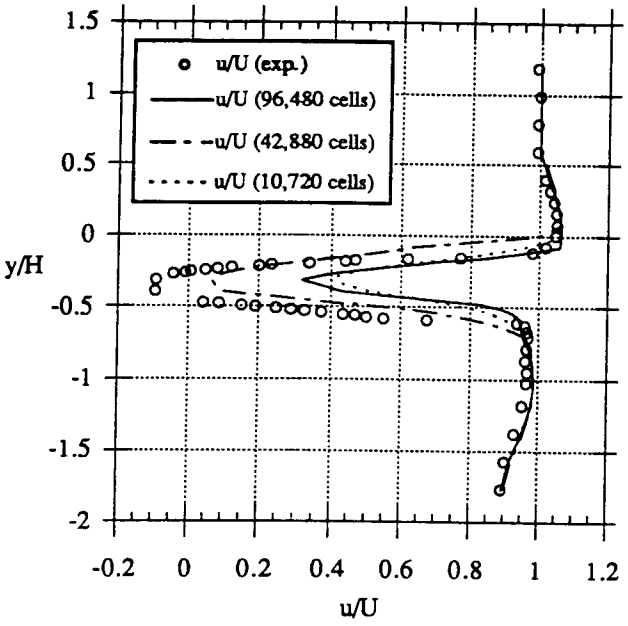


Figure 7: Streamwise velocity profiles for different grid densities at x=30 mm from the base.

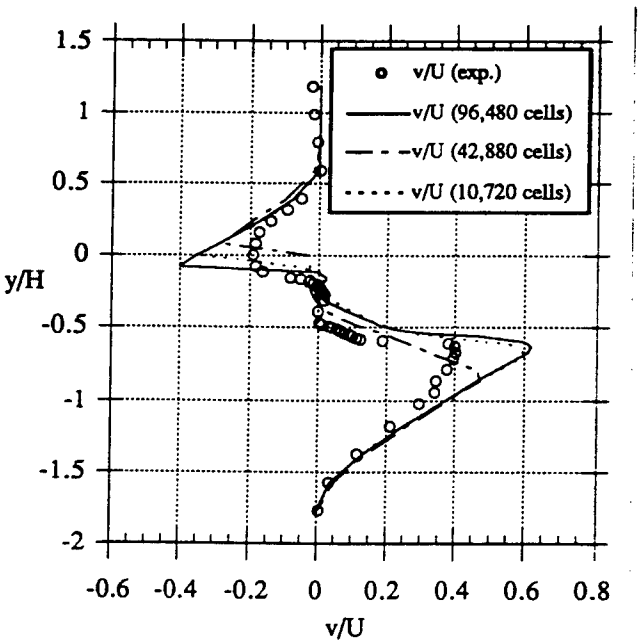


Figure 8: Transverse velocity profiles for different grid densities at x=30 mm from the base.

	Wake Closure (X_R/H)	P_{BASE}
Experiment	1.4	13.8 kPa
10,720 cells	0.72 (-49%)	3.8 kPa (-73%)
42,880 cells	1.02 (-27%)	10.63 kPa (-23%)
96,480 cells	0.72 (-49%)	5.34 kPa (-61%)

Table 1: Numerically obtained values of wake closure and base pressure obtained during grid convergence study. Shown in parentheses are the percentage differences between numerical and experimental values.

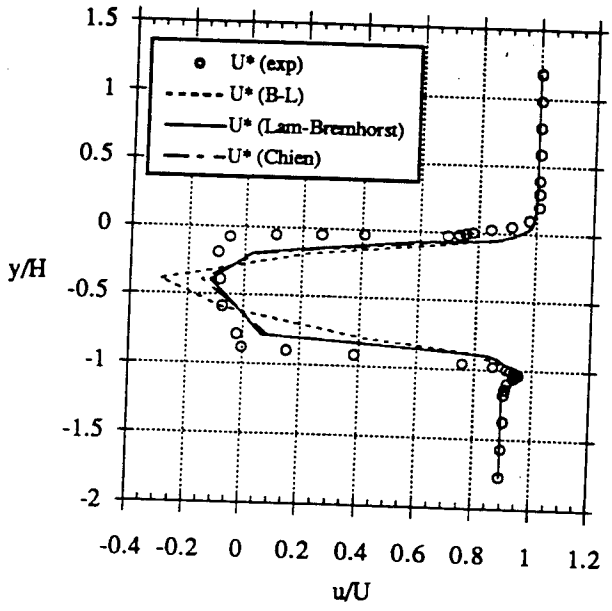


Figure 9: Streamwise velocity profiles for different turbulence models at x=5 mm from the base.

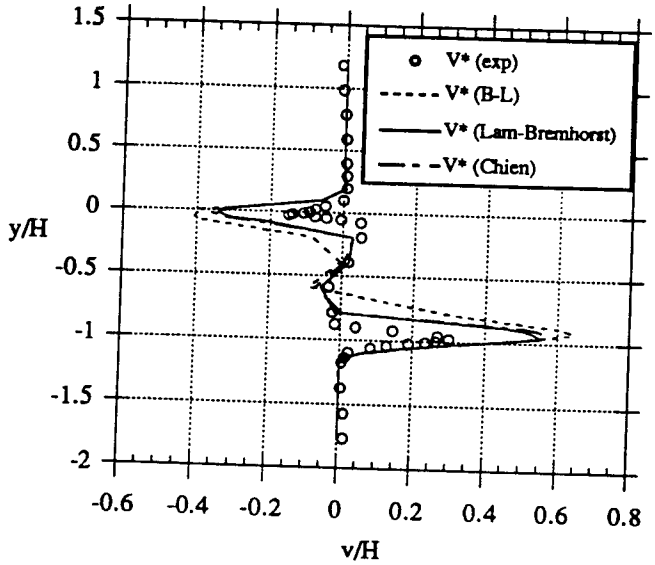


Figure 10: Transverse velocity profiles for different turbulence models at x=5 mm from the base.

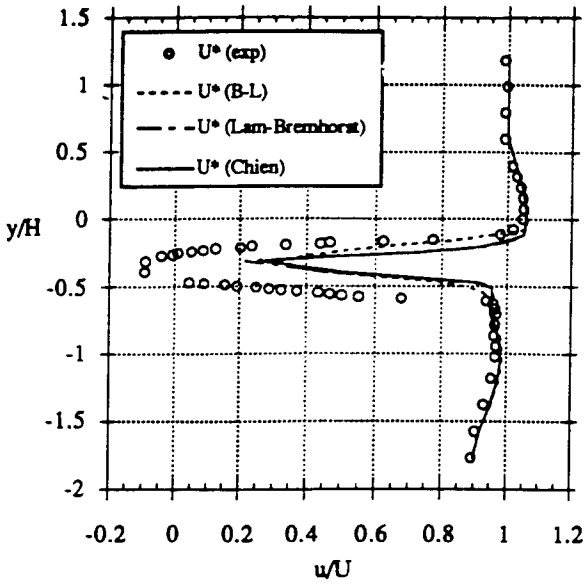


Figure 11: Streamwise velocity profiles for different turbulence models at x=30 mm from the base.

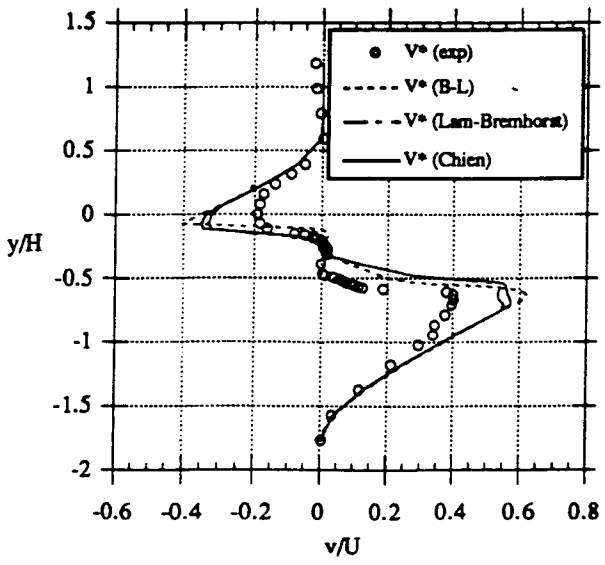


Figure 12: Transverse velocity profiles for different turbulence models at x=30 mm from the base.

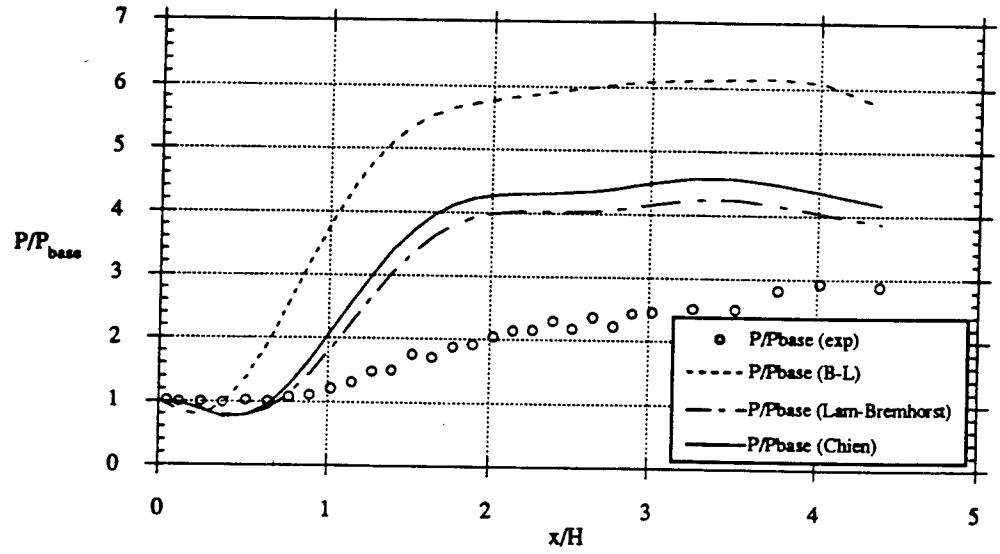


Figure 13: Streamwise variation of static pressure for different turbulence models at y=-0.5 H.

	Wake Closure (X_R/H)	P_{BASE}
Experiment	1.4	13.8 kPa
Baldwin-Lomax	0.72 (-49%)	5.34 kPa (-61%)
Lam-Bremhorst	1.0 (-29%)	8.78 kPa (-36%)
Chien	0.94 (-33%)	8.04 kPa (-42%)

Table 2: Numerically obtained values of wake closure and base pressure obtained during model assessment study. Shown in parentheses are the percentage differences between numerical and experimental values.

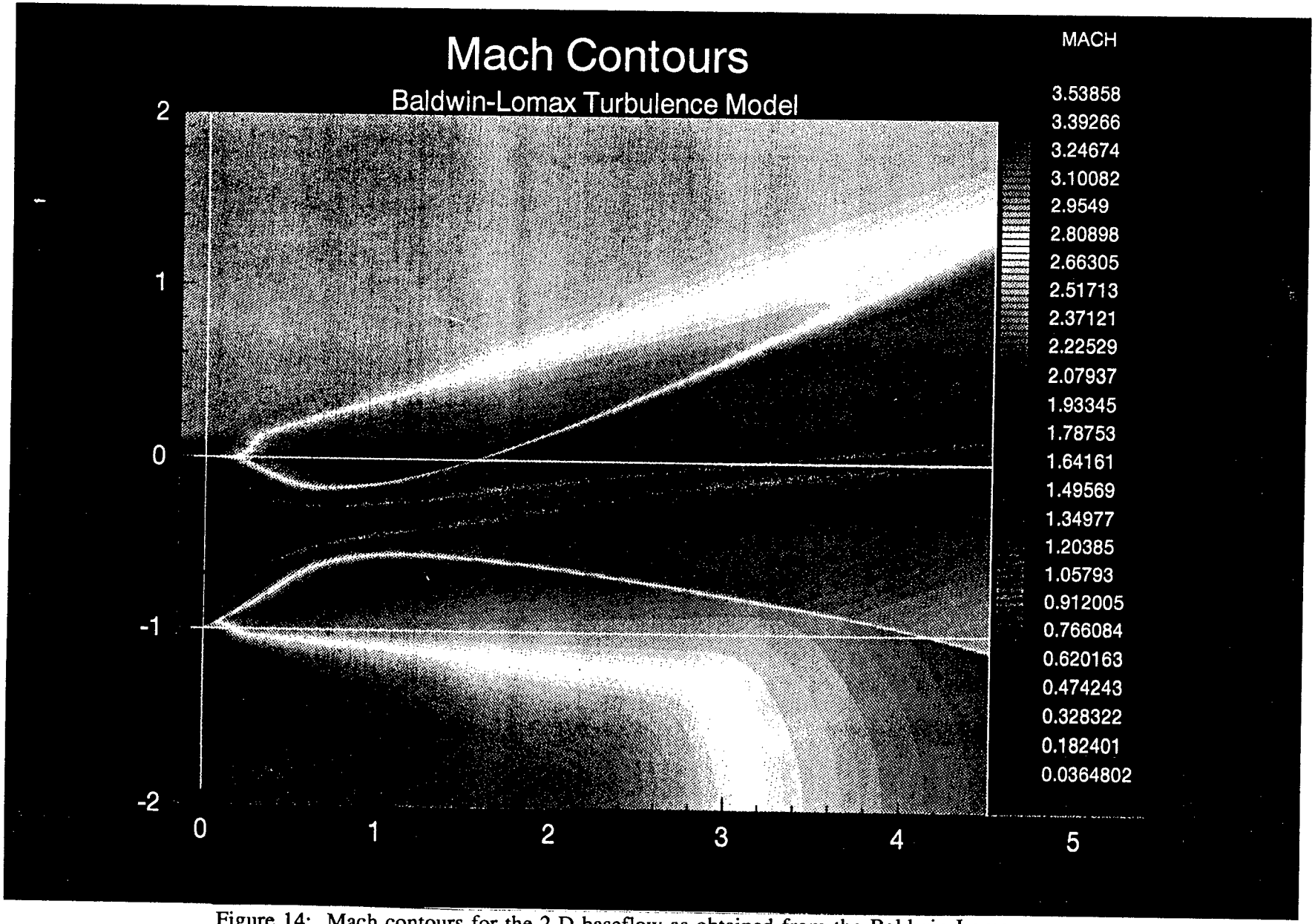


Figure 14: Mach contours for the 2-D baseflow as obtained from the Baldwin-Lomax turbulence model.

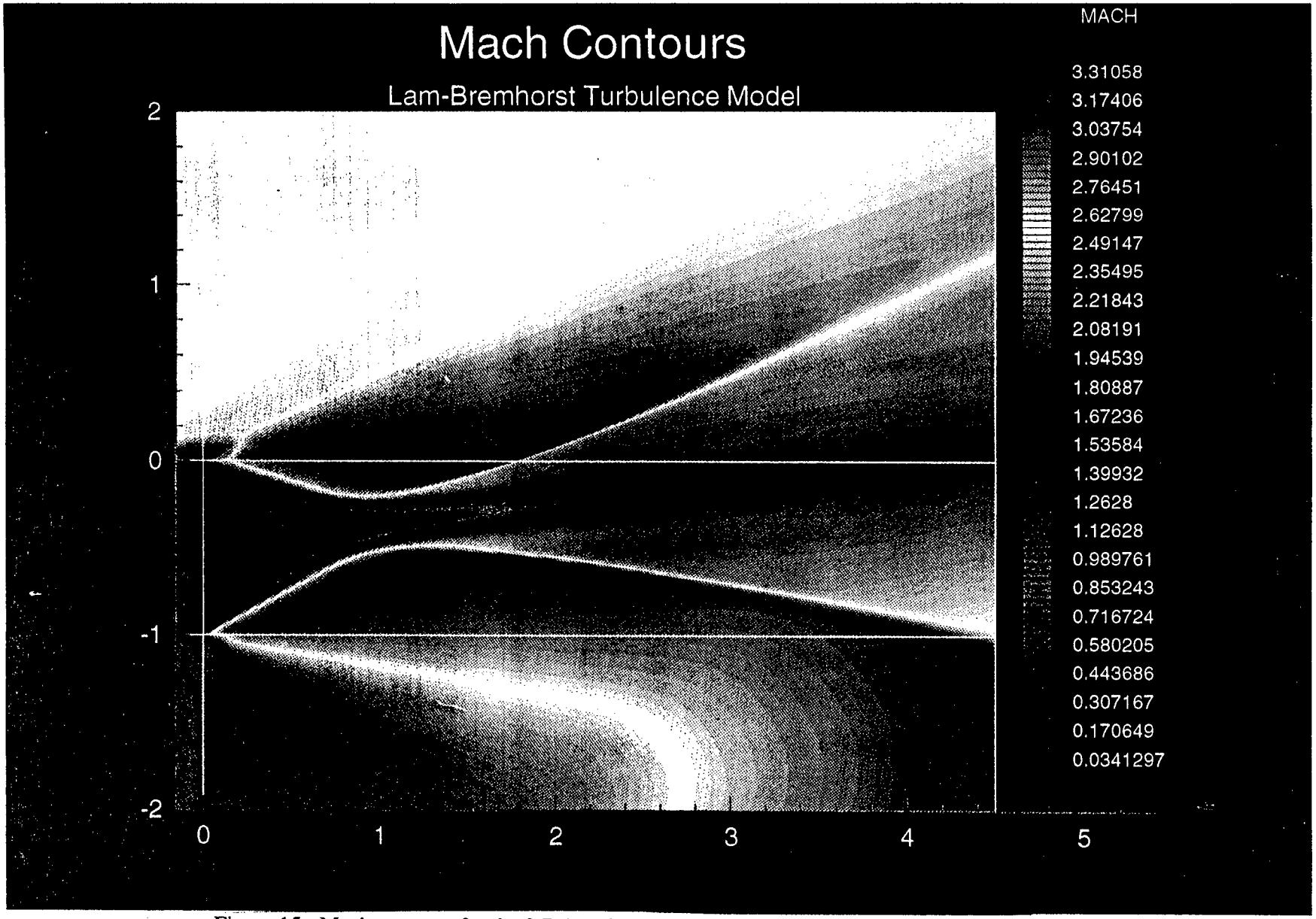


Figure 15: Mach contours for the 2-D baseflow as obtained from the Lam-Bremhorst low Re number k-ε turbulence model.

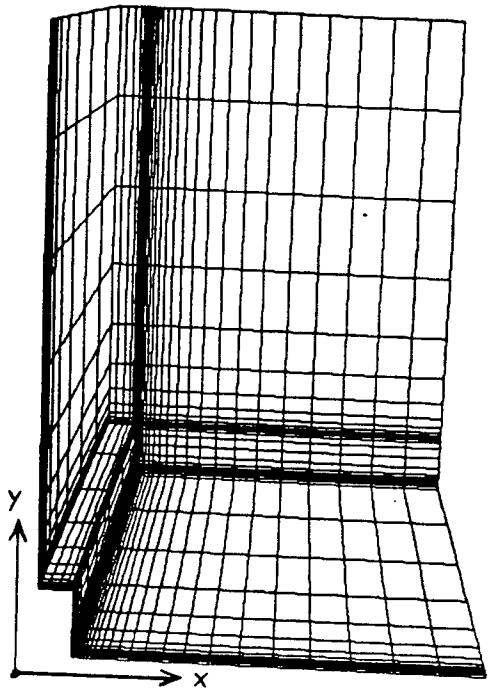


Figure 16: The three-dimensional grid structure used to model the parallel injection of helium into a Mach 2 airstream.

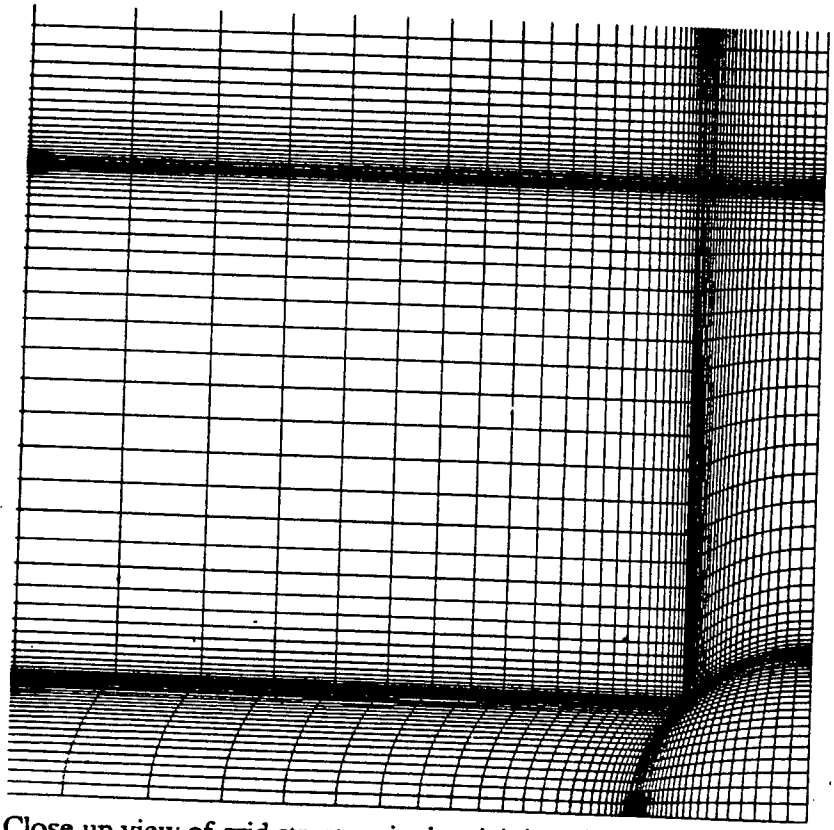


Figure 17: Close up view of grid structure in the vicinity of the helium injector. Only one-quarter of the injector is simulated due to symmetry.

A STUDY OF THE HEAT TRANSFER FOR THE HIGH FLUX HEAT EXCHANGER

Mike Cutbirth
Graduate Student
Department of Mechanical Engineering

Oklahoma State University
218 Engineering North
Stillwater, OK 74078

Final Report for:
Graduate Student Research Program
Wright Laboratories

Sponsored by:
Air Force Office of Scientific Research
Bolling Air Force Base, DC

and

Wright Laboratories

September 1994

A STUDY OF THE HEAT TRANSFER FOR THE HIGH FLUX HEAT EXCHANGER

Mike Cutbirth
Graduate Student
Department of Mechanical Engineering
Oklahoma State University

Abstract

An experimental study was conducted to determine the heat transfer capabilities of the high flux heat exchanger, using Polyalphaolefin (PAO) as the coolant. This study was completed over a range of coolant temperatures from 0 °C to 40 °C with intervals of 10 °C. Because PAO was used as the coolant this study represents an unique example of the performance of the compact high intensity cooler designed by Sundstrand under laminar flow. Previously, the majority of tests performed on the compact high intensity cooler were for turbulent flow. In addition to the heat transfer capabilities, the study also included the examination of the dynamic pressure drop across the high flux heat exchanger, which has a design point pressure drop of 16 psi at 30 °C and 4.5 kg/min. However, this study shows that the pressure drop is 16 psi at 30 °C and 2.5 kg/min. Further dissimilarities include the predicted thermal resistance and the calculated thermal resistance. For example at 20 °C the thermal resistance was calculated at .22 for a flow rate of 3.5 kg/min. and the predicted thermal resistance was .28 for the same flow rate. However, for a flow rate of 1.5 kg/min., the thermal resistance was calculated at .29 while the predicted thermal resistance was .52 for the same flow rate. These dissimilarities indicate the need for an improved correlation between the hydraulic and thermal performances and the input variables for laminar flow.

A STUDY OF THE HEAT TRANSFER CAPABILITIES OF THE HIGH FLUX HEAT EXCHANGERS

Mike Cutbirth

Introduction

As the aircraft electronic systems have become more advanced, the power dissipation has increased while the actual size of the system has decreased. In fact, it is estimated that by the year 2000, the board-level heat loads in these electronic systems will reach 2,000W with local heat fluxes greater than 100 W/cm^2. Therefore, new techniques for more efficient heat exchangers are needed to cool these high-powered electronics. One such technique is the Compact High Intensity Cooler, CHIC, that was developed in 1983 by Sundstrand Aerospace. The CHIC is a liquid single-phase cooler which combines the thermal efficiency of multiple jet impingement with an extended surface area to produce a high effective heat transfer coefficient. This technique consists of a stack of thin copper orifice laminates and spacer laminates that are photo etched and diffusion bonded. The orifice plate contains anywhere from 50 to 200 small circular holes. These plates provide a liquid jet impingement heat transfer on a target plate, then is directed back to a drain manifold and ultimately to a exit port. The electronics are connected to the back side of the target plate. Each CHIC is 1cm x 1cm and allows 100 watts of heat transfer. Taking this concept, McDonnell Douglas developed the High Flux Heat Exchanger, HFHE. The HFHE consists of 20 CHICs in parallel, each orifice plate contains 60 holes, seven laminates, with each laminate being .1 cm thick. From this arrangement each CHIC should be independent of each other. Therefore, the total heat transfer capability of the HFHE is 2000 W. Previously, the CHIC devices have not been tested for laminar flow due to a highly viscous fluid such as PAO. In fact most of all of Sundstrand model predictions are for turbulent flow. Therefore, the performance predictions for the HFHE must be extrapolated to laminar Reynolds numbers.

Methodology

The test procedure for this study consisted of two basic parts, the hydraulic tests and heat transfer tests. Because of the limited space aboard aircraft, the electronic coolant system must be compact. Therefore, the pressure drop across the HFHE needs to be minimized to allow for a small pump. However, as the PAO becomes exceedingly viscous as temperature decreases, the pressure drop across the HFHE becomes exceedingly large. In addition, each chic in the HFHE must be capable of transferring 100 W. With these concepts in mind the following tests were performed.

Test Setup

Figure 1 shows the experimental configuration of the test loop. The coolant starts from a reservoir which is then pumped through a constant volume gear pump to achieve the desired flow rate. The coolant then

is cooled to the desired temperature using a shell and tube heat exchanger with ethylene-glycol as the cooling fluid.

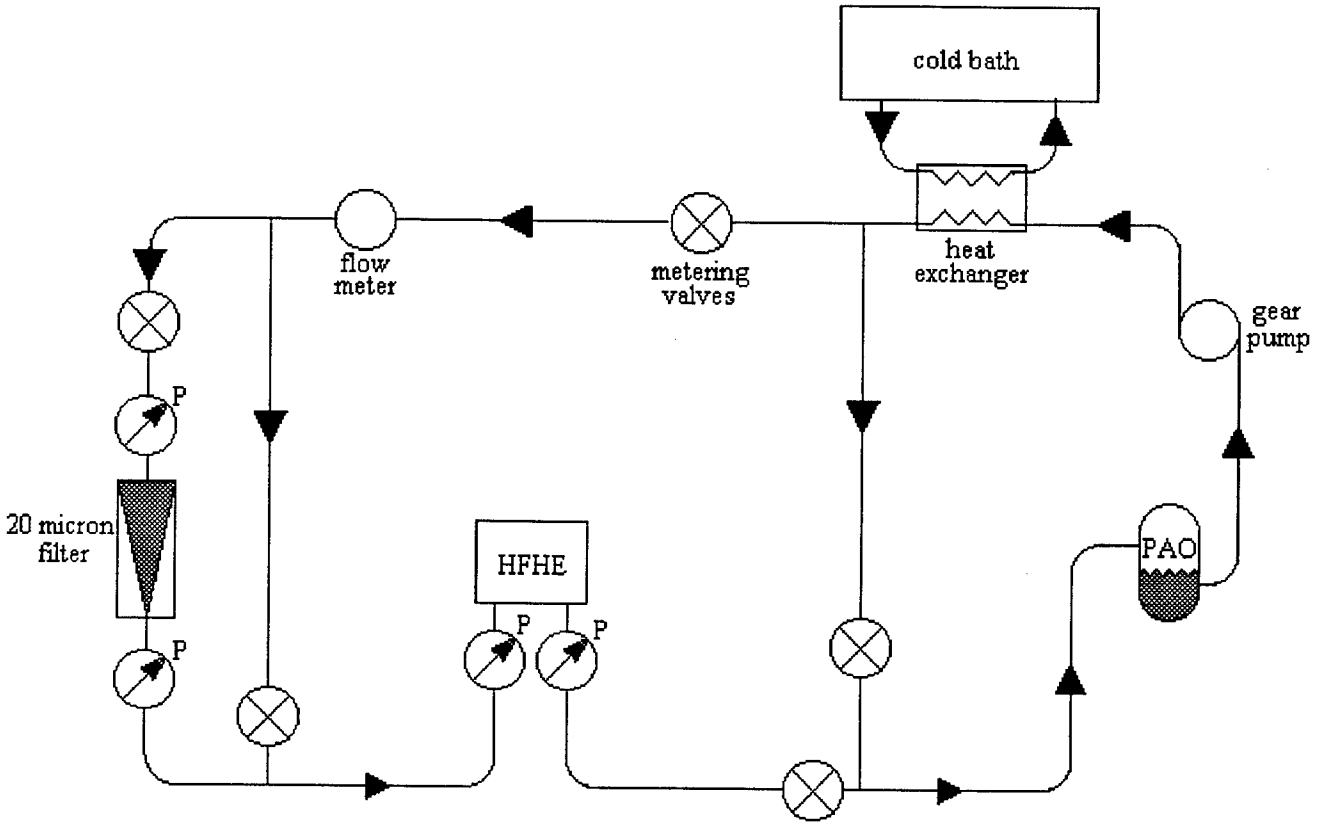


Figure 1. Test Loop

The inlet and outlet pressures are measure using two absolute wet-wet pressure transducers. In addition, the temperature of the inlet coolant supply and the outlet coolant supply are measured by using thermocouple probes. Due to the high watt intensity needed to generate the necessary heat flux and the unavailability of commercial heaters that can handle high watt intensities, a heat flux amplifier, shown in figure 2, was designed. This amplifier allows the use of a commercially bought heater, such as a Minco mica heater. The top of the amplifier is 2.5 inches by 2.5 inches or a surface space of 6.25 inches squared. Therefore, the heater only has to handle a watt intensity of 16 W/ sq. in. The amplifier is then reduced in cross-sectional area to 1cm by 1cm. Thereby creating a heat flux of 100W/sq. cm. To guarantee that the heat flux is uniform throughout the amplifier at any given distance from the CHIC surface, thermocouples are imbedded throughout the cross-section in three different planes. In addition, a thermocouple is located at the heater to indicate when the steady state condition has been satisfied.

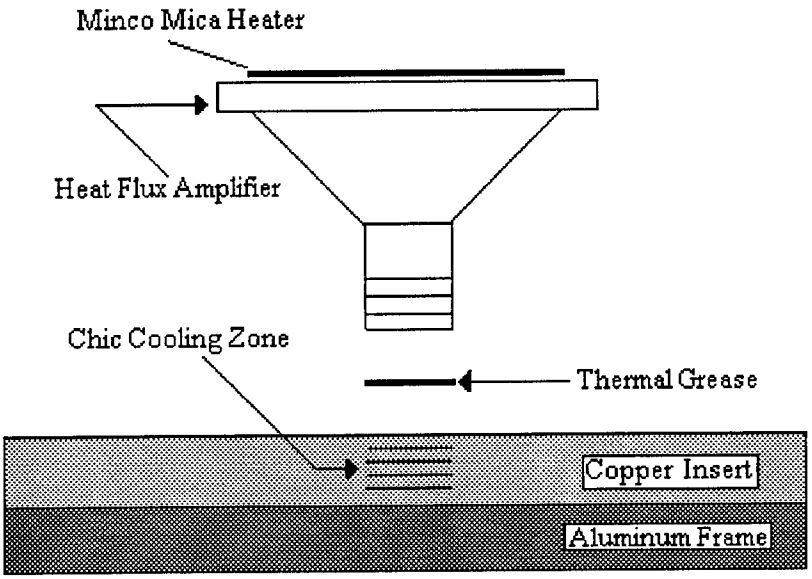


Figure 2. Heat Flux Amplifier

The HFHE itself consists of 20 CHICs arranged in parallel flow. For proper testing of the HFHE, each CHIC should be evaluated. However, due to time constraints, only one CHIC was tested, shown in figure 3. The wall temperature of the CHIC is needed for the heat transfer calculations. Therefore, to alleviate any errors due to interference from the amplifier, a small notch was made in the CHIC. Inside this notch a thermocouple was imbedded.

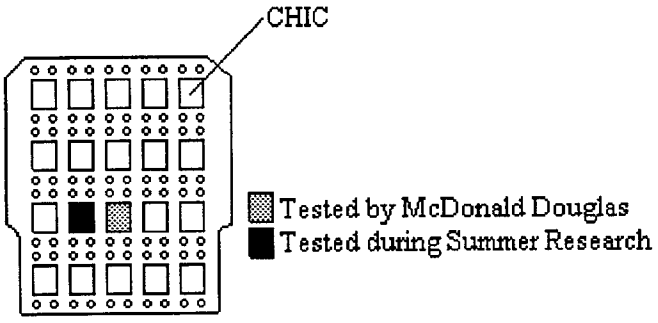


Figure 3. HFHE

For each flow rate, there exists three variables: the heat transfer applied, the wall temperature of the CHIC, and the inlet coolant temperature. Therefore, to reduce this to a single variable, the thermal resistance of the CHIC can be defined as:

$$R_{wf} = \frac{(T_w - T_f)}{Q}$$

However, because only one CHIC is being tested at a time, there is some heat transfer conducted radially from the CHIC. Therefore, the actual heat transferred from the heater to the connected CHIC is less than the applied heat transfer. In McDonnell Douglas experiments, the correlation, shown in figure 4, between the radially conducted heat transfer and the flow rate was approximated by the following equation:

$$\frac{Q_{loss}}{Q_{applied}} = .219 - .000356(\dot{m})$$

Where: mass flow rate is in kg/hr

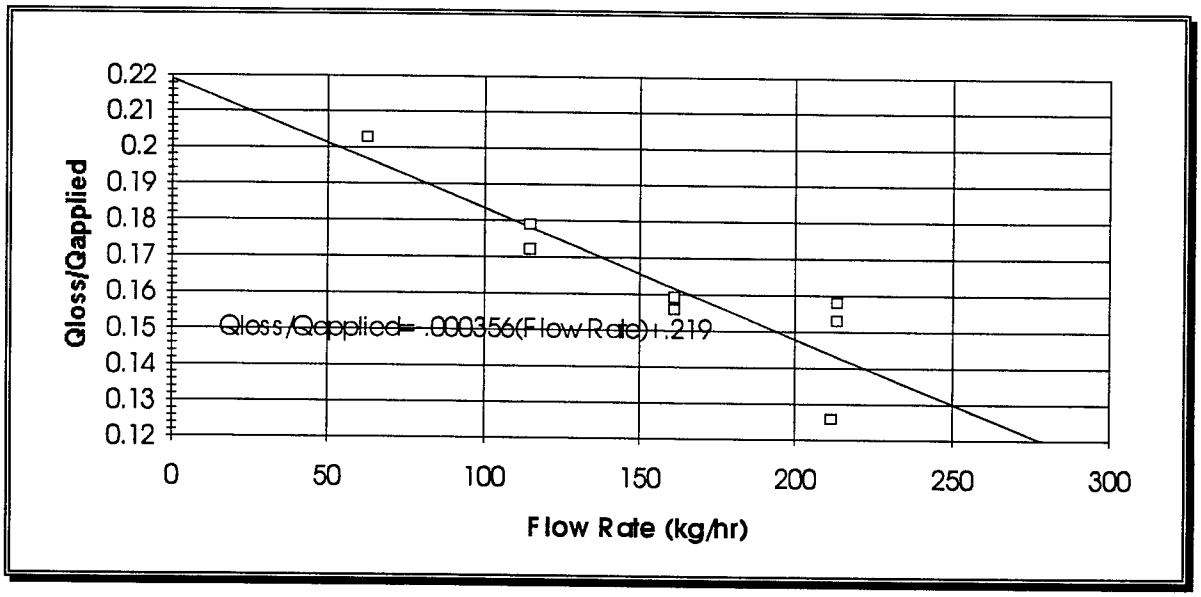


Figure 4. Correlation between Radially Conducted Heat Transfer and Flow Rate

Using this correlation, an actual heat transfer from the heater to the CHIC can be calculated which in turn yields an updated thermal resistance.

Results: Hydraulic Tests

Figure 5 shows the relationship between the pressure drop and the flow rate of the coolant. From this figure, it is evident that the viscosity of the coolant is increasing at a greater rate as the temperature decreases. Noting from this chart that the difference in the pressure drop at 3.5 kg/min. from 30 °C to 20 °C is 3 psi while the difference in the pressure drop at 3.5 kg/min. between 10 °C and 0 °C is 9 °C, thereby leading to the conclusion that the difference between the -10 °C and 0 °C will be much greater than 9 °C. Since each interval, as the temperature decreases, will be larger than the previous, it is evident that at the low end of the possible temperature range, -40 °C, the pressure drop will be much greater than 100 psi, which is specified as the design point pressure drop across the HFHE.

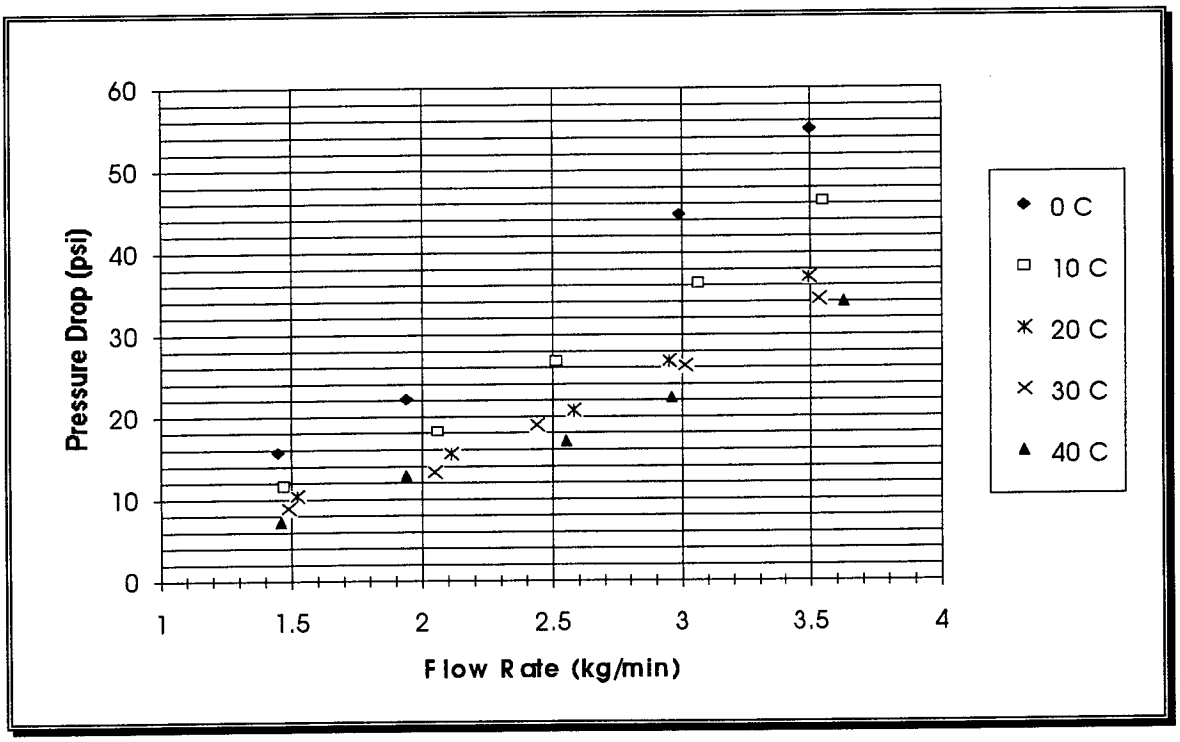


Figure 5. Dynamic Pressure Drop Across the HFHE

Also of interest is the assumption that at the extreme low temperatures, that the only concern with the pressure drop is at the initial startup. In other words, that the pressure drop across the HFHE will decrease as the heat transfer across the CHIC increases. Therefore, the relationship between the pressure drop and the heat transfer was determined and is shown in figure 6.

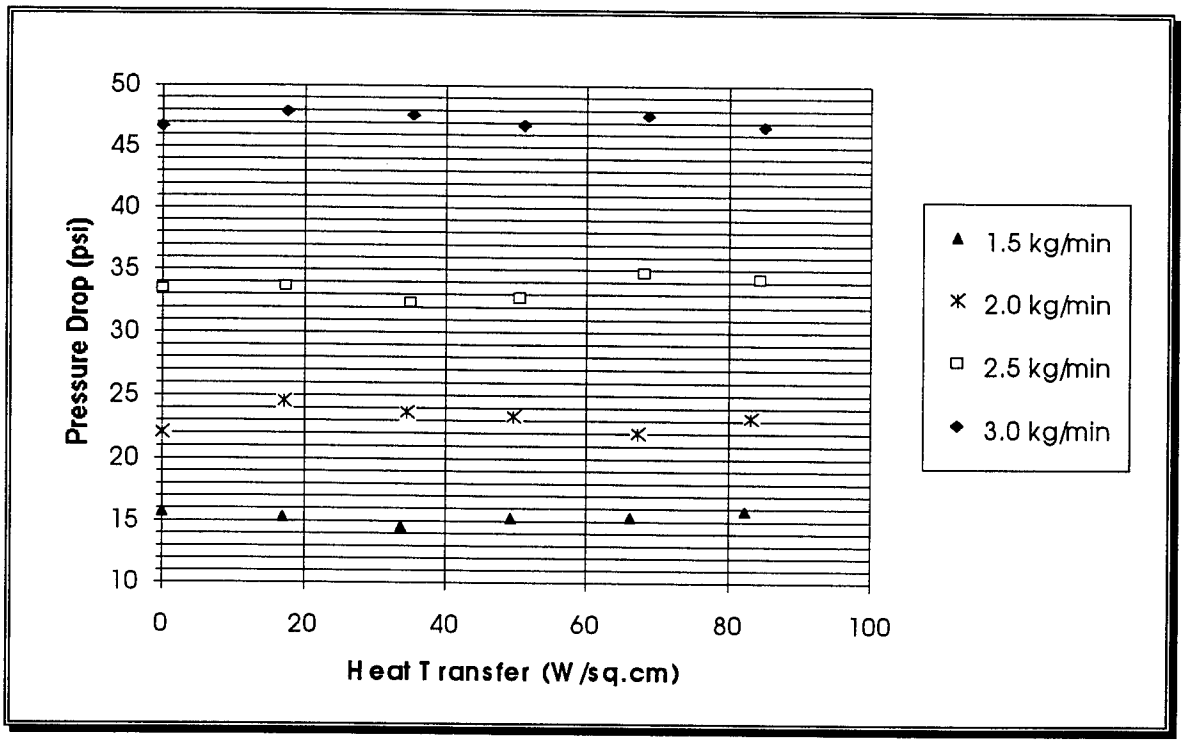


Figure 6. Relationship between the Dynamic Pressure Drop and the Heat Transfer

From this figure, it is evident that the pressure drop is independent of the heat transfer to the CHIC. However, this assumes that the inlet coolant temperature to the HFHE remains constant.

Results: Heat Transfer Steady-State Tests

Figures 7 through 11 show the relationships between the thermal resistance and the flow rate for the coolant temperatures 0°C through 40°C respectively. For each temperature the heat transfer data shown are for the corrected heat transfer and the thermal resistance is the updated thermal resistance. Also, at each temperature the curves are compared to the predicted curve for 100 W of heat transfer to the CHIC. This prediction is given by Sundstrand based on turbulent flow extrapolated to laminar flow and shown in McDonnell Douglas' final report over the HFHE.

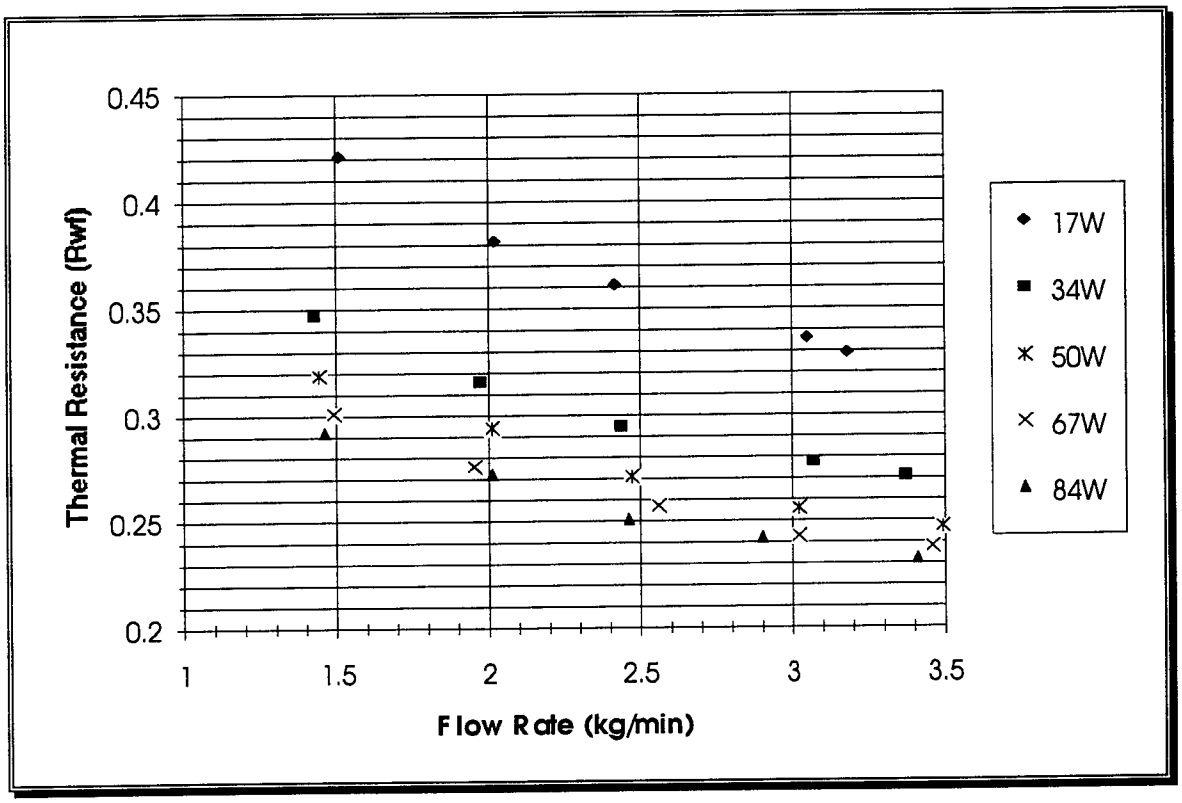


Figure 7. Thermal Resistance for 0 °C

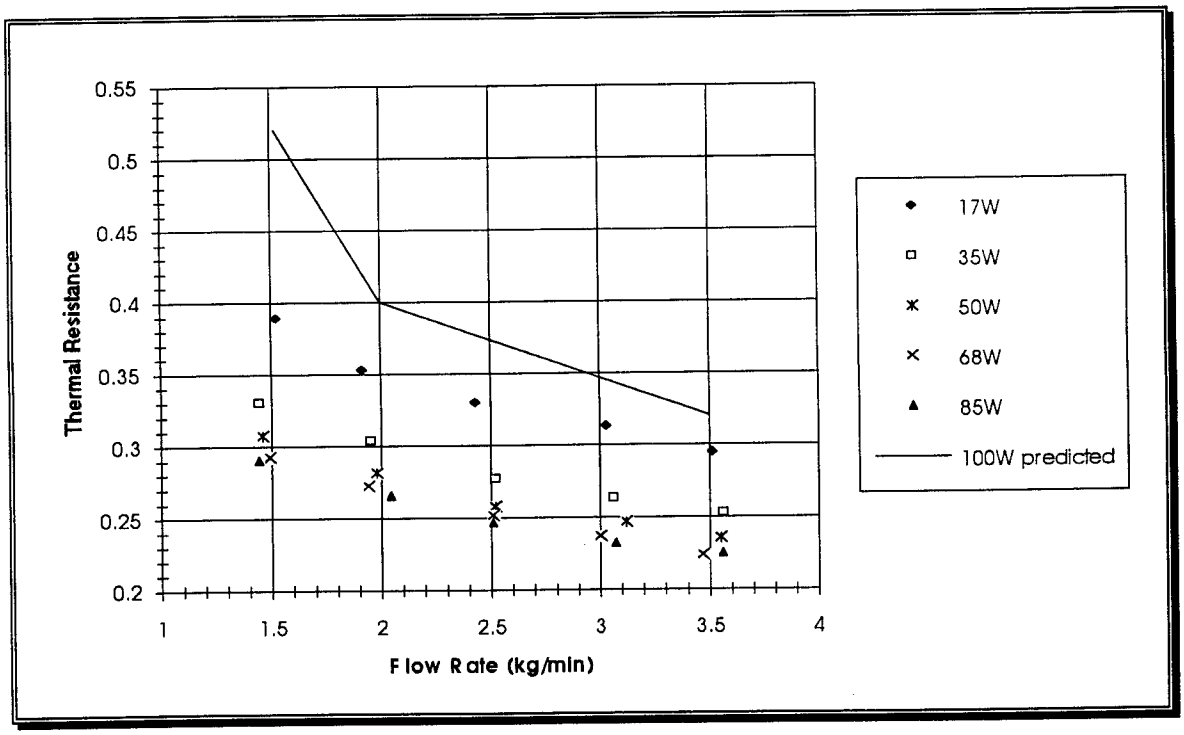


Figure 8. Thermal Resistance for 10 °C

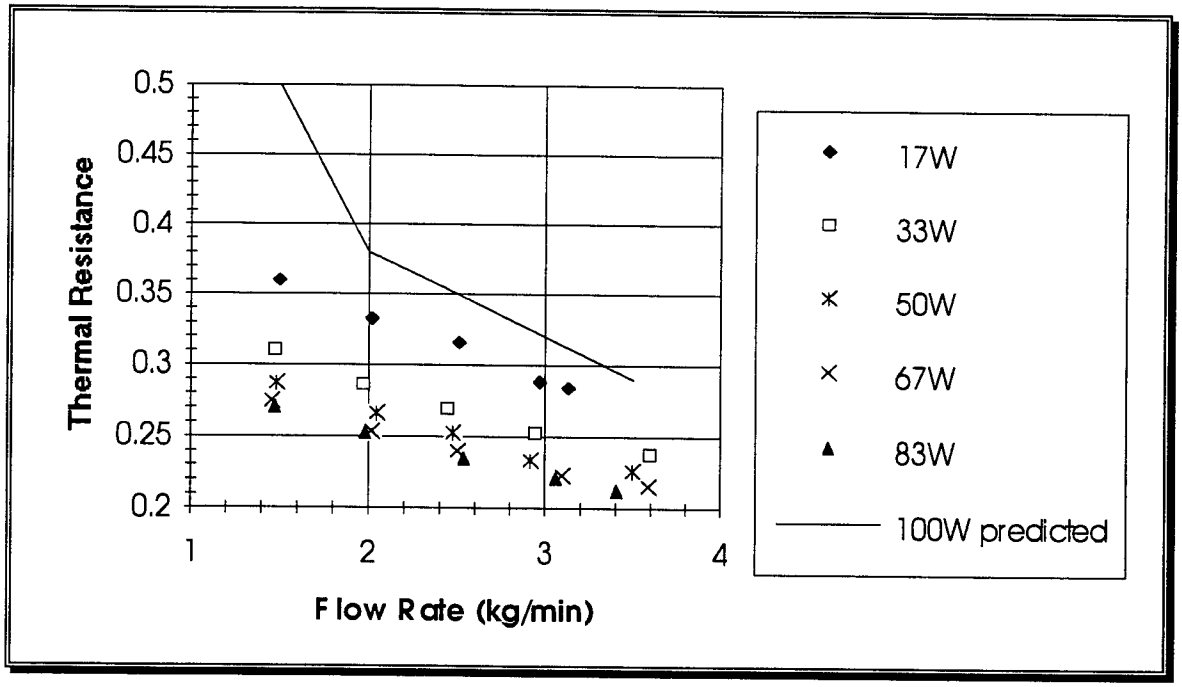


Figure 9. Thermal Resistance for 20 °C

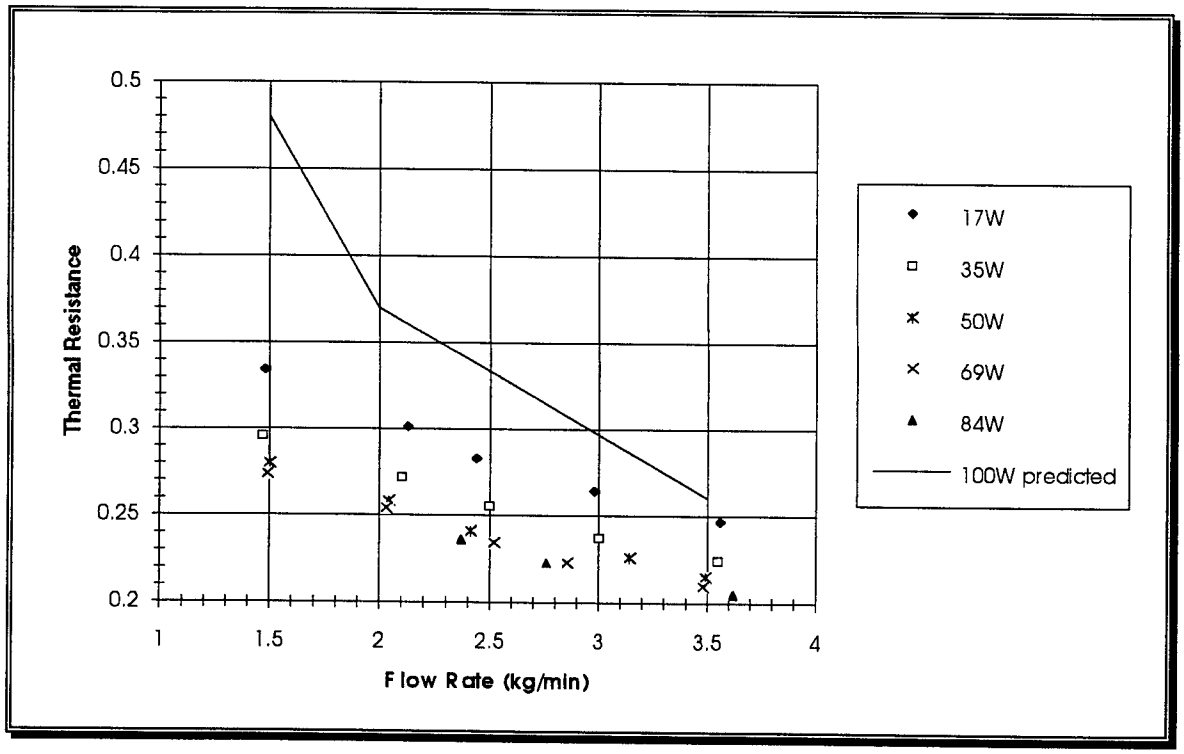


Figure 10. Thermal Resistance for 30 °C

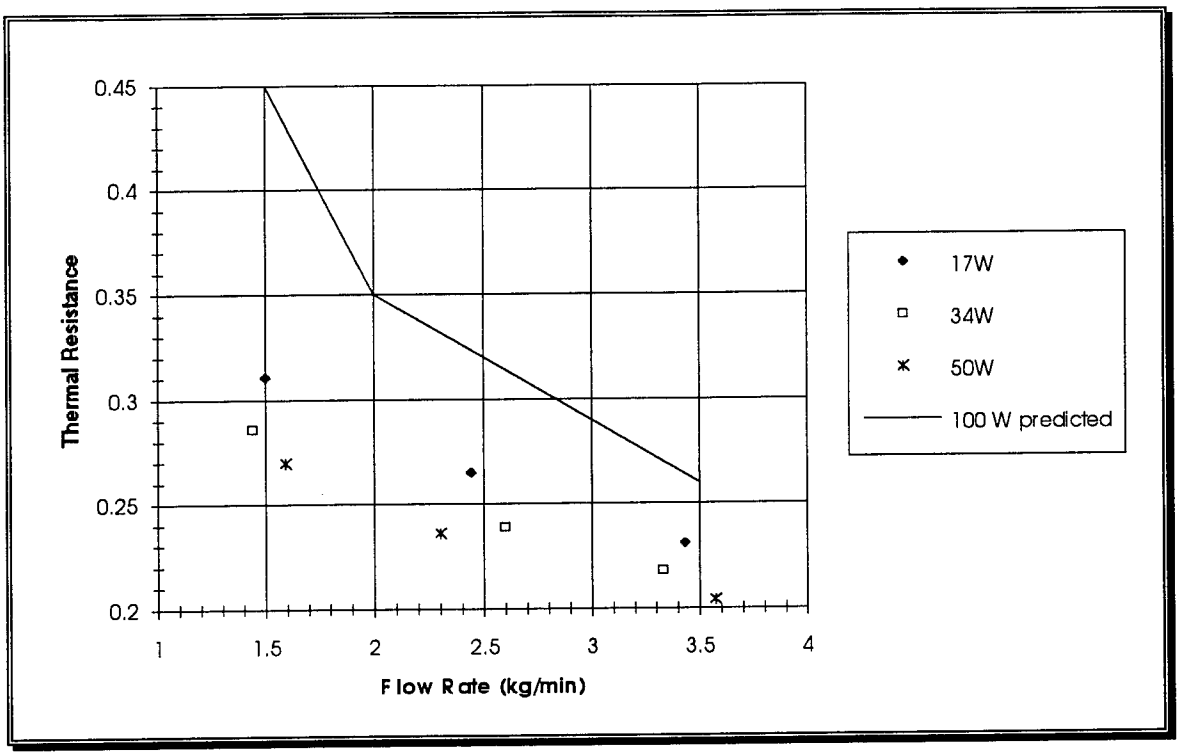


Figure 11. Thermal Resistance for 40 °C

From these figures, it is evident that for the higher flow rates the predicted thermal resistance is fairly accurate. However, for the lower flow rates, the data for the measured and predicted thermal resistance diverges. This leads to the conclusion that the extrapolation from the turbulent flow through the CHICs to the laminar flow through the CHICs is good for high flow rates. However, a new extrapolation is need for the lower flow rates.

Even though the design point for the HFHE is 100 W per square centimeter of heat transfer, the thermal resistance at off-design heat transfer must also be considered. Therefore, the relationship between the thermal resistance and the amount of heat transfer applied to the CHIC is also of interest. Figures 12 through 16 show this relationship for the inlet coolant temperatures of 0 °C through 40 °C, respectively.

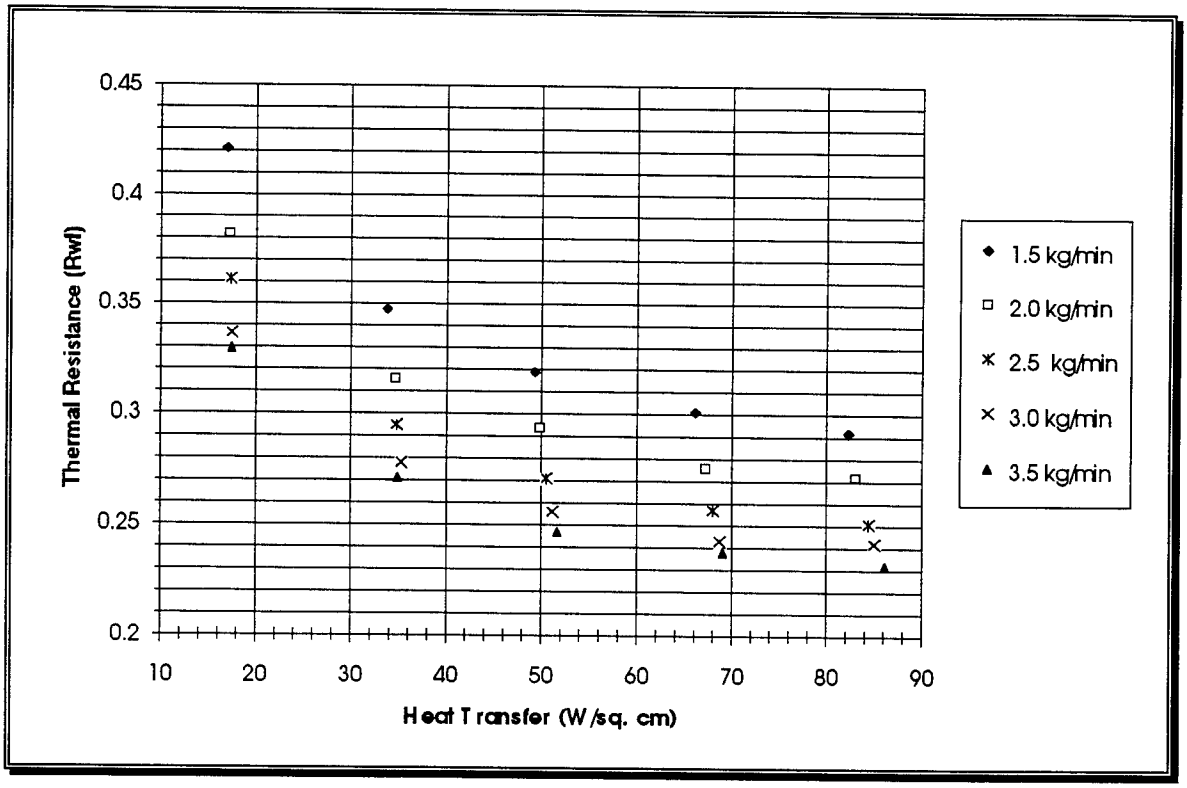


Figure 12. Thermal Resistance at 0 °C

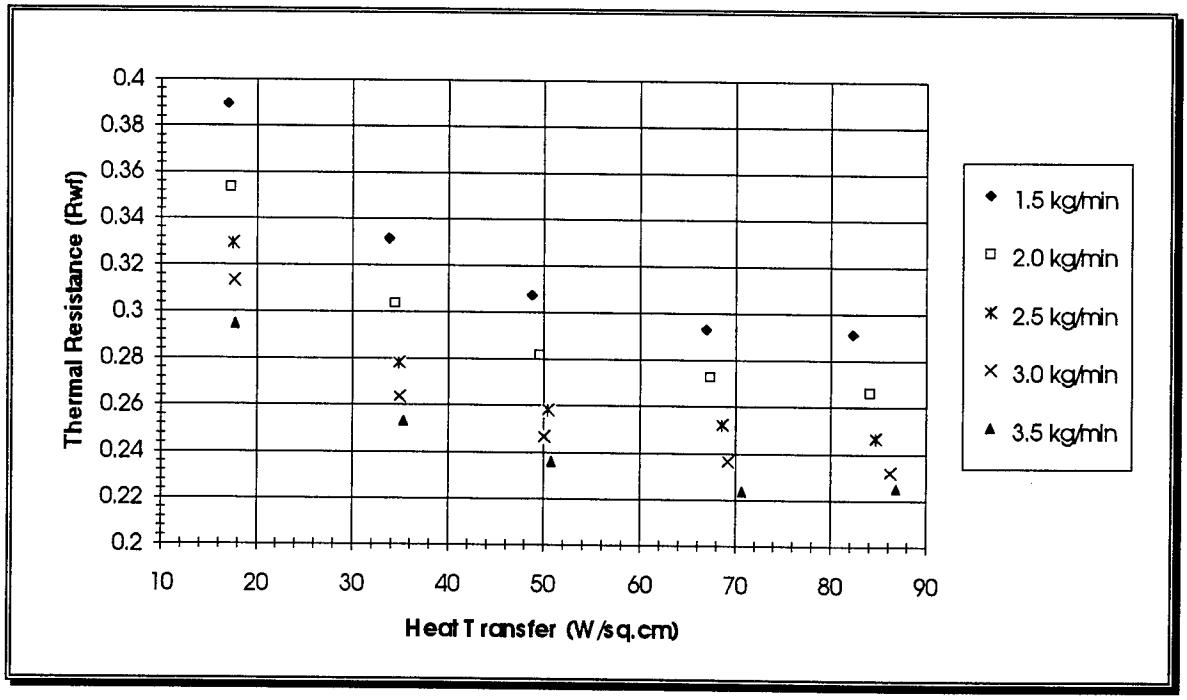


Figure 13. Thermal Resistance at 10 °C

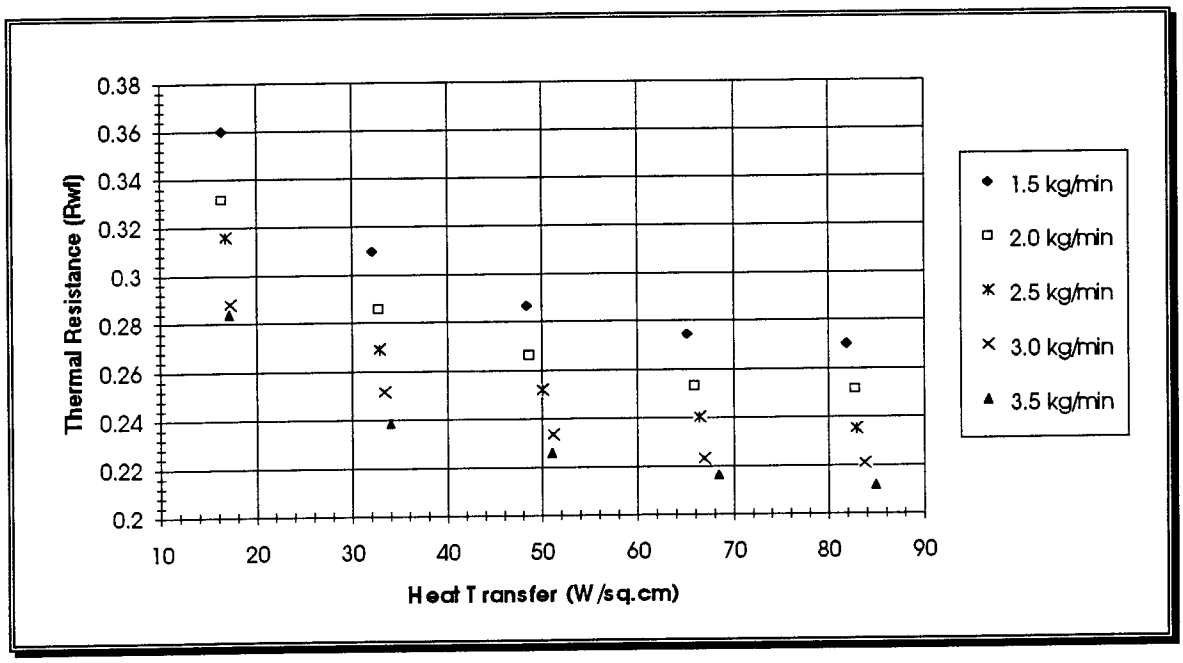


Figure 14. Thermal Resistance at 20 °C

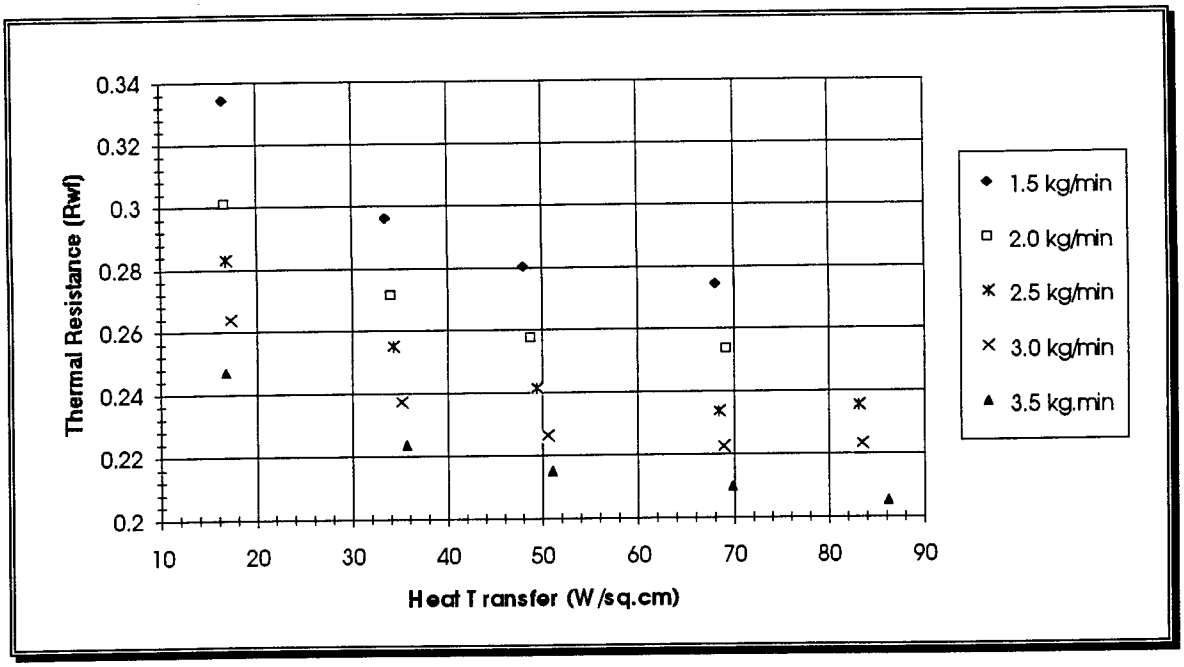


Figure 15. Thermal Resistance at 30 °C

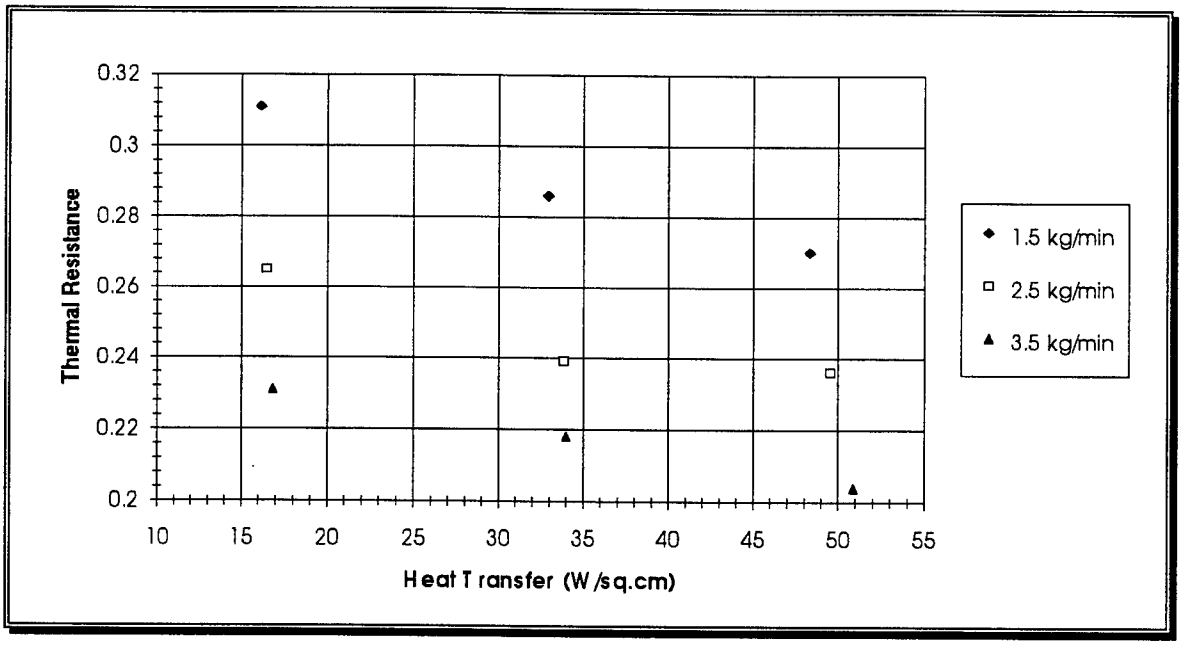


Figure 16. Thermal Resistance at 40 °C

Summary

From this data, it is evident that future study is needed. First, an increase in accuracy for the pressure drop across the HFHE should be determined. To accomplish this, a differential pressure transducer will be used. In addition, the pressure drop needs to be evaluated for the entire range of possible coolant temperatures. Furthermore, all twenty CHICs need to be examined to determine similarity and independence between the CHICs. Another possible experiment would be to test more than one CHIC at a time to achieve a more accurate determination of the heat loss due to conduction radially. Finally, a study that repeats these base line tests involving coolants other than PAO for comparison should be performed to indicate the best possible coolant for the HFHE.

Nomenclature

T_w	≡	wall temperature of the HFHE (C)
T_f	≡	inlet coolant temperature (C)
Q	≡	applied heat transfer (W/cm^2)
Q_{loss}	≡	heat transfer lost due to radial conduction (W/cm^2)
Q_{net}	≡	net heat transfer (W/cm^2)
R_{wf}	≡	thermal coefficient for the CHIC [$C/(W/cm^2)$]
m	≡	mass flow rate (kg/hr)

References

1. T.J. Bland, et al., "A Compact High Intensity Cooler," SAE Thirteenth Intersociety Conference on Environmental Systems, July 1983.

2. T.J. Bland, et al., "The Development of Advanced Cooling Methods for High-Power Electronics," SAE Technical Paper Series, October 1990.

3. Edward M. Flynn, et al, "High Flux Heat Exchanger," Final Report, February 1994

Using a search heuristic in an NP-complete problem in Ashenhurst-Curtis Decomposition.

Craig Files
Masters Student
Department of Electrical Engineering

University of Idaho
Moscow, Idaho 83844-1023
cfiles@gemini.mrc.uidaho.edu

Final Report for:
Graduate Summer Research Program
Wright Laboratory

Sponsored by:
Air Force Office of Scientific Research
Bolling Air Force Base, DC

and

Wright Laboratory

August 1994

Using a search heuristic in an NP-complete problem in Ashenhurst-Curtis Decomposition.

Craig M. Files
Masters Student
Department of Electrical Engineering
University of Idaho

Abstract

This paper reports on the application of several searching algorithms to Ashenhurst-Curtis decomposition. A final search algorithm is then presented that is base on using different values instead of just using column multiplicity to guide the search. The influence behind this algorithm is the analogous behavior of functional decomposition to decision trees. By using this algorithm 2^N possible partitions can be searched by evaluating $\frac{N*(N+1)}{2}$ partitions.

Introduction

This paper reports on the application of a search algorithm to an NP-complete combinatorial problem of pattern theory. Pattern theory is a concept for finding patterns in discrete and continuous mathematical functions. This approach has been developed at Wright Laboratories, in an attempt to find a more formal notation of a pattern. To gain an understanding of the object's "patterness" one has to be able to measure the complexity of a pattern. Measuring this complexity must be robust enough to handle many classes of applications. The applications considered by Wright Laboratories include pattern recognition, algorithm creation, data compression, machine learning, and logic minimization. Their approach is to use the Ashenhurst-Curtis decomposition for a binary function, called functional decomposition[1].

It is well known that functional decomposition is an NP-complete problem. Because of this complexity, the Ashenhurst-Curtis method is rarely used in industry, while algebraic factorization and binary decision diagram methods are used instead. There has been, however, some recent increase of interest in functional decomposition for applications in FPGA mapping and PLA decomposition[9].

The algorithm proposed here uses heuristic search to find close to minimum decomposition. The reference of minimum decomposition, in this paper, means the smallest representation of the function as a composition of two other functions. The advantage of this algorithm is in its ability to find solutions of this exponential problem in polynomial time. The algorithm "Ashenhurst-Curtis Search Heuristic (ASH)" is a reduction method that looks at groups of variables. By

using a figure of merit for each individual variable in the group, the variable with the best merit is then used to construct the next set of groups. The rest of this paper will discuss Ashenhurst-Curtis decomposition, previous work on this topic, the theory of ASH, and results.

2.0 Functional Decomposition

The decomposition of a function is an expression in terms of a composition of other functions. For example, if $f(x_1,x_2,..,x_4)=F(\Phi(\Im(x_1,x_2),x_3),x_4)$ then the term to the right is a set of compositions that are the equivalence of f. This process is called functional decomposition. It must be noted that functional decomposition has been recently formulated for multi-valued[9] and real-valued functions[3], but in this paper binary functions will be used.

In general, an N input function, $f: B^N \rightarrow B$, where $B=\{0,1\}$, has the set of input variables $\{x_1,x_2,..,x_N\} \in X$. In this paper we will use Ashenhurst-Curtis' definition of trivial decomposition to partition the input variables. A partition is a collection of subsets whose union is the whole set and whose intersections are empty. The partition is then used to separate the input variables into different functions to form a decomposition. For example, if $A \cup B=\{x_1,x_2,..,x_N\}$ and $A \cap B=\emptyset$, then the decomposition can be written as $f(A,B)=F(\Phi(A),B)$, where Φ and F are the composite functions of f.

Some simple forms of decomposition:

1. $f(A,B)=F(\Phi(A),B)$
2. $f(A,B)=F(\Phi(A),\Im(B))$

3. $f(A,B,C)=F(\Phi(A),\Im(B), C)$

4. $f(A,B,C)=F(\Phi(\Im(A), B), C)$

In each of these cases $A \cup B \cup C=X$ and $A \cap B=\emptyset$, $B \cap C=\emptyset$, and $A \cap C=\emptyset$. The decomposition $F(\Phi(A),B)$ is the most basic form of decomposition and is used in the implementation described in this paper.

A measure of a function's complexity is called the "function cardinality", and is defined as 2^N*M, for an N input, M output function. For means of representation this is called the decomposed function cardinality(DFC). DFC is defined as a cost of the minimum decomposition. Since we are only evaluating the decomposition of f(A,B) into $F(\Phi(A),B)$, we will denote the expression as the sum of child cardinality(SOCC). Thus, once a partition has been selected, and each of the functions in the composition have been found, the SOCC may be calculated. The SOCC is calculated as the cardinality of Φ, plus the cardinality of F. The example 2.0 illustrates calculating the SOCC of a given function.

Example 2.0

Starting with a 6 input function, cardinality = 2^6=64. After decomposing the function, the netlist of decomposed blocks from Fig 2.0 is created.

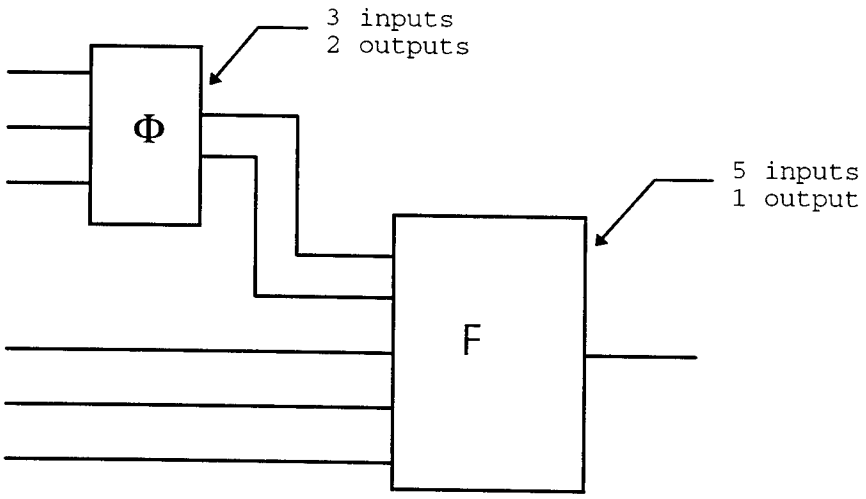


Fig 2.0 - Example of decomposed blocks

$$SOCC = cardinality(\Phi) + cardinality(F)$$

$$SOCC = 2^3 * 2 + 2^5 * 1 = 8 * 2 + 32 = 48$$

The concept of the DFC measure is used at Wright Labs as a robust measure of pattern. Thus, DFC can be used in common pattern recognition applications, such as the following machine learning approaches of geometric, syntactic and artificial intelligence. DFC has also been shown to be related to factors in data compression, time complexity and size complexity of a circuit[8]. SOCC is used because of its simple and obvious implementation of DFC.

A principal reason that Ashenhurst-Curtis decomposition hasn't been used much for practical engineering applications is because of the

search complexity that it involves. To find the minimum SOCC for an N variable input function to be placed in the form $f(A,B)=F(\Phi(A),B)$, there are 2^N partitions that could be evaluated. Because of the number of evaluations, the problem as stated is exponential.

3.0 Previous Work

Several approaches have been examined to reduce the complexity of finding the minimum decomposition. One such approach was the use of the Genetic Algorithm(GA)[6][7]. GAs have been used to find approximate solutions to NP-complete optimization problems[2], so it looked like an appropriate approach to this problem. But, according to the best of our knowledge there has been very few, if any, successful applications of genetic algorithms in the area of logic synthesis.

The GA is an evolutionary learning technique, developed by Holland(1975), that is based on genetic variation and natural selection. The GA is a simulation of the basic processes that are found in nature. Included in these processes are natural selection and reproduction. Highly fit individuals are allowed to reproduce with other individuals in the population. While other, not fit, individuals will be removed from the population to make way for the newly formed individuals. By using this type of selection, hopefully the most promising areas of the search space are explored. The GA should then converge towards an optimal solution of the problem. Figure 3.0 is the basic pseudo-code for a GA.

```
Initialize population

repeat
      evaluate population
      reproduce
until done;
```

Fig. 3.0

The initial population is probably the most important part of the GA. If the population is diverse then the probability of finding solutions will be much greater than if the population is localized in one area of the search space. This gives the GA the variance that it needs to complete the task. Another element in the implementation of the GA is evaluating the population. This is where the individuals of the population are given their fitness, or SOCC in the case of the work that has been conducted with functional decomposition.

Another approach to finding the best partitions in Ashenhurst-Curtis decomposition is the method of increasing row-column ratio(IRC)[5]. This search technique takes advantage of the fact that the minimum SOCC is usually found when there are very few row variables. Row variables are defined as the variables included in the set A of the expression $F(\Phi(A),B)$. Thus, row variables are the input variables to the composite function Φ. Column variables are then defined as the input variables not in A, but are the elements of the set B. The algorithm IRC evaluates the partitions of a given function by starting with all the possibilities of having one row variable. This is continued until all the possibilities of having N row variables have been evaluated.

Both of these approaches, on average, found the minimum SOCC faster than using a random search technique. The problem was that the algorithms didn't guarantee when the minimum SOCC would be found. Since the work was done experimentally, there was no real stopping condition for the algorithms. In some cases, the entire search space, all 2^N, would have to be searched before finding the minimum SOCC.

4.0 ASH

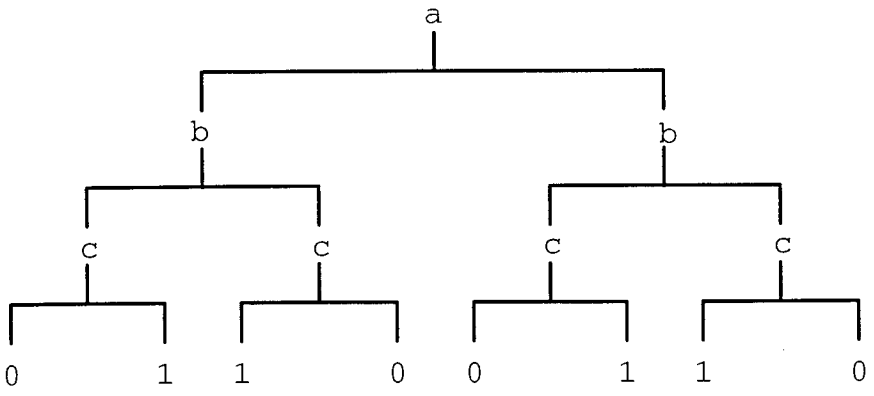
The concept of ASH is based on the idea of representing functional decomposition as a decision tree(DT), in the machine learning paradigm. The most general way of developing a DT is to start building it from the top, or the root. In the case of ASH, we are concerned with building the tree from the bottom, or the leaf nodes. Selecting the bottom node in the DT can be done by going through all N possible variable combinations. The variable or node that has the most folding, or matching elements, is then chosen as the best bottom node. The following is an example of doing this.

Example 4.0 - Decision Trees

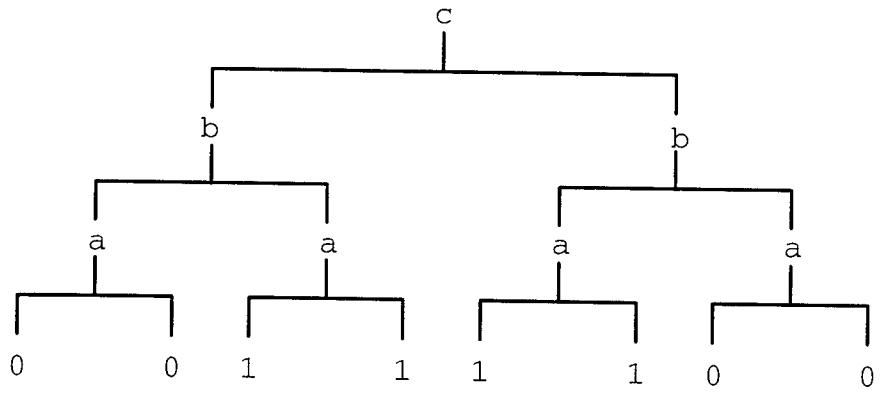
Given the following 3 input function.

f(a, b, c)= 01100110.

Then the following decision tree exists.



In this case, using c as the bottom node in the tree has four mismatches. The term mismatches is used to denote the elements under c that are not equal. The result that is wanted is to fold the elements under c, but this can only occur when the elements are equal. By switching the nodes in the tree such that a is the bottom node, the following tree results.



In this configuration there are no mismatches, thus indicating a is the best candidate for being the bottom node of the tree. Note that since there are no mismatches then a is a vacuous variable, meaning that the variable has no relevant effect on the output of the function.

This process is then continued to select the next level, and proceeding until choosing the top, or root of the tree.

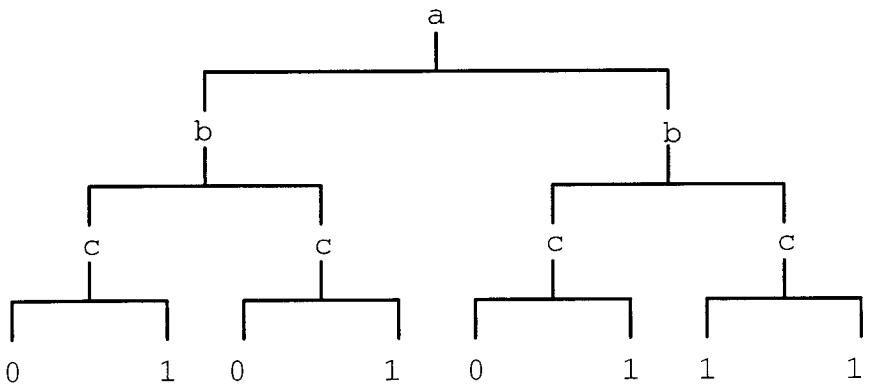
The process of choosing the bottom level of nodes in the tree is the same as selecting all the possible partitions that have only one column variable. The column variable that returns the best properties is then chosen as the best possible column variable. The next set of

partitions that are used will be the best column variable individually paired with all the remaining variables. Which is N-1 possible partitions. This process is continued until there is only 1 possible partition to evaluate.

The best partition is selected using the following cost function. Cost is defined as finding the partition with the smallest column multiplicity, then finding the smallest number of row mismatches. Example 4.1 shows the way ASH uses this Cost function to find the minimum SOCC.

Example 4.1 - Decision tree to functional decomposition

Given the following 3 input function
f(a, b, c) = 01010111
The following decision tree exists



Which can then be represented as the following decomp. table:

ab \ c		
0	1	- Mismatch
0	1	- Mismatch
0	1	- Mismatch
1	1	- Match

column multiplicity ν = 2
number of row mismatches = 3

b as the bottom level of nodes represented as a decomp. table:

ac \ b	
0	0 - Match
1	1 - Match
0	1 - Mismatch
1	1 - Match

column multiplicity ν = 2
number of row mismatches = 1

a as the bottom level of nodes represented as a decomp. table:

bc \ a	
0	1 - Mismatch
1	0 - Mismatch
0	1 - Mismatch
1	1 - Match

column multiplicity ν = 2
number of row mismatches = 3

From the above three partitions, the partition with b as the single column variable is chosen to be the best. So now b is paired with the other 2 variables as column variables.

b and a as column variables.

c \ ba			
0	0	1	1 - Mismatch
0	1	1	1 - Mismatch

column multiplicity ν = 3
number of row mismatches = 2

b and c as column variables.

a \ bc			
0	0	0	1
1	1	1	1

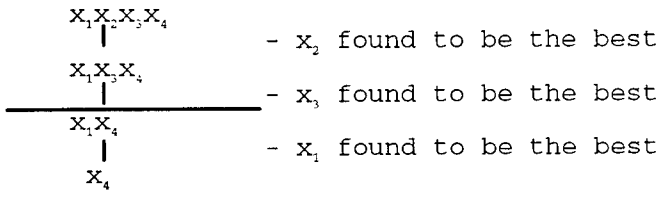
- Mismatch
- Match

column multiplicity ν = 2
number of row mismatches = 1

From the last two partitions, the partition with b and c as the column variables is chosen to be the best. Since the only partition that still exists is the situation when all three variables are column variables, means that ASH is done.

Summary of ASH; at each level of choosing the best partition, the variables in the best partition are then paired with the remaining individual variables. Figure 4.0 is graphical representation of this.

Figure 4.0 - 4 variable function



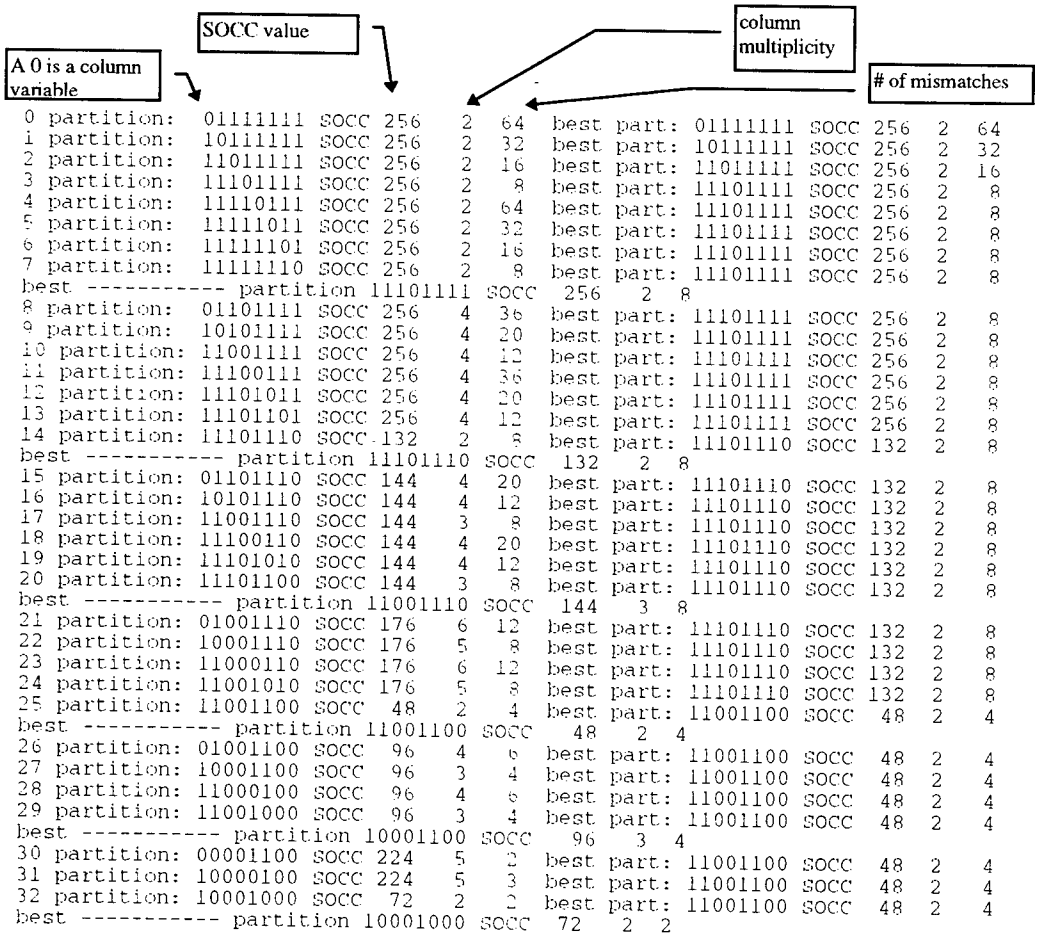
From Figure 4.0, there are four input variables to the function f, by using each variable as an independent column variable the best input variable for the composite function is chosen. That leaves three more variables to look at, and the process continues until there are no more variables to look at. At each level a new variable is selected to be column variable, x_2 is chosen first, then x_3 and so on. This process results in the evaluation of 4+3+2+1=10 partitions, since there are 4 partitions to be evaluated with 4 input variables, 3 partitions to be evaluated with 3 variables, and so on. For an N input function, Eulers

definition gives us $\frac{N*(N+1)}{2}$ evaluated partitions. Which states that ASH is a polynomial algorithm.

At some point, in this search, ASH will hold the best SOCC found during the search. From Figure 4.0, that is denoted by the horizontal line. This is the point when all the column variables chosen up until this point will return the best SOCC. After this point any additional column variables will make the SOCC grow in size.

4.1 ASH Example

The following is an example of the ASH algorithm decomposing an eight variable function.



```
33 partition: 10000000 SOCC 256   3   1  best part: 11001100 SOCC  48  2   4
34 partition: 00001000 SOCC 256   3   1  best part: 11001100 SOCC  48  2   4
best ---------- partition 00000100 SOCC  256   3  1
BEST : partition 11001100 SOCC   48   4   0
```

The next example is used to show how vacuous variables are found and then implemented as column variables. Note, the function being analyzed is completely specified so vacuous variables are specified as column variables.

```
0 partition:  01111111 SOCC 256   2  80  best part: 01111111 SOCC 256  2  80
1 partition:  10111111 SOCC 256   2  48  best part: 10111111 SOCC 256  2  48
2 partition:  11011111 SOCC 128   1   0  best part: 11011111 SOCC 128  1   0
3 partition:  11101111 SOCC 256   2  16  best part: 11011111 SOCC 128  1   0
4 partition:  11110111 SOCC 128   1   0  best part: 11011111 SOCC 128  1   0
5 partition:  11111011 SOCC 256   2  16  best part: 11011111 SOCC 128  1   0
6 partition:  11111101 SOCC 128   1   0  best part: 11011111 SOCC 128  1   0
7 partition:  11111110 SOCC 128   1   0  best part: 11011111 SOCC 128  1   0
vacuous variables
8 partition:  11010100 SOCC  16   1   0  best part: 11010100 SOCC  16  1   0
best ---------- partition 11010100 SOCC   16   1  0
9 partition:  01010100 SOCC  48   2   0  best part: 11010100 SOCC  16  1   0
10 partition: 10010100 SOCC  48   2   0  best part: 11010100 SOCC  16  1   0
11 partition: 11000100 SOCC  48   2   0  best part: 11010100 SOCC  16  1   0
12 partition: 11010000 SOCC  48   2   0  best part: 11010100 SOCC  16  1   0
best ---------- partition 11000100 SOCC   48   2  1
13 partition: 01000100 SOCC 144   3   0  best part: 11010100 SOCC  16  1   0
14 partition: 10000100 SOCC 144   3   0  best part: 11010100 SOCC  16  1   0
15 partition: 11000000 SOCC  72   2   0  best part: 11010100 SOCC  16  1   0
best ---------- partition 11000000 SOCC   72   2  1
16 partition: 01000000 SOCC 256   3   0  best part: 11010100 SOCC  16  1   0
17 partition: 10000000 SOCC 132   2   0  best part: 11010100 SOCC  16  1   0
best ---------- partition 10000000 SOCC  132   2  1
BEST : partition 11010100 SOCC   16   1  0
```

5.0 Results

The results of ASH are analyzed and compared to the other methods that have been implemented for finding the minimum partition. The research group at Wright Laboratories has created 53, 8-variable, and 14, 12-variable benchmark functions that have been used to evaluate the effectiveness of ASH. The results where obtained by using two software packages, FLASH, Function Learning and Synthesis Hotbed, and FLASHETTE. FLASH was implemented by the Systems Concepts Group of the Mission Avionics Division, Wright Laboratory[6]. FLASHETTE is a smaller version of FLASH that is the implementation of ASH.

In determining the effectiveness of the algorithms the following notation is used. The cost for each function is 1.0 if the minimum partition has not been found, 0.0 if the minimum has been found.

$$\text{Normalized Cost} = \frac{\text{Cost of each function}}{\text{number of functions}}$$

This method shows the speed in which the algorithm finds the optimal solution. See figures 5.0 and 5.1.

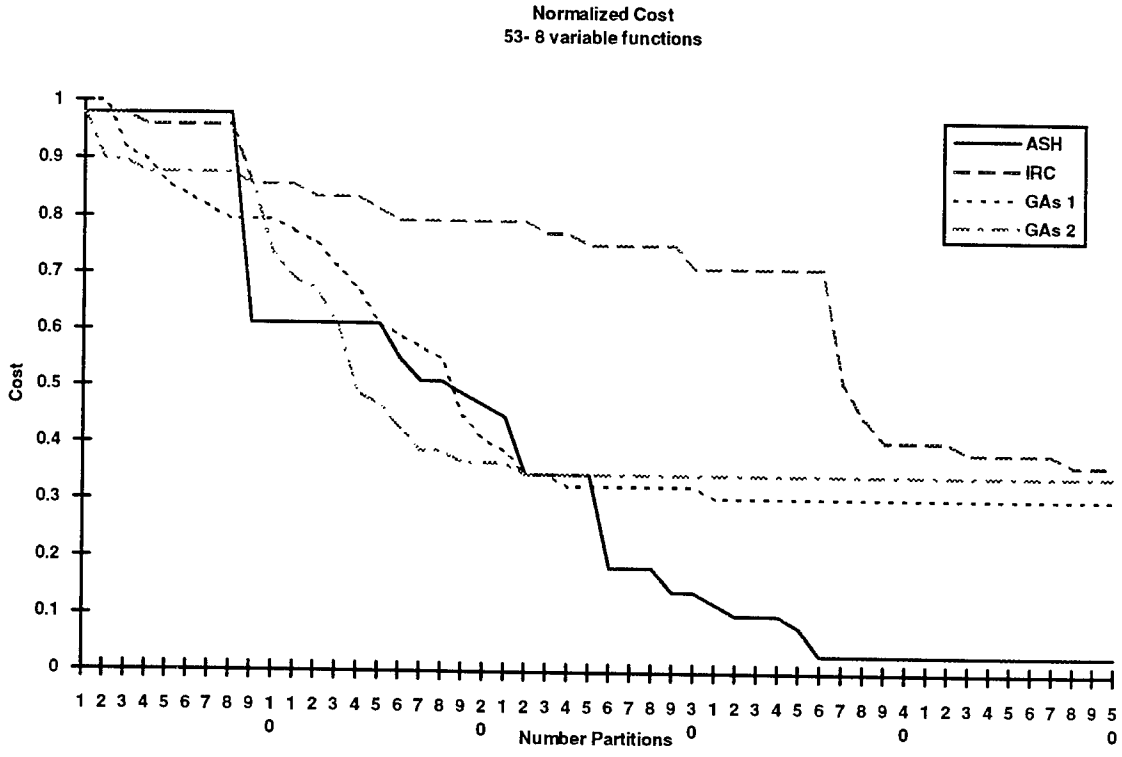


Fig 5.0

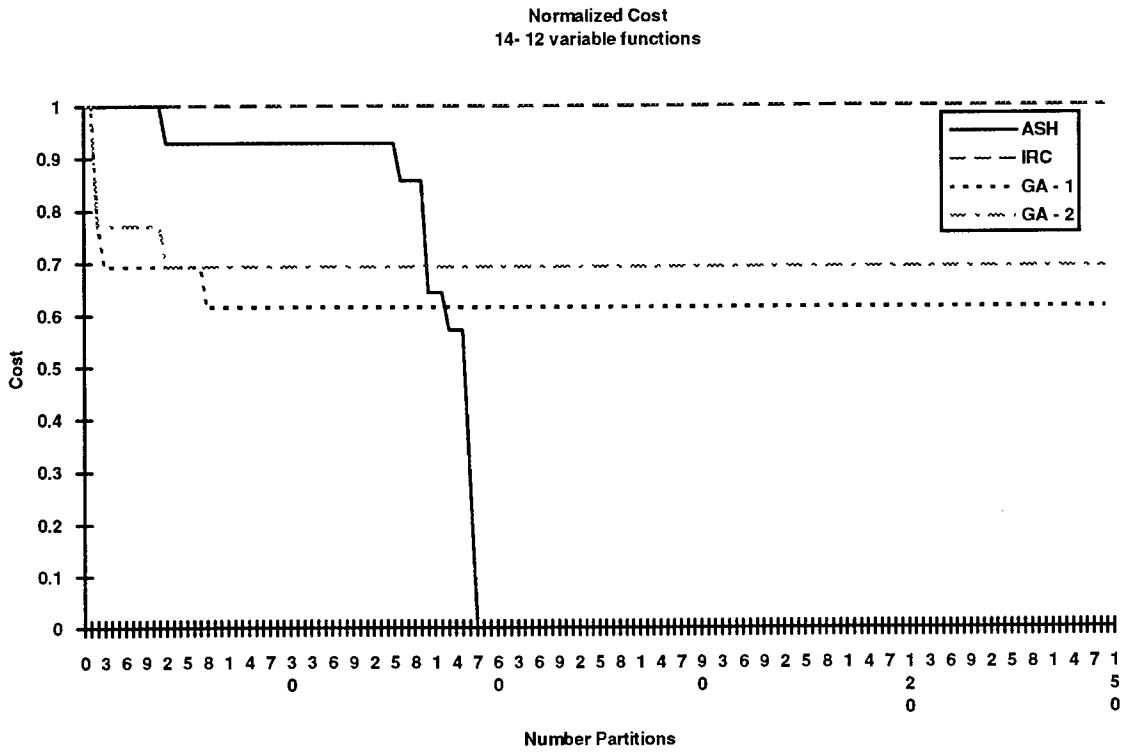


Fig 5.1

The two figures show the effectiveness and speed of ASH. In Fig 5.0, ASH doesn't find the known minimum two times, where in Fig 5.1 it finds the minimum in all 14 cases. The two genetic algorithms that are shown have a stopping condition. This implies that the algorithm will not do any better as the number of partitions increases. The reason for the stopping condition is that without it, the GAs would search all 2^N partitions, and the time that it would take to find new partitions would grow exponentially since it didn't want to reevaluate partitions. IRC in the two graphs will continue to evaluate all 2^N partitions, and so as the number of partitions increases its Normalized Error will approach zero. Thus, IRC will find the minimum partition in the figures shown above.

6.0 Conclusions

The paper proves that an algorithm can be successfully applied to an NP-complete problem of logic synthesis that has been traditionally treated as very difficult to solve. The results demonstrated that our ASH algorithm is able to reduce the search complexity to a polynomial complexity on pattern theory benchmarks.

Even though the algorithm may not find the minimum solution every time, we feel that this is a good start for actually understanding this area of functional decomposition. With more research into this area and other NP complete problems in decomposition, Ashenhurst-Curtis decomposition may be the best way of dealing with problems in machine learning and logic synthesis.

BIBLIOGRAPHY

[1] T. D. Ross et al. Logic Minimization as a Robust Pattern Finder. International Workshop on Logic Synthesis. Lake Tahoe, California. May 1993.

[2] S. Khuri. An Evolutionary Approach to Combinatorial Optimization Problems. Proceedings of CSC 1994. Phoenix Arizona. March 1994.

[3] T. D. Ross et al. On the decomposition of real-valued functions. 3rd International Workshop of Post-Binary VLSI Systems, International Symposium on Multiple Valued Logic. May 24, 1994.

[4] T. D. Ross et al. The Function Learning and Synthesis Hotbed. Wright Laboratory, WL/AART-2. WPAFB, OH 45433-6543. May 4, 1994.

[5] M. L. Axtell. Partition Selection Algorithms: Row/Column Ratio Experiment. Technical report, Veda Incorporated, c/o Wright Laboratory, WL/AART-2. WPAFB, OH 45433-7408. April 1994.

[6] M. J. Noviskey et al. Application of Genetic Algorithms to Functional Decomposition in Pattern Theory. Wright Laboratory, WL/AART-2. WPAFB, OH 4533-5543. Jan 1994.

[7] J. F. Frenzel. Application of Genetic Algorithms to Pattern Theory. Final report for summer faculty research program, AFOSR. Wright Laboratory, July 1993.

[8] T. D. Ross et al. Pattern Theory: An Engineering Paradigm for Algorithm Design. Final report for period Oct. 1988-Oct. 1990. Avionics Directorate, Wright Laboratory. WPAFB, OH 45433-6543. p 46.

[9] T. Luba, R. Lasocki. Decomposition of Multiple-Valued Boolean Functions. Applied Mathematics and Computer Science. Vol. 4 No.1 1994. pp 125-138.

DIRECTION FINDING IN THE PRESENCE OF A NEAR FIELD SCATTERER

Edward Michael Friel
Graduate Student
Department of Electrical Engineering

University of Dayton
300 College Park
Dayton, Ohio 45419-0226

Final Report for:
Graduate Student Research Program
WL/AARM - 3

Sponsored by:
Air Force Office of Scientific Research
Bolling Air Force Base, DC.

and

WL/AARM - 3

August 1994

DIRECTION FINDING IN THE PRESENCE OF A NEAR FIELD SCATTERER

Edward Michael Friel
Graduate Student
Department of Electrical Engineering
University of Dayton

Abstract

In this paper we consider the problem of computing the directions of arrival of two closely spaced signals when there is a scatterer in the near field of the antenna array. The antenna is a linear array of equally spaced dipoles modeled with the method of moments (MoM). The spacing between the dipoles is $\lambda/2$ so that the coupling between the antenna elements is minimized without permitting the array to form grating lobes. The scatterer is a finite length edge modeled with the Uniform Theory of Diffraction (UTD) and equivalent currents. The edge can have any length and any orientation relative to the antenna array. The coupling between the edge and the antenna array is accounted for in the method of moments by using a hybrid technique that combines the Uniform Theory of Diffraction with the method of moments. The final computer program was validated by comparing a special case with previously published results. It is shown that the edge degrades the Multiple Signal Classification (MUSIC) algorithm's ability to resolve two closely spaced plane waves.

Table of Contents

1.0	Introduction	4
2.0	Modeling the Antenna Array	5
2.1	Modeling the Nearby Scatterer	7
2.2	Equations for the Edge	7
2.3	Computer Program Validation	11
3.0	Direction of Arrival Estimation	14
3.1	Results	15
4.0	Summary and Conclusions	18
5.0	References	20

DIRECTION FINDING IN THE PRESENCE OF A NEAR FIELD SCATTERER

Edward Michael Friel

1.0 Introduction:

It is a straight forward problem to determine the angle of arrival of one plane wave. This can be done with many direction finding algorithms. The problem becomes more complicated when two uncorrelated plane waves are present. In this case, the angles can usually be resolved if they are not too close together and the power in the signals is significantly greater than that of the noise.

Sometimes, one of the incident signals will be a reflection from another object. If this object is in the far field of the antenna array, the signal will appear as a correlated plane wave. This problem can be overcome by using a technique known as data smoothing before applying the direction finding algorithm. If the object, however, is in the near field of the antenna, the scattered field will be a spherical wave and not a plane wave. This case results if the nearby scatterer is an airplane wing or even the inside of the antenna's radome. It is the objective of this research to study these near field reflections on a direction finding algorithm's ability to resolve two closely spaced plane waves.

The problem is shown graphically in figure 1. Two uniform plane waves are incident on both the antenna array and a nearby scatterer. Since the scatterer is in the near field of the antenna, the reflected waves from it are spherical and not planar. These interfering waves are also correlated with the incident plane waves and cause errors in calculating the angles of arrival of the two plane waves.

Specifically, the antenna is a linear array of equally spaced dipoles. The scatterer is a nearby finite length edge representing an airplane wing. The antenna array was modeled using the method of moments [1,2,3]. The spherical waves from the edge were computed using the Uniform Theory of Diffraction (UTD) [3,4,5,6]. The Multiple Signal Classification (MUSIC) algorithm was used to determine the angles of arrival [7,8].

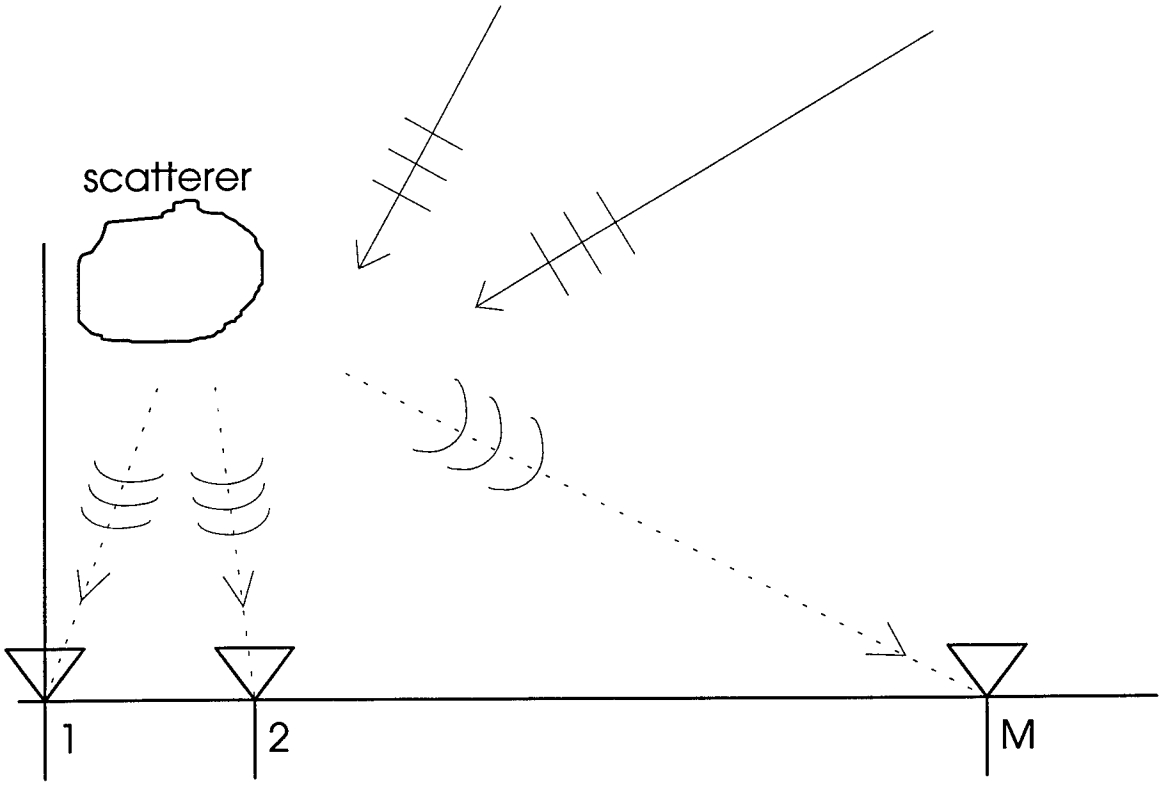


Figure 1: Geometry of the Array and Sources

2.0 Modeling the Antenna Array:

The antenna array is modeled using a reaction integral equation. This equation is reduced to a system of linear equations using the method of moments. The system of equations is solved using linear algebra techniques to yield the current on the antenna. The current at the antenna terminals is multiplied by the load impedance to yield the actual voltages at the terminals.

The reaction integral equation for an arbitrary scatterer is shown below

$$\int_s (\vec{J}_m \cdot \vec{E}^s - \vec{M}_m \cdot \vec{H}^s) ds = -\int_s (\vec{J}_m \cdot \vec{E}^i - \vec{M}_m \cdot \vec{H}^i) ds \qquad (1)$$

$$m = 1, 2, 3, \ldots, N$$

where J_m and M_m are the m^{th} testing functions, E^s and H^s are the scattered fields, and E^i and H^i are the incident fields. Since the wire is non magnetic, the equivalent magnetic current is zero and we have

$$\int_s \vec{J}_m \cdot \vec{E}^s \, ds \;=\; -\int_s \vec{J}_m \cdot \vec{E}^i \, ds. \tag{2}$$

Next, we expand E^s as a series using piecewise sinusoids [3]. This yields

$$\int_s \vec{J}_m \cdot \sum_{n=1}^{N} I_n \, \vec{E}_n^s \, ds \;=\; -\int_s \vec{J}_m \cdot \vec{E}^i \, ds. \tag{3}$$

In this expression E_n^s is the field from one piecewise sinusoidal mode and I_n is the complex current.

The piecewise sinusoidal expansion on one dipole element is shown graphically in figure 2.

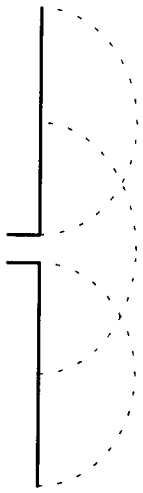


Figure 2: Piecewise Sinusoidal Current Expansion on One Dipole

The testing functions, J_m, are also piecewise sinusoids. In general for the m^{th} mode of the expansion we have

$$\sum_{n=1}^{N} I_n \int_s \vec{J}_m \cdot \vec{E}_n^s \, ds \;=\; -\int_s \vec{J}_m \cdot \vec{E}^i \, ds \qquad \text{m = 1, 2, 3, . . . , N.} \tag{4}$$

This can be expressed as [3]

$$\sum_{n=1}^{N} Z_{mn} \, I_n = V_m \qquad m = 1, 2, \ldots, N \tag{5}$$

$$Z_{mn} \;=\; \int_s \vec{J}_m \cdot \vec{E}_n^s \, ds \qquad V_m \;=\; -\int_s \vec{J}_m \cdot \vec{E}^i \, ds \tag{6}$$

where Z_{mn} is the mutual coupling between modes m and n, I_n and I_m are the currents at mode n and m respectively, V_m is the excitation at mode m, E^i is the incident field and ds is along the dipole.

2.1 Modeling the Nearby Scatterer:

The effects of a nearby scatterer on the antenna array can be included by slightly modifying the method of moments [3 pp. 500-510, 9]. For convenience we first express the reaction integrals using inner product notation. In particular

$$Z_{mn} = < J_m , E_n^s , > \quad \text{and} \quad V_m = < J_m , E^i > \tag{7}$$

To account for the presence of the nearby scatterer, we modify each of these integrals. The terms Z_{mn} and V_m become

$$Z_{mn}^{'} = < J_m , E_n^s + a\, E_n^s > \text{ and } \quad V_m^{'} = < J_m , E^i + b\, E^i > \tag{8}$$

where (a E_n^s) is the field from the n^{th} mode scattered by the edge and (b E^i) is the incident field scattered by the edge. Mathematically we have

$$Z_{mn}^{'} = < J_m , E_n^s > + < J_m , a\, E_n^s > \tag{9}$$

$$Z_{mn}^{'} = Z_{mn} + Z_{mn}^g \tag{10}$$

$$V_m^{'} = < J_m , E^i > + < J_m , b\, E^i > \tag{11}$$

$$V_m^{'} = V_m + V_m^g \tag{12}$$

$$\sum_{n=1}^{N} (Z_{mn} + Z_{mn}^g)\, I_n = (V_m + V_m^g) \qquad m = 1,2,\ldots,N \tag{13}$$

The matrix element Z_{mn} is calculated by reacting the field from the n^{th} mode of current on the array with the current on the m^{th} mode of the array. Similarly the matrix element Z_{mn}^g is calculated by reacting the field scattered by the object from the n^{th} mode of current on the array with the current on the m^{th} mode of the array. In a similar way, the excitation vector, V_m, is calculated by reacting the incident electric field with the m^{th} mode of current. The vector V_m^g is computed by reacting the m^{th} mode of current with the portion of the incident field that is scattered from the nearby object.

2.2 Equations for the Edge:

The geometry used to determine Z_{mn}^g and V_m^g is shown in figure 3

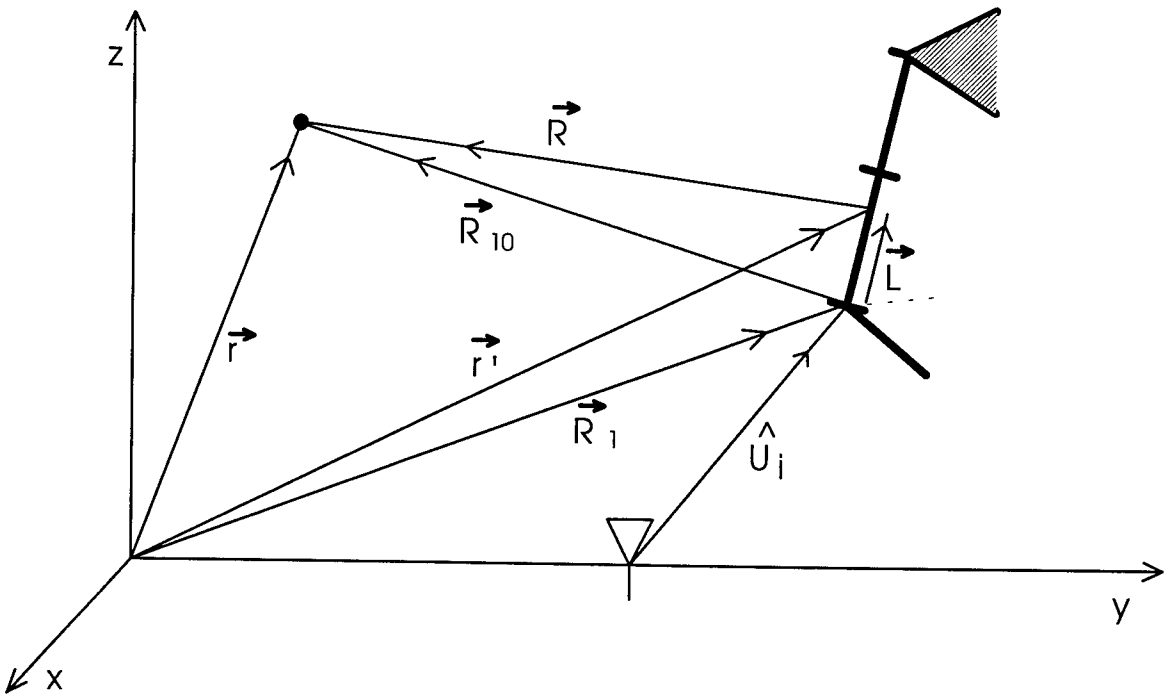


Figure 3: Geometry for Determining Z_{mn}^{g} and V_{m}^{g}

where $\vec{r}'$ = vector from the origin to a point on the segment of the edge

$\vec{r}$ = vector from origin to the observation point

$\vec{R}_1$ = vector from origin to one end of a segment edge

$\vec{l}'$ = vector along the direction of edge

$\vec{R}_{10}$ = vector from one end of a segment on edge to the observation point

$\vec{R}$ = vector from the point on edge to the observation point

$\hat{u}_i$ = unit vector in direction of radiation from the antenna element

The observation point shown is arbitrary but is actually on the dipole array for our particular problem. To calculate the field scattered by the edge we use equivalent currents and UTD. However, the observation point is, in general, in the near field of the edge. Therefore, the edge is broken up into segments such that the observation point is in the far field of each segment. The far field radiation integral may then be used to compute the field scattered by the edge. This analysis is for the impedance matrix Z_{mn}^{g}. However, the vector V_{m}^{g} is computed in a similar way by substituting the incident field for E_{n}^{s} and the direction of arrival for u_i.

To calculate the field scattered by the edge we first define the vector V as

$$\vec{V}(\vec{I}) = \frac{1}{4\pi}\int_{l'}\frac{\vec{I}(l')e^{-j\beta R}}{R}dl' \tag{14}$$

where R is shown in figure 3, β is the propagation constant, I is the equivalent electric or magnetic current on the edge, and the integration is along the length, l', of the edge. Using this vector, the magnetic and electric vector potentials are respectively

$$\vec{A} = \mu\vec{V}(\vec{I}^{e}) \tag{15}$$

$$\vec{F} = \varepsilon\vec{V}(\vec{I}^{m}) \tag{16}$$

where I^e is the equivalent electric current and I^m is the equivalent magnetic current on the edge. To find the scattered field we make the usual far field approximations. Referring back to figure 3, we see that the distance in the denominator of (14) may be approximated by R_{10} while the phase term is more sensitive. To calculate this, we note that

$$\vec{R} = (\vec{r}-\vec{r}') = \vec{r}-(\vec{R}_1+\vec{l}') = (\vec{r}-\vec{R}_1)-\vec{l}' \tag{17}$$

but

$$\vec{R}_{10} = \vec{r} - \vec{R}_1 \tag{18}$$

Therefore,

$$\vec{R} = \vec{R}_{10}-\vec{l}' \tag{19}$$

The magnitude of R is

$$\left|\vec{R}\right| = [(\vec{R}_{10}-\vec{l}')\cdot(\vec{R}_{10}-\vec{l}')]^{\frac{1}{2}} = [R_{10}^2-2\vec{R}_{10}\cdot\vec{l}'+\vec{l}']^{\frac{1}{2}} \tag{20}$$

Using the Binomial expansion, we can express the magnitude of R as

$$\left|\vec{R}\right| \approx \vec{R}_{10}-\hat{R}_{10}\cdot\vec{l}' \tag{21}$$

Using this in (14) we have,

$$\vec{V}(\vec{I}) = \frac{e^{-j\beta R_{10}}}{4\pi R_{10}}\int_{l'}\vec{I}(l')e^{+j\beta\hat{R}_{10}\cdot\vec{l}'}dl'. \tag{22}$$

The equivalent electric current is given by the expression [4]

$$\vec{I}^{e}(l_o') = -\frac{\sqrt{8\pi\beta}}{\eta\beta} e^{-j\frac{\pi}{4}} (\vec{E}_i(l_o') \cdot \hat{l})\, D_s\, e^{-j\beta \vec{l}' \cdot \hat{u}_i}\, \hat{l}\,, \tag{23}$$

where η is the intrinsic impedance of free space, D_S is the soft or parallel diffraction coefficient of the edge, $\vec{E}_i(l_o')$ is the incident electric field at l_o' on the edge, and $\hat{u}_i$ and l' are defined in figure 3. Substituting this expression into (22) yields,

$$\vec{V}(\vec{I}^{e}) = \frac{e^{-j\beta R_{10}}}{4\pi R_{10}} \left(\frac{-\sqrt{8\pi\beta}}{\eta\beta} \right) e^{-j\frac{\pi}{4}} (\vec{E}_i(l_o') \cdot \hat{l})\, D_s\, \hat{l} \int_{l'} e^{j\beta \vec{l}' \cdot (\hat{R}_{10} - \hat{u}_i)}\, dl'. \tag{24}$$

After performing the integration and substituting into (15) we have

$$\vec{A} = \frac{-\mu\sqrt{8\pi\beta} e^{-j\beta R_{10}}}{\eta\beta 4\pi R_{10}} e^{-j\frac{\pi}{4}} (\vec{E}_i(l_o') \cdot \hat{l})\, D_s\, \hat{l}\, e^{j\beta_e \frac{\Delta l}{2}}\, \Delta l \frac{\sin(\beta_e \frac{\Delta l}{2})}{(\beta_e \frac{\Delta l}{2})} \tag{25}$$

where

$$\beta_e = \beta\, \hat{l} \cdot (\hat{R}_{10} - \hat{u}_i). \tag{26}$$

Similarly, the equivalent magnetic current is

$$\vec{I}^{m}(l_0') = -\frac{\eta\sqrt{8\pi\beta}}{\beta} e^{-j\frac{\pi}{4}} (\vec{H}_i(l_0') \cdot \hat{l})\, D_h\, e^{-j\beta \vec{l}' \cdot \hat{u}_i}\, \hat{l} \tag{27}$$

where $\vec{H}_i(l_o')$ is the incident magnetic field on the edge, and D_h is the hard or perpendicular diffraction coefficient. Combining (27), (22), and (16) yields

$$\vec{F} = \frac{-\varepsilon\eta\sqrt{8\pi\beta} e^{-j\beta R_{10}}}{\beta 4\pi R_{10}} e^{-j\frac{\pi}{4}} (\vec{H}_i(l_o') \cdot \hat{l})\, D_h\, \hat{l}\, e^{j\beta_e \frac{\Delta l}{2}}\, \Delta l \frac{\sin(\beta_e \frac{\Delta l}{2})}{(\beta_e \frac{\Delta l}{2})}. \tag{28}$$

The far field due to the equivalent electric current on the edge is

$$\vec{E}_A = -j\omega[\vec{A} - (\vec{A} \cdot \hat{R})] \qquad \vec{H}_A = \frac{1}{\eta}[\hat{R} \times \vec{E}_A] \tag{29}$$

where the radial component of $\vec{E}_A$ has been subtracted out since we are in the far field. Similarly the far field due to the equivalent magnetic current is

$$\vec{H}_F = -j\omega[\hat{F} - (\hat{F}\cdot\hat{R})] \qquad \vec{E}_F = \eta[\vec{H}_F \times \vec{R}]. \tag{30}$$

Since only the electric field affects the wire, the scattered field at the antenna is

$$\vec{E}_{scat} = -j\omega\vec{A} + j\omega(\vec{A}\cdot\hat{R}) - j\omega\eta(\vec{F}\times\hat{R}). \tag{31}$$

From figure 3 we see that since the observation point is in the far field, $\hat{R} \approx \hat{R}_{10}$. This substitution is made because $\hat{R}$ varies along the segment of the edge while $\hat{R}_{10}$ is constant for each segment. Therefore, the expression for the electric field scattered by the edge is

$$\vec{E}_{scat} = -j\omega\vec{A} + j\omega(\vec{A}\cdot\hat{R}_{10}) - j\omega\eta(\vec{F}\times\hat{R}_{10}) \tag{32}$$

where $\vec{A}$ is given by (25) and $\vec{F}$ by (28). This expression is used to compute both Z_{mn}^g and V_m^g. For Z_{mn}^g $\vec{E}_i(l_o')$ in (25) and $\vec{H}_i(l_o')$ in (28) are from the piecewise sinusoidal currents on the antenna. For V_m^g these fields are from the incident plane waves.

2.3 Computer Program Validation:

The dipole array with the nearby edge was programmed in FORTRAN using the method of moments as described previously. Instead of writing the entire code from scratch, an existing thin wire method of moments code was used to model the antenna without the edge [2]. This code can model almost any thin wire antenna and has been validated with several examples. Therefore, it was only necessary to write subroutines to include Z_{mn}^g and V_m^g of (13) and incorporate them into the program. The final program was validated by comparing the results to previously published work.

There are several antenna parameters such as gain, radiation pattern, and input impedance that may be used to validate an antenna code. While the gain and radiation pattern are not very sensitive to modeling errors, it is well known that the input impedance is very sensitive to the antenna model [3]. Therefore, this parameter was used to validate the computer code.

The input impedance is calculated by operating the antenna in the transmitting mode. In this mode the voltage used to excite the antenna is divided by the complex current that results at the antenna terminals.

This operating condition is slightly different from the receiving mode used to determine the angles of arrival. However, it serves to adequately validate the code since, from a programming point of view, it is only a slightly different problem.

To validate the computer code, the input impedance of the antenna in figure 4 was calculated. In this problem, we have a $\lambda/2$ vertical dipole just above a perfectly conducting surface. This surface extends to infinity in one direction but bends by 90° in the other direction. At the bend, the horizontal edge is 20 wavelengths long. This is very similar to the problem in [3 p. 502-504] in which an infinitely long edge is near a monopole mounted on a perfectly conducting surface. In [3] it is shown that as the edge is moved away from the monopole, the input impedance oscillates about the value of the monopole on an infinite ground plane. For our problem in figure 4, we expect a similar behavior.

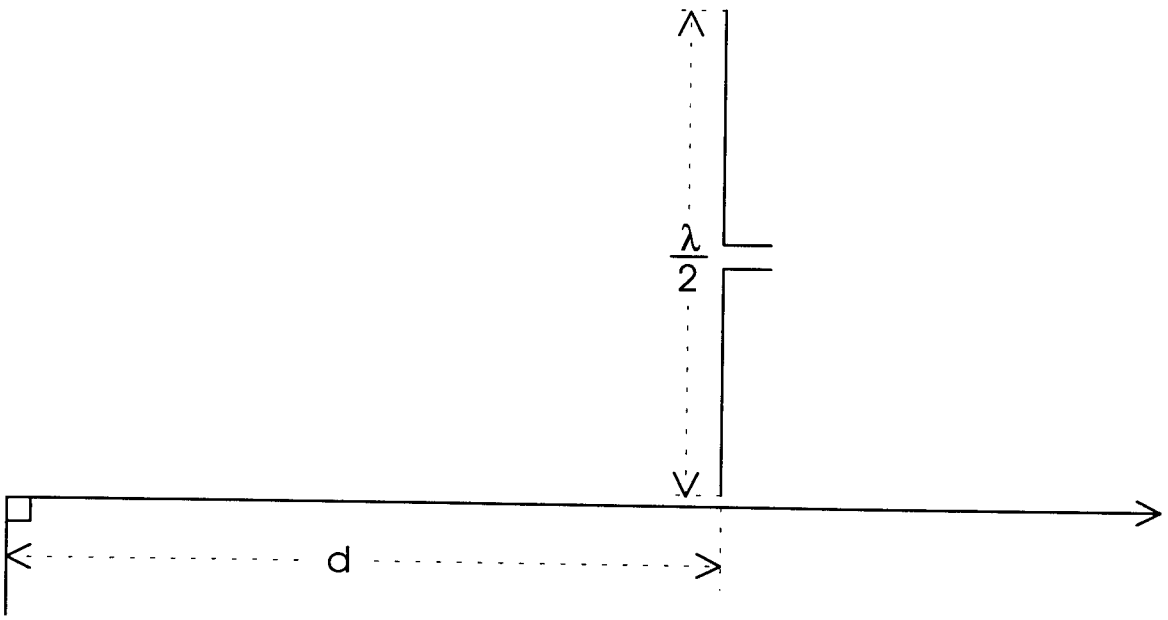


Figure 4: Dipole with Nearby Edge

Figure 5 shows the real and imaginary parts of the input impedance as a function of 'd' for the problem in figure 4. Notice that as the edge is moved away from the dipole, the impedance oscillates as expected. Notice also that the oscillations decay as the edge is moved away from the dipole. This is expected since the edge will naturally have less effect on the dipole. In the limit as 'd' approaches infinity,

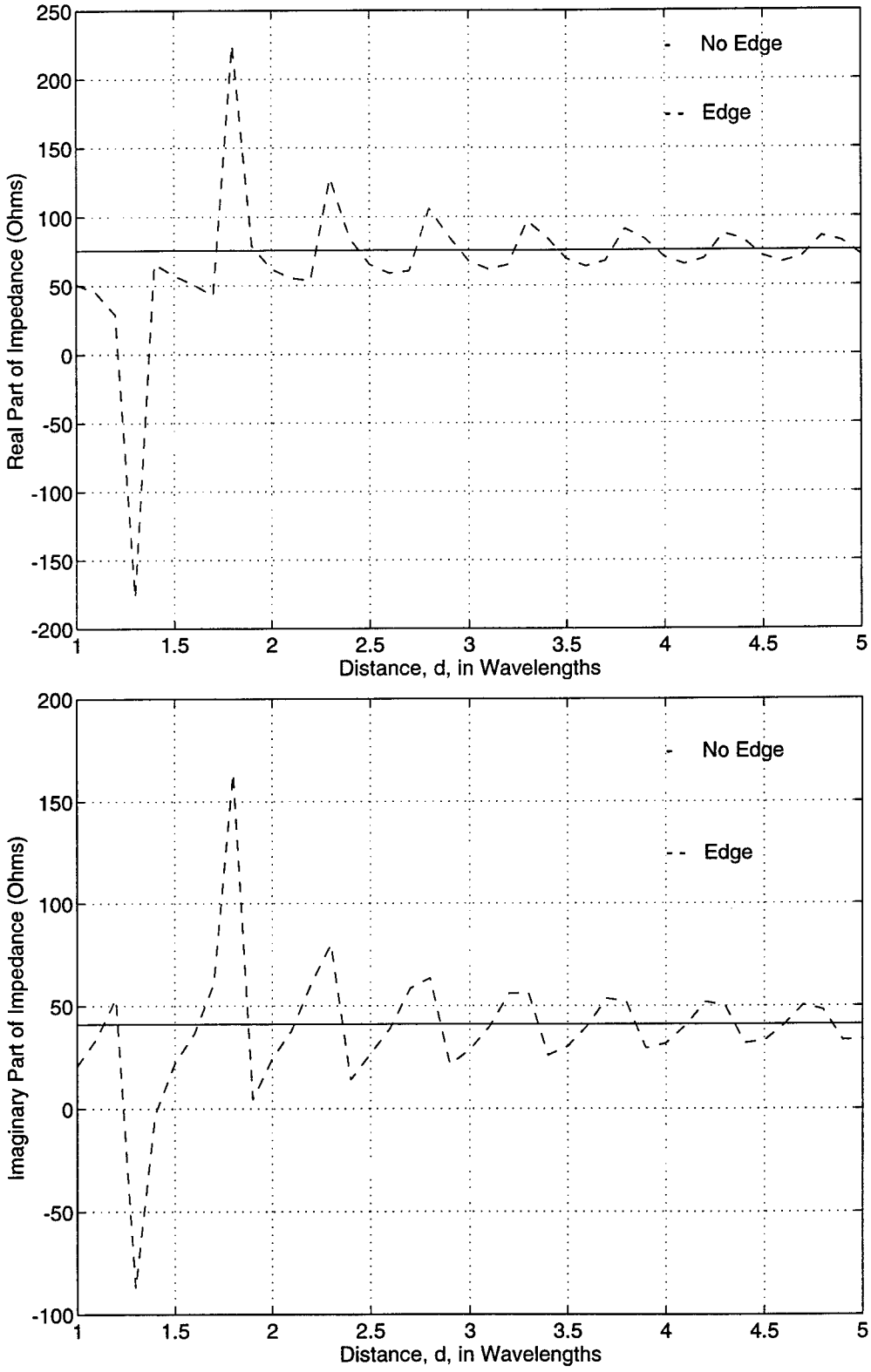


Figure 5: Input Impedance of Dipole with Nearby Edge

the input impedance is equal to the no edge case. These graphs are very similar to the impedance graphs for the monopole on a perfectly conducting surface with a nearby edge [3, p. 504].

3.0 Direction of Arrival Estimation:

The directions of arrival of the incident plane waves were determined using the multiple signal classification (MUSIC) algorithm [7,8]. This method starts by finding the covariance matrix from the output of the antenna array. This matrix is decomposed into its eigenvalues and eigenvectors. By examining the eigenvalues, it is possible to determine the number of signals and which eigenvectors correspond to the signal plus noise subspace and which correspond to the noise only subspace. The pseudo spectrum is determined by searching for the angles of arrival whose direction vector is orthogonal to the noise only subspace.

Mathematically, we have [8]

$$X_i(t) = \sum_{k=1}^{K} u_k(t)\, e^{j\beta d_i \cos(\theta_k)} + n_i(t) \tag{33}$$

where $x_i(t)$ is the signal at the i^{th} sensor, $u_k(t)$ is k^{th} narrow band signal, and θ_k is the angle of arrival of the k^{th} signal with respect to the array axis. In vector notation we have

$$X(t) = \sqrt{M} \sum_{k=1}^{K} u_k(t)\, a(\theta_k) + n(t) \tag{34}$$

where

$$a(\theta_k) = \frac{1}{\sqrt{M}} [e^{-j\beta d_1 \cos(\theta_k)} \quad e^{-j\beta d_2 \cos(\theta_k)} \quad \ldots \quad e^{-j\beta d_M \cos(\theta_k)}]^T \tag{35}$$

In matrix notation we have

$$X(t) = A\, u(t) + n(t) \tag{36}$$

where

$$u(t) = [\, u_1(t), u_2(t), \ldots, u_k(t) \,]^T \tag{37}$$

$$n(t) = [\, n_1(t), n_2(t), \ldots, n_M(t) \,]^T \tag{38}$$

and

$$A = \sqrt{M}\, [\, a(\theta_1), a(\theta_2), \ldots, a(\theta_K) \,]. \tag{39}$$

The covariance matrix for the array is

$$R = E[\, x(t)\, x^H(t)\,] \tag{40}$$

where $x^H(t)$ is the Hermitian transpose of $x(t)$. This simplifies to

$$R = A\, E[\, u(t)\, u^H(t)\,]\, A^H + E[\, n(t)\, n^H(t)\,] = A\, R_u\, A^H + \sigma^2\, I. \tag{41}$$

The covariance matrix, R, is decomposed into its eigenvalues and eigenvectors. There will be K eigenvalues associated with the K signals and M - K eigenvalues associated with the noise power. As long as the signal power is significantly greater than the noise power, it will be possible to identify which eigenvalues correspond to the signals and which to the noise. The noise eigenvectors are then determined from the noise eigenvalues. The pseudo spectrum is then obtained by searching for direction vectors that are orthogonal to the noise only subspace spanned by the noise eigenvectors. This can be expressed mathematically as

$$P_{MUSIC}(\theta) \;=\; \frac{1}{\sum_{i=K+1}^{M} \left|\beta_i^H\, a(\theta)\right|^2} \tag{42}$$

where β_i^H are the noise only eigenvectors and $a(\theta)$ is defined in (35).

3.1 Results:

A near field scatterer will have adverse effects on the MUSIC algorithm's ability to resolve two closely space plane waves. This is demonstrated with the antenna array in figure 6. In this case we have a 10 Element vertical dipole array with a 20 wavelength long horizontal edge in the near field. Two uncorrelated plane waves separated by 5 MHz are incident on both the array and the edge. The edge scatters spherical waves toward the antenna array which degrades the direction finding algorithm's ability to resolve the two plane waves.

Figure 7 demonstrates the results with signals at 45° and 52° relative to the array axis. The ideal curve assumes that there is no edge present and also that there is no coupling between the antenna elements. This is the best possible case and indicates that the signals can be resolved. The solid curve indicated without the edge shows the output of the moment method code without the edge present. This curve takes into account all the mutual coupling between the antenna elements but does not include the coupling due to

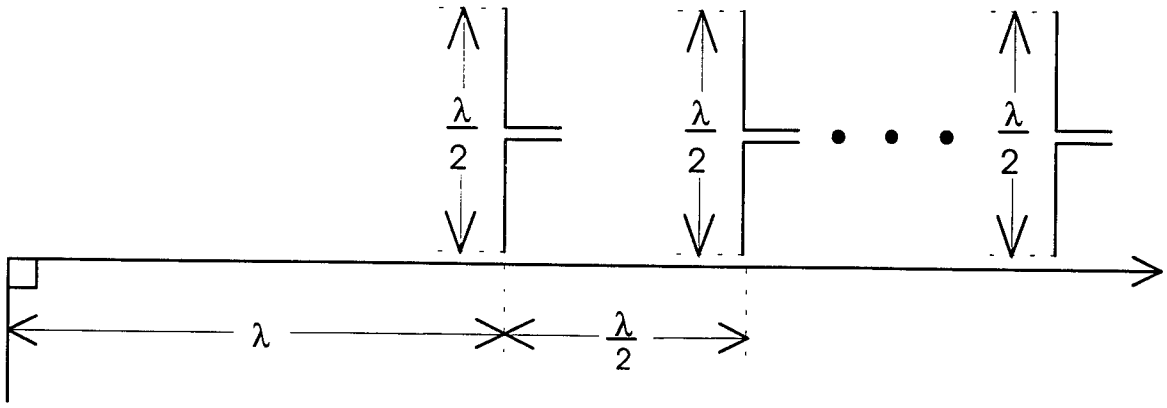


Figure 6: 10 Element Dipole Array with Nearby Horizontal Edge

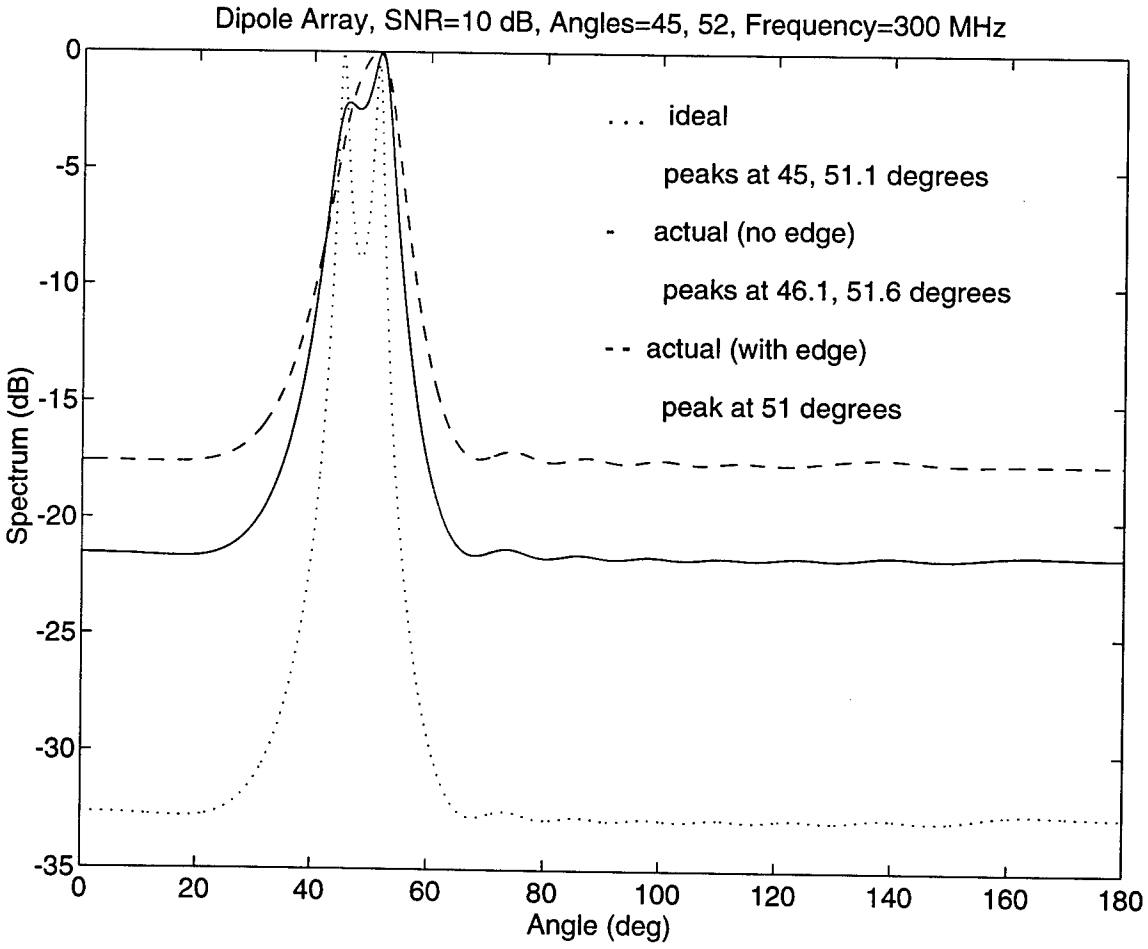


Figure 7: MUSIC Spectrum for 10 Element Array with Nearby Horizontal Edge

the edge. It represents the actual spectrum that would appear at the antenna elements without the edge being present. This is equivalent to setting Z_{mn}^{g} and V_{m}^{g} in (13) to zero. Again, we see that the two signals can be resolved. This case can be greatly improved by compensating for the antenna element coupling as shown in [10,11]. The third curve shows the spectrum when the edge is included. This corresponds to including Z_{mn}^{g} and V_{m}^{g} in (13). In this case we see that the two signals can no longer be resolved.

Figure 8 shows a vertical edge in front of an antenna array. The results for this case are shown in figure 9. Again, the ideal curve assumes that the edge is not in picture and that there is no coupling between the antenna elements. In this case, the two plane waves can be clearly resolved. The solid curve represents the spectrum obtained from the method of moments code without the edge. The two signals can be clearly resolved but their calculated angles of arrival deviate slightly from the true angles. The dotted curve shows the effect of the edge. In this case, only one signal is found in the spectrum. The coupling between the antenna elements and the edge prevent the MUSIC algorithm from separating the two signals even though they are 20° apart.

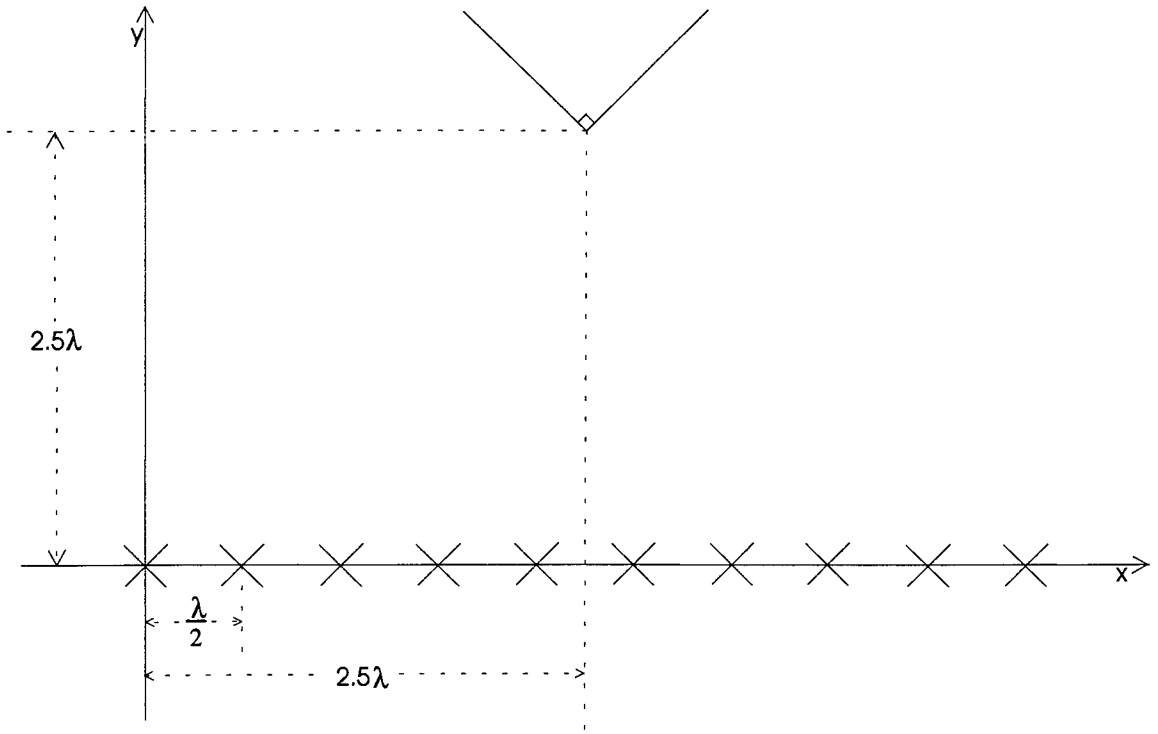


Figure 8: 10 Element Dipole Array with Nearby Vertical Edge

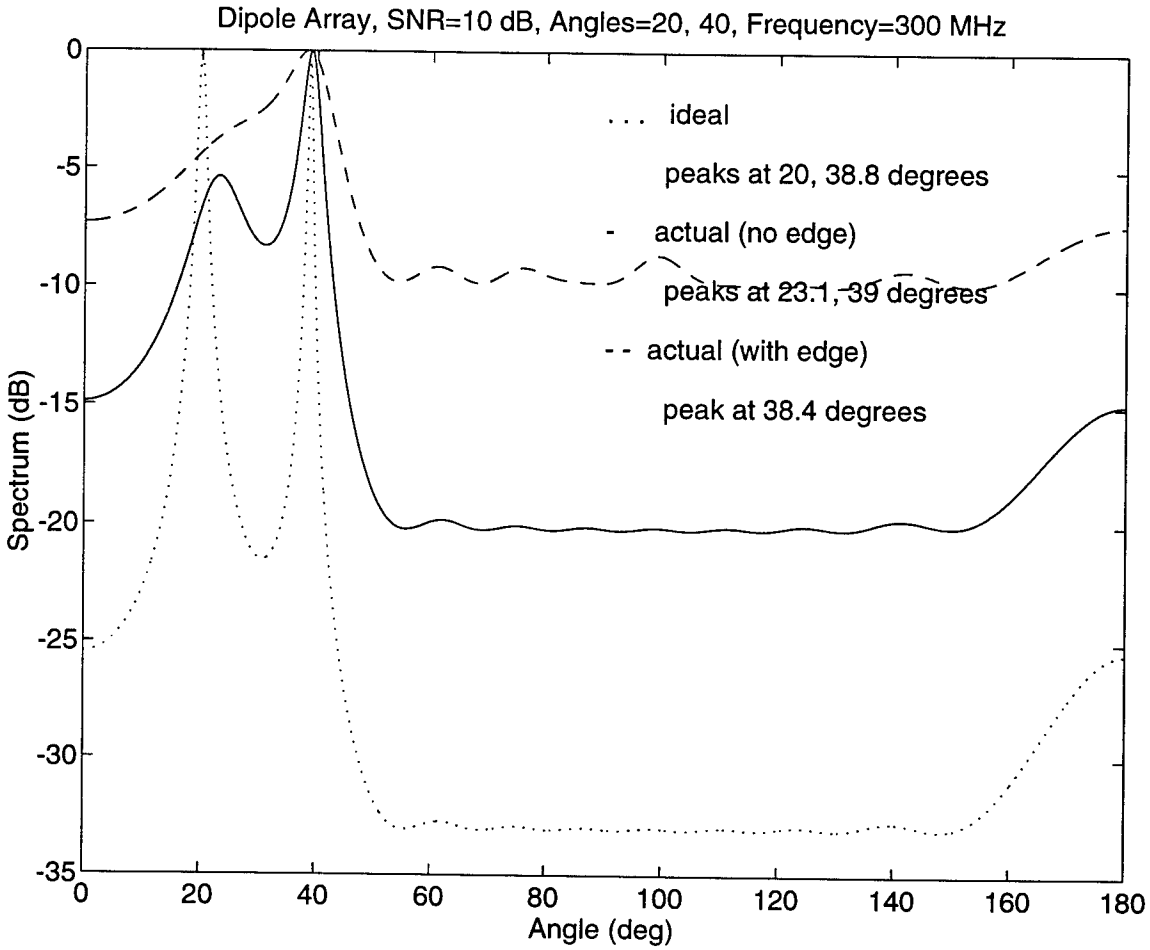


Figure 9: MUSIC Spectrum for 10 Element Array with Nearby Vertical Edge

4.0 Summary and Conclusions:

Aircraft us antenna arrays to determine the angles of arrival of incident radiation. Objects such as a nearby airplane wing or even the inside of the antenna's radome may reflect this energy toward the antenna array that is receiving the signals. As shown in this report, these reflections can alter the calculated angles of arrival or even cause the two signals to appear as one.

The antenna array and near field scatterer were modeled using the method of moments. This was done by expanding a standard computer program. The original code can model virtually any thin wire antenna. However, to simplify calculating the extra terms due to the edge, the program was limited to parallel antenna elements such as dipoles.

The near field scatterer was modeled as a finite length edge. Mathematically, the edge was modeled using the Uniform Theory of Diffraction (UTD). The edge could have any orientation and any length. However, since the length of the edge may cause the array to be in the near field, the edge was broken up into segments. The scattered field from the edge was then calculated by summing up the field from each segment. This simplified the mathematics because the edge could be made small enough so that the array was in the far field of each segment.

The final computer program was validated by comparing a special case to previously published work. This was done by computing the input impedance of a dipole with a nearby horizontal edge. The input impedance was chosen because it is well known that it is very sensitive to modeling errors. It was shown that the impedance behaved as expected thereby validating the computer program.

The nearby edge was shown to have adverse effects on the MUSIC spectrum. In the first case, a horizontal edge was placed in the near field at one end of the array. This represents scattering by an airplane wing. It was seen that the presence of the edge caused the two plane waves to appear as one signal. Next, a vertical edge was placed in front of the antenna array. This represents scattering from a near field object such as the antenna radome. It was shown that this also caused the two plane waves to be inseparable.

It has been shown in previous work that it is possible to compensate for coupling effects. This was shown in [10,11] where it was demonstrated that the mutual coupling between antenna elements can be virtually eliminated so that the actual spectrum is approximately equal to the ideal case. This was done by multiplying the signals at the antenna terminals by a terminal impedance matrix derived from the method of moments impedance matrix. It should be possible to account for the coupling between the dipole and the edge in a similar way. For the edge, it is also important to compensate for the diffraction of the incident waves by the edge. This factor is more difficult to compensate for and needs further investigation.

5.0 References:

1. Richmond, J. H., "Radiation and Scattering by Thin-Wire structures in the Complex Frequency Domain." NASA contractor Report CR-2396, Contract NGL 36-008-138, Hampton, VA, May, 1974.

2. Richmond, J. H., "Computer Program for Thin-Wire Structures in a Homogeneous Conducting Medium" NASA contractor Report CR-2399, June 1974.

3. Stutzman, W. L., Thiele, G. A., Antenna Theory and Design New York, Wiley & Sons, 1981.

4. Balanis, C. A. Advanced Engineering Electromagnetics New York, Wiley & Sons, 1989.

5. Kouyoumijian, R. G., Pathak, P. H., "A Uniform Geometrical Theory of Diffraction for an Edge in a Perfectly Conducting Surface." Proc. IEEE, Vol. 62, pp. 1448-1461, 1974.

6. Kouyoumijian, R. G., "Asymptotic High Frequency Methods", Proc. IEEE, Vol. 53. pp. 864-876, 1965.

7. Pillai, S. U., Array Signal Processing New York Springer-Verlag, 1989.

8. Schmidt, R. O., "Multiple Emitter Location and Signal Parameter Estimation," in Proc. RADC Spectral Est. Workshop, Oct. 1979. pp. 243-258; reprinted in IEEE Trans. on Antennas and Propagation, vol. AP-34, pp. 276-280, March 1986.

9. Thiele, G. A., Newhouse, T. H., "A Hybrid technique for combining moment methods with the geometrical theory of diffraction," Proc. IEEE, Vol. 62, pp. 1438-1447, 1974.

10. Friel, E. M., Pasala, K. M., "Wideband Bearing Estimation with Compensation for Mutual Coupling Effects" in Proceedings of IEEE Antennas & Propagation / URSI Symposium, Seattle WA. 1994, Vol 3, pp. 1556-1559.

11. Pasala, K. M., Friel, E. M. "Mutual Coupling Effects and Their Reduction in Wideband Direction of Arrival Estimation" to appear in IEEE Transactions on Aerospace and Electronic Systems, Vol. 30 No. 4 October, 1994.

OBTAINING THE CORRECTION FACTORS FOR TWO-PHOTON INDUCED FLUORESCENCE COVERING THE Ti:SAPPHIRE TUNING RANGE

Keith D. Grinstead, Jr.
Graduate Student
Department of Chemistry

Purdue University
1393 Brown
West Lafayette, IN 47907-1393

Final Report for:
Graduate Student Research Program
Wright Laboratories

Sponsored by:
Air Force Office of Scientific Research
Bolling Air Force Base, Washington DC

and

Wright Laboratories

October 1994

OBTAINING THE CORRECTION FACTORS FOR TWO-PHOTON INDUCED FLUORESCENCE COVERING THE Ti:SAPPHIRE TUNING RANGE

Keith D. Grinstead, Jr.
Graduate Student
Department of Chemistry
Purdue University

Abstract

A two-photon fluorometer was built using a tunable, single-mode Ti:sapphire laser. Fluorescence excitation spectra obtained using this instrument can be used as a reference to correct for the square of the incident intensity in spectra taken with mode-locked, and some multimode sources. The obvious disadvantage of this instrument was the inherent loss of sensitivity, which was greater than five decades. However, this instrumentation does allow for the collection of two-photon excitation spectra, of molecules with high cross-sections, without noise due to second-order coherence effects.

OBTAINING THE CORRECTION FACTORS FOR TWO-PHOTON INDUCED FLUORESCENCE COVERING THE TI:SAPPHIRE TUNING RANGE

Keith D. Grinstead, Jr.

Introduction

Jet fuel is not only the major fuel of an aircraft, but also serves as the primary coolant and lubricant. Due to this triad of duties, jet fuels have become a complex mixture of hundreds of compounds, each ideally designed for a specific duty. Unfortunately, the fuels are not completely characterized nor are the additives. This means that a fuel or additive is found to be good or bad by trial and error. Serendipitously, it was discovered that the two-photon fluorescence emission spectra were different for each class of fuel. Such data seem capable of determining the quality of the commercially available fuels. In order for any rapid screening technique to be fully developed and robust, the molecules responsible for these signals must be found. To this end, the two-photon excitation spectra of each fuel and the additives must be acquired.

Discussion of Problem

In two-photon excited flour, a molecule simultaneously absorbs two red photons whose energies add to equal that of the energy difference between the ground and first excited state. This absorption process will depend upon, I^2, the squared instantaneous photon flux[1] (since it requires the simultaneous presence of two photons). Also, using the same argument, the absorption is dependant upon the focal spot size.[2] Therefore, the ideal source would pack all of it's photons into a short pulse with a well defined and reproducible spacial profile for tight focusing in hopes that the signal, S, would be proportionate to $\langle I^2 \rangle$. Unfortunately it is difficult to measure the $\langle I^2 \rangle$ directly and generally one only has a reference which follows the average laser intensity squared, $\langle I \rangle^2$. Second-order coherence is then defined as, $\langle I^2 \rangle / \langle I \rangle^2$, which is not independent of wavelength in tunable pulsed lasers and often changes markedly within the tuning range of a dye or solid-state laser.[3] The resultant excitation spectrum therefore has distortions due to second-order coherence and appears 'flared' on its edges. There are several different ways presented in the literature to deal with this problem and many others, including the method we chose.

Three techniques have been established to provide correction factors necessary to correct for second-order coherence while obtaining two-photon excitation spectra; obtain the strength directly by three wave mixing,[4] correct with a second harmonic generation detector,[5] or ratio the signal to a reference compound whose

spectra was obtained with a single-mode laser.[6] Correction by a SHG detector has been done successfully with a 10 Hz Q-switched YAG. This allows for quick acquisition of spectra with the pulsed-dye laser as long as the user is willing to change dye multiple times and deal with a large amount of data manipulation. One disadvantage of this method would be the inability to compare compounds by not being able to obtain their relative two-photon cross-sections.

A method of correcting for the second order coherence of a laser while measuring a nonlinear optical phenomenon is by the use of a chemical standard.[7] Unfortunately, this optimal method, developed by Lytle et. al., of using bis-MSB presently has correction factors that only cover the yellow to red (550 - 700 nm) dye laser region. In order for true two-photon spectroscopic studies to be available to the user of the relatively new self mode-locked Ti:sapphire lasers, chemical standard(s) must be obtained to cover its tuning range (700-1000 nm). The compound used to cover the visible region, bis (o-methylstyryl) benzene, (bis-MSB), would be a poor choice to cover this new region due to its blue absorption. Another group of compounds will have to be evaluated, namely the coumarins. Coumarin 480 has an absorption band that nearly mimics the first mirror set for a mode-locked Ti:sapphire.[8] So using Coumarin 480 and a single-mode Ti:sapphire laser, a two-photon chemical reference will be obtained.

Methodology

A Schwartz single-mode Ti:sapphire (Titan-cw) was pumped with 6 W from an all lines, small frame Spectra Physics Argon ion laser (2020). This resulted in ~300 mW of tunable near infrared radiation which was modulated by a Hinds Instruments (PEM-90) photoelastic modulator. This device produced a 50 kHz trapezoidal polarization modulation on the output beam. The resultant circularly and linearly polarized light passed through a fresnel rhombus and then a polarization cube to select the horizontally polarized modulated light. Part of this beam was monitored by a Coherent LM-2 silicon power detector while the rest traveled through a 20 x microscope objective prior to the sample. Once the laser light exited the one cm cell, it was re-collimated and analyzed by a Burligh optical spectrum analyzer for jumps in single mode operation while data was collected. The resultant fluorescence of the sample was collected at 90 degrees with another 20 x microscope objective. This light was collimated onto a 931A photomultiplier tube which was fast wired[9] and biased at -1000 V. The anode current from this detector was monitored through a 1 kΩ shunt to ground by a Stanford Research Systems 850 digital lock-in amplifier. The lock-in and PMT power supply are powered through an isolation transformer to prevent any leakage of modulation frequencies through the ground or

power. The reference from the PEM-90 controller is filtered of all its higher harmonics to produce a 50 kHz sine wave for the lock-in to synchronize to. This prevents any second-harmonic modulation noise from entering the synchronization or lock-in electronics. The second-harmonic of the modulated fluorescence is detected by the lock-in with a time constant of a second and 30 values averaged. At each wavelength the laser is attenuated by placing two glass slides into the beam at opposite brewster angles,[10] so as to not walk the beam. Signals are obtained at six different powers and the slope of the signal vs. power squared is calculated. This 'sensitivity' is then plotted as a function of wavelength to obtain the complete excitation spectra.

Results

Presently, the collaboration started this summer has continued in hopes of finishing the primary experiment, the acquisition of the two-photon excitation spectra of Coumarin 480. Initial results indicate that this molecule will make a good chemical standard possessing both a relatively smooth spectra and a large cross-section. However even with the poor signal to noise ratios initially achieved, many replicates must be run to average out the noise. Since the instrument is currently running, this is just a time consuming and tedious process which will be accomplished in due time.

Once this data is achieved several experiments are planed. Excitation spectra of the jet fuels, additives and several other reference compounds would be acquired with the mode locked Ti:sapphire at Wright-Patterson AFB. Also, of interest is to initiate some experiments at Purdue using the sync-pumped dye laser facilities there. This collaboration would allow for a complete set of two-photon excitation and emission spectra to be obtained for the above listed compounds. With the separation techniques available at both facilities, determining the bad actors in fuel performance should be possible.

Conclusion

An instrument has been developed which allows for the acquisition of both the two-photon absorption spectra and two-photon cross-section. The excitation spectra will be used to correct for noise that is wavelength dependant while using a tunable, mode-locked Ti:sapphire. This will allow for spectral comparison between molecules excited in the near-infrared, which is not possible without this type of standard reference. Also using the two-photon cross-section data will permit the comparison of data of other research groups interested in the field and with the data obtained with visible dye lasers.

Acknowledgement

The author would like to thank Fred E. Lytle, James R. Gord, Steven R. Buckner, and William L. Weaver for their helpfulness and suggestions during the many trials encountered attempting to complete this experiment. Also thanks must be given to RDL for establishing and maintaining a program which allows this type of technology transfer.

References

1. Kaiser W.; Garrett C. G. B., *Phys. Rev. Lett*, **7**, 229.
2. Wirth, M. J., Fatunmbi, H. O. *Anal. Chem.* 1990, **62**, 973.
3. Hassinger, M. J.; Kennedy, S. M.; Lytle, F. E. *Anal. Instr.,* 1987, **16(4)**, 487.
4. Friedrich, D. M. *J. Chem. Ed.* , 1982, **59,** 472.
5. Jones, R. D.; Callis, P. R., *J. Appl. Phys.,* 1988, **64,** 4301.
6. Kennedy, S. M.; Lytel, F.E., *Anal. Chem.* 1986, **58,** 2643.
7. Freeman, R. G.; Gilland, D. L.; Lytle, F. E., *Anal. Chem.,* 1990, **62,** 2216.
8. Lytle, F. E.; Dinkel, D. M.; Fisher, W. G., *Appl. Spec.* 1993, **47,** 2002.
9. Lytle, F. E. *Anal. Chem.* 1974, **46,** 545A.
10. Wirth, M. J.; Lytle, F. E., *New Application of Lasers to Chemistry,* 1987, Chapter 3.

A RESEARCH PLAN FOR EVALUATING WAVE GUN AS A LOW-LOADING MODEL LAUNCHER FOR HIGH SPEED AEROBALLISTIC TESTS

Robert W. Courter
Associate Professor
Department of Mechanical Engineering

and

Jason J. Hugenroth
Graduate Student
Department of Mechanical Engineering

Louisiana State University
Baton Rouge, LA 70803

Final Report for:
Summer Faculty Research Program
Wright Laboratory - Armament Directorate
Eglin Air Force Base, FL

Sponsored by:
Air Force Office of Scientific Research
Bolling Air Force Base, DC

and

Wright Laboratory - Armament Directorate

August, 1994

A RESEARCH PLAN FOR EVALUATING WAVE GUN AS A LOW-LOADING MODEL LAUNCHER FOR HIGH SPEED AEROBALLISTIC TESTS

Robert W. Courter
Associate Professor
Department of Mechanical Engineering
Louisiana State University

and

Jason J. Hugenroth
Graduate Student
Department of Mechanical Engineering
Louisiana State University

Abstract

A specialized light gas gun firing cycle, developed by Thomas Dahm of Astron Research and Engineering and named by him the Wave Gun, is investigated as a candidate for launching models in a ballistic range to high speed with relatively low model loading. The Wave Gun firing cycle features a very light piston which oscillates during the shot and produces a series of shock impulses on the model. A light gas gun interior ballistics code that simulates the Wave Gun firing cycle was used to evaluate launcher performance for a matrix of launcher geometric and launch parameters. A Wave Gun test facility, designed and constructed by Astron, was used to provide data with which to verify the fidelity of the simulation code. Pressure histories were recorded in the combustion chamber, the pump tube exit, the nozzle exit and at three axial stations along the launch tube. In addition the first-pass piston velocity and the model muzzle velocity were determined. Two test shots were fired. During the second shot a nozzle structural failure occurred and further testing was suspended pending fabrication of a new nozzle. The data acquired from the tests were not sufficient to verify the numerical model. However, the tests did provide experience in operation of the gun and data acquisition, and they provided insight into the status of the numerical model and the direction that future testing should take. A plan is presented for numerical and experimental studies to identify parameter sets that produce high velocity with moderate model loading. Initial testing and analysis will be devoted to validation of the gun cycle simulation code. Then parametric studies, supported by appropriate tests, will be carried out. Six parameters identified for consideration in these studies are propellant type and weight, helium charge pressure, pump tube volume, piston start pressure and model start pressure. Launch tube and model configurations will be held constant.

Acknowledgements

The authors would like to thank Mr. Gerald Winchenbach for selecting them to participate in this summer research program. His enthusiasm and continuing encouragement are sincerely appreciated. We are also indebted to Mr. Charles McClenahan and his staff for setting up the test facility, fabricating apparatus components and carrying out the experimental program. We are grateful to Messrs. John Huntington and John Case of Astron Research and Engineering for providing us with much useful information on the history and technical details of the Wave Gun program. Finally, we acknowledge the support of the Air Force Office of Scientific Research and the Wright Laboratory-Armament Directorate and the program management of Research and Development Laboratories.

A RESEARCH PLAN FOR EVALUATING WAVE GUN AS A LOW-LOADING MODEL LAUNCHER FOR HIGH SPEED AEROBALLISTIC TESTS

Robert W. Courter

Jason J. Hugenroth

Introduction

In 1981 Thomas Dahm of Astron Research and Engineering invented a unique firing cycle that provided the potential for weaponization of the light-gas gun. He called the device Wave Gun[1]. Essentially, it employed a very light piston in conjunction with a long propellant burning time and a high light-gas charge pressure to produce an oscillatory piston motion that, in turn, caused propellant burning rate fluctuations and multiple pressure pulses on the projectile. Analytical studies in conjunction with some crude experiments led to the suggestion that with appropriate tailoring of the gun and shot parameters, a high muzzle velocity could be achieved within the bounds imposed by weapon design. An interesting by-product of that study was the possibility of designing a cycle that could achieve a high muzzle velocity with a relatively low loading on the projectile[1]. It is advantageous in free-flight aeroballistic testing to have the capability of launching fragile models to high speeds without imposing destructive loads on the model. It is this prospect that Wave Gun might be used as a low-loading model launcher that motivates the present study.

In 1992 the Astron Wave Gun test apparatus was acquired by the Ballistics Branch of the Armament Directorate of Wright Laboratory, Eglin AFB, Florida. This facility has been activated for experiments to support the present study. The experimental results achieved will aid in validating a numerical simulation of the Wave Gun firing cycle. The objectives of the present study are to develop a simulation code, initiate the validating experimental program and provide a plan for future research that will produce an evaluation of Wave Gun as a "soft launch" aeroballistic model accelerator.

The Wave Gun Concept

A conventional gun uses an explosive propellant to accelerate a projectile in a launch tube. For a given configuration the muzzle velocity of such a gun is limited because some of the energy from the propellant must be expended to accelerate the heavy propelling gas. This difficulty is circumvented in the two-stage light gas gun. This gun features a chamber of light gas (the pump tube) between the propellant chamber and the projectile, sealed from the propellant gas by a moveable piston and from the projectile by a frangible diaphragm. Here the

propellant gas drives the piston which, in turn, compresses the light gas. Ultimately, the frangible diaphragm ruptures, and the compressed light gas accelerates the projectile through the launch tube. The high velocities attainable by this type of launcher make it attractive for use in free flight aeroballistic testing. It is standard practice in aeroballistic testing to use an "isentropic compression" firing cycle for the light gas gun. This cycle employs a heavy piston to produce a continuous, almost isentropic, pressure rise which eventually propels the model smoothly without large pressure spikes (Figure 1). The Wave Gun cycle, on the other hand, uses a very light piston that simply acts as a barrier separating the propellant gas from the light gas. This firing cycle routinely features an oscillating piston which alternately compresses and expands the propellant gas, producing fluctuations in burning rate and driving pressure. Some characteristics of a typical Wave Gun cycle are shown in Figure 1. It has been shown that this type of cycle can be optimized to produce very high muzzle velocities within the constraints of gun design[2]. It is also believed that high velocity shots with low model loading are possible through judicious selection of launcher geometric and shot parameters.

Firing Cycle Simulation

To investigate the capabilities of Wave Gun as a low-loading launcher a firing cycle simulation program has been constructed. The light gas gun code currently used at the Arnold Engineering Development Center (the "AEDC code") is used as the basic simulation engine. The code was originally developed by Piacesi, Gates and Seigel[3], and it has been extensively modified by DeWitt[4]. The code uses a von Neumann-Richtmyer time-stepping procedure with artificial viscosity for integration of the fundamental equations of motion, a power law relationship for propellant burning rate and a virial-type real gas model for the light gas (in this case, helium). The present authors have modified the code to be compatible with the requirements of the experimental program. In addition provisions are made to alter treatment of propellant conservation laws, piston and model release and friction and pump tube heat transfer . These adjustments will be guided by the results of the experimental program.

Experimental Facility Description

The Astron Wave Gun 30mm test facility was assembled at Eglin AFB to provide experimental support for the present research program. The gun was originally designed to investigate potential firing cycles for light gas gun weaponization, a program requiring flexibility of configuration. This flexibility was achieved by using a massive steel tube to contain the internal parts of the launcher where very high pressures are generated. A schematic of the gun is shown in Figure 2. The main components of the gun are the internal breech plug and ignition system, the propellant chamber, the polypropylux piston, the pump tube liner, the nozzle, the aluminum model and the launch tube. The parts subjected to high pressure are contained under compression in the outer tube by a breech plug at one and and a barrel nut at the other. A spacer is used to permit adequate compression of the internal parts. The original facility had three different sets of components so that the internal volume relationships could be

parametrically investigated. However, only the configuration shown in the figure is possible at the present time. Detail drawings of the gun components are shown in the Appendix.

Helium gas is supplied to the pump tube through a fill valve which is not shown in the figure. A black powder primer is used in the spit tube, and the main propellant is bagged and wrapped around the spit tube. Ignition is with a 50 volt electrical pulse. The piston is actually screwed into the pump tube end of the propellant chamber. Piston motion begins when the combustion pressure is sufficient to shear the polypropylux piston threads. Thus, the number of piston threads engaged determines the piston start pressure. The model is simply an aluminum cylinder with integral flange. Model motion begins when the driving pressure is sufficient to shear the flange. The shot start pressure is therefore determined by the flange thickness and material.

There are thirteen instrumentation ports in the gun, nine in the high pressure tube and four in the launch tube. It is important to note that the positioning of the internal parts must be precise so that these ports are open. In this regard it is essential that when the gun is being sealed prior to firing, the breech plug and barrel nut must be tightened simultaneously so as not to disturb this instrumentatin port alignment. The position of the ports and the designation of those used for the tests of this program are indicated in Figure 3. Transducers 3, 8 and 9 provide, respectively, the propellant chamber pressure, the nozzle entrance pressure and the nozzle exit pressure. Transducers LT1, LT2 and LT3 provide pressures at the repective launch tube locations. Ports 4, 5 and 7 are used for breakwires that signal passage of the piston during its first travel down the pump tube.

Figure 4 is a schematic of the overall setup for the Wave Gun tests. Each quartz pressure transducer was connected through a charge amplifier to a digital oscilloscope. The transducers were set to trigger simultaneously from the signal of the first transducer. The breakwires were connected across two gated digital timers to provide the elapsed time for piston passage between the breakwire stations. Two infrared sky screens were used in the same way to determine the approximate muzzle velocity of the projectile. Finally, a Doppler radar unit was used to determine the projectile trajectory from launch tube exit to the model-catching bunker. It is intended that this unit be used for downbore velocity measurements in later tests. In addition a VISAR unit (Velocity Interferometer System for Any Reflector) will also be available for down-bore measurements in later tests.

Experimental Results

The Astron Wave Gun was assembled and commissioned at Eglin AFB during the present summer research program. In Reference 2 some data from previous firings of the gun are provided. Since the gun had not been fired in about seven years, it was deemed adviseable to initiate the new firing program by duplicating a low performance shot from the previous program. However, even this was not exactly possible because a supply of the

same propellant and a supply of high pressure helium were not available. The propellant deficiency was not of major importance for the first shot, and M30/19 MP propellant was used. The helium deficiency was important. The Wave Gun uses a low volume pump tube and light piston. The low volume necessitates using helium at unusually high pressure in the pump tube. Standard light gas guns use helium pressures of about 200 psi. The Wave Gun pressures are between 2500 and 4000 psi. This high pressure plays an important role in the piston behavior, particularly with regard to piston speed during the cycle. The parameters for the two shots that made up the present experimental program are shown in the table below.

Shot number	Propellant weight (gm)	Primer weight (gm)	Model weight (gm)	Piston start pressure (psi)	Model start pressure (psi)	Helium charge pressure (psi)
1	1304	18.2	111.6	3100	34800	900
2	1304	18.2	111.6	3100	34800	1600

The radar was not available for Shot 1 so the muzzle velocity was estimated from sky screen measurements (see Figure 4). The radar was used instead of the sky screens for Shot 2.

The results of the two shots were disappointing. No data were acquired from Shot 1. The instrumentation trigger was activated by the firing switch. One possible cause for the failure was a delayed ignition which caused the scope to sweep prior to the main part of the firing cycle. Another was a possible short in the trigger circuit. The transducer traces indicated negligible activity, so it is not possible to determine the exact cause. The sky screens did not give an indication of projectile passage, so it seems likely that their circuit suffered a short during the early stages of the shot. The piston, the model and the sheared model flange were all recovered. The piston was partially deformed and wedged in the nozzle throat. The model separated cleanly from the flange in a pure shear failure, indicating failure at a pressure that was near the design value. There was no damage to the steel backing washer or to any of the gun components. Some very mild erosion, probably from blow-by, was detected on the upstream nozzle face. The physical evidence after the shot and the relatively low helium charge pressure suggest that the Wave Gun operated in a fashion close to that of a standard light gas gun. The numerical simulation of this shot indicates something else. A discussion of the numerical simulations and the experimental results for both shots is given in the next section.

The second shot was triggered with the propellant chamber pressure transducer, so ignition delay was removed as a factor in data acquisition. Some experimental data were acquired for this shot. Pressure traces from the nozzle entrance, the nozzle exit and the first launch tube station were recorded. Also, the elapsed time for piston travel between ports 4 and 5 and the radar track of the projectile (including the muzzle velocity) were acquired. The

other sensors failed to provide any data. The data acquired are shown in Figure 5. The radar track, which is very reliable, indicates a muzzle velocity of 5800 fps. The pressure traces, however, are suspect. Since the instrumentation was to have been triggered from the pressure sensor in port 3 (at the propellant chamber), it would be expected that the transducers at the pump tube and nozzle exits would initially indicate a low pressure followed by a sudden rise in pressure as the pump tube gas is compressed by the advancing piston. Each of the actual traces shows a high value at the triggering time and an uncharacteristic trace. These traces do provide an indication of the pressure levels in the gun, but it is surmised from the previous arguments that these are probably not maximum values. The pressure trace from the launch tube transducer has the appropriate characteristics. However, it is impossible to assess the timing of the pulse in light of the triggering difficulties with the other transducers. It is obvious that this shot experienced at least a double compression by the piston. The piston was extruded through the nozzle and launch tube and propelled down range. The model was not recovered, but the model flange had a jagged edge indicating a combined stress failure. This would seem to indicate that the pressure was high enough to disturb the seal between nozzle and launch tube. The steel backing washer was also eroded. Most importantly, however, the upstream nozzle face was found to be severely eroded by blow-by and several stress cracks, one quite severe, were in evidence. In addition, the inside surface of the steel gun shell was eroded at the location of the pump tube-nozzle joint. All of this evidence points to a very powerful shot that was particularly hard on the nozzle structure, probably because the charge pressure of the helium was below that used by Astron in their initial tests with this gun.

Simulation Results

The results of the two simulations are summarized in the following table. In addition the behavior of piston and model for the two cases is show in Figures 6 and 7.

Shot Number	Muzzle Velocity (fps)	Maximum Base Pressure (psi)	Maximum System Pressure (psi)	Total Cycle Time (ms)	Model Release Time (ms)
1	4916	50000	170000	7.27	4.39
2	5805	46000	92000	8.26	5.92

Comparison of these simulations with the experimental results prompts some interesting observations. The simulated results for Shot 2 compare very favorably with the experimental data. The system pressure indicated by the simulations is not consistent with what can be gleaned from the experimental results in that it would be expected for the higher pressures to occur for Shot 2 where some structural damage and complete piston extrusion occurred. Having made these observations, it is now appropriate to consider each simulation separately.

The plots of Figure 6 indicate that the model in Shot 1 was released at the second compression by the piston. The relatively large amplitude of the piston oscillation would suggest a pressure fluctuation that would yield a lower average driving pressure than would occur with smaller piston oscillations. Thus, the muzzle velocity would suffer accordingly. This would also indicate that the release load would be softer. It is apparent from the model trajectory that a third compression reaches the model before it leaves the launch tube.

The simulated results of the second shot tell a different story. The model is launched just at the third compression by the piston. Note that the piston osicillates at a lower amplitude than occurs for the first shot. Thus, a larger load is imposed on the gun structure and the model. The calculated muzzle velocity and maximum base pressure are surprisingly close to the experimental results for this shot. At this point of the investigation the descrepancy that occurs in the maximum base and system pressure for the two shots cannot be adequately explained. It is obvious that we have a long way to go to have a validated simulation code. However, we have made a beginning, and the results achieved so far are not drastically unreasonable.

Future Research

The present research effort has been disappointing in that no measurements have been made that can be used directly in verifying the simulation code. However, the experience gained in assembling and firing the Wave Gun has been valuable, and the lessons learned regarding data acquisition have considerably raised the probability of success with future tests. It is important, then, to plan carefully for the next series of tests so that the maximum benefit can be gained. The following general observations are important:

1. All instrumentation mounted on the gun should be activated with a common trigger. The propellant chamber pressure transducer is a good choice for this trigger.
2. It would be advantageous to connect the breakwires into the system such that the elapsed time from trigger to wire disconnect can be determined for each wire.
3. All sensors should be recorded on a unit with a common time base. It is also advantageous for the data to be easily transferable to a computer. Consideration should be given to activating the 12-channel Soltec recording unit.
4. High pressure helium (over 3000 psi) should be available for the tests
5. If possible, in-bore measurements of velocity with a VISAR or Doppler radar should be made.

At least the first three tests in the new series should be aimed at duplicating results reported by Astron in Reference 2 for three different test conditions. These tests will provide definitive information on the piston and model start conditions, the performance of the propellant and the behavior of the piston. Also, careful attention to the wave

timing and pressure levels should provide some insight into the heat transfer and friction models in the code. Prior to the initiation of new tests the simulation code will be modified to account for spatial property changes in the propellant chamber and mass transfer from the gun liner into the surrounding space. Guidance for these revisions will be provided by the experimental results reported by Astron. Since the objectives of our program are somewhat different from those reported by Astron, it is not possible to specify the testing matrix for the additional tests required to validate the simulation code. As with any investigative effort, the direction taken will depend on the results of the most recent tests and analysis. However, six parameters will be considered initially.during the program. These are propellant type and weight, helium charge pressure, pump tube volume, piston start pressure and model start pressure

References

1. Dahm, T. J. and D. S. Randall, "The Wave Gun Concept for a Hypervelocity Rapid Fire Weapon," presented at the 1984 JANNAF Propulsion Meeting, New Orleans, LA, 8 February 1984.
2. Mawhinney, R. C., D. S. Randall and R. P. Heydt, "Wave Gun Charge Development," Astron Research and Engineering Report Number 7110-01, 29 September 1989.
3. Piacesi, R., D. F. Gates and A. E. Seigel, "Computer Analysis of Two-Stage Hypervelocity model Launchers," Naval Ordnance Laboratory, NOLTR 62-87, February, 1963.
4. Cable, A. J. and J. R. DeWitt, "Optimizing and Scaling of Hypervelocity Launchers and Comparison with Measured Data," Arnold Engineering Development Center, AEDC-TR-67-82, April, 1967.

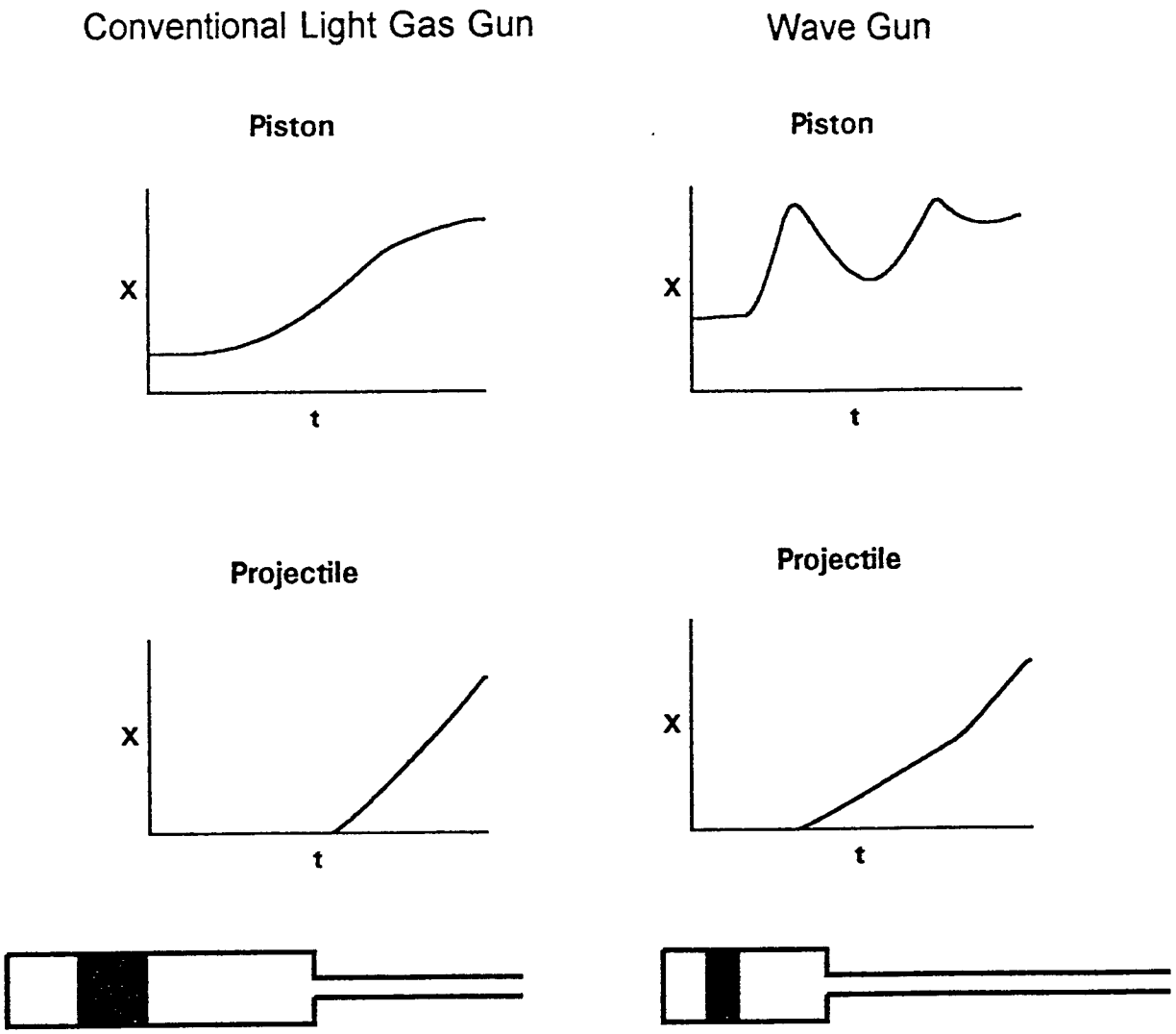
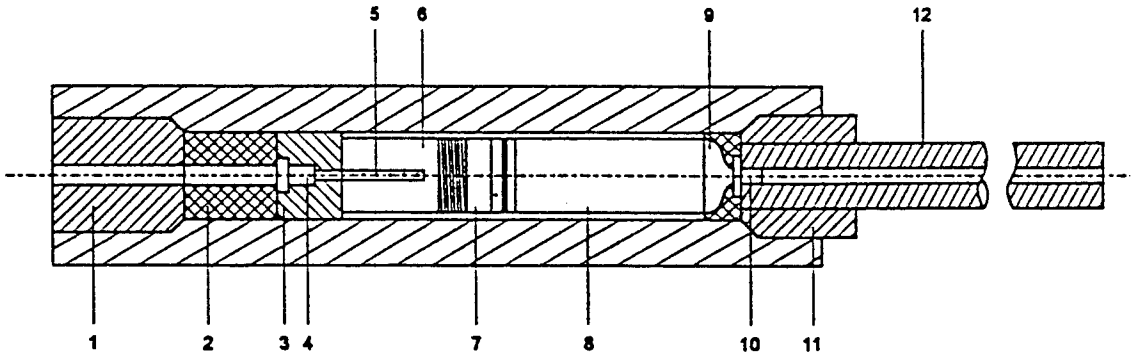
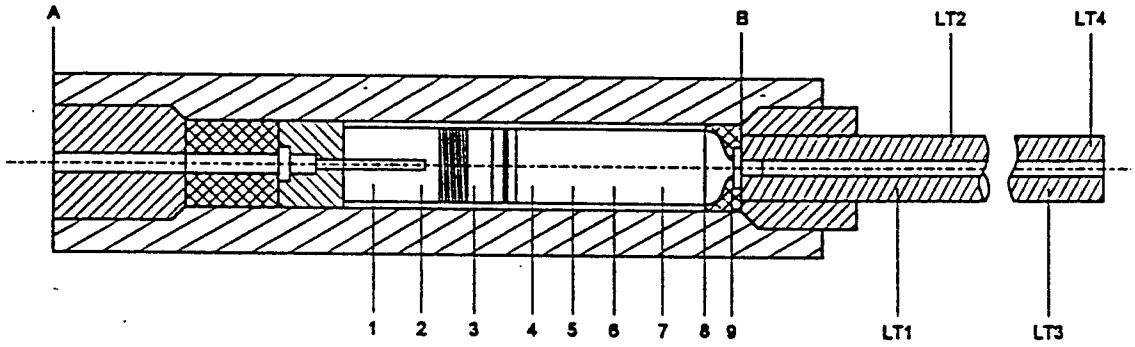


Figure 1. Comparison of Wave Gun and Conventional Light Gas Gun firing cycles.



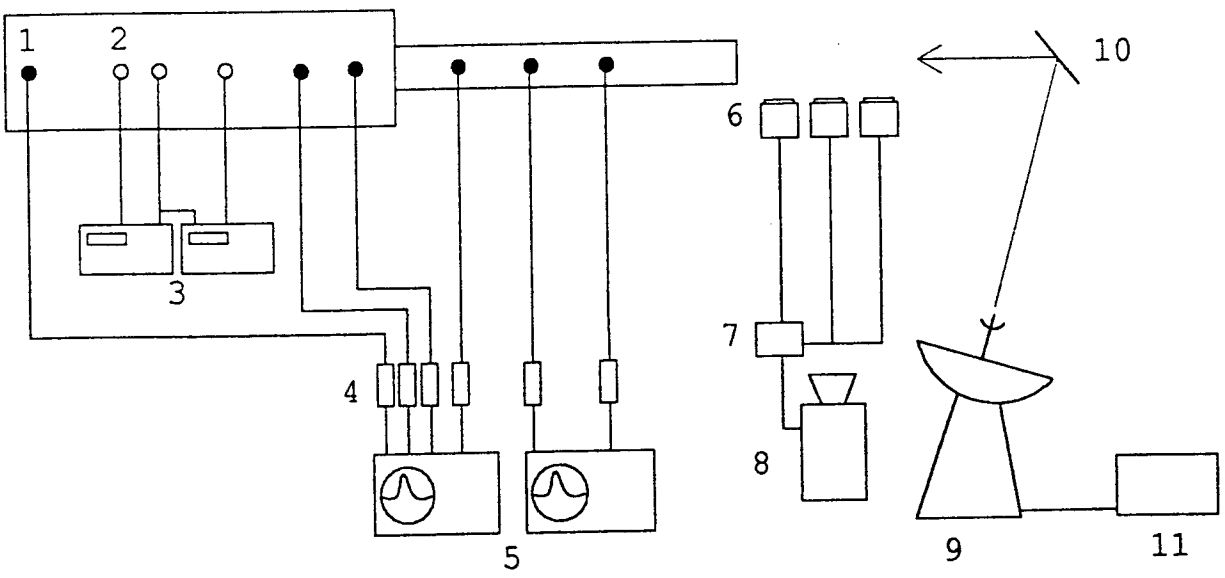
No.	Part	Length (cm.)	Diameter (cm.)	No.	Part	Length (cm.)	Diameter (cm.)
1	Breech plug (outer)	-	-	7	Piston	10.29	11.43
2	Spacers	11.47	13.29	8	Pump tube	49.43	11.43
		16.04	13.29	9	Nozzle	7.67	11.43
		22.91	13.29	10	Projectiles	5.715	3.00
3	Breech plug (inner)	12.07	13.29			6.033	3.00
4	Igniter	-	-			6.350	3.00
5	Spit tube	-	-	11	Barrel nut	-	-
6	Propellant chambers	18.67	11.43	12	Launch tube	243.84	3.00
		23.25	11.43				
		28.19	11.43				

Figure 2. Astron Wave Gun Test Apparatus



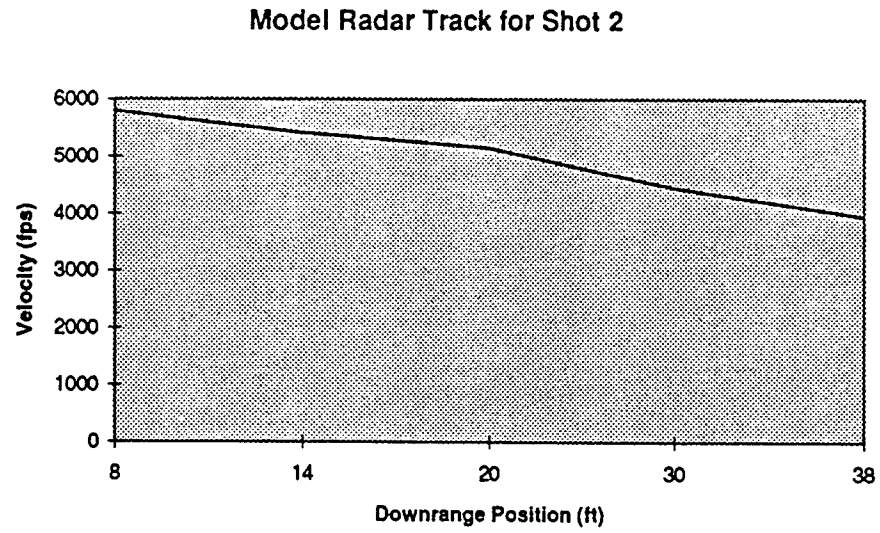
No.	Location (cm.)*	Use	No.	Location (cm.)**	Use
1	45.72	Not active	LT1	45.72	Pressure transducer
2	60.96	Pressure transducer	LT2	76.20	Pressure transducer
3	71.12	Not active	LT3	137.16	Pressure transducer
4	81.28	Break wire	LT4	198.12	Not active
5	91.44	Break wire			
6	101.60	Not active			
7	111.76	Break wire			
8	121.92	Pressure transducer	* Measured from A		
9	128.11	Pressure transducer	** Measured from B		

Figure 3. Instrumentation ports on Astron Wave Gun



No.	Instrument	Model
1	Piezeoelectric pressure transducers	Kistler 60704
2	Breakwires	-
3	Universal counters	HP 5315B
4	Charge amplifiers (1-4)	Kistler 504E4
	Charge amplifiers (5-6)	PCB 463A
5	Digital oscilloscopes	Nicolet 4094B
		Hi Techniques HT-600
6	Flashers	Hadland Photonics
7	Flash control unit	Hadland Photonics CU-2
8	Camera	Hadland Photontics SV-553BR
9	Radar	Opos Electronics
10	Sacrificial mirror	-
11	Radar analyser	Terma DR-5000

Figure 4. Experimental test setup



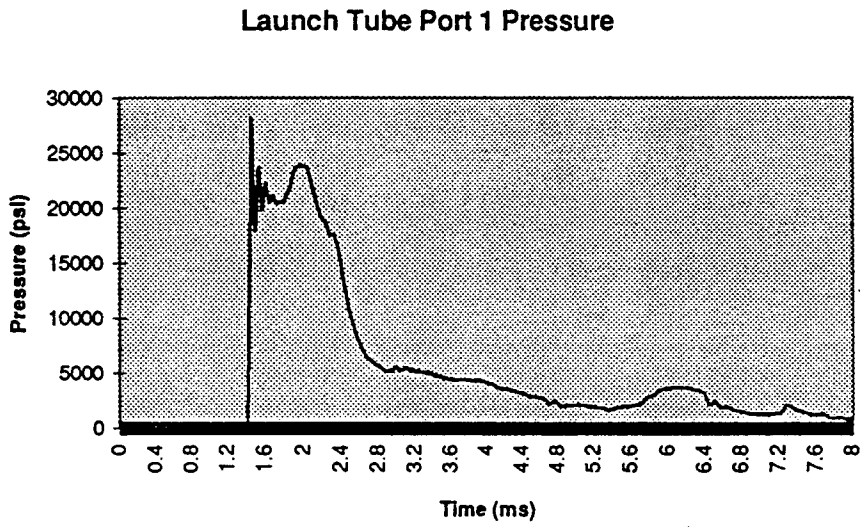
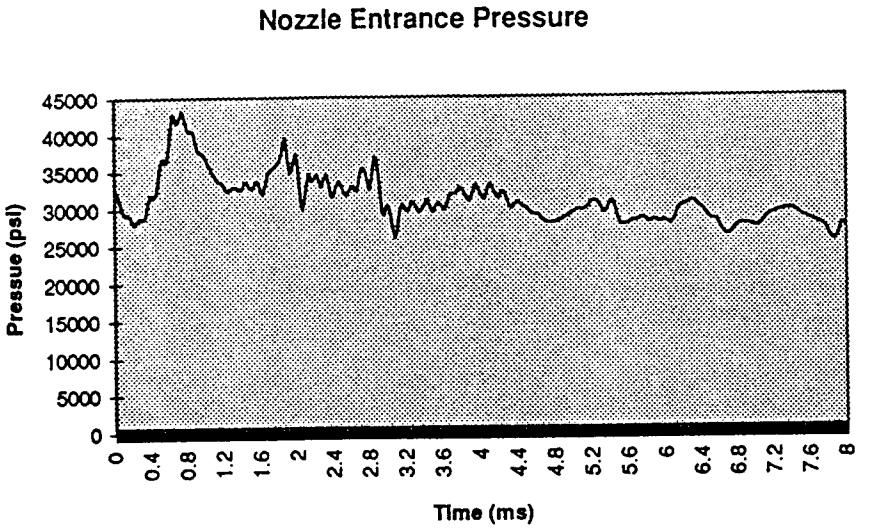


Figure 5. Experimental Results



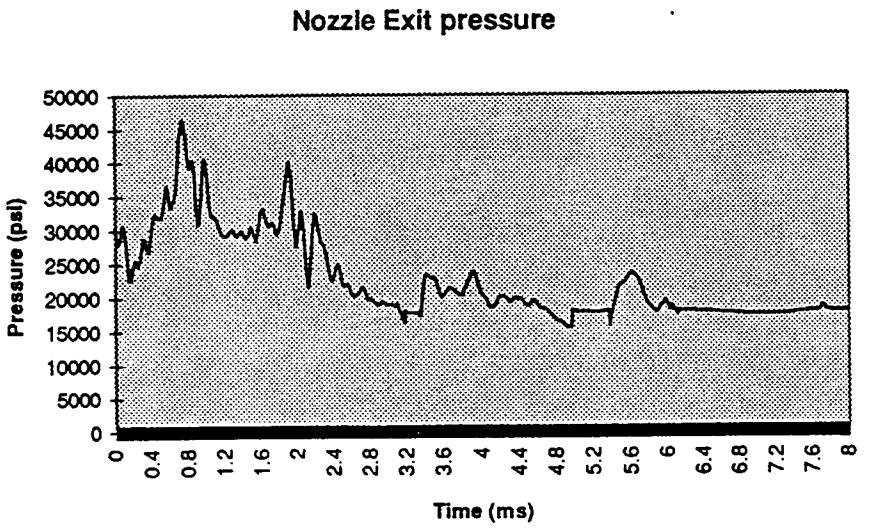
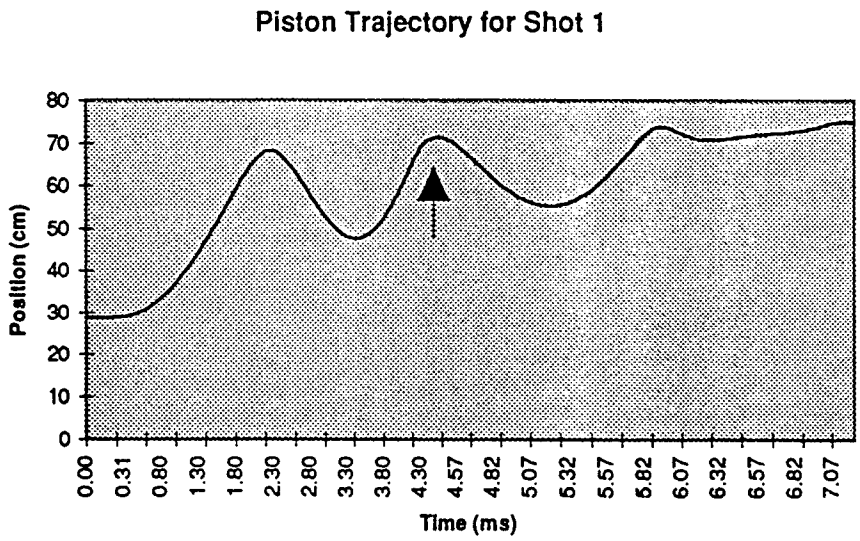


Figure 5. Experimental Results (Concluded)



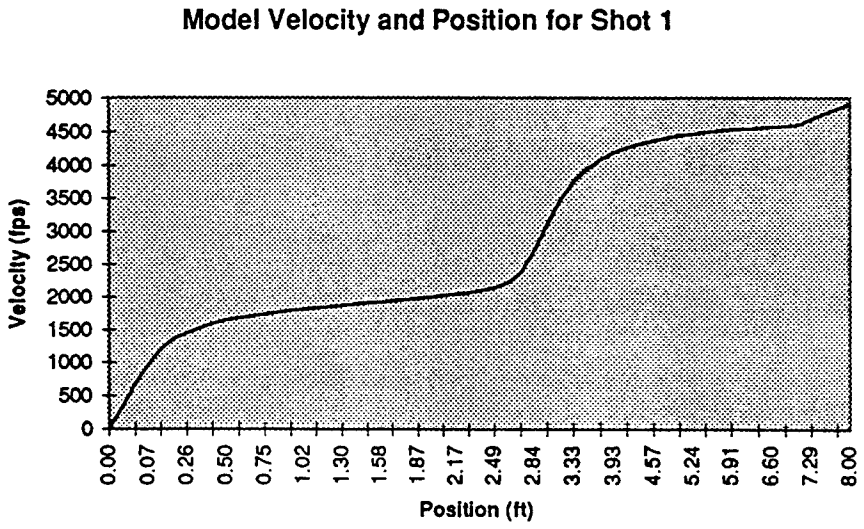
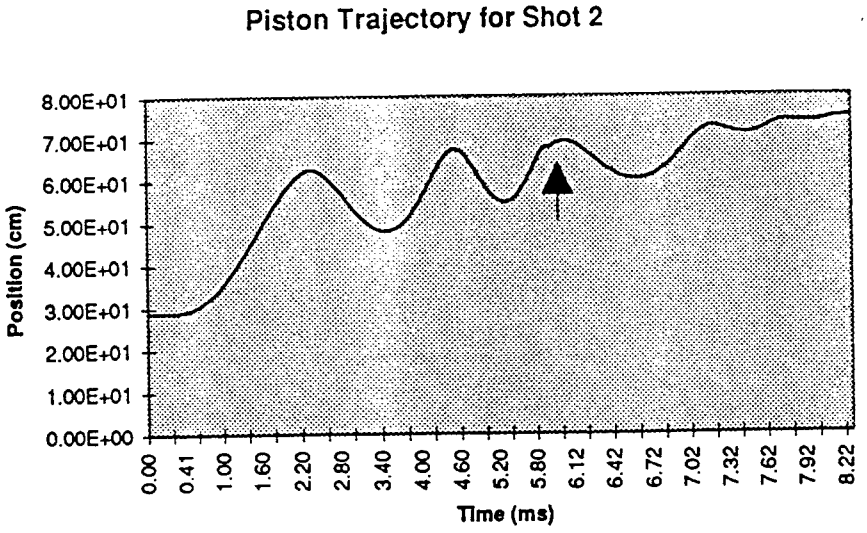


Figure 6. Numerical Results for Shot 1



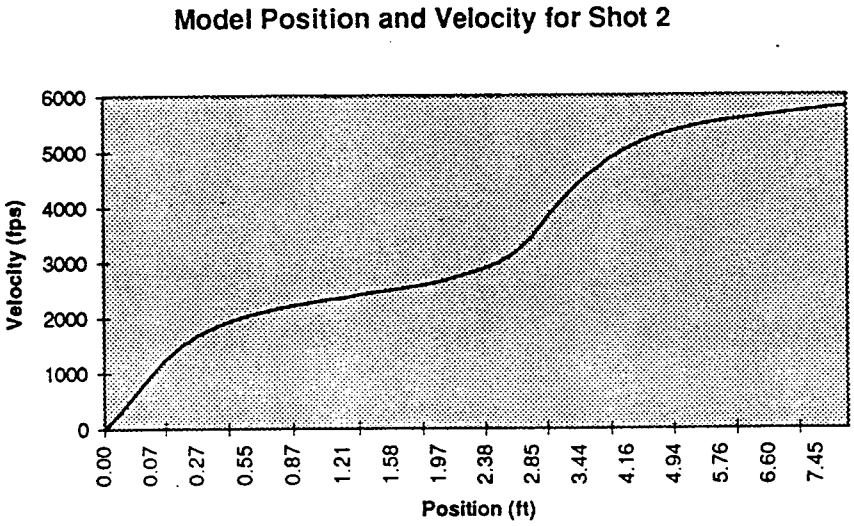
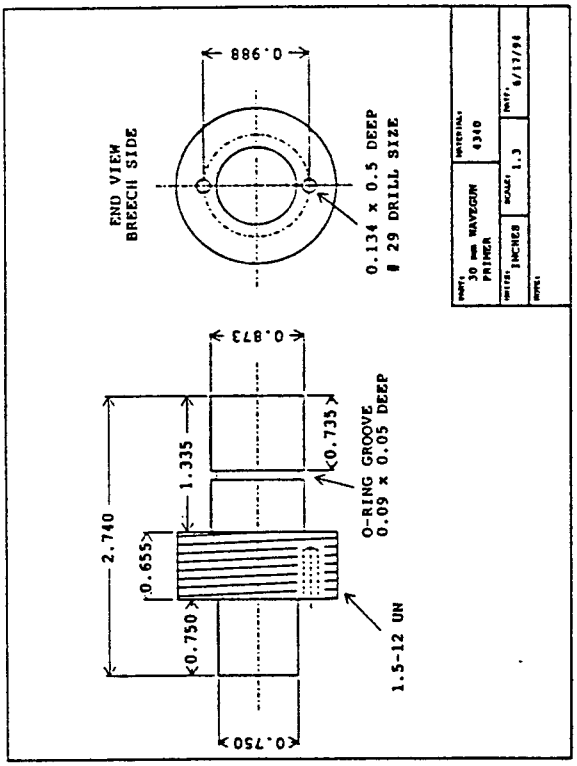
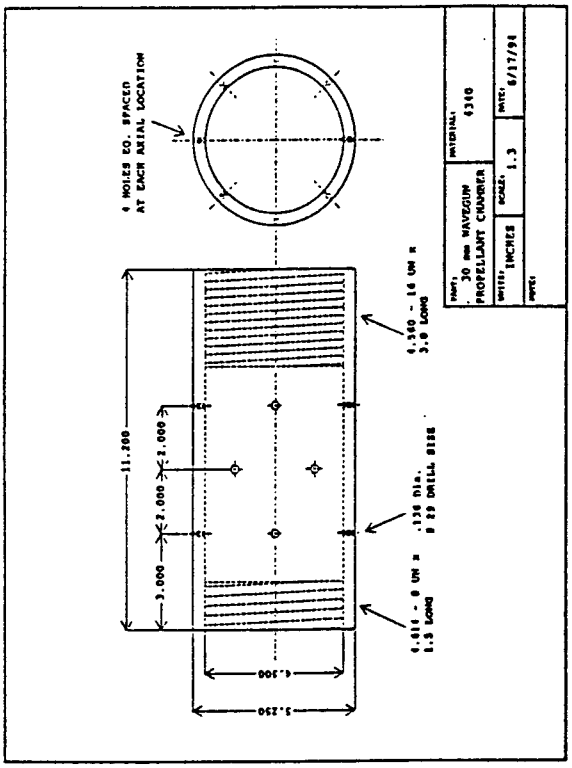
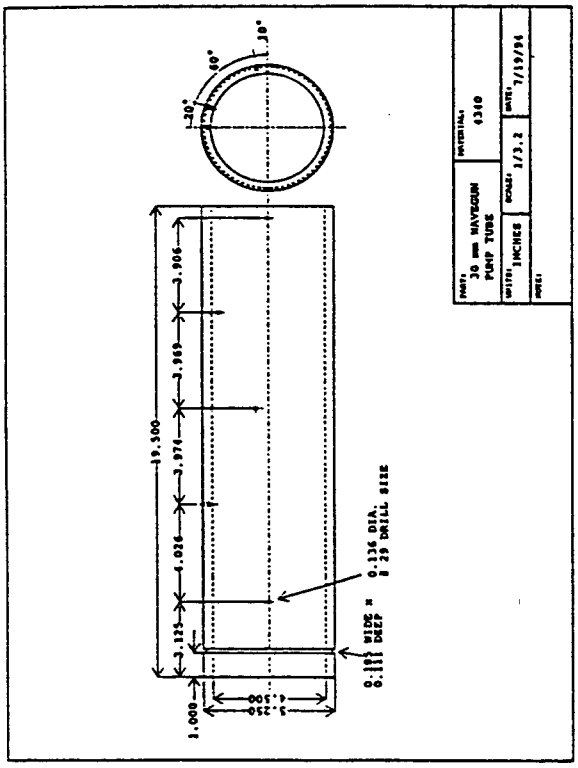


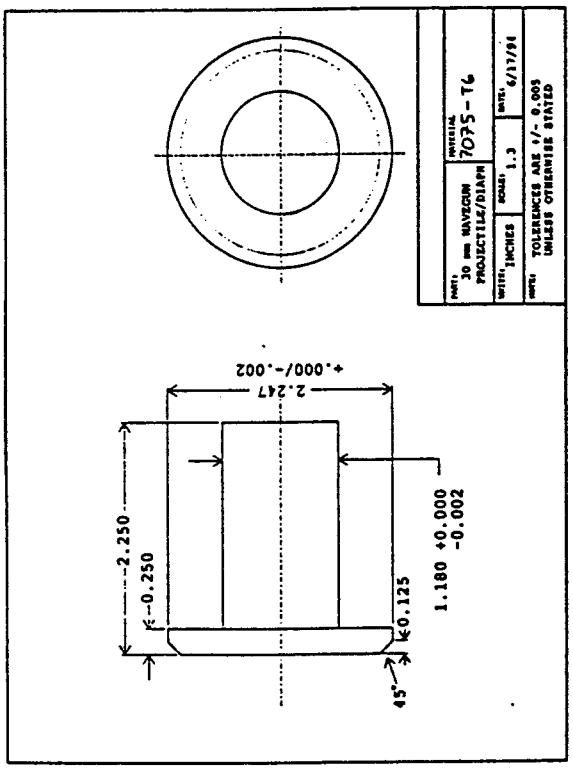
Figure 7. Numerical Results for Shot 2

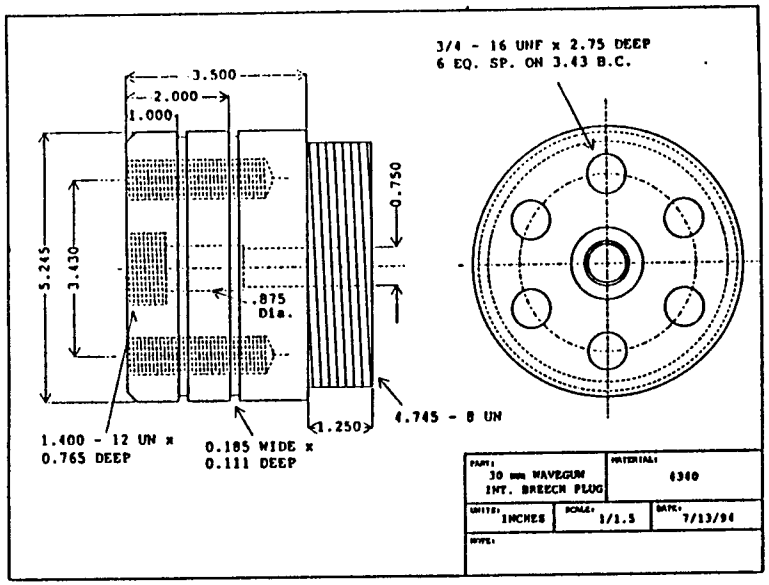
Appendix

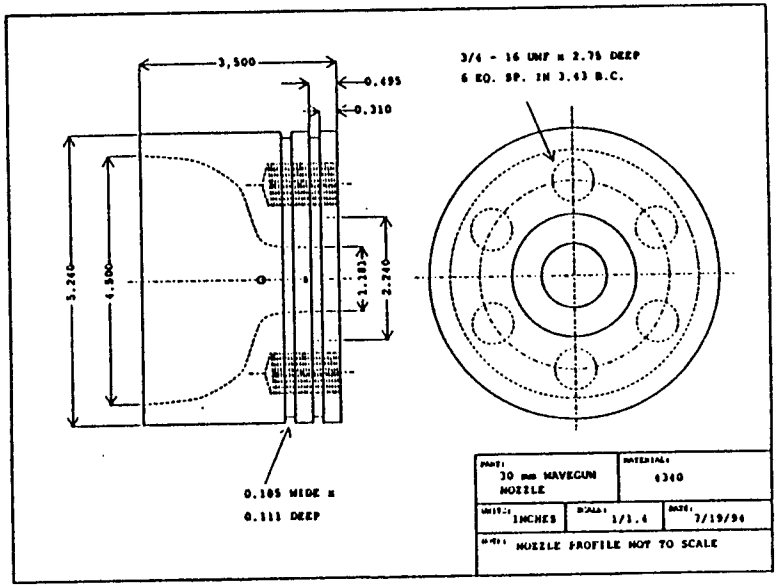

END VIEW
BREECH SIDE
0.988
0.134 x 0.5 DEEP
29 DRILL SIZE
0.873
0.735
1.335
2.740
0.655
0.750
O-RING GROOVE
0.09 x 0.05 DEEP
1.5-12 UN
0.750
30 mm MAVEGUN
PRIMER
4340
INCHES
1.3
6/17/94

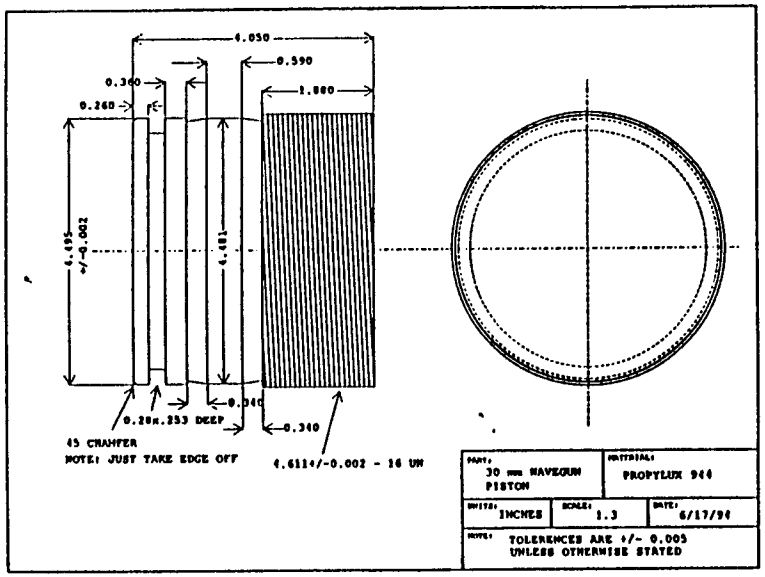

4 HOLES EQ. SPACED
AT EACH AXIAL LOCATION
11.200
2.000
2.000
3.000
5.300
5.250
30 mm MAVEGUN
PROPELLANT CHAMBER
4340
INCHES
1.3
6/17/94

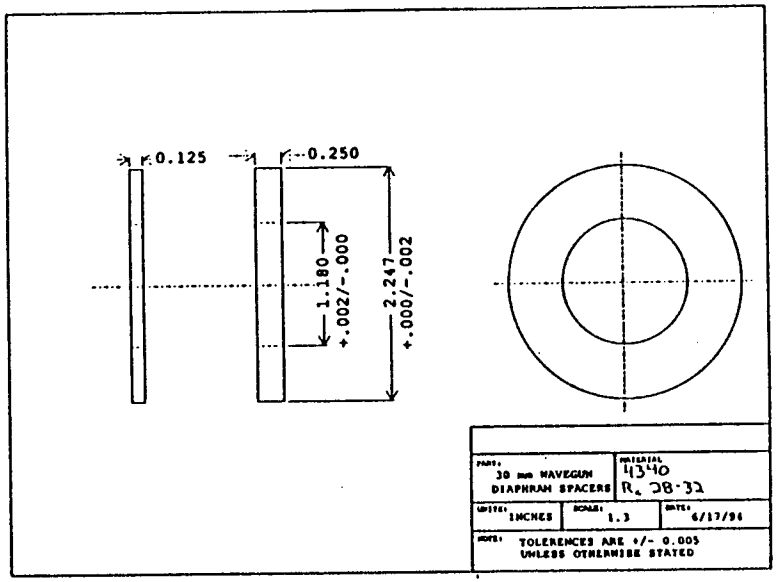

30°
60°
30°
19.500
3.906
3.969
3.937
4.016
3.125
1.000
0.136 DIA.
29 DRILL SIZE
30 mm MAVEGUN
PUMP TUBE
4340
INCHES
1/3.2
7/19/94


2.247
+.000/-.002
2.250
±-0.250
0.125
45°
1.180 +0.000
-0.002
30 mm MAVEGUN
PROJECTILE/DIAPH
7075-T6
INCHES
1.3
6/17/94
TOLERANCES ARE +/- 0.005
UNLESS OTHERWISE STATED


3/4 - 16 UNF x 2.75 DEEP
6 EQ. SP. ON 3.43 B.C.
3.500
2.000
1.000
5.245
3.430
0.750
.875
Dia.
1.400 - 12 UN x
0.765 DEEP
0.185 WIDE x
0.111 DEEP
1.250
4.745 - 8 UN
PART: 30 mm MAVEGUN INT. BREECH PLUG
MATERIAL: 6340
UNITS: INCHES
SCALE: 1/1.5
DATE: 7/13/94
NOTE:


3.500
0.495
0.310
5.240
4.500
1.183
2.240
0.185 WIDE x
0.111 DEEP
3/4 - 16 UNF x 2.75 DEEP
6 EQ. SP. IN 3.43 B.C.
PART: 30 mm MAVEGUN NOZZLE
MATERIAL: 6340
UNITS: INCHES
SCALE: 1/1.4
DATE: 7/19/94
NOTE: NOZZLE PROFILE NOT TO SCALE


4.050
0.590
0.360
0.260
1.880
4.495
+/-0.002
4.481
0.340
0.28W.353 DEEP
0.340
45 CHAMFER
NOTE: JUST TAKE EDGE OFF
4.6114+/-0.002 - 16 UN
PART: 30 mm MAVEGUN PISTON
MATERIAL: PROPYLUX 944
UNITS: INCHES
SCALE: 1.3
DATE: 6/17/94
NOTE: TOLERENCES ARE +/- 0.005 UNLESS OTHERWISE STATED


0.125
0.250
1.180
+.002/-.000
2.247
+.000/-.002
PART: 30 mm MAVEGUN DIAPHRAM SPACERS
MATERIAL: 4340 Rc 28-32
UNITS: INCHES
SCALE: 1.3
DATE: 6/17/94
NOTE: TOLERENCES ARE +/- 0.005 UNLESS OTHERWISE STATED

A Numerical Study of the Effect of Base and Collector Structures on the Performance of ALGaAs/GaAs Multi-finger HBTs

Andrew Kager
Graduate Student
Department of Electrical Engineering

University of Central Florida
Orlando, Fl. 32816

Final Report for:
Graduate Student Research Program
Wright Laboratory

Sponsored by:
Air Force Office of Scientific Research
Bolling Air Force Base, DC

and

Wright Laboratory
Wright-Patterson Air Force Base, OH

August 1994

A Numerical Study of the Effect of Base and Collector Structures on the Performance of AlGaAs/GaAs Multi-Finger HBTs

Andrew Kager
Graduate Student
Department of Electrical and Computer Engineering
University of Central Florida

Abstract

A numerical analysis is presented to investigate different base and collector structures on the dc and ac performance of the AlGaAs/GaAs multi-finger heterojunction bipolar transistor (HBT). The simulation is carried out using a two-dimensional device simulator called MEDICI. Five possible structures are studied and compared. The results show that different structures give rise to different electric fields in the base-collector junction and lattice temperatures in the HBT, which consequently affect the HBT's cutoff frequency and current gain, respectively. The physical mechanisms governing these changes are also discussed in detail.

1. INTRODUCTION

AlGaAs/GaAs heterojunction bipolar transistor (HBT) is a promising device for power amplifiers in microwave applications becuase of its high current handling capability and high cutoff frequency [1]. The HBT's high power performance is often severely limited by the thermal effect, however, due to the poor GaAs thermal conductivity. For a single-emitter finger HBT, the thermal effect arises from the fact that the heat generated in the HBT cannot dissipated quickly to the ambient area, thus increasing the lattice temperature in the HBT (self-heating effect) [2]. To reduce the signal propagation delay time in the HBT, a multi-emitter finger structure is frequently used. For the multi-finger HBT, the thermal effect is more complex. In addition to the self-heating effect in each finger, thermal coupling among the emitter fingers can also occur if the finger spacing is relatively small (thermal-coupling effect) [3]. The thermal-coupling effect causes the inner fingers to be hotter than the outer fingers.

Studies on the HBT thermal design and analysis have been reported in the literature [3-5]. All of them focused on the multi-finger HBT structure in which only the emitter is separated into the island structure (E-island) and both the base and collector are uniform underneath the emitter fingers, as shown in Fig. 1(a). In this paper, we will consider also two other structures which have emitter/base island (E/B-island) and emitter/base/collector island (E/B/C-island) structures, as shown in Figs. 1(b) and 1(c), respectively. Comparing to the E-island HBT, the E/B-island HBT will have a less uniform lattice temperature and current distribution in the base. Similarly, the E/B/C-islander HBT will have less uniform lattice temperature and current distribution in the collector than the other two devices. It is the purpose of the paper then to investigate and compare the dc and ac performance of the three HBTs. As will not shown later, the different

island formations affect considerably the dc current gain and cutoff frequency of the HBTs.

The analysis will be carried out based on results simulated from a two-dimensional device simulator called MEDICI [6], which is a new version of PISCES. Given the proper device structure, doping concentration, and bias condition, MEDICI can solve numerically the electron and hole current equations, Poisson equation, and electron and hole continuity equations. The free-carrier recombination and generation processes in the semiconductor are described by the Shockley-Read-Hall, Auger, and band-to-band radiative statistics. A comprehensive mobility model covering both the low-field and high-field regions is used in MEDICI. Two options are also available in MEDICI. One option called the heterojunction device module provides the means to simulate devices that employ multiple semiconductor materials with varying band structure. Another option called the lattice-temperature module allows the effects of lattice heating to be included in simulation by solving the heat transfer equation in addition to the basic semiconductor equations. Both options will be used in our study.

2. RESULTS AND DISCUSSIONS

Throughout the analysis, all HBT structures considered are N/p^+/n $Al_{0.3}Ga_{0.7}As$/GaAs/GaAs three-finger HBTs with the following typical make-up: a $5x10^{17}$ cm^{-3} and 1000 Å emitter, 300 Å graded layer, 10^{19} cm^{-3} and 1000 Å base, $5x10^{16}$ cm^{-3} and 7000 Å collector, 4x10 μm^2 emitter finger area, and 10 μm finger spacing.

Figs. 2(a) and 2(b) show the current gains β versus the collector current I_C of the three HBTs simulated at V_{CE} at 2 V and 5 V, respectively. The current gain at the high current region (i.e., $I_C > 10^{-4}$ A) decreases as V_{CE} is increased. This is because a larger V_{CE} gives rise to a more

significant thermal effect in the HBT, which subsequently increases the lattice temperature and degrades the current gain. Figs. 3(a) and 3(b) show the lattice temperature contours in the E-island HBT at V_{CE} = 2 and 5 V. Note that the intrinsic HBT is located at $0 < y < 0.93$ μm and 234 μm $< x <$ 266 μm, and the lattice temperature decreases rapidly toward the side-walls and semi-insulating substrate. Also, the middle finger is hotter than the outer fingers due to the thermal coupling among the fingers.

The smallest β found in the E/B-island HBT (Figs. 2(a) and 2(b)) results from the following two mechanisms. First, at high current levels, it is due to the fact that the lattice temperature in such a device is higher than the other two devices. This is evidenced by the lattice temperature contours in Figs. 4(a)-4(c), which indicate that the E-island and E/B-island have the lowest and highest lattice temperatures, respectively. Second, at small current levels, becuase of the different base contact patterns, electron-hole recombination in the base of the E-island HBT is less prominent than that of the E/B- and E/B/C-island HBTs, hence resulting in a smallest base current and largest current gain for the E-island HBT. The hole current density contours in the E-island and E/B-island HBTs are given in Fig. 5(a)-5(b), respectively, to demonstrate this point. While the peak hole current density at the base contacts of the E-island HBT appears to be larger than that of the E/B-island HBT, the total base current density of the E/B-island HBT is actually larger because the device has six contacts (i.e., total base current density equals 1.6×10^4 A/cm^2), rather than just 2 contacts in the E-island HBT (i.e., total base current density equals 1.2×10^4 A/cm^2).

Figs. 6(a) and 6(b) show the cutoff frequencies f_T of the three HBTs simulated at V_{CE} = 2 V and 5 V, respectively. Like the current gain, the high-current f_T degradation at larger V_{CE}

is caused by the thermal effect. At the low current region, however, f_T is slightly higher at larger V_{CE} due to a larger electric field in the base-collector junction and a smaller quasi-neutral base thickness as V_{CE} is increased. Furthermore, the results show that the E/B/C-island HBT has the lowest peak f_T. This can be attributed to the fact the E/B/C-island HBT has the least uniform electric field in the base-collector junction among the three devices. This is demonstrated in Figs. 7(a) and 7(b), which plot the electric field contours in the E-island and E/B/C-island HBTs, respectively. It has been shown in various studies that the free-carrier transit time across the base-collector space-charge region is often the limiting factor for the HBT cutoff frequency [7]. Thus, the lower field in the regions between fingers found in the E/B- and E/B/C-island formations increases the overall base-collector transit time and decreases the overall cutoff frequency of the E/B- and E/B/C-island HBTs.

Next, we consider the HBT structures in which the base and collector contacts are placed everywhere between the islands, not just placed on the two sides of the base and collector as considered in Fig. 1. One of the structures (E-island-multi-contact) is shown in Fig. 8(a), and the other structure (E/B/C-island-multi-contact) is shown in Fig. 8(b).

Figs. 9 and 10 compare the β and f_T, respectively, simulated from the E-island and E/B/C-island HBTs and their two-contact counterparts. The results clearly suggest that placing ohmic contacts between the islands degrades both the high-current dc and ac performance of the HBTs. This can be attributed to the fact that the voltage drops in the quasi-neutral regions of the multi-contact HBTs are smaller compared to those of the two-contact HBTs. As a result, for the same applied voltage, the multi-contact HBTs have higher junction voltages than its two-contact counterparts, which then gives rise to a more significant thermal effect and thus degrades the

HBT performance. Therefore it is sometime beneficial to trade the larger voltage drops for a less significant thermal effect in the HBT. The same concept has led to the use of a ballast emitter resistance for HBT thermal design [3].

Among the five HBT structures studied, the E-island HBT (Fig. 1(a)) appears to be the optimal multi-finger structure for high current gain and/or cutoff frequency applications.

3. CONCLUSION

A numerical study of the effects of the emitter, base, and collector island formations on the dc and ac performance of AlGaAs/GaAs multi-finger HBTs is presented. The results are obtained from a two-dimensional device simulator called MEDICI, which accounts for the spatial-dependent energy bandgap in the heterostructure devices as well as allows the effect of lattice heating to be included in simulation.

The following conclusions can be drawn from the study.

1). Among the five structures considered, the E-island HBT is the optimal structure for both high current gain and cutoff frequency applications.

2). For the dc performance, the E/B- and E/B/C-island HBTs are inferior to the E-island HBT because of the higher lattice temperatures in these devices due to the more significant self-heating and thermal-coupling effects.

3). For the ac performance, the E/B- and E/B/C-island HBTs have lower cutoff frequency than the E-island HBT. This is due to the fact that the electric field in the base-collector junction of these devices are much less uniform than that of the E-island counterpart, which then results in a longer overall base-collector transit time and a smaller overall cutoff frequency for the E/B-

and E/B/C-island HBTs.

4). Placing ohmic contacts everywhere between the islands (multi-contact HBT) degrades the dc and ac performance of the HBT. This is caused by the more significant thermal effect in the multi-contact HBT, because the voltage drops in the quasi-neutral region of these devices are smaller and the junction voltages are larger compared to those of the two-contact HBT.

Acknowledgements--Two of the authors (AK and JJL) acknowledge the support of the summer graduate student and faculty program funded by the Air Force Office of Scientific Research. The donation of MEDICI to the University of Central Florida by Technology Modeling Associates, Inc., Palo Alto, CA is gratefully appreciated.

REFERENCES

[1] For example, see F. Ali and A. Gupta (eds.), HEMTs and HBTs: Devices, Fabrication, and Circuits, Boston: Artech House, 1991.

[2] J. J. Liou, L. L. Liou, C. I. Huang, and B. Bayraktaroglu, "A physics-based heterojunction bipolar transistor model including thermal and high-current effects," IEEE Trans. Electron Devices, vol. 40, pp. 1217, 1993.

[3] G. B. Gao, M. B. Wang, X. Gui, and H. Morkoc, "Thermal design studies of high-power heterojunction bipolar transistors," IEEE Trans. Electron Devices, vol. ED-36, p. 854, 1989.

[4] W. Liu, S. Nelson, D. G. Hill, and A. Khatibzadeh, "Current gain collapse in microwave multifinger heterojunction bipolar transistor operated at very high power densities," IEEE Trans. Electron Devices, vol. 40, p. 1917, 1993.

[5] A. Kager, J. J. Liou, L. L. Liou, and C. I. Huang, "A semi-numerical model for multi-emitter finger AlGaAs/GaAs HBTs," Solid-St. Electron., to appear.

[6] MEDICI Manual, Technology Modeling Associates, Inc., Palo Alto, CA 1993.

[7] J. J. Liou, Advanced Semiconductor Device Physics and Modeling, Boston: Artech House, 1994, Ch. 7.

FIGURE CAPTIONS

Fig. 1 Schematic structures for (a) Emitter-island HBT, (b) emitter/base-island HBT, and (c) emitter/base/collector-island HBT.

Fig. 2 Current gains versus the collector current of the three HBTs simulated at (a) V_{CE} = 2 V, and (b) V_{CE} = 5 V.

Fig. 3 Lattice temperature contours in the E-island HBT at V_{BE} = 1.5 V and (a) V_{CE} = 2 V, and (b) V_{CE} = 5 V.

Fig. 4 Lattice temperature contours simulated at V_{BE} = 1.5 V and V_{CE} = 2 V for (a) E-island HBT, (b) E/B-island HBT, and (c) E/B/C-island HBT.

Fig. 5 Hole current contours simulated at V_{BE} = 1.1 V and V_{CE} = 2 V for (a) E-island HBT, and (b) E/B-island HBT.

Fig. 6 Cutoff frequencies versus the collector current of the three HBTs simulated at (a) V_{CE} = 2 V, and (b) V_{CE} = 5 V.

Fig. 7 Electric field contours simulated at V_{CE} = 2 V for (a) E-island HBT, and (b) E/B/C-island HBT.

Fig. 8 Schematic structures for (a) E-island-multi-contact HBT, and (b) E/B/C-island-multi-contact HBT.

Fig. 9 Comparisons of the current gains of the E-island, E-island-multi-contact, E/B/C-island, and E/B/C-island-multi-contact HBTs at V_{CE} = 2 V.

Fig.10 Comparisons of the cutoff frequencies of the E-island, E-island-multi-contact, E/B/C-island, and E/B/C-island-multi-contact HBTs at V_{CE} = 2 V.

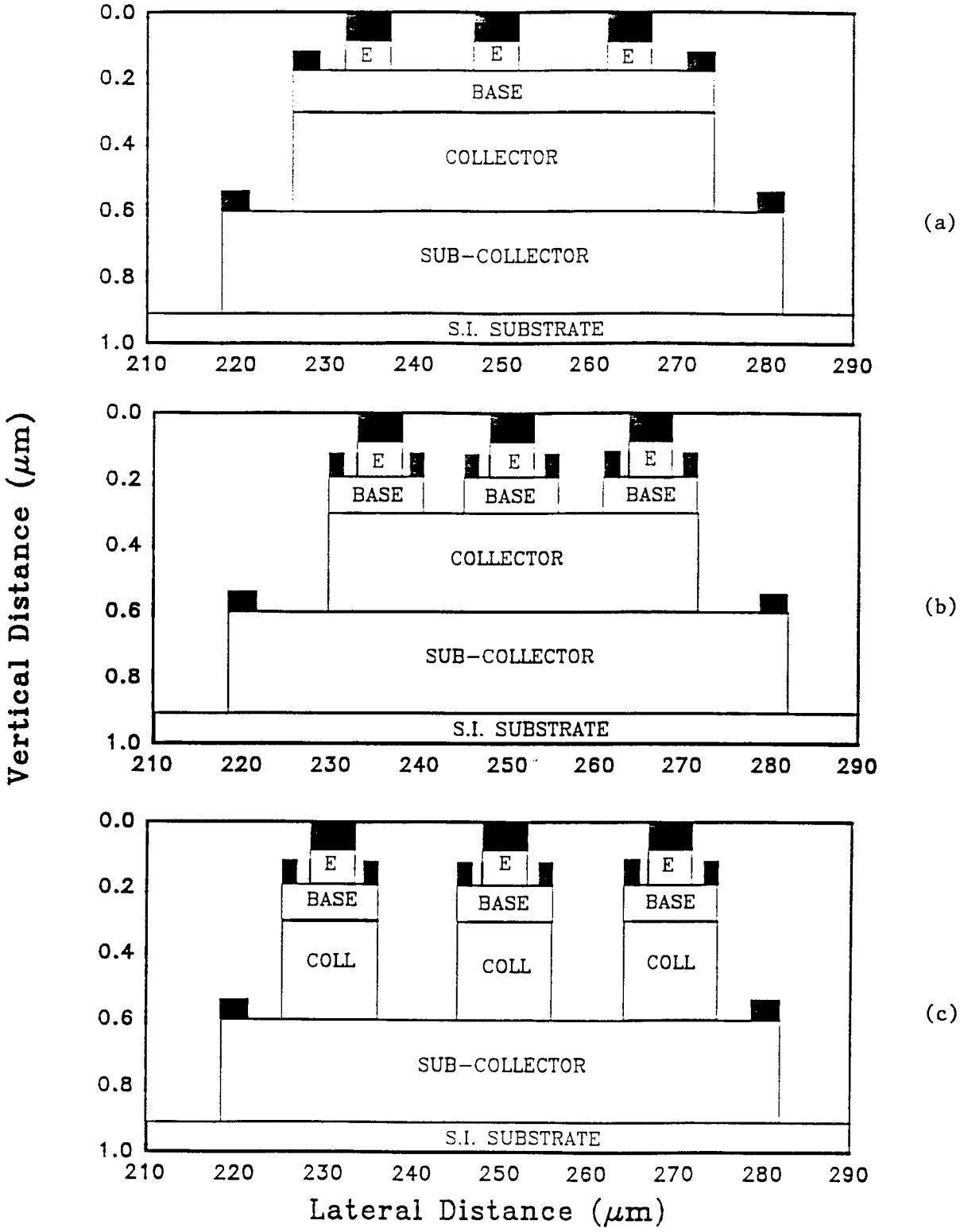
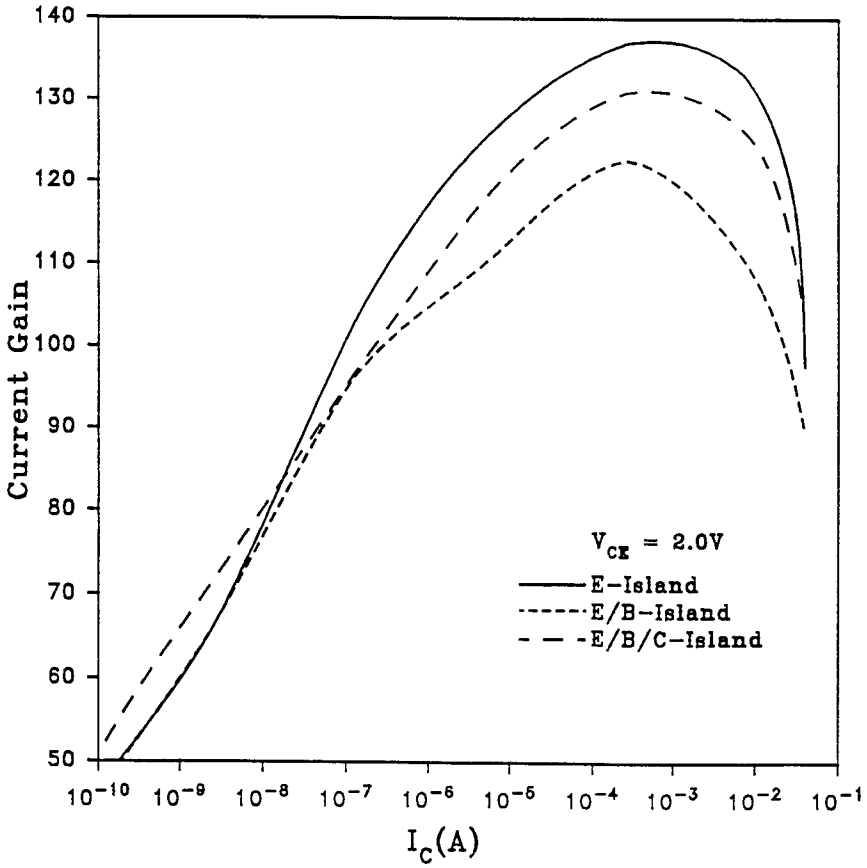
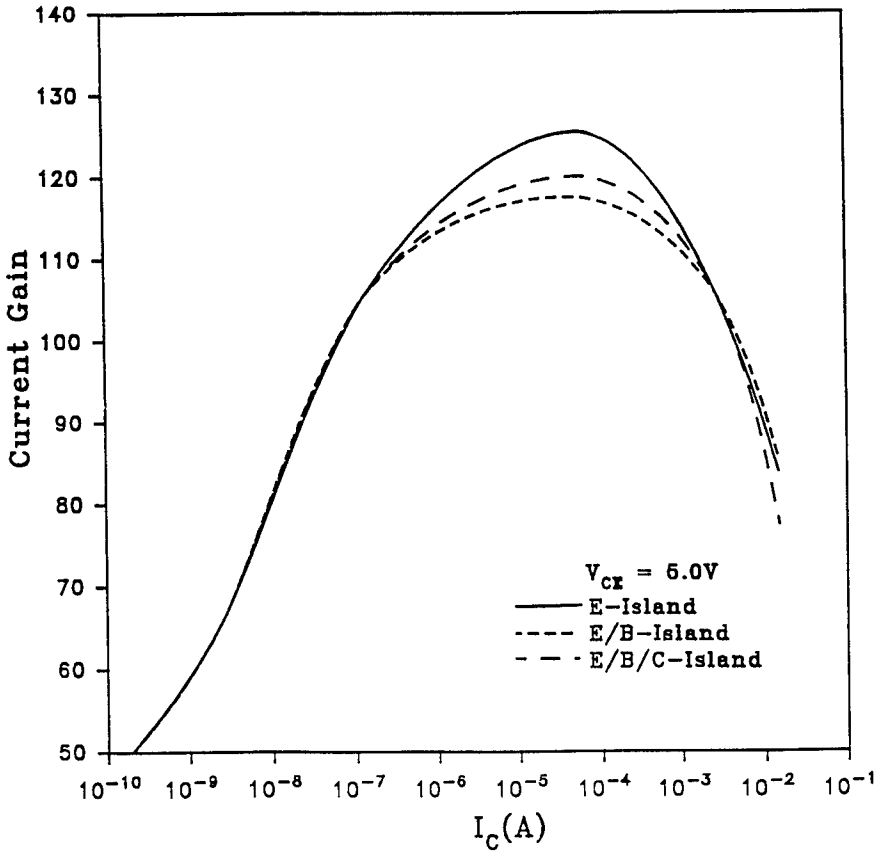


Fig.1 Schematic Structures for (a) Emitter-island HBT, (b) Emitter/Base-island HBT, and (c) Emitter/Base/Collector-island HBT.

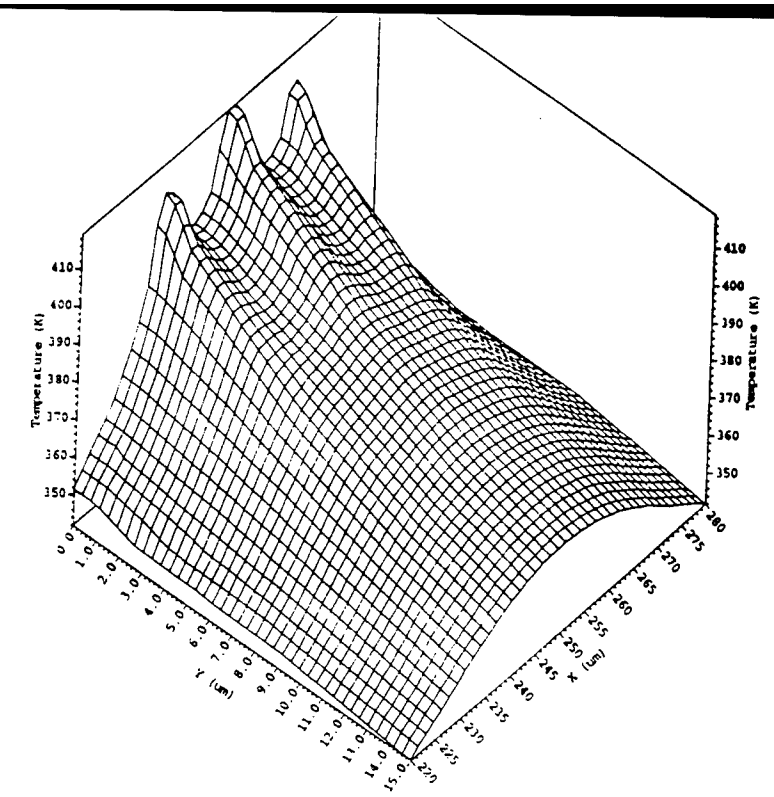


(a)

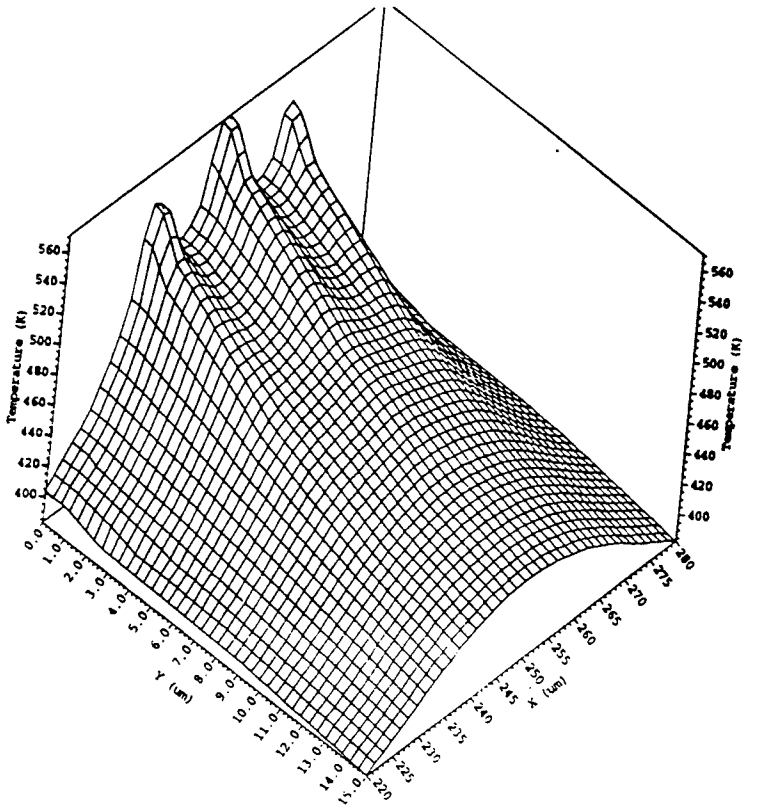


(b)

Fig. 2 Current gains versus the collector current of the three HBTs simulated at (a)V_{CE} = 2V, and (b) V_{CE} = 5V.

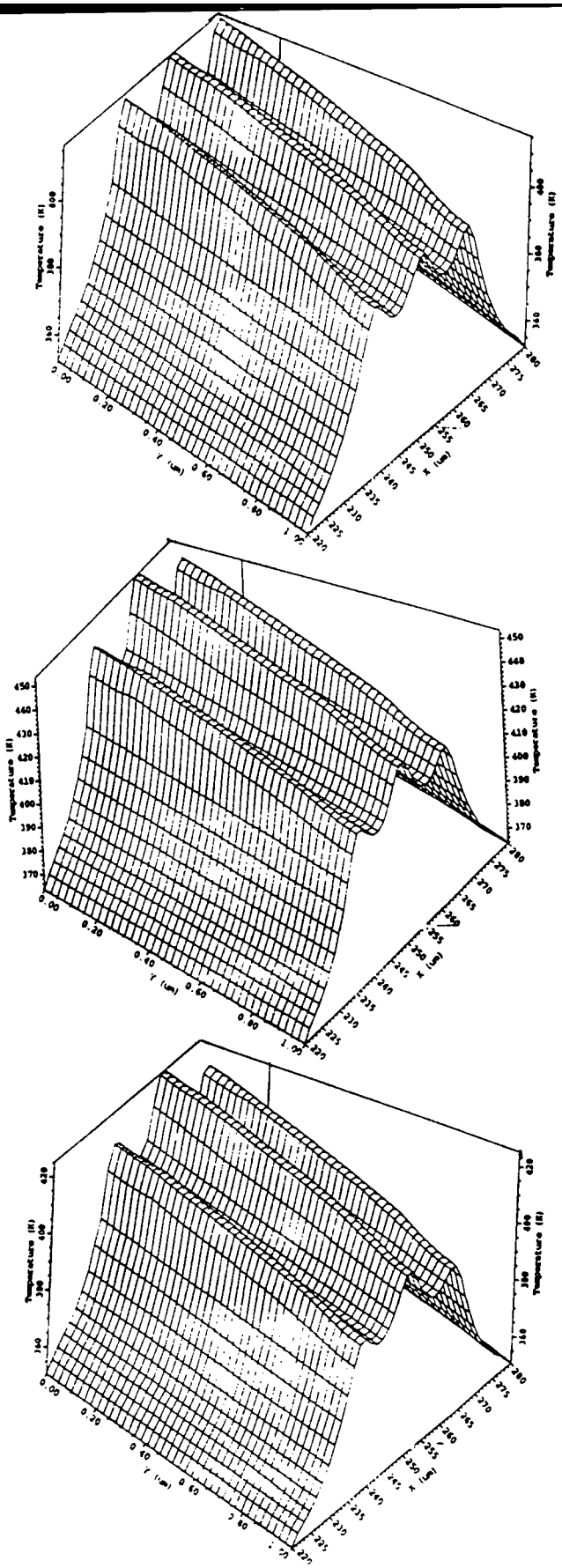


(a)



(b)

Fig. 3 lattice temperature contours in the E-island HBT at V_{BE} = 1.5 V and (a) V_{CE} = 2 V, and (b) V_{CE} = 5 V



(a)

(b)

(c)

Fig. 4 lattice temperature contours simulated at V_{BE} = 1.5 V and V_{CE} = 2 V for (a) E-island HBT, (b) E/B-island HBT, and (c) E/B/C-island HBT.

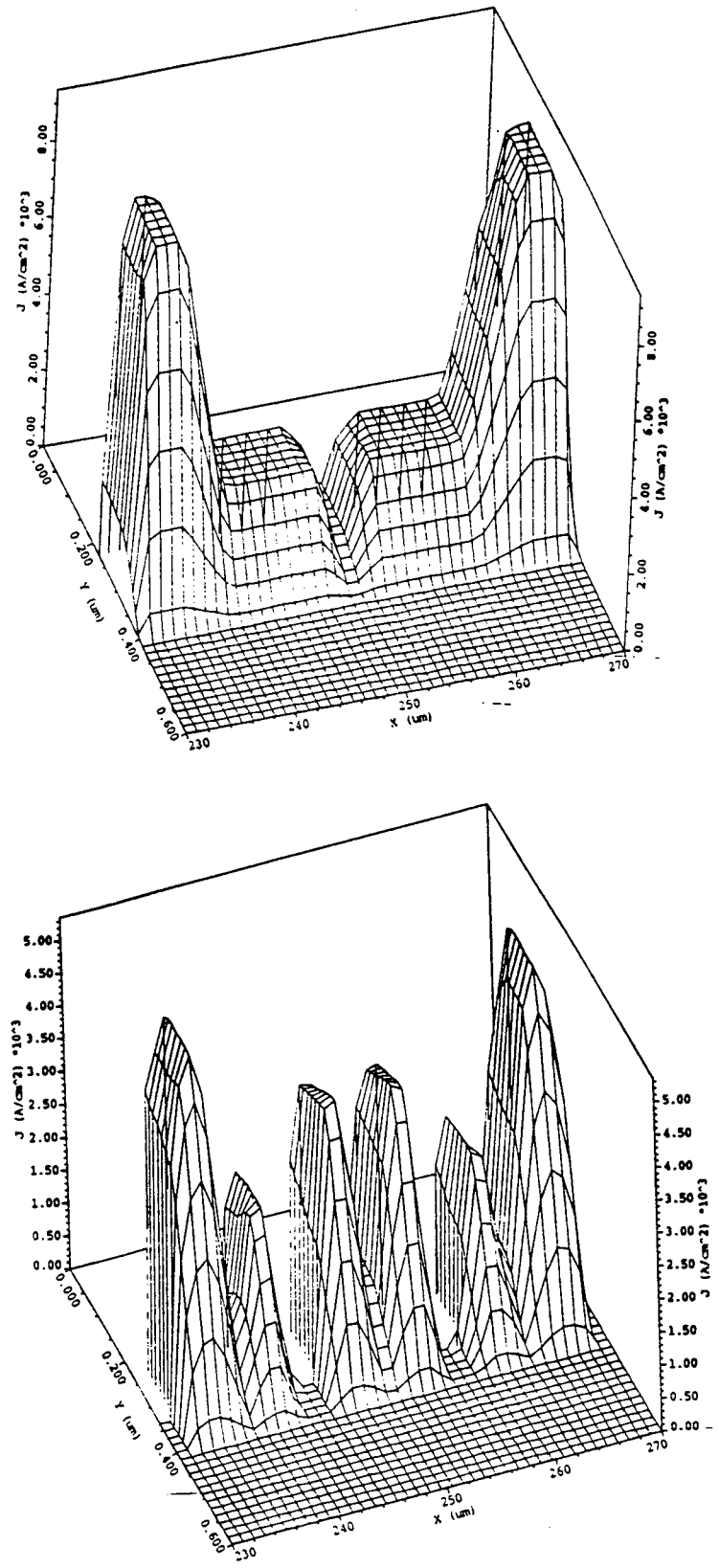
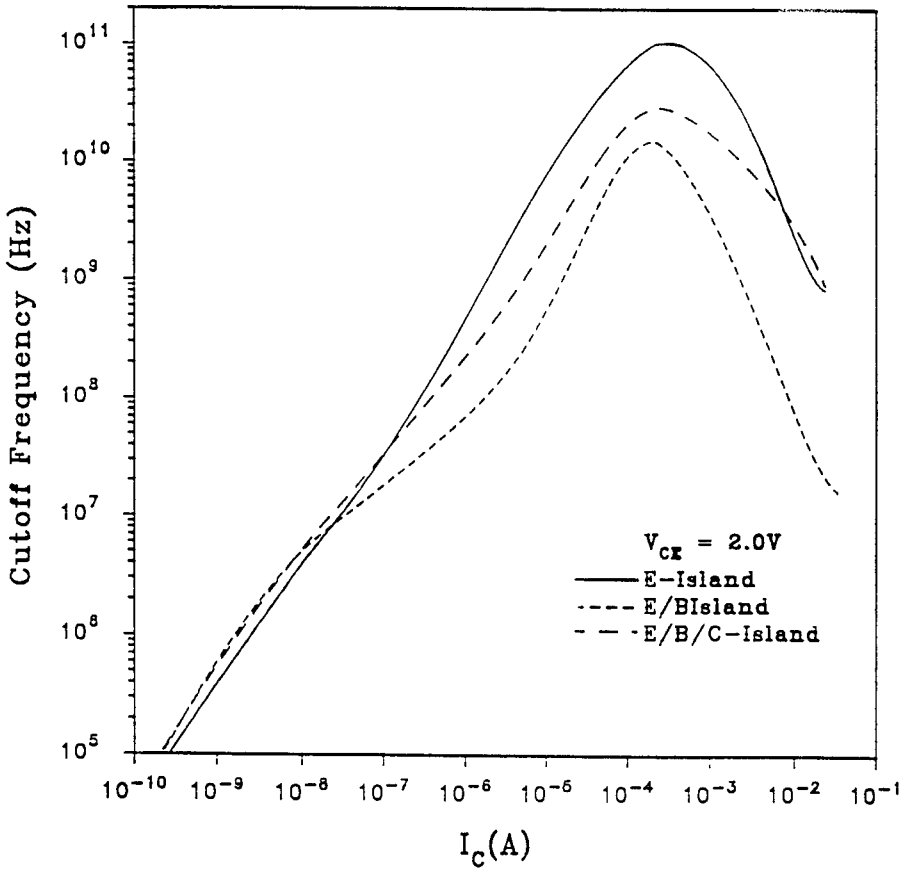
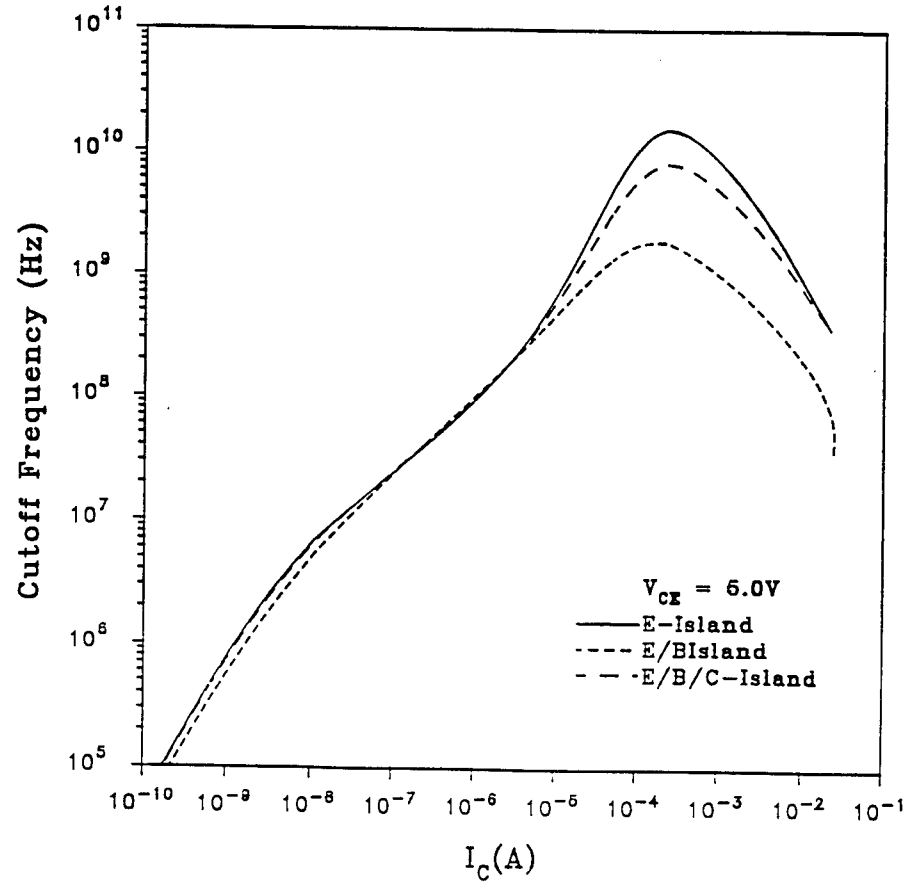


Fig. 5 Hole current contours simulated at V_{BE} = 1.1 V and V_{CE} = 2 V for (a) E-island HBT, (b) E/B-island HBT.

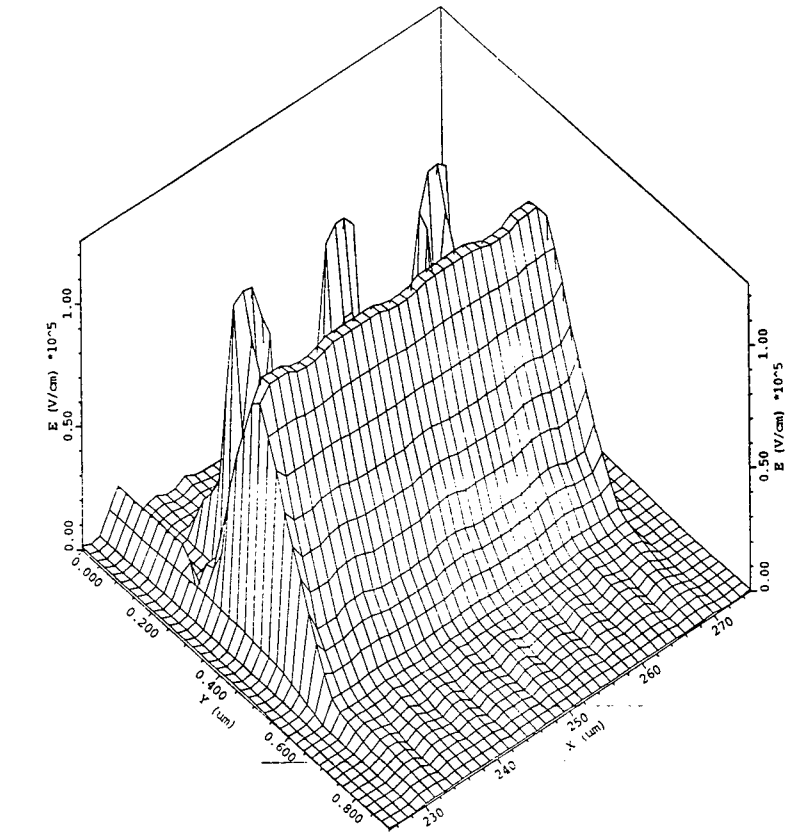


(a)

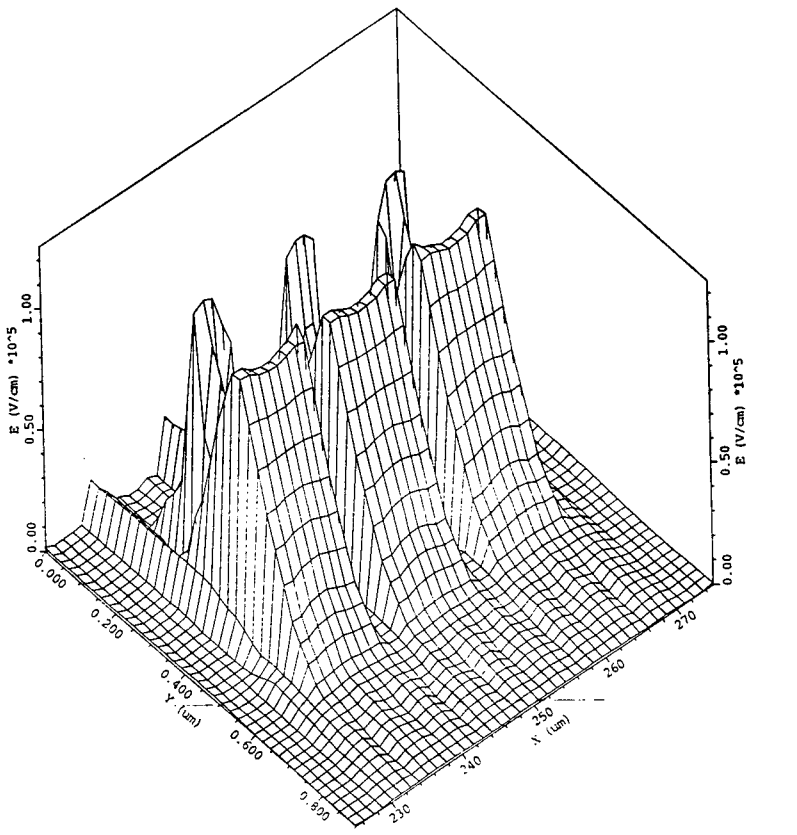


(b)

Fig. 6 Cutoff frequencies versus the collector current of the three HBTs simulated at (a) V_{CE} = 2 V and (b) V_{CE} = 5 V.



(a)



(b)

Fig. 7 Electric Field contours simulated at V_{CE} = 2 V for (a) E-island HBT and (b) E/B/C-island HBT.

A THEORY FOR THE TESTING OF MATERIALS UNDER COMBINED TENSION-TORSION

John C. Lewis
Graduate Student
Department of Materials Engineering

University of Kentucky
177 Anderson Hall
Lexington, KY 40506

Final Report for:
Graduate Student Research Program
Wright Laboratory

Sponsored by:
Air Force Office of Scientific Research
Bolling Air Force Base, DC

and

Wright Laboratory

September 1994

A THEORY FOR THE TESTING OF MATERIALS UNDER COMBINED TENSION-TORSION

John C. Lewis
Graduate Student
Department of Materials Engineering
University of Kentucky

Abstract

This theory for the yielding behavior of materials under combined tension-torsion uses the von Mises yield criteria and accounts for the effects of testing machine stiffness. Experimental results are given for tests performed on 6061-T6 aluminum and a yield surface is constructed from this data. It is concluded that the von Mises criteria may not be totally satisfactory in modelling the yielding response of real materials under multiaxial loading.

A THEORY FOR THE TESTING OF MATERIALS UNDER COMBINED TENSION-TORSION

John C. Lewis

Introduction

For many years, a great deal of interest has been focused on the mechanical response of materials to multiaxial states of stress. For tests conducted under uniaxial stress, the material response can be simply expressed by a single stress-strain curve. This permits a relatively straightforward analysis of the mechanical behavior. For tests conducted under multiaxial stress, an effective stress and an effective strain must be defined if the mechanical response is to be expressed by a single stress-strain curve[1]. For an isotropic material, the two most commonly used initial yield and flow conditions are the von Mises and Tresca criteria. Each can be used to derive corresponding expressions for effective stress and effective strain. Most experimental data for strain-hardening metals, when so reduced, lie between the two theories, but are generally closer to that of von Mises[2].

This paper focuses on the analysis of a thin-walled tube loaded in tension and torsion. This combined loading produces a bi-axial state of stress where σ_z and $\tau_{\theta z}$ are the only non-zero components of the stress tensor. Equations for effective stress and strain are derived using the von Mises yield and flow criterion and considering the effects of machine stiffness[3] for tests where the linear and rotary displacements are given by ramp functions. Also, an experimental yield surface is constructed from tests performed on 6061-T6 aluminum. Finally, the validity of the von Mises theory is briefly discussed.

Theory

Consider a thin-walled tube of axial gage length L, cross-sectional area A, and some average radius R. Let ΔL denote the axial displacement of the combined specimen-machine system and Φ be its angle of twist. During a combined tension-torsion test

$$\Delta L = \Delta L_S^E + \Delta L_S^P + \Delta L_M \tag{1}$$

and

$$\Phi = \Phi_S^E + \Phi_S^P + \Phi_M \, , \tag{2}$$

where the subscripts S and M denote specimen and machine and the superscripts E and P denote elastic and plastic, respectively. In this analysis it is assumed the machine undergoes only elastic deformations. The elastic displacements can be written

$$\Delta L_S^E = PL/AE, \tag{3}$$

$$\Delta L_M = P/k_1 , \tag{4}$$

$$\Phi_S^E = TL/AGR^2, \tag{5}$$

and

$$\Phi_M = T/k_2 . \tag{6}$$

Here P is the axial load, T is the torque, E and G are the elastic and shear moduli, respectively, and k_1 and k_2 are measures of machine stiffness. Using these relations, equations 1 and 2 can be rewritten as

$$\Delta L = (PL/AE)\ (1 + AE/k_1L) + \Delta L_S^P , \tag{7}$$

and

$$\Phi = (TL/AGR^2)\ (1 + AGR^2/k_2L) + \Phi_S^P. \tag{8}$$

Let the axial and angular displacements be given by ramp functions such that $\Delta L = at$ and $\Phi = bt$. In the early stages of deformation (near t=0), $\Delta L_S^P = \Phi_S^P = 0$. So equations 7 and 8 can be equated to their ramp functions and solved for P and T as

$$P = \frac{AEat}{L(1 + AE/k_1L)} \equiv C_1t \tag{9}$$

and

$$T = \frac{AGR^2bt}{L(1 + AGR^2/k_2L)} \equiv C_2t. \tag{10}$$

Here, C_1 and C_2 are the initial slopes of the load-time and torque-time curves, respectively.

After the specimen begins to undergo plastic deformation equations 9 and 10 will no longer represent the load-time and torque-time curves. To determine the amount of plastic deformation the specimen has undergone at some time t, consider figure 1. Here t^* represents the time that would be required to reach load P if there were no plastic deformation and is defined by

$$t^* = P/C_1 . \tag{11}$$

Then the amount of plastic deformation in the specimen can be written

$$\Delta L^P = a(t - t^*). \tag{12}$$

The same idea can be applied to the torque-time curve. Thus the following equations are obtained:

$$\Delta L^P = a(t - P/C_1), \tag{13}$$

and

$$\Phi^P = b(t - T/C_2). \tag{14}$$

The corresponding plastic strains can be written

$$\epsilon_z^P = \Delta L^P/L = (a/L)\ (t - P/C_1) \tag{15}$$

and

$$\gamma_{\theta z}^P = (R/L)\ \Phi^P = (bR/L)\ (t - T/C_2). \tag{16}$$

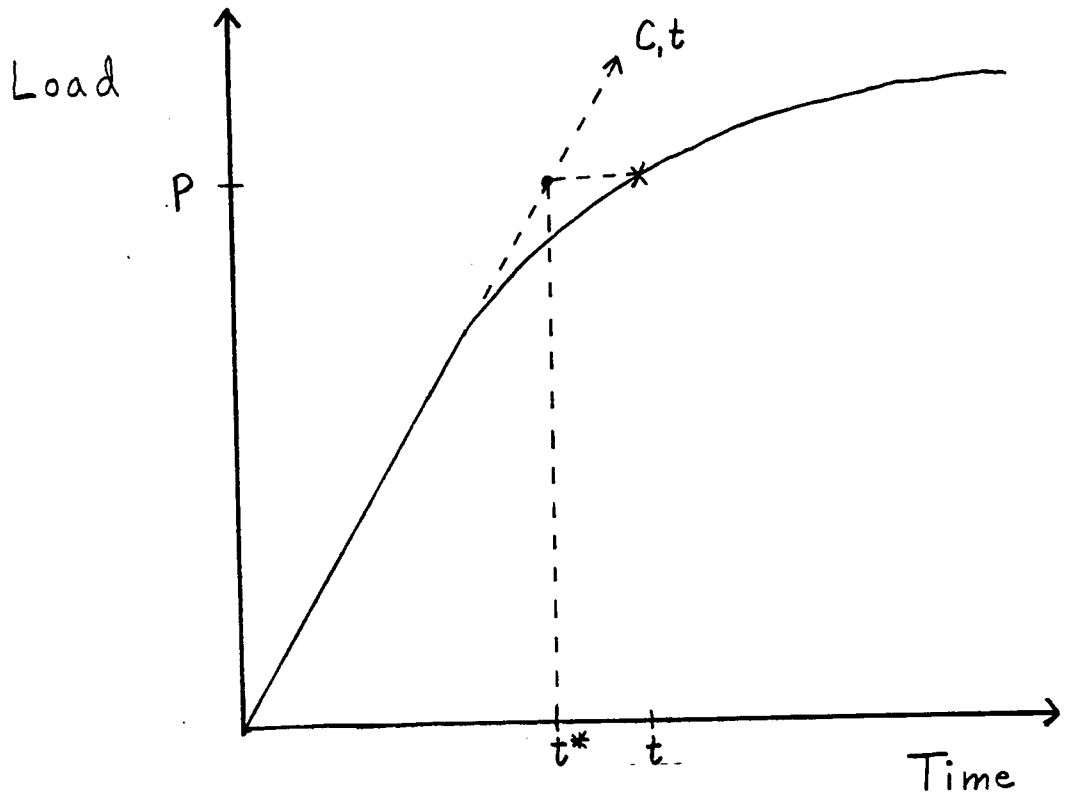


FIGURE 1. A typical load-time curve.

In a uniaxial test, the yield point can be defined by the stress at which the specimen has undergone some set amount of plastic strain. In a multiaxial test, the effective strain can be used in the same manner. For an isotropic material that obeys the von Mises flow criteria the effective plastic strain ϵ_p is defined through

$$d\epsilon_p^2 = d\epsilon^P{}_z^2 + 1/3\ d\gamma^P{}_{\theta z}^2, \tag{17}$$

for tension-torsion, and for proportional strain paths

$$\epsilon_p^2 = \epsilon^P{}_z^2 + 1/3\ \gamma^P{}_{\theta z}^2. \tag{18}$$

Now equations 15 and 16 can be substituted into equation 18 to obtain the following equation for effective plastic strain:

$$\epsilon_p^2 = [a/L\ (t - P/C_1)]^2 + 1/3\ [bR/L\ (t - T/C_2)]^2. \tag{19}$$

By analogy with the offset yield stress often used in uniaxial tension tests, the multiaxial yield point can be defined as the point when ϵ_p reaches some set value.

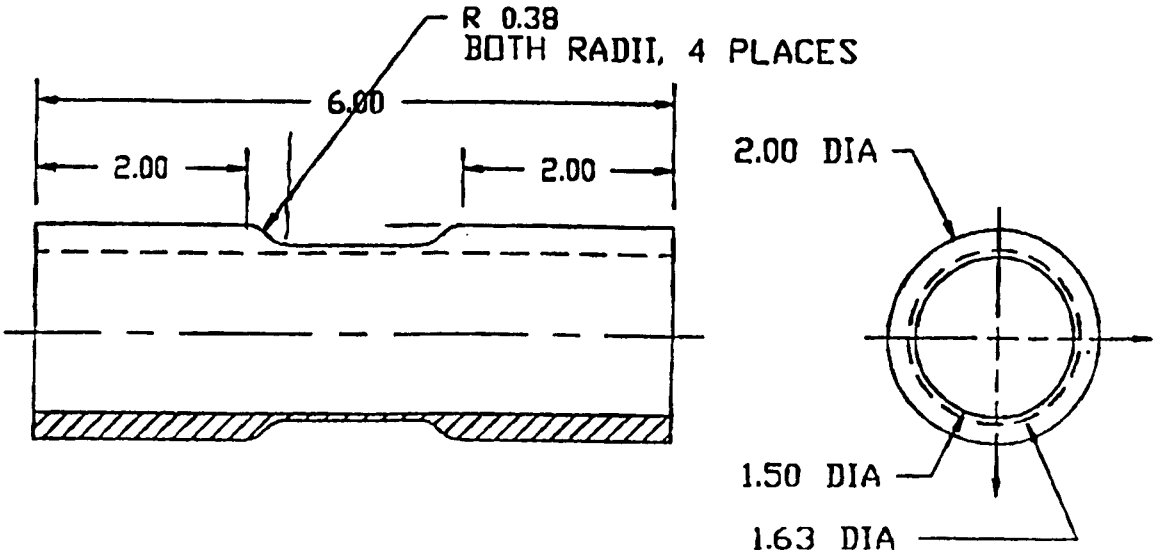


FIGURE 2. A sketch of the biaxial specimen. The units for the dimensions are inches.

Experimental

The specimens were thin-walled tubes of 6061-T6 aluminum machined from round rod stock to within close tolerances. A sketch of the specimens is given in Fig. 2. The tests were performed by deforming the specimen under constant longitudinal displacement and a constant rate of change of the angle of twist. The effective strain rates were in the order of 0.01/s and no pre-stress was applied. The tubes were tested on an Instron model 1323 combined tension-torsion testing machine. The machine was programmed with a digital function generator and a desktop computer was used for data analysis and display.

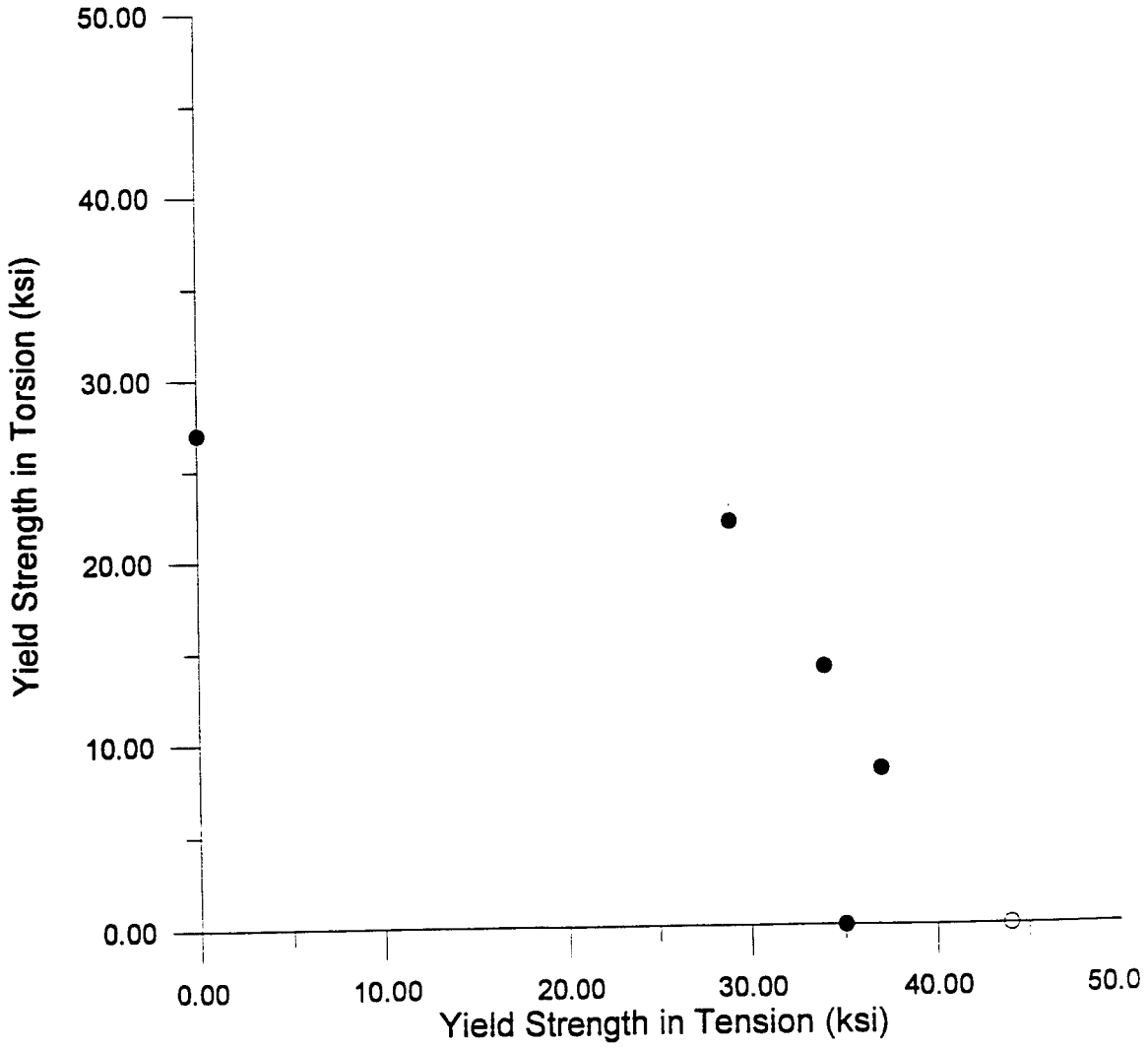


FIGURE 3.

Results and Discussion

For each test, the machine output was in the form of axial load and torque versus time. A yield point was determined from each curve and the results plotted as solid circles in figure 3. The yield point was determined by a 0.2% effective plastic strain. The data point obtained in pure tension is suspiciously low for a 6061-T6 aluminum. Results of tension tests by House[4] report the yield point of a similar stock of 6061-T6 aluminum to be approximately 44 ksi. This value is shown by the open circle in figure 3.

An effective yield stress for each test was also calculated and is reported in Table 1. Theoretically, the effective yield stress should be constant. The variation shown in Table 1 indicates the accuracy with which the von Mises yield criteria correctly modelled the yielding phenomena of this material. Although these values are fairly close, some doubt arises as to the validity of the von Mises criteria in describing the yielding behavior of this material.

TABLE 1.

σ_Y	τ_Y	σ_{EFF}
44	0	44
37	8.4	40
34	14	42
29	22	48
0	27	47

Conclusion

It seems the von Mises effective stress-strain criterion may not be totally satisfactory for predicting the yielding response of real materials to multiaxial loading. However, more tests need to be performed so a better data base can be constructed for further analysis.

References

1. Stout, M.G., S.S. Hecker, and R. Bourcier, "An evaluation of anisotropic stress-strain criteria for the biaxial yield and flow of 2024 aluminum tubes," *J. of Engr. Matl. Tech.* (trans. ASME) **105** 242 (1983).
2. Hecker, S.S., "Yield surfaces in prestrained aluminum and copper," *Metall. Trans.* **2** 2077 (1971).
3. Hockett, John E., and Peter P. Gillis, "Mechanical testing machine stiffness: part I - theory and calculations," *Int. J. Mech. Sci.* **13** 251 (1971).
4. House, J.W., "Taylor Impact Testing," AFATL-TR-89-41, Air Force Armament Laboratory, Eglin AFB, September 1989.

ACTIVE NON-CONTACT 3D MODELING USING AN ACCURATELY CALIBRATED CAMERA/LASER SYSTEM

Kenneth P. Luke
Graduate Teaching Assistant
Department of Electrical Engineering

Wright State University
Dayton, Ohio 45435

Final Report for:
Graduate Student Research Program
Wright Laboratory

Sponsored by:
Air Force Office of Scientific Research
Bolling Air Force Base, DC

and

Wright Laboratory

September 1994

THREE-DIMENSIONAL MODELING USING A CALIBRATED CAMERA/LASER SYSTEM

Kenneth P. Luke
Graduate Teaching Assistant
Department of Electrical Engineering
Wright State University

ABSTRACT

Three dimensional (3D) modeling involves combining a laser and camera to form an active range measuring system. The camera receives an object's three dimensional (3D) projection onto its two dimensional (2D) surface, and in the process, loses the object's depth information. By using a laser along with the camera, we retrieve the lost depth information. This camera/laser range measuring system is then placed on a rotating structure (which is an arch) and rotated completely around an object. By obtaining range measurements to an object's surface at many positions around an object, a three-dimensional (3D) reconstruction of the object's surface can be obtained. In order to optimize speed and measurement density, our 3D modeling system uses a non-contact active triangulation method of measuring. In this method, a known pattern is projected on an object using a laser, and its reflection is observed by the camera. Knowing the observed position of the pattern in the detected image, the range to the scene is computed by triangulation methods.

In order to use active triangulation in our system, proper calibration of the camera and camera/laser is essential. By constructing a multi-plane calibration device, we were able to obtain an accurately calibrated camera and camera/laser. The parameters from the camera calibration included the focal length, lens distortion coefficient, and an uncertainty scale factor due to scanning and sampling error. This method involves solving a linear set of equations, and then applying a nonlinear optimization technique to reduce the error of a perspective transformation. The parameters from the camera/laser calibration include the angle and distance of the laser plane to the optical axis. These parameters are found by certain geometric constraints of the calibration plane. By incorporating the described techniques, the camera calibration gives a mean absolute error of .5 mm (or 1/4000 of the working distance) for measurements made on the calibration plane, and the camera/laser calibration gave a mean absolute error of 5 mm (or 1/400 of the working distance) for the actual measurements of the 3D model.

THREE-DIMENSIONAL MODELING USING A CALIBRATED CAMERA/LASER SYSTEM

Kenneth P. Luke

CHAPTER 1. - INTRODUCTION

In this paper, a laser and camera are combined to form a range measuring system. The camera receives an object's 3D projection onto its 2D surface, and in the process, loses the object's depth information. By using a laser along with the camera, we can retrieve the lost depth information. This camera/laser range measuring system is then placed on a rotating structure (which is an arch) and rotated completely around an object . By obtaining range measurements to an objects surface at many positions around an object, a three-dimensional (3D) reconstruction of the object's surface can be obtained. Since the actual contour and shape of an object can be obtained from a 3D model, applications for 3D modeling could include 'form fitting' helmets, body suites, prosthetics, and/or orthotics. 3D models can be generated for input into CAD applications for automated machining. Other applications include virtual reality interfacing. Military applications include scanning targets for input into data bases which can then be used for target recognition.

In order to optimize speed and efficiency , our 3D modeling system uses a non-contact method, as opposed to a contact method, of measuring. Contact methods using tactile sensors, computer-controlled probes, and profilometers are usually slow and can not thoroughly measure enough points in a short period of time. In order to quickly and efficiently obtain 3D models of real world objects without physical contact, our algorithms must be based on state of the art range imaging technology. State of the art range (non-contact) imaging technology includes two classes of techniques : passive and active triangulation techniques. In active triangulation , a known pattern is projected on a scene (using a laser, projector, etc.) , and its reflection is observed by one or more dectectors. The projected pattern can be in the form of a point, a line, or binary code. Knowing the observed position of the pattern in the detected image, the range to the scene can be computed by triangulation methods. In passive triangulation, a scene is observed by one or more detectors (usually cameras) without any modification to the current illumination . Corresponding points are then extracted from each position's image frame, and the range is calculated to that point. For our application, active triangulation is used for the following reasons.

a) Active triangulation usually requires less computation power than passive triangulation.

b) Passive triangulation requires a model of surface reflection which is difficult to obtain.

c) Many commercial applications exist which include active triangulation. Therefore, evaluation of the performance of an active system is not as difficult to obtain.

d) Active systems have a higher reliability and robustness than do passive system.

In order to use active triangulation in our system, proper calibration of the system is essential. Proper calibration allows us to find otherwise unknown parameters of the system. After finding these parameters, we have enough information about the triangles formed (by the camera, the laser, and the projected laser line) to allow us to obtain depth information. The calibration of the system includes a camera and camera/laser calibration.

In the following paper, we provide a step-by-step approach for the calibrations, the theoretical framework for the calibrations, and the derivation of the laser/camera calibrations. The setup for both calibrations is given and discussed as is the setup for the entire 3D modeling system. Finally, an accuracy assessment is given for the camera calibration, the camera/laser calibration, and the reconstructed real world object.

CHAPTER 2 - SYSTEM CALIBRATION:

2.1. INTRODUCTION

Calibration of a 3D modeling system must be implemented for accurate results. Our calibration for the system is broken down into 2 parts.

1) camera calibration

2) camera/laser calibration

By camera calibration, we are able to obtain both the intrinsic and extrinsic parameters of the camera. The intrinsic parameters include a radial lens distortion coefficient, the focal length, and an uncertainty scale factor due to scanning and sampling error. The extrinsic parameters include the rotation and translation values of a user defined world coordinate system to the camera coordinate system.

The camera's intrinsic parameters, once found from calibration, provide us a way of determining a ray in 3D space that the object point must lie on. The camera's extrinsic parameters will allow us to complete the calibration of the camera/laser.

By camera/laser calibration, we are able to obtain a criteria for getting the angle of the laser plane relative to the optical axis, and the distance between the optical axis to the laser plane (in the plane of the CCD). Furthermore, we can ensure that the laser line and the columns of the CCD are parallel in the plane of the CCD and are aligned with the center of the arch. These parameters are not only necessary for the range measuring system, but (as later seen) help to describe the rotation of the arch.

2.2. CAMERA CALIBRATION

As already mentioned, the camera's intrinsic and extrinsic parameters must be found for our system. The camera calibration technique which was implemented is taken from [1].

2.3 LASER/CAMERA CALIBRATION

2.3.1. INTRODUCTION

Now that we have obtained the camera's intrinsic and extrinsic parameters, we are ready to calibrate the laser with the camera. This, once again, allows us to find the angle of the laser plane relative to the optical axis, and it allows us to find the distance between the laser plane and the optical axis (in the

plane of the CCD). We also can ensure that the laser line (in the plane of the CCD) is parallel to the verticle elements on the CCD.

2.3.2. LASER/CAMERA MODEL

Referring to figure #5, we have a model for the laser/camera setup. Notice that the camera model is not drawn with a back projection of the image plane. This is because we are looking for parameters that are dependent on the physical setup. The back projection model would not be accurate here.

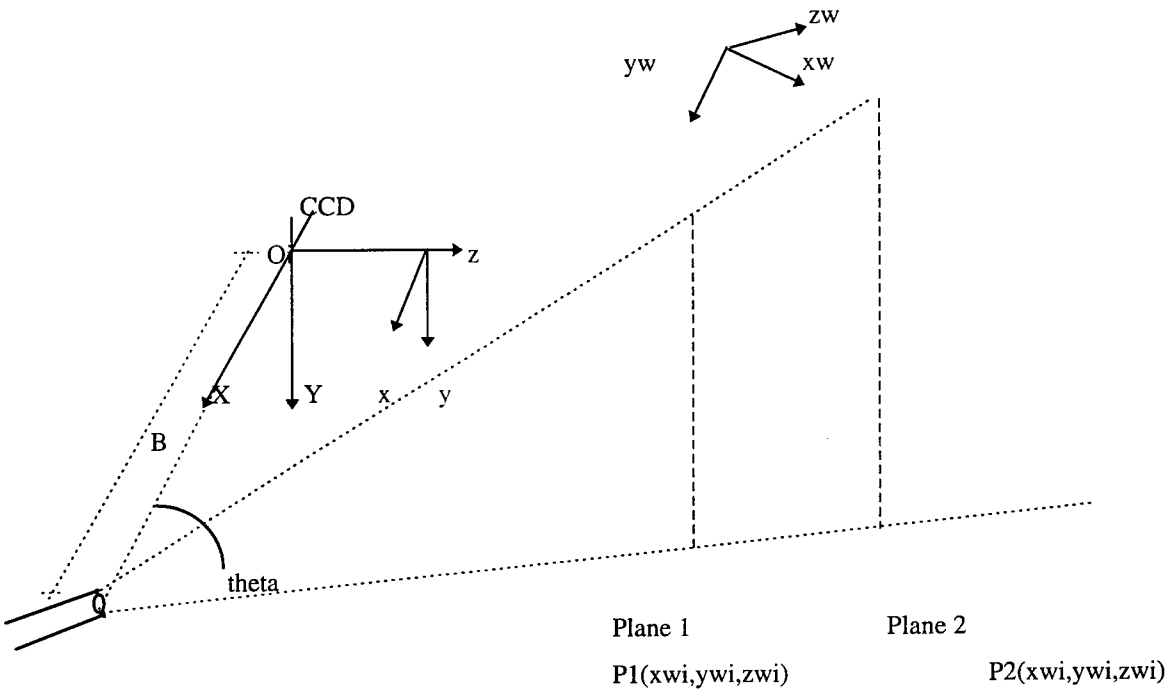


Figure 5. Laser and Camera Model

Once again, the vectors **x,y,z** form the camera coordinate system centered at O (the center of the lens). Vectors **X,Y** form the axis of the CCD center at Oi.Focal length is the distance between the planes of **X,Y** and **x,y.** The vectors **xw,yw,zw** form the world coordinate system.

Theta is the angle of the laser relative to the optical axis. This angle is constant in any plane formed by a row of the CCD. B is the distance from the optical axis to the laser line (again constant in any plane formed on a row of the CCD). P1(xwi,ywi,zwi) is the series of points formed on the first calibration plane by the laser line. Pn(xwi,ywi,zwi) is the series of points formed on the nth calibration plane by the laser line.

2.3.3. ASSUMPTIONS

The assumptions here are based on the physical setup. They are as follows. a) We assume that by the adjustments of the calibration plane during physical setup, we can obtain a calibration plane which is

completely perpendicular to the laser line. In order to obtain this, the laser line must bisect a whole column of LEDs for any and all depths of the plane.

b)We assume from this constraint that the world coordinates (formed by the laser line) are known. Since we know the location of all LEDs, we know the world coordinates formed by the laser line.

2.3.4. TRANSFORMATION FROM THE 3D WORLD COORDINATE SYSTEM (AS GENERATED BY THE LASER) TO THE CAMERA COORDINATE SYSTEM

The rotation matrix and translation vector from the first plane of the world coordinate system to the camera coordinate system is given by

(8a)
$$\begin{pmatrix} x_{c1} \\ y_{c1} \\ z_{c1} \end{pmatrix} = \begin{pmatrix} r_1 & r_2 & r_3 \\ r_4 & r_5 & r_6 \\ r_7 & r_8 & r_9 \end{pmatrix} \begin{pmatrix} x_{w1} \\ y_{w1} \\ z_{w1} \end{pmatrix} + \begin{pmatrix} T_x \\ T_y \\ T_z \end{pmatrix}$$

The rotation and translation of a second plane of the world coordinate system to the camera coordinate system is

(8b)
$$\begin{pmatrix} x_{c2} \\ y_{c2} \\ z_{c2} \end{pmatrix} = \begin{pmatrix} r_1 & r_2 & r_3 \\ r_4 & r_5 & r_6 \\ r_7 & r_8 & r_9 \end{pmatrix} \begin{pmatrix} x_{w2} \\ y_{w2} \\ z_{w2} \end{pmatrix} + \begin{pmatrix} T_x \\ T_y \\ T_z \end{pmatrix}$$

where all xwi,ywi,zwi are world coordinates on the calibration plane, but generated by the laser.

The difference between the two camera coordinates can be described by

(9)
$$\begin{pmatrix} x_{c1} - x_{c2} \\ y_{c1} - y_{c2} \\ z_{c1} - z_{c2} \end{pmatrix} = \begin{pmatrix} r_1 & r_2 & r_3 \\ r_4 & r_5 & r_6 \\ r_7 & r_8 & r_9 \end{pmatrix} \begin{pmatrix} x_{w1} - x_{w2} \\ y_{w1} - y_{w2} \\ z_{w1} - z_{w2} \end{pmatrix} + \begin{pmatrix} T_x - T_x \\ T_y - T_y \\ T_z - T_z \end{pmatrix}$$

referring to figure #6, we see from the model that

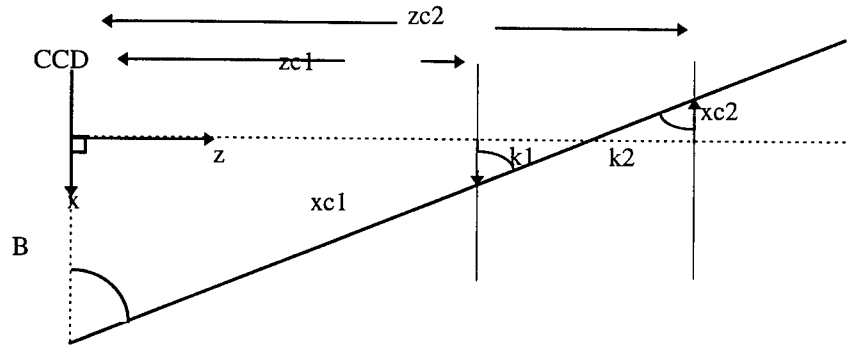


Figure 6: View of the laser/camera looking down the y axis

zc2-zc1=k1+k2

where k1=xc1tan(theta) and k2=-xc2tan(theta)

therefore

$$zc2 - zc1 = (xc1 - xc2)\tan(\vartheta)$$

By solving for theta

(10) $$\vartheta = \tan^{-1}\left(\frac{(zc2 - zc1)}{(xc1 - xc2)}\right)$$

Now that theta has been found, we nee a relationship to find B. Again referring to figure #6.

(11) $$B\tan(\vartheta) = Zc1 + f + k1 = Zc1 + f + xc1\tan(\vartheta)$$

(12) $$B = \frac{Zc1 + f + xc1\tan(\vartheta)}{\tan(\vartheta)}$$

2.3.5. PROBLEM DEFINITION

The problem to be addressed is 'How do we calibrate the laser and camera so that accurate range measurements can be made?'. The next section provides the algorithm for solving the stated question.

2.3.6. CAMERA/LASER CALIBRATION USING A MONOVIEW NONCOPLANAR SET OF POINTS

a) PROCEDURE: Obtain the coordinates of the laser line on the calibration plane. This should be simple since the laser line is set up to bisect a whole column of already known LED coordinates.

b) PROCEDURE: Compute theta from

$$\vartheta = \tan^{-1}\left(\frac{-r9}{r3}\right)$$

DERIVATION: This part of the procedure follows directly from the setup constraint discussed in Appendix B. This simple setup technique simplifies computation procedures.

Again, the constraint gaurentees that the calibration plane will be exactly perpendicular to the laser line. With this in mind, we locate which column of LEDs the laser line bisects for all planes.

From equation (9) we have

$$\begin{pmatrix} x_{c1} - x_{c2} \\ y_{c1} - y_{c2} \\ z_{c1} - z_{c2} \end{pmatrix} = \begin{pmatrix} r_1 & r_2 & r_3 \\ r_4 & r_5 & r_6 \\ r_7 & r_8 & r_9 \end{pmatrix} \begin{pmatrix} x_{w1} - x_{w2} \\ y_{w1} - y_{w2} \\ z_{w1} - z_{w2} \end{pmatrix} + \begin{pmatrix} T_x - T_x \\ T_y - T_y \\ T_z - T_z \end{pmatrix} = \begin{pmatrix} r_1 & r_2 & r_3 \\ r_4 & r_5 & r_6 \\ r_7 & r_8 & r_9 \end{pmatrix} \begin{pmatrix} 0 \\ 0 \\ z_{w1} - z_{w2} \end{pmatrix} + \begin{pmatrix} 0 \\ 0 \\ 0 \end{pmatrix}$$

Therefore, solving for the difference,

xc1-xc2=r3(zw1-zw2)

and

zc1-zc2=r9(zw1-zw2)

From equation (10)

$$\vartheta = \tan^{-1}\left(\frac{-r9(zw1 - zw2)}{r3(zw1 - zw2)}\right) = \tan^{-1}\left(\frac{-r9}{r3}\right)$$

C) PROCEDURE: From the known value of theta, calculate B from equation (12)

$$B = \frac{Zc1 + f + xc1\tan(\vartheta)}{\tan(\vartheta)}$$

where zc1=r7xw+r8yw+r9zw+Tz and

xc1=r1xw+r2yw+r3zw+Tx

DERIVATION: Derivation is straight from the equations derived in the last section.

CHAPTER 3 - OBTAINING 3D INFORMATION FROM THE CALIBRATED SYSTEM

3.1. INTRODUCTION

In this section, it is necessary to introduce a set of equations for finding range information from the laser line coordinates in the computer's image frame. Additionally, we need a set of equations which relate the range information obtained at each location back to one initial position. In the upcoming sections, we introduce these equations and show their derivation

3.2 ASSUMPTIONS

The following assumptions are neccessary in order to obtain a 3D model.

1) The center of rotation is found.

2) The center column of the camera's CCD is aligned on the center of rotation.

3) The laser line is projecting onto the center of rotation.

In order to ensure these assumptions, the following steps are necessary.

Step 1

In order to obtain information (later in the calibration) about the path of the laser/camera system, we must know were the center of rotation is. We obtain the center as follows. With a plum-bob hanging from a string which hangs from the center of rotation, we rotate the arch to position zero degrees. We pick a fixed point on the string, mark it, and then find it in the image of the camera. Call this point (Xf1,Yf1). Rotate the arch to position 180 degrees. Do the same except call the point (Xf2,Yf2). Now move the string such that it is at the half way point between Xf1 and Xf2. Go back and do the exact same procedure for position 90 degrees and position 270 degrees. Now verify this centering procedure by rotating the arch 360 degrees while watching the marked point on the string. This point should lie on the same image pixel for the whole rotation.

Step 2

With the string fixed on the center of rotation, align the camera such that the string lies on the image frames center column.

Step 3

Adjust the laser line onto the center string.

Step 4

Remove the center string and bring in the calibration plane. With the arch in a fixed position, a calibration device was placed in the center of the arch. The half way point between the two used planes was placed at almost the exact center of the arch. Next, make sure that the first plane of the calibration device almost completely filled the field of view of the camera (we made sure that all LEDs were in the field of view).

Step 5

At this point, the laser was turned on and a whole line of LEDs were lined up on a whole laser line. We then move the calibration plane back (we used 20 inches) and aligned the same line of LEDs with the whole line of the laser. This ensures that the calibration plane is completely perpendicular to the laser line.

Step 6

The world coordinates for this laser line should be recorded. The xw for each plane is a constant, and the yw varies through the length of you calibration plane.

3.2. EQUATIONS DIRECTLY RELATING THE LASER'S PROJECTED WORLD COORDINATES AND THE DIGITIZED COMPUTER'S IMAGE FRAME COORDINATES

From equations (2a) and (2b), we have the relationships

$$\frac{zc1}{xc1} = \frac{f}{Xu}$$

(13a) and (13b) *and*

$$\frac{zc1}{yc1} = \frac{f}{Yu}$$

where xc1,yc1,and zc1 are camera coordinates, f is the focal length, and Xu,Yu are undistorted image coordinates on the CCD plane.

By combination of equation (12) with equation (13a) solved for zc1 , we get

(14) $$xc1 = \frac{B\tan\vartheta - f}{\tan\vartheta + f / Xu}$$

and combination of (14) and (13a) solved for zc1, we get

(15) $$zc1 = \frac{fB\tan\vartheta - f^2}{Xu\tan\vartheta + f}$$

and by combination of (15) with (13b) solved for yc1, we get

(16) $$yc1 = \frac{YuB\tan\vartheta - Yuf}{Xu\tan\vartheta + f}$$

The physical significance here is that given a calibrated system, any Xu, and Yu coordinate will give us a range from the optical center.

3.3. EQUATIONS RELATING ROTATIONAL COORDINATE SYSTEMS TO THE INITIAL COORDINATE SYSTEM.

As was discussed earlier, the transformation from one coordinate system to another can performed using the rotational matrix and translational matrix. As the position of the camera/laser system changes during rotation about the arch, so does its coordinate orientation. Each position in which depth information is obtained, there needs to be a translation and rotation from each position back to the initial position. The rotation matrix can be described by the rotation about each axis as shown below.

$$\begin{pmatrix} r1 & r2 & r3 \\ r4 & r5 & r6 \\ r7 & r8 & r9 \end{pmatrix} = \begin{pmatrix} 1 & 0 & 0 \\ 0 & \cos\varphi & \sin\varphi \\ 0 & -\sin\phi & \cos\phi \end{pmatrix} \begin{pmatrix} \cos\theta & 0 & -\sin\theta \\ 0 & 1 & 0 \\ \sin\theta & 0 & \cos\theta \end{pmatrix} \begin{pmatrix} \cos\psi & \sin\psi & 0 \\ -\sin\psi & \cos\psi & 0 \\ 0 & 0 & 1 \end{pmatrix} =$$

Since the system described ensures alignment of the center column of the image with the center of the rotation, the only rotation occuring is the rotation about the y axis.Therefore, by setting the angles of rotation about x and z to zero (or phi=0 and psi = 0), we get the following rotation matrix.

17)
$$R = \begin{pmatrix} \cos\vartheta & 0 & -\sin\vartheta \\ 0 & 1 & 0 \\ \sin\vartheta & 0 & \cos\vartheta \end{pmatrix}$$

Now, in order to find the translation vector, we refer to figure 4a below.

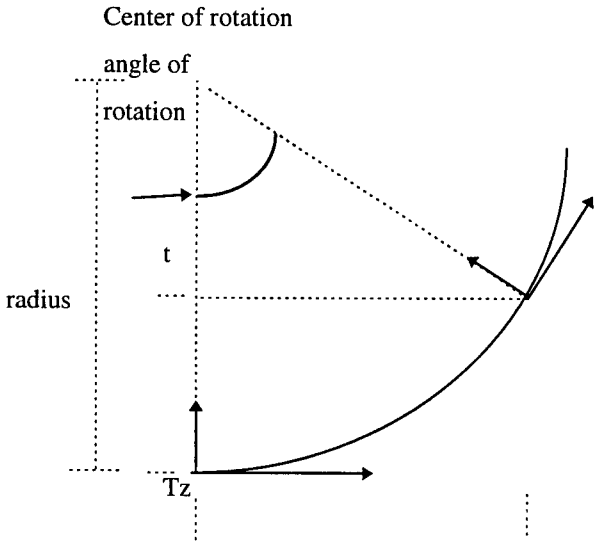


Figure 8: Quarter of the rotation of the arch. Rotation is based only on the rotation about y axis. The translation Ty is always zero.

From figure 8, if we let the angle of rotation be alpha, then we see that theta is equivelant to alpha. Therefore, the angle of rotation of the arch is the same as the angle of rotation of the camera coordinate system. Now, from simple geometrical relationships, we get the translation vector. Since

$$radius = B\cos\theta$$

$$\sin\alpha = \frac{T_x}{radius}$$

$$then$$

$$T_x = radius * \sin\alpha$$

Furthermore, from figure 8, since

$$\cos\alpha = \frac{t}{radius}$$

(19) $$then$$

$$x = radius * \cos\alpha$$

then

(20) $$T_z = radius - x = radius - radius * \cos\alpha = radius(1 - \cos\alpha)$$

Therefore, the transformation back to the original position is

(21) $$\begin{pmatrix} x_{c1} \\ y_{c1} \\ z_{c1} \end{pmatrix} = \begin{pmatrix} \cos\vartheta & 0 & -\sin\vartheta \\ 0 & 1 & 0 \\ \sin\vartheta & 0 & \cos\vartheta \end{pmatrix} \begin{pmatrix} x_{ci} \\ y_{ci} \\ z_{ci} \end{pmatrix} + \begin{pmatrix} T_x \\ T_y \\ T_z \end{pmatrix}$$

3.4 THREE DIMENSIONAL MODELING

At this point, we now have all the necessary equations to obtain the 3D model. This section is based on the actual procedures so that the reader can incorporate the information into their own algorithms. Steps:

1) We assume that the system is completely calibrated at this time.

2) An object is placed in the center of the rotating arch.

3) Ambient light should be reduced to a minimum

4) Start the stepper motor moving and at the same time receive enoder feedback. At equal increments in the rotation, snap an image and save it. The position of each image must be recorded.

5) After completion of the rotation we are now ready to start processing the images.

6) Open each image file and extract a single line (image of the laser line). This information is in the computers image frame coordinates (Xfi,Yfi).

7) By using equations (6a) and (6b), solve for Xdi, Ydi

8) By equations (3a) and (3b) , solve for Xui,Yui

9) From equations (14) , (15), and (16), calculate the corresponding xci,yci,zci for each point.

10) For each position, theta should be calculated and all xci,yci,zci points at that position should be transformed by equation (21) back to the initial starting position

11) MATLAB was used to image the 3D surface at this point.

3.5 RESULTS OF 3D MODELING

The results of the 3D modeling system presented here are purely qualitative. In the following diagrams, the actual object is shown along with its reconstructed surface. The next section describes the accuracy assessment.

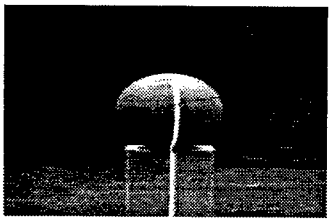


Figure 9

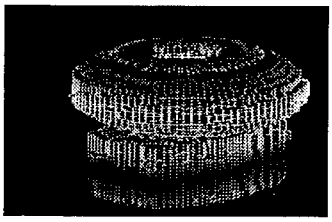


Figure 10

Qualitatively, we make the following observations from our present results.

1) The top,bottom, and deep crevices of objects is a problem for modeling.

2) Error in the described method gives us a noisy surface.

3) Worping of the plots occur due to inadequate plotting algorithms.

CHAPTER 4 - ACCURACY ASSESSMENT

In this section, an accuracy assessment will be presented for the camera calibration, the camera laser calibration, and finally the 3D model.

4.1 CAMERA CALIBRATION ACCURACY ASSESSMENT

The camera calibration's accuracy was assessed by actually using the camera to measure the world coordinates of an unknown object on the calibration plane. By using the first plane of the calibration device, the unknowns to solve for were xw and yw. For each result, we obtain error for 64 calculated xw and yw points. From these we obtain a mean absolute error. Our results give:

Mean absolute error = .5mm

4.2 CAMERA/LASER ACCURACY ASSESSMENT

The camera/laser accuracy assessment was performed by grabbing two images. Each image would have one pixel element in its image frame. This was obtained by allowing the laser line to intersect a small object at two different known points. By finding the xc,yc,zc for each position (from the equations in (14), (15), and (16)) , we can calculate the absolute distance in 3D space by

$$dist = \sqrt{(x_{c1} - x_{c2})^2 + (y_{c1} - y_{c2})^2 + (z_{c1} - z_{c2})^2}$$

From this technique, we achieved the following: Mean absolute error = 5mm

CHAPTER 5 - CONCLUSION

Our approach to system calibration for 3D modeling was by way of camera calibration, and then camera/laser calibration. Camera calibration gave us a way to obtain the camera's intrinsic parameters which included the coefficient of lens distortion, the focal length, and an uncertainty scale factor. The camera calibration also gave us a way to obtain the camera's extrinsic parameters which included the rotation and translation constants. The extrinsic parameters were then used as a constraint to find the camera/laser parameters. These parameters included the distance from the CCD center to the laser plane, and the angle of the laser plane relative to the optical axis.

From the approach described, an error analysis was done for the camera calibration, the camera/laser calibration, and the final 3D model. From the results for camera calibration, we obtained an error of approximately 1/4000 of our working distance. From the results for the camera/laser calibration, we obtain an error of approximately 1/400 of our working distance.

Simple and effective techniques have been presented for calibrating a camera and camera laser system. From our experience, problems occur in the methods :

1) for finding the center of rotation during setup

2) for aligning the column of the CCD and the laser plane

3) for ensuring a perpendicular calibration plane to the laser line

If an accurate 3D model is to be obtained, solutions for the above problems will need to be developed.

Bibliography

[1] R.Y. Tsai, "A versatile camera calibration technique for high accuracy 3D machine vision metrology using off-the-shelf TV cameras and lenses," IBM RC 11413, October 1985.

[2] M. Hebert and T. Kanade, "State of the Art in Range Imaging Technology",1990

[3] Kefu Xue, "Imaging Geometry and Camera Model", 1992

[4] Rafael C. Gonzalez and Richard E. Woods, Digital Image Processing, Addison-Wesley Publishing, Copyright 1992.

Preliminary Characterization and Calibration of Micro Shear Stress Sensors in a Compressible Flow.

John D. H. Mai
Graduate Student, Aerospace Engineering
Department of Mechanical, Aerospace, and Nuclear Engineering

University of California, Los Angeles
MANE Dept., Engineering Bldg. IV
420 Westwood Blvd.
Los Angeles, CA 90024

Final Report
Graduate Student Research Program
Wright Laboratory

Sponsored by:
Air Force Office of Scientific Research
Bolling Air Force Base, Washington D.C.
and
Wright Laboratory

September 1994

Preliminary Characterization and Calibration of Micro Shear Stress Sensors in a Compressible Flow.

John D. H. Mai
Graduate Student
Mechanical, Aerospace, and Nuclear Engineering Department
University of California, Los Angeles

Abstract

The feasibility of using a Caltech/UCLA designed micro shear stress sensor in a compressible flow environment has been proved. Uniformly and non-uniformly doped micro sensors (designed using MEMS technology) were tested in the Mach 3 High Reynolds Number Facility at Wright Laboratories. Using a polynomial fit-extrapolation (of previous data) for the skin friction coefficient within the tunnel, the sensor voltage output versus wall shear stress compared well with empirical calibration models derived from hot film sensor operating in incompressible flows. The frequency spectrum of the data obtained from the micro sensors displayed the characteristic 5/3 power slope associated with the inertial subrange. Some frequency regions in the power spectrum of the results were identified, after applying frequency compensation methods, as having potential for future investigation, as well as future research and applications are outlined.

Preliminary Characterization and Calibration of Micro Shear Stress Sensors in a Compressible Flow.

John. D. H. Mai

Introduction

The measurement of wall shear stress, especially in the compressible flow regime, is a daunting technical challenge. Yet the important role that this phenomena plays in fluid dynamics promises great rewards in efforts towards understanding and controlling the mechanisms at work in turbulent boundary layer flows. The difficulty in obtaining quantitative values arises, in part, from the limited number of practical measurement devices available to the experimentalist. Since shear stress at the wall is proportional to du/dy, a direct approach would dictate that a streamwise-component velocity profile in the y-direction is necessary in order to unequivocally arrive at a quantitative value for the shear stress. However, traditional measurement techniques have inherent problems near the wall region. Simple Pitot/Preston tubes have proven to be too bulky to measure adequate, high resolution velocity profiles, and are inadequate at obtaining fluctuation r.m.s. values at the wall. A hotwire experiences detrimental heat conduction effects, and a bulky laser Doppler anemometry system encounters severe reflection problems when they are brought too near a wall. Although a hot film sensor can be flushed mounted, its application remains limited due to formidable calibration and drift problems. Surveys in shear stress measurement techniques can be referenced to works by Settles [1986], Hakkinen [1992], and Haritonidis [1989]. However, the body of literature available on the subject of wall shear stress measurements in a high Reynolds number, compressible flow, until very recently, is quite limited. Early works in the supersonic flow regime, pertinent to this study, include Moore and Harkness [1964], Brinich and Diaconis [1952], and Eimer [1955]. These researchers obtained their results via floating element balances or Preston tubes.

More recent trends in shear stress research has been towards innovative miniature devices, such as those developed by Higuchi [1983], Murthy & Rose [1997], and Schmidt, et al [1988] . It has only been within the last decade that the technology has become available, as a spin-off from CMOS VLSI processing, to produce micron scale sensors, and thus it is only natural that shear stress sensor designs take advantage of this opportunity. With the recent advances in micro-electromechanical-machine systems (MEMS) design and fabrication, researchers at the California Institute of Technology, in collaboration with the University of California, Los Angeles have produced a viable shear stress sensor.

There are many advantages that a MEMS shear stress sensor has over conventional shear stress measurement methods. The primary advantage is that the short sensor height, typically less than 1.0 μm, creates limited disturbances in the boundary layer flow, unlike the protruding Preston and Stanton probes.

As a consequence of this advantage, these micro sensors can be placed downstream of each other, in order to follow changes in the flow, without creating substantial disturbances which would influence the upstream sensor. Compared to floating element balances, a MEMS sensor is at least three orders of magnitude smaller. Although these balances give a direct measurement of shear stress, many mechanical problems, as well as calibration problems, have manifested themselves during trials. (Tcheng, Holmes, and Supplee, [1989] and White [1984].) Also, these devices are difficult to mount on curved, thin surfaces such as airfoils. In addition, Hakkinen [1993] estimates that for a typical airfoil with a chord c= 1.0 m and $C_f = 0.002$, a gap height (the distance between the floating element and the surface on which it is mounted) of t = 0.1 mm should result in a 50% error in measurements. This MEMS shear stress sensor is also a superior design when compared to orifice and surface fence gages since there are no holes or breaks in the surface that could also disturb the flow. Finally, normal miniature gages are difficult to mass produce. They are usually produced by hand, a time consuming, expensive process, that invariably lead to minor manufacturing differences between sensors that can cause radical, unpredictable changes in behavior and data results. This is not true for the MEMS micro sensor. Once its manufacturing process is characterized, thousands of identical sensors can be cheaply made by the automated, assembly line-like process available at several commercial CMOS foundries.

Sensor Design

The sensor was designed by Liu and Tai at Caltech, with support and initial testing done by Huang and Ho at UCLA [1994, to be published]. Each MEMS shear stress sensor is essentially a polysilicon line, 80-200 μm long, 2μm wide and 0.45 μm thick, that acts as a thermistor, resting on a vacuum sealed cavity. (Ref. Figure 1.) Two variations (uniformly and non-uniformly doped) of this sensor, with 16 sensors per microchip, were available for supersonic testing. For the uniformly doped chip, each polysilicon line has a resistance of 50 Ω/□, due to ion implantation. For the non-uniformly doped chip, the doping profile is similar except for a 2 μm long segment at the center, which is doped to 21 kΩ/□. The polysilicon rests on a 1 μm thick layer of low stress silicon nitride, that acts as an extremely strong and flat diaphragm material. The diaphragm covers a 200 μm by 200 μm cavity that originally contained phosphosilicate glass (PSG), which was sacrificially etched by hydrofluoric acid. The cavity's etch facilitating holes were sealed during a low pressure chemical vapor deposition (LPCVD) step with silicon nitride at 300 mTorr. This creates a cavity approximately 2 μm deep, with an assumed internal pressure of 300 mTorr. Since the sensor operates according to the heat-shear stress analogy, the cavity was necessary in order to decrease heat conduction to the substrate (by isolating the sensor over a vacuum) and thus improve the sensor's sensitivity.

Earlier testing of the MEMS sensors with and without cavities found that the sensors with the cavity underneath has a thermal resistance seventeen times greater than the sensor without a cavity. This design has led to an unprecedented sensitivity of 1 V/V-kP, while also maintaining electrical time constants on the order of 10 μs and diaphragm/heating time constants around 350 μs. This design circumvents the trends observed by Moen and Schneider [1993] in their comparison experiments with conventional hot-film sensors. They concluded that frequency responsivity increased as sensor size decreased, but there was a penalty in the form of a decrease in sensitivity for the conventional design. This substrate conduction problem has plagued many other miniature shear stress sensor design, such as Houdeville's quartz element gages [1984], and Flittie and Covert's wire cavity shear gage [1992].

Operating Theory

Reynolds Analogy

The sensors work on the principle known as Reynold's analogy for turbulent flow over a flat plate. It can be referenced in most elementary heat transfer books such as Incropera and Witt's *Fundamentals of Heat and Mass Transfer* [1990]. Based on the assumption that the Prandtl number is approximately equal to unity, the analogy relates heat transfer with skin friction, which is directly proportional to wall shear stress.

The following is a synopsis of the relationship: Given the relation between shear stress and the appropriate velocity component

$$\tau_{xy} = \mu \frac{\partial u}{\partial y}$$

and Fourier's law of heat convection (where q is heat flux per unit area, and T is temperature)

$$q = -k \frac{dT}{dy}$$

this results in

$$q = -\tau_{xy} \frac{k}{\mu} \frac{dT}{du}$$

Making the assumption that the limits of integration are from the wall conditions to the free stream conditions, also noting that for Pr = 1 that Cp= k/μ , and knowing the definitions of heat convection coefficient, Nusselt number, and Stanton number the following skin friction coefficient relation results

$$NuRe^{-1}Pr^{-1/3} = StPr^{2/3} = C_f/2$$

This gives the final proportionality between shear stress and heat flux as

$$q \sim \tau^{1/3}$$

Based on hot film anemometry results, the empirical, incompressible relation between the sensor voltage output, E, and shear stress should follow this relation:

$$E^2 = A + B\tau^{1/3} \qquad (1)$$

where A and B are experimentally obtained calibration coefficients.

Sensor Response/Time Constant

Following Kovasznay's notation, a hot wire system can be modeled according to the following energy relation:

change in total heat stored = Joule heating produced - heat loss due to convection in wire element

$$dQ/dt = P(i,T) - F(U, T)$$

where

$$dQ/dt = cm\, dT/dt$$

$$P = i^2R(T)$$

$$F = hA(T - T_0)$$

where c is the specific heat of the wire material, m is the mass, T is temperature, i is current, U is velocity, R (a function of temperature) is the material resistance, h is the convection coefficient, and A is the surface area of the sensor.

For a standard hot wire, R is modeled in the usual manner

$$R = R_0\{1+\alpha(T-T_0)\}$$

where "o" signifies reference values, and α is the temperature coefficient of resistivity. However, for the case of the micro shear stress sensor, it should be modeled as a thermistor, which follows this relation:

$$R = R_0 \exp\beta(1/T - 1/T_0)$$

where β is a constant coefficient based on thermistor characteristics.

The general heat transfer coefficient relation can be derived from an expression for the Nussult number

$$Nu = [A + B\,\mathrm{Re}^n](1 + {}^{a_T}\!/_2)^m$$

the overheat ratio (a_T) exponent, m, is approximately zero and is usually ignored in incompressible analysis.

Noting that P and F can be decomposed into average and fluctuation quantities (e.g. P =

P(average) + ΔP), and also noting that a long time average means that P (average) = F (average), this results in

$$cm\frac{d\Delta T}{dt} = \Delta P - \Delta F$$

Also, when small fluctuation approximations are made, an example of which is

$$\Delta F = dF = \left.\frac{\partial F}{\partial U}\right|_T dU + \left.\frac{\partial F}{\partial T}\right|_U dT$$

this results in the following relation:

$$cm\ \frac{d\Delta T}{dt} + \left(\left.\frac{\partial F}{\partial T}\right|_u - \left.\frac{\partial P}{\partial T}\right|_i \right)\Delta T\ = \left.\frac{\partial P}{\partial i}\right|_T \Delta i - \left.\frac{\partial F}{\partial U}\right|_T \Delta U$$

Note that Δi = 0 in the constant current operating mode. When the above relation is placed in the form of a first order system :

$$Md\Delta T/dt + \Delta T = f(t)$$

it is apparent that the frequency response is given by

$$M = \frac{cm}{\left(\left.\frac{\partial F}{\partial T}\right|_u - \left.\frac{\partial P}{\partial T}\right|_i \right)} \qquad (2)$$

which, when evaluated for a hot wire, in constant current operating conditions, in terms of temperature and resistance is

$$M = \frac{cm(\overline{T} - T_o)}{i^2 R_o \alpha} = \frac{\rho cAl(\overline{R} - R_o)}{i^2 \alpha R_o}$$

these relations assume m = 0 in the heat transfer relations, and all fluctuations are small.

The time constant relation for a thermistor-type sensor is more complicated due to the exponential nature of the governing equation. Based on the linearized definition (2), the time constant is

$$M = \frac{cm}{\frac{Ak_f}{d}\left[(1 + a_T/2)^m [A + B\mathrm{Re}^n]\right] - i^2 \exp\left(\frac{1}{T} - \frac{1}{T_o}\right)\ln TR_o}$$

In this case, using the relation that P (average) = F (average) does not lead to simplifications as in the case of a normal resistance hotwire. Additionally, both results assume that fluctuation quantities are small.

Quantitative fluctuation values are being estimated, and future work will be aimed towards verifying the fluctuation results. The main difficulty in obtaining reliable fluctuation values lies in the inherent difficulty with calibrating the sensor in a facility with only a fixed Mach number capability.

It is apparent from the aforementioned theoretical results for the sensor's frequency response, that the frequency response is highly dependent on the operating current used, which also manifests in the overheat ratio. Since the operating current is usually a fraction of a millivolt, a smaller operating current results in an increased frequency response, but this is balanced by a loss in sensitivity. However, due to delicate nature of the electronics, and the difficulty in replacing a sensor, it was decided to cautiously only use low operating currents in order to avoid burning out the sensors.

Experimental Facilities and Setup

Testing was conducted in the Mach 3 High Reynolds Number Facility operated by Wright Aeronautical Laboratories at Wright-Patterson Air Force Base, Ohio. A fixed, two dimensional nozzle produces a Mach 3 flow into a 8 inch wide, 8.2 inch high, and 23.2 inch long test section. Since air supplied to the tunnel is unheated, the tunnel stagnation temperature decreases during tunnel operation. The tunnel has a variable stagnation pressure capability, ranging from 65 psia to 560 psia. Technical support was provided by the experimental aerodynamics research branch at Wright Laboratories (WL/FIME).

The chip containing the sensor that was tested is mounted on a PC board type backing. Gold wires are then wire bonded between the bond pads on the chip, to pads on the PC board. The PC board facilitates the attachment of more robust lead wires out the backside of the board. These wires link the sensor to the constant current anemometer designed by Huang [Ref. Figure 4; 1994, to be published]. The chip and board is then mounted in a 0.09 in. deep, 0.85 in. square recess that had been milled into a 2.25 in. diameter anodized aluminum plug that would be inserted into the upper wall of the tunnel. The plug had been ground and marked so that it's surface is flush with the tunnel walls. (Ref. Figure 2 and 3) The plug also contains a type J iron/constantan thermocouple, used to measure local wall temperature, and a 0.125 in. diameter static pressure tap. They are located on each side of the square recess and are centered 0.125 in. away from the recess edge. The daunting problem of protecting the fragile gold bond wires to the rigors of the starting and stopping tunnel shocks/loads, as well as the general supersonic flow conditions is overcome via the use of non conducting epoxy.

The plug is inserted 14.5 inches from the tunnel nozzle (measured to the center of the plug), and all data is taken at this location. Due to the orientation of the chip to the flow, and the need for no obstructions upstream of the sensors (such as bond wires and epoxy), limitations were place on the

number of sensors that could be active on a chip, during a given trial. The setup only allows for the testing of 1 row of sensors, along the back edge of a chip. These sensors are the only ones oriented in the correct position to the flow, and their bond wires are connected to pads behind them, in reference to the flow. This effectively reduces the total possible number of sensors available to five per chip. Also, since only one constant current anemometer was constructed to operate with the sensors, only one sensor is active per trial.

Previous Results

Fiore [1977] wrote a summary of his experiences with Preston tube and force balance measurement in the M3 HRNF at WPAFB. In his analysis, the assumption is made that there is a zero pressure gradient inside the test section and there are near adiabatic wall conditions. This assumption is based on the result that there is a 0.00651 psia/inch gradient at P_0 = 85 psia, and a 0.0429 psia/inch gradient at P_0 = 560 psia. This slight, but negligible longitudinal pressure gradient is due to the fact that the walls of the downstream extension section of the tunnel are not adjustable. Also, Fiore makes the reasonable assumption that the static pressure throughout the boundary layer is constant and equal to the wall pressure. Finally, there is the assumption that the temperature distribution through the boundary layer is linear, as a function of y/δ, between the wall temperature and the total temperature at the outer edge of the boundary layer.

Experimental results

Sensor Characteristics

Before placing the sensors inside the tunnel, the frequency response is obtained by inputting a square wave into the circuit with the sensor attached. For the non uniformly doped sensor with a resistance of 150.9 kΩ, and operating at 0.12 mA the cut off frequency is 1.0 kHz, and operating at 0.10 mA the frequency response increased to 1.17 kHz. The uniformly doped sensor, with a resistance of 2.91 kΩ had a worse frequency response. Tested at 1.32 mA, the response is approximately 295 Hz, while the bandwidth slightly increased to 310 Hz when the operating setting was decreased to 0.85 mA. Additionally, Huang provided frequency response curves for the uniformly and non uniformly doped sensors so that frequency compensation methods could be applied to the raw data. (Ref. Figure 9 for the non uniformly doped sensor response) A third order polynomial fit was used to digitize Huang's normalized data and it was used as a weighing function in order to clear up any inherent signal amplification, in the higher frequency range, in the raw Fourier transform results .

Test Matrix

The test matrix is broken into 3 general groups. The first group (runs 1-3) involve the non uniformly doped sensor operating at 0.12 mA while the second group (runs 4-6) are similar trials, but with the same sensor operating at 0.10 mA. The third group (runs 7-10) uses the uniformly doped sensor, but the trials are conducted almost in the exact same manner as the previous two groups.

Run	Sensor	Stagnation Pressure		operating conditions
1	non uniform	100	psia	I=0.12 mA, sampled at 10kHz for 0.5 sec
2	non uniform	150	psia	I=0.12 mA, sampled at 10kHz for 0.5 sec
3	non uniform	100-500	psia	I=0.12mA, 1000 pts averaged per sec.
4	non uniform	100-550	psia	I=0.10mA, 1000 pts averaged per sec.
5	non uniform	250	psia	I=0.10mA, sampled at 10kHz for 0.5 sec.
6	non uniform	400	psia	I=0.10mA, sampled at 10kHz for 0.5 sec.
7	uniform	100-500	psia	I= 0.88 mA, 1000 pts averaged per sec.
8	uniform	150	psia	I= 0.88 mA, sampled at 10 kHz for 1.6 sec
9	uniform	250	psia	I= 0.88 mA, sampled at 10 kHz for 1.6 sec
10	uniform	350	psia	I= 0.88 mA, sampled at 10 kHz for 1.6 sec

The results of these trials have shed new light on the capabilities of these sensors. However, the delicate nature of the bond wires led to the loss of all but two sensors (1 uniformly doped, and 1 non-uniformly doped) in the installation process. The cause has not been verified, but it is suspected that irregular mixing of the epoxy led to a buildup of residual stress concentrations within the epoxy after it dried. This could contribute to some of the lost sensors, since they usually were not lost until a day after the epoxy was applied. However, once the epoxy hardened, the remaining sensors were quite robust. They both survived all the rigors of supersonic testing, including the extreme pressure and temperature effects of several cycles of the starting and stopping tunnel loads.

Figures 5a and 5b show time averaged data for the uniformly and non-uniformly doped sensors, respectively. Each data point represents 1000 data samples averaged per second and plotted as a function of actual run time. Po and To are stagnation pressure and temperature, T1 is wall temperature according to the plug thermocouple, P1 is the static wall pressure, and "sens" is the sensor output in voltage. These quantities are in English units, e.g. temperature is in degrees Rankine and pressure is in pounds per square inch. Figures 6a and 6b are the same temperature, pressure, and voltage data graphed as functions of stagnation pressure, which was the only operational variable during each trial.

The trends observed during all the trials were repeatable and similar, even between the non-uniformly and uniformly doped sensors. The two noticeable differences are due to the inherent designed characteristics of the sensors. First the non-uniformly doped sensor output decreases with increases in

stagnation pressure. This shows a potential direct measurement of shear stress, since Fiore recorded that the skin friction coefficient, C_f, decreases linearly with linear increases in Po. The uniformly doped sensor shows a similar, but opposite, rise in voltage output when shear stress decreases at increasing Po. This trend is explained by the fact that the uniformly doped sensor has a negative thermal coefficient relative to the non-uniformly doped sensor. The other glaring difference is that the sensitivity difference between the sensors is an order of magnitude. The increase in sensitivity was the major design consideration which led to the development of the non-uniformly doped sensor, thus these results verify the superiority of this configuration over that of the uniformly doped sensor.

Referring to Figures 5a and 5b again, since P1(wall) moves in a stepwise fashion (due to the controlled stepwise increments of Po and the continuous data sampling technique) and the voltage decreases linearly, it is concluded that the sensor has a negligible pressure sensitivity. However, the same cannot be concluded about the sensor's temperature sensitivity. Figure 7 (output voltage squared vs. wall shear stress cube rooted based on Fiore's data) presents the crucial data that is necessary to extract the nature of the temperature dependence, if any, of the sensor. The wall thermocouple shows a linear 9.4% decrease in temperature near the sensor as each run progresses. Since both temperature and sensor output seemingly vary linearly with increased Po (Ref. Figures 6a and 6b), it is difficult to determine the effects of temperature contamination on the sensor's ability to detect the experimentally verified decrease in C_f as Po increases in the M3 HRNF. Before going further into temperature effects, the method used to correlate Fiore's data with the present data, and how Figure 7 was produced, will be explained.

The comparison with Fiore's data is conducted in the following manner. His nearest data to the data taken in the present trial (14.5 in.) is at a location 27.28 in. (pt. 1) downstream from the nozzle. Fiore's next five points are 43.28 in., 58.28 in., 70.28 in., 82.28 in., 94.28 in. downstream (pt. 2,3,4, and 5, respectively). Since Fiore gives data for C_f with respect to Po at each x location, this information was graphed and a linear fit was performed at each location. The slopes at each x location were then graphed and a third order polynomial fit was obtained. This resulted in a method for estimating C_f at the present trial location since Po is known. The wall shear stress, τ, value was easily obtained from this point since Q ($=1/2\rho V^2$) is automatically calculated by the data acquisition program. Figure 7, based on Run 3 is representative of data trends from Run 4 also. When the square of the sensor output (at 14.5 in.) is graphed with the cubed root of the wall shear stress, this gives a linear fit, which exactly matches the empirical trend hoped for in Equation 1. Additionally, there are differences between Runs 3 and 4 in the values for the A and B coefficients obtained by this linear fit. Therefore, it seems that the instrument operating settings and operating conditions, such as the temperature variation, only play a role in the calibration coefficients. Otherwise, this sensor seems to operate according to the empirical calibration correlation, similar to other hot film sensor operating in the incompressible regime. This also shows that

the simpler resistor model (as opposed to the thermistor model) should be adequate for modeling the MEMS sensor. More trials must be conducted to verify this calibration correlation, but there seems to be little relation between changes in operating temperature and the linear calibration.

Although the long time average data from both sensors showed similar trends , the sensitivity of the uniformly doped sensor was not adequate enough to provide a meaningful voltage time trace. Changes in the voltage output from the uniformly doped sensor were at the detection threshold (approximately 1 mV) of the data acquisition system. Therefore, compensated Fourier transform analysis was only performed on the non-uniformly doped data. The following discussion is thus centered around the non-uniformly doped sensor results, but it must be remembered that the long time average trends of the uniformly doped sensor were almost identical, so that all aspects of the previous discussion are applicable to both sensor types.

Figure 10 compares the compensated and uncompensated frequency spectrum of the sensor output at 150 psia. Figure 11 shows the compensated frequency spectrum of the data taken at 250 psia and 400 psia. Spectrum peaks below 100 Hz should be ignored since definite 60 Hz noise was identified in the system during preliminary sensor setup. The cause has not been isolated, but it is either due to incompatibilities between UCLA's anemometer and the M3 HRNF data acquisition system, or interference generated by other equipment in the facility. All of the spectrums follow a definite 5/3 power slope, which points towards the sensor's ability to detect and resolve small scale structures on the order of the Kolmogorov scale. Referring to Figure 10, for the 150 psia case, a distinct harmonic structure is apparent near 250 Hz, 500 Hz, and 1 kHz. In the 250 psia case, these peaks are not as prominent, and they seemed to have shifted to approximately 375 Hz and 750 Hz. By the time the stagnation pressure reached 400 psia, the peak amplitudes have decreased further, but there are still identifiable isolated peaks near 500 Hz and 1 kHz. These results identify possible structures in the compressible turbulent boundary layer, and isolate the frequency range in which to search for them. This phenomena warrants further, future investigation, if nothing else, than to expand our understanding of these sensor's abilities to resolve small scale structures within a flow field.

Conclusion

First, these trials confirm the ability of micro sensor to survive and operate under the rigors of a compressible flow environment. The simple solution which remedied the problem of protecting the bond wires was by burying them under non-conducting epoxy. Next, the superiority of the non-uniformly doped sensor over the uniformly doped sensor is apparent. This improvement in the non-uniformly doped design manifests in a higher frequency response and increased sensitivity, as compared to a uniformly

doped sensor. The feasibility of practical applications for the sensor is only limited by the lack of a simple, accurate calibration method. Using previous skin friction coefficient data and correlating it with present results, a linear fit between the square of the sensor output and the cubed root of the wall shear stress value is identified. This leads to the preliminary, tentative conclusion that the sensor can be modeled as a resistor and seems to closely emulate incompressible hot film calibration results. Additionally, frequency spectrum characteristics of the inertial sublayer were verified and regions were identified where influential flow structures might be characterized, thus providing new paths for future research.

A goal for the immediate future is the refinement of constant temperature circuitry for use with the sensors. This should hopefully lead to an increase in frequency response. Along the same lines, research into constant voltage circuitry should be explored. Preliminary and theoretical studies into the constant voltage anemometer designed by Sarma in 1991 show improvements over standard constant temperature and current systems. These studies show increases in sensitivity as well a a large bandwidth, and the minimization of adverse cable capacitance effects. There are many applications for a viable micro shear stress sensor. Pertinent to ongoing research at Wright Laboratories, Wang, Qiu, and Zhang [1988] developed a method for using shear stress sensors in order to quantitatively identify the onset of buffet of wings. Also, Cole [1990] identified a phase relationship between flush mounted shear stress sensors that can be used to identify the location of boundary layer separation and reattachment. Therefore, the refinement of these micro sensors should greatly enhance our understanding of boundary layer phenomena, as well as provide a useful instrument in many practical applications.

Appendix- Infrared Results

Currently, at UCLA's Fluid Dynamics Laboratory, MEMS sensors and actuators are being integrated in an attempt to influence the vortices generated by a vortex generator within an effectively 2-D channel flow. The actuator was designed and documented by Liu, Tsao, et al [1994] at Caltech, and although it was designed to operate under the influence of external magnetic fields, it was found that the differences in the coefficients of expansions between the polysilicon and metal layers produced a bimetal-like effect when subjected to I^2R Joule heating. Consequently, approximately 20 to 50 degrees of actuation could be achieved with an input of 20-40 mA.

In preliminary experiments at UCLA with the vortex generator aligned in front of a row of actuators, followed by a MEMS shear stress sensor behind the actuator chip, a 15% decreases in DC shear stress level was detected by the sensor. However, at that time, facilities were not available to determine what percentage of this decrease was actually due to the actuator motion, and what was due to temperature contamination of the sensor by the heated actuators.

Since the sensor operates on the heat transfer-shear stress analogy, it is important to determine

the temperature distributions around the sensor and actuator. An AGEMA Thermovision System 900 (SW/TE) infrared camera and analyzer was available at the M3/M6 HRNF at WPAFB. Operating a single 54.4 Ω actuator using thermally induced movement with a 31.2 mA current (in a zero flow setting), a typical actuator operating value, the temperature difference jumped from an ambient value of 71.0 ^{o}F to 122.9 ^{o}F. According to images generated by the Sony video and printing system connected to the infrared analyzer, this single actuator was able to raise the temperature of the entire 1.0 cm by 1.0 cm chip (that the actuator is a part of) to at least 100 ^{o}F. In addition, it was found that a 119.0 kΩ sensor, operating at a typical value of 0.356 mA, created less than a 1.0 ^{o}F change in ambient conditions, an insignificant value when operating next to an actuator.

With a 10^{o} narrow field of view lens on the IR camera and a 119.38 cm focal length, each image contains 17920 pixels per frame. Given an image size of 20.89 cm by 13.04 cm, this results in a resolution of 1.23 mm per pixel. Using this information, and based on the IR pictures (Ref. Figure 8), it is estimated that five actuators aligned along an edge of the 1.0 cm square chip, operating in the 30 mA range, would easily raise the temperature of the air within a 5 cm radius by at least 10 ^{o}F. Since the sensor and actuator grouping at UCLA is less that 5 cm apart, it is apparent that most of the sensor output is contaminated by the actuator heating, which is now obviously heating the sensor to an order of magnitude greater than its usual operating conditions.

Acknowledgments

There are many people who made this research possible. I would like to first thank Mr. N. Scaggs and the Experimental Aeromechanics Section for their support and the use of their facilities this summer. Thanks to M. Wagner for familiarizing me with the facilities and aiding in the IR experiments. Milling of the plug and mounting of the sensors was done by K. Shoffstall. Additional wire bonding was done by J. Comtois at AFIT. The professionalism of the tunnel operators, T. Norris and R. Allen, was conducive to supporting a flexible test schedule. Special thanks to J. Scheuring who operated the computer facilities during the data acquisition and reduction phase. Electronics support was provided by D. Gehring and H. Baust.

I would also like to thank Caltech and J.B. Huang for providing the sensors and anemometer. Thanks to my advisor Dr. C.M. Ho for his support in this summer project and to Dr. S. Tung at UCLA for reviewing the raw data. Thanks does not seem adequate to acknowledge the countless enlightening discussions with Dr. R. J. Hakkinen, whose advice has saved me a lot of grief. My gratitude to L. Nguyen for her support and understanding. This research is funded by AFOSR.

References

1. G.S. Settles, "Recent Skin Friction Techniques for Compressible Flows", AIAA Paper 86-1099, May 1986.
2. R.J. Hakkinen, "Survey of Skin Friction Measurement Techniques," University of Dayton Research Institute, Ohio, 1992.
3. J. H. Haritonidis, "The Measurement of Wall Shear Stress", Advances in Fluid Mechanics Measurements, Springer-Verlag, pp.229-261,1989.
4. D.R. Moore, J. Harkness, "Experimental Investigation of the Compressible Turbulent Boundary Layer at Very High Reynolds Numbers, M=2.8", Report No. 0-71000/4R-9, April 1964.
5. P.F. Brinich, N.S. Diaconis, "Boundary Layer Development and Skin Friction at Mach Number 3.05", NACA TN 2742 July 1952.
6. M. Eimer, "Direct Measurement of Laminar Skin Friction at Hypersonic Speeds", Ph.D. thesis, California Institute of Technology, 1955.
7. D.G. Mabey, L. Gaudet, "Some Performance of Small Skin Friction Balances at Supersonic Speeds," *J. Aircraft*, Vol. 12, p.819-825, 1975.
8. P.Tcheng, H.K. Holmes, F.H. Supplee, Jr., "High Temperature Skin Friction Measurement," NASA LaC internal report, 1986.
9. E.L. White, "Experiences with a Simple Skin Friction Balance Design," USAF, Wright Laboratories, Wright-Patterson AFB, Ohio, Technical Memorandum AFWAL-TM-85- 246-FIMN, Nov. 1985.
10. H. Higuchi, "A Miniature, Directional Surface- Fence Gage for 3-D Turbulent Boundary Layer Measurements", AIAA 16th. Fluid and Plasma Dynamics Conference, AIAA-83-1722, July 1983.
12. V.S. Murthy, W.C. Rose, "Direct Measurements of Wall Shear Stress by Buried Wire Gages in a Shock Wave-Boundary Layer Interaction Region", AIAA 10th Fluids and Plasma Dynamics Conference, AIAA 77-691, 1977.
14. M.A. Schmidt, R.T. Howe, et al, "Design and Calibration of a Microfabricated Floating-Element Shear-Stress Sensor," *IEEE Trans. Electronic Devices*, Vol 35 No. 6, p 750-757, 1988.
15. C. Liu, J.B. Huang, et al, "Surface-Micromachined Thermal Shear-Stress Sensors," to be presented at the Symposium on Micro Structures, Sensors and Actuators of the the ASME Winter Annual Meeting, Nov. 26-Dec 1, 1994.
16. M.J. Moen, S.P. Schneider, "The Effect of Sensor Size and Substrate Properties on the Performance of Flush Mounted Hot Film Sensors", Proceedings of the 3rd. International Symposium on Thermal Anemometry, ASME, July 1993.
17. J. Shajii, K.Y. Ng, M.A. Schmidt, "A Microfabricated Floating-Element Shear Stress Sensor Using Wafer-Bonding Technology," *Journal of Microelectromechanical Systems*, Vol. 1, No. 2, June 1992, p. 89-94.
18. K.J. Flittie, E.E. Covert, "Unsteady Turbulent Skin-Friction Measurement in an Adverse Pressure Gradient," *AIAA Journal*, Vol. 30 No. 11, Nov. 1992, p. 2647-2652.
19. A.W. Fiore, "M=3 Turbulent Boundary Layer Measurements at Very High Reynolds Numbers," USAF, Wright-Patterson AFB, Ohio, Technical Report AFFDL-TR-77-80, Oct. 1977.
20. C. Liu, T. Tsao, Y.C. Tai, C.M. Ho, "Surface Micromachined Magnetic Actuators", 7th IEEE Workshop on Micro Electro-Mechanical Systems, MEMS'94, Oiso, Japan, pp.57-62, 1994.
21. F. Incropera, D. DeWitt, *Fundamentals of Heat and Mass Transfer*, 3rd ed., John Wiley & Sons, New York, 1990.
22. S.M. Mangalam, G.R. Sarma, et al, "A New Approach to High-Speed Flow Measurements Using Constant Voltage Anemometry", AIAA paper 92-3957, 1992.
23. K.D. Cole, "Separation Detection with Stochastic Signals from Flush-mounted Hot-film Sensors", Fluid Measurement and Instrumentation Forum:1990 Proceedings of the ASME Spring Meeting, Toronto, Canada, June 1990.

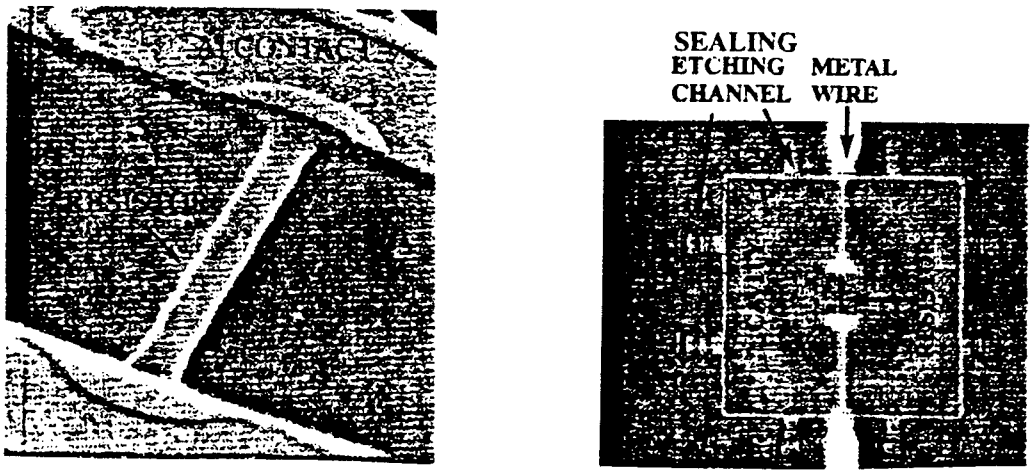


Figure.1 Electron micrographs of MEMS shear stress sensor (by Tai, Caltech).

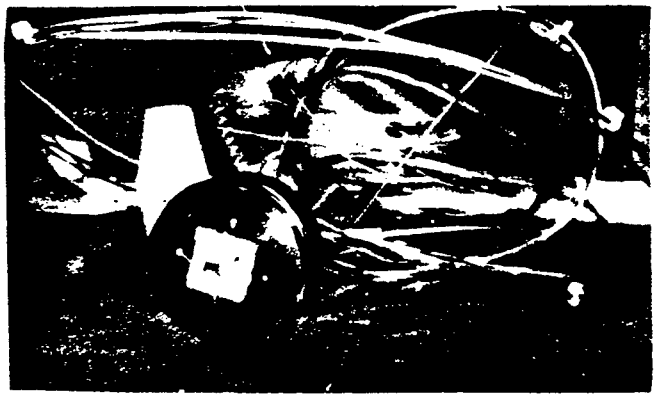


Figure 2. MEMS shear stress sensor mounted in test plug, with sensor wiring in background



Figure 3. Sensor and Plug inside of M3 HRNF test section

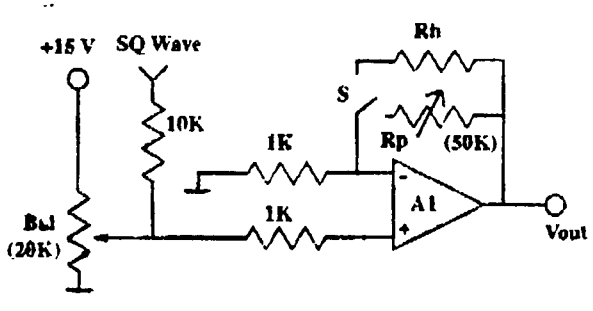
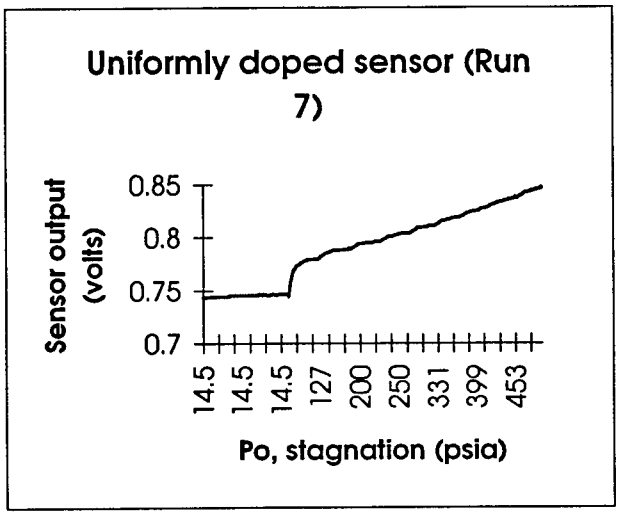
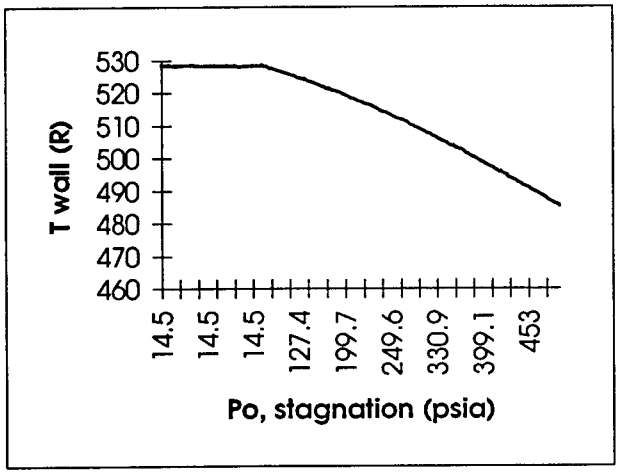


Figure 4. Constant current circuit (by Huang, UCLA)





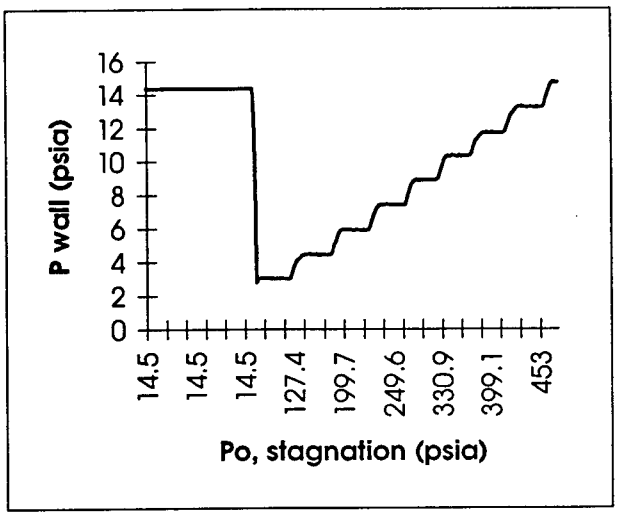
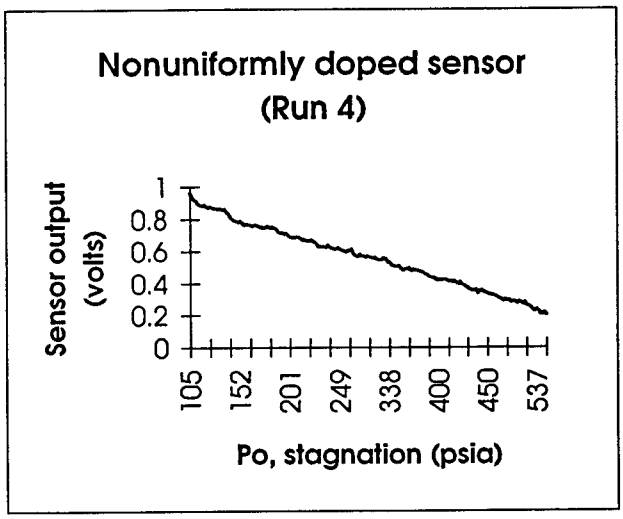
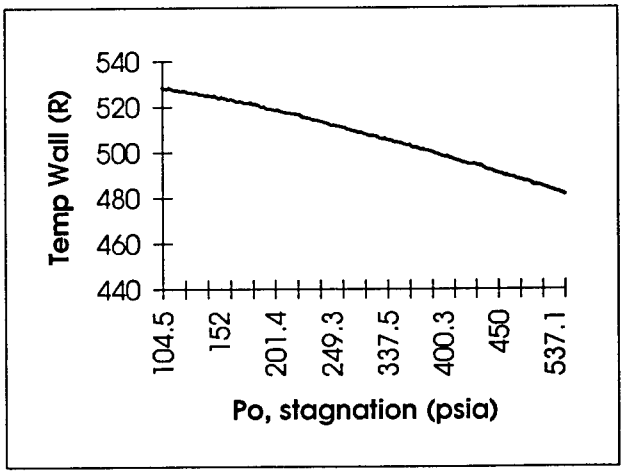


Figure 6a. Uniformly Doped Sensor Data





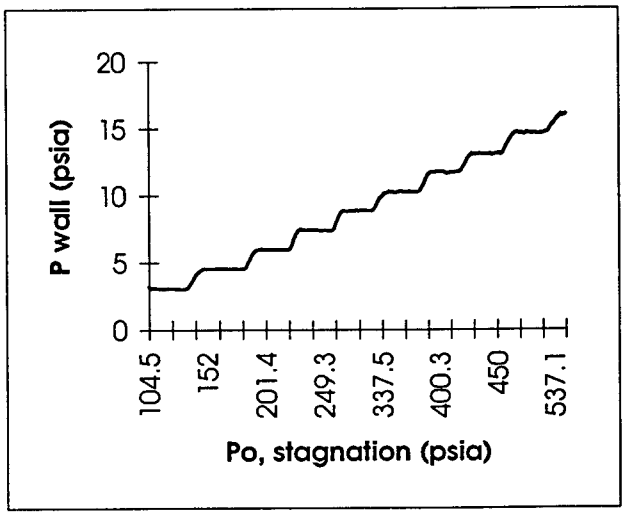


Figure 6b. Non Uniformly Doped Sensor Data

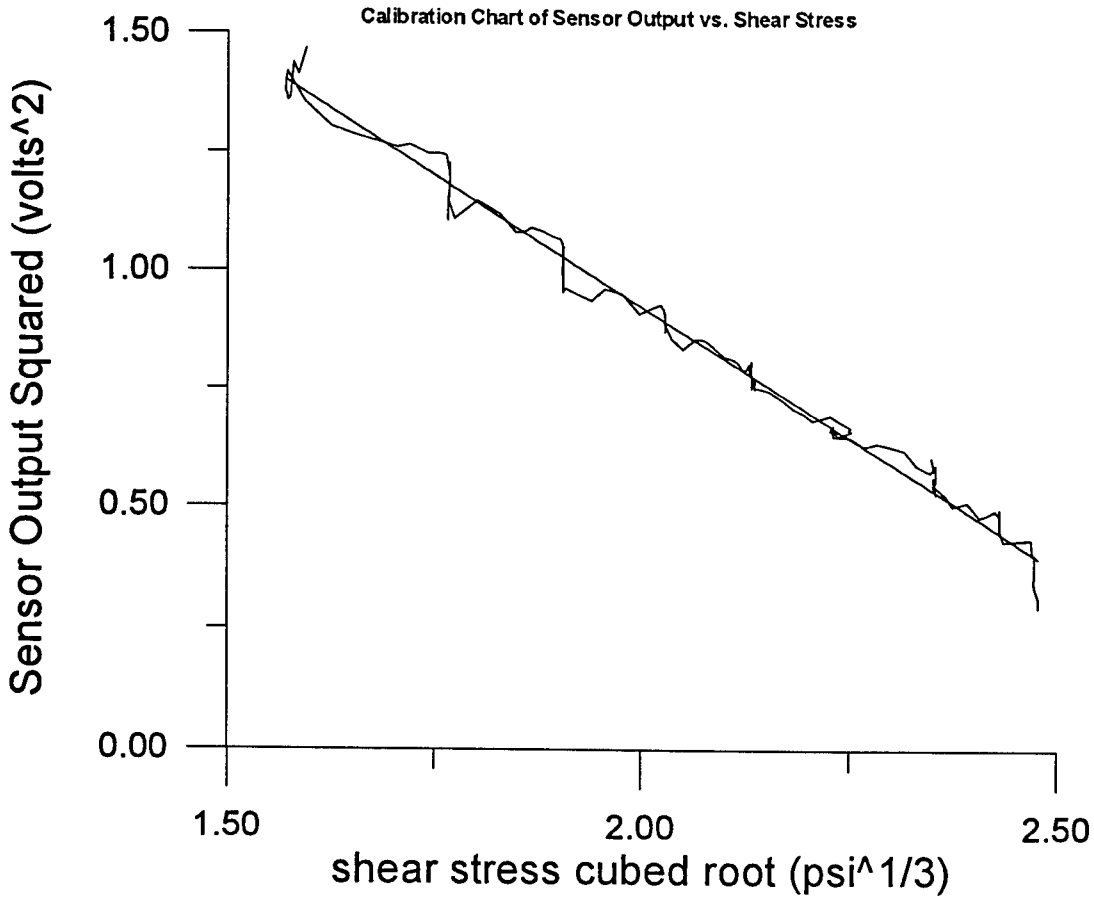


Figure 7 MEMS Shear Stress Sensor Calibration Chart

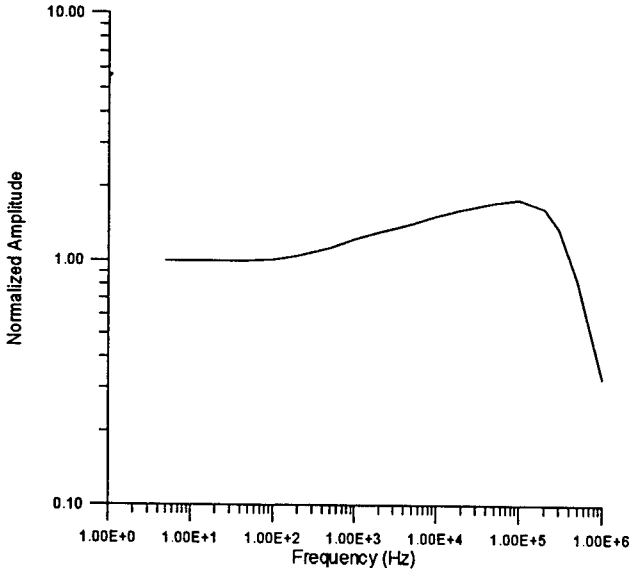
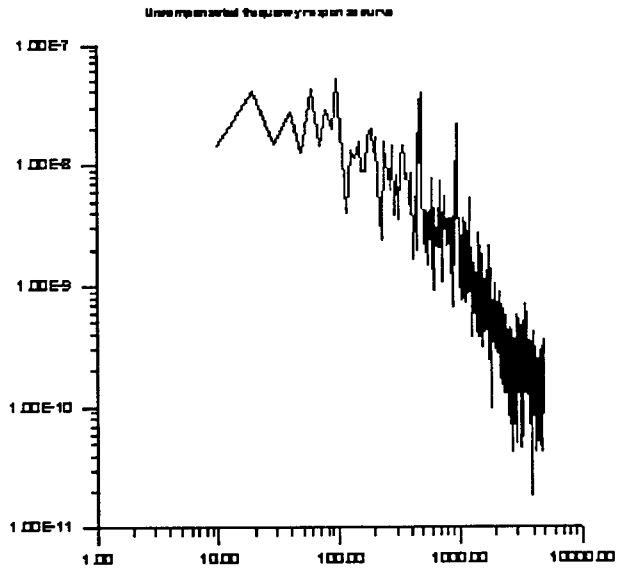
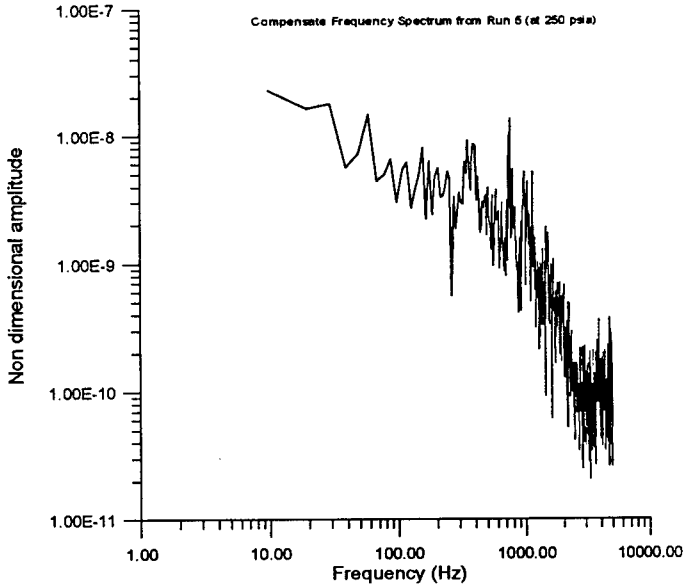
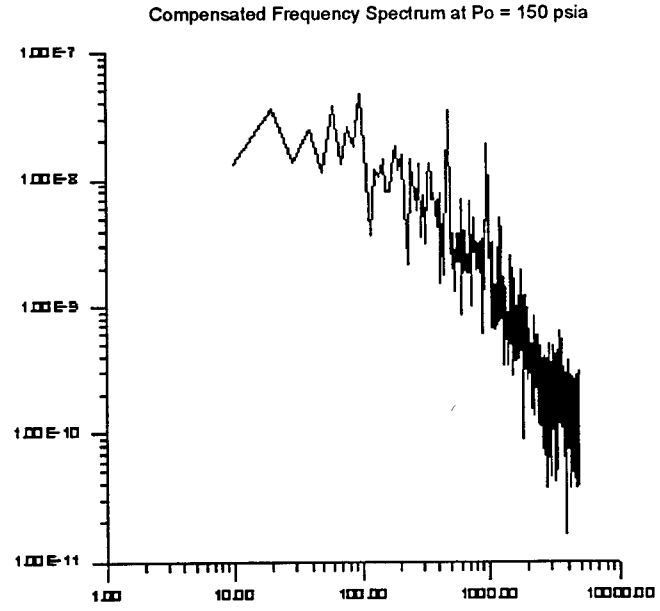


Figure 9 Normalized Non Uniformly Doped Sensor
Frequency Response Curve (Courtesy of J.B. Huang)







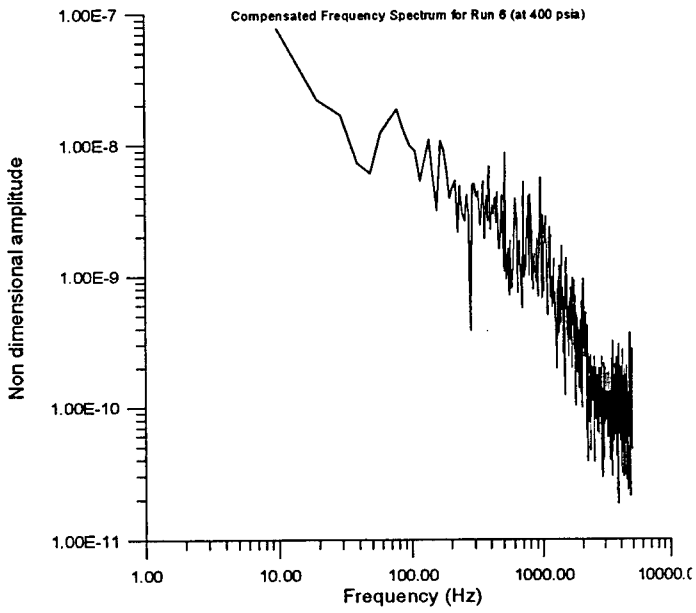


Figure 10 Uncompensated and Compensated Spectrum at Po = 150 psia.

Figure 11 Compensated Frequency Spectra at Various Stagnation Pressures

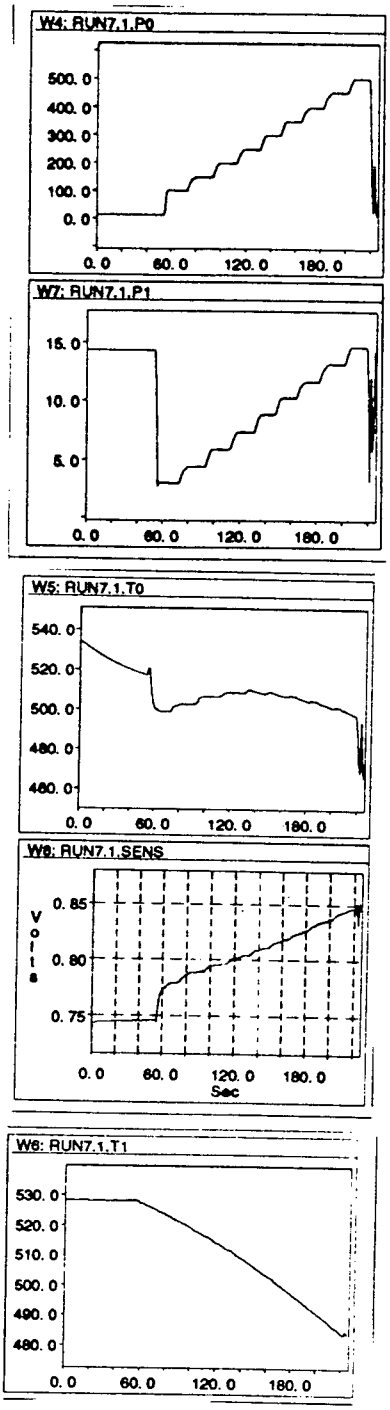


Fig. 5a Uniformly doped sensor

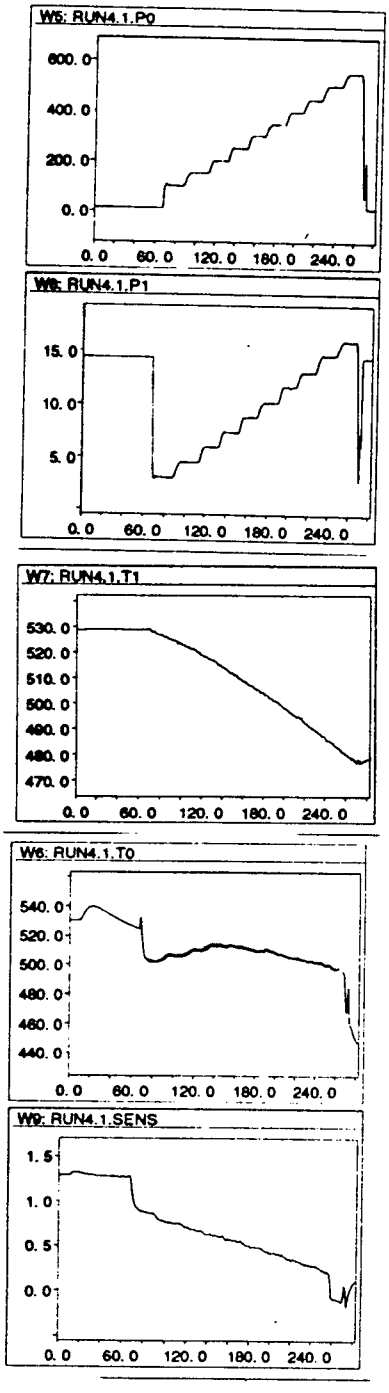


Fig. 5b Non-Uniformly doped sensor

HIGH SPEED IMAGING INFRARED POLARIMETRY

Mark A. Manzardo
Graduate Student
Department of Physics

University of Alabama in Huntsville
301 Sparkman Drive
Huntsville, Alabama 35805

Final Report for:
Graduate Student Research Program
Wright Laboratory Munitions Division

Sponsored by:
Air Force Office of Scientific Research
Bolling Air Force Base, DC

and

Wright Laboratory Munitions Division
Eglin Air Force Base, FL

September 1994

HIGH SPEED IMAGING INFRARED POLARIMETRY

Mark A. Manzardo
Graduate Student
Department of Physics
University of Alabama in Huntsville

ABSTRACT

High Speed Imaging Infrared Polarimetry is a technique which enables the Stokes Vector of a scene to be determined on a pixel by pixel basis. This technique can be used to measure the circular component of the Stokes vector using a Photoelastic Modulator and a Linear Polarizer. When a Quarter Wave Linear Retarder is added the technique is capable of measuring the linear components of the Stokes Vector. The Photoelastic Modulator oscillates at a rate of 37 kHz. Measurements of this oscillating signal can be used to determine the Stokes Vector of the detected light. A 3 x 3 array of HgCdTe detectors are used to aid in the imaging process. The DC detected signal is amplified with nine custom circuit boards developed at University of Alabama in Huntsville. The data is acquired and analyzed with custom computer software on a 486/33 PC using 5 dual channel GageScope oscilloscope boards. The calibration consists of determining a Polarization Measurement Matrix which is then used to determine the incident Stokes Vector from the time varying detected signal. This matrix should be determined for the system operating in both the circular and linear mode. Measurements taken of blackbody radiation sources of simple geometries can be used to verify the technique.

HIGH SPEED IMAGING INFRARED POLARIMETRY

Mark A. Manzardo

INTRODUCTION

Polarimetry is a technique used to measure the polarization state of light. There are many ways in which the polarization state of light can be measured. Interferometric methods can be used to measure the amplitude and phase of the light. These methods usually lead to representing the light in a form known as a Jones Vector [1]. The polarization state can also be determined by intensity measurements through known polarizing elements. When only the intensity of the light is measured, the polarization state is better represented by a Stokes Vector [2]. The polarimetry method described here is one which falls into the latter category. Therefore, the terminology used will be in reference to the Stokes parameters and the instantaneous amplitude and phase of the light will not be considered.

In the *Theory* section of this report: (1) a general definition of polarization will be given, (2) the representation of any polarization state will be seen to be given by a point within the Poincaré Sphere or equivalently by a general Stokes Vector, (3) the relationship between the Stokes Vector and the Poincaré Sphere will be given, and (4) the Mueller Calculus will be described. The *Polarization Components* section gives a Mueller Matrix representation and explanation of each of the polarization components to be used. The *Polarimetric Measurement Matrix* section shows how the output (detected signal) of a polarimeter system can be used to determine the input Stokes Vector. The *Polarimetry Systems* section will give a description and explain the calibration and measurement method for the two polarimeters to be used: (1) the High Speed Imaging Infrared Linear Polarimeter (HSIILP) and (2) the High Speed Imaging Infrared Circular Polarimeter (HSIICP). The *Experiments* section describes work accomplished during the summer and future potential experiments to be run using the polarimeter. The *Conclusion* section draws conclusions and provides suggestions for future measurements.

THEORY

Polarization:

Polarized light is in general elliptical, where a line and a circle are special cases of an ellipse. By this it is meant that the tip of electric field vector will trace out an ellipse as the light propagates. The trace can proceed in either a clockwise or a counter-clockwise direction as one looks into the beam; clockwise implies Left Elliptical and counter-clockwise implies Right Elliptical polarization (see Figure: "The Polarization Ellipse").

The Stokes Vector:

The Stokes Vector is a mathematical construct which is used to describe any state of polarized light using only properties of the intensity of the light. This vector is defined as:

$$\underline{S} = \begin{bmatrix} S_0 \\ S_1 \\ S_2 \\ S_3 \end{bmatrix} = \begin{bmatrix} P_0 + P_{90} \\ P_0 - P_{90} \\ P_{45} - P_{135} \\ P_R - P_L \end{bmatrix}$$

where P_X - represents the signal that would be detected through a perfect X polarizer and X - either implies a linear polarizer at 'X' orientation or a Right or Left circular polarizer. S_0 represents the total intensity of the light beam and can be equivalently represented by: $P_0 + P_{90} = P_{45} + P_{135} = P_R + P_L$. S_1 represents the tendency of linear polarization at 0 compared to 90 degrees. S_2 represents the tendency of linear polarization at 45 compared to 135 degrees. S_3 represents the tendency of Right compared to Left circular polarization.

It is often convenient and sometimes necessary to use a Normalized Stokes Vector to represent the polarization state of light. The Normalized Stokes Vector is defined as:

$$\underline{Sn} = \begin{bmatrix} Sn_0 \\ Sn_1 \\ Sn_2 \\ Sn_3 \end{bmatrix} = \begin{bmatrix} 1 \\ S_1/S_0 \\ S_2/S_0 \\ S_3/S_0 \end{bmatrix}$$

In this form, the absolute radiant intensity is not considered. This alleviates the need for well calibrated detector systems, only a linear detector system is required. Also, any overall intensity transmission of the detection system can also be ignored.

The Poincaré Sphere:

The Stokes Vector is related to the Poincaré Sphere in a relatively straight forward sense. The radius of the Poincaré Sphere has a length equal to S_0. Any point *on* the Poincaré Sphere describes a unique state of completely polarized light. Points on the sphere that are mirror images about the origin are orthogonal states of polarization. Light that is partially polarized is described by points that are *within* the sphere. All points that lie along the same radial direction correspond to light having the same elliptical orientation and rotation. The three Cartesian axes represent, by definition, the Stokes Vector components S_1, S_2, and S_3 [3].

Any point in (or on) the Poincaré Sphere can be given by the vector:

$$\underline{r} = \begin{bmatrix} S_1 \\ S_2 \\ S_3 \end{bmatrix}$$

The magnitude of the this vector is used to define the *Degree of Polarization* (DOP) given by:

$$DOP = \frac{\sqrt{S_1^2 + S_2^2 + S_3^2}}{S_0} = \sqrt{Sn_1^2 + Sn_2^2 + Sn_3^2}$$

where the DOP is equal to 1 if and only if the light is completely polarized. The Normalized Poincaré Sphere is given by letting $S_0 = 1$ and using the Normalized Stokes Parameters. Using the Poincaré Sphere, the orientation of the major axis of the ellipse and the ellipticity angle are given

by:

$$\theta = \frac{1}{2}\arctan\left(\frac{S_2}{S_1}\right) = \frac{1}{2}\arctan\left(\frac{Sn_2}{Sn_1}\right)$$

$$\epsilon = \frac{1}{2}\arcsin\left(\frac{S_3}{\sqrt{S_1^2 + S_2^2 + S_3^2}}\right) = \frac{1}{2}\arcsin\left(\frac{Sn_3}{\sqrt{Sn_1^2 + Sn_2^2 + Sn_3^2}}\right)$$

The orientation of the major axis of the ellipse has the range $0 \le \theta \le \pi$. The ellipticity angle has the range $-\pi/4 \le \epsilon \le \pi/4$ (negative for Left and positive for Right circular polarization). These definitions allow any normalized polarization state to be determined by the Normalized Stokes Vector or equivalently by the DOP and the two angles θ and ϵ given above. Figure: "The Poincaré Sphere", graphically illustrates how these quantities are related.

Mueller Calculus:

Mueller Calculus is used to explain how the polarization state of light changes as it transverses an optical system. The general procedure is to represent an optical component as a 4 x 4 matrix. Such a matrix is defined so that when it is dotted into the incident Stokes Vector the resulting vector is the transmitted (or reflected) Stokes Vector. These matrices are given the name Mueller Matrices [2]. Mathematically, the output Stokes Vector is given by:

$$\begin{bmatrix} S_0 \\ S_1 \\ S_2 \\ S_3 \end{bmatrix}_{out} = \begin{bmatrix} m_{1,1} & m_{1,2} & m_{1,3} & m_{1,4} \\ m_{2,1} & m_{2,2} & m_{2,3} & m_{2,4} \\ m_{3,1} & m_{3,2} & m_{3,3} & m_{3,4} \\ m_{4,1} & m_{4,2} & m_{4,3} & m_{4,4} \end{bmatrix} \begin{bmatrix} S_0 \\ S_1 \\ S_2 \\ S_3 \end{bmatrix}_{in}$$

$$\begin{bmatrix} S_0 \\ S_1 \\ S_2 \\ S_3 \end{bmatrix}_{out} = \begin{bmatrix} m_{1,1}S_{0,in} + m_{1,2}S_{1,in} + m_{1,3}S_{2,in} + m_{1,4}S_{3,in} \\ m_{2,1}S_{0,in} + m_{2,2}S_{1,in} + m_{2,3}S_{2,in} + m_{2,4}S_{3,in} \\ m_{3,1}S_{0,in} + m_{3,2}S_{1,in} + m_{3,3}S_{2,in} + m_{3,4}S_{3,in} \\ m_{4,1}S_{0,in} + m_{4,2}S_{1,in} + m_{4,3}S_{2,in} + m_{4,4}S_{3,in} \end{bmatrix}$$

If the optical system of interest has many components in it, then a cascade of Mueller Matrices

representing these components can be combined into a signal *System Mueller Matrix*. This System Mueller Matrix is formed by multiplying the individual Mueller Matrices from left to right reversing the order in which the element is encountered. In other words, the first element is represented by the right most Mueller Matrix, the second to the left of the first, and so on. This procedure is illustrated as:

$$\underline{\underline{S}}_{out} = (\cdots \underline{\underline{M}}_{second} \underline{\underline{M}}_{first}) \underline{\underline{S}}_{in}$$

$$\underline{\underline{S}}_{out} = \underline{\underline{M}}_{system} \underline{\underline{S}}_{in}$$

This Calculus allows one to determine the change of the polarization state of the light as it transverses the optical system. All that is needed is to know the Mueller Matrix representation for all of the components in the system.

POLARIZATION COMPONENTS

Linear Polarizer:

A Linear Polarizer is a device which transmits only the component of the electric field along its pass axis. In Mueller Calculus a Perfect Linear Polarizer with its pass axis at an angle α, with respect to the horizontal, is given by:

$$LP(\alpha) = \frac{1}{2}\begin{bmatrix} 1 & \cos(2\alpha) & \sin(2\alpha) & 0 \\ \cos(2\alpha) & \cos^2(2\alpha) & \cos(2\alpha)\sin(2\alpha) & 0 \\ \sin(2\alpha) & \cos(2\alpha)\sin(2\alpha) & \sin^2(2\alpha) & 0 \\ 0 & 0 & 0 & 0 \end{bmatrix}$$

Quarter Wave Linear Retarder (QWLR):

A QWLR is a device which has a so called *fast* and *slow* axis. The electric field component oscillating along the fast axis will encounter a negative quarter wave phase shift with respect to the electric field oscillating along the slow axis. The QWLR with its fast axis at an angle β, with respect

to the horizontal, is given by:

$$QWLR(\beta) = \begin{bmatrix} 1 & 0 & 0 & 0 \\ 0 & \cos^2(2\beta) & \sin(2\beta)\cos(2\beta) & -\sin(2\beta) \\ 0 & \sin(2\beta)\cos(2\beta) & \sin^2(2\beta) & \cos(2\beta) \\ 0 & \sin(2\beta) & -\cos(2\beta) & 0 \end{bmatrix}$$

Photoelastic Modulator (PEM):

The PEM is a device which acts as a time varying linear retarder. In this case, a ZnSe crystal is made to mechanically resonate using a piezoelectric driver. As the crystal vibrates the effect is to change the index of refraction with time. This will cause a time dependent retardance between the induced fast and slow axes. The PEM with its fast axis originally at an angle θ, with respect to the horizontal, and having a retardance of δ(t) is given by:

$$PEM(\theta,\delta(t)) = \begin{bmatrix} 1 & 0 & 0 & 0 \\ 0 & \cos^2(2\theta)+\sin^2(2\theta)\cos(\delta(t)) & \sin(2\theta)\cos(2\theta)[1-\cos(\delta(t))] & -\sin(2\theta)\sin(\delta(t)) \\ 0 & \sin(2\theta)\cos(2\theta)[1-\cos(\delta(t))] & \sin^2(2\theta)+\cos^2(2\theta)\cos(\delta(t)) & \cos(2\theta)\sin(\delta(t)) \\ 0 & \sin(2\theta)\sin(\delta(t)) & -\cos(2\theta)\sin(\delta(t)) & \cos(\delta(t)) \end{bmatrix}$$

POLARIMETRIC MEASUREMENT MATRIX

An entire polarization analysis system can be modelled by a complete "Polarimetric Measurement Matrix" (PMM) which takes into account the polarization properties of all components (i.e. lenses, polarizers, retarders, and even the detector). The concept is based on the assumption that all effects occurring are linear optical effects (i.e. independent of the intensity of the light).

If the system is to be operated over a well defined variety of configurations, then six "perfect" polarization states of equal incident amplitude should be prepared. Four of the incident states are linear at orientations of 0, 45, 90, and 135 degrees. The remaining two state are Right and Left circular polarization. For each of the six input polarization states, detected signal measurements are made corresponding to the different system configurations (e.g. a system with five different

configurations will require at least 30 measurement: 5 x 6 = 30).

Once the input polarization states have been generated and the measurements made, a unique "Analyzer Vector" is determined for each system configuration. The Analyzer Vector is given by:

$$\underline{A}_n = \begin{bmatrix} a_0 \\ a_1 \\ a_2 \\ a_3 \end{bmatrix}_n = \begin{bmatrix} P_0 + P_{90} \\ P_0 - P_{90} \\ P_{45} - P_{135} \\ P_R - P_L \end{bmatrix}_n$$

where: P - the response of the system (voltage, current, etc...)

n - the system configuration index

Given any input polarization state, represented by a Stokes Vector, the response of the system for a particular system configuration will be:

$$P_n = \underline{A}_n \bullet \underline{S} = a_{n,0}\, S_0 + a_{n,1}\, S_1 + a_{n,2}\, S_2 + a_{n,3}\, S_3$$

Assuming that the incident Stokes Vector is stationary for the time it takes the system to be measured for all possible configurations, a "Response Vector" and "PMM" can be formed. If there are Q different well defined system configurations, then the PMM relates the incident Stokes Vector to the Response Vector via:

$$\underline{P} = \begin{bmatrix} P_0 \\ P_1 \\ \cdot \\ \cdot \\ \cdot \\ P_{Q-1} \end{bmatrix} = \underline{\underline{W}}\,\underline{S} = \begin{bmatrix} a_{0,0} & a_{0,1} & a_{0,2} & a_{0,3} \\ a_{1,0} & a_{1,1} & a_{1,2} & a_{1,3} \\ \cdot & \cdot & \cdot & \cdot \\ \cdot & \cdot & \cdot & \cdot \\ \cdot & \cdot & \cdot & \cdot \\ a_{Q-1,0} & a_{Q-1,1} & a_{Q-1,2} & a_{Q-1,3} \end{bmatrix} \begin{bmatrix} S_0 \\ S_1 \\ S_2 \\ S_3 \end{bmatrix}$$

Once the PMM ($\underline{\underline{W}}$) has been determined, a least squares pseudoinverse is performed to relate the actual measured response of an arbitrary input polarization state to its corresponding Stokes Vector. The least squares pseudoinverse is given by:

$$\underline{\underline{W}}_p^{-1} = [\,\underline{\underline{W}}^T\,\underline{\underline{W}}\,]^{-1}\,\underline{\underline{W}}^T$$

Therefor the "Measured Stokes Vector" is given by:

$$\underline{S}_m = \underline{\underline{W}}_p^{-1}\,\underline{P}$$

The Measured Stokes Vector may differ from the actually Stokes Vector due to system noise and/or poor calibration.

The beauty of this method is that it allows the determination of an incident Stokes Vector without knowledge of all internal polarization effects. As long as the system is a linear optical system and the PMM can be inverted, the Polarimetric measurement should be successful.

POLARIMETRY SYSTEMS

High Speed Imaging Infrared Linear Polarimeter (HSIILP):

The linear component of polarization is described by the S_1 and S_2 components of the Stokes Vector. These components are defined as: $S_1 = P_0 - P_{90}$ and $S_2 = P_{45} - P_{135}$, where P is representative of the signal value measured on the detector through the indicated polarizer. The normalized linear components are given by $Sn_1 = (P_0 - P_{90})/(P_0 + P_{90})$ and $Sn_2 = (P_{45} - P_{135})/(P_0 + P_{90})$. By using a Quarter Wave Linear Retarder (QWLR), Photoelastic Modulator (PEM), and Linear Polarizer it is possible to measure S_1 and S_2 (see Figure: "High Speed Imaging Infrared Linear Polarimeter").

The general System Matrix of this combination is given by: $SYS = LP(\alpha) \bullet PEM(\theta,\delta(t)) \bullet QWLR(\beta)$. Assuming the PEM has its fast axis at $\theta = 45$ degrees, the Polarizer is rotated at $\alpha = 0$ degrees, and the QWLR is rotated at $\beta = 0$ degrees the System Matrix is given by:

$$SYS(\delta(t)) = \frac{1}{2}\begin{bmatrix}1&1&0&0\\1&1&0&0\\0&0&0&0\\0&0&0&0\end{bmatrix}\begin{bmatrix}1&0&0&0\\0&\cos(\delta(t))&0&-\sin(\delta(t))\\0&0&1&0\\0&\sin(\delta(t))&0&\cos(\delta(t))\end{bmatrix}\begin{bmatrix}1&0&0&0\\0&1&0&0\\0&0&0&1\\0&0&-1&0\end{bmatrix}$$

$$SYS(\delta(t)) = \frac{1}{2}\begin{bmatrix}1&\cos(\delta(t))&\sin(\delta(t))&0\\1&\cos(\delta(t))&\sin(\delta(t))&0\\0&0&0&0\\0&0&0&0\end{bmatrix}$$

The output measured intensity for any general input polarization state is given by:

$$I(t) = \begin{bmatrix}1\\0\\0\\0\end{bmatrix} \cdot \left\{ \frac{1}{2}\begin{bmatrix}1&\cos(\delta(t))&\sin(\delta(t))&0\\1&\cos(\delta(t))&\sin(\delta(t))&0\\0&0&0&0\\0&0&0&0\end{bmatrix} \cdot \begin{bmatrix}S_0\\S_1\\S_2\\S_3\end{bmatrix} \right\}$$

$$I(t) = \frac{1}{2}\begin{bmatrix}1\\0\\0\\0\end{bmatrix} \cdot \begin{bmatrix}S_0 + S_1\cos(\delta(t)) + S_2\sin(\delta(t))\\S_0 + S_1\cos(\delta(t)) + S_2\sin(\delta(t))\\0\\0\end{bmatrix}$$

$$I(t) = \tfrac{1}{2}\left[S_0 + S_1\cos(\delta(t)) + S_2\sin(\delta(t)) \right]$$

The time variation of the retardance of the PEM is given by: $\delta(t) = \delta_0\sin(\omega t)$, where ω is the resonant angular frequency of the PEM and δ_0 is the amplitude of the retardance. The output intensity as a function of time becomes:

$$I(t) = \tfrac{1}{2}\left[S_0 + S_1\cos(\delta_0\sin(\omega t)) + S_2\sin(\delta_0\sin(\omega t)) \right]$$

Using Bessel Function expansions it is possible to write I(t) as a Fourier Series given by:

$$\cos(\delta_0 \sin(\omega t)) = J_0(\delta_0) + 2J_2(\delta_0)\cos(2\omega t) + \ldots$$

$$\sin(\delta_0 \sin(\omega t)) = 2J_1(\delta_0)\sin(\omega t) + 2J_3(\delta_0)\sin(3\omega t) + \ldots$$

$$I(t) = \tfrac{1}{2}\{S_0 + S_1 [J_0(\delta_0) + 2J_2(\delta_0)\cos(2\omega t) + \ldots] + S_2 [2J_1(\delta_0)\sin(\omega t) + \ldots]\}$$

$$I(t) = \frac{a_0}{2} + b_1 \sin(\omega t) + a_2 \cos(2\omega t) + \ldots$$

where the Fourier Transform coefficients are:

$$a_0 = S_0 + S_1 J_0(\delta_0) \quad , \quad b_1 = S_2 J_1(\delta_0) \quad , \quad a_2 = S_1 J_2(\delta_0)$$

The linear Stokes Vector parameters are then determined by:

$$S_0 = a_0 - \frac{J_0(\delta_0)}{J_2(\delta_0)} a_2 \quad , \quad S_1 = \frac{a_2}{J_2(\delta_0)} \quad , \quad S_2 = \frac{b_1}{J_1(\delta_0)}$$

Similarity, the linear Normalized Stokes Vector parameters are determined by:

$$Sn_0 = 1$$

$$Sn_1 = \frac{S_1}{S_0} = \frac{\dfrac{a_2}{J_2(\delta_0)}}{a_0 - \dfrac{J_0(\delta_0)}{J_2(\delta_0)} a_2} = \frac{a_2}{a_0 J_2(\delta_0) - a_2 J_0(\delta_0)}$$

$$Sn_2 = \frac{S_2}{S_0} = \frac{\dfrac{b_1}{J_1(\delta_0)}}{a_0 - \dfrac{J_0(\delta_0)}{J_2(\delta_0)} a_2} = \frac{b_1 J_2(\delta_0)}{J_1(\delta_0)[a_0 J_2(\delta_0) - a_2 J_0(\delta_0)]}$$

In this configuration, the polarimeter is theoretically capable of measuring S_0, S_1, and S_2. The circular component S_3 is undetermined. The Analyzer Vector, for this configuration, must be represented by:

$$\underline{A}_n = \begin{bmatrix} a_0 \\ a_1 \\ a_2 \end{bmatrix}_n = \begin{bmatrix} P_0 + P_{90} \\ P_0 - P_{90} \\ P_{45} - P_{135} \end{bmatrix}_n$$

Therefore, it is only necessary to generate the four linear polarization states. This leads to a Response Vector, PMM, and partial Stokes Vector relationship given by:

$$\underline{P} = \begin{bmatrix} P_0 \\ P_1 \\ \cdot \\ \cdot \\ \cdot \\ P_{Q-1} \end{bmatrix} = \underline{\underline{W}}\,\underline{S} = \begin{bmatrix} a_{0,0} & a_{0,1} & a_{0,2} \\ a_{1,0} & a_{1,1} & a_{1,2} \\ \cdot & \cdot & \cdot \\ \cdot & \cdot & \cdot \\ \cdot & \cdot & \cdot \\ a_{Q-1,0} & a_{Q-1,1} & a_{Q-1,2} \end{bmatrix} \begin{bmatrix} S_0 \\ S_1 \\ S_2 \end{bmatrix}$$

The measured partial Stokes Vector is then determined by the pseudoinverse of $\underline{\underline{W}}$ as given by the PMM method. The procedure would be as follows:

1) Establish the 4 necessary input linear polarization states of equal incident intensity
2) Capture data from each of the 9 detectors using the PEM as a trigger source
   - this is done once for each of the 4 input linear polarization states
3) Construct a PMM and perform the least squares pseudoinverse
4) Use the pseudoinverse matrix to determine the partial Stokes Vector of any source

High Speed Imaging Infrared Circular Polarimeter (HSIICP):

The circular component of polarization is described by the S_3 component of the Stokes Vector. This component is defined as: $S_3 = P_R - P_L$, where P is representative of the signal value measured on the detector through the indicated polarizer. The normalized circular component is given by $Sn_3 = (P_R - P_L) / (P_R + P_L)$. By using a Photoelastic Modulator (PEM) and a Linear Polarizer it is possible to measure Sn_3 (see Figure "High Speed Imaging Infrared Circular Polarimeter").

The general System Matrix of this combination is given by: $SYS = LP(\alpha) \bullet PEM(\theta,\delta(t))$. Assuming the PEM has its fast axis at $\theta = 45$ degrees and the Polarizer is rotated at $\alpha = 0$ degrees,

the System Matrix is given by:

$$SYS(\delta(t)) = \frac{1}{2}\begin{bmatrix} 1 & 1 & 0 & 0 \\ 1 & 1 & 0 & 0 \\ 0 & 0 & 0 & 0 \\ 0 & 0 & 0 & 0 \end{bmatrix}\begin{bmatrix} 1 & 0 & 0 & 0 \\ 0 & \cos(\delta(t)) & 0 & -\sin(\delta(t)) \\ 0 & 0 & 1 & 0 \\ 0 & \sin(\delta(t)) & 0 & \cos(\delta(t)) \end{bmatrix}$$

$$SYS(\delta(t)) = \frac{1}{2}\begin{bmatrix} 1 & 0 & \cos(\delta(t)) & 0 & -\sin(\delta(t)) \\ 1 & 0 & \cos(\delta(t)) & 0 & -\sin(\delta(t)) \\ 0 & 0 & 0 & 0 & \\ 0 & 0 & 0 & 0 & \end{bmatrix}$$

The output measured intensity for any general input polarization state is given by:

$$I(t) = \begin{bmatrix} 1 \\ 0 \\ 0 \\ 0 \end{bmatrix} \cdot \left\{ \frac{1}{2}\begin{bmatrix} 1 & \cos(\delta(t)) & 0 & -\sin(\delta(t)) \\ 1 & \cos(\delta(t)) & 0 & -\sin(\delta(t)) \\ 0 & 0 & 0 & 0 \\ 0 & 0 & 0 & 0 \end{bmatrix} \cdot \begin{bmatrix} S_0 \\ S_1 \\ S_2 \\ S_3 \end{bmatrix} \right\}$$

$$I(t) = \frac{1}{2}\begin{bmatrix} 1 \\ 0 \\ 0 \\ 0 \end{bmatrix} \cdot \begin{bmatrix} S_0 + S_1\cos(\delta(t)) - S_3\sin(\delta(t)) \\ S_0 + S_1\cos(\delta(t)) - S_3\sin(\delta(t)) \\ 0 \\ 0 \end{bmatrix}$$

$$I(t) = \tfrac{1}{2}\left[S_0 + S_1\cos(\delta(t)) - S_3\sin(\delta(t)) \right]$$

Due to the similarity between this and the output for the HSIILP it is obvious that all of the conclusions of the HSIILP section hold for the HSIICP if S_2 is replaced by $-S_3$.

In this configuration, the polarimeter is theoretically capable of measuring S_0, S_1, and S_3. The linear component S_2 is undetermined. The Analyzer Vector, for this configuration, must be represented by:

$$\underline{A}_n = \begin{bmatrix} a_0 \\ a_1 \\ a_3 \end{bmatrix}_n = \begin{bmatrix} P_0 + P_{90} \\ P_0 - P_{90} \\ P_R - P_L \end{bmatrix}_n$$

Therefore, it is only necessary to generate two linear polarization states and two circular polarization states. This leads to a Response Vector, PMM, and partial Stokes Vector relationship given by:

$$\underline{P} = \begin{bmatrix} P_0 \\ P_1 \\ \cdot \\ \cdot \\ \cdot \\ P_{Q-1} \end{bmatrix} = \underline{\underline{W}}\,\underline{S} = \begin{bmatrix} a_{0,0} & a_{0,1} & a_{0,3} \\ a_{1,0} & a_{1,1} & a_{1,3} \\ \cdot & \cdot & \cdot \\ \cdot & \cdot & \cdot \\ \cdot & \cdot & \cdot \\ a_{Q-1,0} & a_{Q-1,1} & a_{Q-1,3} \end{bmatrix} \begin{bmatrix} S_0 \\ S_1 \\ S_3 \end{bmatrix}$$

The measured partial Stokes Vector is then determined by the pseudoinverse of $\underline{\underline{W}}$ as given by the PMM method. The procedure would be as follows:

1) Establish the 4 necessary input polarization states of equal incident intensity
2) Capture data from each of the 9 detectors using the PEM as a trigger source
   - this is done once for each of the 4 input polarization states
3) Construct a PMM and perform the least squares pseudoinverse
4) Use the pseudoinverse matrix to determine the partial Stokes Vector of any source

EXPERIMENTS

Summer Work:

During the course of the summer a number of experiments were performed to attempt to calibrate and prepare the HSIIP to measure polarization signatures. Using available optical components, *known* states of polarization were prepared and subject to measurement. It was quickly observed that the signals recorded did not match those expected from theory. For instance, signals recorded for a 0 degree 100% polarized beam were analyzed and determined to come from a beam

of 30% polarization. Similar effects were observed for other *known* input polarization states. Thus, either the HSIIP system was not operating properly or the initial *"known"* polarization was not correct.

An investigation of each optical component was performed to determine its current condition and usefulness in the HSIIP project. In order to evaluate the available optical components, a well calibrated prism quarter wave linear retarder (QWLR) and a brewster window polarizer were borrowed. It was assumed that these borrowed components were ideal. When the brewster window polarizer was used in conjunction with the original polarizers it was determined that two of the Optics for Research (OFR) polarizers were not properly internally aligned. In fact, using these two OFR polarizers together an extinction ratio of only about 5:1 was observed (Ideally this ratio should be about 100:1). When the prism QWLR was compared to the Cleveland Crystal QWLR under an identical setup there was a noticeable difference in their output (The setup was simply to generate a circular polarization state using the brewster window polarizer and either QWLR). Upon visual inspection of the Cleveland Crystal QWLR it was observed that the interior coatings on the waveplates had begun to severely delaminate. To correct for these problems it was determined necessary to return the QWLR to Cleveland Crystal and to purchase their IR 1600 Polarizer. The IR 1600's purpose would be to generate known polarization states used for the calibration procedure. The IR 1600 Polarizer is specified as having an extinction coefficient of at least 10000:1.

The PEM was observed to modulate the intensity even without any other polarization components (i.e. laser light was detected through the PEM alone). It was determined that the cause of this unwanted modulation was due to the coherence of the laser beam itself. It turns out that as the PEM oscillates its retardance value the front and rear surfaces also oscillate their position with respect to each other. This causes a time varying thickness of the PEM. This changing thickness causes interference effects due to the coherence of the laser. It was determined that it would be advantageous to use a blackbody radiation source for calibrating the system. A Barnes Engineering blackbody source was obtained but it soon failed to operate. The control electronics appeared to be the cause. A Wahl blackbody source was then obtained and was used for the rest of the summer. Using the blackbody source proved to eliminate the unwanted modulation signal caused by the interference of the source (i.e. a blackbody source is incoherent).

The amplification circuitry developed at University of Alabama in Huntsville (UAH) was connected to the detectors. Using the blackbody source it was immediately apparent that there was too much noise associated with the UAH amplifiers. Many steps were taking to eliminate the noise; a battery was used to remove the background 60Hz noise, a single amplifier was individually mounted and any possibility of ground loops was removed, the amplifier was completely shielded from other background sources, and direct BNC type connectors and cables were use to connect from the amplifier board to the detector and to the oscilloscope. Unfortunately, the noise was still too severe to allow for any measurements (i.e. the output modulated signal was only about 100-200 mV and the noise was at least 40 mV). Besides the noise problems it was observed that the output signal drifted too quickly to allow for setup and measurement of the signal. It was finally determined that in their current condition these amplifiers could not be used with the HSIIP system at Eglin AFB.

Efforts to correct the amplifier and optical problems are currently under way. Once these set backs are dealt with it should be possible to calibrate the HSIIP system and prepare to measure polarization signatures.

Future HSIIP work:

To gain familiarity with the HSIIP, a series of measurements of the polarization signatures of simple geometrical configurations can be performed. These experiments could include the polarization of blackbody cavities as a function of direction of emission, reflection of polarized light from smooth and rough surfaces, and blackbody emission from spheres or cylinders. These experiments can be used to verify that the HSIIP is making measurements which conform to theoretical predictions while providing new and important experimental insights into infrared polarization.

Once the HSIIP system is calibrated and successfully predicting polarization signatures of simple geometries, investigations of more complicated geometries can be initiated. These *measured* polarization signatures can be used to help validate current signal prediction codes.

The polarization signatures of natural scenes may possess information which can be used to help distinguish man-made from natural objects. The HSIIP can be used to make these and other measurement which cannot be easily modeled on a computer.

CONCLUSION

The HSIIP is a powerful measurement device which allows for the determination of polarization signatures at a rate of 37 kHz. The polarization signatures can be determined by performing a Fourier analysis of the detected signal or by determining a Polarization Measurement Matrix. Polarization signatures of static as well as rapidly varying scenes can be experimentally measured. Thus, signatures of simple geometries can be measured and compared to theoretical predictions. Furthermore, signatures of more complicated geometries, which can only be modeled on a computer, can also be measured. These signatures can be used to validate signature prediction codes which are a subject of current interest and development.

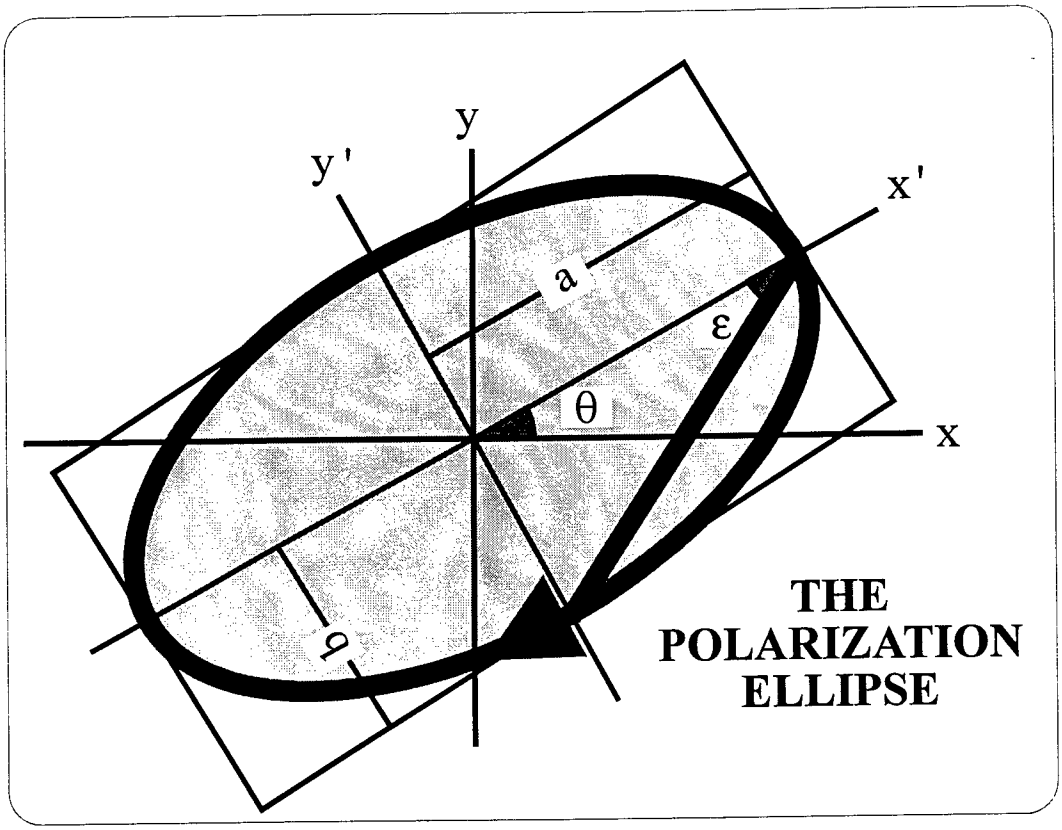
REFERENCES

1). Yariv, A., and P. Yeh, *Optical Waves in Crystals* (Wiley, New York, New York, 1984).

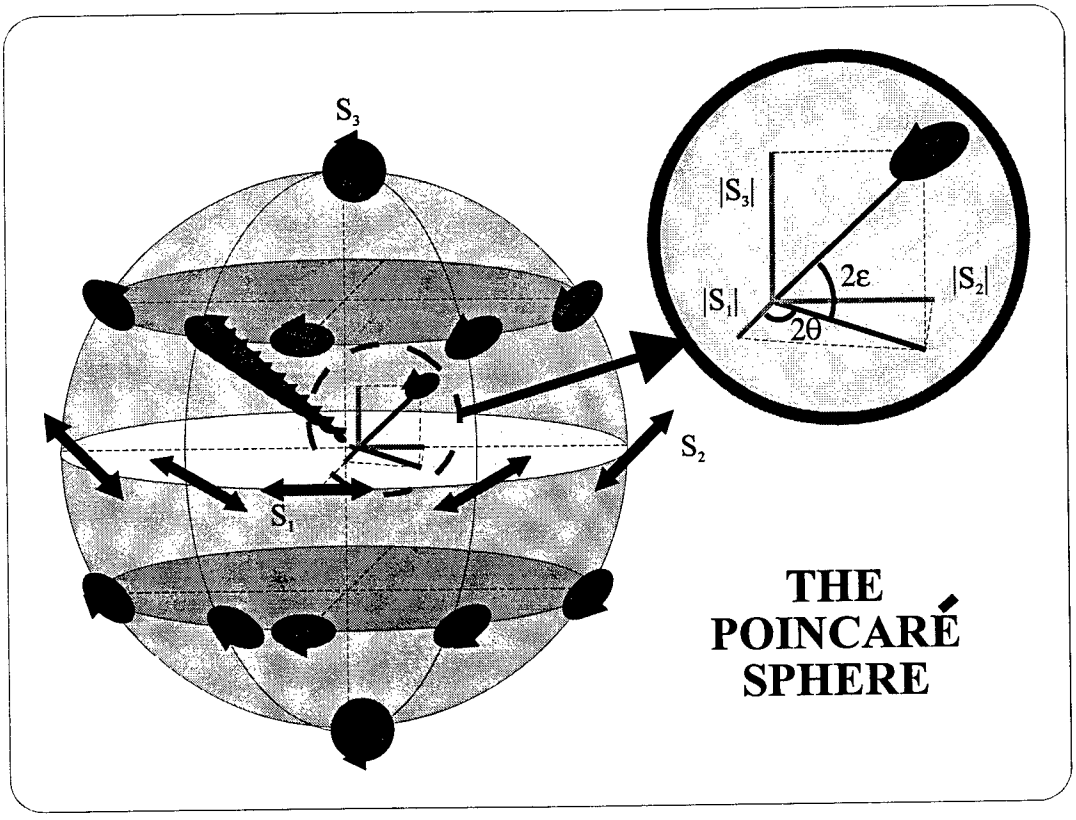
2). Shurcliff, W. A., *Polarized Light* (Harvard University Press, Cambridge, Massachusetts, 1962).

3). Azzam, R. M. A., and N. M. Bashara, *Ellipsometry and Polarized Light*, 1st ed. (Horth-Holland, Amsterdam, 1977).

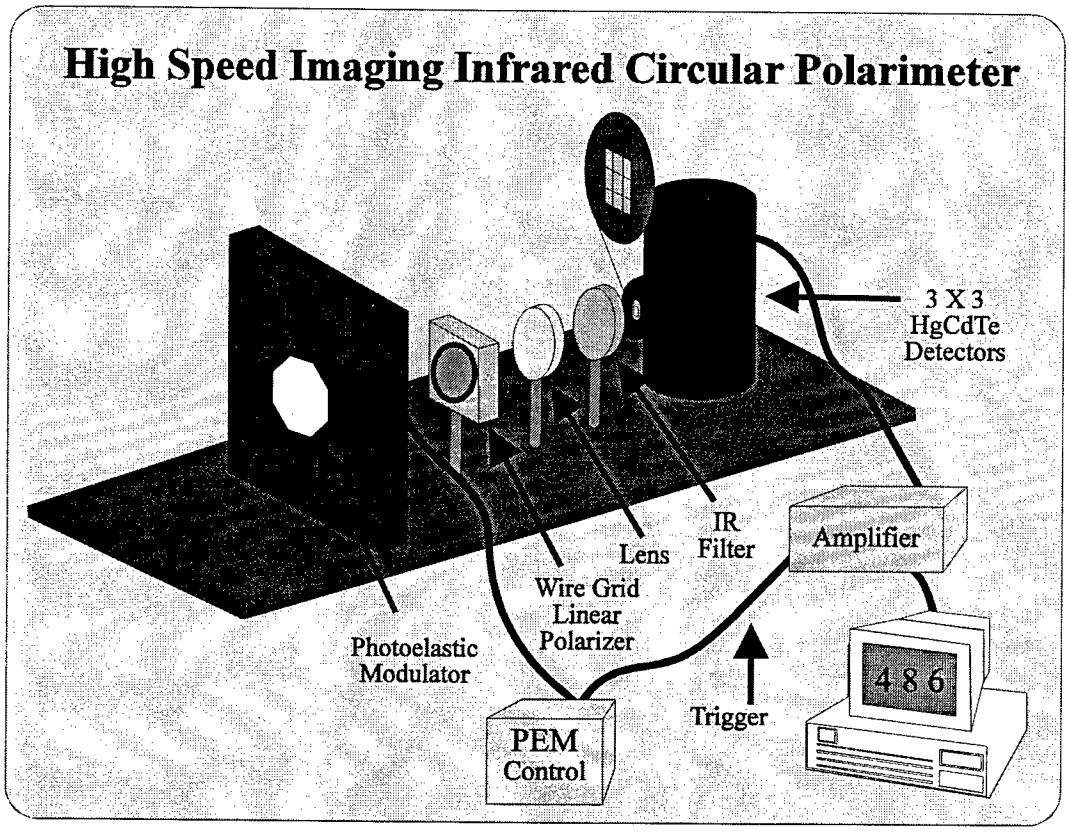
4). Alexander, C., D. Goldstein, R. Chipman, and S. McClain, - private communication.

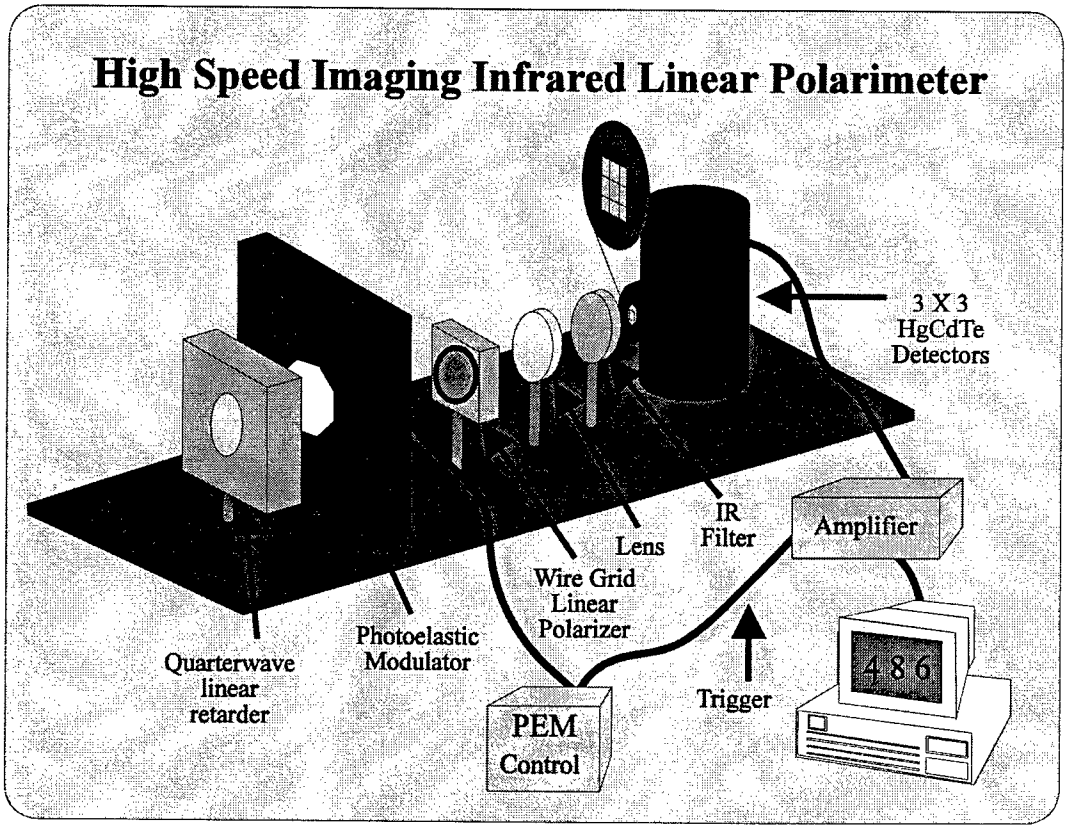


THE POLARIZATION ELLIPSE



THE POINCARÉ SPHERE


High Speed Imaging Infrared Circular Polarimeter
3 X 3
HgCdTe
Detectors
Amplifier
IR
Filter
Lens
Wire Grid
Linear
Polarizer
Photoelastic
Modulator
PEM
Control
Trigger
4 8 6


High Speed Imaging Infrared Linear Polarimeter
3 X 3
HgCdTe
Detectors
Amplifier
IR
Filter
Lens
Wire Grid
Linear
Polarizer
Photoelastic
Modulator
Quarterwave
linear
retarder
PEM
Control
Trigger
4 8 6

FABRICATION AND WHITE-LIGHT CHARACTERIZATION OF ANNEALED PROTON EXCHANGED CHANNEL WAVEGUIDES IN LITHIUM TANTALATE

David B. Maring
Student
Department of Electrical Engineering

University of Florida
Gainesville, FL 32611

Final Report for:
Summer Graduate Research Program
Wright Laboratory

Sponsored by:
Air Force Office of Scientific Research
Bolling Air Force Base, DC

and

Wright Laboratory

September 1994

FABRICATION AND WHITE-LIGHT CHARACTERIZATION OF ANNEALED PROTON EXCHANGED CHANNEL WAVEGUIDES IN LITHIUM TANTALATE

David B. Maring
Student
Department of Electrical Engineering
University of Florida

Abstract

The conditions for the fabrication of single mode channel waveguides in lithium tantalate at 1.31μm are given, followed by a characterization of the guides using a white light source in order to accurately define the regions of cutoff and modal operation. Channel waveguides were implanted in a z-cut lithium tantalate substrate by the Annealed Proton Exchange technique. Single mode operation at 1.31μm was verified for guides of mask widths 3.5μm to 8μm by exciting them from a laser source and focusing the output onto an IR camera. Waveguides of widths 2μm to 10μm were then excited from a white light source and their output power measured as a function of wavelength from 870nm to 1700nm. From these plots, a single graph was constructed giving the value of cutoff wavelength versus channel mask width for the fundamental through fourth order modes. Near-field profile measurements were also made on various guides at 0.890μm and 1.31μm.

FABRICATION AND WHITE-LIGHT CHARACTERIZATION OF ANNEALED PROTON EXCHANGED CHANNEL WAVEGUIDES IN LITHIUM TANTALATE

David B. Maring

Introduction

Channel waveguides are produced by creating an area of higher refractive index in a dielectric substrate material. Unlike planar waveguides, channel waveguides confine the optical wave in two directions. Most processes result in a roughly semi-elliptical, graded-index guide that decreases monotonically from the substrate surface [1]. Such a guide is illustrated in Fig. 1, where the propagation direction of the optical wave is also shown. These waveguides form the basis for the construction of such devices as amplitude modulators used in communications systems, high-speed optical switchers, non-linear frequency doublers, and several other integrated optical devices.

Recently, the most common ferroelectric materials used as substrates for the production of channel waveguides are Lithium Niobate ($LiNbO_3$) and Lithium Tantalate ($LiTaO_3$), which is isomorphous to $LiNbO_3$. Though much research has been performed and reported on the fabrication, characterization, and modeling of channel waveguides in $LiNbO_3$, $LiTaO_3$ has proven to be advantageous over $LiNbO_3$. $LiTaO_3$ has been shown to be harder and demonstrate a threshold for optical damage which is two to three times higher than that of $LiNbO_3$ [2,3,8]. $LiTaO_3$ also exhibits an improved photorefractive resistance, resulting in better stability of power transmission in the guide [3,5,6]. A large nonlinear coefficient combined with $LiTaO_3$'s much lower waveguide propagation loss also make it ideal for the generation of blue light by QPM-SHG, capable of output power levels far exceeding those of $LiNbO_3$ [11,14].

The process of creating waveguides in the substrate by forming an area of higher refractive index can be achieved in several ways, the most popular of which are by diffusion of Ti into the substrate surface at high temperatures, or by exchanging Li^+ ions in the substrate with H^+ ions supplied by an acid source (proton exchange method) [1]. As was discovered by Jackel, Rice and Veselka in 1982, this proton exchange (PE) process results in a large increase in the extraordinary refractive index n_e of $LiNbO_3$ [12]. The technique was later shown to also be effective in forming waveguides in $LiTaO_3$ by Spillman, Sanford, and Soref in 1983 [2]. Like in $LiNbO_3$, PE in $LiTaO_3$ only increases the extraordinary index [15]. Though the PE process initially causes a reduction of the electro-optic effect, the r_{33} coefficient can be completely recovered through post-exchange annealing of the substrate [13,15]. This entire process is referred to as the Annealed Proton Exchange (APE) technique. Annealing also causes further diffusion of the H^+ ions into the substrate after exchange, increasing the area of the guide and decreasing the losses in the guide [9].

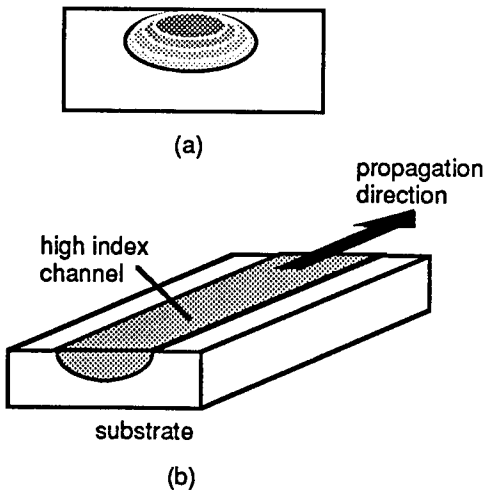


Fig.1. Channel waveguide.

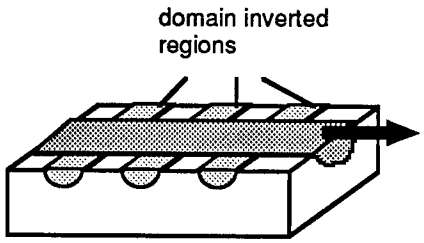


Fig.2. Channel waveguide laid across regions of domain inversion.

In the case of $LiTaO_3$, though its index increment Δn_e has been shown to be less than that of $LiNbO_3$ after proton exchange, annealing causes an additional increase in the surface index n_e for $LiTaO_3$, compared to a decrease in n_e for $LiNbO_3$ [13,15,16].

The APE technique is among the most common for fabricating channel waveguides in $LiTaO_3$ since it is also one of the few methods used to produce regions of domain inversion in $LiTaO_3$. Domain inversion is frequently required in the fabrication of integrated optical devices such as modulators and in nonlinear optical applications, like blue light generation by frequency doubling of infrared, where phase matching is required [7,15]. For this case, the APE process is done on the c^- surface of $LiTaO_3$ (as opposed to the c^+ surface for $LiNbO_3$) since domain inversion can only be achieved on the c^- surface [7,8]. When using patterns of domain inversion such as in QPM, the waveguides are patterned on top of the existing inverted regions, perpendicular to them as in Fig. 2. Since proton exchange and post-exchange annealing for waveguide fabrication can be done at temperatures well below 450°C, they do not affect the existing inverted regions which have also been created by APE but annealed at temperatures near the Curie temperature of about 600°C [4,10].

The exchange portion of the APE process is depicted in Fig. 3. The substrate is first covered by a metal masking layer (usually Al or Ta), in which narrow stripe patterns are delineated, exposing the substrate where the exchange is to take place. The substrate is then immersed in a hot melt of high H^+ concentration, usually benzoic or pyrophosphoric acid, where Li^+ diffuses out and is

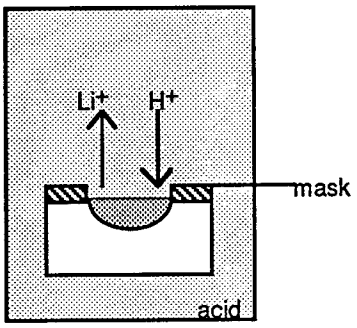


Fig.3. Proton exchange process.

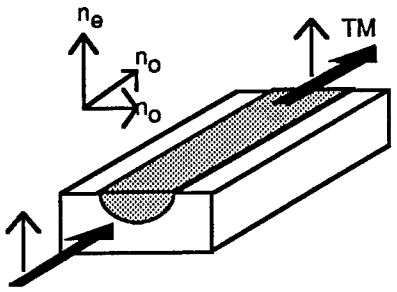


Fig.4. TM polarization due to increase in extraordinary index only.

replaced by H^+ from the source. Pyrophosphoric acid is normally preferred as the H^+ source because it results in an increase of the extraordinary Δn_e which is 15% higher than what is attainable with benzoic acid [9]. In addition, pyrophosphoric acid has no boiling (it is liquid up to 300°C) and a low vapor pressure, allowing work at high temperatures where diffusion is rapid and with more control over diffusion depth than is possible with benzoic acid [17]. However, when using pyrophosphoric acid, Ta must be used as the mask since the pyrophosphoric acid will attack an Al mask.

In the fabrication of integrated optical components incorporating channel waveguides, it is often necessary to accurately ensure single mode, or a higher order mode, region of operation in order to guarantee proper device performance. As a result, it is important to be able to fabricate channel waveguides where the regions of single mode, single mode cutoff, and double mode operation are known. This paper presents the conditions for the fabrication of channel waveguides in $LiTaO_3$ with the aim of single mode operation at 1.31μm. Single mode characterization is initially checked at 1.31μm by coupling into various width guides from a single mode fiber and focusing the output onto an IR camera while observing the mode pattern on a monitor. A more accurate characterization is then performed by exciting the waveguides with a white light source and plotting the transmitted power as a function of wavelength from 870nm to 1700nm. From this data, a graph is constructed displaying the cutoff wavelength as a function of channel mask width for the fundamental through fourth order modes. In addition, the near field profiles of various guides are measured at 0.890μm and 1.31μm, the data from which could be combined with the data for the wavelength region of modal cutoff taken previously to further model the refractive index profile in the guiding region.

Fabrication

Using the APE technique, single mode channel waveguides were fabricated on the c^- surface of a z-cut $LiTaO_3$ substrate purchased from Crystal Technology, Inc. As seen in Fig. 4, only the TM polarization is sustained.

The c^+ and c^- surfaces of the raw crystal were identified by taking advantage of the piezoelectric effect of the ferroelectric substrate. Fig. 5 demonstrates how a voltmeter was used to quickly press down and release on the surface of the substrate. Because of the internal field set up by the polarization of the crystal, free charges exist on the surfaces to counteract this field and maintain electrical neutrality. For example, the c^+ and c^- surfaces have negative and positive free surface charges, respectively. By rapidly pressing on the crystal and releasing, the internal field due to polarization is momentarily reduced and the voltmeter can read the potential due to the now unbalanced surface charges, so the individual positive and negative surfaces can be quickly identified. The substrate was then cut into several smaller pieces where y-propagating waveguides could be implanted. These samples were then annealed at 200°C for 1 hour, to help relieve stresses incurred during cutting.

Samples were subjected to the standard photolithographic process. After pre-baking at 120°C for 5 minutes, Microposit S-1400-23 photo resist (PR) was spun on the c^- surface at 4000 rpm for 35 seconds, after which it was baked at 100°C for 35 minutes. This resulted in a measured PR thickness of 920nm. Each substrate was then covered with a clear-field mask containing waveguide patterns of widths ranging from 1μm to 10μm, in 0.5μm intervals and running parallel to the y-direction. Upon a 3 second exposure to ultraviolet (UV) light, the samples were then held in Microposit MF-319 developer for 50 seconds, whereby the areas of PR not covered by the mask guide patterns, and hence exposed to the UV, were removed. A Ta mask was sputtered on at a thickness of 120nm and the substrates were then cleaned in acetone to lift off the remaining PR and leave a sample which was ready for the proton exchange, as was depicted in Fig. 3. The entire process up through lift-off is illustrated in Fig. 6.

Proton exchange was performed in a horizontal furnace using pyrophosphoric acid at 260°C for a period of 18 minutes. Each sample and the acid source were heated from room temperature to 260°C in 36 minutes before the sample was immersed in the acid for a duration of 18 minutes. After the 18 minutes, the sample was removed from the acid and allowed to cool to room temperature slowly, in order to reduce thermal strain. Each sample was exchanged independently and new acid was used each time.

Once cooled, the samples were washed in deionized water to remove the remaining acid and the Ta mask was etched off using a Ta etchant consisting of hydrofluoric and nitric acids. The samples were next annealed at 300°C for 30 minutes in a horizontal furnace. This time does not

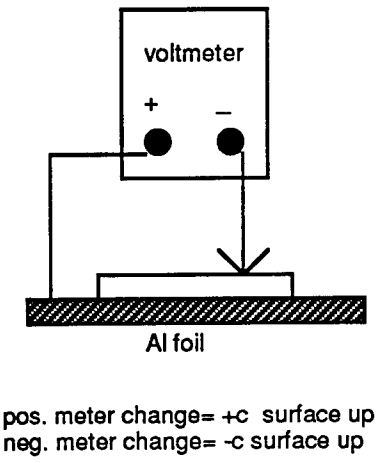


Fig.5.

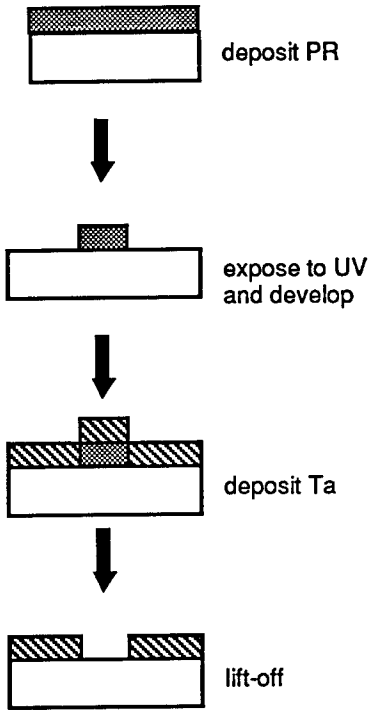


Fig.6. Fabrication process up through lift-off.

include the 30 minute rise and fall durations. As a final step, the end faces of each sample were lapped and polished with 1μm diamond paste for end-fire coupling and characterization.

Experiment

Light from a 1.31μm diode laser was coupled into each of the channel waveguides as illustrated in Fig. 7. The output was focused with a x20 objective lens onto an IR camera where the mode field could be observed on a monitor. By observation, single mode propagation was obtained for waveguide widths of the range 3.5μm to 8μm. Guides below 3.5μm allowed no propagation, whereas guides of widths above 8μm permitted the propagation of two modes, denoted by two adjacent spots on the monitor.

While this characterization procedure gives an idea of the region of single mode operation, often times much more accuracy is desired as to the exact value of cutoff wavelength for a mode as well as accurately defined regions of single and double mode operation. To obtain these results, each of the waveguides was excited by a white light source and the transmitted power was

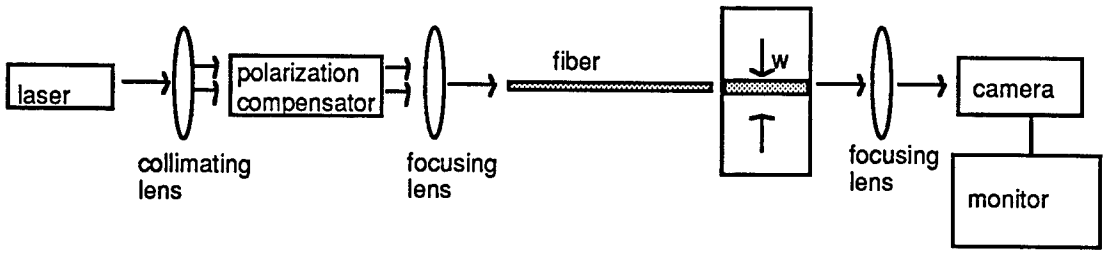


Fig.7. Experimental set-up for initial characterization of channel waveguides.

measured as a function of wavelength. This process was greatly simplified with the aid of a Hewlett Packard HP71451A Optical Spectrum Analyzer (OSA). The experimental setup is given in Fig. 8. White light from a Tungsten Halogen Lamp inside the OSA is coupled into each guide via a single mode fiber and index matching fluid (1.52). The guide output is coupled with a multi mode fiber and index matching fluid (1.52) and sent into the monochromator input of the OSA. The transmitted power is scanned over the wavelength range 870nm to 1700nm with a resolution bandwidth of 10nm. Each scan is simultaneously normalized to a calibration trace, defined previous to guide measurements by butt-coupling the single and multi mode fibers together, and averaged over 50 traces to reduce noise and error. Fig. 9 shows the resulting scans for various width guides.

In order to better understand the data presented, examine the scan for the 6μm guide, Fig. 10. It is seen that up to three modes can be present at lower wavelengths in this guide, with the

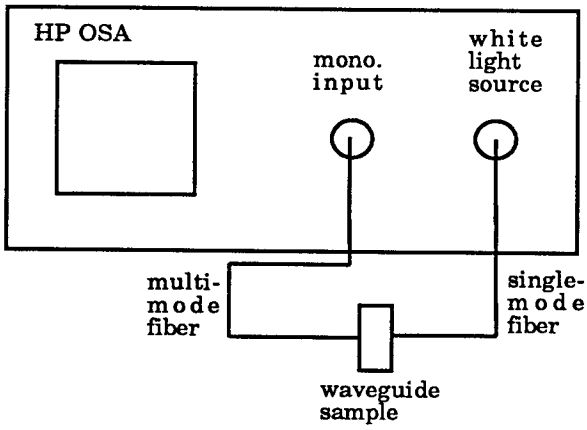


Fig.8. Set-up for measuring optical power transmission as a function of wavelength.

fundamental mode being the right-most peak. For this width guide, the exact region of single mode, double mode, triple mode, or cutoff for any of these modes can be accurately defined in terms of wavelength. As can be seen from the traces of Fig. 9, when the waveguide width is increased, the trace pattern shifts to the right since the cutoff value for the modes increases, eventually allowing more modes to propagate. For the data presented here, cutoff was defined as the point 3dB below the peak value for each of the modes. With this definition in mind, the data from the scans of all width guides, 2-10μm, can be combined to create one very useful chart, Fig. 11. This figure gives the cutoff wavelength, as defined above, as a function of channel waveguide mask width for the fundamental through fourth order modes. From this chart, a channel waveguide width can be determined at a given frequency, for a desired region of modal operation.

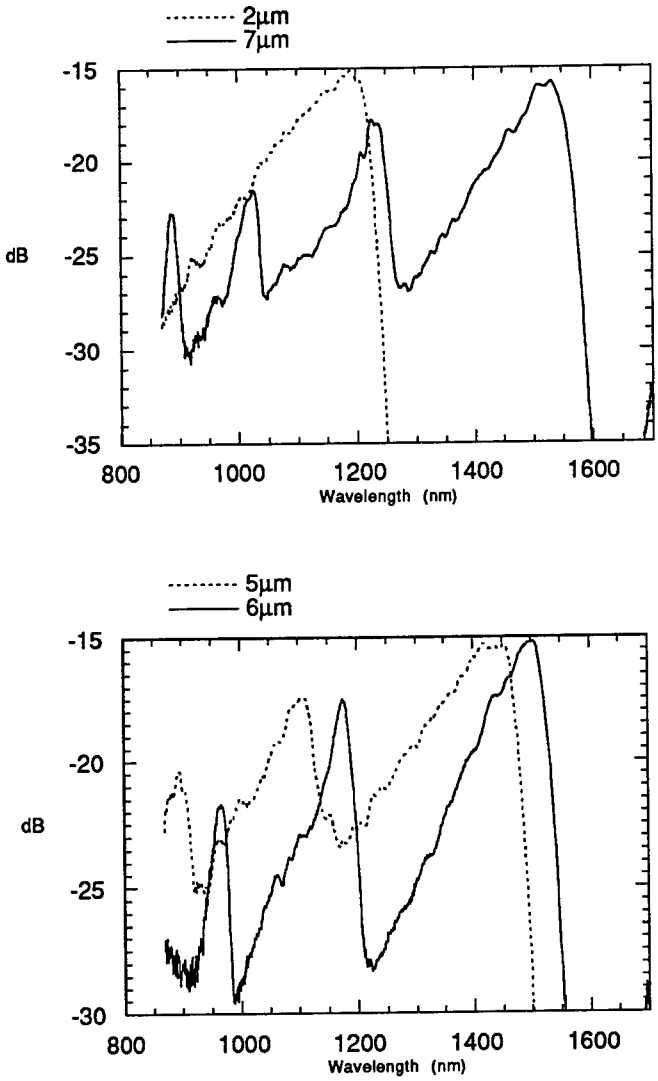


Fig.9. Scans of optical power transmission as a function of wavelength for various width guides excited by a white light source.

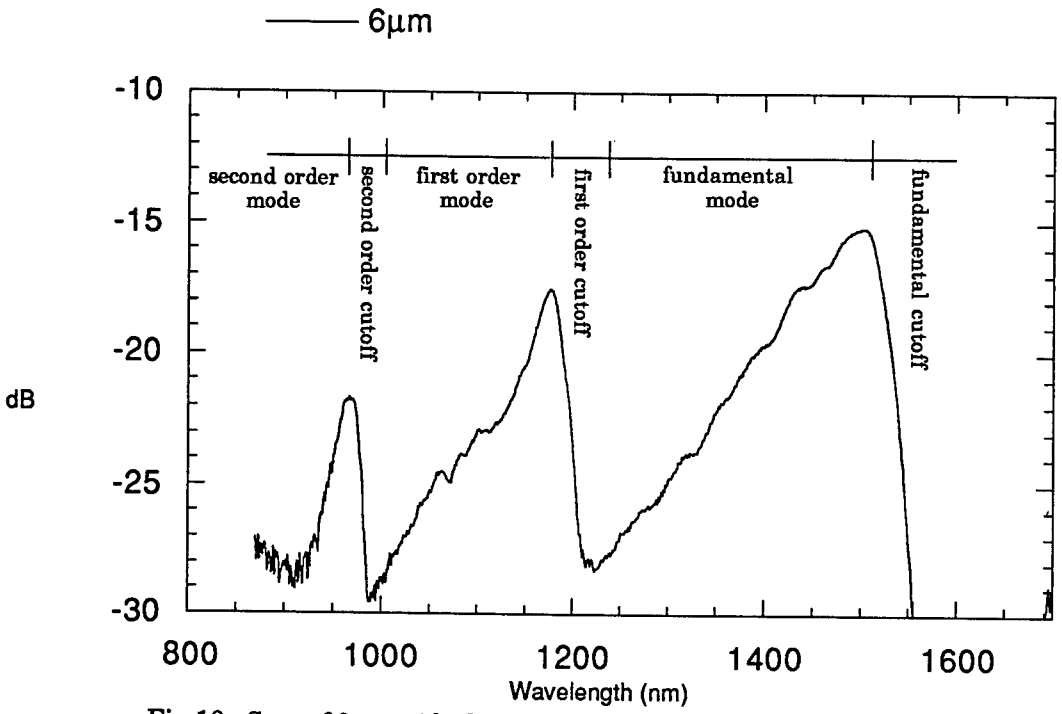


Fig.10. Scan of 6μm guide that indicates the regions of cutoff and modal operation.

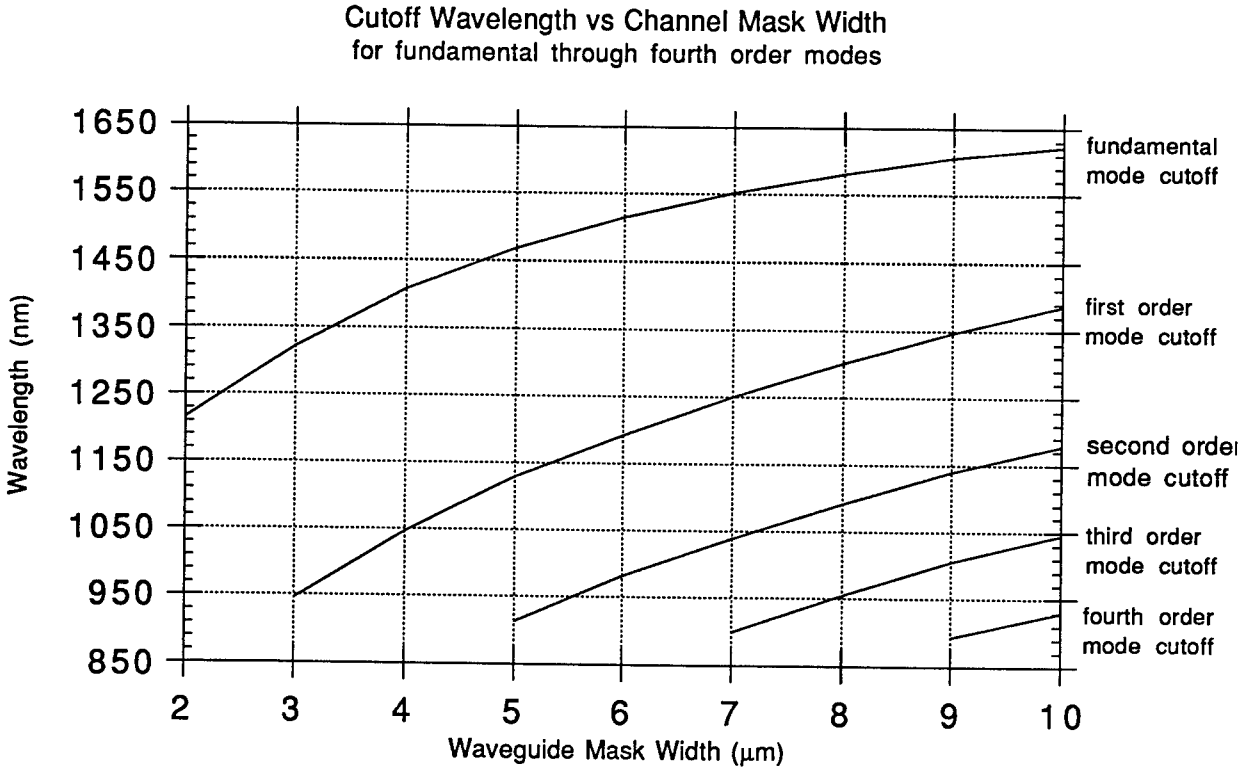


Fig.11. Cutoff wavelengths for each mode as a function of channel mask width.

The experimental setup for the near-field mode profile measurements of the channel waveguides is given in Fig. 12. Laser sources of 0.890μm and 1.31μm were coupled to the guides via a single mode fiber and the guide output profile was focused onto the image plane of a Ge detector mounted on an X-Y micropositioning translation stage. The Ge detector, and accompanying 10μm pinhole, scanned the profile image in the horizontal and vertical directions while simultaneously sending the corresponding data to a computer where it was plotted as a function of stage position. A chopper and lock-in amplifier were added to improve the signal-to-noise ratio. The resulting scan was converted, by a magnification factor, to represent the profile versus width and depth of each guide. Fig. 13 depicts the resulting profile scans of the 2μm and 5μm wide guides at 0.890μm and 1.31μm, respectively. The data obtained from these plots can be used in conjunction with the data for cutoff wavelength of the same guides, found earlier, to further model the channel waveguides by reconstructing the refractive index distribution in the depth and width directions of the guide. Research in this direction is continuing.

Conclusion

The conditions for the fabrication of single mode channel waveguides in lithium tantalate were presented. Channel waveguides of widths 2μm to 10μm were implanted on the c^- surface of a z-cut substrate by the Annealed Proton Exchange technique. Single mode operation was initially verified at 1.31μm by exciting individual guides and focusing the guide output onto an IR camera where the mode pattern could be observed on a monitor. By observation, guides of widths 3.5μm to 8μm were found to be single mode whereas guides of widths below this region showed no propagation and guides above this region propagated two modes. A more accurate characterization was then performed by exciting each of the waveguides with a white light source and measuring the transmitted power as a function of channel mask width over the range 870nm to 1700nm. These

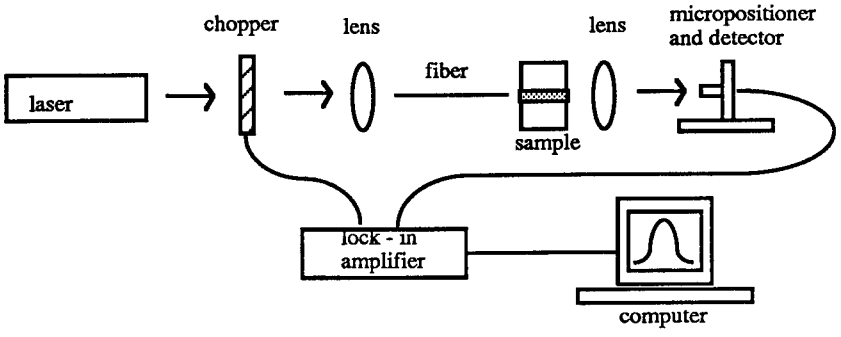


Fig.12. Experimental set-up for near-field mode profile measurement.

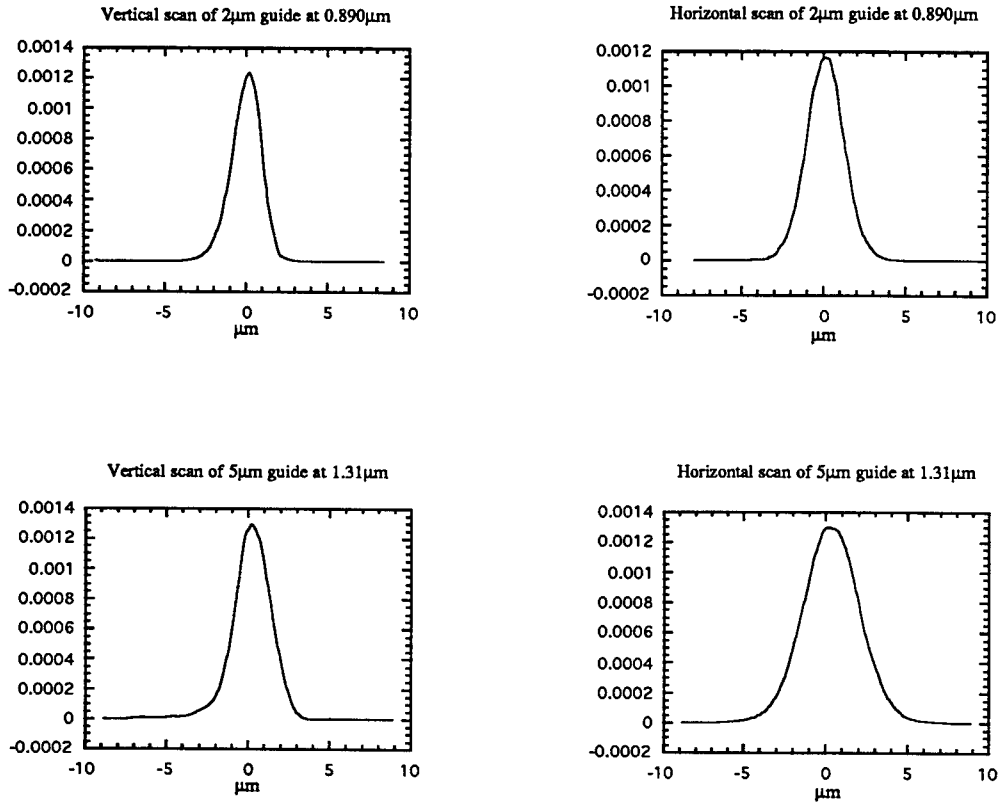


Fig.13. Near-field profiles for various guides at 0.890μm and 1.31μm.

plots accurately defined the wavelength region of cutoff and modal operation for each of the guide widths. As was observed, at 1.31μm these plots detailed the same range of mask width to obtain single mode operation as was found by previous examination of the guides using an IR camera and monitor. The data from the individual scans of all the guides was combined into one chart defining the value of cutoff wavelength as a function of channel mask width for the fundamental through fourth order modes. This chart simplifies the determination of required channel mask width at a given wavelength, for a desired region of modal operation.

Near-field profile measurements were also performed on various width guides at 0.890μm and 1.31μm. The data collected from these measurements can be combined with the previously collected data to model these channel waveguides by reconstructing their refractive index profiles. Such a technique would be simpler than current conventional methods and research on this subject will be continued.

References

[1] R. Syms and J. Cozens, *"Optical Guided Waves and Devices"*, McGraw-Hill Pub., London, 1992.

[2] W. B. Spillman, Jr., N. A. Sanford, and R. A. Soref, "Optical waveguides in $LiTaO_3$ formed by proton exchange", *Opt. Lett.*, vol. 8, no. 9, p. 497, Sept. 1983.

[3] K. Mizuuchi, K. Yamamoto, and T. Taniuchi, "Blue-light generation by quasi-phase-matched second-harmonic generaton in $LiTaO_3$", *CLEO,* 1991, p. 164, CTuV3.

[4] T. Findakly, P. Suchoski, and F. Leonberger, "High-quality $LiTaO_3$ integrated-optical waveguides and devices fabricated by the annealed-proton-exchange technique", *Opt. Lett.*, vol. 13, no. 9, p. 797, Sept. 1988.

[5] W. K. Burns, M. McWright Howerton, and R. P. Moeller, "Performance and Modeling of Proton Exchanged $LiTaO_3$ Branching Modulators", *J. Lightwave Technol.*, vol. 10, no. 10, p. 1403, Oct. 1992.

[6] M. McWright Howerton and W. K. Burns, "Photorefractive effects in proton exchanged $LiTaO_3$ optical waveguides", *J. Lightwave Technol.*, vol. 10, no. 2, p. 142, Feb. 1992.

[7] K. Nakamura and H. Shimizu, "Ferroelectric inversion layers formed by heat treatment of proton-exchanged $LiTaO_3$", *Appl. Phys. Lett.* **56** (16), p. 1535, April 1990.

[8] I. Sawaki and S. Kurimura, "Second-harmonic generation in periodically domain-inverted lithium tantalate channel waveguides", *CLEO,* 1991, p. 166, CTuV4.

[9] D. Kan and G. L. Yip, "Annealed proton-exchanged lithium tantalate waveguides fabricated in concentrated and diluted pyrophosphoric acid", *GRIN,* 1994.

[10] K. Mizuuchi and K. Yamamoto, "Domain inversion in $LiTaO_3$ using proton exchange followed by heat treatment", *J. Appl. Phys.* **75** (3), p. 1311, Feb. 1994.

[11] K. Yamamoto, K. Mizuuchi, K. Takeshige, Y. Sasai, and T. Taniuchi, "Characteristics of periodically domain-inverted $LiNbO_3$ and $LiTaO_3$ waveguides for second harmonic generation", *J. Appl. Phys.* **70** (4), p. 1947, Aug. 1991.

[12] J. L. Jackel, C. E. Rice, and J. J. Vesselka, "Proton-exchange for high index waveguides in $LiNbO_3$", *Appl. Phys. Lett.* **41**, p. 607, 1982.

[13] T. Yuhara, K. Tada, and Y. S. Li, "Anomalous refractive index change and recovery of electro-optic coefficient r_{33} in proton-exchanged $LiTaO_3$ optical waveguides after annealing", *J. Appl. Phys.* **71** (8), p. 3966, April 1992.

[14] K. Yamamoto and K. Mizuuchi, "Blue-Light Generation by Frequency Doubling of a Laser Diode in a Periodically Domain-Inverted $LiTaO_3$ Waveguide", *Photon. Tech. Lett.*, vol. 4, no. 5, p. 435, May 1992.

[15] H. Åhlfeldt, J. Webjörn, F. Laurell, and G. Arvidsson, "Postfabrication changes and dependence on hydrogen concentration of the refractive index of proton-exchanged lithium tantalate waveguides", *J. Appl. Phys.* **75** (2), p. 717, Jan. 1994.

[16] P. Matthews and A. Mickelson, "Properties of proton exchange waveguides in lithium tantalate", *J. Appl. Phys.* **72** (7), p. 2562, Oct. 1992.

[17] K. Mizuuchi and K. Yamamoto, "Characteristics of periodically domain-inverted $LiTaO_3$", *J. Appl. Phys.* **72** (11), p. 5061, Dec. 1992.

SCANNING IMAGE ALGEBRA NETWORKS FOR VEHICLE IDENTIFICATION

Paul Gader, Assistant Professor
Joseph R. Miramonti, Graduate Research Assistant
Department of Electrical and Computer Engineering
University of Missouri - Columbia
Columbia, MO 65211

Final Report for:
Summer Faculty Research Program
Armament Directorate, Wright Laboratory
Eglin Air Force Base

Sponsored by:
Air Force Office of Scientific Research
Bolling Air Force Base, DC

and

Armament Directorate, Wright Laboratory
Eglin Air Force Base

August 1994

Scanning Image Algebra Networks for Vehicle Identification

Paul Gader, Assistant Professor
Joseph R. Miramonti, Graduate Research Assistant
Department of Electrical and Computer Engineering
University of Missouri - Columbia
Columbia, MO 65211

ABSTRACT

Digital image analysis techniques for identifying vehicles in complex scenes were studied. Neural networks that learn image algebra operations for feature extraction and classification simultaneously were applied to the problems of detecting tanks in Infrared (IR) imagery and Chevrolet Blazers in visible imagery. Results on the tanks reconfirmed earlier results with different networks that show networks are capable of generalizing from a much smaller set of examples than matched filters. The Blazers were in parking lots filled with a variety of vehicles. Several test Blazers were in the lot at a variety of ranges, aspects, and depression angles. Empirical results show that the image algebra networks can store a variety of representations of Blazers, including range, aspect and plane rotation angles. In addition, the networks exhibited the capability of generalizing to Blazers with different paint and options in some cases and could detect partially occluded Blazers. Further research is required to suppress network output on complex backgrounds.

Scanning Image Algebra Networks for Vehicle Identification

Paul Gader and Joseph R. Miramonti

I. INTRODUCTION

This report describes the results of experiments in which Image Algebra networks were applied to the problem of vehicle identification in digital images. The general problem can be stated as follows: Given a digital image of a scene that may or may not contain one or more vehicles of a certain type, indicate the location of each vehicle of that type in the scene. The vehicles in the scenes can be at a variety of aspect, depression, and plane rotation angles and ranges, can be occluded, can have a variety of paints, and can have various accessories attached. In addition, there may be vehicles in the scenes that are very similar to the vehicles sought but which are different.

We considered two types of vehicles: tanks and Chevrolet Blazers. In the first set of experiments, infrared images of tanks were used. Each image contained one vehicle. Image algebra networks were trained on a subset of the images and applied to all images with 100% success in confidently locating the tanks in the images. In the second set of experiments, much more complex visible images were used. The images consisted of scenes of a parking lot which was filled with vehicles. There were three different Blazers that appeared in the image set. One particular Blazer was used to train a variety of Image Algebra networks. The Image Algebra networks were able to find the particular Blazer at a variety of ranges that differed from the training set, at aspect angles that differed by as much as approximately 45° from those found in the training set, and which were partially occluded. The networks had difficulty generalizing to other Blazers but exhibited some capability of doing so. The difficulty lies in the fact that several vehicle types look extremely similar to Blazers and suppression of output on these vehicle types leads to suppression of output on Blazers that look different from the training Blazer.

An Image Algebra network is a variation of a multilayer feedforward neural network that learns feature extraction and classification operations simultaneously. The feature extraction operations are represented using generalized image algebra operations. The classification is performed using standard, feedforward multilayer neural networks. The Image Algebra network structure has roots in many places[1-11]. Le Cun et al at ATT [1] used the shared weight concept, also discussed in [12], to design feedforward neural networks that combine linear feature extraction and classification. In the case of linear feature extraction, our networks are also shared weight networks. Krishnapuram and Lee have used operations that range from below min to above max to learn generalized fuzzy set operations for pattern classification[13]. Yuille et. al. used a similar idea to design linear or morphological operations depending on the choice of parameters[14]. Our networks incorporate all of these notions into a network structure that can learn both linear and morphological operations [15 - 17].

Many researchers are considering the problems of vehicle identification for automatic target recognition. One popular approach is the matched filter. Several impressive studies have been done utilizing a variety of design methodologies [18 - 21]. Theoretically, a multilayer feedforward neural network can form more complex decision boundaries than matched filters and can therefore solve more complex pattern recognition problems. We have

previously shown empirically that neural networks can successfully generalize from a significantly smaller set of examples than a MACE type matched filter [20, 22]. Thus, neural network have several good properties with respect to vehicle identification. It is possible that several matched filters can achieve the same level of performance as the multilayer neural network for a lower computational cost, either due to optical implementations or to efficient digital implementations. A thorough comparison of well developed methodologies utilizing each approach on standard data sets would be useful.

Several authors have applied neural networks to target recognition, cf. [23]. Image Algebra networks have been successfully applied to character recognition and chromosome recognition problems. The results have been good in both cases. In the case of handwritten digit recognition, the classification rates computed from several thousands of test images were in the 96% - 98% range [17]. These rates are at the state of the art. In the case of chromosome recognition, the classification rates were also high, around 89%. The approach taken for vehicle identification in this study differs from these other applications in some respects. In both chromosome and character recognition, there are a large number of classes (e.g. 24 chromosome classes or anywhere from 10 to 62 character classes). Also, the characters and chromosomes were segmented from the background whereas we are not segmenting the vehicles from the background.

In section II, we describe Image Algebra networks. Following that, we describe our experimental approach. Finally, we present some results and observations from the experiments.

II. IMAGE ALGEBRA NETWORKS

Operations and Properties

Let $X \subseteq Z$ or $Z \times Z$ be a coordinate set, where Z = set of integers and F be a value set (such as the integers or reals). An image on X with values in F is a function $a : X \to F$. We denote the set of such images as F^X. A template on X is a function $t : X \to F^X$. For $x,y \in X$, we write t_y for t(y). Thus, t_y denotes an image on X and $t_y(x)$ denotes the value of the image at the location x. A template is called translation invariant if $t_y(x) = t_{\phi(y)}(\phi(x))$ for all translations ϕ with $\phi(y)$, $\phi(x)$, $x, y \in X$. The supports S_0, S_∞ , $S_{-\infty}$ are defined by $S_i(t_y) = \{ x \in X : t_y(x) \neq i \}$ $i = 0, \infty, -\infty$. If t is a template, then t* is the template defined by $t^*_y(x) = -t_y(-x)$.

The standard operations of image algebra, $\oplus$, $\boxed{\vee}$, and $\boxed{\wedge}$ are defined in [15 - 17, 24]. The $\oplus$ operation represents all linear operations. In the translation invariant case, the other operations are related to the standard gray-level morphological operations as follows: $b = a \boxed{\vee} t$ represents the dilation of a by the structuring element t and $b = a \boxed{\wedge} t$ represents the erosion of a by the structuring element t^*.

We define a hit-or-miss transform for gray-scale morphological operations as follows: Let a be an image on X and let h and m be structuring elements on X. Let b = (h,m). The hit-or-miss transform is

$$a \otimes b = a \otimes (h, m) \equiv a \boxed{\wedge} h - a \boxed{\vee} m^* .$$

This definition is motivated by the umbra transform and is fully described in [17].

We also define three generalized operations used in an Image Algebra network: weighted erosion, weighted dilation, and weighted hit-or-miss transform. For these operations, we require that F = [0,1]. Let r(x) be a non-decreasing, real-valued function defined for all real numbers with values in F = [0,1]. We define operations $\boxed{\vee}_r$ and $\boxed{\wedge}_r$ by b = a $\boxed{\wedge}_r$ t where

$$b(y) = \bigwedge_{S_1(t_y)} r[a(x) - t_y(x)]$$

and b = a $\boxed{\vee}_r$ t where

$$b(y) = \bigvee_{S_1(t_y)} r[\, a(x) + t_y(x)\,].$$

Given A = {(x, a(x)): x ∈ X} and T = {w, t; p} where w and t are templates on X and p is a real, nonzero value, we define the weighted erosion operation by:

$$E: \quad (A \boxed{\textcircled{\scriptsize}} T)(y) = [\sum_x w_y(x) r[a(x) - t_y(x)\,]^p)]^{1/p})$$

The properties below follow from those for the generalized mean [13].

$$\text{If } w_y(x) = \frac{1}{N} \text{ for all y and x and } p \to -\infty, \text{ then } E = a \boxed{\wedge}_r t$$

and that

$$\text{If } p = 1 \text{ and } t_y(x) = 0 \text{ for all y and x, then } E = a \oplus t.$$

We define the weighted dilation operation similarly [17].

Finally, we define the **weighted hit-or-miss transform**, denoted by A ⊗ B, by letting H = {w^h, t^h; p^h} and M = {w^m, t^m; p^m} and setting

$$A \otimes B = (A \boxed{\textcircled{\scriptsize}} H) - (A \boxed{\textcircled{\scriptsize}} M^*)$$

where M* = {$-w^m(-x)$, $-t^m(-x)$; p^m}. An example is shown [17]. These operations can all be used and optimized as the feature extraction portion of an Image Algebra network as described in the next section.

Network Structure

The image algebra network is composed of two parts: a feature extraction network followed by the feedforward network. The feature extraction network can consist of one or more layers, and each layer can also consist of one or more feature maps. Each layer performs feature extraction by template operations over the input to that layer. The sizes of the feature maps are determined by the undersampling rate for the convolution over their input. The feedforward network performs classification based on the outputs from the feature extraction network. Figure 1 shows the whole network structure for two-dimensional inputs.

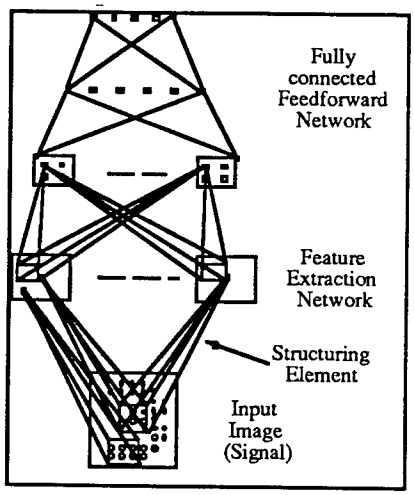


Figure 1. Network Structure.

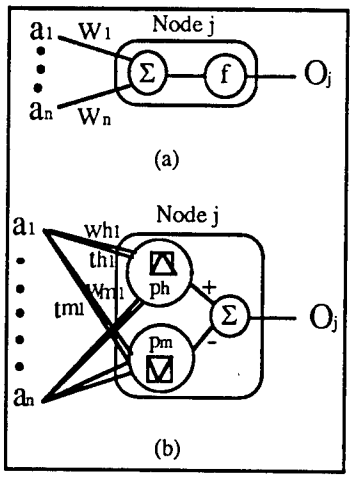


Figure 2 Node operations for the feature extraction network. Linear operation (a) and Morphological Hit-or-Miss operation (b).

The nodes in the feedforward network, except those in the input layer, compute a net input by a weighted sum of its inputs from others and produces the output by a sigmoid activation function. The input nodes for this network are simple buffers which just bypass the input (the output from the feature extraction layer) to their output.

By choosing appropriate values of p in the weighted generalized erosion operation, the nodes in the feature extraction network can perform two different operations: a weighted sum operation and an (approximate) morphological operation (We have also extended this approach to perform exact morphological operations, but this has not yet been published and was not utilized in this work). The weighted sum operation is the usual one for neural networks described above. The morphological operation node performs the weighted Hit-or-Miss transformation which is defined in the previous section. Figure 2 (a) and (b) show the node operation for those two different networks.

In our previous work (and most other neural network pattern classifiers of this type), the standard mode of operation for these networks has been that the input image or signal represents an isolated pattern (such as an image of an isolated character). The outputs of the network are class-coded. That is, there is one output for each pattern class and if the input pattern is from class i, then the i^{th} output is required to be high (typically 1.0) and all other outputs are required to be low (typically 0). In this study, we extended the standard mode of operation to allow the Image Algebra networks to operate on images which can contain one or more of the vehicles of interest in relatively small subregions of the input image. We describe the standard mode of operation more precisely here. We then describe the extension to scanning mode.

Assume we have a network with inputs that are images on a rectangular coordinate set X. Assume the network has L feature map layers and that the i^{th} feature map layer has M_i feature maps, i = 1, 2, ..., L. Each feature map is a

coordinate set. Denote the j^{th} feature map of the i^{th} layer by F_{ij}. We let $F_{00} = X$. Each feature map has several templates associated with it. In the case that the feature extraction is linear, there is one for each feature map in the previous feature map layer. In the morphological case, there are two templates for each feature map in the previous feature map layer. Assume for concreteness that the network is performing linear feature extraction. Denote by t_{ijk} the template associated with the j^{th} feature map in feature map layer i connected to the k^{th} in feature map layer i-1. Given an input image a on X, the output of the feature extraction network is computed as follows:

Let $a_{00} = a$ and $s(x) = \dfrac{1}{1 + e^{-x}}$ be the standard unipolar sigmoid function.

FOR i = 1, ..., L

FOR j = 1, ..., M_i

$$a_{ij} = s\left(\sum_{k=1}^{M_{i-1}} a_{i-1\ k} \oplus t_{ijk} \right)$$ (a_{ij} is an image on the feature map Fij)

$$a_{out} = \bigcup_{j=1}^{M_L} a_{Lj}$$ (a_{out} is an image on the union of feature maps $\bigcup_{j=1}^{M_L} F_{Lj}$)

The image aout is the output of the feature extraction network and is also the input to the classification network. Ritter et al have described the operation of the classification network in terms of image algebra [25]. In the morphological feature extraction case, we replace the templates t_{ijk} by pairs of templates h_{ijk} and m_{ijk} and replace the linear operation $\oplus$ by the generalized hit-or-miss operation $\boxed{\Omega}$.

For example, one architecture used in this study had one feature map layer with two feature maps, three hidden units in the classification network, and two output units. The values of the outputs range between 0 and 1 and represent the confidences that the input represents a Blazer or a non-Blazer. The output confidences are computed by the feedforward propagation as follows:

(AL1) Feedforward Propagation in Class Coded Mode:

a = input pattern image, (e. g. a 50 x 80 subimage extracted from a scene).

$a_{11} = s(a \oplus t_{110})$.

$a_{12} = s(a \oplus t_{120})$.

$a_F = a_{11} \cup a_{12}$.

$h_1 = s(\sum (a_F \bullet W_1))$.

$h_2 = s(\sum (a_F \bullet W_2))$.

$h_3 = s(\sum (a_F \bullet W_3))$.

$C_{target} = s(c_{t1}h_1 + c_{t2}h_2 + c_{t3}h_3)$.

$C_{background} = s(c_{b1}h_1 + c_{b2}h_2 + c_{b3}h_3)$.

where t_{110}, t_{120}, are templates from F_{11} to X and F_{12} to X respectively, W_1, W_2, and W_3, are images on $F_{11} \cup F_{12}$, c_{ij}, i = t,b; j = 1,2,3 are scalars, and • denotes the pointwise (Hadamard) image product. The weights of all the templates, images, and scalars involved are learned by a backpropagation type algorithm for the generalized image algebra operations. The algorithm is derived in [17].

An Image Algebra network operating in scanning mode is an image-to-image transformation. Only the target output confidence is used to a form the output image, which can be thought of as a (nonlinear) correlation plane. A typical example is depicted in Figure 3; an analogous depiction of a class-coded network is shown in Figure 4.

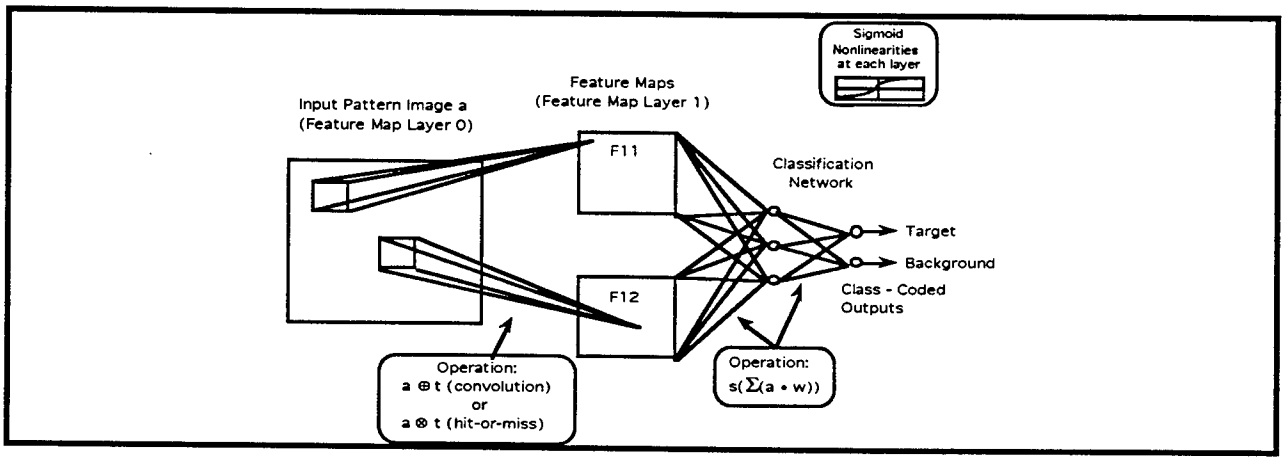


Figure 3. Typical Network Architecture in Class-Coded Mode.

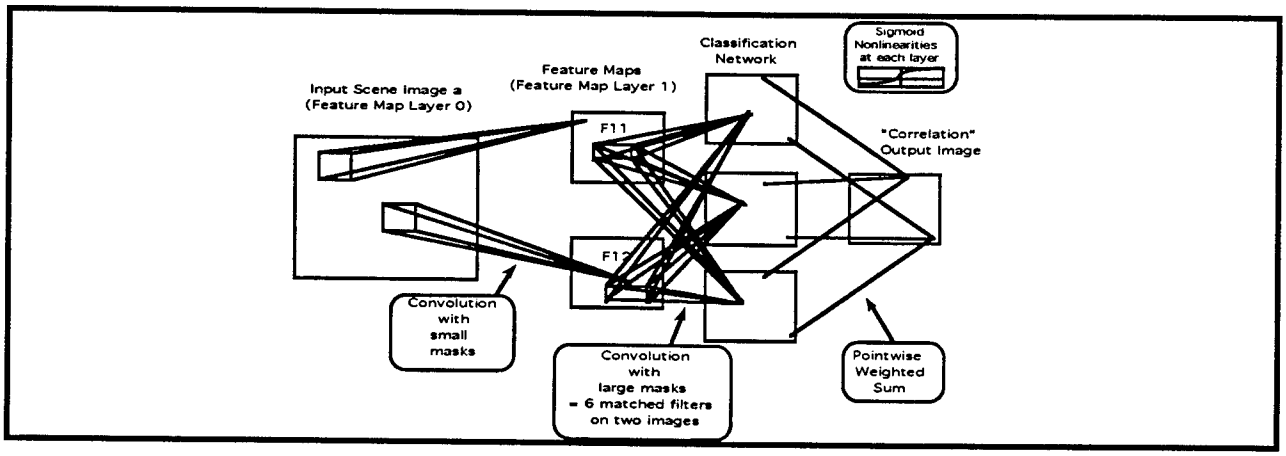


Figure 4. The Same Architecture as in Figure 3 but extended to Scanning Mode.

An Image Algebra representation of the feedforward propagation in scanning mode for the example with input image a, two feature maps, three hidden units, and two outputs is the following:

$a_{11} = s(a \oplus t_{110})$.

$a_{12} = s(a \oplus t_{120})$.

$h_1 = s((a11 \oplus W_{11}) + (a12 \oplus W_{12}))$

$h_2 = s((a11 \oplus W_{21}) + (a12 \oplus W_{22}))$

$$h_3 = s((a11 \oplus W_{31}) + (a12 \oplus W_{32}))$$
$$C_{target} = s(c_{t1}h_1 + c_{t2}h_2 + c_{t3}h_3).$$

where t_{110}, t_{120}, are templates from F_{11} to X and F_{12} to X respectively; W_{11}, W_{21}, and W_{31}, are translation invariant templates obtained by restricting W_1, W_2, and W_3 to F_{11} and W_{12}, W_{22}, and W_{32}, are translation invariant templates obtained by restricting W_1, W_2, and W_3 to F_{12}. The supports of the Wij are called the scanning windows. In scanning mode, h_1, h_2, h_3, and C_{target} are images whereas in class-coded mode they are scalars.

It is interesting to note that the Image Algebra networks in scanning mode are feature extraction networks. One can now consider the possibility of training the network using techniques similar to those used to train matched filters. We will discuss how this observation may help to develop better methods for training the networks using constrained optimization in the analysis and conclusions section.

III EXPERIMENTAL APPROACH

Two data sets were used in our experiments: a Tank data set and a Blazer data set. The tanks data set consists of 35 infrared images of a tank in a field and was obtained from MICOM [22]. We divided the data set into two subsets: a training subset and a testing subset. These are shown in Figure 5(a) and (b)

The Blazer data set was collected during the study at Eglin. A camera mounted on a roof was focused on the parking lot. We drove a particular Blazer, which we refer to as the training Blazer, around the parking lot and captured images on video tape. The parking lot contained other Blazers and related vehicles such as Jeep Cherokees. Eighty eight 512 x 512 images were digitized from the video tape. They were categorized into the following subcategories:

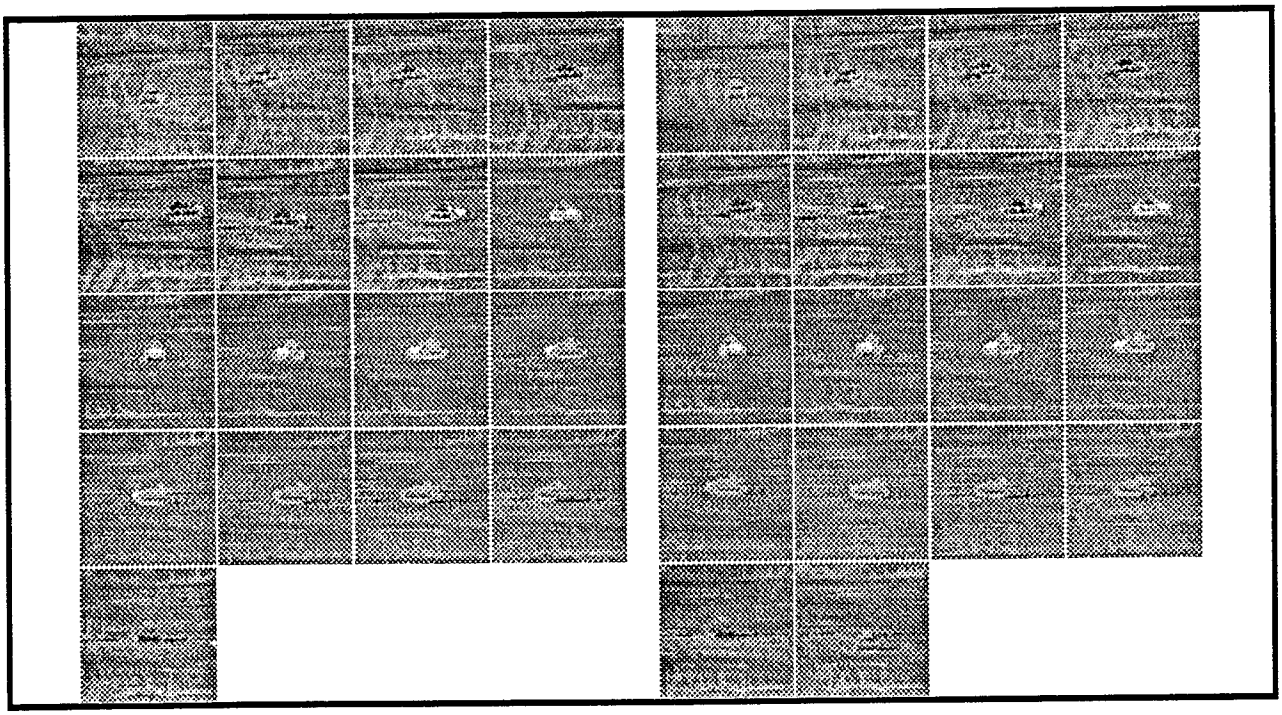


Figure 5. Tank training set (left) testing set (right).

Rotation Sequence A: A set of sixteen images containing the training Blazer at approximately the same location in the front of the lot but at intervals of approximately 20^0 in aspect Half these images are shown in Figure 6. The training Blazer is the vehicle moving between frames. The first vehicle in the row to the left of the training Blazer is also a Blazer and further back in the same row is a Jeep . All or parts of this sequence are used in training.

Rotation Sequence B: A set of twenty images containing the training Blazer at approximately the same location in the back of the lot with different views in aspect angle. Half these images are shown in Figure 6. All or parts of this sequence are used in training.

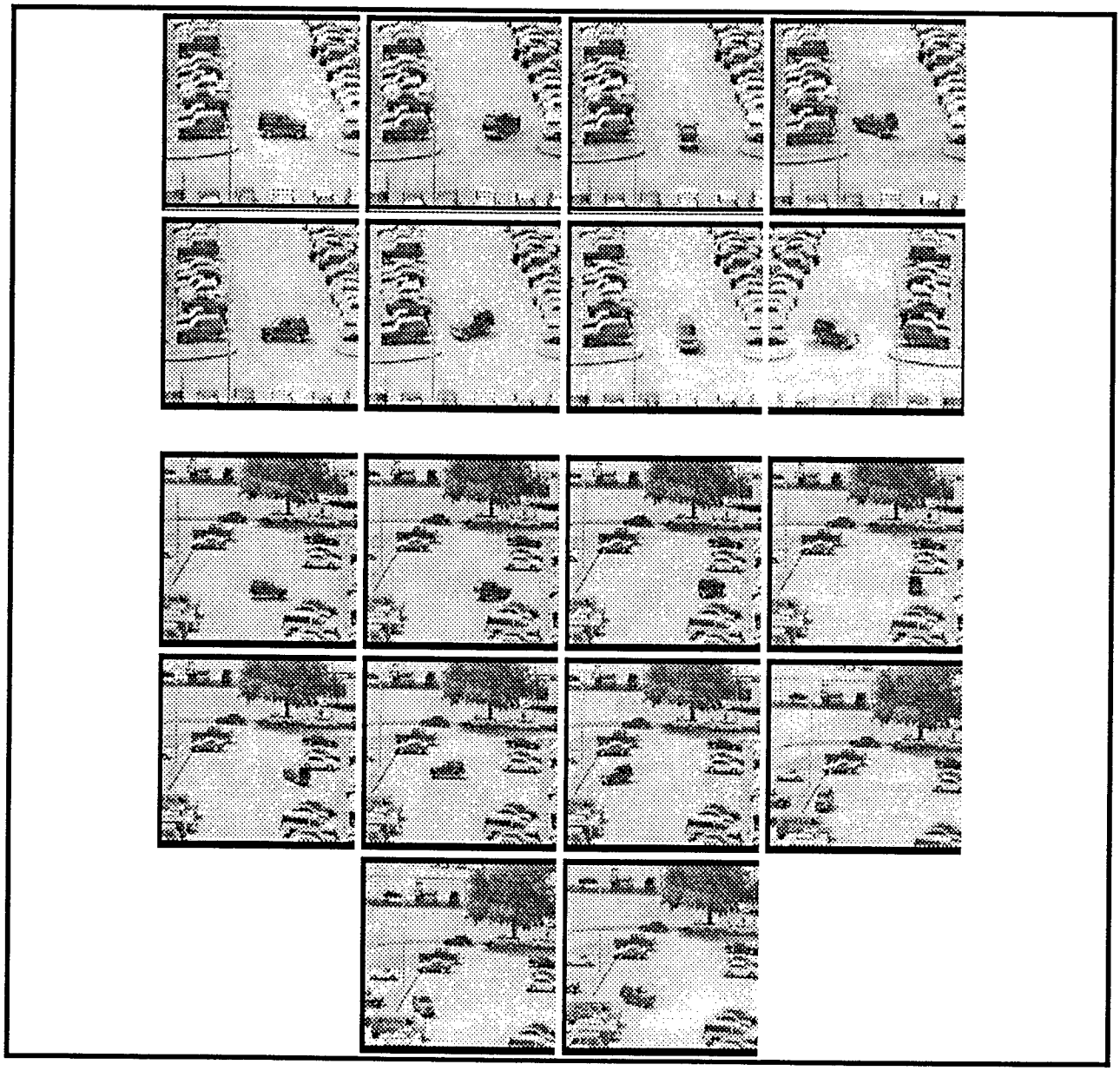


Figure 6. The Blazer training set. The Blazer driving around in the lot is the only one used to train the network.

Parking Sequence: A set of forty two images consisting of eight sequences. Each sequence consists of five or six images with the training Blazer pulling into or out of a parking space. The training Blazer ranges from no occlusion to almost full occlusion in each sequence. This sequence is used for testing only.

Jeep Sequence: A set of four images. Each image contains the training Blazer, a different Blazer, and two different styles of Jeep Cherokee. This sequence is used for testing only.

Extra Sequence: A sequence of six images of the training Blazer driving along the front of the parking lot. The training Blazer is partially occluded in some of the views. This sequence is used for testing only.

Some of the images in the testing sequences will be shown in the Analysis and Conclusion section of this report.

Training

Training consists of three basic steps: (1) Creation of a set of patterns (the training set) that is used to form the network, (2) choosing network parameters, and (3) iteratively presenting patterns to the network and applying modified backpropagation rule to update the weights. The implementation of each step requires resolution of several issues which have some generality across problem domains but which are also somewhat problem dependent.

The creation of the training set is an important function which can significantly affect the features that are learned by a neural network. As noted by Kallman and Goldstein [19], if we embed a vehicle in a constant background image, the overwhelming feature of the image is the background. It is possible that a classifier can learn to classify objects based on the background rather than the object. On the other hand, embedding vehicles in noisy backgrounds can create difficulties in training and can result in the networks learning to recognize the vehicle in specific backgrounds.

In our experiments, we tried a variety of strategies of preparing training sets and training networks. In each strategy, we used "cutout" images. Cutout images are images of vehicles with no background. Our strategies fell into two major categories: Preselected Backgrounds and Dynamically Selected Backgrounds. They are described as follows:

Preselected Background Training Algorithm:

```
Inputs:   List of subimages containing vehicles to be detected, T.
          List of randomly selected background subimages, B

Epoch = 1;
WHILE (Epoch < MaxIter AND Error > ErrorThresh) DO
      FOR i = 1 to number of patterns in T
            Select background image, a,  from B using random selection;
            Perform Forward and Backward propagation with a;
            Select target image, a,  from T using random selection;
            Perform Forward and Backward propagation with a;
            Update Error
      ENDFOR
      Epoch = Epoch + 1;
ENDWHILE
```

The lists of targets and backgrounds are created before training and held fixed. Some target images may be cutouts and some extracted directly from the scene image so that they are embedded in the background they appear in. Shifted versions of each target are collected into the list. In our experiments, we considered shifts by as much as three pixels in each direction. Thus, 49 x 2 = 98 versions of the training vehicle from each scene were included in the training set, 49 shifts of images in backgrounds and cutouts The number of backgrounds chosen is equal to the number of targets chosen. This algorithm converges to a low RMS error and consistently trains to 100% classification accuracy. Networks trained with this algorithm do not always generate low output on test backgrounds.

Dynamically Selected Background Training Algorithm:

```
Inputs:       List of images of scenes containing training vehicles, S
              List of bounding boxes of training vehicles in scenes.
Epoch = 1
WHILE (Epoch < MaxIter AND Error > ErrorThresh) DO
      FOR i = 1 to number of scenes in T
            Select a subimage, a, containing the training vehicle subimage;
            Perform Forward and Backward propagation with a;
            Randomly select a background subimage, a;
            Perform Forward and Backward propagation with a;
            Update Error
      ENDFOR
      Epoch = Epoch + 1;
ENDWHILE
```

This algorithm is significantly different. It is much more memory efficient than the first algorithm. The backgrounds that are shown to the network are different each Epoch. This algorithm tends not to converge, although it does achieve a low error and networks trained with it perform as well as the first algorithm in scanning mode.

IV. RESULTS

We first discuss tank results. The tanks were trained using the preselected background training algorithm. No preprocessing was performed on the imagery. Half the data set was used for training and half the data set was used for testing. The images were of size 256 x 256. A network was training with two feature maps of size 5 x 5 and had two hidden units in the classification network. The scanning window was of size 50 x 80.

The scanning network was 100% accurate at detecting the tanks in both the training and testing sets. Detection was performed by selecting the maximum output of the "correlation" plane. Sample outputs on testing images are shown in Figure 7. Four examples are shown. For each example, the image in the upper left is the input. The image in the lower left is the nonlinear correlation output. The graph in the lower right is the peak obtained by setting all output values to zero except the maximum output value. The image in the upper right depicts the pixel(s) that contains that maximum output (black pixels) overlaid on the original image; the aimpoint.

These results show that a single network trained with views of a vehicle every 20^0 can represent a vehicle at virtually all rotations in aspect angle (at the same depression angle). Matched filters do not seem to be able to do this.

The Blazer networks were trained using the dynamically selected background algorithm. The images were 512 x 512. The images were preprocessed using the Prewitt edge operator. Thus, all network operations were performed on edge map images. Several different network architectures were tried. We show results from a network that had one feature map of size 5 x 5, and five hidden units in the classification network. The scanning window was of size 100 x 160.

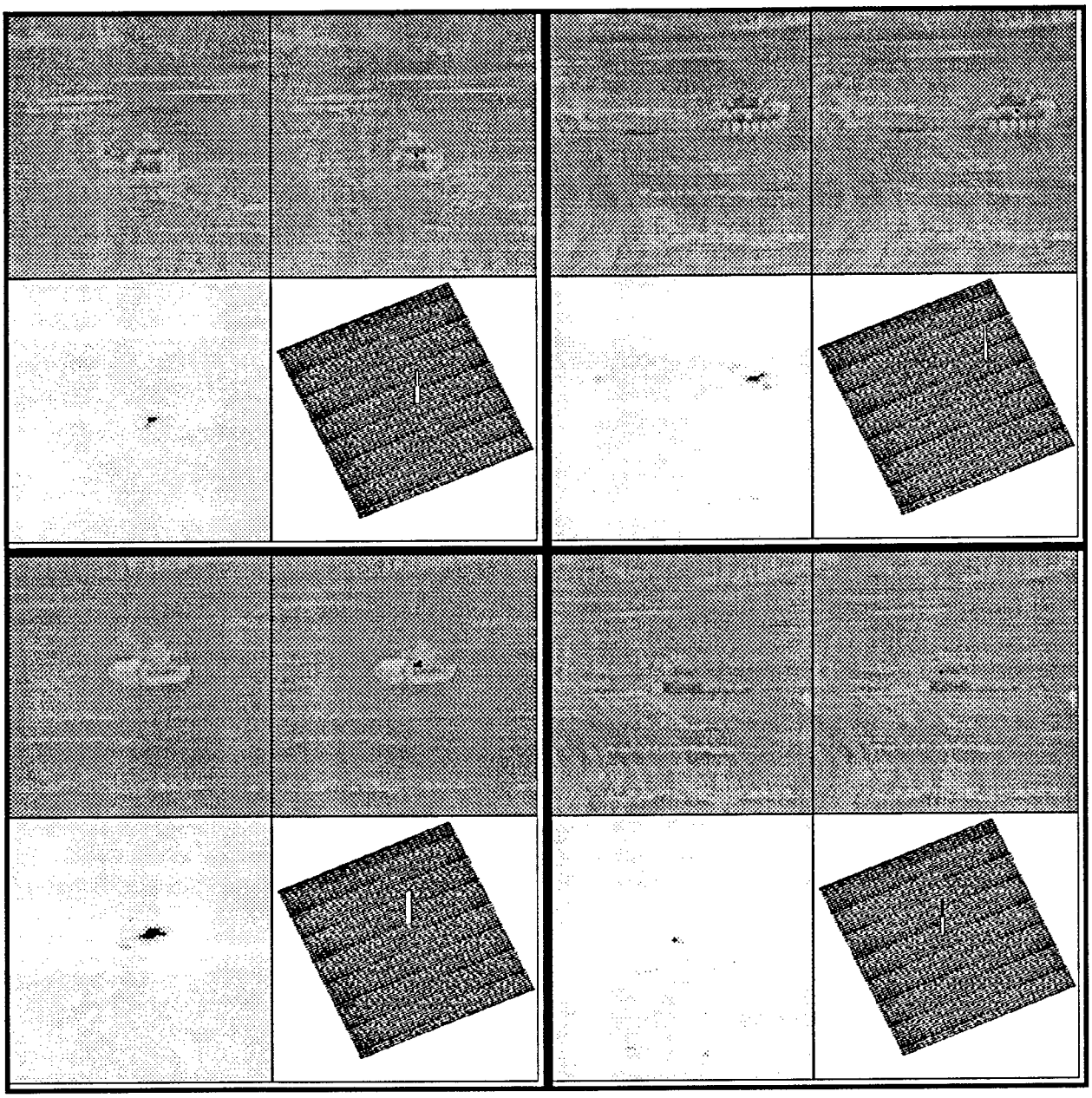


Figure 7. Sample testing results for the tank detection network.

The networks detected the training Blazer image in a variety of testing images. Precise performance measurements were not performed because of time constraints. However, inspection showed that in most images in which the training Blazer was not occluded, the network had high confidence output on the training Blazer The network sometimes detected the Blazer under partial occlusion. The network generally had medium outputs on different Blazers, but also had medium outputs on other objects such as vans, cars, and non-vehicles. Occasionally, false alarms would have high outputs. Thus, further research is needed to fully exploit the potential of these networks.

Figures 8-10 show some of the results. Each figure shows one or more examples of results on testing images. Each example is a set of four images. The upper left image is the edge map of the input. The lower left image is the thresholded, nonlinear correlation plane (the threshold was set on the training set). The lower right graph shows all values that were above the threshold. The upper right image shows the pixels above the threshold (white pixels).

Figure 8 shows the ability of the network to discriminate between a Blazer and a Jeep in a scene. The Jeep is pulling into a parking place and is not detected by the network whereas the training Blazer, which is at a different range than the training images, is detected. Another Jeep which is parked is not detected. However, the vehicle in the front of the left row of cars is a Blazer and is not detected. In Figure 9, the training Blazer undergoes various levels of occlusion. The Blazer is detected with partial occlusion, but not with a large amount of occlusion. Finally, in Figure 10 an example of a false alarm is shown.

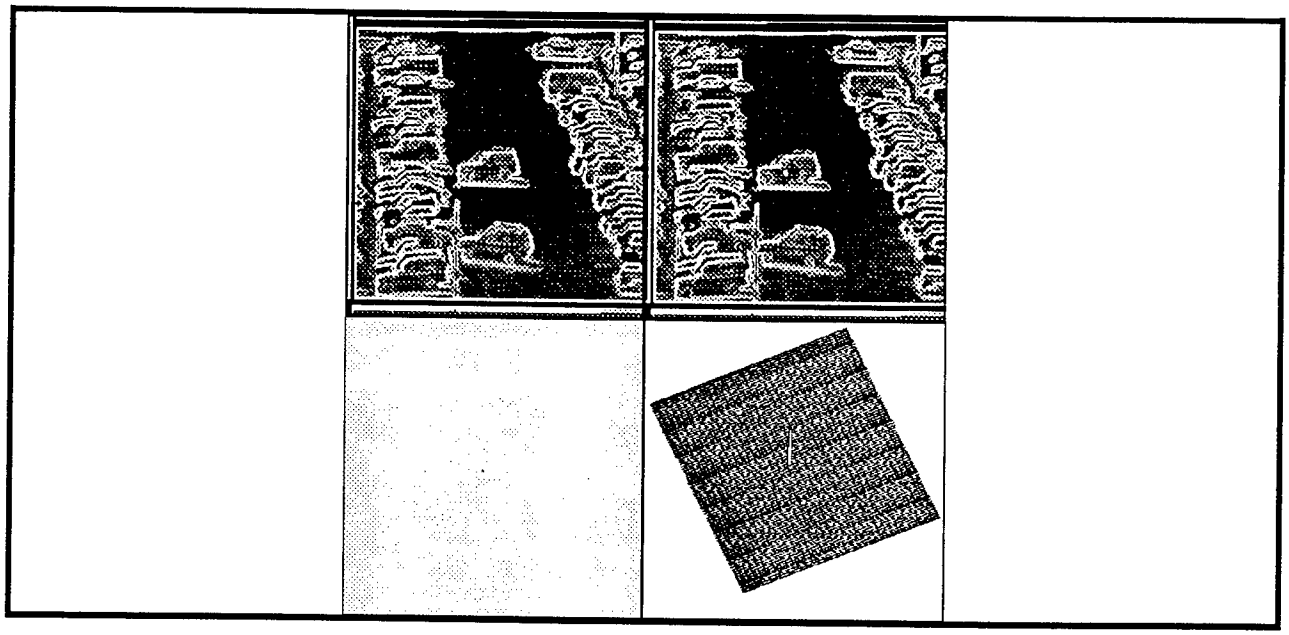


Figure 8. Testing results of Blazer network showing ability to disciminate between Blazer and Jeep but inability to generalize from one Blazer to another

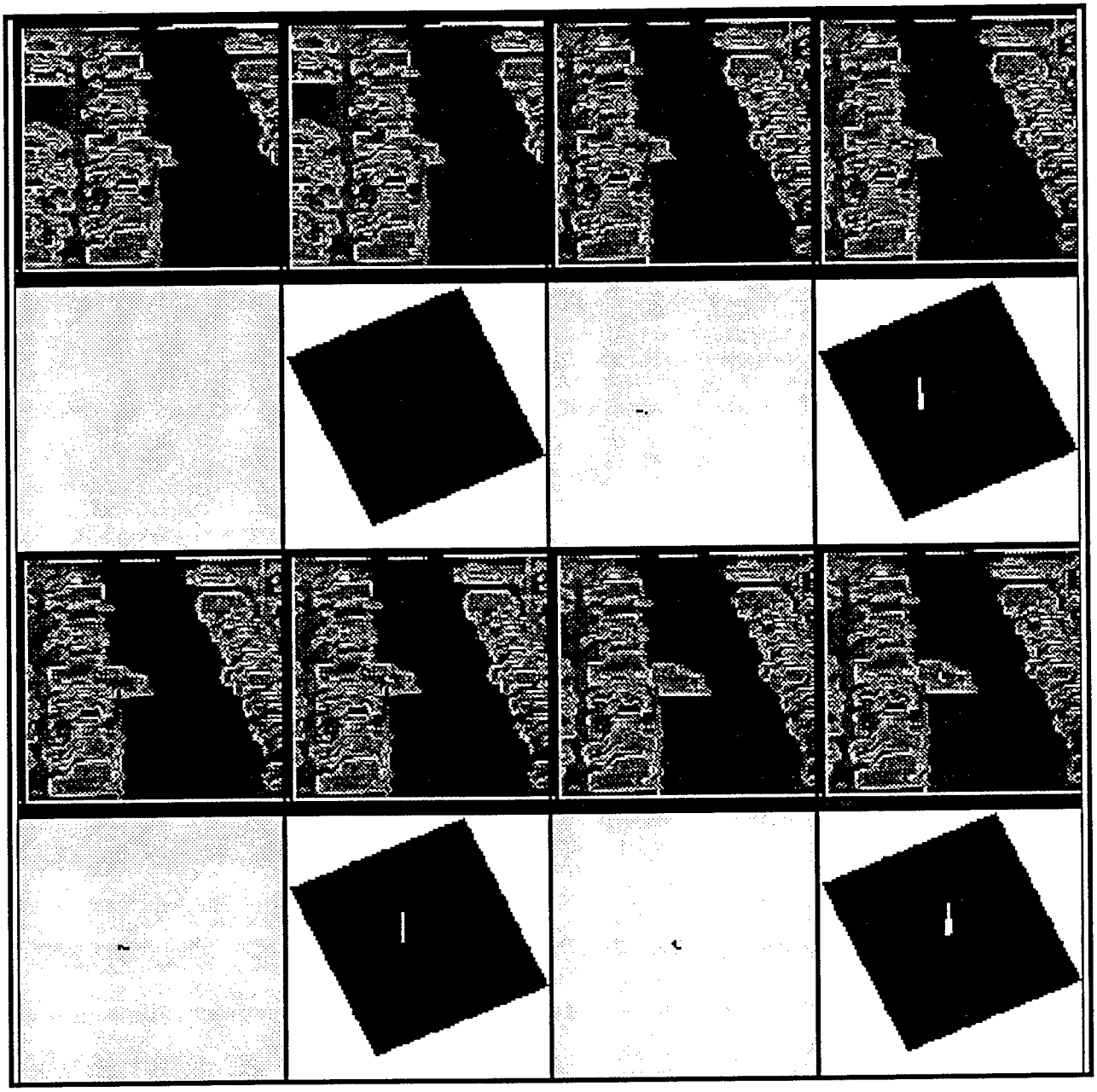


Figure 9. Testing results of Blazer network showing ability to detect Blazer under partial occlusion but not large amounts of occlusion .

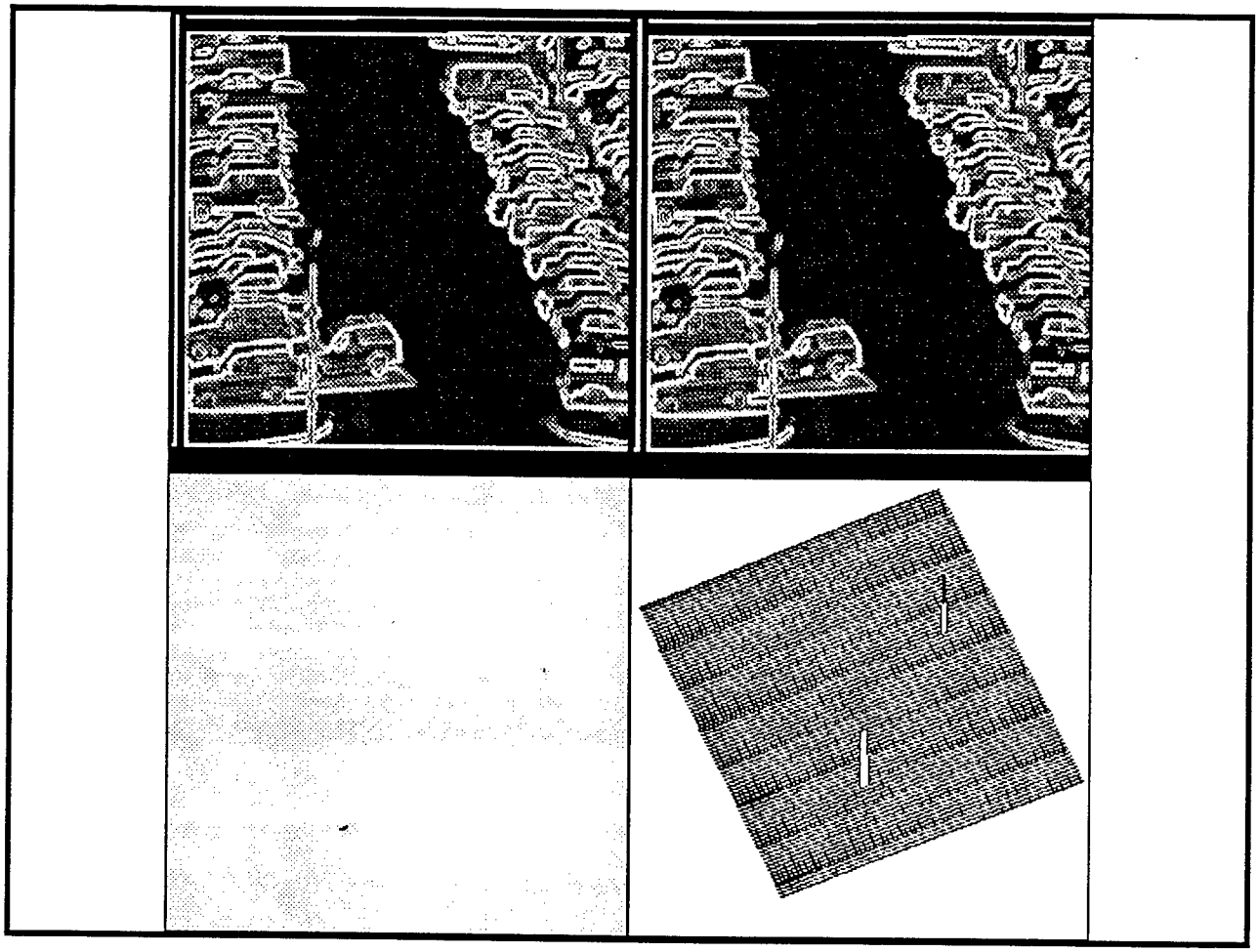


Figure 10. Testing results on Blazer showing false alarm in cluttered region consisting of cars, detection of training Blazer, and missed detection of non-training Blazer.

V. ANALYSIS AND CONCLUSION

The Image Algebra scanning network approach to detecting vehicles in complex scenes is a promising approach that needs further investigation. The universal approximation property of neural networks provides a theoretical basis for believing that the networks can provide improved detection rates. Training methodologies need to be developed that can minimize spurious outputs and computational requirements must be fully understood. Once mature, the networks should be compared to existing techniques on standard data sets using meaningful measures of comparison. Detection and false alarm rates, computational complexity, training or design requirements should be considered.

An important conceptual result obtained in this study was the idea that the Image Algebra networks in scanning mode should be trained as image-to-image transformations rather than image-to-class-coded outputs transformations. This idea allows us to consider better design criteria. Feedforward neural networks are usually trained using unconstrained optimization. This is analogous to designing a Synthetic Discriminant Function (SDF).

However, SDF's do not perform well, producing many spurious outputs. Thus, much research in the design of matched filters has focused on the development of constrained optimization criteria [19,20]. These constrained optimization criteria produce extremely significant enhancements of the matched filter performance, producing sharp correlation peaks without the spurious outputs associated with the SDF's. It is reasonable to assume that using such criteria will lead to equally significant enhancements of the scanning Image Algebra network performance.

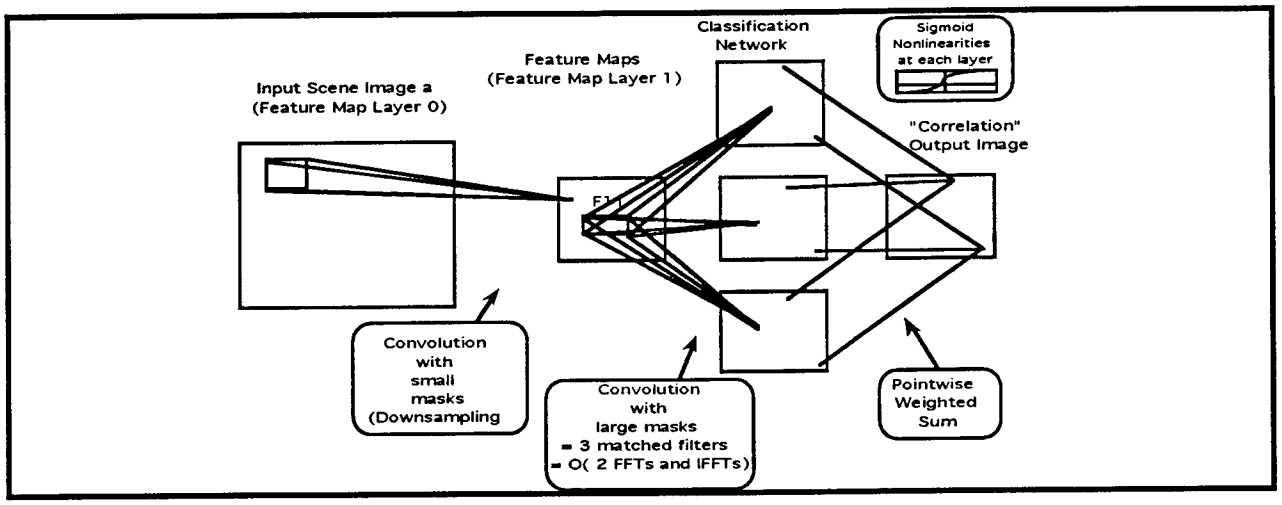


Figure 11. A Network Architecture in Scanning Mode with only one Feature Map and Feature Map Layer. In this case, the Feature Extraction Network performs a Downsampling Operation which is optimized

Frequency domain techniques in the design process have helped to produce better filter designs. We can modify our training procedure in the scanning mode to operate in the frequency domain. For example, consider the network shown in Figure 11. This network has one feature map, say for concreteness of size 5 x 5, which essentially performs downsampling. In the current mode of operation, this stage is followed by scanning with a window large enough to contain all the targets. This scanning window could be replaced by a frequency domain filtering approach. Training could be performed in the frequency domain using a modification of backpropagation.

Let us be more precise. Assume there is no downsampling layer. The forward propagation of an image, a, through a network with n_h hidden units is given by:

$$h_i = s\,(F^{-1}(F(a) \cdot Hi)) \qquad i = 1, 2, \ldots, n_h$$

$$C(a) = s\Big(\sum_{i=1}^{n_h} w_i\, h_i\Big)$$

where F (a) denotes the Fourier transform of a and F^{-1} denotes the inverse Fourier transform. Note that each h_i is an image and can be thought of as the output of a matched filtering operation with filter H_i. In this view, the scanning Image Algebra network is a collection of matched filters that are trained simultaneously. The outputs of the matched filters are combined to produce an output image. Thus, the network servers as a generalization of a matched filter and is identical to a matched filter if the number of hidden units is 1. The beauty of this view of the scanning

network, as mentioned previously, is that we can now modify the weights, or filter coefficients, according to a constrained optimization criteria. For example, a Minimum Average Correlation Energy type constraint could take the following form:

Given training images $a_1, a_2, ..., a_s$, each with associated target points $\{x_{i1}, x_{i2}, ..., x_{ini}\}$

Minimize $$\sum_{i=1}^{s} \left(\sum C(a_i)^2\right)$$

subject to the constraints that $C(a_i)(x_{ij}) = d_{ij}$.

One approach to solving this would be to use Lagrange multipliers, i.e.,

Minimize $$E = \sum_{i=1}^{s} \left(\sum C(a_i)^2\right) + \lambda \left(\sum_i \sum_j \left(C(a_i)(x_{ij}) - d_{ij}\right)\right).$$

The approach to minimizing this expression would be to mimic the backpropagation procedure using the forward propagation equations provided above. This requires differentiating the output of the matched filtering process with respect to the filter coefficients in the frequency domain, which is not difficult. The use of constrained optimization in training neural networks has received a small amount of attention recently in the neural network community and a review of proposed techniques should be helpful for this application [26-28].

Furthermore, in this new scheme, the initial weights of the frequency domain filters could be picked in more intelligent ways than purely random. For example, Kallman and Goldstein use the notion of a Basic False Target to initialize several frequencies to zero in the matched filter and they require that the frequencies remain zero during the constrained optimization process. This process can be utilized as well to enhance the network training.

In addition to investigating the implications of the idea of training the scanning networks in image-to-image mode, many other experiments can be performed. These include the following:

Training the network with morphological feature extractors rather than linear feature extractors. This approach could result in faster processing and more appropriate features in some cases.

Train the network with morphological classification networks. This could result in faster processing. These networks have been investigated by Ritter et el.

Investigate the potential of a single network to produce outputs for several target types. More generally, characterize the extent of the variance that can be included in a single network.

Investigate the affects of small changes in the input on the state of the network; an analysis of variance. Characterize the outputs of the network in a more predictable fashion.

REFERENCES

1. Y.L Cun, B. Boser, J. Denker, D. Henderson, R. Howard, W Hubbvard, L. Jackel, and H. Baird. "Constrained Neural Network for Unconstrained Handwritten Digit Recognition, Proc. Frontiers in Handwriting Recognition, CENPARMI, Concordia University, Montreal CA, April 1990.
2. P.D. Gader, and M.A. Khabou, "Automated Feature Generation for Handwritten Digit Recognition," submitted to *IEEE Trans. Pattern Analysis and Machine Intelligence.*, 1993.
3. A. M. Gillies, "Automatic generation of morphological template features", SPIE Image Algebra and Morphological Image Processing I, vol-1350, pp 252 - 262, San Diego CA, July 1990.
4. Wm. F. Pont and P.D. Gader,"Gradient Descent Techniques for Feature Detection Template Generation," SPIE Image Algebra and Morphological Image Processing II, vol-1568, San Diego CA, July 1991.
5. M. Ritzki, L. Tamburino, M. Zmuda, "Adaptive search for morphological feature detectors", SPIE Image Algebra and Morphological Image Processing I, vol-1350, pp 150 - 160, San Diego CA, July 1990.
6. S. Wilson,"Unsupervised Training of Structuring Elements", SPIE Image Algebra and Morphological Image Processing II, vol-1568, San Diego CA, July 1991.
7. F. Stentiford, "Automatic Feature Design For Optical Character Recognition Using An Evolutionary Search Procedure." IEEE Trans. Pattern Anal. Machine Intell., Vol. PAMI-7, pp. 349-355, May 1985.
8. E. Dougherty, "Optimal Mean-Square N-Observation Digital Morphological Filters I Optimal Binary Filters II Optimal Gray-Scale Filters", CVGIP vol-55, pp 36-72, Jan 1992.
9. E. Dougherty and R. Loce, "Optimal Mean-Absolute-Error Hit-or-Miss filters: Morphological Representation and Esitmation of the Binary Conditional Expectation", Optical Engineering, Vol 32. No. 4, April 1993, pp.815-827.
10. R. Loce, *Morphological Filter Mean-Absolute-Error Representation Theorems and Their Application to Optimal Morphological Filter Design*, Ph.D. Thesis, Rochester Institute of Technology, May 1993.
11. J. Davidson and K. Sun,"Template Learning in morpohological nets,"SPIE Image Algebra and Morphological Image Processing II, vol-1568, pp 176-187, San Diego CA, July 1991.
12. D. Rumelhart and J. McClelland, Parallel Distributed Processing,MIT Press, Cambridge Mass, 1986.
13. R. Krishnapuram and J. Lee,"Fuzzy-Set-Based Hierarchical Networks for Information Fusion in Computer Vison", Neural Networks, Vol. 5, pp 335-350, 1992.
14. A. Yuille, D. Geiger, and L. Vincent, "Statistical Physics Interpretation of Mathematical Morphology", SPIE Image Algebra and Morphological Image Processing II, vol-1568, San Diego CA, July 1991.
15. P.D. Gader, "Template Generation for Pattern Classification," *Proceedings of the SPIE Conference on Image Algebra and Morphological Image Processing III*, Vol. 1796, July 1992.
16. P.D. Gader, "Fuzzy Morphological Networks, " *Proceedings of the First Midwest Electro-Technology Conference*, Ames, Iowa, April 1992.
17. P. D. Gader, Y. Won, M. A. Khabou, "Image Algebra Networks for Pattern Classification", *Proceedings of the SPIE Conference on Image Algebra and Morphological Image Processing V*, Vol. 2300, July 1994.
18. *Optical Engineering*, Special Section on Optical Pattern Recognition, J. Horner and B. Javidi (guest eds.), Vol. 33, No. 6, June 1994.
19. R. R. Kallman and D. H. Goldstein, "Phase-encoding input images for Optical Pattern Recognition", Optical Engineering, Vol. 33, No. 6, June 1994, pp. 1806-1813.
20. A. Mahalanobis, BVK Vijaya Kumar, and D. Casasent, "Minimum average correlation energy filters," *Appl. Opt.* Vol. 26, 1987, pp. 3633-3640.
21. S. R. Sims, J. Epperson, B. V. K. Kumar, A. Mahalanobis, "Synthetic Discriminant Functions Using Relaxed Constraints", Proc. SPIE Automatic Object Recognition IV, Orlando, April 1993.
22. G. Hobson, S. R. Sims, P. Gader, J. Keller, "MACE Prefilter Networks for Automatic Target Recognition", Proc. SPIE Automatic Object Recognition IV, Orlando, April 1994.
23. C. Daniell, D. Kemsley, W. Lincoln, W. Tackett, and G. Baraghimian, "Artificial Neural Networks for Automatic Target Recognition", *Optical Engineering*, Special Section on Automatic Target Recognition, F. Sadjadi (guest ed.), Vol. 31, No. 12, December, 1992, pp. 2521-2531.

24. G. Ritter, J. Wilson, and J. Davidson, "Image Algebra: An overview", *CVGIP*, vol. 49, Mar. 1990, pp 297-331,.

25. G. Ritter, D. Li, and J. Wilson, "Image Algebra and its Relationship to Neural Networks, in Proc SPIE Technical Symposium Southeast on Optics, Electro-Optics, and Sensors, Orlando FL, March 1989.

26. F. Fogelman Soulie, "Integrating Neural Networks for Real World Applications" ,in Computational Intelligence: Imitating Life, Zurada, Marks, Robinson(eds), IEEE Press, 1994.

27 D. Mckay, "A Practical Bayesian Framework for Backpropagation Networks", *Neural Computation*, vol. 4, 1992, pp. 448-472.

28 S. Nowlan, G. Hinton, "Simplifying Neural Networks by Soft Weight Sharing", Neural Computation, vol. 4, 1992, pp. 473 - 493.

AUTOMATIC CONTROL ISSUES IN THE DEVELOPMENT OF AN ARTIFICIAL PANCREAS

Jennifer Naylor
Department of Electrical Engineering
Auburn University

200 Broun Hall
Auburn, AL 36849

Final Report for:
Summer Faculty Research Program
Wright Laboratory/MNAG

Sponsored by:
Air Force Office of Scientific Research
Bolling Air Force Base, DC
and
Armstrong Laboratory

August 1994

AUTOMATIC CONTROL ISSUES IN THE DEVELOPMENT OF AN ARTIFICIAL PANCREAS

Jennifer Naylor
Department of Electrical Engineering
Auburn University

Abstract

Recent developments in technology for the treatment of diabetes mellitus enable sensing and control of key chemical/hormone species related to the disease. Further, it is expected that non-invasive (infrared) blood glucose sensing techniques will permit continuous on-line sensing of blood glucose levels in insulin-dependent diabetics. It is thus desired to apply modern control systems design techniques in the design of an artificial pancreas in order to provide a robust, fault-tolerant design suitable for clinical and at-home use. A preliminary effort toward this goal was undertaken during the 1994 Summer Faculty/Graduate Student Research program at Eglin Air Force Base; a complementary study is presented by Dr. A. S. Hodel in Summer Research Program Report 29. The effort presented in this report comprises the development of (1) strong background necessary for understanding the dynamics of glucose metabolism (2) a qualitative model of endocrine kinematics related to glucose management and (3) control applications to the glucose regulation models developed.

AUTOMATIC CONTROL ISSUES IN THE DEVELOPMENT OF AN ARTIFICIAL PANCREAS

Jennifer S. Naylor

1 Introduction

The main objectives of this summer research project involve understanding and developing an accurate model of the blood glucose regulation system for type I diabetic patients. Type I diabetes is characterized by the absence of insulin, a key factor in glucose uptake, resulting in prolonged hyperglycemia (elevated glucose levels). The ultimate goal is to apply various control techniques on a glucose regulation model and regulate plasma glucose levels in the body via controlled insulin infusion. In order to accomplish this goal, the mathematical representations must include the essential dynamics of glucose production and removal systems. This report details the steps toward developing an accurate model of the glucose regulation system, the implementation of several models developed and found in literature, and attempts at controlling insulin infusion to the models in order to achieve desirable glucose levels. The project is of interest to Wright Lab/MNAG due to the following common properties between the treatment of diabetes and missile guidance:

1. The subject dynamic systems (a missile or a patient's glucose/insulin kinematics) are inherently non-linear and, often, are poorly modeled relative to required performance levels.
2. The subject dynamic systems are subject to external disturbances that that are not under the authority of the control system (wind gusts, target motion, physical activity or food consumption by the diabetic patient).
3. The subject dynamic systems have limited actuator authority (limited fin deflection, insulin delivery rates).
4. Safe operation of the subject dynamic systems requires that system state variables be kept within a prescribed operating range.

This work was performed in tandem with Dr. A. S. Hodel, from Auburn University, and with Johnny Evers and Dr. Darren Schumacher, both of MNAG branch, Wright Lab, Eglin Air Force Base. All simulations were performed using Matlab.

2 Background Information: Physiology of Glucose Regulation

In order to develop an accurate model of the glucose regulation system, the dynamics, involving the endocrine system and the physical demands of the body, must be understood. Many factors affect the level of plasma

glucose. One of the factors stems from the glucose demand to fulfill energy requirements. Other factors involved are meals, stress, temperature changes and various hormones including insulin, glucagon, seratonin, growth hormone, and a number of other counter-regulatory hormones. Of the hormones involved, insulin and glucagon are major contributors to glucose uptake and glucose production respectively, but several factors affect the secretion of insulin and glucagon. In type I diabetes, no insulin is secreted by the β cells of the pancreas, which results in elevated glucose levels. The following sections summarize the important modelling issues such as factors affecting insulin and glucagon secretion, glucose production, and glucose uptake in normal and type I diabetic patients.

Factors Affecting Dynamics of the Glucose Regulation System

The desired glucose regulation model must consider the controllable inputs, such as meals, insulin injection, and exercise, but more importantly it should accurately describe the physiological responses involved in keeping the glucose levels within the normal range (80-100 mg/dl)[11]. The key hormones involved in glucose counterregulation are insulin, glucagon, and in cases of glucagon deficiency, adrenaline [2]. Other hormones become involved during prolonged cases of hypoglycemia to elevate blood glucose levels, but insulin, secreted from the β cells in the pancreas, is the only hormone involved in lowering glucose levels.

2.1 Glucose Production

In the basal state, the metabolic condition after a 10-14 hour fast, glucose production is approximately 2 mg/kg per minute. In this state, gluconeogenesis, the formation of glucose or glycogen from non-carbohydrate sources, contributes 30 % of glucose production in the liver, and this percentage increases as fasting continues[3]. The remaining hepatic production relies on glycogenolysis, the conversion of glycogen to glucose. Fasting liver depletes glycogen stores at a rate of 11 % per hour. As fasting continues, glycogen stores are depleted thus increasing the role of gluconeogenesis. Glycogen stores consist of 60 grams, in a 1.5kg liver, and 250 grams in 28kg muscle tissue[4].

Increases in glucose production are controlled by several hormones including glucagon, adrenaline, cortisol, and growth hormone [15]. Glucagon and adrenalin have an immediate affect on raising blood glucose levels, by promoting glycogenolysis, and in prolonged hypoglycemia they activate gluconeogenesis. Cortisol and glucagon, in the presence of prolonged hyperglycemia, promote gluconeogenesis. Adrenaline acts within seconds to elevate glucose concentration, while glucagon affects can be observed within minutes. A rise in blood glucose level inhibits glucagon secretion, and conversely, a fall in blood glucose levels stimulates glucagon secretion. During acute insulin induced hypoglycemia, glucagon levels increase by a factor of four[15] in attempts to return glucose levels within the normal range. Glucagon is secreted from the α cells of the pancreas during periods of low glucose concentrations and is suppressed by high insulin levels

[8]. Somastatin, secreted from the δ cells of the pancreas, inhibits glucagon and insulin secretion [15]. The normal fasting concentration of glucagon is approximately 100-150 pg/ml and has a half-life of approximately 5-10 minutes in circulating blood[7]. Growth hormone and cortisol act to increase glucose concentrations by suppressing glucose uptake as well as increasing hepatic glucose production [1]. Cortisol, growth hormone and thyroxin have slower onsets and more prolonged affects to increasing the glucose level.[15].

Glucose production is inhibited by an increase in insulin concentration. In the liver, a 5-7 μU/ml increase of plasma insulin concentration will result in a half-maximum suppression of hepatic glucose production [1], and an increment of 100 μU/ml will decrease hepatic glucose production to less than 10-15 % of basal production [5]. The inhibition of hepatic glucose production is three times as sensitive to insulin than peripheral glucose uptake[4].

2.2 Glucose Uptake

Insulin acts to lower blood glucose levels by increasing cellular glucose uptake [15]. Insulin increases cell membrane permeability to glucose, amino acids and potassium and decreases intracellular cyclic adenosin mono-phosphate (cAMP), the basic regulator of cell metabolism. Glycogenolysis and gluconeogenesis are decreased by high insulin levels[3], which in part is due to the reduction of circulating glucagon[3]. Classic insulin-sensitive tissues are adipocyte,m brown fat, skeletal, heart and smooth muscle[4], this constitutes only a fraction of the tissues involving glucose uptake. The brain, liver, kidneys, and intestines undergo insulin independent glucose uptake. The brain requires $\approx$ 1 mg/kg of glucose per minute, and glucose oxidation provides almost 90 % of the energy required for the brain and nervous system to operate properly. Basal glucose uptake is $\approx$ 2 mg/kg per minute of which 50 % is required by the brain, 25 % by the splanchnic (liver and gut) tissues, and the other 25 % by insulin dependent tissues.Under normal circumstances the rate limiting step for glucose uptake is the phosphorylation within the cell by hexokinase[1]. Glucose uptake is inhibited other hormones, as seen in Figure1, and half-maximal glucose utilization is produced when insulin concentration increase by a factor of $\approx$ 3.

Insulin secretion is stimulated by glucagon [8], a rise in glucose levels, a rise in blood ketones and by glucagon from the α cell. In contrast, insulin is inhibited by the secretion of somastatin, adrenaline and by decreased blood glucose levels[15]. Normal basal rate of insulin release from the β cell is 1 iu/hour (1μU=0.04ng [14]). Insulin degrades in the liver by 50% each time it passes through, but this fraction varies among individuals and in an individual under different instances [9].Typical fasting levels of insulin concentration are 10-50 μ iu/ml, and have a half-life of 5-10 minutes in circulating blood [7]. The insulin response to a glucose bolus, geared to increase glucose levels, is highly nonlinear. It is a predominantly biphasic response with the first impulse occurring within 3-5 minutes followed by a second response, a slower prolonged response, that is proportionate to the glucose concentration preceeding the glucose infusion[14].

Input	Target	Action/Mechanism
Glucose↑	Insulin	secretion↑
Glucose↓	Glucagon	secretion↑
Insulin	Glucose↓	increased cell uptake
Glucagon	Glucose↑	hepatic glycogenolysis (fast)
adrenalin	Glucose↑	hepatic glycogenolysis (fast)
cortisol	Glucose↑	slower than Glucagon and adrenalin
ACTH	cortisol	↑
growth hormone	Glucose↑	slower elevation of glucose levels
adrenaline	insulin	↓
Glucagon	Glycogen	inhibits synthesis
Insulin	Glycogen	promotes synthesis
Insulin	cells	promotes Glucose uptake
Glucose↓	FFA	↑
Glucose↓	epinephrine	↑ (limits cell uptake)
Glucose↓	cortisol	↑
Glucose↓	growth hormone	↑
high FFA/ketones	insulin	inhibits secretion
Glucose↑	glucagon	↓
insulin level ↑	insulin	inhibits secretion

Insulin stimulated by:	**Insulin Inhibited by:**
High glucose levels	Adrenaline
Fructose, Mannose	Noradrenaline
High level of ketones	Insulin
Amino Acids	Starvation
Glucagon	α-mannoheptulose
Growth Hormone	2-Deoxyglucose
Sulphonyl ureas	Diazoxide
cyclic AMP	Vagotomy
secretin	
Pancreozymin	
Vagal stimulation	
Thyroxin	

Figure 1: Summary of dynamics

One of the problems with insulin therapy is insulin-induced hypoglycemia, which occurs when blood glucose levels fall below $\approx$ 50 % of basal levels [7].The brain requires a certain glucose flux as mentioned above, and only has reserves sufficient for a few minutes, at most. When glucose levels drop below 60 mg/dl, neurophysiological deterioration may occur[1]. In attempts to overcome hypoglycemia, the first defense mechanism is increased hepatic glucose output, and the second defense is the suppression of glucose utilization, which may occur 2 - 2.5 hours after the onset of hypoglycemia [1]. The factors affecting hypoglycemia and the dangerous resulting from this condition are important considerations for modelling and controller design.

Factors affecting glucose dynamics are collectively summarized in Figure 1 from references [15] and [1].

3 Modelling Techniques

To include all of the previously detailed dynamics involved in the glucose regulatory system in a model would be an enormous task. The idea is to develop a simple model based on the most important factors affecting glucose levels. The following sections describe previously developed models as well as models constructed during this research program.

3.1 Initial Modelling Attempts

During initial attempts to model the intricate glucose regulation system as described in Figure 1, the following mathematical model was constructed to estimate the effects of the various hormones on glucose concentration.

Inputs:
gi: glucose input rate (mg/dl-min)
u2: adrenaline disturbance (pg/ml-min)
ui: external insulin delivery (units/min)

State Variables:
IN: insulin (U/ml)
BG: blood glucose (mg/dl)
EPI: epinephrine (pg/ml)
GLP: pancreas glucagon (pg/ml)
GL: liver glucagon (pg/ml)
COR: cortisol (μg/dl)
GRTH: growth hormone (ng/ml)

Constants:
Kbg: BG insulin trigger rate
Kbg3: BG/GL inhibitor rate
Kc: insulin decay (5-10 min half life)
Kg: growth hormone rate
Kgl3: GL/BG glycogenolysis rate
Ki3: IN/BG update rate
BGhi: insulin trigger level
w: growth hormone disturbance
Kbg2: BG/GL trigger rate
Kbg4: BG/cortisol rate
Kcell: insulin decay
Kgl: insulin decay rate
Ki: insulin decay rate
BGd: desired BG level
BGlo: GL trigger level

The constants were selected and adjusted arbitrarily. A switching value for insulin production term is set up so that if BGhi<BG, then the switching term GINsw = tanh((BG-BGhi)/5), and otherwise zero. The insulin equation includes a decay term, the blood glucose trigger, and an external input. The liver glucagon equation includes a decay term, a low blood glucose trigger, high blood glucose suppressor. The blood glucose level depends on cell uptake, cell uptake due to insulin, glycogenolysis due to glucagon, and glucose input. The cortisol and growth hormones involve decay terms and a trigger level at low glucose levels. The epinephrine term is set to zero for simplicity.

$$\dot{IN} = -Ki \cdot IN + GINsw \cdot Kbg \cdot max(0, BG - BGhi) + ui \quad (1)$$

$$\dot{GL} = -Kgl \cdot GL + Kbg2 \cdot max(0, BGlo - BG) - Kbg3 \cdot max(0, BG - BGhi) \quad (2)$$

$$\dot{BG} = -Kcell \cdot BG - Ki3 \cdot IN \cdot BG + Kgl3 \cdot GL + gi \quad (3)$$

$$\dot{COR} = -Kc \cdot COR + Kbg4 \cdot max(0, BG - BGlo) \quad (4)$$

$$\dot{EPI} = 0 \quad (5)$$

$$\dot{GRTH} = -Kg \cdot GRTH + Kbg \cdot max(0, BG - BGlo) + w \quad (6)$$

Results

While qualitatively unsatisfactory, the results from this model did provide insight on modelling issues to be considered in future modelling endeavors.

3.2 Previously developed models

Bergman's Minimal Model

This nonlinear model, described in a glucose-clamp experiment[10], was examined because it uses minimal data to describe various parameters related to glucose metabolism. The model produces a parameter which reflects insulin secretion ability, a parameter estimating insulin's ability to stimulate glucose metabolism, and an index of glucose disposal. This model has been criticized because it fails to accomplish it's ambitious goal of describing all aspects of glucose tolerance with minimum data. It fails to accomplish this goal because it does not accurately describe situations of diabetic conditions[4]. Therefore, the "minimal" model was used as a guide for future modelling endeavors and not for simulation purposes.

Model involving stress hormone effects

A model describing the glucose response to stress hormone exposure by Waldhausal et al. [13] introduced several important issues relating to glucose regulation. The "glucose submodels" provided insight on glucose utilization and production. The nonlinear dynamics in this model were analyzed to improve modelling techniques previously described in Section 3.1.

Celeste/Ackerman Model

A mathematical representation of the glucose regulatory system involving glucose, insulin, and glucagon concentrations is presented in reference [12]. The system of equations are designed to describe the response to a insulin infusion test. It is a gain-scheduled model that switches between two linear models based on a function of blood glucose concentration. A new trigger function, a hyperbolic-tangent based function, is added to the model dynamics to replace the switch and represent the sensitivity of various compartments to their inputs. The trigger function is used to model secretion responses that are suppressed below a

lower threshold and limit the secretion above a higher threshold, simulating a saturation curve. The trigger function output is a value between 0 and 1. This function is further detailed in Figure 2 in report 29 by Dr. A. S. Hodel. The variables involved in the trigger functions include the input variable (G,I,E), $XYlo$ and $XYhi$, where X is the affected variable (g,i,e), Y is the measured variable (g,i,e), and lo and hi are the lower and upper threshold values respectively.

Further modifications were made to the state equations which replace the terms involving the trigger values with the triggering function previously described. The inputs to the system are u_1, external glucose input, and u_2, external insulin input. The state variables include G,I, and E (glucose, insulin, and glucagon concentrations respectively). The coefficients were selected in order to achieve basal level characteristics (as described in section 2) at steady state. For the diabetic patient, the b_1 coefficient is set to zero. The following equations are include all modifications involved.

$$\dot{G} = -a_1 \cdot trig(G, gglo, gghi) - a_2 \cdot trig(I, gilo, gihi) + a_3 \cdot trig(E, gelo, gehi) + u_1 \quad (7)$$

$$\dot{I} = b_1 \cdot trig(G, iglo, ighi) - b_2 \cdot I + u_2 \quad (8)$$

$$\dot{E} = c_1 \cdot trig(G, eglo, eghi) - c2 \cdot E \quad (9)$$

The simulation results failed to accurately describe the response to an external glucose infusion. The main problem with the model lies in the glucagon response to elevated glucose levels. Another problem with this model is that hypoglycemia cannot be achieved even with external insulin infusion. However, since the results were qualitatively better than previous modelling attempts, several control algorithms (H_2,H_∞ and H_2 with a fuzzy logic advisor see Section 4.1) were implemented to regulate glucose levels in the diabetic case. Healthy patient and controlled diabetic patient simulation results can be found in Figures 4.1 and 4.1.

3.3 Further Modelling Attempts

Taking into consideration all the kinematics involved in regulating glucose described in section 2, the following model was derived based on the work of Celeste et. al, described in section 3.2.

$\dot{G}$ = (production via glucagon) + (other production) + (glucose input)
−(insulin independent glucose uptake) − (insulin dependent uptake)
+(activation by stress hormones)

$\dot{I}$ = (secretion activated by high glucose levels) − (decay of insulin) − (insulin binding) + (insulin input)
−(suppression from stress hormones)

$\dot{E}$ = (secretion activiated by low glucose levels) − (suppression by high glucose levels)
−(suppression by insulin) − (decay of glucagon) − (conversion to glucose)

The corresponding mathematical representations are as follows.

$$\dot{G} = (a_1 \cdot trigh(G, gghi, gglo) \cdot E - a_2 \cdot G - a_3 \cdot trigh(I, gilo, gihi) \cdot G + u_1) \quad (10)$$

$$\dot{I} = u_3 \cdot b_1 \cdot trigh(G, iglo, ighi) - b_2 \cdot I + u_2 \quad (11)$$

$$\dot{E} = u_3 \cdot c_1 \cdot trigh(G, eglo, eghi) - c_2 \cdot E - c_3 \cdot trigh(I, eilo, eihi) + (1 - u_3) \cdot c_4 \cdot trigh(G, egloD, eghiD) \quad (12)$$

For simplification, the glucose production terms have been collectively represented, and the stress hormone contribution has been neglected at this time.

Details of the dynamics The inputs to the system are u_1 and u_2, which are external glucose and insulin infusion respectively. The term u_3 is used to designate the health of the patient because type I diabetic patients produce no insulin and tend to have elevated levels of glucagon. For normal, non-diabetic patients, u_3 is set to 1, and for insulin deficient diabetic patients, u_3 is set to zero. For this model, the glucose production term is dependent on the amount of glucagon, and the trigger function depends on the glucose concentration. The insulin dependent glucose uptake is dependent on the amount of insulin present, and also contains a trigger function dependent on the glucose concentration. In a healthy patient, the insulin produced depends on the trigger value from the glucose concentration. The decay terms for insulin and glucagon will be such that the half life is 10 - 15 minutes in the blood stream. The amount of glucagon secreted depends on the health of the patient, as mentioned above, and on the trigger value from the glucose concentration. Glucagon secretion is suppressed by high insulin levels, therefore it is assumed to be triggered by the insulin concentration. (Note: The values for the trigger functions were chosen using the information found in the literature and were adjusted to yield desirable results.)

Glucose dynamics coefficients At equilibrium, where G=geq, I=ieq, and E=eeq, the resulting changes in glucose, insulin and glucagon concentrations are zero. Therefore the glucose uptake and production are equivalent, and chosen to be the basal amount, $basalG \approx 2mg/kg \cdot min$. The fact that $\approx 75\%$ of glucose uptake, in the basal state, occurs in insulin independent tissues was used to determine the coefficients a_2 and a_3.

Glucose dynamics coefficients

$$a_1 = (basalG \cdot Mass)/(eeq \cdot trigh(geq, gghi, gglo) \cdot Vol \cdot 10)$$
$$a_2 = 0.75 \cdot basalG \cdot Mass/(geq \cdot Vol \cdot 10)$$
$$a_3 = 0.25 \cdot basalG \cdot Mass/(geq \cdot trigh(ieq, gilo, gihi) \cdot Vol \cdot 10)$$

Insulin dynamics coefficients

$$b_1 = b_2 \cdot ieq/trigh(geq, iglo, ighi)$$
$$b_2 = 0.0924$$
$$b_3 = 5/Vol \cdot 1000$$

Glucagon dynamics coefficients

$c_2 = 0.0924$

$c_1 = c_2 \cdot eeq/trigh(geq, eglo, eghi)$ glucose based glucagon production

$c_3 = 150$

$c_4 = c_1 \cdot 0.8$

Other parameters The variable $Mass$ is the patient body mass in kg, chosen as 80 kg, and blood volume, Vol, approximated at 6.0 liters. The equilibrium constants are chosen from typical fasting values. The desired glucose level, geq, insulin level, ieq, and glucagon level,eeq, are 100.0 mg/dl, 10.0 μU/ml, and 150.0 pg/ml respectively. The trigger values were selected based on a qualitative understanding of the endocrinology involved.

Results from the model simulation The open-loop responses to a constant glucose infusion are located in Figure 4.2 plots 1 and 2. The results provide a more accurate description of the physiological responses than previous simulations. The model allows for insulin-induced hypoglycemia to occur in both healthy and diabetic cases, and the concentrations settle to normal steady state values. The model requires improvements in the area of glucose production, but it is unlikely that this three state model can incorporate the myriad of factors involved. A variable structure control algorithm was implemented on this model (see Section 4.2).

Factors to consider for Future Model modifications Glucagon stimulates insulin release. In normal insulin secretion, the second phase is directly proportionate to the steady state glucose concentration immediately preceding glucose increase due to infusion. An increase of insulin of 100 μU/ml decreases glucose production to less thatn 10 to 15 %of basal levels. At insulin levels 60-90 mU/l 50-70% of glucose flux is disposed in muscle tissues. Limits for maximum glucose, glucagon, insulin production and consumption should be considered in determining the coefficients. Inhibition of hepatic glucose production is 3 times more sensitive to insulin than glucose uptake. Gluconeogenesis accounts for 30% of hepatic glucose production at fasting states. Insulin infusion reduces circulatory glucagon levels by 20 - 30 %, and a increase in glucose concentration of 36.16 mg/dl reduces glucose production by 80%.

4 Controllers for the models

4.1 State Space Control Applications

d H_2, H_∞, and fuzzy logic control strategies were used on the model described in Section 3.2. Taking into consideration the fact that the measurement of glucose alone does not give a controller the ability to assess patient health (i.e. insulin sensitivity, glucagon responses,etc.), and for a model such as

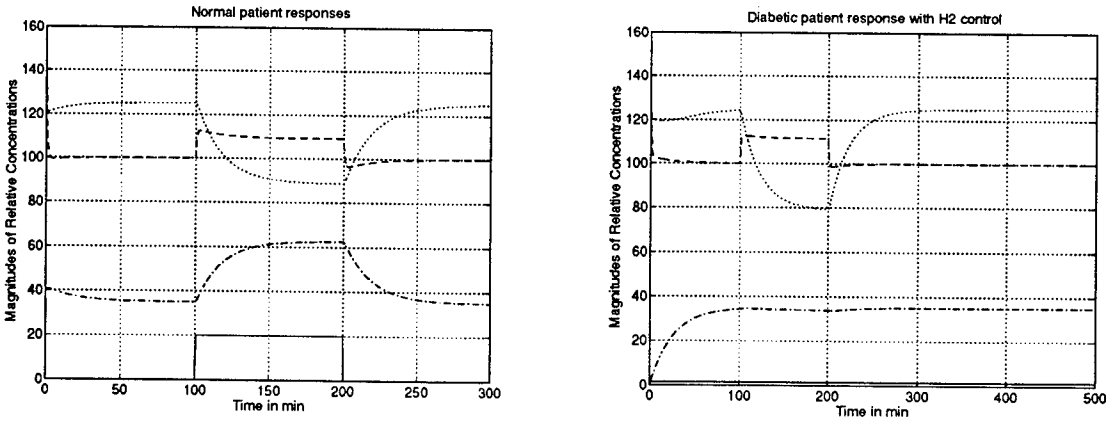


Figure 2: Left: Normal Patient response Right: Controlled with H_2 design

$$\begin{aligned} \dot{x} &= A \cdot x + B_1 \cdot w + B_2 \cdot u \\ z &= C_1 \cdot x + D_{12} \cdot u \\ y &= C_2 \cdot x + D_2 \cdot w \end{aligned}$$

the vector z must include glucose and either insulin or glucagon, or both, in order for the system to be observable. The simulation therefore involves linearizing the model about an operating point (i.e. equilibrium point), finding the transfer function realization from insulin to glucose, and proceeding with an H_2 or H_∞ design scheme. The design procedures used in the simulations follow the guidelines presented in reference [6]. Results of the Normal patient response, the diabetic patient with controlled insulin infusion using H_2 and H_∞ control schemes are located in Figures 4.1 and 4.1.

Fuzzy Logic Application Another control strategy was implemented using a fuzzy logic advisor for several H_2 controllers designed about different operating points. For this design, three H_2 controllers were designed for a slightly high glucose level, nominal fasting glucose level, and a lower glucose level. The "fuzzy" advisor is set up to weight the contribution of each controller depending on the glucose concentration, G and an estimated derivative $\dot{G} = 10s/10s + 1$. The corresponding nominal insulin rate is also determined, by the same fuzzy rules, and is added to the final output of the advised H_2 controller. Hyperbolic-tangent based membership functions were used in the simulations, and the fuzzy rules were set up for conservative control at low to acceptable glucose concentrations. Results of the H_2 controllers with the fuzzy logic advisor are located in Figure 4.1.

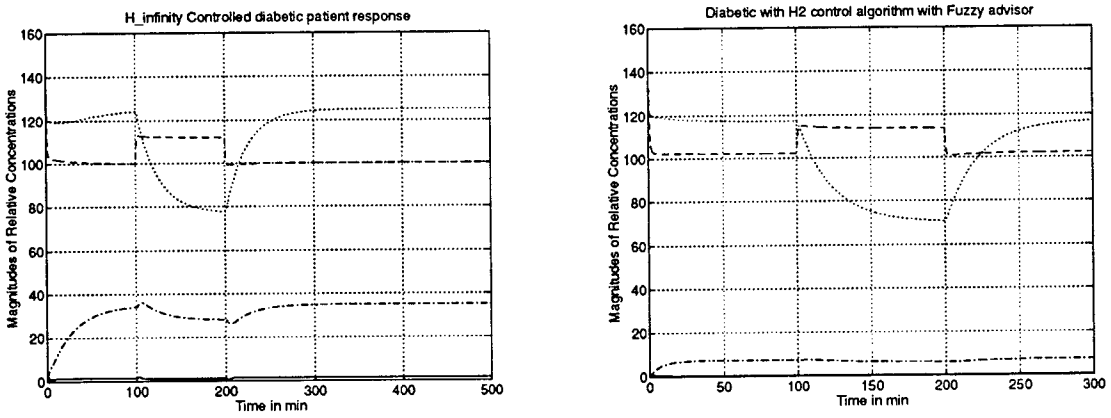


Figure 3: Left: Diabetic patient with H_∞ controller Right: Diabetic patient with H_2 controller with Fuzzy logic advisor

4.2 Variable Structure Control Application

For the model described in section 3.3, a Variable Structure Controller (VSC) was applied.

Inputs to the controller:	Glucose concentration, G
	"Estimated" derviative of glucose concentration, dG/dt
Output of the controller:	Piecewise constant insulin infusion

Implementation Choose a desired glucose level, say 100 mg/dl. For levels of low glucose concentration, no insulin required, therefore no control action needed. For glucose levels above the desired glucose level, the control action depends on the change in glucose concentration. Ordinarily the division for the control output, as seen in Figure 4.2, would be linear. But, for this application, a more conservative control response is desired as the derivative decreases. The reason behind the conservatism, is to prevent overshoot which could result in severe hypoglycemic affects. Therefore, the trigger function described in section 3.2 is used to provide the desired control characteristics, and the slope is adjusted to prevent hypoglycemic effects of aggressive insulin therapy.

VSC Simulation results The results of the VSC control strategy show that effective glucose control can be implemented without extensive knowledge of the plant dynamics. Another important advantage of the VSC design over the state-space controllers (H_2 and H_∞) is that the plant behavior is not altered through linearization methods. The simulation results are located in plot 3 in Figure 4.2.

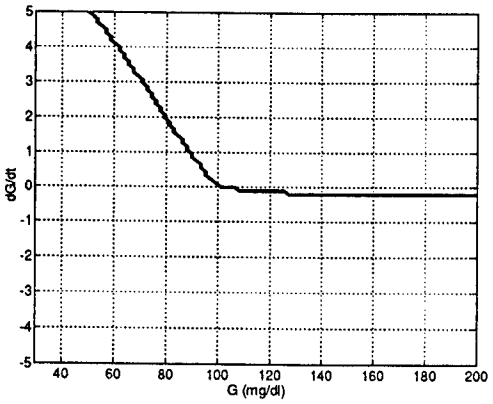


Figure 4: Operating region for VSC strategy

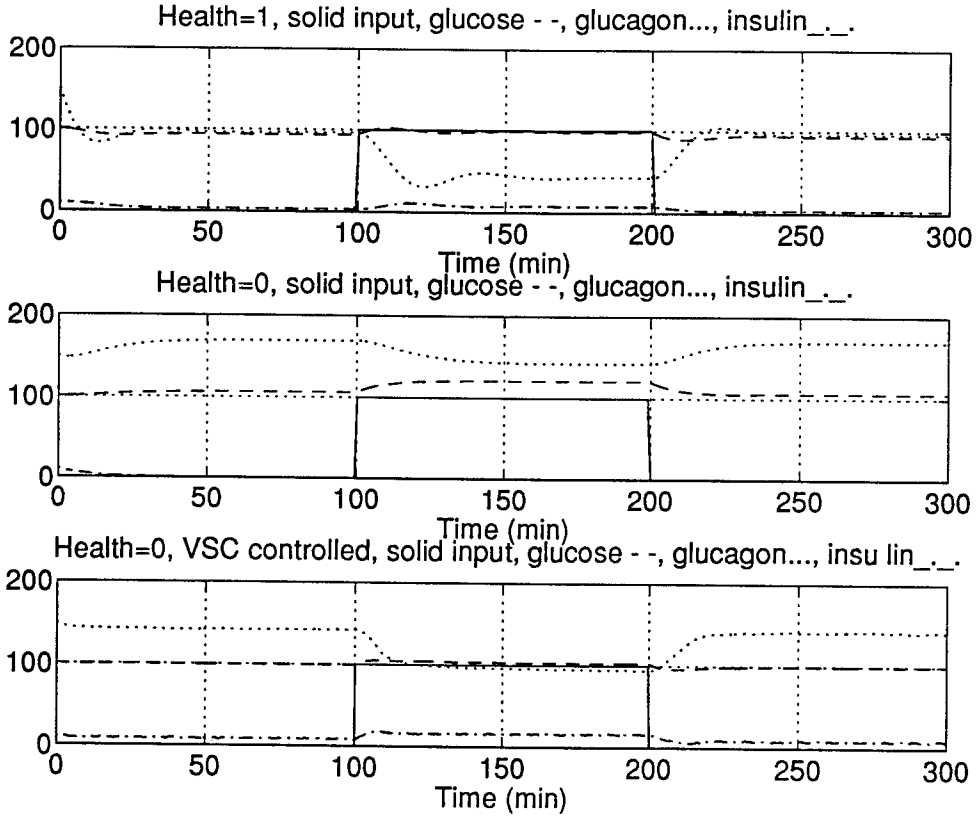


Figure 5: Responses of 1)open loop healthy patient 2) open-loop diabetic patient and 3) VSC controlled diabetic patient.

5 New directions modelling

Another step towards developing a model for the glucose regulation system, is a "model estimation" technique. Given a desired output waveform (i.e. hormone/glucose levels), construct a model to replicate this data. The solution involves constructing a linear, or nonlinear, model with unknown coefficients (or parameters), taking an initial guess at the coefficients, then using the following gradient descent method to minimize the error of the output from the estimated parameters to the actual output desired.

Algorithm details Given a function $f(x)$, compute its gradient with respect to x, $\nabla_x(f(x))$. Next compute the Hessian matrix, $H = \nabla_x(\nabla_x(f(x)))$. Next, one would optimally select α such that the solution $x_{new} = x - \alpha H^{-1}\nabla_x(f(x))$ results in $f(x_{new}) = 0$.

Implementation Given the set of unknown parameters, ξ, which yields a certain error function, $\eta(\xi)$, for the system, first compute $\Gamma = \nabla_\xi(\eta(\xi))$. Next compute the Hessian matrix, $H = \nabla_\xi(\Gamma)$. Finally, select α to minimize $\eta(\xi_{new})$, where $\xi_{new} = \xi - \alpha H^{-1}\Gamma$.

Method of Dirt Cheap Partials Given an initial guess of the "N" unknown system parameters, $\xi^0 = \begin{bmatrix} \xi_1 & \cdots & \xi_N \end{bmatrix}^T$, first determine ξ^j.

$$\xi^j = \xi^0 + \varepsilon * e_j = \begin{bmatrix} \xi_1 & \cdots & \xi_j + \varepsilon & \cdots & \xi_N \end{bmatrix}^T \tag{13}$$

where ε is some small deviation. Next, compute the error related to ξ^j, which will be denoted as η_j, where $\eta_j = \eta(\xi^j)$. Γ can now be determined via a estimated derivative.

$$\Gamma(\xi^0) = \frac{1}{\varepsilon}\begin{bmatrix} \eta_1 - \eta_0 \\ \vdots \\ \eta_N - \eta_0 \end{bmatrix} \approx \begin{bmatrix} \frac{\partial \eta}{\partial \xi_1} \\ \vdots \\ \frac{\partial \eta}{\partial \xi_N} \end{bmatrix} \tag{14}$$

In order to compute the Hessian matrix, H, evaluate $\Gamma_0, \ldots \Gamma_N = \Gamma(\xi^0), \ldots, \Gamma(\xi^N)$, then determine H via another estimated derivative.

$$H = \frac{1}{\varepsilon}\left[\ (\Gamma_1 - \Gamma_0) \ \middle|\ \cdots\cdots\cdots \ \middle|\ (\Gamma_N - \Gamma_0)\ \right] \tag{15}$$

The ultimate goal of this process is to determine an estimate of the parameters, ξ, that minimizes the error $\eta(\xi)$. To accomplish this goal, α must be chosen to minimize the error on the updated estimate ξ_{new}.

$$\xi_{new} = \xi^i - \alpha H^{-1}\Gamma \tag{16}$$

Where ξ^i is the present estimate of the parameters. After α is determined for the j^{th} estimate, ξ_{new} is computed as the new estimate, and the entire process is repeated until a tolerable error is accomplished.

6 Conclusions

Careful regulation of glucose levels is the key element for the treatment of diabetes mellitus. During this program, preliminary steps toward developing a glucose regulation model suitable for applying a robust, fault-tolerant controller have been made. After investigating the factors involved in glucoregulation, it appears that a highly nonlinear model would provide the best dynamic description. Experimentation indicates that a variable structure controller, would provide a more effective control of glucose levels in diabetic patient models than an H_2, H_∞, or a μ synthesis type control which require linearized models. Further developments are expected to provide useful two-way technology transfer between control strategies developed at Wright Lab/MNAG and the biomedical community.

References

[1] Geremia B. Bolli and Edwin A. M. Gale. Hypoglycemia. In K.G.M.M. Alberti, R.A. DeFronzo, H. Keen, and P. Zimmet, editors, *International Textbook of Diabetes Mellitus*, pages 1131–1149. John Wiley &Sons, 1992.

[2] P.E. Cryer. Counterregulation to hypoglycaemia in type i diabetes. In P. Brunetti and W.K.Waldhăusl, editors, *Advanced Models for the Therapy for Insulin-Dependent Diabetes*, pages 13–16. Raven Press, New York, 1987.

[3] Ralph A. DeFronzo, Riccardo C. Bonadonna, and Eleuterio Ferannini. Pathogenesis of niddm: A precarious balance between insulin action and insulin secretion. In K.G.M.M. Alberti, R.A. DeFronzo, H. Keen, and P. Zimmet, editors, *International Textbook of Diabetes Mellitus*, chapter 22, pages 569–633. John Wiley & Sons, 1992.

[4] Ralph A. DeFronzo and Eleuterio Ferrannini. Insulin actions in vivo: Protein metabolism. In K.G.M.M. Alberti, R.A. DeFronzo, H. Keen, and P. Zimmet, editors, *International Textbook of Diabetes Mellitus*, chapter 18d, pages 467–511. John Wiley &Sons, 1992.

[5] Ralph A. DeFronzo, Jordan D. Tobin, and Reubin Andres. Glucose clamp technique: a method for quantifying insulin secretion and resistance. *American Journal of Physiology*, 237:E214–E223, 1979.

[6] John C. Doyle, Keith Glover, Pramad P. Khargonekar, and Bruce A. Francis. State-space solutions to standard h_2 and h_∞ control problems. *IEEE Transactions on Automatic Control*, 34(8):831–847, August 1989.

[7] Keele, Neil, and Joels. *Samson Wright's Applied Physiology*. Oxford University Press, 1982.

[8] Pierre J. Lefèbvre. Biosynthesis, secretion and action of glucagon. In K.G.M.M. Alberti, R.A. DeFronzo, H. Keen, and P. Zimmet, editors, *International Textbook of Diabetes Mellitus*, chapter 14, pages 331–339. John Wiley & Sons, 1992.

[9] Sten Madsbad, Svend G. Hartling, and Ole K. Faber. C-peptide and proinsulin. In K.G.M.M. Alberti, R.A. DeFronzo, H. Keen, and P. Zimmet, editors, *International Textbook of Diabetes Mellitus*, chapter 13, pages 303–332. John Wiley & Sons, 1992.

[10] Patrizio Palazzo and Vittorio Viti. A new glucose-clamp algorithm — theotetical considerations and computer simulations. *IEEE Transactions on Biomedical Engineering*, 37(5):535–543, 1990.

[11] Donald C. Simonson, Luciano Rossetti, Andrea Giaccari, and Ralph A. DeFronzo. Glucose toxicity. In K.G.M.M. Alberti, R.A. DeFronzo, H. Keen, and P. Zimmet, editors, *International Textbook of Diabetes Mellitus*, chapter 23, pages 635–667. John Wiley &Sons, 1992.

[12] G. W. Swan. *Applications of Optimal Control Theory in Biomedicine*, chapter 3, pages 75–116. 1984.

[13] Werner K. Waldhăsl, Paul Bratusch-Marrain, Martin Komjati, Felix Breitenecker, and Inge Troch. Blood glucose response to stress hormone exposuure in helathy man and insulin dependent diabetic patients: Prediction by computer modeling. *IEEE Transactions on Biomedical Engineering*, 39(8):779–790, 1992.

[14] Brad J. Wallum, Steven E. Kahn, David K. McCulloch, and Daniel Porte Jr. Insulin secretion in the normal and diabetic human. In K.G.M.M. Alberti, R.A. DeFronzo, H. Keen, and P. Zimmet, editors, *International Textbook of Diabetes Mellitus*, chapter 12, pages 224–259. John Wiley & Sons, 1992.

[15] S. Wright. *Applied Physiology*. Oxford University Press, 1971.

A STUDY OF RF FIBER OPTIC COMMUNICATION LINK TECHNOLOGY

Ned F. O'Brien
Research Assistant
Department of Electro-Optics

University of Dayton
KL-463, 300 College Park
Dayton, OH 45469-0140

Final Report for:
Graduate Student Research Program
Air Force Office of Scientific Research

and

Wright Laboratory
Wright-Patterson Air Force Base, OH

September, 1994

A STUDY OF RF FIBER OPTIC COMMUNICATION LINK TECHNOLOGY

Ned F. O'Brien
Research Assistant
Department of Electro-Optics
University of Dayton

Abstract

In this paper the design, application and performance of RF fiber optic communication links (FO links) are considered for integration in the Pave Pace avionics architecture. Included is a comprehensive definition of relevant terminology, the reasoning behind present device selection, characterization, performance, and suggestions for future development. Particular attention is given to achieving the minimum detectable signal (MDS) and dynamic range required for RF avionics application. Various network configurations and optimization techniques are discussed, including: central versus remote data mixing, dedicated FO links, analog wavelength division multiplexed (WDM) FO links, and digital time division multiplexed (TDM) FO links. It is proposed that a composite FO network combining remote data mixing and external optical fiber modulation techniques will be most likely to achieve the MDS and dynamic range requirements.

A STUDY OF RF FIBER OPTIC COMMUNICATION LINK TECHNOLOGY

Ned O'Brien

Introduction:

The development of the Air Force avionics baseline architecture can be segmented into four basic progressions as outlined by Wilgus.{1} Roughly speaking these architectures are identified as independent avionics, federated avionics, integrated avionics, and advanced integrated avionics. The first architecture employed few avionics functions. It was possible to have independent processors, antennas, cockpit displays, and communication links for each function. The design was direct to implement and maintain, although advances in the complexity of the avionics suite made it necessary to improve the architecture. Cockpit displays became too numerous for the pilot to work with, aircraft performance was compromised by the weight and size of the avionics architecture, and system reliability was limited due to nonreconfigurability. These difficulties resulted in a progression toward shared resources in avionics design. The first step in this direction was the federated architecture.

Resource sharing began with display generators which were integrated into the cockpit processors to better utilize the limited display area available to the pilot. This is the present state of the avionics suite in Air Force aircraft. Restricted to coherent communication links the federated avionics is limited by long, heavy, lossy and inflexible paths of coaxial cable. Furthermore, the attenuation in coaxial cable rises proportionally to increasing frequency and inversely proportional to the cables cross section.{2,3} Therefore weight and size must be compromised to limit communication losses at high RF frequencies.

A rapid growth in computer technology, particularly in the development of very high-speed integrated circuitry, has made it possible to realize increasingly complex avionics functions. These functions are separated into 3 classes: electronic warfare (EW), communication/navigation/identification (CNI), and radar. Since each function has it own set of transmitted and received RF signals it is necessary to either co-locate the processors at the antennas in order to limit communication link losses or to down convert the signals before transmission over the coaxial cables. The large number of functions have also resulted in the

development of multifunction antennas (MFA).{4,5} This development is part of the next step in the evolution of the avionics architecture presently underway.

The Integrated Avionics architecture, also known as PAVE PILLAR, is the current baseline for the Air Force and is being developed for integration into the Air Force F-22 advanced tactical fighter and the Army's RAH-66 attack helicopter.{1} This architecture incorporates a small family of modular processors to realize multifunction processing. This allows for reconfigurable processing, minimizing the possibility of critical failure, and time-sharing among the processors, allowing the coordination of EW, CNI, radar to operate on a priority basis without interfering with each other.

PAVE PILLAR also includes the first implementation of optical communication links. This will first be realized with several 400 Mb/s point-to-point fiber optic links that will help to distribute high-speed sensor data to the centrally located digital processors.{1} This small step toward optical communications is an indication of broad advances to come.

Although PAVE PILLAR is yet to be implemented, progress has begun toward an advanced integrated avionics architecture, known as PAVE PACE.{6,7,8} The stated goal of PAVE PACE is to promote shared resources, system reliability, system maintainability, and reconfigurability. It is a progression to implement new technologies, optimizing the avionics architecture with respect to cost, weight, power and reliability. Critical technologies are outlined that need to be developed in order to integrate the avionics into the RF sensor suite. Optical communication links, parallel optical interconnects and advanced optical processing techniques are proposed to replace the long paths of coaxial cable and to reduce the burden on the processors. The advantages of FO links include light weight, small size, flexibility, flat transmission loss over a very broad bandwidth, EMI/EMP immunity, multiple link RF phase coherence, and high channel-to-channel isolation. The integration of optical components in PAVE PACE promise to vastly improve the avionics architecture, although much work is required to meet military aircraft environment requirements. A few of the more challenging requirements are: performance over the temperature range (-50°C to +125°C), thermal shock, mechanical shock, random vibrations, sinusoidal vibrations, dirt, dust and sand.

For CNI applications, a wideband optical communication link will need to provide a dynamic range of greater than 80 dB over the frequency range of 4 MHz to 6 GHz, with a minimum sensitivity of less than -130 dBm. The MFA further restricts the communication link to operate under EW and radar specifications as well, increasing the dynamic range to over 110 dB over a frequency range of 4 MHz to 18 GHz. A detailed listing of specific functions and their signal requirements is given in {8}.

Design Specifications

In this section, the individual devices of an RF FO link are discussed. Attention is given to the advantages and disadvantages of various component selections as well as the chosen mode of operation. Link loss, MDS, and dynamic range are defined as link performance criteria, and specific link configurations are specified.

LASER:

The laser diode is preferred over an LED source for communications applications above 100 to 200 Mb/s, since diodes typically provide a more intense, coherent, narrowband spectral output confined to within a smaller divergence angle. They typically have a linear response over much of the stimulated emission regime, and can have 30⇒40% quantum efficiency. The laser diode can also be as small as 250 ⇒500 μm long, 5 ⇒15 μm wide, 0.1 ⇒0.2 μm thick, which directly improves the coupling efficiency into a fiber while reducing packaging size.{9} Much research has been performed with the InGaAsP diode laser. It is well suited for operation in the range 1100-1600 nm, which makes it the diode laser of choice for operation at 1.3 μm or 1.55 μm. The disadvantages of the diode laser are the more complicated construction, the temperature sensitivity, and reduced lifetime at high current operation. A new approach to laser design is the optical fiber laser. It is too early to make a comparison, although it is hoped that one day the optical fiber laser will provide similar performance to the diode laser without the coupling difficulties for fiber applications.

WAVELENGTH:

For broadband communications, 1.3 μm sources are preferred since there is zero dispersion in typical optical fibers at this wavelength, although in long distance communications 1.5μm is typically used to minimize attenuation and scattering losses. In such systems, waveguide dispersion can be adjusted to counterbalance material dispersion, thus achieving a dispersion shifted fiber that will combine the advantages of both minimum loss and zero dispersion at 1.55 μm. This would seem to make a 1.55 μm source advantageous, although this is not presently the case. 1.55 μm lasers are very expensive and research within the analog RF regime at this wavelength has been limited. Erbium-doped optical fiber ring lasers are promoting interest in generating very closely spaced, coupled WDM/TDM optical solitons for dispersion free transmission, although their application is limited due to the digital nature of the TDM.

Since the optical fiber has such low losses, it is possible to ignore scattering and attenuation and choose 1.3 μm operation to avoid dispersion problems, especially for such short lengths. This is why the PAVE PACE architecture calls for 1.3μm optical communication links.

MODULATION:

The laser diode source modulation can be achieved either externally from the laser or directly by modulating the drive current to the laser. The direct modulation can achieve both a linear amplitude modulation and a pulse modulation up to a few GHz for present lasers. For higher frequency modulation it is necessary to go to external modulation. Externally modulated sources operate the laser in a continuous wave mode while modulating the light separately with either an electro-optic or acousto-optic modulator. Presently, externally modulated lasers are available at 20 GHz, although they are not yet economically viable. Since the laser is operated in the continuous wave mode the external modulated source will have lower noise although the external modulator may add as much as 10 dB of additional loss to the system. The lower noise is more significant since the loss can be compensated with pre- or post-amplification.

OPTICAL FIBER:

The specifications of the optical fiber cable will be dependent upon the number of parallel communication links required within each cable. This is a packaging issue which has not yet been studied, although certain specifications for the optical fiber can be made. The high frequency modulation of the source makes the light non monochromatic, resulting in a wide spectral width. A multimode optical fiber would suffer significant intermodal dispersion. This suggests that a single-mode optical fiber would be best for this application.

As mentioned in the introduction, the present avionics architecture depends upon coaxial cable communication links, which suffer very high attenuation (semi-rigid coaxial cable 790 dB/km, and flexible coaxial cable 1115 dB/km), and limits the amount of remote processing that can be done within weight and space requirements.{10} The attenuation of optical fibers (0.48 dB/km) is very low in comparison, and even more interesting is the fact that attenuation is flat with respect to the modulation frequency. This demonstrates a symbiosis between the desire to move the communications into the RF sensor suite, the application of optical fiber communication links, and remote processing. Implementing RF communications makes optical fiber systems very attractive, which in turn enables remote processing.

The application of rare-earth doped fibers is also finding application in present systems since they can provide signal amplification or even operate as the light source themselves. For

avionics applications the link lengths are so short that this may not be necessary within a dedicated FO link design, although advanced designs may incorporate optical signal amplification.

DRIVE CIRCUITRY:

There are at least two requirements of the drive circuitry to achieve stable operation of an FO link. These are to account for the laser output variations as a function of temperature, and for loss of maximum power with age. Since the diode is highly temperature dependent, it necessary to include an adjustable dc bias current level to drive the laser to the right intensity. This can be achieved with an optical-feedback scheme, a temperature-matching transistor, or a threshold-sensing circuit. The temperature dependence is governed by the threshold current given by,

$$I_{th}(T) = I_z e^{T/T_o},$$

where T_o and I_z are constants dependent upon material and design specifications of the diode laser.

The life expectancy of the diode laser is also a function of the temperature as well as the drive current density. In general the higher the temperature or drive current density, the shorter the operational life of the device. The typical diode laser can work for several years before experiencing a 3 dB loss, although at 200°C it may degrade in less than a year.{9}

IMPEDANCE MATCHING CIRCUITRY:

The purpose of impedance matching circuitry is to optimize the input and output impedance of the link to minimize resistance reflection losses. The input impedance to a laser diode is characteristically very low whereas the Avalanche photodiode (APD) output impedance is characteristically very high. Both poorly match the RF communications input/output impedance (50Ω). Typically a trade-off is enacted between return loss, insertion loss, and bandwidth resulting in a 5 - 10 dB reduction in link loss.{3}

Lossless passive matching makes use of RCL networks to perform impedance transformations to the laser over a finite bandwidth. Active matching uses bipolar and field-effect transistors, in addition to the passive elements, to effect a match to the laser. The active matching can add gain to the overall network while allowing the 50 Ω match to be made to an active device such as the external modulator.

Fano's Rule is used to determine the amount of lossless matching that is achievable for a circuit.{11} Fano's Rule states that there is a minimum insertion loss that can be achieved with impedance matching for a given bandwidth and Q of the circuit. It is expressed as,

$$\int_0^\infty \ln\frac{1}{\Gamma}d\omega = \frac{\pi\omega_o}{Q_1} \quad ,$$

where ω_o is the frequency, Q_1 is the quality factor of the circuit or device, and Γ is the reflection coefficient that is to be minimized. Γ is defined as,

$$\Gamma = \frac{Z_{MATCH} - Z_{CIR}}{Z_{MATCH} + Z_{CIR}},$$

where Z_{MATCH} is the complex impedance of the matching circuit and Z_{CIR} is the complex impedance of the circuit. Minimizing Γ for the frequency range ω_a to ω_b gives,

$$\Gamma = \exp\left[-\pi(\omega_b - \omega_a)/R_oC\right], \qquad \omega_a < \omega_o < \omega_b$$

$$\Gamma = 1, \qquad \text{elsewhere.}$$

where R_o and C are the laser small circuit resistance and capacitance.

The voltage standing wave ratio (VSWR) is typically used to describe the performance of the transmission line independently of its shape, attenuation, or electromagnetic wave properties. The VSWR is related to the amplitude of the reflection coefficient as follows {12},

$$|\Gamma| = \frac{VSWR - 1}{VSWR + 1}.$$

If there were no reflections then the VSWR would be 1, if the reflections were 100% then the VSWR would be infinite. Typically this should be as close to 1 as possible, for properly matched circuitry.

COUPLING:

In any optical fiber system, coupling is a source of significant loss. Several optical techniques are used to improve the coupling efficiency. Typical examples are the use of imaging microspheres, nonimaging microspheres, or cylindrical lenses between the source and fiber to match numerical apertures. These techniques are typically optimized by the manufacturer for many laser diodes and photodetectors. Typically the source or detector will come with a 1 meter length of optical fiber directly connected to the device in an optimum configuration. This is called a pigtail or a fly-lead. For application to a communications link the pigtail would then be

connected to the transmission fiber via an expanded optical connector. Using microlenses with a laser diode source of between 3 and 9μm FWHM, coupling efficiencies of 50% (3 dB) to as high as 80% (1 dB) should be attainable.

CONNECTOR:

Although fusion splicing is the optimum method of connecting fiber ends, a single-mode optical fiber connector would be more appropriate under the PAVE PACE architecture. This would improve the systems maintainability and reliability by allowing for the direct replacement of the optical fiber without exposing the fiber cleave, a fusion splicer, or a specially trained technician. The Air Force and AT&T Bell Laboratories have developed a card-edge, multimode connector which is capable of surviving in the harsh military environment. Work on a single mode connector is underway. These connectors are called Robust Optical Connectors.{1}

DETECTOR:

Detector specification is generally coupled to the laser and modulation selection. In general an APD is required to respond to the high frequency RF modulation. Often the APD will be made out of the same material used in the laser to optimize the detectors sensitivity at the particular wavelength. Furthermore it also provides a statistical amplification of the detected signal thereby improving the devices minimum sensitivity. Several sources of noise arise from the quantum conversion, such as the shot noise arising from the discrete nature of current flow in the device, thermal noise arising from the random motion of electrons in the conductor, and dark current noise arising from electron-hole pair creation in the absence of optical quanta. Typically, these devices come with a 1 meter fiber pigtail to provide optimum coupling and have an optical conversion efficiency greater than 50%.

LINK LOSS:

The link loss of the FO link describes the degradation of the input signal due to the inefficiency of each of the components. The amplitude loss to the signal can be preconditioned or restored with either a pre- or post-link amplifier. The loss is significant since it limits the minimum detectable signal that can be discerned above the noise threshold of the detector. Therefore it is important to minimize the losses in order to reduce the minimum detectable signal and to improve the links dynamic range. The link loss is defined as the sum (in dB) of the loss of all components of the link. A simple equation can be written that describes this as,

$$L_{link} = L_{LE} + L_{LC} + L_C + L_{OF} + L_{DC} + L_{DE} + L_\Omega$$

L_{LE}	=	laser quantum efficiency loss
L_{LC}	=	laser coupling loss
L_C	=	connector loss
L_{OF}	=	optical fiber loss = $2a_f l_f$
		a_f = fiber attenuation [dB/km]
		l_f = fiber length [km]
L_{DC}	=	detector coupling loss
L_{DE}	=	detector quantum efficiency loss
L_Ω	=	reflection & ohmic loss

The results of a study of present device technology is given by Koffman.{3} Koffman found relative losses of $L_{LE} + L_{LC}$ = 13 dB (36%), L_Ω = 13.5 dB (37%), $L_{DE} + L_{DC}$ = 7.5 dB (21%), L_C = 2.0 dB (5%), L_{OF} = 0.01 dB (0.03%). Plotting these values in a pie chart, as shown in Figure 1, illustrates the relative loss of each component.

The loss of each component is indicative of the specific link design, although the relative losses between components suggests where improvements can be made. In the study the 13.5 dB of ohmic and resistive losses were reduced by as much as 10 dB when reactive impedance matching circuitry was added. Connector and coupling optimization techniques have been discussed that minimize there respective contributions, therefore the next major improvement in MDS and dynamic range will have to come from improved quantum conversion efficiency at the laser and detector. One technique to overcome the laser inefficiency is to modulate the laser externally after it has been coupled into the fiber. In this way the laser quantum efficiency would be replaced with the modulator efficiency.

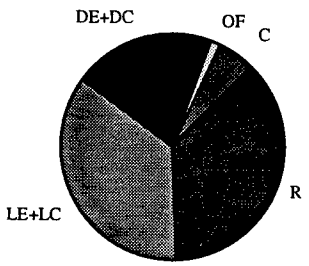


Figure 1. Relative losses of FO link without impedance matching.

AMPLIFICATION:

Electrical amplification is required to boost a transmission signal before the antenna. This must be provided after the transmit FO link due to the limited power output of the detector.{see Figure 4} Since the signal processors can put out a 0 dBm signal, post FO link amplification will be sufficient to overcome the link losses. This is not the case for the receive FO link. Received signals may be just above the thermal noise level (-174 dBm/Hz), which is below the MDS of present links, therefore the received signal must be amplified before the FO link. This amplification stage should also provide any required gain so that post link amplification is not necessary.

NOISE:

For long lengths of fiber, the signal is significantly attenuated, and the system is receiver noise limited, although in this study the fiber lengths are short and the system is transmitter noise limited. Typically a noise figure is defined as the S/N at an input of -174 dBm/Hz (thermal noise) divided by S/N at the output of FO link. This results in a noise figure given by,

$$F_{link} = 1 + \frac{N_t}{L_{link} kT},$$

where N_t is the total noise of the optical link, k is the Boltzmann constant, and T is the temperature in Kelvin. A preamplifier can be added to reduce the noise figure, or a post amplifier to restore the signal amplitude. The noise figure is them determined as the sum of the cascaded stages given by,

$$F_{sys} = F_1 + \frac{(F_{link} - 1)}{G_1} + \frac{(F_2 - 1)}{G_1 L_1},$$

where G is the gain, 1 indicates the preamplifier, and 2 the post amplifier.

LINEARITY:

At high intensity the optical link begins to compress the signal. The compression results in a nonlinear relationship between the input and output signals, and may occur as low as 50 mW. It is very important to know at what intensity the 1 dB compression occurs since the S/N ratio and dynamic range are defined by this point.

DYNAMIC RANGE:

The dynamic range of the optical link is a measure of the variation of signal levels that can be carried by the link. It is typically defined in one of three ways, and it is important to distinguish which way is being used. The three ways are as follow:

1) the ratio of the fundamental output to the third order intermodulation product (IMP).
2) the level of IMP suppression achieved when that level equals the link S/N ratio.
3) the range of power between the MDS and the point at which the link gain exhibits 1 dB of compression.

The 1 dB compression point is usually determined as 10 dB below the third order intercept point of the laser diode, which is dependent upon the laser structure and material. Definition (1) is limited in use since the IMP decreases faster than the fundamental with decreasing input power. Therefore by definition (1) any required dynamic range can be stated for low enough power. Definition (2) accounts for this by specifying the dynamic range at the point where the IMP equals the noise floor. Since the noise is constant for any specific bandwidth, this will indicate the maximum possible dynamic range. Definition (3) applies when only one signal is present. This definition yields a higher dynamic range but if more than one signal is present it does not indicate whether the signals can be distinguished from harmonic and IMP spurs. spur free dynamic range is defined as 2/3 of definition (3). Definition (2) is generally preferred.

MINIMUM DETECTABLE SIGNAL:

The MDS is a critical specification for PAVE PACE communication link integration. It is a function of the room temperature thermal noise, -174 dBm/Hz, the link noise factor and the bandwidth of the signal, $\Delta\nu$. It can be expressed as,

$$MDS[dB] = -174[\frac{dBm}{Hz}] + F_{link} + 10\log\Delta\nu$$

L-CROSSOVER LENGTH:

The L-Crossover point is a method of comparing two communication links in terms of total link attenuation. It specifies the length in meters were the two links have equal attenuation for a given signal modulation. This is particularly useful in demonstrating the benefits of an FO link at high RF modulations.{3}

Optical Communication Link Designs

The typical FO link has central data mixing (CDM) as shown in Figure 2. In this architecture the FO link signal is modulated directly by the combined data and reference signal. The data is upconverted to the reference signal before transmission. The linearity and high noise level near the relaxation oscillation frequency of the laser puts severe restraints on this type of system.

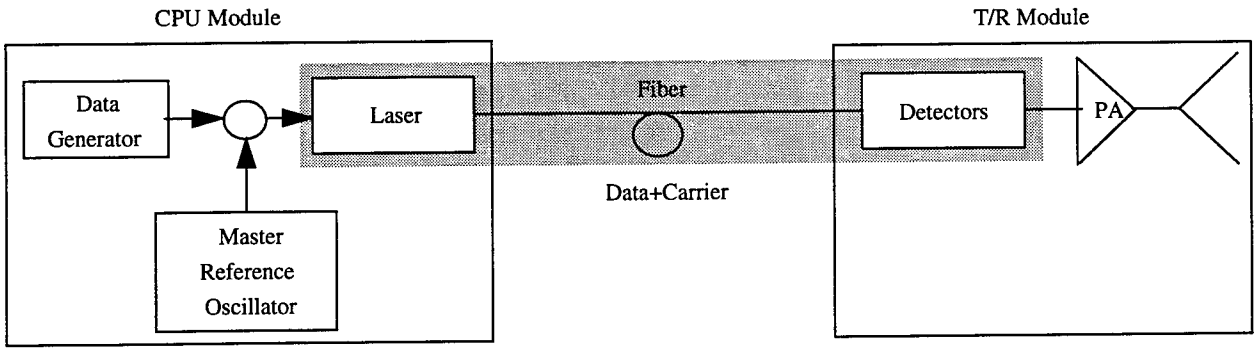


Figure 2. Central data mixing FO link.

An improved system employs remote data mixing (RDM), shown in Figure 3. This FO link actually has two separate links, one narrow bandwidth link for the data transmission and one high frequency carrier for the microwave transmission. These two links are then mixed at the antenna.

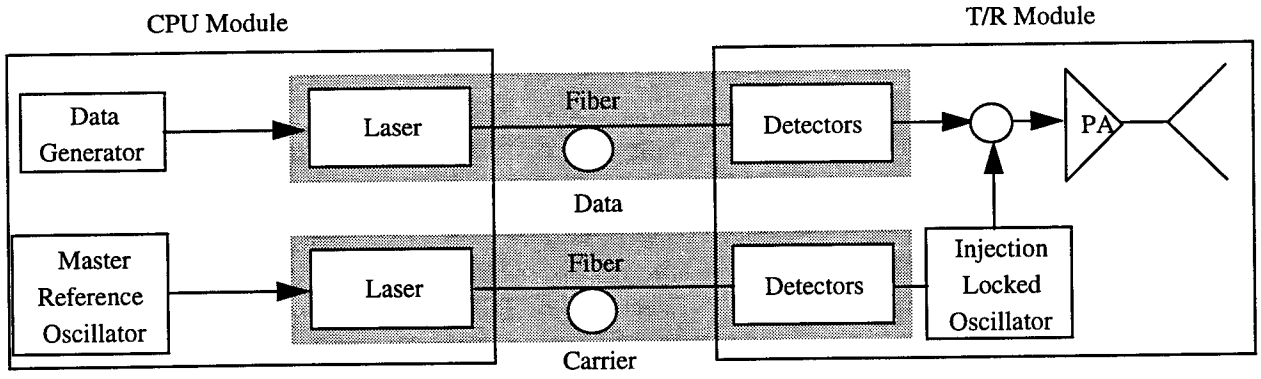


Figure 3. Remote data mixing FO link.

With the RDM, each link can be optimized independently to reduce noise and improve dynamic range. Since the RF signal is not carrying data and is not modulated from the carrier frequency, nonlinearities of its operation can be utilized to extend the operating frequency well beyond the laser relaxation frequency.

Since the data link is now modulated at much lower frequencies (0.5 GHz), reactively matched microwave circuitry can be designed to better match the impedance of the laser and detector modules. Using this technique, Stephens and Joseph {3} have demonstrated a 13 dB reduction of link loss, with an improvement in dynamic range of 15 dB. L-Crossover lengths are also determined for 5, 10, and 20 GHz. The most interesting comparison is between the RDM and semi-rigid coaxial cable resulting in L-Crossovers of 25, 12, and 5 meters.

In designing the two-way optical communication links for phased array antenna applications two different sets of criteria must be considered, that is, one set for the transmit link and one set for the receive link. Additional criteria apply according to the specified functions of the antenna. In general, the criteria for the receive FO link will be more stringent than those for the transmit FO link. The receive link will need to provide the required dynamic range and SNR to a signal with a minimum input as low as $\approx$ -137 dBm). This requires direct amplification before optical conversion or else the noise of the link will significantly degrade the signal. The pre-amplification significantly reduces the noise figure. This is an advantageous situation since present transmit/receive (T/R) modules provide this amplification of received signals.

If the input to the FO link is a well formed RF signals (0 dBm), such as would be obtained directly from the processors, it is not necessary to pre-amplify the signal, although post-amplification will be necessary to make up for link losses and to provide any necessary gain before transmitting from the antenna. Once again present T/R modules provide this amplification.

Figures 4 shows a direct FO network for 8 point-to-point links from the central processor to the T/R module. The separate transmit and receive modules are identified and are shown to be similar. The optical connectors are the robust optical connectors previously discussed. They allow for independent replacement of the lasers, fibers or detectors. The connectors external to the modules are electrical connectors. The packaging of the lasers and detectors can be very small and the size of the optical fibers is a significant reduction over coaxial cables.

The direct FO link network provides independent devices for each FO link. This provides a graceful degradation in case of device failure (reliability, survivability), while reducing the need for additional complicated optics or electronics. Common to all networks are the impedance matching networks, and both the electrical and optical connectors.

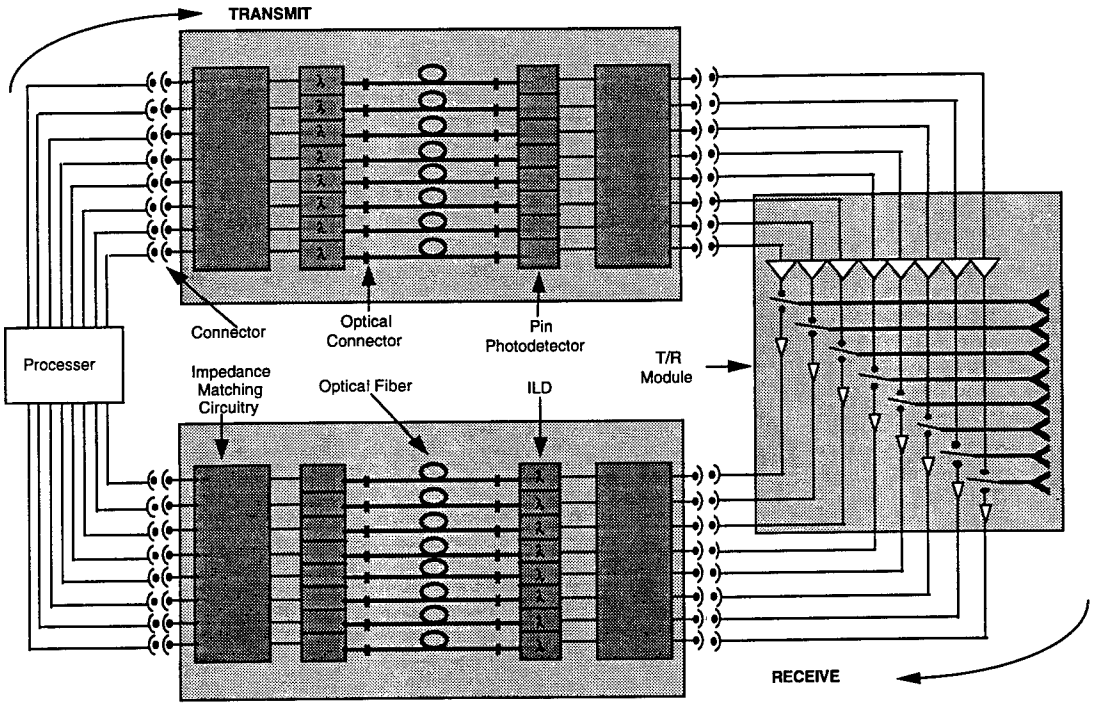


Figure 4. Direct FO link.

Since the fiber has an extremely wide bandwidth, further reductions can be achieved by applying TDM or WDM techniques to the network as shown in Figure 5 and Figure 6.

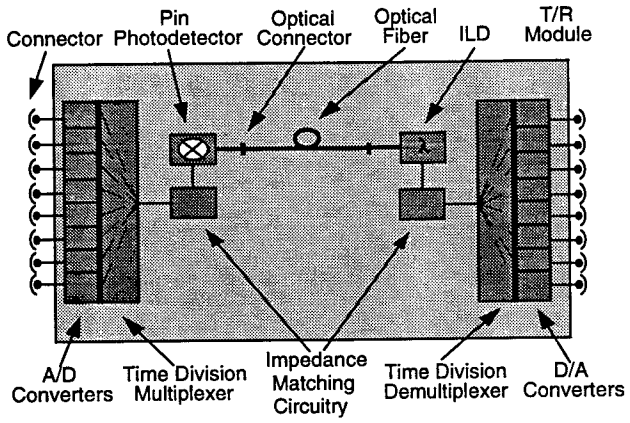


Figure 5. Time division multiplexed FO link.

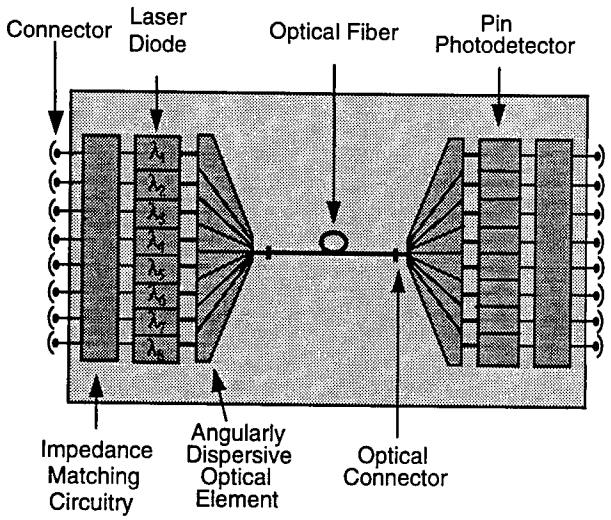


Figure 6. Wavelength division multiplexed FO link.

The TDM FO link has the advantage of multiplexing all of the optical signals onto a single fiber, while reducing the impedance matching circuitry to a single laser/detector pair. This design requires significant development of present technology in two areas. The first is dependent upon much higher laser modulation rates, since the multiplexed signal will have to be a large factor faster than each of the parallel modulators to assure signal quality. The second required technological development is an A/D and D/A converter that can provide the conversions fast enough to sample the RF signal modulation, satisfying the dynamic range, SNR, and MDS requirements, and minimizing size and energy consumption.

The WDM network utilizes parallel lasers with unique wavelengths launched onto a single fiber. This has the advantage of being an all analog network that provides a similar reliability and survivability for the quantum devices while reducing the number of fibers in the system. A very simple WDM system is shown in Figure 7. In principle, it consists of an angularly dispersive element, most likely a thin film, that will redirect the light dependent upon its wavelength. If traveling to the right the light is then focused to separate locations for independent detection. If traveling to the left the light is then focused into a single FO link. Figure 7 demonstrates another advantage of a WDM FO link. Since the angularly dispersive element is bi-directional, the possibility arises to reduce the independent transmit and receive FO networks into a single fiber, bi-directional, analog network. There are at least three limiting factors to this configuration, increased coupling loss, finite channel width, and increased channel cross talk.{9,13}

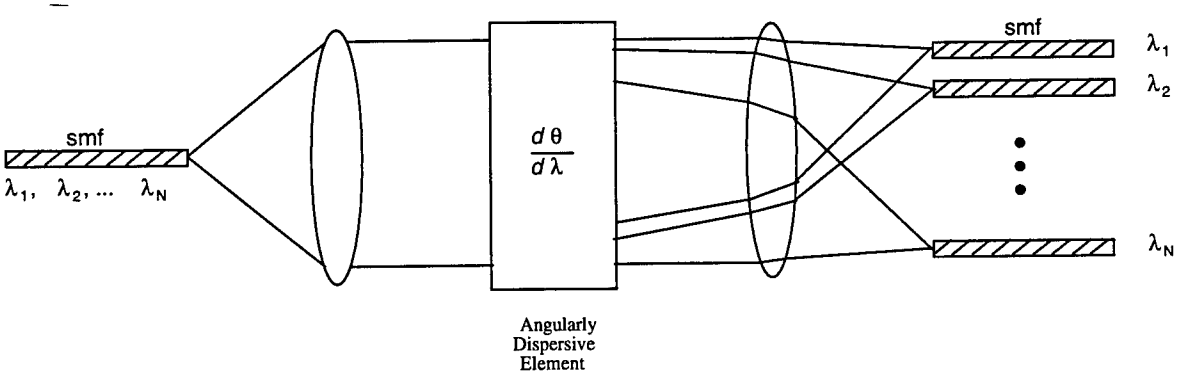


Figure 7. Wavelength division multiplexed optical signals.

Figure 8 demonstrates a single FO link employing external modulation and remote data mixing techniques. Unlike the three previously discussed links, this configuration has unique transmit and receive modules. Both modules utilize optical fiber electro-optic modulators, and a single continuous wave laser that is coupled and split to each link.

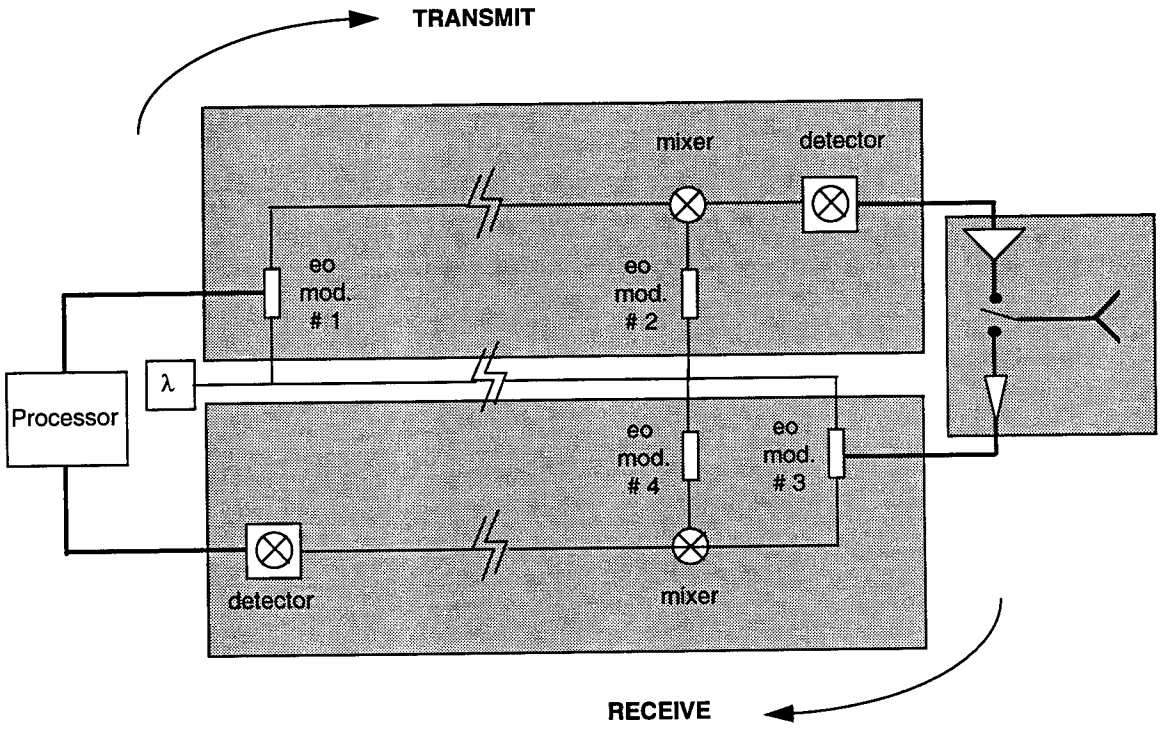


Figure 8. Externally modulated, remote data mixing FO link.

This configuration combines several of the FO link techniques to extend the performance of the network. The external fiber optic modulators (eo mod.) avoid unnecessary coupling and decoupling losses of the modulated signal. The remote mixing reduces the modulation bandwidth of the eo modulators. resulting in improved dynamic range. The transmit module consists of two links. The first link is modulated with the data signal by eo mod. #1. The signal is then remotely, optically up converted to the carrier RF signal by mixing it with the signal from eo mod. #2. The receive module performs a similar down conversion by mixing the incoming signal from eo mod. #3, with the selected RF carrier frequency to strip off and send only the data signal to the processor. In this optical heterodyne detection technique, the optical mixing significantly reduces the amount of electrical hardware while providing a wideband signal modulation. Although characterization of the mixer and modulator performance measures have not yet been determined, it is hoped they will be improved by minimizing the number of optical-to-electrical and electrical-to-optical conversions and by reducing the detected modulation rate of the receiver signal.

Conclusion

The development of avionics over the past 50 years has greatly improved the effectiveness of all military aircraft, and the progress will most certainly continue into the 21 century. The trends in avionics design show a commitment toward shared resources, modularity, reliability and the reduction of weight, size and cost. The small attenuation, large bandwidth, light weight and small size of FO links directly supports each of these trends. The integration of FO links into avionics is a fundamental progression of technology, although several advances must be made before their application will be realized. The most significant improvements are needed from the diode lasers and detectors. Quantum efficiency, modulation frequency, and stability must be increased while reducing noise, in order to meet the high dynamic range and low MDS requirements. A literature search shows that each year these advances are being made.

References

1) Wilgus, Joseph S., "An optical approach to a post-2000 avionics architecture: PAVE PACE," SPIE Vol. 2153 Optoelectronic Interconnects II (1994), pp. 96-100.

2) W.R. Stephens and T.R. Joseph, "RF fiber optic links for avionics applications," SPIE Vol. 716, High Frequency Optical Communications (1986) p. 2.

3) I. Koffman, P.R. Herczfeld, A.S. Daryoush, "High speed fiber optic links for short-haul microwave applications," IEEE MTT-S Digest (1988), pp. 983-986.

4) Tenbarge, Joseph A., et.al., "Shared Antenna Concepts for integrated avionics systems," Wright Laboratory, WPAFB, OH.

5) R. A. Reilly, et. al., "Modulated multi-function multi-band airborne radio system," AFWAL TR-81-1077, Vol. 1, Avionics Laboratory, WPAFB, October 1981.

6) R. D. Varga, and K. G. Mathews, "Advanced system avionics technology and application assessment (PAVE PACE)," System Requirements Specifications, WL-TR-93-1072, McDonnell Douglass Co., September 1990.

7) R. D. Varga, and K. G. Mathews, "Advanced system avionics technology and application assessment (PAVE PACE)," Technology Roadmap and Integration Strategy, WL-TR-93 -1075, McDonnell Douglass Co., 1992.

8) W. A. Whitehouse, et. al., "PAVE PACE system segment specifications," WL-TR-93-1069, Boeing Defense and Space Group, April 1993.

9) Keiser, Gerd, Optical Fiber Communications, McGraw Hill Inc., New York, 1991.

10) W.E. Stephens, and T.R. Joseph, "System Characteristics of Direct Modulated and Externally Modulated RF Fiber-Optic Links," JLT vol. LT-5, No. 3, March (1987), p 380-387.

11) R.J. Fano, "Theoretical limitations on broadband matching of arbitrary impedances," J. Franklin Ind. pp, 57-84, 139-154, Jan. and Feb. 1950.

12) M. Skolnik, Radar Handbook, McGraw-Hill Book Co., New York: 1970, p. 8-2.

13) Brackett, Charles A., "Dense Wavelength Division Multiplexing networks: Principles and Applications," IEEE Journal on Selected Areas in Communications Vol. 8(6), August 1990, pp. 948-964.

A NUMERICAL STUDY OF DROPLET-VORTEX INTERACTIONS IN AN EVAPORATING SPRAY

Tae W. Park
Graduate Student
Department of Mechanical Engineering

University of Illinois at Chicago
842 West Taylor Street
Chicago, IL 60607

Final Report for:
Graduate Student Research Program
Wright Laboratory

Sponsored by:
Air Force Office of Scientific Research
Bolling Air Force Base, DC

and

Wright Laboratory

September 1994

A NUMERICAL STUDY OF DROPLET-VORTEX INTERACTIONS IN AN EVAPORATING SPRAY

Tae W. Park
Graduate Student
Department of Mechanical Engineering
University of Illinois at Chicago

Abstract

In this paper, we present the time-dependent axisymmetric numerical simulation of an unsteady n-heptane evaporating spray, and investigate the droplet-vortex interactions which determine the structural and dynamic characteristics of a spray jet flow. The spray is formed between a droplet-laden heated nitrogen jet and a coflowing air stream. A detailed, multidimensional, two-phase algorithm is developed for the simulation. A comprehensive vaporization model is employed to calculate the instantaneous droplet size and surface temperature along the trajectory of each droplet group. Monodisperse spray in introduced into the large vortex structures that are generated due to the presence of buoyancy-induced hydrodynamic instability of the heated jet. Results focused on the two-way interactions between vortical structures and droplets, and the dynamics of both non-evaporating and evaporating sprays. The vortex structures cause droplets to disperse radially outward, and this in turn determines the fuel vapor distribution and also modifies the vortex dynamics. Thus, the dynamics and structural characteristics of the evaporating spray are strongly influenced by the two-way transient interactions. The effects of initial droplet size, injection location, and liquid-to-gas mass loading ratio on these interactions are also investigated.

A NUMERICAL STUDY OF DROPLET-VORTEX INTERACTIONS IN AN EVAPORATING SPRAY

Tae W. Park

Introduction

Large-scale, coherent vortical structures have been found to exist in a variety of shear flows including those involving combustion and multiple phases [1-5]. In two-phase shear flows involving solid particles or liquid droplets, transient interactions between the dispersed phase and the large vortical structures are expected to play a central role in determining the dynamics and structural characteristics of these flows. The transient interactions pertain to the effect of large vortical structures on the behavior of droplets/particles, and the influence of droplets on the dynamics of large vortical structures. These two effects are coupled in a nonlinear manner; the vortex structures determine the droplet dispersion and gasification behavior, which in turn affects the local environment surrounding each droplet and thereby the dynamics of two-phase system under consideration. Several numerical [6,7] and experimental [8-11] studies in recent years have focused on the one-way coupling, examining the influence of large vortical structures on the dynamics of droplets/particles injected into a shear flow. These studies show that the effect of large structures on particle motion is characterized by the ratio of the particle response time to the characteristic time of structures. This ratio is defined as the Stokes number (St). When the particle response time is of the same order of magnitude as the vortex time scale, $St \sim O(1)$, particles can disperse significantly more than the fluid particles, the enhanced dispersion being attributed to the centrifugal action of vortices. For small Stokes number, $St << 1.0$, particles behave similar to the fluid particles, while for large Stokes number, particles remain largely unaffected by the vortices. More recent work [12,13] on particle-laden flows have examined the effect of external forcing on the particle dispersion behavior. A general conclusion from those studies [12,13] is that the dynamics of vortex structures, and thereby the dispersion behavior of particles in a shear layer can be manipulated by a sub harmonic periodic forcing of the shear layer.

Particle-laden shear flows in practical applications involve two-way, nonlinear interactions between the continuous phase and the dispersed phase. Previous studies cited above have mostly focused on the one-way interactions, i.e. on characterizing the effect of vortex structures on the droplet motion and dispersion behavior. The effects of dispersed phase on the vortex dynamics, and subsequently on fuel vapor distribution and flame behavior remain largely unexplored. In this paper, we report a numerical study of two-way droplet-vortex interactions in an unsteady evaporating spray. The spray is formed between a droplet-laden heated nitrogen jet and a coflowing air stream. The jet velocity and temperature are considered in a range where the large vortical structures are generated due to the buoyancy-induced hydrodynamic instability rather than the shear-induced Kelvin-Helmholtz instability. The vaporization characteristics of n-heptane fuel spray under the influence of two-way droplet-vortex interactions are

investigated. The dynamics of a non-evaporating spray is also analyzed in order to distinguish the interactions involving only momentum transfer between the phases from those involving mass, momentum, and energy transfer.

Physical Model

The evaporating spray investigated in the present study is shown schematically in Fig. 1. It consists of a central fuel jet which is a two-phase mixture of gaseous nitrogen and liquid fuel droplets and a low-speed coannulus air flow. The central jet is heated primarily to enhance the fuel evaporation; however, in the present studies, it also plays a key role for the formation of buoyancy induced vortical structures. Numerical studies on the two-way interactions between the vortex structures and the evaporating droplets are conducted by solving the unsteady, axisymmetric gas-phase equations that include the droplet source terms, and the appropriate droplet equations.

The unsteady, axisymmetric governing equations in cylindrical (z, r) coordinate system for heated jet are

$$\frac{\partial(\rho\Phi)}{\partial t}+\frac{\partial(\rho u\Phi)}{\partial z}+\frac{\partial(\rho v\Phi)}{\partial r}=\frac{\partial}{\partial z}\left(\Gamma^{\Phi}\frac{\partial\Phi}{\partial z}\right)+\frac{\partial}{\partial r}\left(\Gamma^{\Phi}\frac{\partial\Phi}{\partial r}\right)-\frac{\rho v\Phi}{r}+\frac{\Gamma^{\Phi}}{r}\frac{\partial\Phi}{\partial r}+S_g{}^{\Phi}+S_\ell{}^{\Phi}. \qquad (1)$$

The general form of Eq. (1) represents the continuity, momentum, species, or energy conservation equation depending on the variable used for Φ. Table 1 gives the transport coefficients Γ^{Φ} and the source terms $S_g{}^{\Phi}$, $S_\ell{}^{\Phi}$ that appear in the governing equations. In this table, μ, λ, and c_p represent the viscosity, the thermal conductivity, and the specific heat, respectively. They are considered functions of temperature and species concentration.

In order to evaluate the source terms in the gas-phase equations due to the presence of droplets, it is necessary to establish droplet trajectories, size and temperature histories. The Lagrangian approach is employed to solve the liquid-phase governing equations for the dynamics and vaporization history of each droplet group. The spray is characterized by a discrete number of droplet groups, distinguished by their injection location, initial size, and time of injection. The effect of dispersed phase is incorporated through the source/sink terms, representing the exchange of mass, momentum, and energy between the gas and liquid phases. The equations governing the variation of position, velocity, and size for each droplet group and other expressions are available in Ref. [14]. A comprehensive vaporization model is employed to calculate the instantaneous droplet size and surface temperature along the trajectory of each group. The model includes the effects of variable thermophysical properties, non-unity Lewis number in the gas film outside the droplet, the effect of Stefan flow on the heat and mass transfer between the droplet and the gas, and the effect of transient liquid heating. The variable thermophysical properties are calculated at reference film temperature and concentrations, obtained by using the 1/3 rule, except for the gas density which is calculated at the free stream value [15]. The Wilke rule [16] is used to calculate the dynamic viscosity and thermal conductivity of the gas film. The droplet (nC_7H_{16}) properties are collected from the various sources and approximated as a function of the temperature [14]. The effect of transient liquid heating is incorporated by using the conduction-limit model [17]. This model is deemed satisfactory in the present study, since the maximum droplet

Reynolds number during droplet lifetime is less than ten and thus the effect of internal circulation is expected to be negligible. For the same reason, the effects of gas-phase convection on the heat and mass transport are represented by the Ranz-Marshall correlation [17].

Solution Procedure

The numerical solution of the unsteady two-phase equations employs an implicit algorithm for solving the gas-phase equations, and an explicit Runge-Kutta procedure for the liquid-phase equations. The finite-difference forms of the momentum equations are obtained using an implicit QUICKEST scheme [18], while those of the species and energy equations are obtained using an hybrid scheme of Spalding [19]. A "finite control volume" approach with a staggered, non-uniform grid system is utilized. Body force term due to gravitational field is included in the axial momentum equation for gas-phase and the droplet motion equation for liquid-phase. An iterative ADI (Alternative Direction Implicit) technique is used for solving the resulting sets of algebraic equations. A stable numerical integration procedure is achieved by coupling the species and energy equations through the source terms (cf. Table. 1). At every time step, the pressure field is calculated by solving the pressure Poisson equations simultaneously and utilizing the LU (Lower and Upper diagonal) matrix decomposition technique. It should be noted that the pressure Poisson equations consider the effect of mass transfer from the liquid phase to the gas phase, represented by a source term in the gas-phase mass continuity equation.

The liquid-phase equations are advanced in time by a second-order accurate Runge-Kutta method. Since the gas-phase solution employs an implicit procedure, the temporal step size used for integrating the liquid-phase equations is smaller than that for gas-phase equations. An automatic procedure is implemented in order to select an optimum liquid-phase time step. The procedure involves calculating the characteristic thermal response time, velocity response time, and vaporization time for each droplet group, and then selecting the temporal step size as a fraction (two-hundredth) of the smallest of these time scales. A detailed examination of the various time scales, based on numerical experiments, revealed that the temporal step size is determined by either the thermal response time or the velocity response time of a given droplet group. The number of sub cycles for advancing the liquid-phase solution for each gas-phase cycle typically varies from two to ten, depending upon the droplet size.

The procedure to advance the two-phase solution over one gas-phase time step is as follows. Using the known gas-phase properties, the liquid-phase equations are solved over a specified number of liquid-phase subcycles. A third-order accurate Lagrangian polynomial method is used for interpolating the gas-phase properties from the non-uniform fixed grid to the droplet characteristic location. It should be noted that the interpolation scheme for the gas-phase velocities u and v is based on their respective grid cells because of the use of a staggered grid in gas-phase calculation. The droplet properties are updated after every liquid-phase subcycle. Also, during each subcycle, the liquid-phase source terms appearing in the gas-phase equations are calculated at the characteristic location, and then

distributed to the surrounding gas-phase grid points. These source terms are added at each gas-phase grid points during one gas-phase time step and then used in the implicit solution of the gas-phase equations.

Results

The jet diameter of the vertically mounted evaporating spray considered in the present study is 2.54 cm. The jet velocities for the central fuel and coannular air streams are 1.0 and 0.2 m/s, respectively. Flat velocity profiles are used as the inflow conditions. Temperature chosen for the fuel jet is 1200 K while that of the surrounding annulus air is 294 K. Calculations are made for a physical domain having dimensions of 15 and 40 cm in the radial and axial direction, respectively. It should be noted that the physical domain used in the calculations is much larger than the domain of interest (3 x 20 cm) and hence, the results are not influenced by the computational boundaries.

Results reported in the present paper are obtained using a grid system having 151 and 61 points in the axial and radial directions, respectively. Calculations are advanced in time utilizing a low CFL number of 0.2. In an earlier study of gas-phase simulations [14] it was found that the results obtained on a 151 X 61 grid system and using a CFL number of < 0.5 are grid independent and time accurate.

Calculations are initially made without injecting droplets into the fuel stream. The shear layer between the 1200 K-nitrogen jet and the cold annulus air flow became unsteady with the development of large-scale vortices. Iso-temperature contours of this heated jet are shown in Fig. 2(a). It is important to note that these vortical structures are generated without using any external forcing, and their dynamics is found to be highly periodic. The numerical experiments [14] have indicated that the large-scale toroidal vortices appear as a result of the buoyancy-induced instability of the heated-jet shear layer. In other words, the buoyant acceleration of the got gasses in the shear layer is primarily responsible for this instability.

Numerical experiments are conducted by injecting different groups of droplets into the fuel stream to examine the changes in the flow structure due to the two-way nonlinear, two-phase interactions. The injection process consists of introducing a group of monodisperse droplets at a given instant of time. The number of droplets in each group depends on the mass loading (mass ratio between the liquid fuel and the nitrogen gas), initial droplet size, and injection time interval. As a base case for the spray calculations reported in this work, a monodisperse n-heptane spray with an initial diameter of 200 μm and mass loading of 1 is considered. The droplets are injected continuously into the jet shear layer from a radial location of 1.25 cm. A time difference of 1.428 ms is used between two consecutive injections for all the spray calculations reported in this work. This time interval was determined based on the constraint that the spatial separation between two successive droplet groups is large enough for neglecting the interaction between the droplets. This yields the number of droplets in each group to be 76.

The instantaneous iso-temperature contours for the base spray case are shown in Fig. 2(b). All the droplet source terms (cf Table 1) are incorporated in the gas-phase equations. No effort is made in matching the phases of the gaseous and spray jets of Fig. 2. It is apparent from this figure that the injection of 200 μm droplets into the shear layer weakened the vortical structures and decreased the spreading of the heated jet. The latter is as expected due to the fact that the addition of fuel spray to the nitrogen gas increases the jet momentum. On the other hand, the reason for the former effect (i.e., weakening of vortices) is not clear. However, it may be attributed to the non-linear coupling of two-phase flow.

The dynamics of the vortex structures is examined by plotting time evolution of temperature contours in Fig. 3. Temperature data along the radial location at an axial location of 10 cm above the jet exit for the gaseous and spray cases are recorded over a time period of 250 ms and shown in this figure. It can be seen from Fig. 3(a) that the vortex structures in the case of gaseous jet are highly coherent and periodic. The frequency of oscillation is 15.8 Hz. With the addition of fuel spray the dynamics of jet has become aperiodic and also the vortex crossing frequency has increased by about 30 % (from 15.8 to 20.5 Hz).

Effect of Liquid Mass Loading

The structural changes noted in a buoyancy driven heated jet with the addition of fuel spray are resulting from 1) liquid mass loading, 2) droplet evaporation, and 3) the two-way interaction between the vortices and the droplets. To further understand the impact of the above individual parameters, numerical experiments are made by changing the liquid mass loading, evaporation characteristics, spray injection location and the droplet size.

1. Non-Evaporating Spray

The instantaneous iso-temperature contours for five different mass loading values (M = 0, 0.125, 0.25, 0.5, and 1.0) for a non-evaporating spray case are shown in Fig. 4. Here, the mass loading M is defined as the ratio between the mass of the liquid droplets and that of the nitrogen gas. Liquid mass flow rates are controlled by changing the number of droplets in each injected group. As the droplets are assumed to be non-evaporating ones in this case, only the source terms in the momentum equation (cf Table 1) are considered in gas-phase equations. In other words, only the momentums are exchanged in this two-phase flow calculations. The single-phase gaseous flow shown in Fig. 2(a) may be approximated as a non-evaporating spray in the limiting case of M = 0 [Fig. 4(a)]. It seems that the structural characteristics of low mass loading cases like M = 0.125 and 0.25 are similar to that of single-phase flow even though the vortex-crossing frequencies in these flows are somewhat different.

The time history plots of the dynamic heated jets for different mass loading values are shown in Fig. 5. This plot clearly shows the changes in the sizes of the vortex structures and their crossing frequency for different cases. It may be observed from Fig. 5 that as the mass loading ratio is increased, the crossing frequency of vortex

structures is also increasing. At higher mass loading values (M = 0.5 and 1.0), the structural characteristics seem to change more significantly.

2. Evaporating Spray

The effect of mass loading in an evaporating spray is depicted by plotting the instantaneous temperature contours for several mass loading values (M = 0.25, 0.5 and 1.0) in Figure 6. The gas-phase governing equations for this case include all the source/sink terms due to the exchange of mass, momentum and energy due to droplets dynamics and vaporization. Structure of the heated jet seems to change more significantly with the addition of evaporating spray compared to that of a non-evaporating one.

Figure 7 shows the time evolution of temperature contours at z = 7.5 cm for the three cases shown in Fig. 6. It is interesting to compare the structures of high mass loading values (M = 0.5 & 1.0) for the evaporating (Fig. 7) and non-evaporating (Fig. 5) cases. The development of vortical structures for evaporating spray is more periodic than that observed in the corresponding non-evaporating cases.

Effect of Injection Location

The effect of initial droplet distribution on the structural characteristics and dynamics of the heated spray jet is studied by changing the injection locations. The mass loading ratio and the size of the droplet are fixed at 1.0 and 200 mm, respectively. Evaporating spray jets are simulated in this study. The instantaneous temperature contours for three cases having different droplet injection locations are shown in Fig. 8. The three distributions of injection locations used are as follows; 1) r_k = 1.25 cm, 2) r_k = 0.625 and 1.25 cm, and 3) r_k = 0.25, 0.50, 0.75, 1.00 and 1.25 cm. The mass loading ratio is kept constant by using different number of droplets in each group for different cases. It is shown that the characteristics of core region near nozzle exit are quite different for all the three cases due to different initial droplet injection process. The use more injection locations apparently led to a dynamic heated spray jet with well-organized vortical structures [Fig. 8(c)]. It is known that the vaporization of liquid droplet absorbs thermal energy and hence reduces the local temperature. This is evident in Figs. 8(b) and 8(c). In the former figure a valley in the temperature contours developed in the downstream region of the inner injection location (i.e., r_k = 0.625 cm) as the injected droplet vaporizes. However, in the latter figure, the choice of more injection locations reduced the entire jet temperature uniformly leading to near flat contours for 1000 and 1100 K [Nos. 7 and 8 in Fig. 8(c)].

The time evolution for temperature contours at an axial location of 7.5 cm for the three cases of injection locations are plotted in Fig. 9. It clearly shows that the vortex structures are well organized and highly periodic similar to that of a single-phase flow [Fig. 2(a)] when the number of injection locations is large.

Effect of Droplet Size

The instantaneous temperature contours represented in Figs. 10(a), 10(b), and 10(c) show the structures of three different n-heptane evaporating sprays with initial droplet diameters (d_o) of 50, 100, and 200 μm, respectively. A constant mass loading ratio of M = 1.0 is obtained for different cases by increasing the number of droplets in each group as its initial size is decreased. Droplets in all the three cases are injected in the shear layer (r_k = 1.25 cm). The important observation made from these calculations is that the initial droplet size has a strong influence on the structural characteristics of the evaporating sprays. Vortex structures of the 50-μm evaporating spray [Fig. 10(a)] seem to be destroyed in the downstream of z = 10 cm.

Reduction of temperature due to vaporization of the liquid fuel is evident in these calculations made with different sizes of initial droplet sizes. In fact, when the droplet size is very small (~ 50 μm) the temperature of the entire fuel/N_2 jet downstream of z = 100 cm has dropped down to less than 400 K from the initial temperature of 1200 K. The time evolution of temperature contours for the three evaporating sprays with different initial droplet sizes are shown in Fig. 11. The structural dynamics is very different for all the three cases. Due to subsequent vortex pairing phenomena between the axial locations z = 2.5 and 5 cm (not shown in the figures), the structures of 50-μm case became large and their crossing frequency has decreased. It seems that the two-way nonlinear interactions became stronger due to the high concentrated fuel vapor in a jet shear layer region by fast vaporization of 50-μm evaporating spray.

Conclusions

In this paper, the droplet/vortex interactions on the dynamics of evaporating spray and their structural characteristics are studied by developing a detailed multidimensional numerical algorithm. An implicit, third-order accurate QUICKEST scheme for momentum equations and hybrid scheme of Spalding for species and energy equations are used to solve the unsteady axisymmetric gas-phase equations. The Lagrangian approach is employed to study the droplet dynamics and vaporization history in an evaporating spray. The effect of dispersed phase is incorporated through the source/sink terms in the gas-phase governing equations, representing the exchange of mass, momentum, and energy between the gas and liquid phases.

Snapshots and time evolution plots of temperature contours are employed to analyze the structural characteristics and their dynamics of the non-evaporating and evaporating spray jet flow. The presence of gravity introduces the buoyancy-induced hydrodynamic instability, causing the large vortical structures to appear without any external perturbation. The vortex structures cause droplets to disperse radially outward, and this in turn determines the fuel vapor distribution and also modifies the vortex dynamics. Thus, the dynamics and structural characteristics of the evaporating spray are strongly influenced by these interactions. The effects of initial droplet size, injection

location, and liquid-to-gas mass loading ratio on the droplet/vortex interaction are also investigated by performing numerical experiments.

The important observations made from this study are: (1) A strong two-way nonlinear, two-phase interactions between large vortex structures and droplets are found in non-evaporating and evaporating spray. (2) The structural characteristics and their dynamics for both non-evaporating and evaporating spray are significantly affected at high liquid-to-gas mass loading ratios ($M \geq 0.5$). (3) The vortex structures become highly coherent and periodic as the multiple injection locations are chosen for the high liquid-to-gas mass loading case ($M = 1.0$). (4) The initial droplet size has a strong effect on the structural characteristics and their dynamics. Also, the subsequent vortex pairing phenomena is observed for the 50-μm evaporating spray.

References

1. Brown, G. L., Roshko, A., "Density Effects and Large Scales in the Developing Mixing Layer," J. Fluid Mech., Vol. 64, pp. 775-816, 1974.

2. Yule, A. J., "Large Scale Structure in the Mixing Layer of a Round Jet," J. Fluid Mech., Vol 89, pp. 413-432, 1978.

3. Katta, V. R., Goss, L. P., and Roquemore, W. M., "Effect of Nonunity Lewis Number and Finite-Rate Chemistry on the Dynamics of a Hydrogen-Air Jet Diffusion Flame," Combustion and Flame, Vol. 96, pp. 60-74, 1994.

4. Longmire, E. K. and Eaton, J. K., "Structure of a Particle-Laden Round Jet," J. Fluid Mech., Vol. 236, pp. 217-257, 1992.

5. Park, T. W., Aggarwal, S. K., and Katta, V. R., "Effect of Gravity on the Structure of an Unsteady Spray Diffusion Flame," to appear in Combustion and Flame of the Twenty-Fifth Symposium (International) on Combustion, 1994.

6. Chung, J. N., and Troutt, T. R., "Simulation of Particle Dispersion in an Axisymmetric Jet," Journal of Fluid Mechanics," Vol. 186, pp. 199-222, 1988.

7. Hansell, D., Kennedy I. M., and Kollmann, W., "A Simulation of Particle Dispersion in a Turbulent Jet," International Journal of Multiphase Flow, Vol. 18, No. 4, pp. 559-576 1988,.

8. Lazaro, B. J., and Lasheras, J. C., "Particle Dispersion in the Developing Free Shear Layer, Part 1- Unforced Flow," Journal of Fluid Mechanics, Vol. 235, pp. 143- 178, 1992.

9. Lazaro, B. J., and Lasheras, J. C., "Particle Dispersion in the Developing Free Shear Layer, Part 2- Forced Flow," Journal of Fluid Mechanics, Vol. 235, pp. 179- 221, 1992.

10. Samimy, M., and Lele, S. K., "Motion of Particles with Inertia in a Compressible Free Layer," Physics of Fluids, Vol A 3, pp. 1915-1923, 1991.

11. Hishida K., Ando, A., and Maeda, M., "Experiments on Particle Dispersion in a Turbulent Mixing Layer," International Journal of Multiphase Flow, Vol 18, pp. 181-194, 1992.

12. Uthuppan, J., Aggarwal, S. K., Grinstein, F. F., and Kailasanath, K., "Particle Dispersion in a Transitional Axisymmetric Jet : A Numerical Simulation," AIAA 93-0105, 31st Aerospace Sciences Meeting and Exhibit, Reno, Nevada, 1993. Also to appear in AIAA Journal.

13. Aggarwal, S. K., "Relationship Between Stokes Number and Intrinsic Frequencies in Particle Laden Flows," to appear in AIAA Journal, 1994.

14. Park, T. W., Aggarwal, S. K., and Katta, V. R., "Gravity Effects on the Dynamics of Evaporating Droplets in a Heated Jet," AIAA Paper 94-0684, 32nd Aerospace Sciences Meeting and Exhibit, Reno, 1994. Also submitted to AIAA J. of Propulsion and Power.

15. Abramzon, B. and Sirignano, W. A., Int. J. Heat Mass Transfer, 32 (9): 1605-1618 (1989).

16. Edwards, D. K., Denny, V. E. and Mills, A. F., Transfer Processes: An Introduction to Diffusion, Convection and Radiation (2nd Edn.), McGraw-Hill, New York, 1979.

17. Aggarwal, S. K., Tong, A. and Sirignano, W. A., "A Comparison of Vaporization Models for Spray Calculation," AIAA Journal, Vol. 22, No. 10, pp. 1448-1457, 1984.

18. Leonard, B.P., A Stable and Accurate Convective Modelling Procedure Based on Quadratic Upstream Interpolation, Comput. Methods in Applied Mechanics and Engineering, Vol. 19, pp. 59-98, 1979.

19. Spalding, D. B., Int. J. Num. Meth. Eng., Vol. 4, pp. 551-559, 1972.

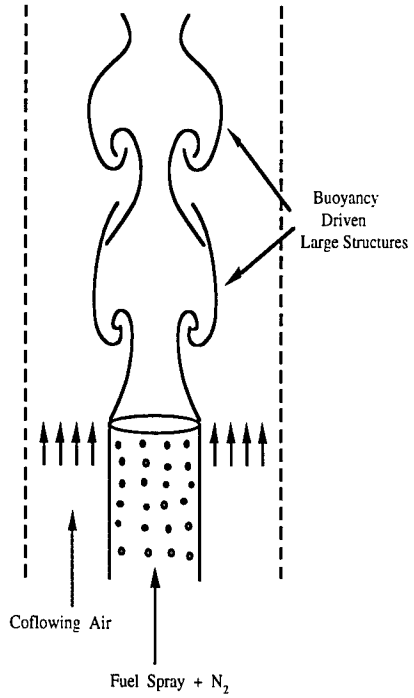


Figure 1: A schematic of evaporating spray jet at 1g.

Table 1: Transport coefficients and source terms appearing in governing equations

Equations	Φ	Γ^{Φ}	S_g^{Φ}	S_ℓ^{Φ}
Continuity	1	0	0	$\sum_k n_k \dot{m}_k$
Axial momentum	u	μ	$-\frac{\partial p}{\partial z} + (\rho_o - \rho)g + \frac{\partial}{\partial z}\left(\mu\frac{\partial u}{\partial z}\right) + \frac{\partial}{\partial r}\left(\mu\frac{\partial v}{\partial z}\right) + \frac{\mu}{r}\frac{\partial v}{\partial z} - \frac{2}{3}\left\{\frac{\partial}{\partial z}\left(\mu\frac{\partial u}{\partial z}\right) + \frac{\partial}{\partial z}\left(\mu\frac{\partial v}{\partial r}\right) + \frac{\partial}{\partial z}\left(\mu\frac{v}{r}\right)\right\}$	$\sum_k \left(n_k \dot{m}_k u_k - n_k M_k \frac{du_k}{dt}\right)$
Radial momentum	v	μ	$-\frac{\partial p}{\partial r} + \frac{\partial}{\partial z}\left(\mu\frac{\partial u}{\partial r}\right) + \frac{\partial}{\partial r}\left(\mu\frac{\partial v}{\partial r}\right) + \frac{\mu}{r}\frac{\partial v}{\partial r} - 2\mu\frac{v}{r2} - \frac{2}{3}\left\{\frac{\partial}{\partial r}\left(\mu\frac{\partial u}{\partial z}\right) + \frac{\partial}{\partial r}\left(\mu\frac{\partial v}{\partial r}\right) + \frac{\partial}{\partial r}\left(\mu\frac{v}{r}\right)\right\}$	$\sum_k \left(n_k \dot{m}_k v_k - n_k M_k \frac{dv_k}{dt}\right)$
Mass fraction of fuel	Y_F	ρD	0	$\sum_k n_k \dot{m}_k$
Energy	T	λ/C_p	0	$\sum_k n_k \dot{m}_k \left(h_{fs} - \ell_{k,eff}\right)$

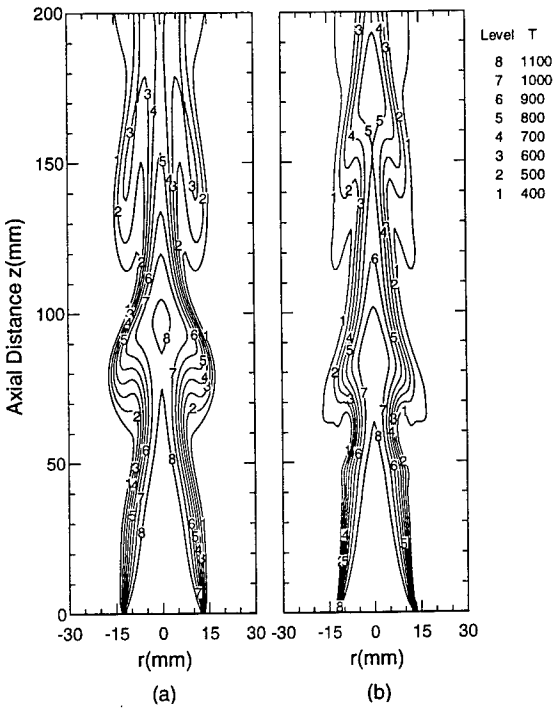


Figure 2: Instantaneous iso-temperature contours for the heated N_2 jet (a) without fuel spray (b) with fuel spray.

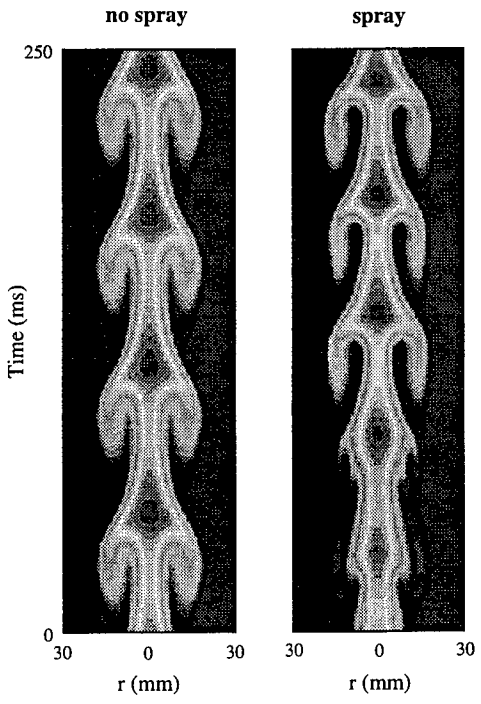


Figure 3: Time evolution of temperature contours at axial location of 10 cm above inlet for the cases of for Fig. 2.

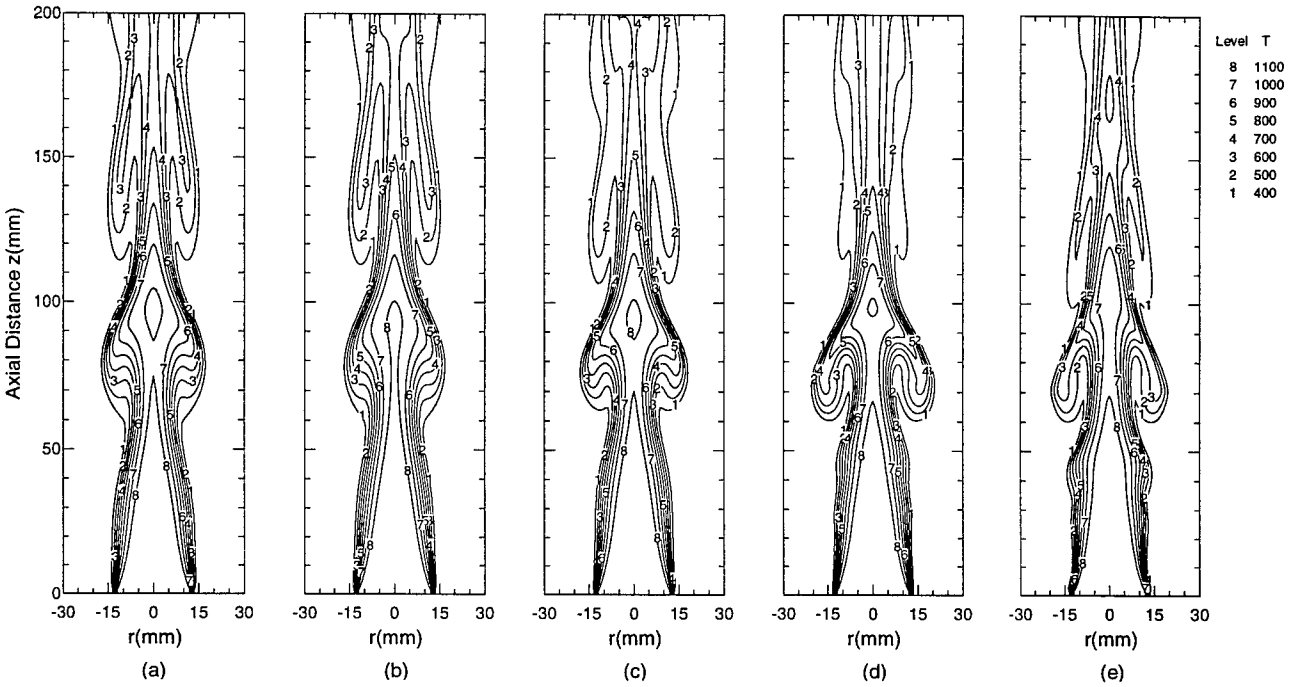


Figure 4: Instantaneous iso-temperature contours for a non-evaporating spray jet with five different mass loading values; (a) M = 0 (b) M = 0.125 (c) M = 0.25 (d) M = 0.5 (e) M = 1.0.

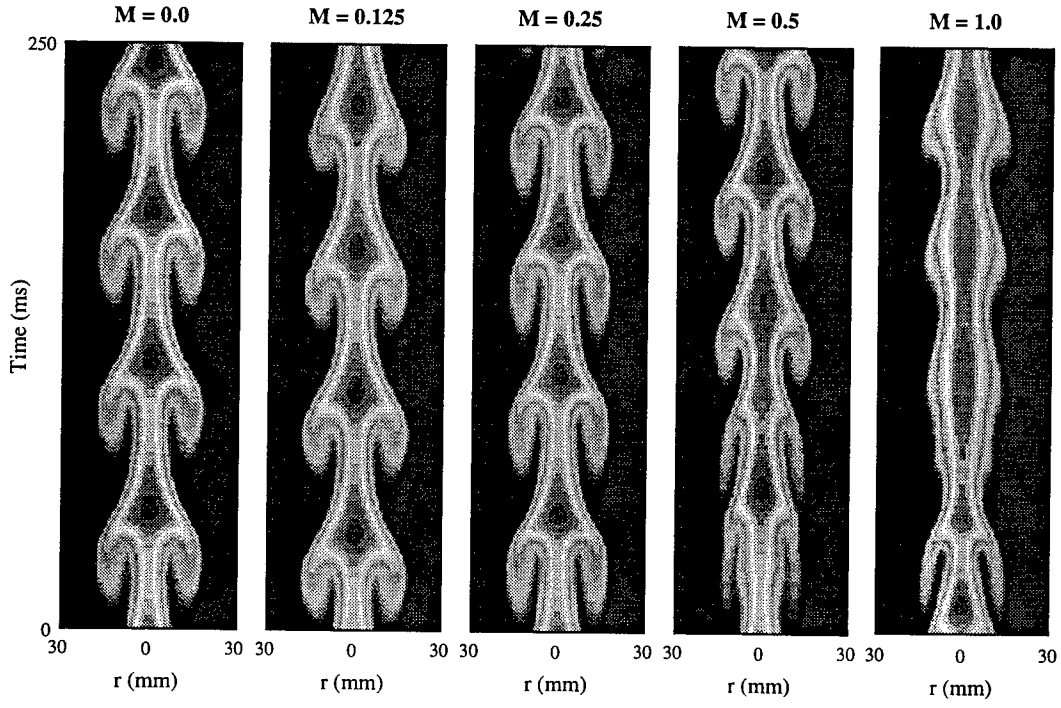


Figure 5: Time evolution of temperature contours at axial location of 10 cm above the inlet for the cases of Fig. 4.

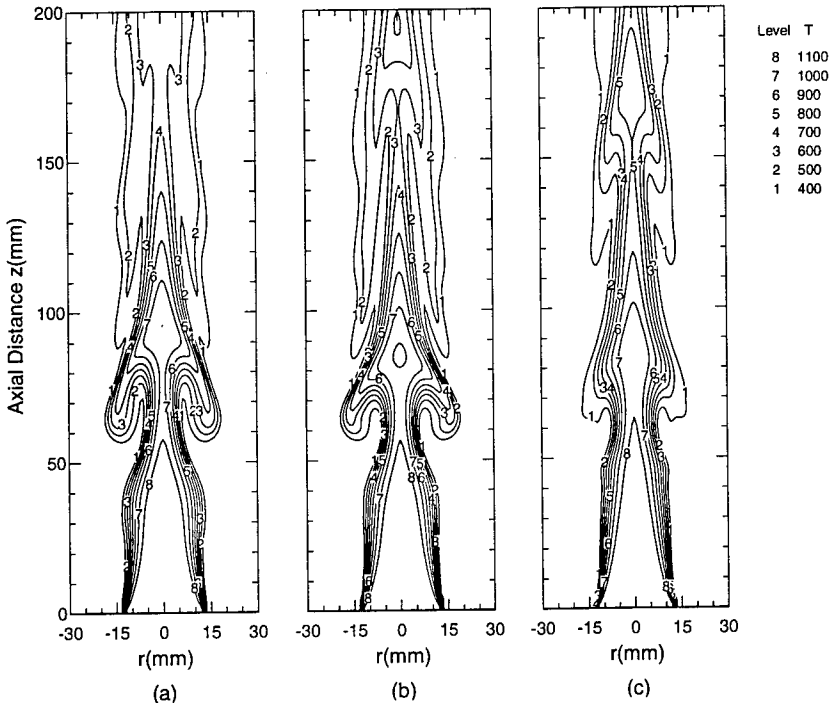


Figure 6: Instantaneous iso-temperature contours for an evaporating spray jet with three different mass loading values; (a) M = 0.25, (b) M = 0.5, and (c) M = 1.0.

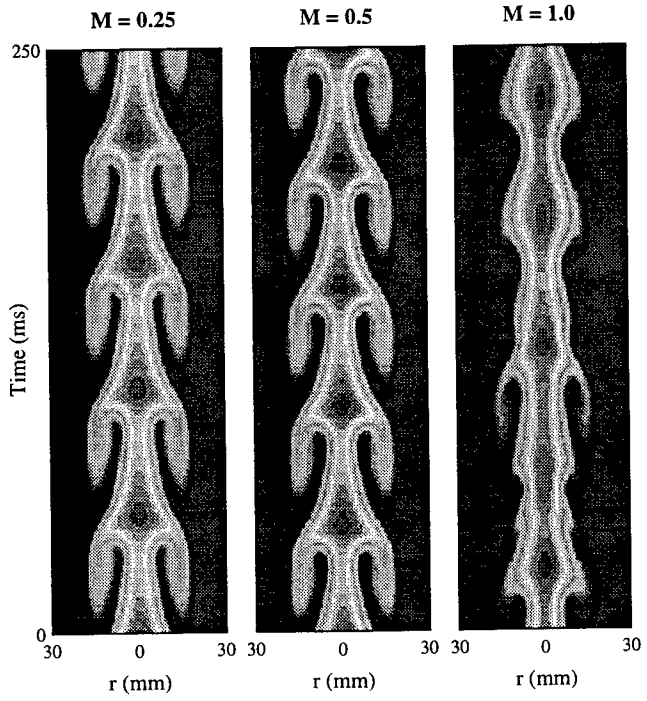


Figure 7: Time evolution of temperature contours at a location of 7.5 cm above the inlet for the cases of Fig. 6.

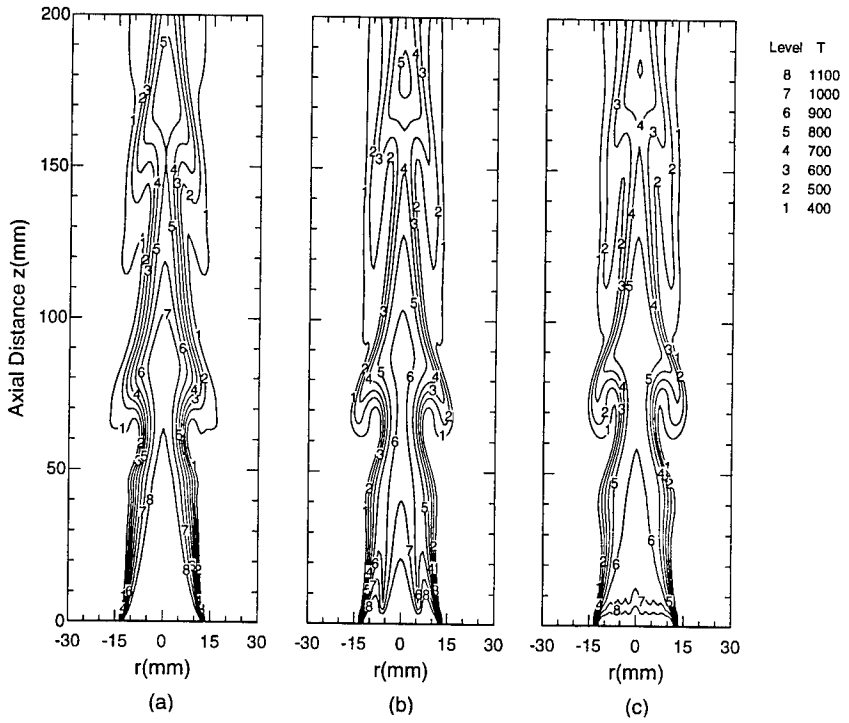


Figure 8: Instantaneous iso-temperature contours for an evaporating spray jet with three different injection distributions; (a) r_k = 1.25 cm, (b) r_k = 0.625 cm and 1.25 cm, and (c) r_k = 0.25, 0.5, 0.75, 1.0 and 1.25 cm.

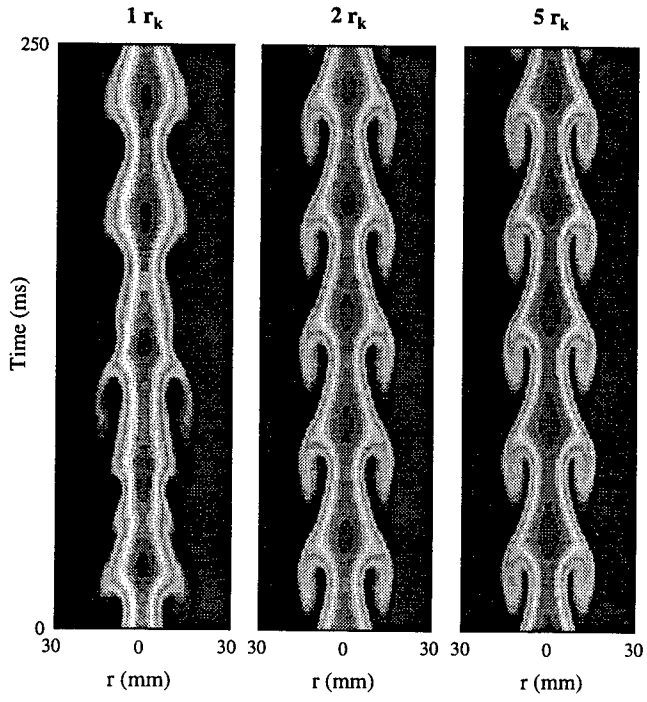


Figure 9: Time evolution of temperature contours at axial location of 7.5 cm above the inlet for the cases of Fig. 8.

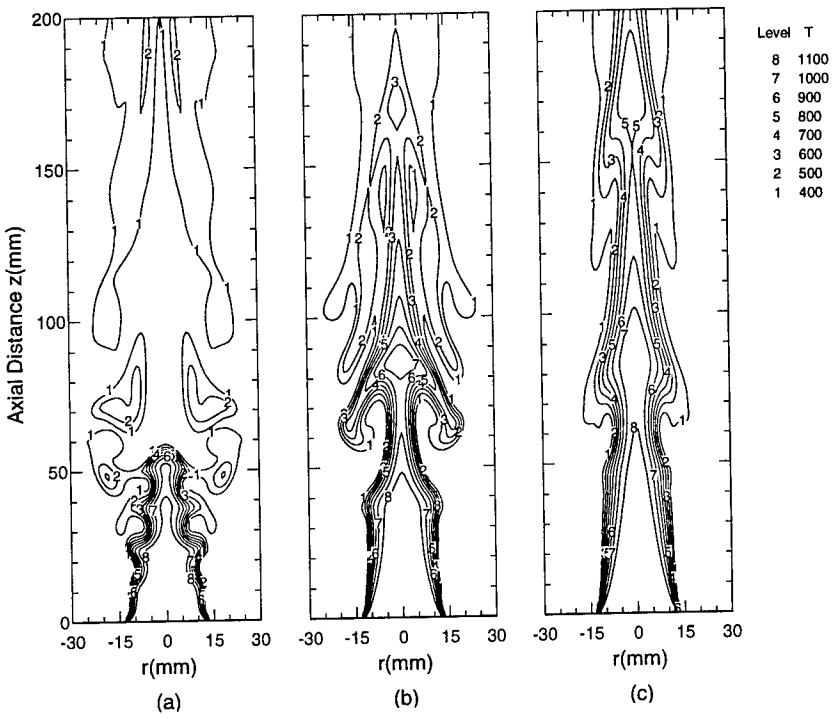


Figure 10: Instantaneous iso-temperature contours for an evaporating spray jet with three different initial droplet diameters; (a) $d_O = 50$ μm, (b) $d_O = 100$ μm, and (c) $d_O = 200$ μm.

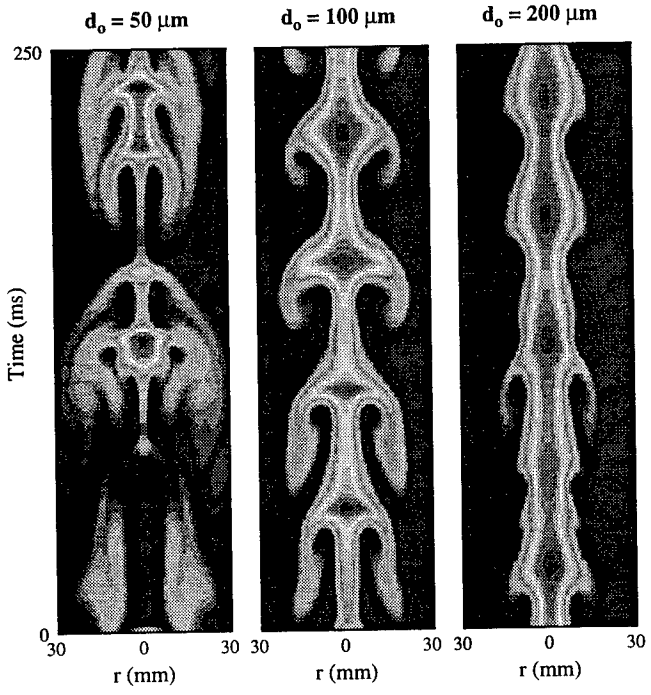


Figure 11: Time evolution of temperature contours at a location of 7.5 cm above the inlet for the cases of Fig. 10.

A PARAMETRIC STUDY OF THE FACTORS AFFECTING THE OPEN AND FILLED HOLE PERFORMANCE OF FIBER REINFORCED COMPOSITE MATERIALS

Margaret F. Pinnell
Graduate Student
Department of Materials Engineering

University of Dayton
300 College Park Drive
Dayton, Ohio 45469

Sponsored by:
Air Force Office of Scientific Research
Bolling Air Force Base, DC

and

Wright Laboratory

August 1994

A PARAMETRIC STUDY OF THE FACTORS AFFECTING THE OPEN AND FILLED HOLE PERFORMANCE OF FIBER REINFORCED COMPOSITE MATERIALS

Margaret F. Pinnell
Graduate Student
Department of Materials Engineering
University of Dayton

Abstract

The effect of fiber stiffness, matrix toughness and fiber orientation on the open and filled, drilled hole tension and compression performance and drilled hole bearing performance of continuous fiber, polymer matrix composites was investigated. Failure characteristics of tested specimens were studied using fractographic techniques. Fiber type and lay-up were found to have the biggest effect on the tensile data while test type (open hole versus filled hole) had little effect on the data. Test type and lay-up were the parameters having the largest effect for the compressive data. Hole size most significantly affected the bearing data. Results of an extended isotropic analysis showed that the stress concentration factor for materials 1 (AS-4/3501-6) and 2 (IM-8/3501-6) was greater for stacking sequences 3 ($[60/0_2/-60]_{2}]_{2S}$) and 4 ($[60/-60/0_2]_{2S}$) than for stacking sequences 1 ($[45/90/-45/0]_{2S}$) and 2 ($[45/-45/0/90]_{2S}$). This result was consistent with the data obtained through testing. Fractographic examination of tested specimens showed that test type, stacking sequence, fiber type or matrix type had little effect on the failure characteristics for the open and filled hole tension specimens but test type, matrix type and stacking sequence had some effect on failure characteristics of the open and filled hole compression specimens. All of the bearing specimens failed in a bearing type mode. For both materials the damage appeared to be slightly more significant for the 0.125 inch diameter hole bearing specimens than for the 0.250 inch diameter hole bearing specimens. The failures appeared to be independent of lay-up or fiber type but somewhat dependent on matrix type.

A PARAMETRIC STUDY OF THE FACTORS AFFECTING THE OPEN AND FILLED HOLE PERFORMANCE OF FIBER REINFORCED COMPOSITE MATERIALS

Margaret F. Pinnell

Introduction

Although considered to be a relatively new class of materials, continuous fiber, polymer matrix composite materials are finding increasing applications in the aerospace industry. Although composite materials are being widely used in the aerospace industry, they are, by no means, trouble free. One problem associated with composite materials arises from the nearly inevitable need to join composite parts in the assembly of an aerospace structure. The most common method of joining composite parts is through the use of single- or multiple-bolted mechanical fasteners. The main problem with the use of mechanical fasteners is that they require that a hole be drilled in the composite part. Drilled holes significantly disturb the internal structure of the composite since the material in the hole region is cut out, breaking the continuity of the fibers. This material discontinuity produces areas of high stress concentrations which reduce the load carrying capability of the composite structure [1-5]. The load carrying efficiency of a properly designed and manufactured bolted composite joint has been reported to be as low as 70% as compared with 20% for traditional isotropic materials [6]. Many parameters are believed to affect the overall performance of a bolted composite joint. Among these include the mechanical properties of the composite constituent materials, fiber orientation of the composite laminate, number and spacing of bolts, end distance, bolt clearance and load distribution among the bolts [3,7,8].

In an effort to avoid the problems associated with drilled hole bolted composite joints several joining alternatives have been suggested and/or attempted. Perhaps the most prevalent of these alternatives is the use of adhesively bonded joints. Although this alternative is becoming more viable with improvements in adhesives technology, several problems arise with the use of bonded joints. One such problem is that only relatively low rates of load transfer can be attained with bonded joints due to the low shear strengths of the adhesive and composite laminate. Other problems with bonded joints include the existence of high thermal strains in the bonded region due to the relatively high cure temperatures of the adhesives and the environmental degradation of adhesive properties. Additionally, bonded joints prohibit easy disassembly of composite

structures, thus making maintenance and repair difficult [2,9]. Another proposed alternative to bolted composite joints is the use of a multi-shim joint consisting of thin metal shims interleaved with composite layers. This method is not attractive since the multi-shim joint is difficult to fabricate and therefore cost prohibitive [9]. Molded hole composites is another method which has been proposed to replace drilled holes for use in bolted composite joints. This method generates bolt holes by routing the fibers around a circular mold during fabrication of the composite structures. Although molded hole composites have been shown to provide significant strength increases as compared to drilled hole composites, fabrication of molded hole structures is tedious and time consuming and would be expensive to manufacture into parts for aerospace structures. Therefore, fabrication of molded hole composites must be simplified or automated before this concept can be incorporated into the aerospace industry [5,4,10,11]. Modification of hole shape to minimize stress concentrations, reinforcing the region near the hole and embedding the hole in a soft high strain material are some other alternatives suggested for reducing the problems associated with drilled hole bolted composite joints [12-14].

It is apparent that none of the aforementioned alternatives provide sufficient solutions to the problems associated with drilled hole bolted composite joints. Perhaps the only way in which some of the problems can be resolved is through optimization by design. Before optimum designs can be achieved, engineers require information concerning the parameters which affect composite joint performance. Although many studies have been conducted in the area of bearing, open hole tension and compression performance of composite materials, none of these studies systematically looked at the anticipated important parameters associated with bolted composite performance. Little effort has been exerted to correlate material parameters, material performance and failure characteristics. Furthermore, there is little reference in the open literature to any work being done in the area of filled hole composite performance. It is for these reasons that a systematic and parametric study needs to be conducted in the area of bearing and open and filled hole tension and compression performance of composite materials.

The overall objective of this research is to experimentally and analytically determine the effect of fiber stiffness, matrix toughness and fiber orientation on the open and filled, drilled hole tension and compression performance as well as the drilled hole bearing performance of continuous fiber, polymer matrix composites. An emphasis shall be placed on determining the effect of these parameters on the specimen failure characteristics.

Experimental Approach:

In order to determine the effect of fiber stiffness on the mechanical properties and failure modes two graphite fibers having significantly different elastic modulus were studied. These fibers include::

Fiber	Tensile Strength [psi]	Tensile Modulus [psi]
AS-4	570 E 3	36 E 6
IM-8	790 E 3	44 E 6

The AS-4 fiber was chosen because it represents a baseline composite constituent for which a large database and much experience exists, which is commercially available in a variety of matrices and is relatively inexpensive. The IM-8 fiber was chosen because this fiber has significantly higher stiffness and strength than the AS-4 fiber.

It is well known that the matrix material provides lateral support to the fibers when a composite structure is subjected to a compressive load. In general, strong lateral support of the fibers is provided by high stiffness matrix materials. In this case, the compressive failure mode is dominated by shearing of the fibers. Conversely, low stiffness matrix materials do not provide strong lateral support to the fibers and the resulting compressive failure mode is dominated by fiber buckling [15, 16]. The matrix material also governs the notch sensitivity of a composite [17-20]. The notch sensitivity of composite materials is related to the toughness of the matrix material where brittle matrix materials are regarded as notch sensitive and ductile matrix materials as notch insensitive [21]. Since thermoplastic and thermoset matrix materials have significantly different toughness and mechanical properties, both matrix materials were used in this investigation. This difference in matrix properties provided information concerning the effect of matrix toughness on the open and filled hole compression and tension and bearing performance of composite materials and the respective failure characteristics. The 3501-6 and the APC-2 materials were chosen for this project because they represent baseline epoxy and thermoplastic matrices, respectively. These materials are well studied, relatively inexpensive, commercially available, have large data bases and can be successfully processed with relative ease. The 3501-6 epoxy matrix material has a tensile modulus of 643 ksi and is considered to be somewhat brittle in nature. The APC-2 matrix material has a tensile modulus of 520 ksi and is considered to be more ductile than the epoxy material.

Stiffness discontinuities between plies result in the generation of interlaminar stresses near free edge regions during in-plane loading of composite laminates. Interlaminar stresses have a notable effect on the damage initiation and growth mechanisms in composite laminates. Hence, the strength of the laminate may be

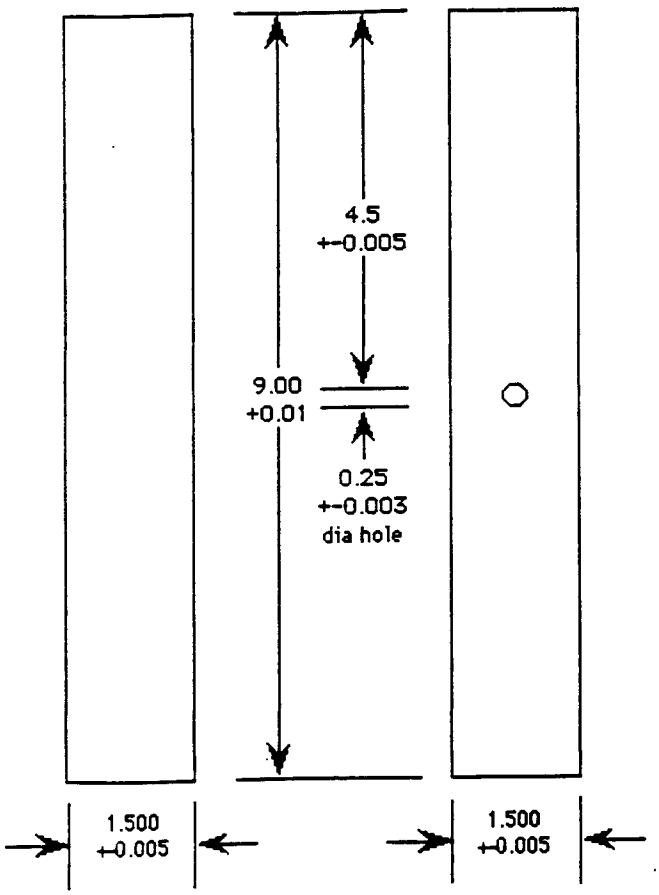
significantly reduced by the occurrence of premature delamination and matrix cracking resulting from interlaminar stresses [22,23,24,25-28]. This situation is further complicated in areas of material discontinuities, such as a notch or bolt hole. The nature and magnitude of interlaminar stresses is largely determined by the laminates stacking sequence and fiber orientation [22]. In order to determine the effect of stacking sequence and interlaminar stresses on the properties and failure modes of composite materials a variety of lay-ups and stacking sequences were examined. The resulting material/lay-up systems examined are shown below:

Thermoset Mat.	Lay-ups:	Thermoplastic Mat.	Lay-up
(1) AS-4/3501-6	(1) $[45/90/-45/0]_{2S}$	(3) AS-4/APC-2	(1*) $[-45/0/45/90]_{2S}$
(2) IM-8/3501-6	(2) $[45/-45/0/90]_{2S}$	(4) IM-8/APC-2	(2*) $[-45-45/90/0]_{2S}$
	(3) $[60/0_2/-60]_{2S}$		(4) $[60/-60/0_2]_{2S}$
	(4) $[60/-60/0_2]_{2S}$		

Specimens were labeled using the following codes: X-Y-TEST-# where X represents the materials as labeled above (1-4); Y represents the lay-up as labeled above (1*,2* and 4); TEST represents the type of test and # corresponds to the specimen number for that particular test group.

All panels were fabricated then processed in an autoclave in accordance with their respective curing/processing cycles. Prior to machining, all processed panels were subjected to a series of quality control and physical property tests. These tests included ultrasonic inspection, cross-sectional photomicrographs, fiber and void content and density and specific gravity measurements. Panels were then machined using a water cooled diamond impregnated saw and the holes were drilled in the open and filled hole specimens. Open and filled hole specimens were subjected to a second ultrasonic inspection to check for possible material damage resulting from the drilling process.

Mechanical testing of the materials included laminate property tests, unnotched, open and filled hole tension tests, unnotched, open and filled hole compression tests and bearing tests. Laminate property tests including longitudinal and transverse tension and in-plane shear tests were conducted to provide basic laminate property data for the four materials being studied. Specimen configurations were standard for these tests. Specimen configurations for the open and filled hole compression and tension tests are shown in figure 1. Tabless specimens were used to avoid problems with specimen tabs including tab failure and variability in the data generated resulting from tab material, tab geometry and adhesive selection [29]. Global buckling of the compression specimens was prevented by using an edge stabilized compression fixture described in [29]. Titanium, 0.249 diameter bolts with accompanying washers and nuts were used in the testing of the filled hole tension and compression tests. The bolts were installed as



Note:

1. All dimensions in inches;
2. Longitudinal edge to be parallelto 0 degree fiber within 2.0 degrees ;
3. Hole must be free of backface damage, delaminations or other damege;
4. Machined surfaces to be lightly sanded.

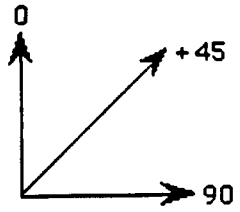


Figure 1. Open and filled hole tension and compression specimen configuration.

protruding head fasteners and tightened to a torque of 30 in-lbs using a torque wrench. A minimum of three specimens per setup were tested to failure. Bearing tests were conducted for two bearing hole diameters, (a) 0.125 inch and (b) 0.250 inch. An E/D (end distance/diameter) ratio of four and W/D (width/diameter) ratio of six was maintained throughout the bearing tests. With exception of specimen dimensions, bearing tests were conducted in accordance with the SACMA Recommended method [30]. A post failure analysis was conducted on representative tension and compression specimens. Representative tested open and filled hole tension and compression test specimens were photographed macroscopically to provide some information concerning the overall failure mode of these specimens. These specimens were subsequently cross-sectioned and the cross-sections examined under a microscope. A preliminary statistical analysis was done using the difference of means technique as described in references [31] and [32]. The extended isotropic analysis described in reference [33] was applied to the open hole tensile data to determine the effect of the various parameters on the

materials ability to dissipate the stress concentration [33-35]. An analysis using data obtained from [36] was conducted for the graphite/epoxy open hole tension and compression specimens. Predicted failures were compared with the information obtained from the fractographic analysis.

Results:

Results of the laminate property tests, tension, and compression tests and bearing tests are shown in Tables 1,2 and 3, respectively. Results of the tension and compression tests and bearing tests are shown graphically in figures 2 and 3, respectively.

Table 1. Laminate Property Data

Material	E_L [MSI]	E_T [MSI]	G_{LT} [KSI]	s_L [KSI]	s_T [KSI]	s_{LT} [KSI]	n_{LT}
AS-4/3501-6	17.8	1.4	701	237	8.31	11.7	.31
IM-8/3501-6	24.1	1.5	790	268	6.59	12.8	.32
AS-4/APC-2	16.2	1.6	905	294	10.62	27.5	.32
AS-4/APC-2	23.3	1.2	901	316	14.02	27.5	.32

Results of the preliminary statistical analysis using the difference of means technique are shown in Table 4.

Table 4. Results of the Difference of Means Technique

	Loading Condition		
Main Effect	Tension [%]	Compression [%]	Bearing [%]
Test	0.26	39.20	14.33
Fiber	35.62	4.11	0.56
Matrix	2.23	4.55	9.97
Lay-up	42.65	17.19	0.60
Stacking Seq.	0.20	3.11	2.04

In this analysis large values correspond to parameters which have a significant effect on the failure strength. As indicated in the above table, lay-up and fiber type have the largest effect on the tensile strength. Test type (i.e. open versus closed hole) and stacking sequence appear to have very little effect on the resulting tensile data. Conversely, test type appears to be the factor which most significantly influences the outcome of the compressive data. Lay-up also appears to have a significant affect on the compressive data. Stacking sequence appears to have a greater affect on the compressive data than on the tensile data, but this affect does not appear to be a dominating parameter. Test type (0.250 versus 0.125 inch diameter hole size) and matrix type have the largest effect on the bearing results, however these effects are relatively small. Stacking sequence appears to be an insignificant parameter in the bearing data.

Table 2. Unnotched, Open and Filled Hole Tension and Compression Results

TENSION

Material	Failure Stress (psi)	Stress Std. Dev. (psi)	Long. Strain (in/in)	Trans. Strain (in/in)	Initial Modulus (psi)	Average Vf (%)	Open Hole σN/σo	Filled Hole σN/σo	Normalized Strength (psi)
11	99475	*6737*	1.38E-02	4.14E-03	7.60E+06	62.42	0.622	0.630	95618
12	88412	*2491*	1.32E-02	4.49E-03	7.20E+06	59.22	0.616	0.638	89576
13	128503	*3204*	1.22E-02	3.74E-03	1.01E+07	61.86	0.671	0.649	124639
14	131137	*9542*	1.29E-02	3.53E-03	1.00E+07	60.27	0.693	0.673	130550
21	114726	*6721*	1.25E-02	4.05E-03	9.47E+06	60.84	0.695	0.717	113142
22	121394	*2938*	1.22E-02	4.06E-03	9.85E+06	61.68	0.651	0.683	118088
23	171702	*9941*	1.16E-02	3.62E-03	1.40E+07	60.81	0.737	0.749	169415
24	187317	*14130*	1.22E-02	3.73E-03	1.37E+07	61.00	0.709	0.666	184246
31*	112879	*8571*	1.57E-02	4.93E-03	7.22E+06	59.03	0.540	0.566	114734
32*	107239	*10960*	1.49E-02	4.73E-03	7.56E+06	59.92	0.585	0.630	107382
34	156052	*16793*	1.02E-02	6.15E-03	1.03E+07	59.77	0.590	0.583	156653
41*	148108	*11002*	1.51E-02	5.42E-03	9.37E+06	56.68	0.545	0.614	156783
44*	104925	*4323*	1.29E-02	2.51E-03	7.84E+06	56.11	0.717	0.761	112199

OPEN HOLE TENSION

Material	Failure Stress (psi)	Stress Std. Dev. (psi)	Long. Strain (in/in)	Trans. Strain (in/in)	Initial Modulus (psi)	Average Vf (%)	Normalized Strength (psi)
11	61847	*3339*	4.91E-03	1.52E-03	1.17E+07	62.42	59449
12	54463	*5068*	4.73E-03	1.58E-03	1.04E+07	59.22	55180
13	86253	*6861*	5.03E-03	1.89E-03	1.60E+07	61.86	83660
14	90816	*3102*	5.59E-03	1.42E-03	1.49E+07	60.27	90409
21	79709	*9300*	5.14E-03	1.71E-03	1.41E+07	60.84	78608
22	78991	*7536*	5.44E-03	1.44E-03	1.37E+07	61.68	76839
23	126496	*11878*	4.80E-03	1.23E-03	2.15E+07	60.81	124811
24	132884	*6592*	4.98E-03	2.45E-03	2.21E+07	61.00	130706
31*	80925	*8218*	5.14E-03	1.55E-03	1.11E+07	59.03	61926
32*	62784	*2070*	4.46E-03	1.51E-03	1.14E+07	59.92	62868
34	92125	*3770*	5.03E-03	1.88E-03	1.63E+07	59.77	92480
41*	80673	*4336*	5.28E-03	1.61E-03	1.42E+07	56.68	85398
44*	75249	*2387*	6.26E-03	1.07E-03	1.19E+07	56.11	80466

FILLED HOLE TENSION

Material	Failure Stress (psi)	Stress Std. Dev. (psi)	Long. Strain (in/in)	Trans. Strain (in/in)	Initial Modulus (psi)	Average Vf (%)	Normalized Strength (psi)
11	62625	*4286*	5.66E-03	1.51E-03	9.48E+06	62.42	60197
12	56398	*1834*	5.27E-03	1.49E-03	9.41E+06	59.22	57141
13	83438	*6966*	5.04E-03	1.84E-03	1.42E+07	61.86	80929
14	88217	*2750*	5.76E-03	1.43E-03	1.40E+07	60.27	87822
21	82217	*3327*	5.70E-03	1.80E-03	1.22E+07	60.84	81082
22	82856	*2742*	5.55E-03	1.65E-03	1.28E+07	61.68	80599
23	128681	*4504*	5.24E-03	1.35E-03	2.11E+07	60.81	126967
24	124827	*5932*	5.06E-03	2.05E-03	1.82E+07	61.00	122781
31*	63896	*2982*	5.91E-03	1.80E-03	9.05E+06	59.03	64946
32*	67592	*4895*	6.49E-03	1.70E-03	8.35E+06	59.92	67682
34	90938	*1577*	5.40E-03	1.77E-03	1.28E+07	59.77	91288
41*	90988	*4469*	6.32E-03	1.88E-03	1.88E+07	56.68	96318
44*	79861	*2507*	7.07E-03	1.02E-03	1.13E+07	56.11	85398

COMPRESSION

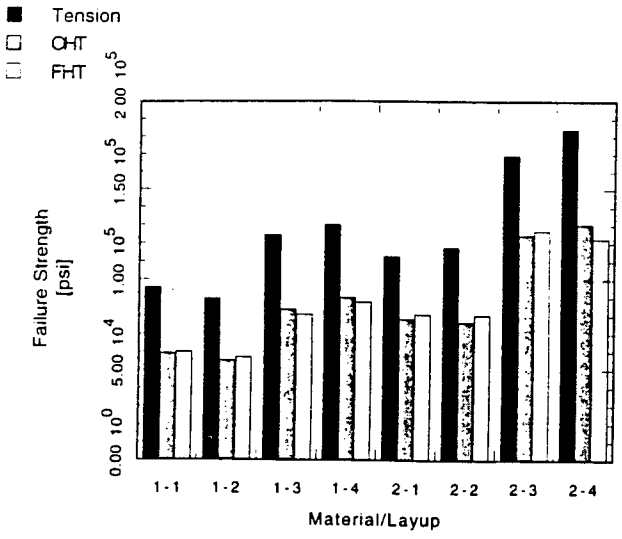
Material	Failure Stress (psi)	Average Vf (%)	Open Hole σN/σo	Filled Hole σN/σo	Normalized Strength (psi)
11	83401	62.42	0.692	1.272	80168
12	94568	59.22	0.584	1.035	95814
13	97101	61.86	0.844	1.051	94181
14	113716	60.27	0.726	0.934	113207
21	92206	60.84	0.631	1.024	90933
22	96714	61.68	0.589	0.944	94080
23	92499	60.81	0.866	1.144	91267
24	111278	61.00	0.636	0.939	109454
31*	86895	59.03	0.599	1.104	88323
32*	92954	59.92	0.613	1.105	93078
34	84486	59.77	0.859	1.276	84811
41*	84101	56.68	0.610	1.113	89027
44*	69084	56.11	0.611	1.126	73873

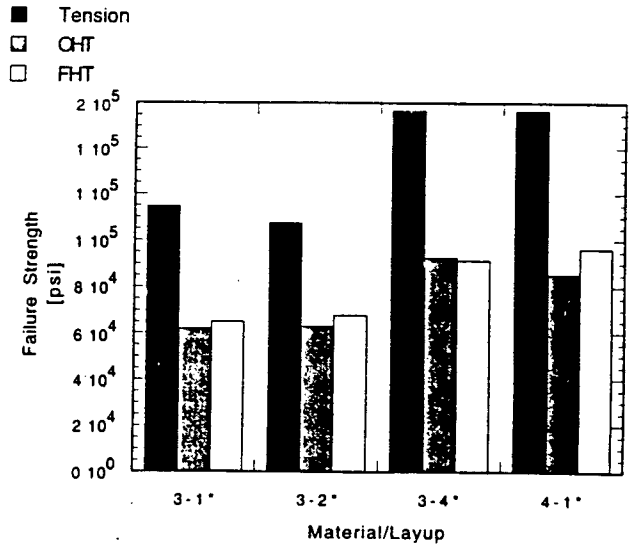
OPEN HOLE COMPRESSION

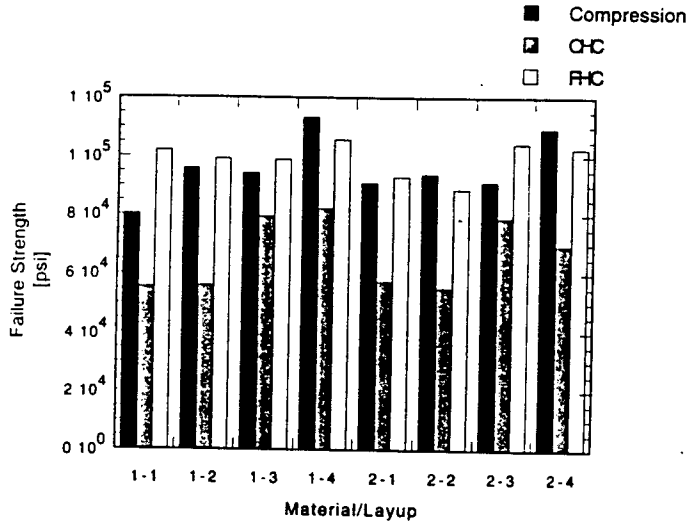
Material	Failure Stress (psi)	Stress Std. Dev. (psi)	Long. Strain (in/in)	Trans. Strain (in/in)	Initial Modulus (psi)	Average Vf (%)	Normalized Strength (psi)
11	57672	*5128*	4.84E-03	1.37E-03	1.10E+07	62.42	55436
12	55218	*1842*	4.88E-03	1.05E-03	1.12E+07	59.22	55945
13	81933	*3552*	5.03E-03	1.07E-03	1.63E+07	61.86	79469
14	82561	*6111*	5.40E-03	2.23E-03	1.63E+07	60.27	82191
21	58155	*1495*	4.16E-03	1.08E-03	1.39E+07	60.84	57352
22	56918	*5773*	3.45E-03	7.80E-04	1.42E+07	61.68	55368
23	80067	*6513*	3.68E-03	2.22E-03	2.03E+07	60.81	79000
24	70729	*10531*	2.78E-03	6.45E-03	2.13E+07	61.00	69570
31*	52077	*3803*	4.27E-03	1.47E-03	1.17E+07	59.03	52933
32*	57002	*1715*	4.95E-03	1.20E-03	1.13E+07	59.92	57078
34	72568	*6080*	4.33E-03	1.36E-03	1.60E+07	59.77	72847
41*	51342	*4336*	3.62E-03	1.01E-03	1.47E+07	56.68	54349
44*	58002	*2387*	4.46E-03	3.00E-04	1.11E+07	56.11	59885

FILLED HOLE COMPRESSION

Material	Failure Stress (psi)	Stress Std. Dev. (psi)	Long. Strain (in/in)	Trans. Strain (in/in)	Initial Modulus (psi)	Average Vf (%)	Normalized Strength (psi)
11	106121	*9527*	9.38E-03	3.42E-03	9.36E+06	62.42	102007
12	97882	*5412*	9.87E-03	3.76E-03	9.76E+06	59.22	99171
13	102022	*7282*	7.62E-03	3.75E-03	1.39E+07	61.86	98954
14	106170	*5230*	7.64E-03	3.38E-03	1.32E+07	60.27	105694
21	94398	*7815*	8.29E-03	2.13E-03	1.21E+07	60.84	93095
22	91259	*4831*	7.67E-03	1.70E-03	1.32E+07	61.68	88773
23	105825	*4288*	5.81E-03	2.22E-03	1.90E+07	60.81	104415
24	104445	*5408*	6.26E-03	1.83E-03	1.79E+07	61.00	102733
31*	95943	*3190*	9.15E-03	2.91E-03	8.90E+06	59.03	97520
32*	102896	*7258*	9.30E-03	3.92E-03	9.40E+06	59.92	102833
34	107770	*6787*	7.65E-03	2.42E-03	1.19E+07	59.77	108185
41*	93577	*5288*	7.80E-03	2.85E-03	1.23E+07	56.68	99058
44*	77793	*3386*	8.06E-03	1.22E-03	2.01E+07	56.11	83186







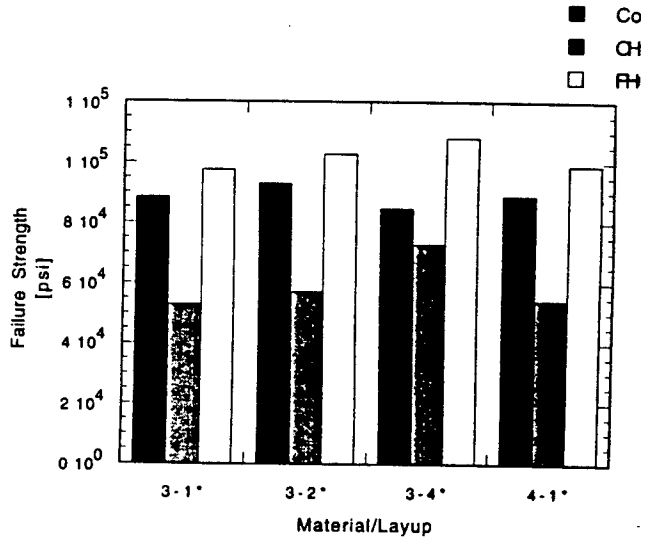


Figure 2, Open and filled hole compressiona and tension data

Table 3. Bearing Data

Material	Bearing a Stress [psi]	Normalized Bearing a [psi]	Bearing b Stress [psi]	Normalized Bearing b [psi]	Average Vf [%]
11	66490	*63912*			62.42
12	70570	*71499*	58700	*59473*	59.22
13	68720	*66654*			61.86
14	71450	*71130*	56350	*56098*	60.27
21	69930	*68964*	61700	*60848*	60.84
22	68860	*66984*	61260	*59591*	61.68
23	67600	*66700*	60720	*59911*	60.81
31*	74880	*76110*	70640	*71801*	59.03
32*	73920	*74019*	73220	*73318*	59.92
34	72500	*72779*	68710	*68974*	59.77
41*	67980	*71962*	69450	*73518*	56.68

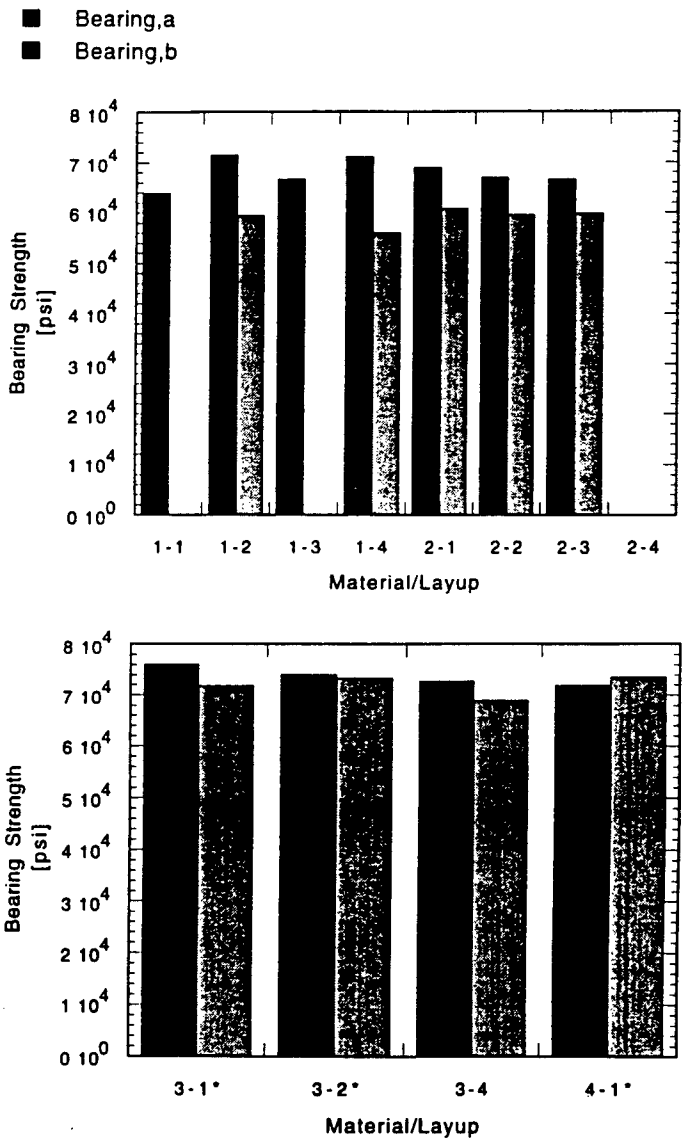


Figure 3, Bearing data.

Results from the extended isotropic analysis are shown in figure 4. From this figure it can be seer that for all materials the tensile stress at the hole edge is greater for stacking sequences 3 and 4 than for stacking sequences 1 and 2. The magnitude of the stress concentration factor appears to be fiber independent. This result is consistent with the statistical analysis but contradicts information provided in the literature which suggests that higher modulus fibers result in lower stress concentration factors [37]. Similarly, examination of the data provided in Table 2 shows slightly better open hole performance for the higher modulus IM-8 fiber material systems. As expected, the analysis suggests that the thermoplastic matrix materials provide slightly better notched strength performance. This information is consistent with results presented in the literature which suggests that tough matrix materials are less notch sensitive than brittle matrix materials [37]. Tensile data provided in Table 2 supports this result also. In all cases it appears as though the remote stress is regained at about one half inch from the center of the hole (.375 in from hole edge).

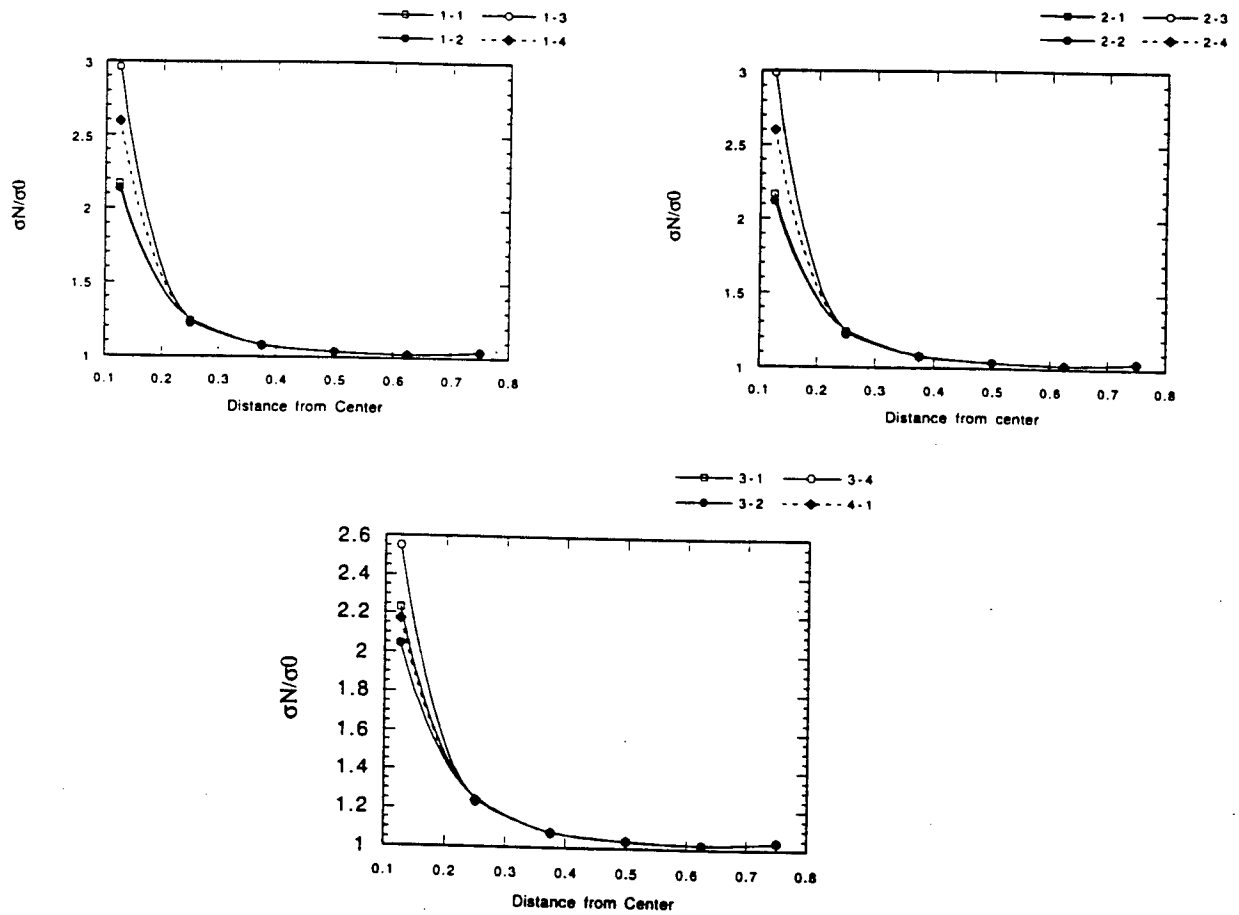


Figure 4. Normalized tensile stress in vicinity of the hole.

Data generated from a spline approximation of a three-dimensional stress analysis in a laminated composite with a hole as described in reference [36] was used to estimate the stress at which delamination would initiate for lay-ups 1 through 4 of material 1. This data was compared with the information obtained through the fractographic analysis. Results of this analysis are shown in Table 5. Based on the continuity of the delamination through the center damage region and the information provided in Table 5 it is possible that delamination is an initial failure mode for lay-ups 3 and 4. Using similar rational, it is doubtful that delamination is the initial failure mode for the remaining lay-ups. It should be noted that once initial delamination occurs then the distribution and magnitude of the interlaminar stresses changes. This may explain the lack of correlation between noted delaminations and the corresponding data at high values of calculated delamination stress. It should also be noted that fractographic cross-sections were taken at the 90 degree location while this analysis predicts maximum interlaminar stress at varying locations.

Macroscopic examination of tested open and filled hole tension and compression specimens indicated that failures were fairly consistent within a given specimen group. With the exception of the unnotched compression specimens, the majority of the specimens failed within the gage area. For the notched specimens these failures generally took place at the hole. For the tension specimens the presence of the bolt/washer appeared to have little effect on the macroscopic failure mode. For the compression specimens, however the presence of the bolt/washer appeared to suppress damage to a region outside of the bolt/washer area. This is consistent with the data provided in Tables 2 and 4 where it was found that the presence of the washer has little effect on the tensile data but a rather large effect on the compressive data. Microscopic examination of specimen cross-sections support this result in that there was little difference noted for the tensile case and a large difference in failure modes for the compressive case. Both the open and filled hole tensile specimen failed by a tensile failure mode occurring at the hole center. In the filled hole compression (FHC) case the delaminations generally appear to be suppressed to a region outside of the washer area. The dominant failure mode appears to be a buckling or kink band formation occurring at the washer edge. If damage occurs at hole center for these specimens it is dominated by a shear type mode. Conversely, for the open hole compression (OHC) case failure is characterized by a shear/compressive mode at the hole.

Comparing the failure mode for the different stacking sequences and lay-ups it was found that for both the OHT and FHT case the overall failures are quite similar. For materials 1 and 2, the amount of delamination appears to be most significant for stacking

sequence 3 and least significant for stacking sequence 1. Face ply delamination was found to occur for all cases. Failures of the OHC specimen appear to be somewhat stacking sequence and lay-up dependent. For materials 1 and 2, the overall failure mode is dominated by shear and compression accompanied by delamination. The extent and location of these delaminations appears to be depended upon the stacking sequence for that material. For example, for material 1, delaminations appear to be more significant for stacking sequence 2 than for stacking sequence 1. For stacking sequences 3 and 4 of that same material, delaminations are comparable in extent. Both stacking sequences contain

Table 5. Calculation of Critical Applied Stress in Relation to Interlaminar Failure

Open Hole Tension								
Material: 1	**Layup: 1**							
Value	**0/0**	**0/-45**	**-45/90**	**90/45**	**45/0**	**0/-45**	**-45/90**	**90/45**
σ33/σ0	0.18	0.11	0.32	0.26	0.10	0.07	0.24	0.30
Location (degrees)	106.45	108.39	69.68	103.74	61.94	106.45	77.42	101.42
Inter. Fail Stress (ksi)	45.16	74.86	26.30	32.33	79.90	118.71	34.20	28.07
Material: 1	**Layup: 2**							
Value	**90/90**	**90/0**	**0/-45**	**-45/45**	**45/90**	**90/0**	**0/-45**	**-45/45**
σ33/σ0	0.28	0.28	0.05	0.09	0.22	0.37	0.07	0.01
Location (degrees)	87.08	87.08	109.52	51.47	109.91	86.69	103.72	129.65
Inter. Fail Stress (ksi)	29.31	29.31	175.95	91.46	38.10	22.41	127.05	764.63
Material: 1	**Layup: 3**							
Open Hole Tension								
Value	**-60/-60**	**-60/0**	**0/0**	**0/60**	**60/-60**	**-60/0**	**0/0**	**0/60**
σ33/σ0	0.28	0.19	0.10	0.34	0.28	0.34	0.08	0.09
Location (degrees)	123.87	109.16	84.77	64.65	57.29	116.13	48.39	80.13
Inter. Fail Stress (ksi)	30.20	43.65	81.00	24.76	29.55	24.76	110.29	88.87
Material: 1	**Layup: 4**							
Value	**Midsurf**	**0/0**	**0/-60**	**-60/60**	**60/0**	**0/0**	**0/-60**	**-60/60**
σ33/σ0	0.15	0.14	0.26	0.28	0.28	0.08	0.22	0.19
Location (degrees)	83.46	83.46	111.29	59.27	65.32	85.28	110.08	122.18
Inter. Fail Stress (ksi)	53.94	60.29	32.04	29.28	30.14	102.49	37.96	42.70
Open Hole Compression								
Material: 1	**Layup: 1**							
Value	**0/0**	**0/-45**	**-45/90**	**90/45**	**45/0**	**0/-45**	**-45/90**	**90/45**
σ33/σ0	0.28	0.16	0.05	0.02	0.32	0.29		0.02
Location (degrees)	120.00	69.68	170.32	143.23	114.19	68.90		10.45
Inter. Fail Stress (ksi)	29.86	53.09	159.20	340.91	25.97	28.44		477.04
Material: 1	**Layup: 2**							
Value	**90/90**	**90/0**	**0/-45**	**-45/45**	**45/90**	**90/0**	**0/-45**	**-45/45**
σ33/σ0	0.14	0.19	0.23	0.26		0.18	0.22	0.17
Location (degrees)	171.49	0.00	69.29	90.97		0.00	65.81	87.10
Inter. Fail Stress (ksi)	59.02	44.30	36.58	31.57		45.16	37.77	50.06
Material: 1	**Layup: 3**							
Value	**-60/-60**	**-60/0**	**0/0**	**0/60**	**60/-60**	**-60/0**	**0/0**	**0/60**
σ33/σ0	0.03	0.12	0.13	0.21		0.24	0.16	0.09
Location (degrees)	27.10	48.39	8.52	115.74		63.87	44.52	113.03
Inter. Fail Stress (ksi)	314.77	67.19	62.58	39.80		34.74	50.92	89.09
Material: 1	**Layup: 4**							
Value	**Midsurf**	**0/0**	**0/-60**	**-60/60**	**60/0**	**0/0**	**0/-60**	**-60/60**
σ33/σ0	0.18	0.18	0.18		0.50	0.20	0.26	0.03
Location (degrees)	36.77	12.77	65.03		10.45	38.71	20.90	83.61
Inter. Fail Stress (ksi)	47.30	45.30	46.61		16.61	42.31	31.82	296.26

a significant amount of delamination. Continuity of these delaminations through major failure regions and the fact that the aforementioned change in direction of failure generally corresponds with a major delamination may indicate that delamination is an initial failure mode. As mentioned previously, for FHC the predominant failure mode appears to be ply buckling at the washer edge. For materials 1 and 2 and stacking sequences 1 through 4 it appears as if the specimen delaminated near the midply, resulting in two sublaminates. One of these sublaminates appears to fail in the aforementioned ply buckling mode. This failure characterized by multiple intra and translaminar fractures and displacement of plies. The remaining sublaminate consists of plies which are displaced away from the midply and appear to fail by shear. In all cases delamination appears to be somewhat suppressed to a region outside of the washer area. Also in all cases there appears to be some minor damage at the hole center.

By comparing the failure characteristics for materials 1 and 2 for a given lay-up, information concerning the effect of the fiber type on the failure mode was obtained. For the OHT and FHT case failures were found to be very similar for the two materials. Both materials failed by tensile failures occurring at the hole center. For the FHT case specimens of material 1 appear to contain slightly more intralamaninar cracking than for material 2. Additionally, slightly more face ply delamination was noted for material 2 than for material 1. Failures of the OHC specimens for materials 1 and 2 were found to be somewhat similar, consisting of a shear dominated center damage region occurring at the hole center. Material 2 has significantly more face ply delamination than material 1. Based on the observed continuity through the shear dominated center damage region it is likely that the OHC specimens for material 2 delaminated before failing in shear. The OHC specimens of material 1, however most likely delaminated subsequent to the center damage shear failure. Longitudinal cross-sections of FHC specimens for materials 1 and 2 show areas of shear failure which terminate at a large delamination occurring at the midply interface. The continuity of the delamination reveals that it is possible that delamination occurred as a first failure mode for specimens 1-1-FHC, 2-1-FHC and 2-3-FHC. Nothing can be inferred from the information available for the 1-3-FHC case.

In order to determine the effect of matrix material on the failure mode, fractographic data obtained from specimens of materials 1 and 3 were compared. For the OHT and FHT case no major difference was noted in the failure modes for the two materials. OHT and FHT specimens of both materials failed in the tensile failure mode described previously. Specimens of both material exhibited comparable amounts of delamination and intralaminar (through the thickness) damage, figure 5.

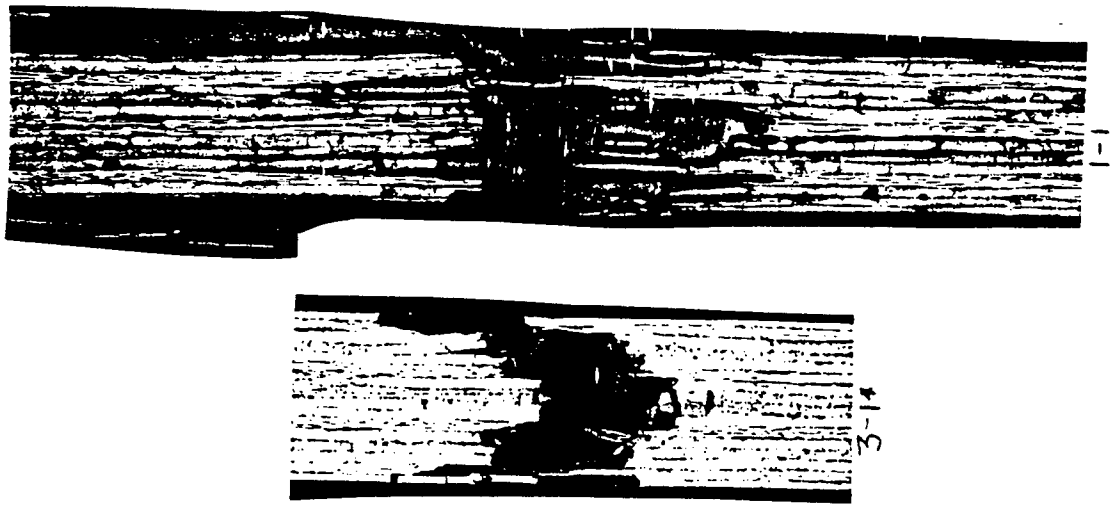


Figure 5, Comparison of OHT failures for different matrix materials.

For the OHC case specimens of both materials appear to be dominated by a compressive and shear failure of the plies. However, for material 1 it appears as though the plies just pressed together after shear failure whereas for material 3 it appears as if the plies bent back after failure. Based on nature of delaminations it is possible that specimens of material 3 delaminated prior to shear failure of the plies. However, it is postulated that had this been the case, the delaminated plies would have immediately kinked and no kinking of fibers was observed. It is possible that delamination proceeded shear failure for specimens of material 1 also. Matrix material appears to have a significant effect on the failure mode of FHC specimens since the failures were found to be very different from each other for materials 1 and 3. FHC specimens of material 1 have a failure characterized by a definite kink band consisting of multiple plies (12 plies). Specimens of material 3, however consist of individually and multiple kinked plies. Delamination appears to surround areas of kinked plies for this material, figure 6.

All of the bearing specimens failed in a bearing type mode, Figure 7. For both materials the damage appeared to be slightly more significant for the 0.125 inch diameter hole specimens than for the 0.250 inch diameter hole specimens. The failures appeared to be independent of lay-up or fiber type but somewhat dependent on matrix type. For the thermoset matrix specimens, the failure was characterized by limited local yielding with delamination propagating from the hole edge. For the thermoplastic matrix specimens a significant amount of local yielding was found to occur in the immediate vicinity of the hole. Very limited to no delamination was observed for these specimens.

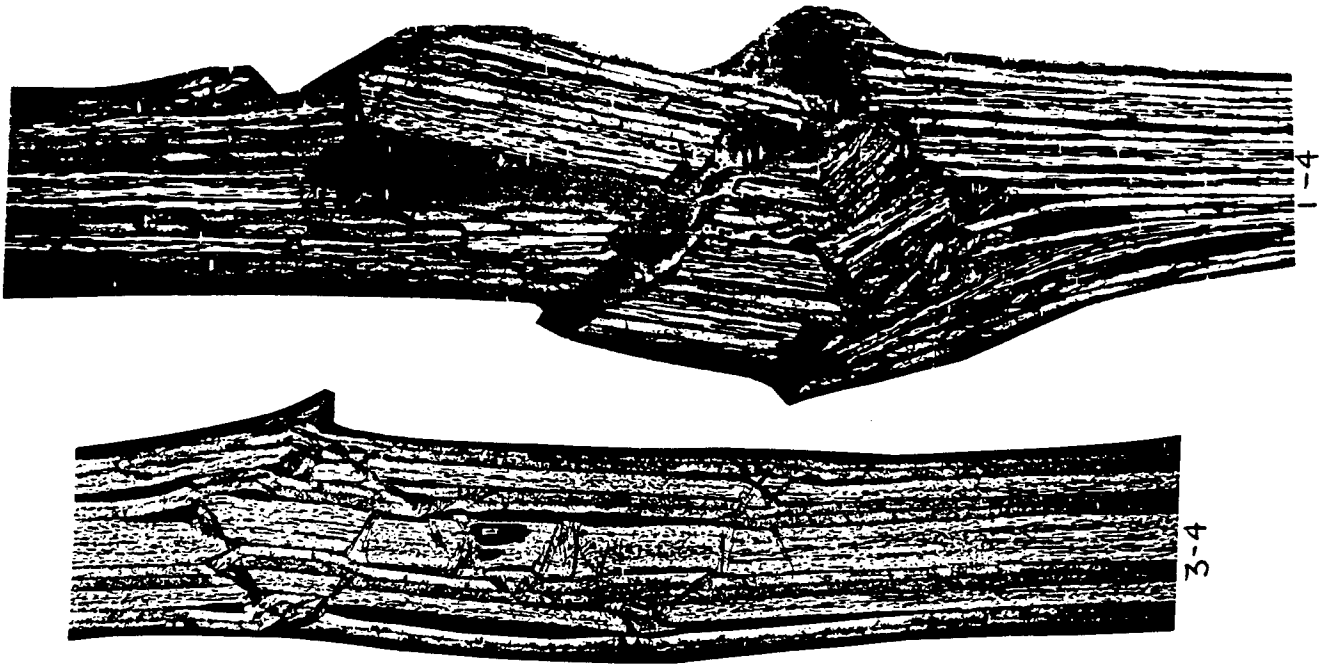


Figure 6, The effect of matrix material on the failure of FHC specimens.

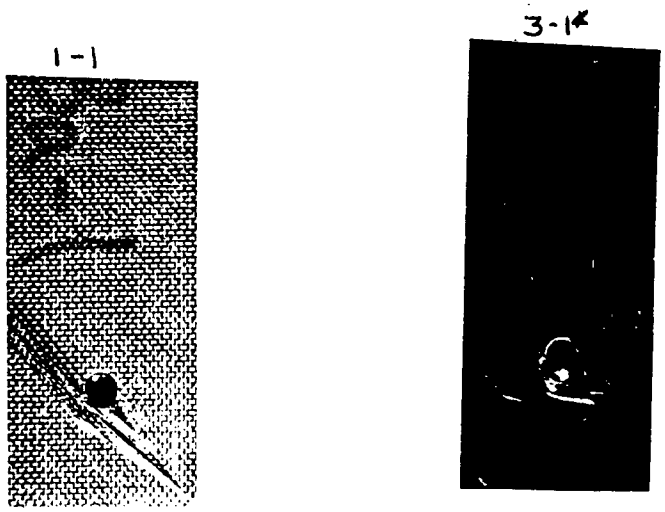


Figure 7, Failure of thermoplastic and thermoset matrix bearing specimens.

Conclusions:

The open and filled, drilled hole tension and compression performance and drilled hole bearing performance was evaluated for four materials of various lay-ups and stacking sequences. The data generated from this testing provided information concerning the effect of test technique (open hole versus filled hole), fiber stiffness, matrix toughness and fiber orientation on failure characteristics and failure strengths. Through this testing it was found that fiber type and lay-up have the biggest effect on the tensile data while test type (open hole versus filled hole) had little effect on the data. Conversely, test technique was the parameter having the largest effect for the

compressive data. Lay-up also significantly affected the compressive data. Hole size most significantly affected the bearing data. Results of an extended isotropic analysis showed that the stress concentration factor for materials 1 (AS-4/3501-6) and 2 (IM-8/3501-6) was greater for stacking sequences 3 ($[60/0_2/-60]_{2}]_{2S}$) and 4 ($[60/-60/0_2]_{2S}$) than for stacking sequences 1 ($[45/90/-45/0]_{2S}$) and 2 ($[45/-45/0/90]_{2S}$). This result was consistent with the data obtained through testing. Fractographic examination of tested specimens showed that test type, stacking sequence, fiber type or matrix type had little effect on the failure characteristics for the open and filled hole tension specimens.

All tensile specimens failed by tension through the hole. The predominant failure mode for the open hole compression specimens was shear or compression occurring at the hole center. The extent and location of delamination occurring in these specimens appears to be stacking sequence dependent. Fiber type appears to control the extent of face ply delamination for the thermoset (3501-6) matrix specimens. This may indicate a difference in fiber matrix interface or a higher energy failure for the IM-8 fibers. As expected, the thermoplastic matrix open hole compression specimens fail in a much more ductile manner whereas the thermoset matrix specimens fail in a more brittle manner. Delamination and damage in the filled hole compression specimens appeared to be suppressed by the presence of the bolt and washer. This may account for the dramatic improvement in strength over the open hole compression case. Failure of the filled hole compression specimens is dominated by a center damage region consisting of sheared plies and a region of dramatic ply buckling occurring at the washer edge. Stacking sequence and fiber type does not appear to have a significant effect on the failure characteristics for the filled hole case. However, matrix material does seem to have a large effect on the failure mode. The thermoset matrix material fails by the formation of a definite kink band consisting of multiple plies whereas the thermoplastic matrix material fails by individually kinked plies. All of the bearing specimens failed in a bearing type mode, Figure 7. For both materials the damage appeared to be slightly more significant for the 0.125 inch diameter hole specimens than for the 0.250 inch diameter hole specimens. The failures appeared to be independent of lay-up or fiber type but somewhat dependent on matrix type.

References:

[1] Cole, R.T., et al, *Photoelastic Investigation of Bolted Joints in Composites,* Composites, July 1982, pp. 253-256.

[2] Zimmerman, K.B., *Mechanical Fastening of Composite Materials,* Experimental Techniques, July/August 1992, p. 36-40.
[3] Rowlands, R.E., et al, *Single- and Multiple-Bolted Joints in Orthotropic Materials,* Composites, July, 1982, pp. 273-279.
[4] Lin, H. J., *Strength of Composite Laminates with Continuous Fiber around a Circular Hole,* Composite Structures, Vol. 21, pp. 155-162.
[5] Nejhad, M.N.G., Chou, T.W., *Compression Behavior of Woven Carbon Fiber-Reinforced Epoxy Composites with Moulded-In and Drilled Holes* Composites, Vol. 21, No. 1, Jan. 1990, p. 33.
[6] Packman, P.F., Hietala, H.J., Schulz, K.C., *An Experimental and Statistical Analysis of Some Fastener Anomalies on the Bolted Joint Strength of Graphite/Epoxy Laminates,* Advanced Materials Performance Through Technology Insertion: Proceedings of the 38th International SAMPE Symposium and Exhibition, V. Bailey, G. Janicki and T. Haulik, eds., Anaheim, CA, May 10-13, 1993, pp. 65-79.
[7] Xue, Y.,Zhang, S., Xu, G., *Effect of Laminate Configuration on Failure of Bolted Composite Joint,* Proceedings of International Symposium on Composite Materials and Structures, T.T. Loo and C. T. Sun, eds., Technomic Publishing, June 10-13, 1986, p. 422.
[8] Arnold, W.S., Marshall, I.H., Wood, J., *Optimum Design Considerations for Mechanically Fastened Composite Joints,* Composite Structures, Vol. 16, 1990, p. 85.
[9] Collings, T.A., *The Strength of Bolted Joints in Multi-Directional CFRP Laminates,* Composites, January 1977, p. 43.
[10] Gunderson, S.L., Hall, R.B., *Preformed Holes for Improved Mechanical Properties of Laminated Composites with Unidirectional Plies,* Advanced Materials Performance Through Technology Insertion: proceedings of the 38th International SAMPE Symposium and Exhibition, V. Bailey, G. Janicki and T. Haulik, eds., Anaheim, CA, May 10-13, 1993, pp. 81-91.
[11] Gunderson, S.L., Lute, J.A., *The Use of Preformed Holes for Increased Strength and Damage Tolerance of Advanced Composites,* Fatigue/Fracture/Damage I., pp. 460-470.
[12] Katz, Y., Haftka, R.T., Altus, E., *Optimization of Fiber Directions for Increasing the Failure Load of a Plate with a Hole,* Proceedings of The American Society For Composites: Fourth Technical Conference, Technomic Publishing, October 3-5, 1989, p. 62.
[13] Eriksson, I., *On the Bearing Strength of Bolted Graphite/Epoxy Laminates,* Journal of Composite Materials, Vol. 24, Dec. 1990, pp. 1246-1269.
[14] Lee, J.H., Mall, S., *Strength of Composite Laminate with Reinforced Hole,* Journal of Composite Materials, Vol. 23, April 1989, p. 337.
[15] Poon, C., et al, *Damage Progression Under Compressive Loading in Composite Laminates Containing an Open Hole,* AGARD, San Diego, CA, 1992.
[16] Guynn, E.G., Bradley, W.L., *A Detailed Investigation of the Micromechanisms of Compressive Failure in Open Hole Composite Laminates,* Journal of Composite Materials, Vol. 23, May 1989, p. 479-504.
[17] Soutis, C., Fleck, N.A., Smith, P.A., *Failure Prediction Technique for Compression Loaded Carbon Fiber-Epoxy Laminate with Open Holes,* Journal of Composite Materials, Vol. 25, November 1991, p.1476-1498.
[18] Starnes, J.H., Williams, J.G., *Failure Characteristics of Graphite-Epoxy Structural Components Loaded in Compression,* Mechanics of Composite Materials: Recent Advances , Z. Hashin and C. T. Herakovich, eds., Pergamon Press, New York, August 1982, p. 253.

[19] Soutis, C., Fleck, N.A., *Static compression Failure of Carbon Fiber T800/924C Composite Plate with a Single Hole,* Journal of Composite Materials, Vol. 22, Nov. 1990, p. 211.
[20] Soutis, C., Fleck, N.A., *Static Compression Failure of Carbon Fiber T800/924C Composite Plate with a Single Hole,* Journal of Composite Materials, Vol. 24, May 1990, p. 536-558.
[21] Guynn, E.G., Bradley, W.L., *Measurement of the Stress Supported by the Crush Zone in Open Hole Composite Laminates Loaded in Compression,* Journal of Reinforced Plastics and Composites, Vol. 8, March 1989, p. 133.
[22] Whitney, J.M., Kim, R.Y., *Effect of Stacking Sequence on the Notched Strength of Laminated Composites,* Composite Materials: Testing and Design (Fourth Conference), ASTM STP 617, American Society for Testing and Materials, 1977, pp. 229-242.
[23] Jen, M.H.R., Kau, Y.S., Hsu, J.M., *Initiation and Propagation of Delamination in a Centrally Notched Composite Laminate,* Journal of Composite Materials , Vol. 27, No 3, 1993, p. 272.
[24] Ko, C.C., and Chien-Chang Lin, *Method for Calculating the Interlaminar Stresses in Symmetric Laminates Containing a Circular Hole,* AIAA Journal , Vol. 30, No.1, January 1992, p. 197.
[25] Ko, C.C., Chien-Chang Lin, Hsiang Chin, *Prediction for Delamination Initiation Around Holes in Symmetric Laminates,* Composite Structures:22, 1992, p. 187-191.
[26] Rybicki, E.F., Schmueser, D.W., *Effect of Stacking Sequence and Lay-Up Angle on a Free Edge Stresses Around a Hole in a Laminated Plate Under Tension,* Journal of Composite Materials, Vol. 12, July 1978, p. 300.
[27] Ratwani, M.M., Kan, H.P., *Effect of Stacking Sequence on Damage Propagation and Failure Modes in Composite Laminates,* Damage In Composite Materials, ASTM STP 775, 1982, pp. 211-228.
[28] Pagano, N.J., Pipes, R.B., *The Influence of Stacking Sequence on Laminate Strength,* Journal of Composite Materials, Vol. 5, Jan. 1971, p. 50.
[29] Zabora, R. F., *Edge Stabilized Compression Testing of Composite Laminates,* Advanced Materials: Performance Through Technology Insertion, 38th International SAMPE Symposium and Exhibition Vol; 28, V. Bailey, et al, eds. May 10-13, 1993.
[30] SACMA Recommended Test Method for Bearing Strength Properties of Oriented Fiber Resin Composites, SRM 9-89.
[31] Caulcutt, R., Statistics in Research and Development, Chapman and Hall, London & New York, 1983.
[32] Box, G.E.P., et.al., Statistics for Experimenters, John Wiley and Sons, New York, 1978.
[33] Konish, H.J., Whitney, J.M., *Approximate Stresses in an Orthotropic Plate Containing a Hole,* Journal of Composites, Vol. 9., April 1975, p.157.
[34] Whitney, J.M., Structural Analysis of Laminated Isotropic Plates, Technomic Publishing Co, Inc., Lancaster, 1987.
[35] Whitney, J.M., Nuismer, R.J., *Stress Fracture Criteria for Laminated Composites Containing Stress Concentrations,* Journal of Composite Materials, Vol. 8, July 1974, p. 253.
[36] Iarve, E., Failed Stress Modeling for Molded and Drilled-Hole Composites, Final Technical Report, AdTech Systems Research, Inc., Dayton, 1994.
[37] Naik, N.K., Sai Ram, K.S., *Effect of Fiber and Resin Properties on Stress Gradients Around Openings in FRP Orthotropic Plates,* Proceedings of International Symposium of Composite Materials and Structures, T.T. Loo, C.T. Sun, Eds., Technomic, June 10-13, 1986, pp. 100-105.

S-PARAMETER MEASUREMENTS OF A GaAsFET VARIABLE-GAIN AMPLIFIER

by

Seth Pinsky
Graduate Student
Department of Electrical Engineering
Oregon Graduate Institute of Science and Technology
20000 Walker Road
Portland, OR 97291-1000

and

Rafael A. Pappaterra
Electronics Engineer
Wright Laboratories
Solid State Electronics Directorate, Microwave Division
2241 Avionics Circle Ste 25
Wright-Patterson AFB, OH 45433-7327

Final Report for:
Summer Graduate Student Research Program
Wright Laboratories

September, 1994

S-PARAMETER MEASUREMENTS ON A GaAsFET VARIABLE-GAIN AMPLIFIER

Seth Pinsky
Graduate Student
Department of Electrical Engineering
Oregon Graduate Institute of Science and Technology

and

Rafael A. Pappaterra
Wright Laboratories

Abstract

A project was done to study the performance of a two-stage GaAsFET variable gain amplifier. We performed tests on several samples of this device, and each sample was tested in 128 different states of variable gain. We made S-parameter measurements over the frequency range of 4.0 - 9.0 GHz for each of the 128 states and compared these measurements against published performance specifications for the device. We went to great lengths to perfect the grounding scheme of our experimental setup so that we could achieve results that accorded with the published specifications.

S-PARAMETER MEASUREMENTS ON A GaAsFET VARIABLE-GAIN AMPLIFIER

Seth Pinsky

and

Rafael A. Pappaterra

DESCRIPTION OF DEVICE TESTED

The device that we tested is designated as a C-Band Dual VGA. The amplifier has a total of fifteen leads to which DC bias must be supplied: there is one pin for VDD, one pin for gate bias, one pin for ground, and twelve gain-control pins.

Of the twelve gain-control pins, there are six pins for each of the two (cascaded) stages. The gain is controlled by supplying a binary number in the range of 0 to 63 to the six gain-control pins of each stage. For any of the control pins, ground potential represents binary zero and -5 volts represents binary 1.

We designate the gain state of a given stage with an integer in the range of 0-63 (0=maximum gain, 63=minimum gain). The gain state is recognized as the value of the binary number that is applied to the six control pins of that stage, following the conventions elaborated above (e.g., state '0' means that all six pins are held at ground; state '63' means that all six pins are held at -5 volts.)

The VGA in the form in which we tested it was housed in an open package and had wirebond connections for all fifteen pins requiring DC voltage. The chip did not, however, have wirebonds for input and output signal power; we thus used Cascade MICROPROBES to probe the input and output ports. The lack of wirebonding on AC signal leads means that our measured S-parameters correspond to those of the unpackaged chip.

DESCRIPTION OF EXPERIMENTAL SETUP.

Figure 1 (p. 25-6) details our experimental setup. A pair of Cascade MICROPROBES was used to probe the input and output ports of the amplifier. These probes are connected via 50-ohm coaxial cables to the ports of our HP 8720A network analyzer. The network analyzer is connected via a GPIB bus to a 286-PC (not shown) on which we ran ANACAT 3.0 to extract our data.

In this setup, special note should be taken of our power supply and ground connections. The salient features of this setup are as follows:

- Each power supply has its own path to a "ground mecca", thus preventing IR drops on ground wires from finding their way to undesired parts of the circuit.

- The VDD and ground wires are shielding so as to prevent

radiation due to possible AC signal currents on these wires.

- An outer conductor shield is never used to supply ground to the VGA. This point deserves special discussion. The leftmost supply shown in fig. 1 can be called upon to supply not only -5 vdc but also 0 vdc to the control pins of the VGA, as determined by switch position. The ground side of the supply is therefore connected to an "inner shield" which is itself shielded by an "outer shield". The outer shield protects the inner shield from induced noise and allows us to use the inner shield as a reliable 0 vdc that can be connected (via the switch assembly) to appropriate pins of the VGA, without fear of AC pickup's getting coupled into the VGA.

The microprobe ground wire shown in fig. 1 should be recognized as a redundant ground path and was not included in our initial setup. We introduced it later since we observed that its inclusion resulted in improved performance (see below).

DESCRIPTION OF EXPERIMENTAL PROCEDURE

The six gain-control pins per stage allow each stage to be operated in 64 ($=2^6$) states of variable gain. This two-stage device can therefore be operated in a total of 4096 ($=64^2$) distinct states.

In order to simplify our experimental task, we performed measurements in only 128 of the 4096 possible gain states. In our experiment, we left one of the two stages in its maximum gain state (state '0'), while we varied the gain state of the other stage through each of its 64 values. While one stage was left in state '0', we placed the other stage in each of 64 possible gain states and made measurements in every such state. All told, we made 128 series of S-parameter measurements for each device tested.

Our experimental procedure was as follows. First we connected our switch cable assembly to the six control pins of stage #1 and left the control pins of stage #2 in an open-circuit condition; we then performed S-parameter measurements for the 64 states of stage #1. Having made S-parameter measurements for all 64 gain states of stage #1, we proceeded to make measurements on stage #2 in a similar manner: We disconnected the switch cable assembly from the control pins of stage #1 and re-connected it to the control pins of stage #2, leaving stage #1's pins open-circuited; we then made measurements in all 64 gain states of stage #2.

OBSERVED VGA PERFORMANCE AND DISCUSSION OF RESULTS

The VGA is advertised to provide an input and output impedance match over the range of 5.0 to 6.0 GHz, and we were able to observe this match without any difficulty. The Smith chart in figure 2 (p. 25-8) shows S11 for a typical sample of the VGA. This chart indicates an input SWR of 2.0:1 or better over the frequency range of interest. The Smith chart in figure 3 (p. 25-9) is a typical

contour for S22 and indicates an output SWR of 2.2:1 or better over the same range of frequencies.

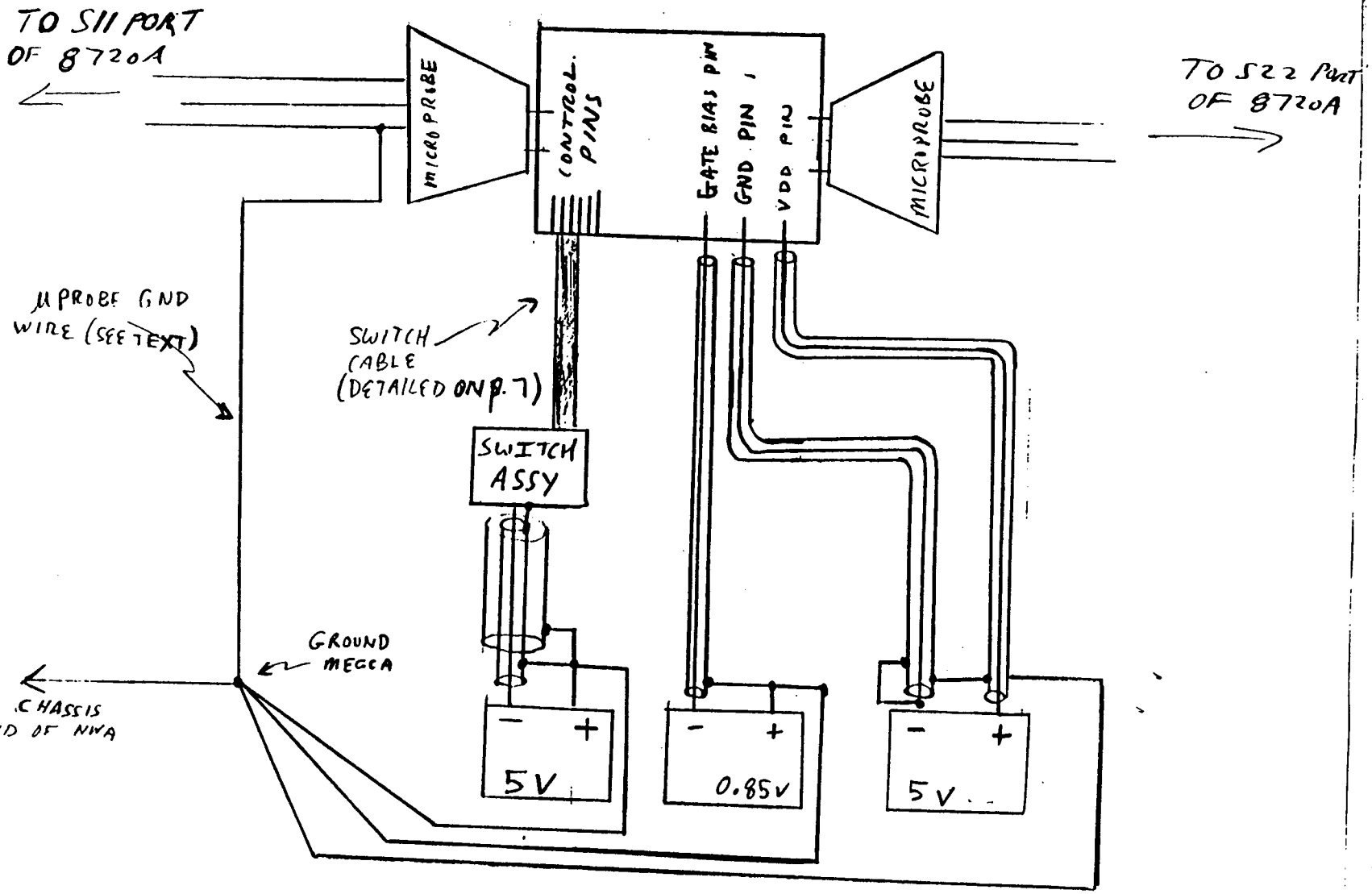
The VGA is advertised to provide an S21 of at least 13.5 dB over the range 5.0 to 6.0 GHz when both stages are in gain state 0. In the early stages of our experimentation, we were not able to achieve this figure, and we routinely measured S21 that was as much as 10 dB below the expected minimum of 13.5 dB. Our continual problems of "low gain" are believed to be due to AC pickup, which causes modulation of the test signal and results in intermodulation products that lie within the passband of the HP 8720A. The microprobe ground wire shown on in figure 1 and mentioned above was the end result of a large amount of experimentation with different grounding schemes. The inclusion of this wire in our test setup is found experimentally to result in values of S21 that reside within specified limits. The discovery of the microprobe ground wire's ability to improve the VGA's performance was the most significant achievement in our experimental work. The data that are presented below were all taken with the microprobe ground included as shown.

PRESENTATION OF EXPERIMENTAL DATA

The following pages provide detailed experimental data for four of the VGA's that we tested. The data are presented as follows:

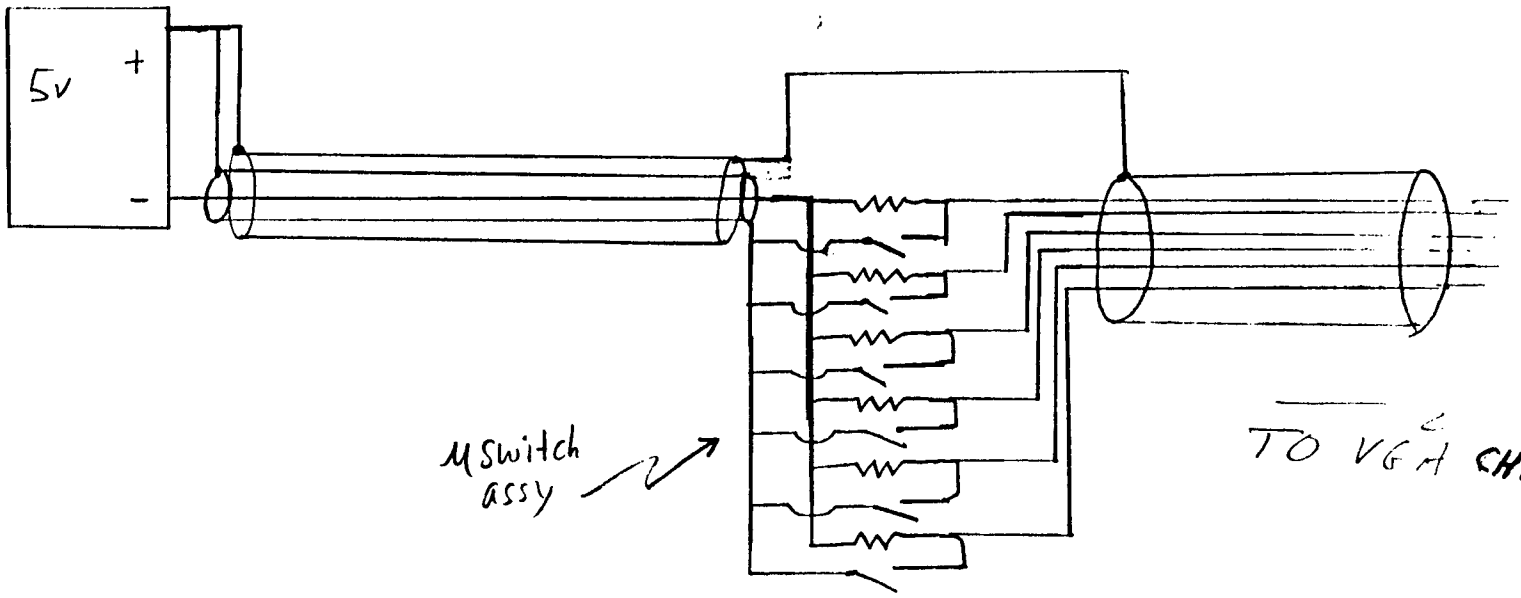
Chip no.	serial no.	s-parameter data for maximum gain state	gain control data, stage #1	gain control data, stage #2
9	B1-21	p. 25-10	p. 25-11	p. 25-12
10	D6-8	p. 25-13	p. 25-14	p. 25-15
11	D6-4	p. 25-16	p. 25-17	p. 25-18
13	D8-16	p. 25-19	p. 25-20	p. 25-21

Figure 1



POWER SUPPLY AND GROUND CONNECTION

Figure 1B



DETAIL OF GAIN CONTROL SWITCH CABLE

Fig 2

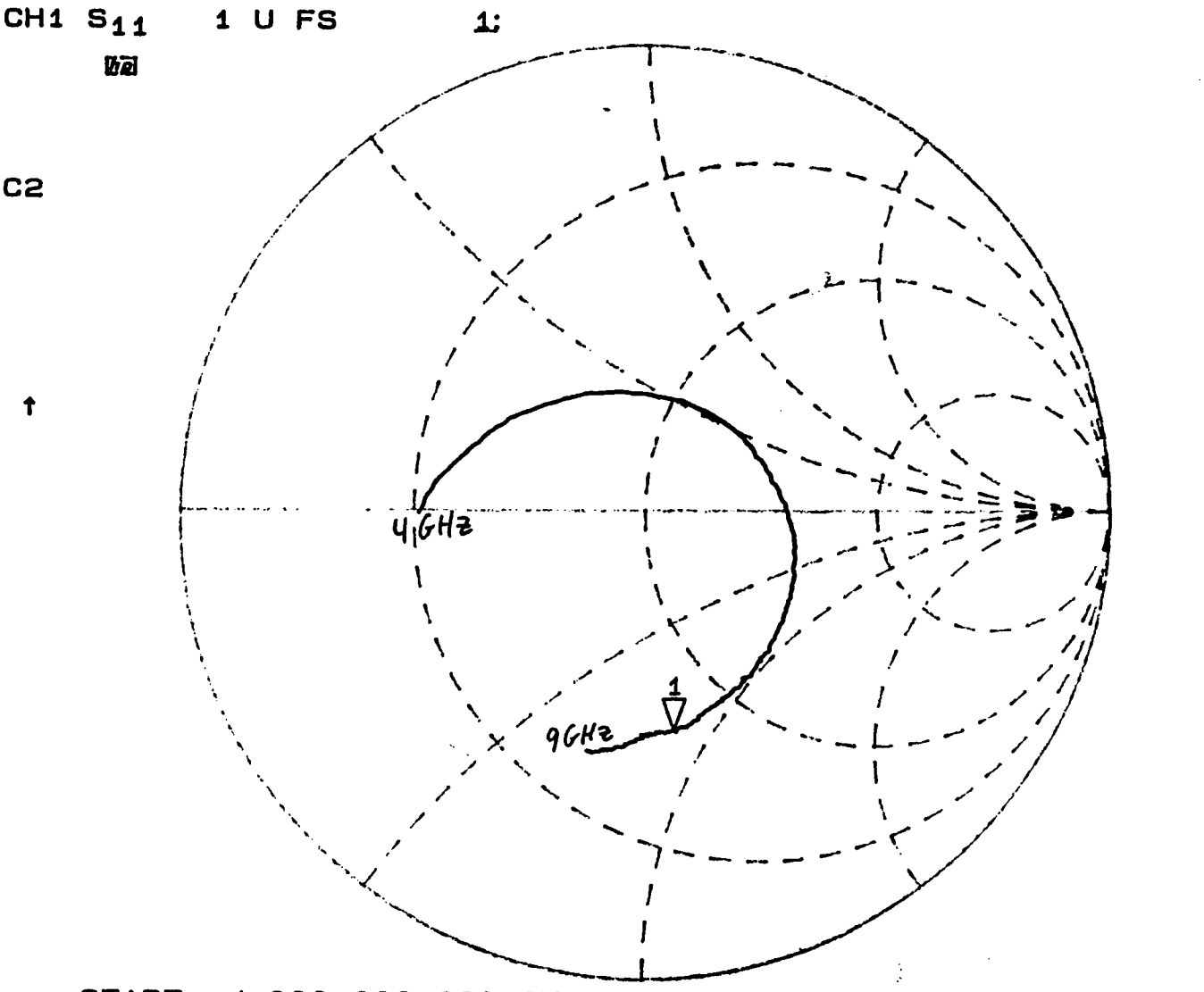
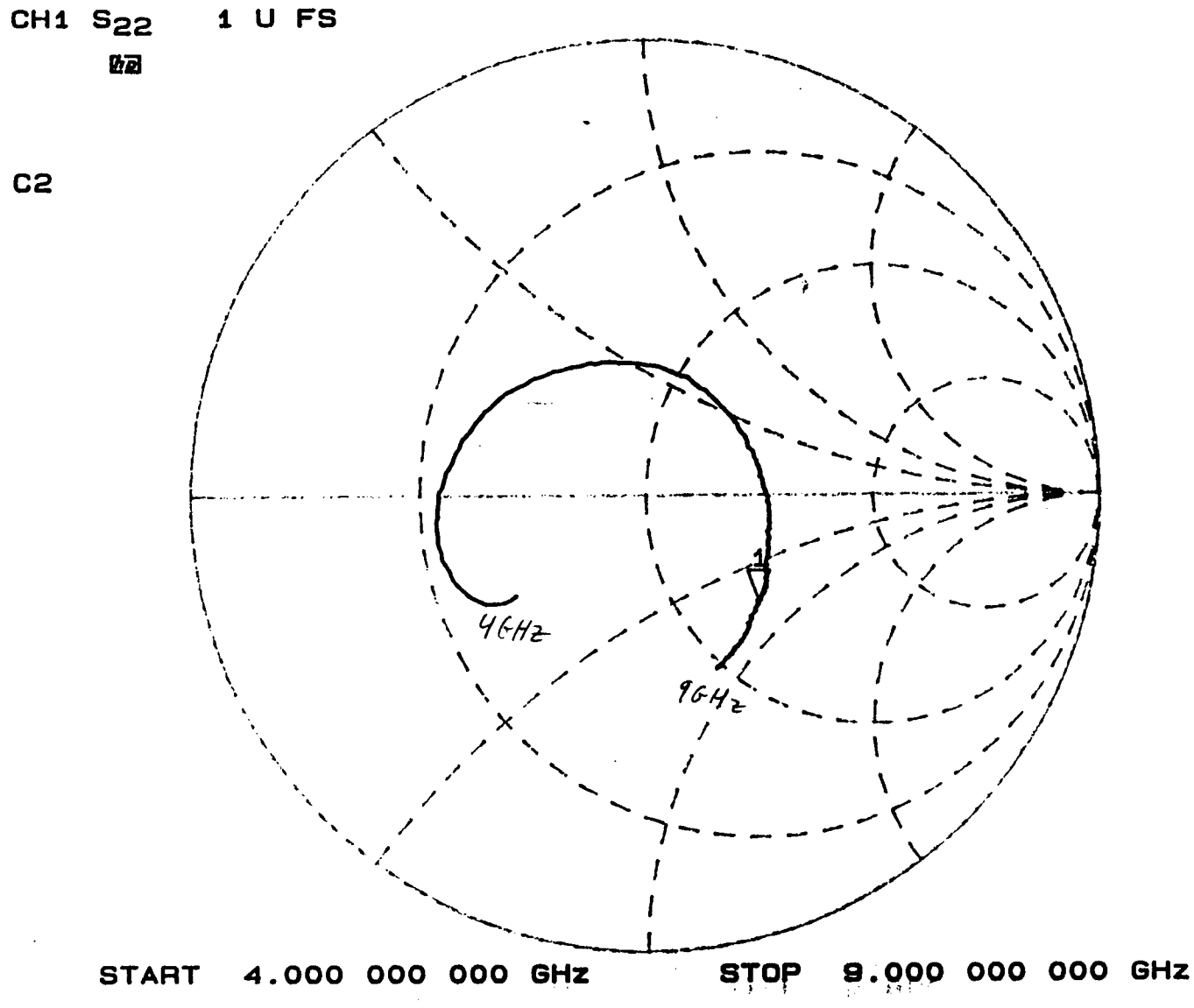
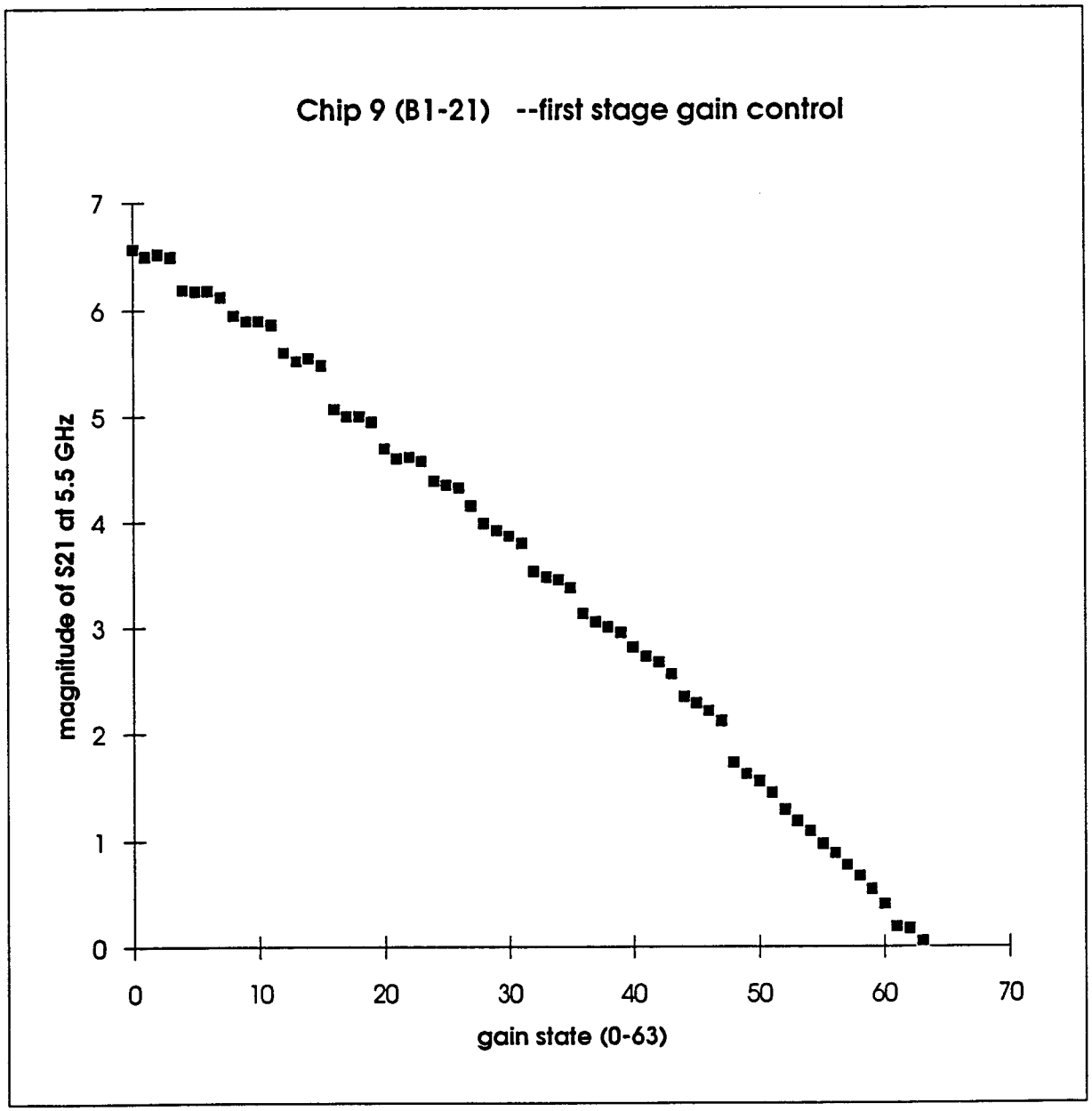

CH1 S11 1 U FS 1:
C2
4GHz
9GHz
1
START 4.000 000 000 GHz
STOP 9.000 000 000 GHz

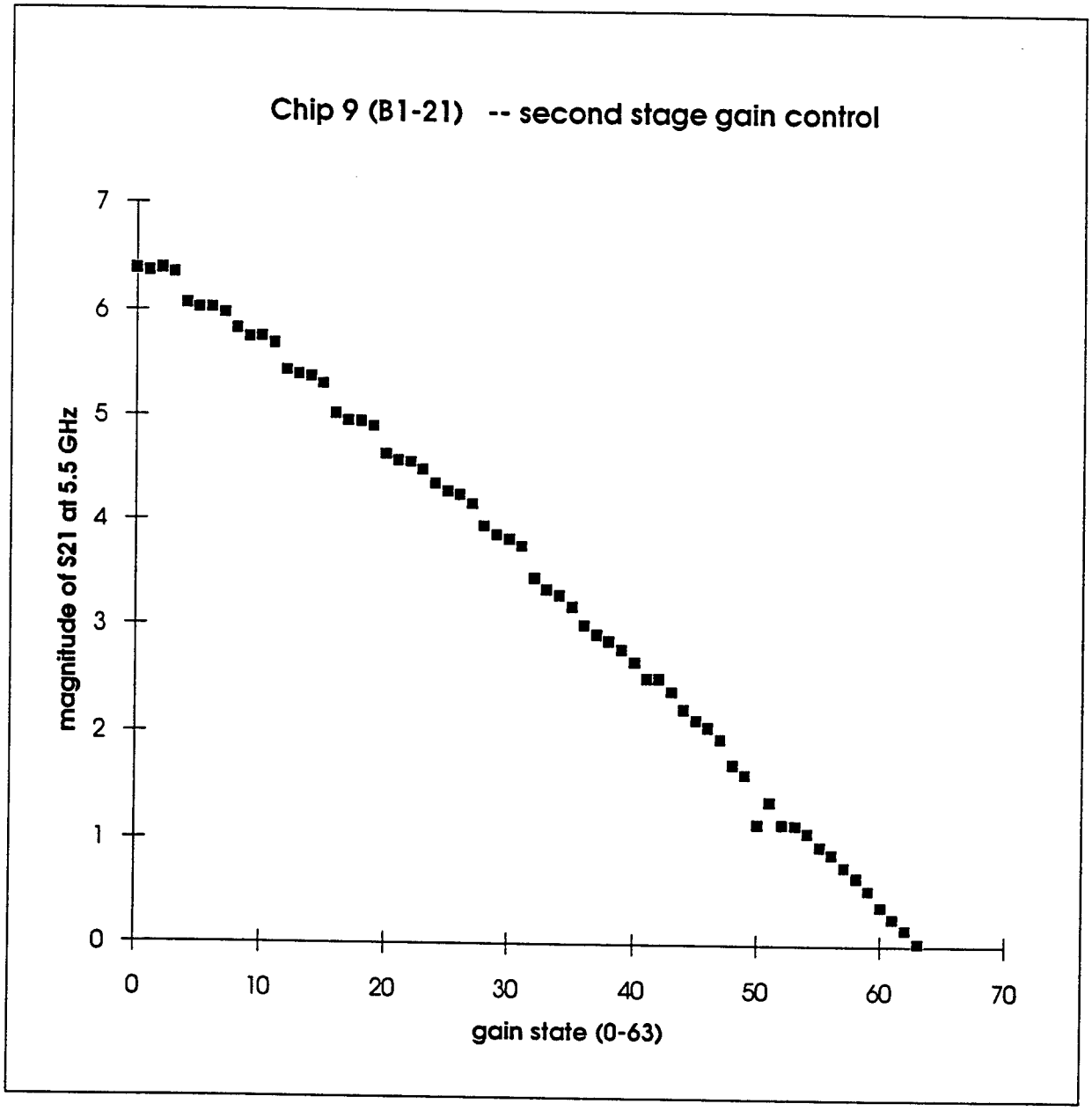
Figure 3


CH1 S22 1 U FS
C2
4GHz
9GHz
START 4.000 000 000 GHz
STOP 9.000 000 000 GHz

Chip 9 (B1-21)
S-parameters in maximum gain state

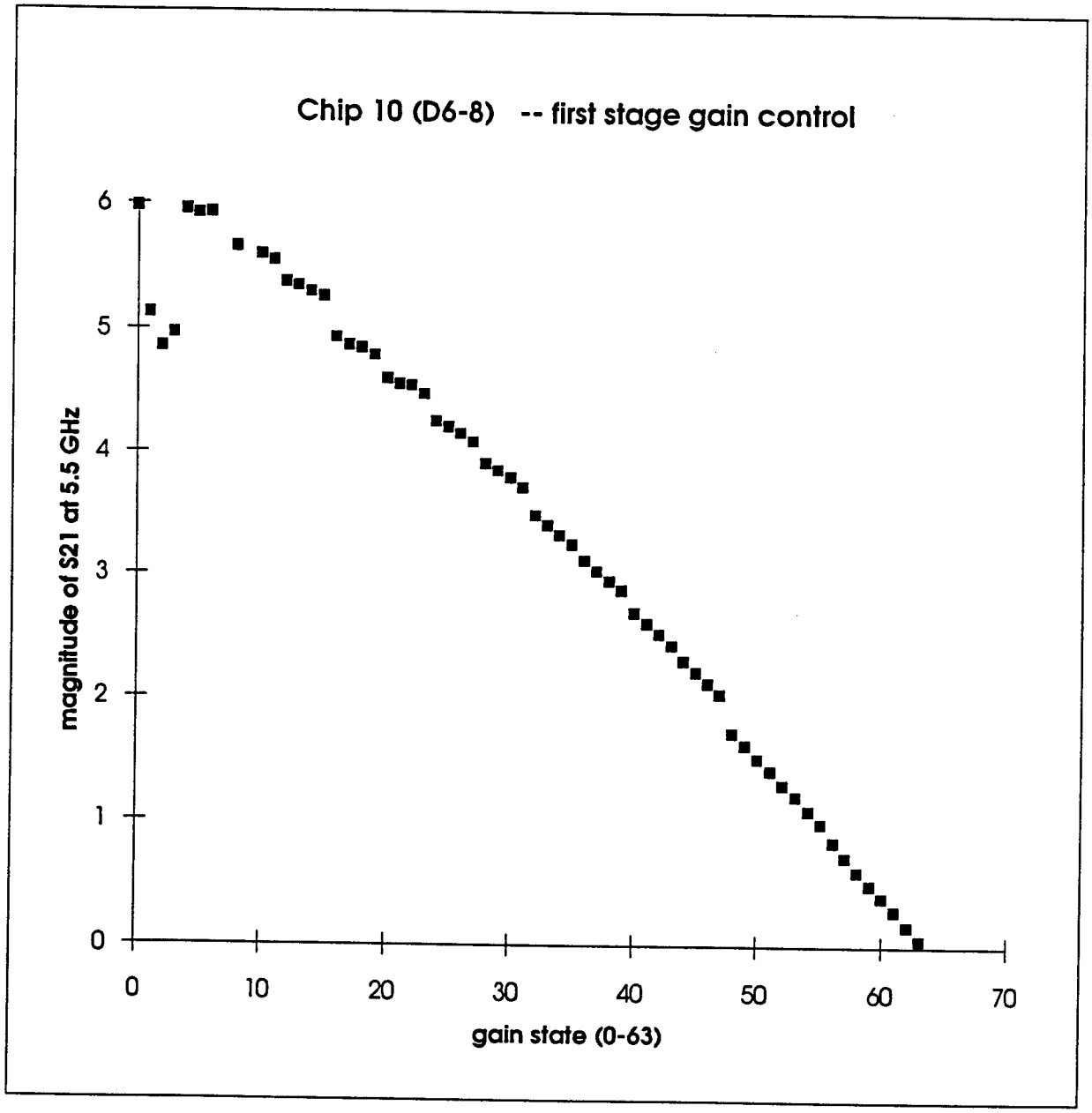
freq (GHz)	mag S11	ang S11	mag S21	ang S21	mag S12	ang S12	mag S22	ang S22
4.0	0.465	-175.2	2.109	-131.4	0.011	111.9	0.360	-138.2
4.1	0.428	176.7	2.280	-147.0	0.011	89.1	0.415	-141.0
4.2	0.383	168.3	2.481	-160.4	0.009	68.0	0.448	-146.5
4.3	0.354	161.0	2.758	-172.6	0.006	55.2	0.464	-154.2
4.4	0.327	150.5	3.031	175.4	0.004	59.4	0.467	-161.1
4.5	0.288	139.5	3.351	163.6	0.005	67.5	0.464	-169.3
4.6	0.258	127.8	3.601	151.9	0.004	49.5	0.456	-177.1
4.7	0.234	114.9	3.937	141.5	0.005	40.4	0.435	175.4
4.8	0.216	101.0	4.267	130.1	0.004	24.8	0.419	167.1
4.9	0.205	86.3	4.601	119.7	0.003	16.7	0.402	159.4
5.0	0.202	72.1	4.989	108.0	0.003	7.1	0.382	150.2
5.1	0.210	57.2	5.279	97.1	0.002	11.6	0.357	141.4
5.2	0.218	43.8	5.562	87.0	0.002	6.7	0.338	132.6
5.3	0.231	31.6	5.998	76.3	0.002	-16.9	0.321	123.4
5.4	0.244	21.0	6.218	65.5	0.002	-15.8	0.306	113.1
5.5	0.259	11.3	6.567	54.9	0.002	-42.7	0.293	102.8
5.6	0.274	1.8	6.800	44.2	0.002	-48.5	0.278	91.9
5.7	0.295	-6.0	6.896	34.3	0.002	-76.3	0.265	80.6
5.8	0.310	-14.2	7.060	24.1	0.002	-87.9	0.254	70.1
5.9	0.324	-21.3	7.093	13.7	0.002	-93.8	0.242	59.5
6.0	0.333	-27.5	7.258	4.9	0.001	-93.2	0.236	51.0
6.1	0.348	-32.6	7.293	-5.3	0.002	-112.4	0.233	41.6
6.2	0.357	-37.2	7.172	-14.9	0.002	-119.1	0.232	33.3
6.3	0.365	-40.9	7.161	-24.6	0.002	-108.0	0.233	26.1
6.4	0.372	-44.2	6.989	-32.6	0.002	-119.0	0.236	19.1
6.5	0.382	-47.1	6.900	-41.0	0.003	-137.9	0.243	12.6
6.6	0.390	-51.8	6.728	-49.9	0.003	-139.2	0.255	5.2
6.7	0.400	-54.6	6.693	-57.5	0.003	-140.6	0.255	-2.3
6.8	0.409	-58.0	6.418	-65.9	0.003	-147.0	0.264	-7.8
6.9	0.414	-60.8	6.210	-73.6	0.003	-148.2	0.269	-14.2
7.0	0.422	-63.5	5.958	-81.1	0.003	-156.2	0.271	-19.1

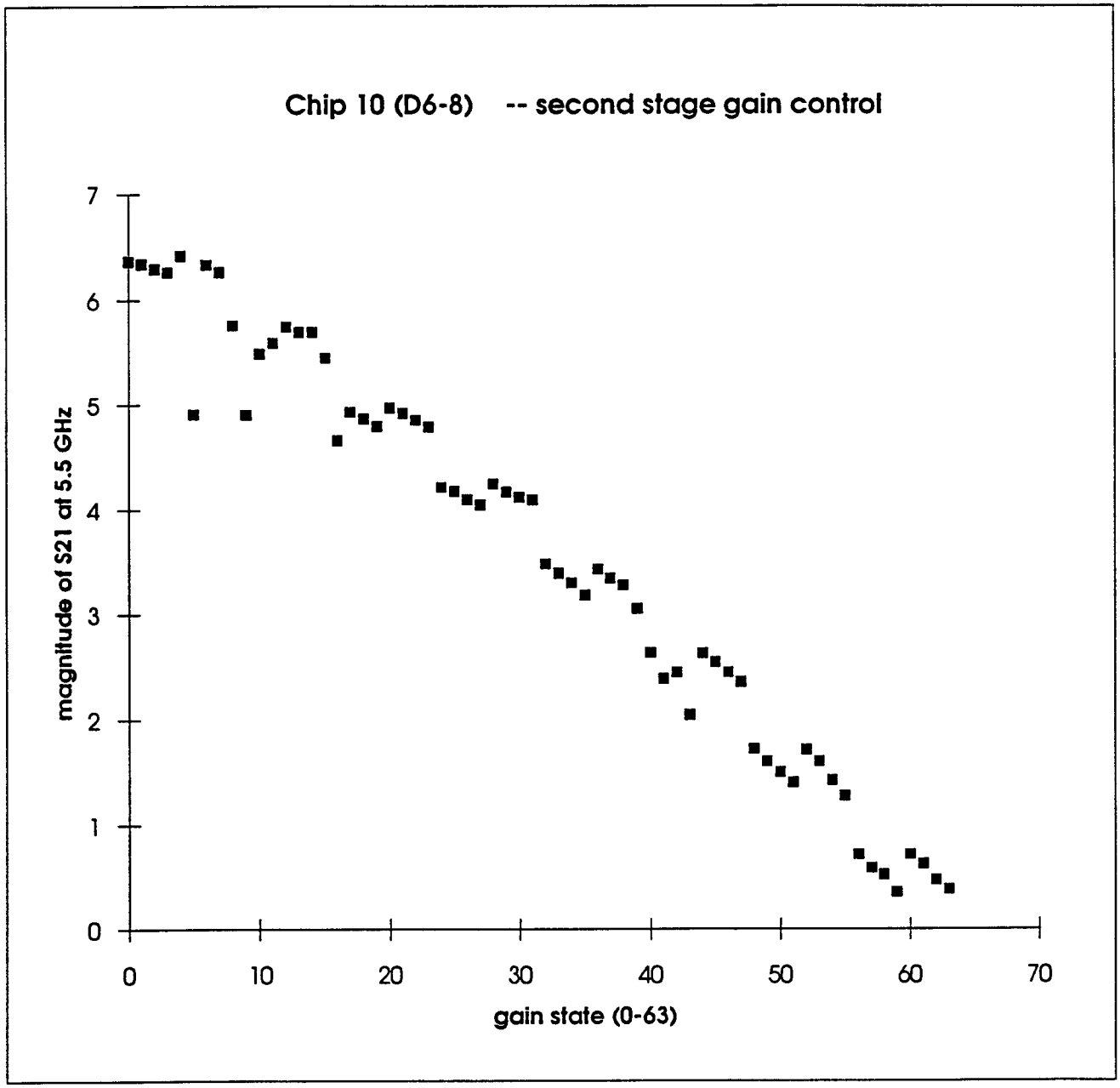

Chip 9 (B1-21) --first stage gain control
magnitude of S21 at 5.5 GHz
0
1
2
3
4
5
6
7
0
10
20
30
40
50
60
70
gain state (0-63)


Chip 9 (B1-21) -- second stage gain control
magnitude of S21 at 5.5 GHz
gain state (0-63)
0
1
2
3
4
5
6
7
0
10
20
30
40
50
60
70

Chip 10 (D6-8)
S-parameters in maximum gain state

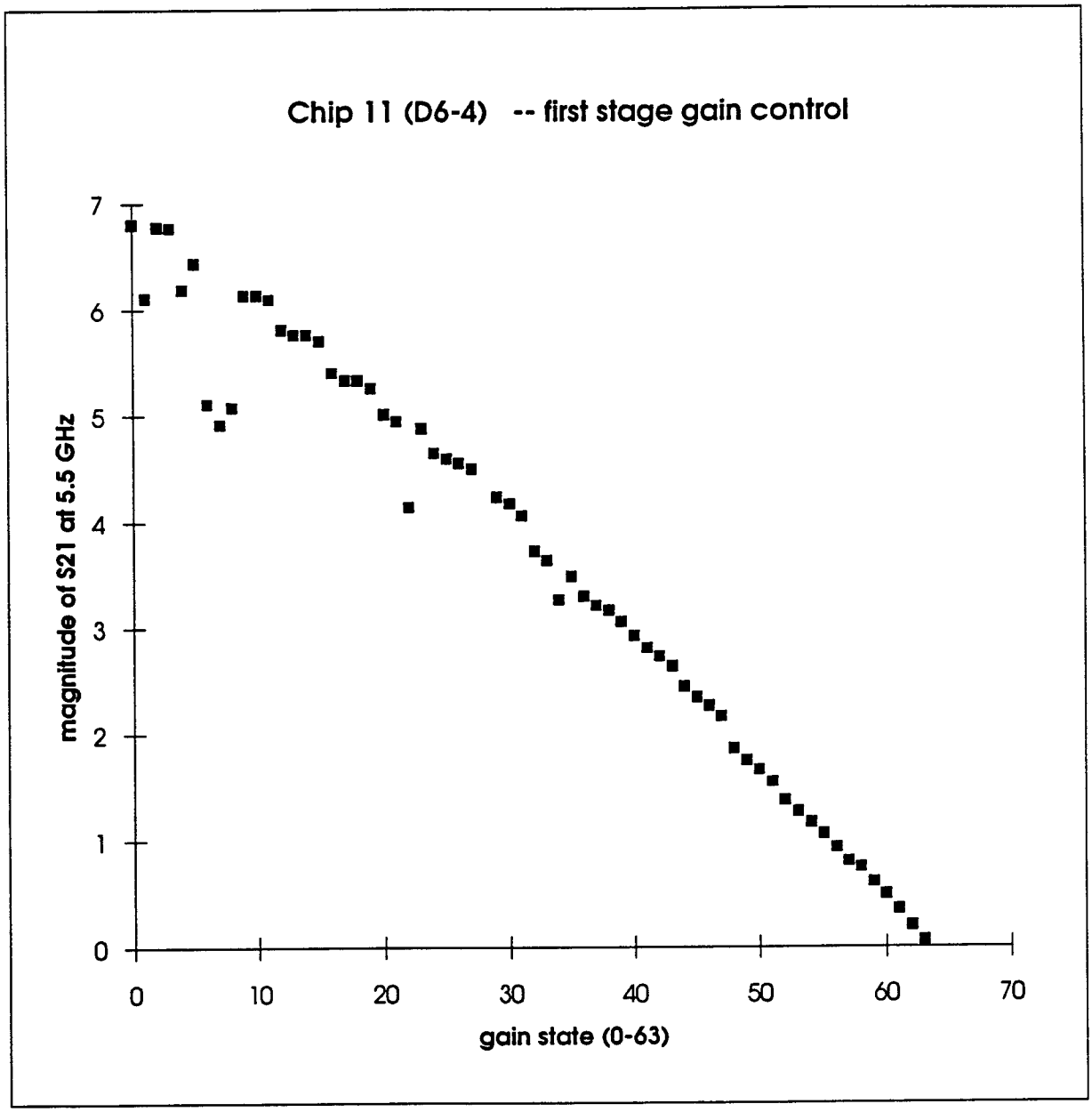
freq (GHz)	mag S11	ang S11	mag S21	ang S21	mag S12	ang S12	mag S22	ang S22
4.0	0.477	179.6	2.036	-134.4	0.011	103.2	0.365	-143.8
4.1	0.437	171.0	2.286	-148.0	0.010	79.2	0.414	-145.9
4.2	0.394	162.9	2.510	-162.0	0.008	58.3	0.447	-151.8
4.3	0.367	154.7	2.725	-174.5	0.006	47.1	0.461	-158.8
4.4	0.336	144.4	2.908	172.8	0.004	36.8	0.467	-166.0
4.5	0.301	134.2	3.098	160.5	0.003	52.9	0.461	-174.1
4.6	0.274	123.3	3.476	151.3	0.004	54.5	0.453	177.9
4.7	0.254	110.4	3.822	140.6	0.004	41.0	0.433	169.9
4.8	0.243	98.1	4.122	129.3	0.003	34.5	0.421	162.0
4.9	0.232	84.8	4.420	118.9	0.002	12.4	0.401	153.9
5.0	0.229	71.9	4.567	105.3	0.002	16.1	0.376	144.6
5.1	0.232	56.9	4.815	94.4	0.002	32.9	0.352	136.5
5.2	0.238	44.0	5.304	87.4	0.002	21.1	0.332	127.7
5.3	0.251	32.8	5.615	77.0	0.002	15.1	0.314	118.6
5.4	0.262	21.8	5.951	66.9	0.002	-24.0	0.297	109.0
5.5	0.279	11.6	5.973	55.0	0.002	-39.6	0.281	98.9
5.6	0.291	2.2	6.122	43.8	0.002	-57.3	0.269	88.2
5.7	0.305	-5.8	6.582	36.0	0.002	-81.8	0.257	76.5
5.8	0.323	-12.6	6.798	26.4	0.002	-84.2	0.245	65.5
5.9	0.337	-19.6	6.843	17.4	0.002	-83.5	0.235	54.0
6.0	0.349	-25.0	7.055	7.7	0.002	-97.5	0.227	43.4
6.1	0.362	-30.7	7.117	-1.3	0.002	-118.2	0.223	33.6
6.2	0.368	-35.8	7.089	-10.9	0.002	-113.3	0.226	25.2
6.3	0.379	-40.0	7.194	-19.3	0.002	-113.7	0.227	17.3
6.4	0.389	-44.2	7.175	-28.6	0.002	-130.0	0.233	10.9
6.5	0.400	-47.7	7.041	-38.1	0.002	-129.7	0.240	3.6
6.6	0.410	-52.7	6.571	-47.5	0.003	-139.3	0.254	-2.5
6.7	0.416	-55.5	7.043	-54.2	0.003	-155.7	0.262	-8.6
6.8	0.424	-58.9	6.821	-63.8	0.003	-148.3	0.269	-19.9
6.9	0.430	-61.7	6.624	-72.1	0.003	-146.5	0.276	-18.3
7.0	0.436	-64.7	6.160	-80.8	0.003	-158.7	0.283	-22.7

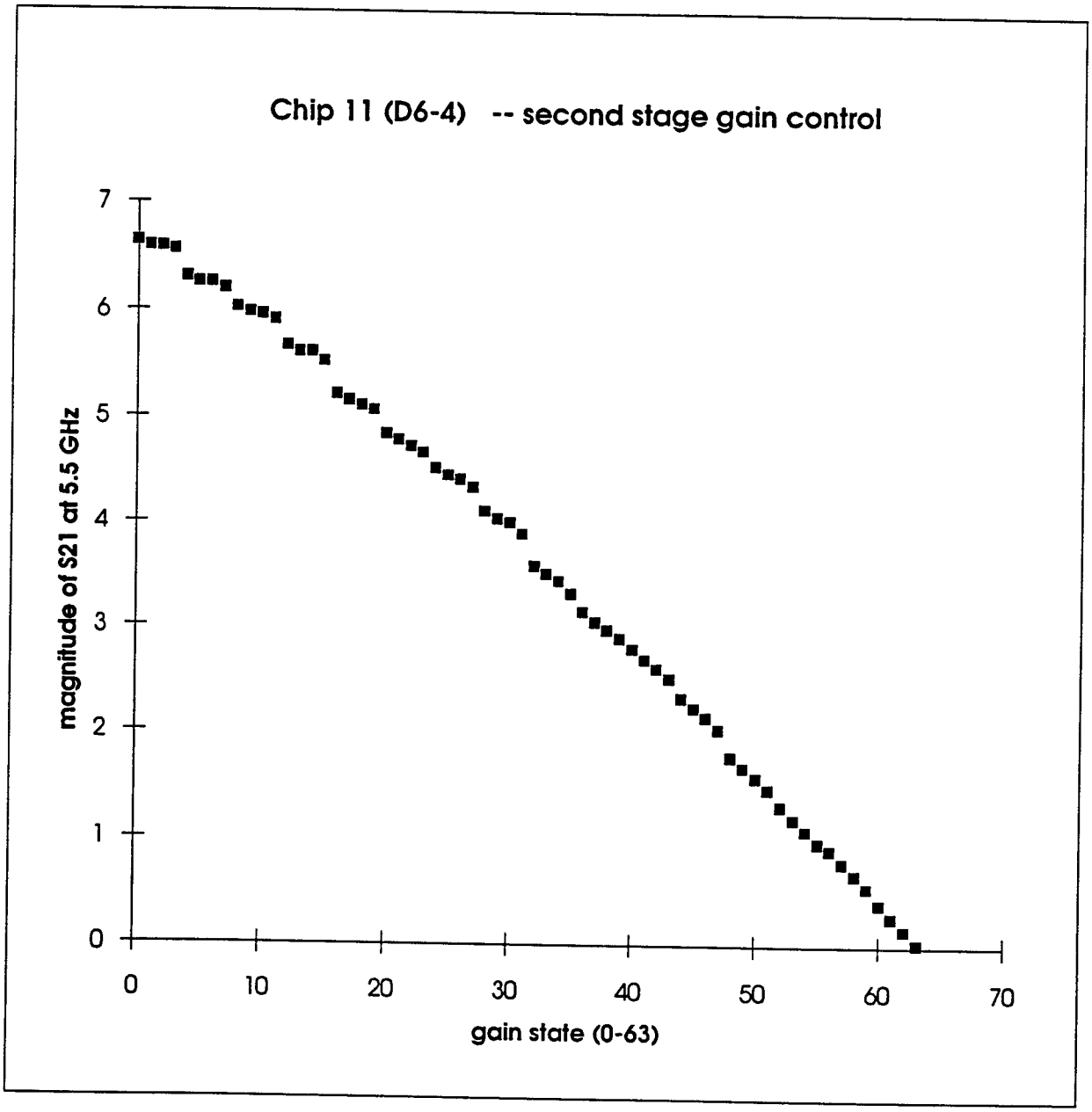

Chip 10 (D6-8) -- first stage gain control
magnitude of S21 at 5.5 GHz
0
1
2
3
4
5
6
0
10
20
30
40
50
60
70
gain state (0-63)


Chip 10 (D6-8) -- second stage gain control
magnitude of S21 at 5.5 GHz
gain state (0-63)
0
1
2
3
4
5
6
7
0
10
20
30
40
50
60
70

Chip 11 (D6-4)
S-parameters in maximum gain state

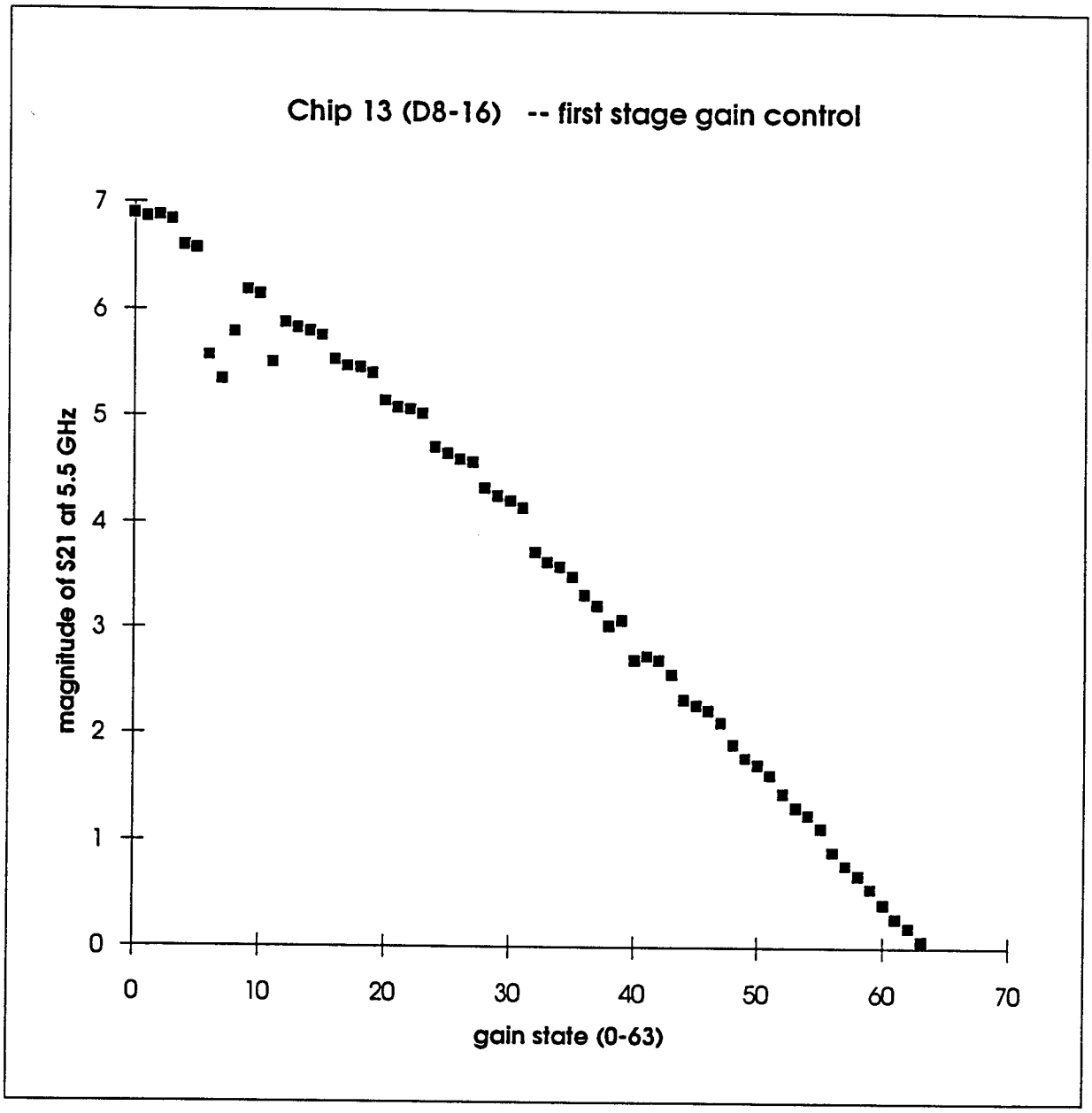
freq (GHz)	mag S11	ang S11	mag S21	ang S21	mag S12	ang S12	mag S22	ang S22
4.0	0.469	-178.7	2.397	-138.3	0.011	104.6	0.359	-142.7
4.1	0.429	172.3	2.559	-153.2	0.011	77.3	0.417	-146.0
4.2	0.386	164.1	2.773	-165.7	0.008	59.1	0.453	-152.0
4.3	0.357	156.1	3.038	-178.2	0.006	49.2	0.471	-159.2
4.4	0.334	145.0	3.336	170.2	0.003	55.6	0.479	-166.8
4.5	0.298	133.0	3.620	158.2	0.005	60.3	0.474	-174.4
4.6	0.270	121.2	3.907	146.9	0.005	55.3	0.466	178.2
4.7	0.249	108.5	4.229	136.4	0.005	34.8	0.453	170.4
4.8	0.235	95.2	4.568	125.8	0.004	30.1	0.440	162.9
4.9	0.228	80.7	4.911	115.1	0.003	8.3	0.429	155.1
5.0	0.225	66.8	5.265	104.9	0.003	5.2	0.416	147.2
5.1	0.231	53.6	5.588	94.1	0.003	-3.9	0.399	138.8
5.2	0.241	41.1	5.933	84.1	0.001	-16.0	0.381	130.5
5.3	0.255	29.8	6.233	73.1	0.001	-21.1	0.361	122.2
5.4	0.273	20.2	6.540	63.2	0.001	-22.2	0.344	113.8
5.5	0.294	10.2	6.799	53.6	0.002	-45.3	0.328	104.9
5.6	0.314	1.2	7.101	43.7	0.001	-38.7	0.313	96.7
5.7	0.329	-7.1	7.340	33.7	0.001	-59.4	0.298	88.4
5.8	0.341	-13.6	7.592	23.9	0.001	-87.5	0.283	79.4
5.9	0.354	-20.0	7.787	13.7	0.002	-80.6	0.276	70.6
6.0	0.365	-25.5	7.930	3.8	0.002	-92.4	0.263	61.9
6.1	0.378	-30.3	7.983	-5.8	0.002	-102.7	0.257	52.9
6.2	0.387	-35.6	7.990	-15.6	0.002	-116.0	0.250	43.7
6.3	0.398	-39.5	7.931	-25.5	0.002	-124.8	0.244	35.0
6.4	0.408	-43.6	7.821	-34.7	0.003	-144.5	0.238	26.8
6.5	0.415	-47.5	7.651	-43.5	0.003	-138.9	0.233	18.2
6.6	0.424	-51.1	7.499	-51.9	0.003	-156.7	0.227	10.8
6.7	0.425	-55.1	7.288	-60.5	0.003	-158.0	0.225	3.6
6.8	0.430	-57.6	7.014	-67.9	0.003	-159.1	0.229	-2.5
6.9	0.440	-60.4	6.829	-75.3	0.003	-159.6	0.232	-7.9
7.0	0.444	-63.3	6.591	-83.0	0.002	-161.6	0.236	-13.4


Chip 11 (D6-4) -- first stage gain control
magnitude of S21 at 5.5 GHz
gain state (0-63)
0
1
2
3
4
5
6
7
0
10
20
30
40
50
60
70


Chip 11 (D6-4) -- second stage gain control
magnitude of S21 at 5.5 GHz
0
1
2
3
4
5
6
7
0
10
20
30
40
50
60
70
gain state (0-63)

Chip 13 (D8-16)
S-parameters in maximum gain state

freq (GHz)	mag S11	ang S11	mag S21	ang S21	mag S12	ang S12	mag S22	ang S22
4.0	0.473	178.8	2.278	-140.3	0.012	104.5	0.384	-138.4
4.1	0.431	169.6	2.462	-155.0	0.010	84.8	0.435	-144.1
4.2	0.388	161.3	2.689	-167.3	0.009	63.9	0.461	-150.9
4.3	0.363	153.1	2.966	-179.5	0.006	45.7	0.471	-158.3
4.4	0.332	140.7	3.230	168.8	0.004	55.2	0.472	-165.8
4.5	0.294	129.9	3.540	156.9	0.004	50.7	0.468	-174.0
4.6	0.267	118.1	3.799	145.5	0.004	47.6	0.455	178.4
4.7	0.249	104.8	4.177	135.2	0.004	33.4	0.437	170.0
4.8	0.234	91.3	4.524	123.6	0.003	28.7	0.423	161.9
4.9	0.226	77.4	4.872	113.3	0.002	11.9	0.399	153.7
5.0	0.227	63.3	5.252	101.4	0.002	24.0	0.377	144.8
5.1	0.234	49.1	5.596	90.4	0.002	13.3	0.353	136.4
5.2	0.245	36.5	5.899	80.2	0.002	16.2	0.333	127.6
5.3	0.258	24.7	6.287	69.5	0.002	-6.6	0.316	118.4
5.4	0.274	15.0	6.616	58.4	0.002	-21.6	0.301	108.4
5.5	0.289	5.7	6.901	47.9	0.002	-30.0	0.287	98.3
5.6	0.310	-3.3	7.125	36.8	0.002	-49.9	0.276	86.9
5.7	0.329	-10.2	7.219	26.6	0.002	-91.0	0.260	74.7
5.8	0.342	-17.7	7.387	16.2	0.002	-90.5	0.252	63.6
5.9	0.354	-24.4	7.413	5.6	0.002	-108.9	0.243	54.3
6.0	0.364	-30.3	7.506	-4.0	0.001	-116.0	0.237	43.9
6.1	0.376	-34.8	7.453	-14.3	0.002	-120.2	0.236	35.0
6.2	0.379	-39.8	7.362	-23.6	0.002	-104.0	0.235	25.9
6.3	0.390	-43.5	7.248	-31.9	0.002	-123.7	0.235	18.0
6.4	0.398	-47.2	7.045	-40.5	0.002	-132.3	0.241	10.4
6.5	0.409	-50.2	6.956	-48.9	0.003	-135.1	0.243	3.8
6.6	0.417	-54.2	6.795	-57.2	0.003	-144.7	0.248	-1.6
6.7	0.424	-57.4	6.765	-64.7	0.003	-154.7	0.252	-7.1
6.8	0.433	-61.0	6.544	-73.4	0.003	-155.0	0.262	-11.9
6.9	0.438	-63.4	6.288	-81.4	0.002	-156.5	0.268	-16.5
7.0	0.446	-66.0	6.024	-88.7	0.003	-159.8	0.271	-21.0


Chip 13 (D8-16) -- first stage gain control
magnitude of S21 at 5.5 GHz
gain state (0-63)
0
1
2
3
4
5
6
7
0
10
20
30
40
50
60
70

MODIFICATIONS TO THE THINKER DISCOVERY SYSTEM

David A. Ress
Graduate Student
Department of Industrial Engineering

Tennessee Technological University
Cookeville TN 38505

Final Report for:
Graduate Student Research Program
Wright Laboratory

Sponsored by:
Air Force Office of Scientific Research
Bolling Air Force Base, DC

and

Wright Laboratory

September 1994

MODIFICATIONS TO THE THINKER DISCOVERY SYSTEM

David A. Ress
Graduate Student
Department of Industrial Engineering
Tennessee Technological University

Abstract

A discovery system is a computer program which utilizes a little knowledge and vast amounts of data to discover rules and relationships which exist in the data. The discovery system Thinker is comprised of algorithms, graphical displays, control procedures, and a knowledge base. The work this summer focused on improving the capabilities of the discovery system Thinker by modifying a regression algorithm, the consulting session, and redesigning the knowledge base - giving the discovery system greater flexibility.

MODIFICATIONS TO THE DISCOVERY SYSTEM THINKER

David A. Ress

Introduction

Discovery is the art of obtaining knowledge through observation, search, study, or chance. In 1928 Alexander Fleming noticed a green mold in a petri dish which prevented various bacteria from growing. This green mold is known today as penicillin, an important pharmaceutical drug for fighting infections.

The computer has been hailed as a great advancement in technology, and in the past ten years the personal computer has come of age. The computer of twenty years ago occupied an entire classroom, but today computers are as small as books and have improved many orders of magnitude in the areas of memory, disk storage, and computational speed. Likewise, computer hardware and software applications (such as Windows) have developed and improved by making the interface simple to increase its user friendliness, but even with these advancements man is still largely responsible for the synthesis of data.

Recently, a new class of computer programs has emerged - discovery systems. Discovery systems are a branch of the artificial intelligence field that endeavor to model human concept formation and pattern recognition in computers. A discovery system utilizes a limited amount of knowledge and vast amounts of data in its attempts to discover the relationships and meanings contained within the data, leading to the discovery of new knowledge. The input to the discovery process is

typically data and general knowledge (relationships) about the domain of the data, but this varies from system to system. The discovery process itself also varies from system to system, but it generally contains a knowledge base which drives and directs the discovery process. The output is interpolated knowledge about the inputs which can be represented as graphs, frames, rules, or simple cause and effect relationships. Furthermore, depending upon the system design, the new knowledge may be added to the knowledge base to enhance the domain of knowledge.

The discovery process has been described as a means of solving problems (Langley, 1987). Mathematics is a common means of solving problems and hence assists in the extraction of knowledge from data. One method from mathematics which is considered to be a discovery tool is regression analysis, and it has been successfully implemented as part of a discovery process(Blum, 1982).

Another means of discovery which has recently become popular is that of defining rules which describe a set of data. The rules are implemented in the form of logical "IF...THEN..." statements where the premise clause represents facts about the data and the conclusion clause asserts a fact given that the premise facts are true. Various methods have been developed to help derive logical rule statements such as the ID3 algorithm (Quinlan, 1986) and ICLN, Inductive Concept Learning Network (Pao, 1991).

The Thinker Discovery System

Thinker was developed on the Macintosh platform using the HyperCard 2.2 application. A HyperCard file is referred to as a stack; hence, Thinker is a HyperCard stack. The language used in writing the algorithms is known as HyperTalk, a scripting language. A scripting language is a program language that is very English-oriented and uses a message hierarchy. Another characteristic of a scripting language is that unlike most higher level programming languages such a BASIC, C, or FORTRAN, HyperTalk uses many short procedures instead of a few long procedures of code.

Developed in early 1994, the Thinker discovery system includes algorithms, graphical displays, control procedures, and a knowledge base. The heart of Thinker's discovery capability lies within the rummaging algorithm which is a self-directed control procedure for analyzing data sets and extracting knowledge from the data sets. The knowledge is extracted in the forms of mathematical models and logical "IF...THEN" statements. The knowledge is then stored in the knowledge base which originally had two areas: the primary knowledge base and the temporary knowledge base.

The discovery system performed better than anticipated, but as with all new discovery systems, a few components needed to be either modified or created. The first area which started to show problems was the knowledge base. After running only two experiments, it was quite obvious that the knowledge base needed to be enlarged and partitioned. The next requiring modifications was the regression algorithm. This algorithm was initially designed to perform linear regression; however,

it became clear that the algorithm needed to be able to handle nonlinear data and interactions between the variables. Finally, the consulting procedures for accessing the knowledge base needed to be upgraded. Specifically, if the consulting session produces an answer, then it needs the capability to explain where the answers came from.

The Knowledge Base

A knowledge base is an area which stores information beneficial to a specific task. The initial domain of Thinker is in families of semiconductor compounds. After a few experiments it became apparent that the knowledge base needed to be partitioned further than initially designed. The basic problem in the initial design revolved around the problem that a set of rules and mathematical models developed with one family of data would not predict the values of another family of compounds very well. Hence the knowledge base was segmented into "areas," or pages, of knowledge where each area contained rules and mathematical models specific to one family of compounds. However, there is also an area referred to as "mixed" since it contains knowledge from multiple families of compounds.

Each page of the knowledge base is further divided into clusters. Each cluster contains either rules or mathematical models for one particular attribute of a compound. For example, the cluster name "cPara r000" indicates that this cluster contains rules (denoted by the r) for the attribute "cPara" (a lattice parameter), and it is the first cluster (number 000) for this attribute's rules. Likewise, the cluster name "gap_energy m002" represents the third cluster of mathematical models for the attribute "gap_energy."

The structure of a knowledge base is also dependent on the way the knowledge is to be represented. Thinker represents knowledge by two means: (1) mathematical relationships, and (2) logical "IF...THEN" statements (i.e., rules). Examples of a mathematical relationship and a logical "IF...THEN" statements contained in clusters are shown below. In both cases, an "IF" statement checks to be sure that the rule can fire or the mathematical relationship can be evaluated. The resulting answer, or answers for the case of rules, are stored in a variable(s) which are returned to the calling procedure. It should be pointed out that any rule which fires stores its output in the last line of the return variable(s). This step is necessary since more that one rule can fire, and hence, more than one response can be returned from a group.

```
if bPara is a number then
  put 0.0 + 1.0 * bPara into (the number of lines of myAnswers+1)
    of myAnswers
  add 1 to numFiredMath
  put "m," & numFiredMath & "," before the first char of line
    (the number of lines of rulesFired+1) of rulesFired
  put "aPara = 0.0 + 1.0 * bPara" after rulesFired
end if
```

Figure 1 Mathematical Model Implementation in HyperTalk

```
if bPara > 5.815 and bPara ≤ 5.977666666667 then
  put 5.815 into line (the number of lines of loValues+1) of loValues
  put 5.977666666667 into line (the number of lines of hiValues+1)
    of hiValues
  add 1 to numFiredRules
  put "r," & numFiredRules & "," into line (the number of lines of
    rulesFired+1) of rulesFired
  put "if bPara > 5.815 and bPara ≤ 5.977666666667 then " after
    rulesFired
end if
```

Figure 2 Rule Implementation in HyperTalk

The knowledge base was further modified to support the new consulting session. Feedback from users of the system explained that it would be beneficial to know which rules or mathematical models were fired to give the answers returned from the knowledge base. This required adding the following lines to each occurrence of a mathematical model or rule in each cluster contained in the knowledge base:

```
add 1 to numFiredRules
put "r," & numFiredRules & "," into line (the number of lines
  of rulesFired+1) of rulesFired
put "if bPara > 5.815 and bPara ≤ 5.977666666667 then " after
  rulesFired
```

Figure 3 HyperTalk Code Additions

Essentially as each cluster is parsed in a consulting session and a rule fires, the rule is numbered and copied into a global variable for later de-referencing in the consulting session.

The Regression Algorithm

It is often desirable to be able to predict the value of an unknown attribute from other known attributes. A logical method of predicting the unknown attribute is through a mathematical model. The discovery of these models is a difficult task since the question of which attributes should be in the model is often asked. Previously implemented in the Thinker discovery system is a stepwise regression algorithm. Stepwise regression is a multiple regression procedure for finding the "best" variables to include in a model where the variables are selected based on the amount of variation the variable explains. If the variable is determined to be significant enough to enter the model by the f-test, then the variable is included in the model.

The stepwise regression algorithm is an enhancement to the forward selection and backward elimination methods in that every time a variable is entered into the model, the algorithm removes any redundant variables from the model. The removal of a variable from a model indicates that two of the independent variables are closely related. The stepwise regression is a two-step procedure with the second step being repeated until the addition of more variables does not significantly increase the capability of the model to explain the variation in the data.

In this discussion, it is assumed that there are four independent variables, x_1, x_2, x_3, and x_4. In the first step, a simple linear regression model is fitted for each of the independent variables. The sums of squares for each model are then compared, and the variable which gives the largest sum of squares is the variable selected to enter the model first. An F-test is used to determine if the variable is significant enough to enter the model. The computed f is the ratio of the sum of squares, $SSR(B_1)$, divided by the mean square error, s^2, where

$$SSR = \sum_{i=1}^{n} (\hat{y}_i - \bar{y})^2,$$

and if

$$f_\alpha(\nu_1, \nu_2) < f_{comp} = \frac{SSR(\beta_1)}{s^2}$$

then the variable is entered into the model; otherwise, the algorithm stops with no variables in the model.

Proceeding with the assumption that the variable x_1 entered the model in the first step, three regression equations are fitted with x_1 in each combination (i.e., x_1 & x_2, x_1 & x_3, and x_1 & x_4) for the second

step. The incremental change in sum of squares regression given that x_1 is already in the model is calculated for each of the three models. The incremental change in sum of squares regression for the model of x_1 and x_2 is

$$SSR(\beta_2|\beta_1) = SSR(\beta_1,\beta_2) - SSR(\beta_1).$$

If the model containing variable x_4 has the greatest change in sum of squares regression, and if

$$f_\alpha(\nu_1,\nu_2) < f_{comp} = \frac{SSR(\beta_4|\beta_1)}{s^2}$$

is true, where s^2 is the mean square error for the regression model involving x_1 and x_4, then variable x_4 is added to the model. The variable x_1 is submitted to an F-test in the presence of x_4 to see if x_1 will remain in the model. That is, if

$$f_a(\nu_1,\nu_2) < f_{comp} = \frac{SSR(\beta_1|\beta_4)}{s^2}$$

then x_1 is retained in the model with x_4.

This process of adding variables that are significant and then checking for variables to be removed which are no longer significant is repeated until no variable is entered into the model. Even with the advantage of removing variables which are no longer significant, the stepwise regression procedure will not necessarily give the optimum regression model every time. This is because the stepwise regression algorithm may not examine every variable in the data set before the algorithm stops. The only procedure which will consistently develop the optimum model is the all models procedure; however, due to the length involved in executing the all models procedure when the number of

variables becomes large, the stepwise regression procedure is a good compromise.

The modification performed to the stepwise regression algorithm was to implement a pre-processor for the data set. The pre-processor allows the user to create additional variables which are non-linear in nature. The following figure shows the dialog box the user utilizes in choosing the degree of nonlinearity to use in the model. The dialog box also allows the user to enable interactions between variables, i.e., create new variables such as x_1*x_2, x_1*x_3, etc...

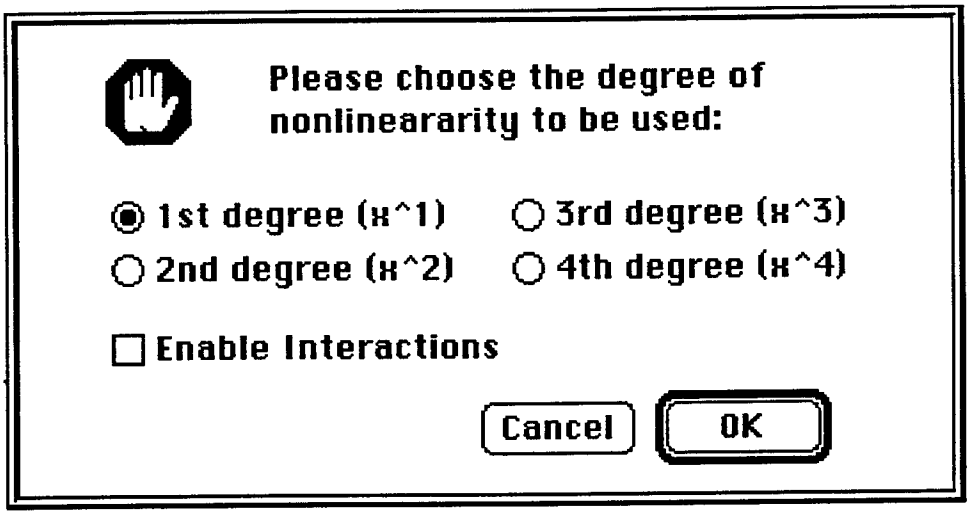


Figure 4 Nonlinearity Dialog Box

While the pre-processor allows the creation of nonlinear variables in the data set, it still performs a linear fit. This modification, while it did not alter the main regression algorithm, allows the user to discover mathematical relationships that otherwise would not have been discovered if this feature was not included.

The Consulting Session

The consulting session part of the Thinker discovery system allows the user to query the knowledge base about attributes of compounds which are unknown. The initial consulting session was a rudimentary design in that it lacked the ability to explain where its answers to queries came from. This defect was corrected by adding code to each instance of a rule and mathematical model as described before and by adding code to the consulting session which allowed the consulting session to keep track of which mathematical model or rule is being queried in detail.

The consulting session was also modified to allow the user to add an answer from a query of the knowledge base to the database. One of the basic tenants of the system which Thinker belongs to is that every data point has a reference number attached to it. This reference number points to a reference record which includes the reference's title, publication information, date of publication, and the author. For the Thinker stack, the reference number defaults to a value of zero when the user adds an attribute value to the database from within the consulting session.

Conclusions

This paper summarizes the modifications made to the Thinker discovery system. The main modifications included redesigning the knowledge base, adding nonlinear models to a stepwise regression algorithm, and implementing a consulting procedure for accessing the knowledge base.

References

Blum, Robert L., *Discovery and Representation of Causal Relationships from a Large Time-Oriented Clinical Database: The RX Project*, 1982, New York, Springer-Verlag, also Ph.D. Dissertation, Stanford University, 1982.

Langley, P., H. Simon, G. Bradshaw, and J. Zytkow, *Scientific Discovery: Computational Explorations of the Creative Process*, Cambridge, MIT Press, 1987.

Pao, Y.H. and W. Hafez, "Analog Computational Models of Concept Formation," *International Journal of Analog Circuits and Systems*, 1992.

Quinlan, J. R., "Decision Trees and Multivalued Attributes," in J. E. Hayes and D. Michie (eds.) *Machine Intelligence II*, Oxford, London, 1987.

A STUDY OF DELAMINATION DAMAGE AND ENERGY EXCHANGE OF COMPOSITE PANELS IMPACTED AT LOW VELOCITY

Mohammed A. Samad
Graduate student
Department of Mechanical Engineering

University of New Orleans
Lake Front
New Orleans, LA 70043

Final Report for:
Summer Graduated student Research Program
Wright Patterson Air Force Base

Sponsored by:
Air Force Office of Scientific Research
Bolling Air Force Base, DC

and

Wright Patterson Air Force Base, Dayton, OH

September 1994

A STUDY OF DELAMINATION DAMAGE AND ENERGY EXCHANGE OF COMPOSITE PANELS IMPACTED AT LOW VELOCITY

Mohammed A. Samad
Graduate student
Department of Mechanical Engineering

Abstract

The of mismatch angle on the damage morphology and energy that occurs during low velocity (below V50) impact of continuous fiber epoxy matrix laminated composite plates was studied experimentally. Composite plates in which the featured a different but uniform value of the change of fiber direction angle (mismatch angle) between adjacent plies on the same plate were impacted over a range of velocities from 100 to 300 feet per second, below their perforation threshold by rigid steel sphere projectiles of one-half inch diameter. The layup of 32 ply thick AS 3501 graphite epoxy plates involved constant mismatch angles between plies on each plate with the plies arranged in a symmetrical spiral staircase manner on each side of the midplane in order to produce a balanced layup. The mismatch angles employed had the value: 90, 45, 22.5, and 11.25 degree.

Projectile velocities approaching and bounce back from the plate were measured to enable the quantitation of the energy transferred to the target plates. Measurement of the change in weight of the plates provided an independent on the mass of spall generated at each velocity.

A STUDY OF DELAMINATION DAMAGE AND ENERGY EXCHANGE OF COMPOSITE PANELS IMPACTED AT LOW VELOCITY

Mohammed A. Samad

Introduction:

Graphite epoxy composite material consists of fibers of graphite embedded in a matrix, currently used in aircraft and many other applications. composite materials (graphite epoxy) are more strong and stiff as compared to other materials like steel or aluminum and can be molded into any complicated structure.

Research on damage due to impact of composite materials at low velocity has been studied for many years. The impact resistance of a multidirectional laminate depends on the specific orientation of the plies. The mismatch angle has a significant effect on damage and in bending stiffness between two plies. In low velocities it was seen that as the mismatch angle between the plies decreases, energy absorbed increases.

Methodology:

The experimental work was done in Wright Patterson Air Force Base, Dayton, Ohio. Graphite epoxy panel with different mismatch angle layups, provided by Wright Laboratory WL/FIVS branch. The two different layups are 1) $[(0/90)_8)]_s$, and 2) $[(0/+45/90/-45)_4]_s$.

The composite plates were impacted at preselected velocities with one-half inch diameter steel sphere at low velocities (below

V_{50}) from 100 to 300 feet per second. Figure 1 shows the setup of gas gun, fixture, composite panel, coil tube, and light screens. The dimensions of the plate was 5" x 5", 32 plies and incorporated with a constant angle change between the fiber direction on adjacent plies. Initial and residual weight of the panel and thickness at the point of impact were measured. Before the panel was impacted, a few test shots were done to get the exact gas (helium) pressure for the required velocity.

There are two methods to calculate the initial velocity: 1) by using graphite 2) by using light screens. To calculate the initial of the projectile, a small piece of graphite is placed across the barrel and also a small piece is placed in front of the fixtures shown in fig. 1. The graphite pencil lead is connected to a circuit. As the projectile break the graphite, a signal is sent to an oscilloscope made by Kontron. The kontron oscilloscope is used to determine the time between the two pieces of graphite. Then by knowing the distance between the two graphite pieces of graphite, and the distance interval, the velocity can be calculated.

To calculate the initial velocity, two light screen were placed between the barrel and the fixture spaced 15 inches apart as shown. When the projectile passes through these screens an interrupted light beam results in a signal on the Kontron. The velocity can be calculated by knowing the time and distance between the two screens. Residual velocity is also calculated by the light screens. When the projectile bounce back after impacting the panel

because of low velocity, passes through light screens and bounce back or residual velocity is calculated by knowing the time and distance between the screens.

After the panels were impacted, soaked in gold chloride solution for two days and heated to 500 ^{0} C for about 30 minutes. By using deplying technique, the panels are deplied ply by ply and the delamination damage area of each ply was measured by image analyzer. The total delamination area and energy absorbed was plotted versus impact velocity.

Conclusions:

Following are the main findings of the experimental investigation:

i) The total delamination area increases with increasing velocity.

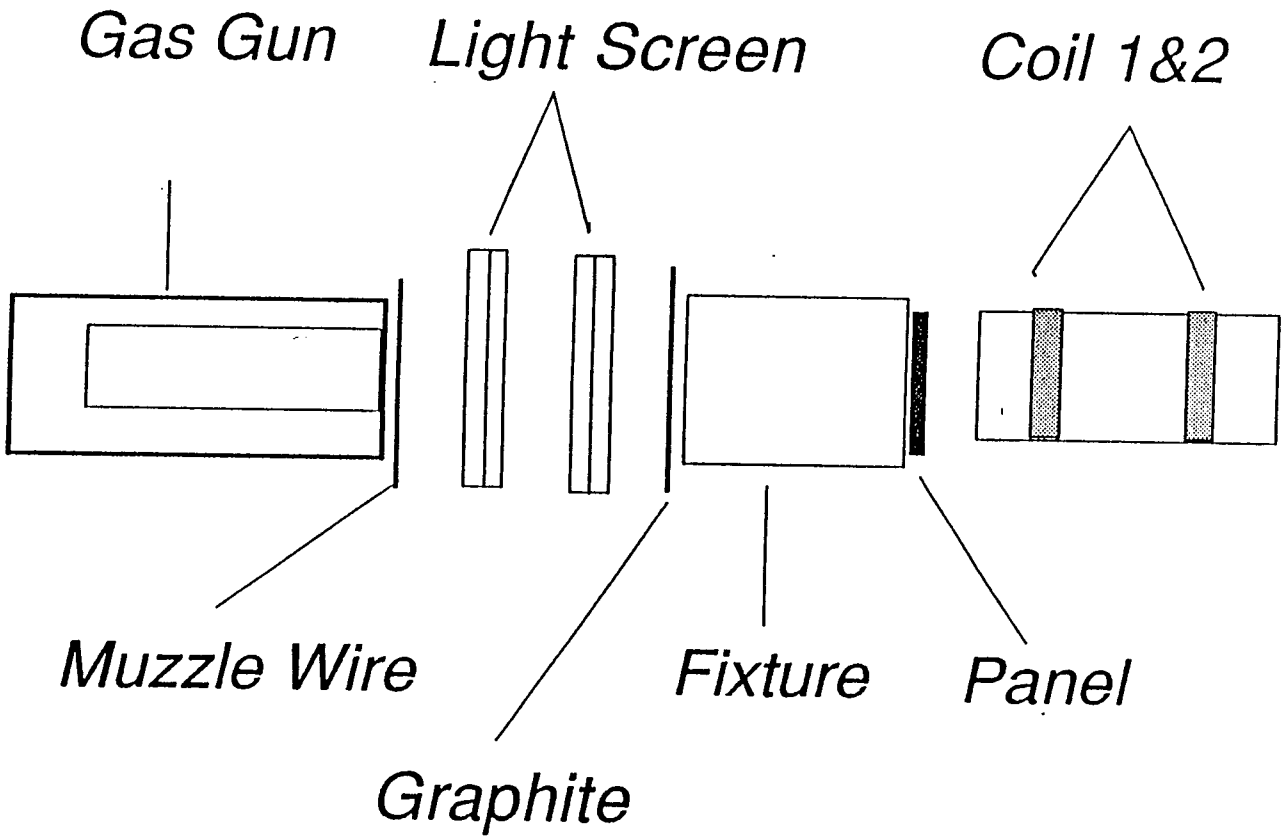
ii) Energy absorbed increases as the impact velocity increases.

Acknowledgement:

I would like to thank the Vehicle Sub System Division WL/FIVS, Wright Patterson Air Force Base, Ohio, for supplying the graphite epoxy plates and allowed me to performed experimental work in their laboratory. I wish to thank Dr. Arnold H. MAyer and Greg Czarnecki for their guidance and support to make this project successful.

Table 1

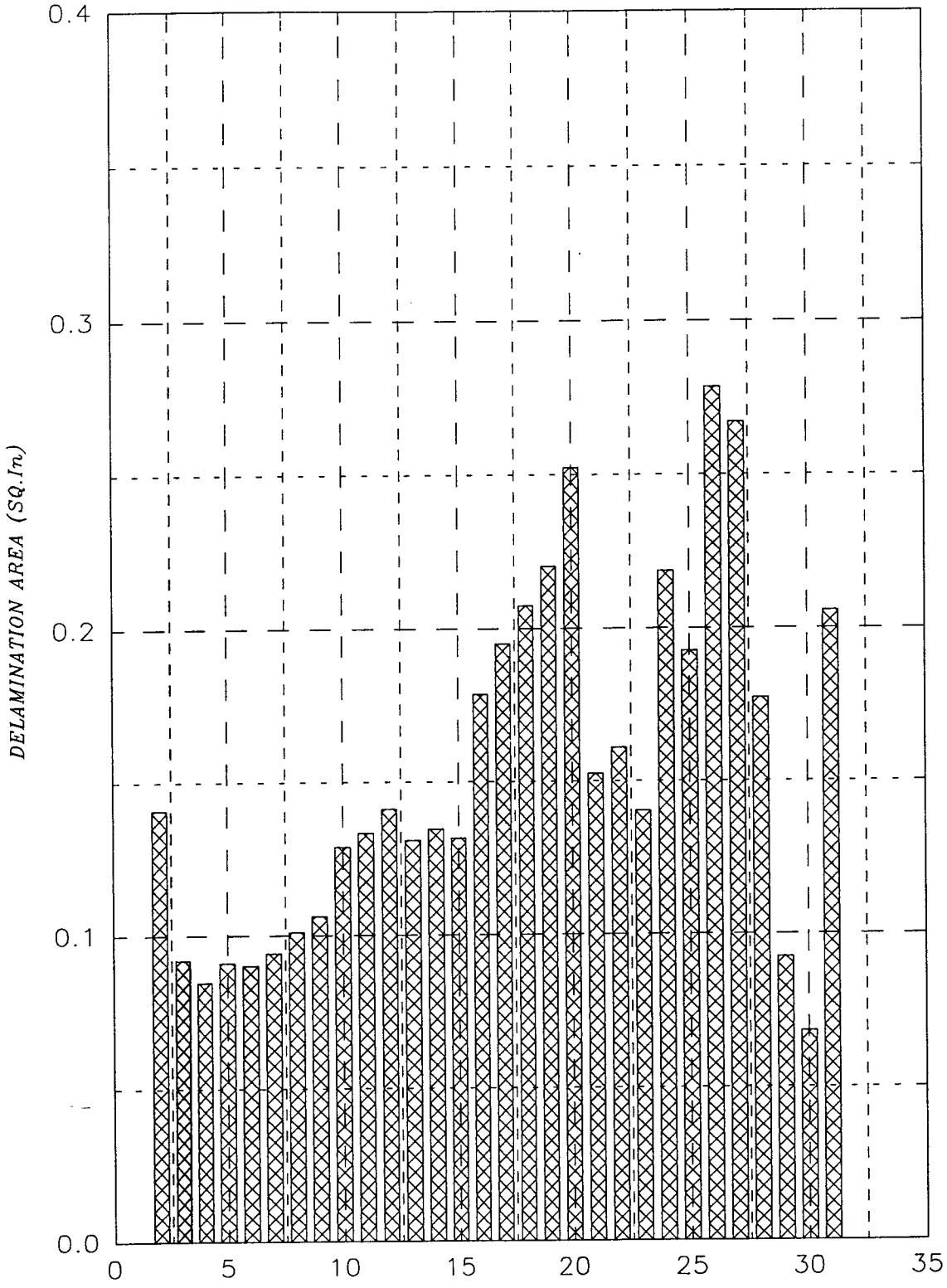
Panel no.	Ini. Vel (ft/sec)	Resi. Vel (ft/sec)	Energy Abs. (ft-lb)	Delmi. area (sq.in)
A-39	117.59	48.84	106.98	4.61
A-26	202.41	103.34	283.22	11.46
A-42	250.01	95.88	498.45	30.18
A-18	300.38	58.34	811.81	30.19



GAS GUN SETUP

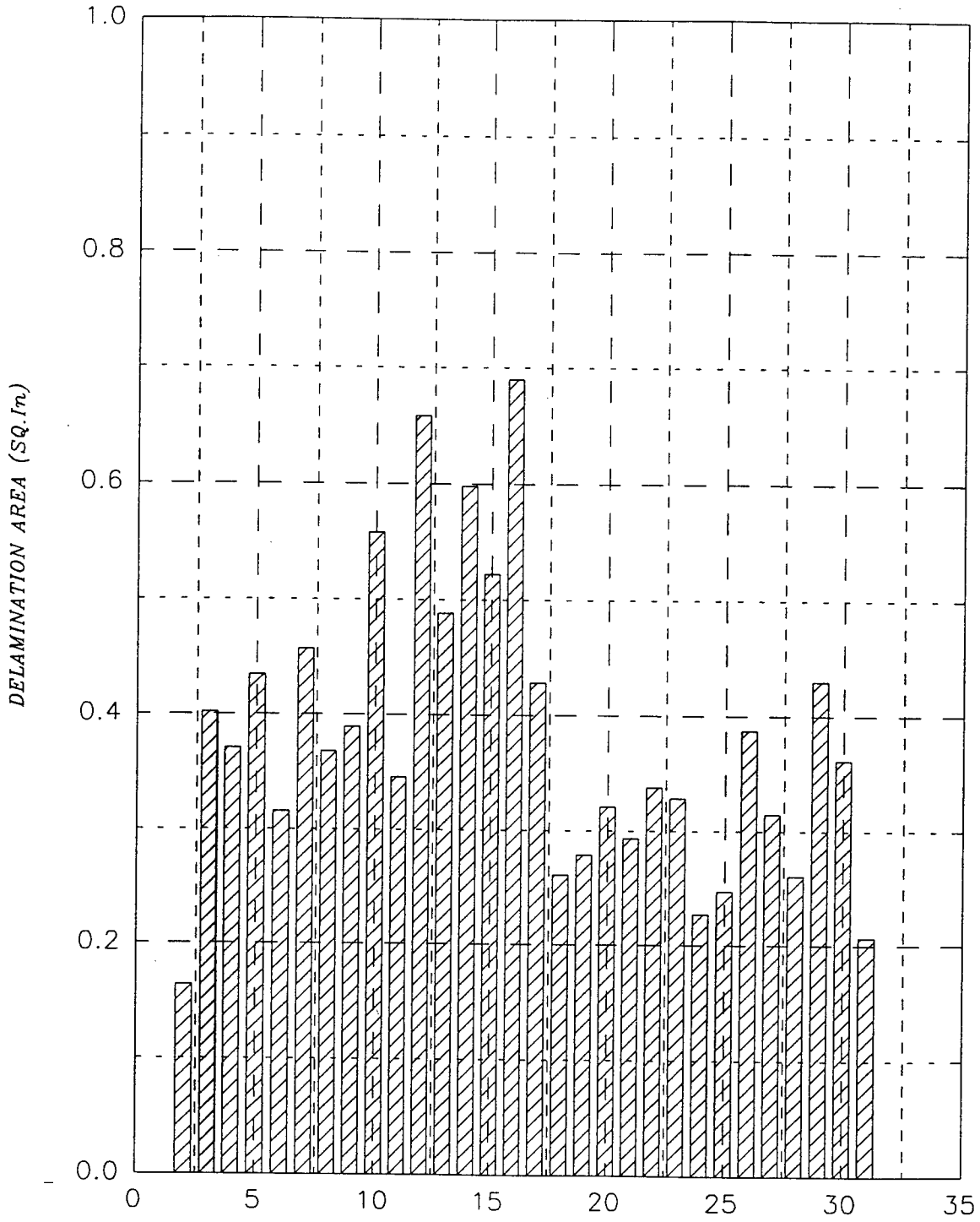
FIGURE: 1

DELAMINATION DAMAGE



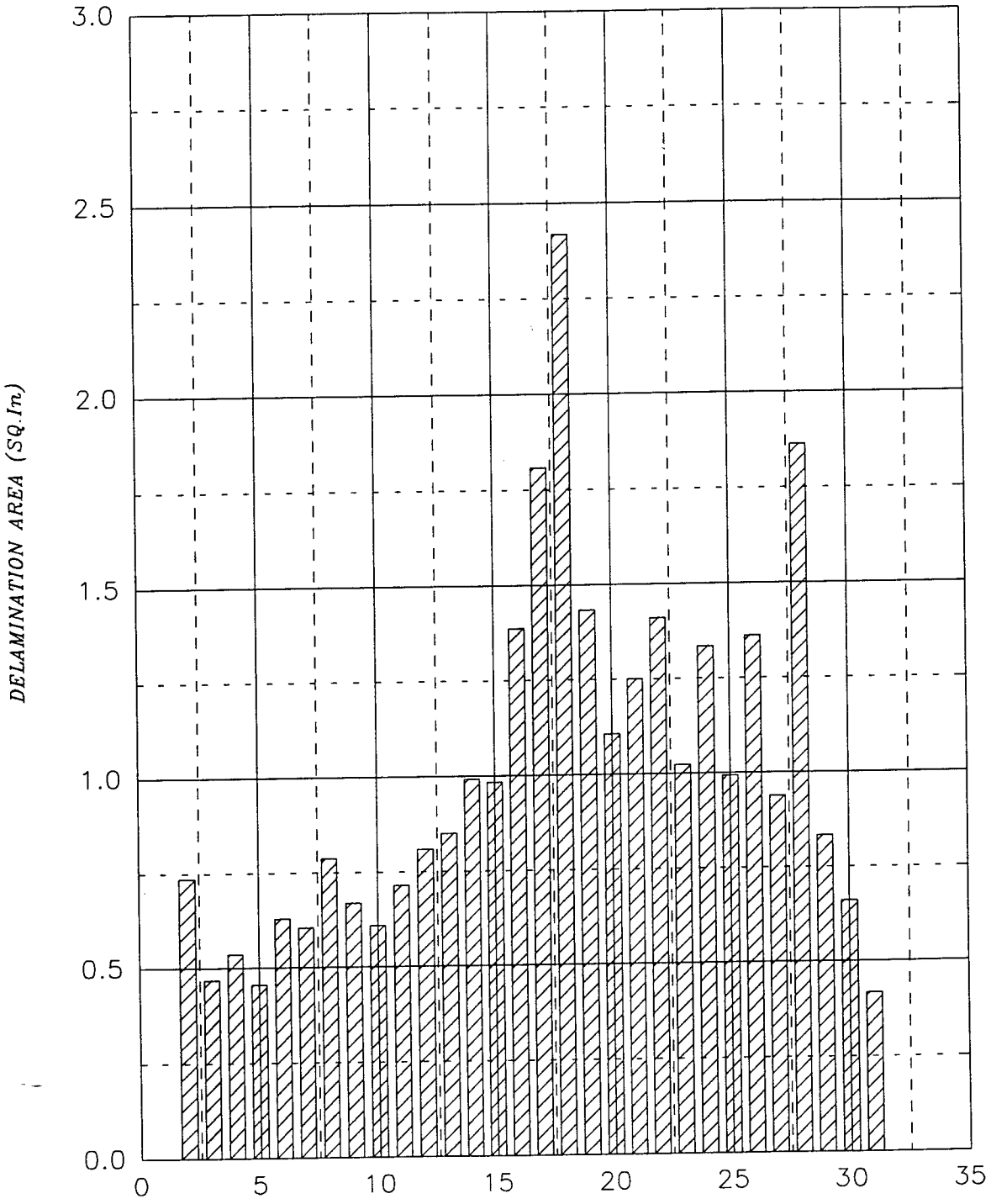
PANEL # A-39, VELOCITY 117.59 ft/sec
MISMATCH ANGLE (0/90)

DELAMINATION DAMAGE



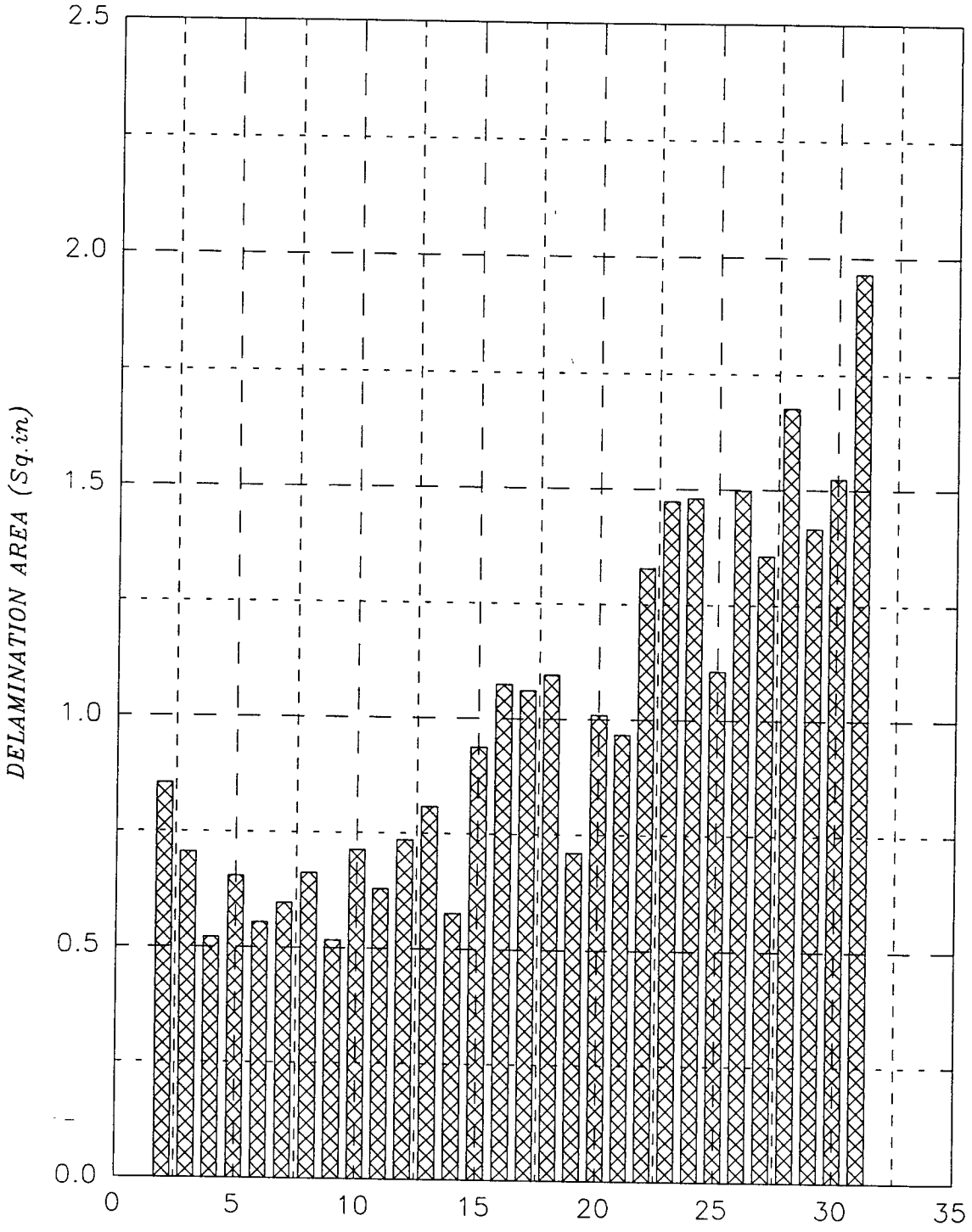
PANEL # A-26, VELOCITY 202 ft/sec
MISMATCH ANGLE (0/90)

DELAMINATION DAMAGE



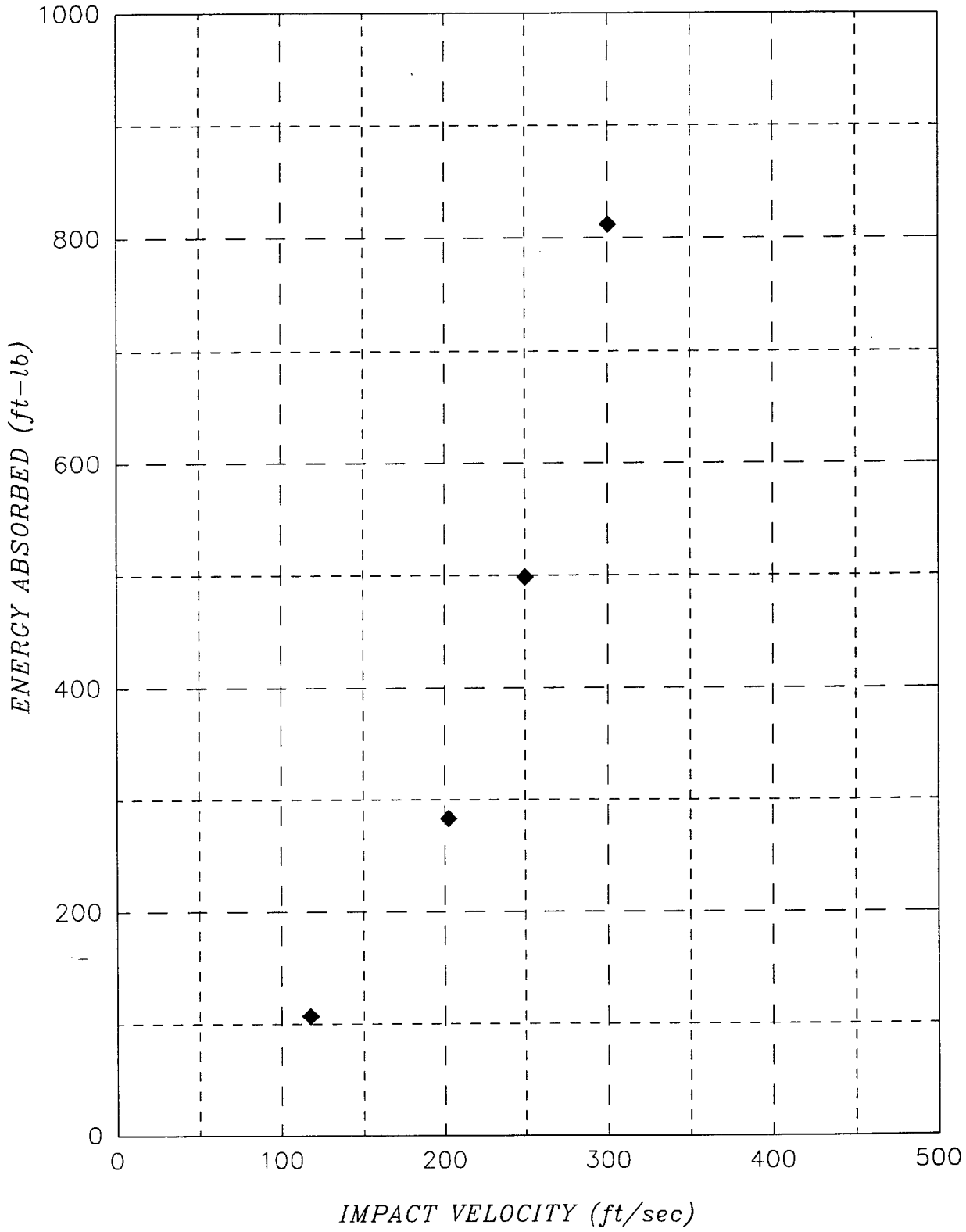
PANEL # A 42 , VELOCITY 250 ft/sec

DELAMINATION DAMAGE

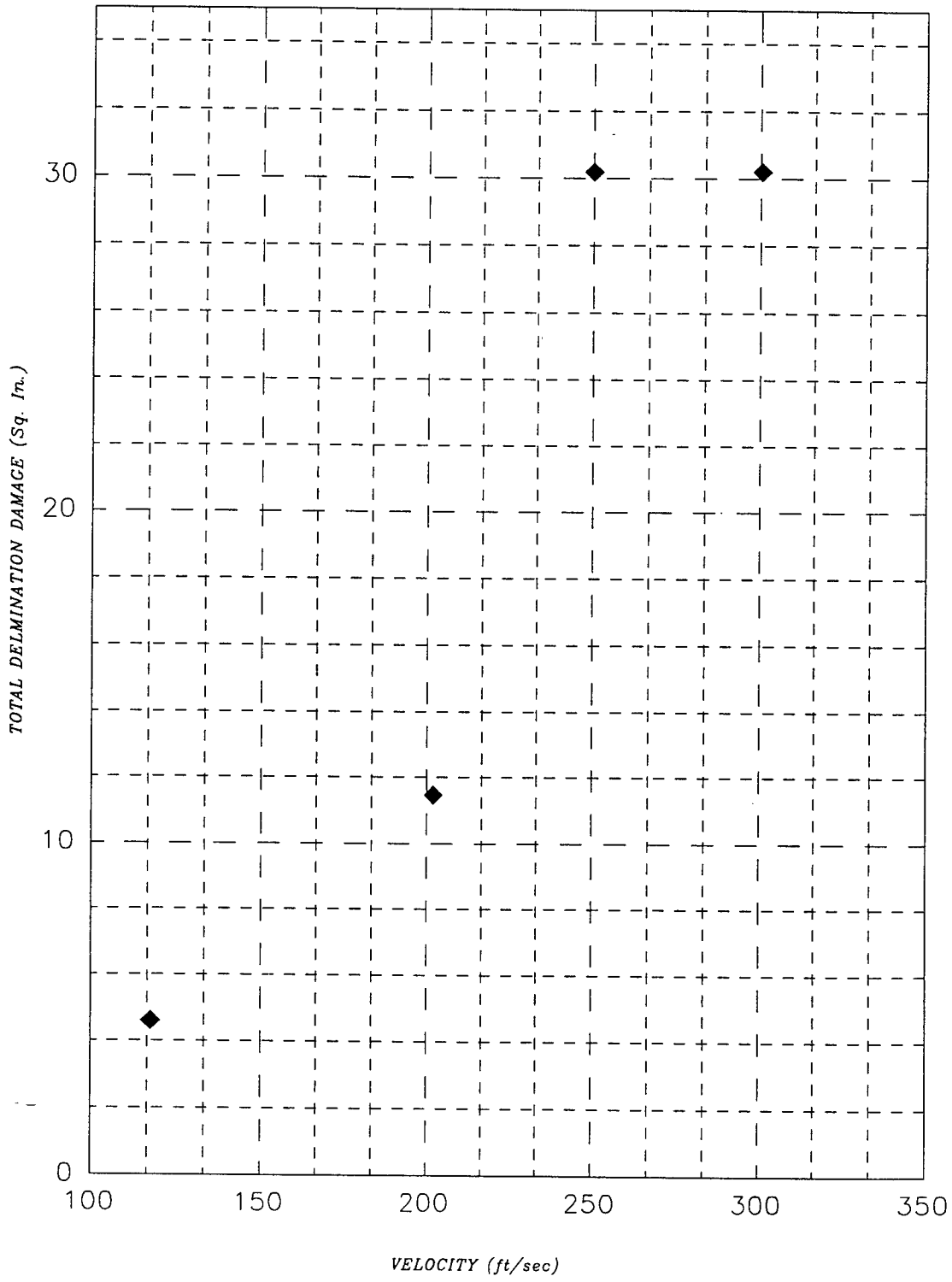


PANEL # A-18, VEOCITY 300.38 ft/sec

TOTAL ENERGY ABSORBED Vs IMPACT VELOCITY



TOTAOL DELAMINATION AREA Vs VELOCITY



LOW-VELOCITY IMPACT OF MOISTURE-CONDITIONED LAMINATED COMPOSITES

Rob Slater
Department of Mechanical, Industrial, and Nuclear Engineering

University of Cincinnati
Cincinnati OH 45221

Final Report for:
Graduate Student Research Program
Wright Laboratory

Sponsored by:
Air Force Office of Scientific Research
Bolling Air Force DC

and

Wright Laboratory

September 1994

LOW-VELOCITY IMPACT OF MOISTURE-CONDITIONED LAMINATED COMPOSITES

Rob Slater
Department of Mechanical, Industrial, and Nuclear Engineering
University of Cincinnati

Abstract

Composite laminates are frequently used in aircraft structures, because they offer high strength and stiffness at a considerable weight savings over metals. The design criteria for composites are different from those for metals. For metals, fatigue and fracture are the major considerations. Design of laminated composites requires consideration of foreign object damage, voids in the material, and propagation of delaminations. Composite laminates are very susceptible to damage from low-velocity impacts. These events may occur during flight operations, such as impact of runway debris, or during maintenance, such as tool drop. The impact frequently leaves only a slight indentation on the surface, but there may be significant internal damage, including matrix cracking, delaminations, and fiber breakage. For this reason this type of damage is often referred to as barely visible impact damage (BVID).

During its lifetime an aircraft, and its composite structures, will be exposed to widely varying atmospheric conditions. All composite materials are hydrophilic and will absorb atmospheric moisture. Research is necessary to determine the effect of moisture on composite laminates. A number of composite specimens were moisture-conditioned in a humidity chamber to 0.7% (by weight) moisture content, heated to 350° F, and then impacted in the laboratory. The impact energies were chosen to conform to the Air Force specifications for damage tolerance. Indentation depth was measured for each specimen. The damaged composite specimens will be subjected to non-destructive evaluation to determine the size of the delaminated areas and then tested to find the post-impact compression strength.

LOW-VELOCITY IMPACT OF MOISTURE-CONDITIONED LAMINATED COMPOSITES

Rob Slater

Introduction

Laminated composite materials have become increasingly popular in the design of high-performance aircraft. They offer high strength and stiffness at a significant weight savings over metals. The design of composites requires a new set of design criteria. For metals the prime considerations are fatigue and fracture. For composites issues such as foreign impact damage must be considered. Numerous researchers have attempted, through analysis and experiment, to determine the behavior of composites due to low-velocity impact and to predict the extent of damage due to a given impact event. Subsequently, models are proposed to predict the residual strength of the laminate and the propagation of damage under loading. Unfortunately this has turned out to be an extremely difficult task. There are many variables that must be considered in a low-velocity impact event and there are no accepted standards for testing. No reliable scaling laws exist to relate tests performed with differing parameters. Also, tests on laboratory coupons are hard to relate to actual built-up structures.

The behavior of composite materials subject to extreme environments was the area in which my summer research was concentrated. Aircraft, rotated through all parts of the world, will be exposed to atmospheric conditions varying from tropical heat and humidity to Arctic cold. Composite materials will absorb moisture from the air that causes a reduction in strength. Composites also suffer from reduced strength at elevated temperatures such as may be experienced near the engine exhausts. Moisture absorption or high temperature alone do not cause a dangerous loss of integrity of the composite structure. But together they exhibit a synergistic effect that needs to be quantified in order to design damage-resistant composite structures.

Methods

Testing for low-velocity impact characteristics of composites at elevated service temperatures and at in-service moisture levels was in progress when I arrived for my summer tour. Tests had already been completed for room temperature-dry and elevated temperature-dry composite specimens. There were two materials tested: IM7/5260 graphite-bismalieimide and AS4/PEEK carbon-thermoplastic. Both materials were tested at room temperature without moisture conditioning to gather baseline data for comparison to their behavior under more extreme conditions. The PEEK matrix does not absorb a significant amount of moisture from the atmosphere so it was tested in the 'dry' (unconditioned) state at 180° F, which approaches its maximum service temperature . The IM7/5260 will absorb moisture up to 2% of its weight and has a glass transition temperature of approximately 425° F. The hot-wet test conditions chosen were 350° F and 0.7% moisture content. These tests were to be performed on panels of five different nominal thicknesses: 9, 27, 48, 74, and 96 plies. Each ply is 0.055 inch thick. There were two lay-up sequences chosen to be tested. One was a relatively 'soft' laminate made up of approximately 10% 0° plies, 80% 45° plies, and 10% 90° plies. The second was a "harder" stacking sequence made up of 40% 0°, 50% 45°, and 10% 90° plies. In order to better match these percentages for the second lay-up the actual number of plies for the five thicknesses were 9, 26, 49, 74, and 96, slightly different than the nominal number of plies but not significantly affecting the overall thickness. For each thickness and lay-up there were four replicates for a total of 40 specimens to be impacted.

The Air Force standard for impact tolerance requires the designer to assume initial damage in the composite laminate. This damage is that which is caused by an impact rersulting in a 0.1 inch deep dent, up to an impact energy of 100 ft-lbf. For the thicker laminates (74 and 96 ply) the allowable impact will be governed by the 100 ft-lbf. impact energy limit i.e., the dent depth will be less than 0.1 inch. For the thinner laminates it is necessary to determine the proper impact energy to cause a 0.1 inch deep dent. For this reason there are an extra three replicates for the 9, 27, and 48 ply specimens with which trial indentation tests are performed. Finally there are 16-ply unidirectional specimens made of each material for finding the material properties and strength in tension, compression, and shear in both the fiber and transverse

directions, and panels of all five thicknesses that are not impacted for determining the undamaged compression strength.

The test equipment used for impacting is a Dynatup 5260 drop tester. This machine features an instrumented tup attached to a crosshead of variable weight, up to 100 lbf. The maximum available drop height is approximately four feet, giving an impact velocity of about 16 feet per second. For the tests it was desired to vary the impact energies by changing the crosshead weights and maintain a constant velocity. But the crosshead weight can only be set to a few discrete values so to effect changes in the impact energy it is necessary to change the drop height. Further, there is a minimum crosshead weight of approximately six lbf. The thinnest specimens would be extensively damaged by an impact with a six pound impactor dropped from four feet so the drop height must be reduced to provide a dent consistent with the standard.

As a result of these limitations, the goal of performing all the impact test at the same velocity (and thus eliminating this as a variable) could not be achieved. The other hurdle to overcome in performing the testing was the heating of the specimens to 350 F. Previous high temperature tests were performed on PEEK specimens at 180 °F. These were heated using a hot air gun that has a maximum temperature of 1000° F and a power rating of 1600 W. For the 350° F tests there was also available a convection-type industrial oven with a maximum temperature of 500° F and a heater of similar power rating. I attempted to make some preliminary calculations to determine how long it would take to heat specimens of varying number of plies to a reasonably uniform 350° F through the thickness. Since the plates are at least an order of magnitude wider than they are thick (even for the 96-ply specimens) they were modeled as infinite slabs, since there are straight-forward solutions available for transient conduction in infinite slabs. The fiber and matrix properties were to be smeared into an equivalent homogeneous under the assumption that the matrix properties dominate transverse heat transfer, as in a slab, and the additional heat transfer through the edges would serve to make the estimates conservative. Unfortunately there is little published heat transfer property data for composite materials, and telephone calls to the manufacturer were not fruitful. Without precise values for thermal conductivity and diffusivity of the materials it was not possible to make accurate predictions of the necessary heating times in the oven to reach a specified temperature. One important fact

was determined from this analysis: the temperature gradients through the thickness of the specimens would not be very great. This was important to know because the temperature could only be measured (with attached thermocouples) on the surface on the panel during heating. There were no thermocouples embedded inside the panels to guarantee the interior had reached the test temperature. In the absence of heat transfer coefficients to make good analytical predictions I performed some experiments on some panels left over from previous tests. These panels were not moisture-conditioned, but since the water adds less than 1% extra mass its effects were judged to be minimal.

The top priority during testing of the specimens was to minimize moisture loss during the heating and impacting because re-conditioning the specimens would be such a time-consuming process. Heating in the oven was preferred because it offered much better temperature control and uniform heating than a heat gun. It was believed that it would also be necessary to heat the fixture in which the composite specimens were to be clamped for impacting. The fixture is two metal plates, each with a 5 inch by 5 inch 'window' in the center, between which the panel to be tested is sandwiched. The top plate is aluminum and is approximately one-half inch thick, and the bottom plate is one inch thick steel. The edges of the panel to be tested (one inch wide on the sides; 2.5 inches on the ends) are in direct contact with the fixture and it serves as a relatively large heat sink, so it must be heated.

Thermocouples were attached to the surfaces of panels with heat-resistant tape and the panels were placed in a pre-heated oven. Temperature versus time was recorded for specimens representing the different thicknesses to be tested. The beads of the thermocouples were in contact with the surface of the panels, but there exists some uncertainty as to whether or not the indicated temperature accurately represents the surface temperature of the panel. The tape resists peeling and cracking at high temperatures but it is doubtful that it is a very effective insulator. The convection oven circulates hot air and the temperature sensed by the thermocouple bead is higher than the true surface temperature. When the panel is removed from the oven this phenomenon is evident as the temperature drops very rapidly at first , as the air temperature around the thermocouple bead drops, then slowly as the panel itself cools. Of course this indicates that the temperature indicated when the panel is removed from the oven is also inaccurate; it is lower than the actual surface temperature because the thermocouple bead is also exposed to room-

temperature air. However, it is believed that the magnitude of the error is less for this situation because the cool ambient air is not circulating as it is in the oven. Convective heat transfer is much less for free convection than it is for forced convection.

Time versus temperature charts were made for 9, 26, and 48-ply panels and also for the fixture. The fixture takes a much longer time to heat up (and cool down) than the thickest panel, so it was decided to heat the panel and fixture separately, with each reaching the necessary temperature at approximately the same time. The panel would be placed in the fixture and impacted immediately. It is necessary to heat both panel and fixture to a temperature higher than the test temperature to allow for the cooling which takes place in the 4 to 5 minute period between removing them from the oven and impacting.

The 9-ply specimens heated and cooled so quickly that it was impossible to heat them in the oven and run the test at the desired 350° F. The maximum oven temperature is 500° F, and even if heated to that temperature the panels would cool too much by the time they were placed in the test fixture and impacted. Further, exceeding the glass transition temperature of the IM7/5260 system, which is approximately 425° F, was to be avoided in order to preserve the material properties of the specimens. So it was decided to use an alternate method of heating the 9-ply panels. A heat gun, with air temperature adjustable up to 1000° F, was used. The specimen to be tested was placed in the pre-heated fixture, in order to minimize the fixture's effect as a heat sink, and then heated with the heat gun. The test temperature could be achieved in a few minutes, but extreme care had to be taken in order to heat the panel uniformly. A few panels blistered during heating. It is not known if this was due to local overheating at the point of the blister, or if the heating rate was too fast and vapor pressure built up inside the panel until the normal interlaminar strength was exceeded.

Once the heating schemes had been determined for all the specimens testing on the actual moisture-conditioned specimens began. These panels had been conditioned to 0.7% moisture (by weight) in a humidity chamber and sealed in aluminum foil bags to preserve the water content. The weight of several panels had been tracked during the conditioning process, which took up to 2 months for the 96-ply specimens. These specimens were called travelers and the weight data was used to estimate the moisture

content of other similar panels. All panels were first dried and then subjected to the same conditions in the humidity chamber so it was assumed panels of similar thickness and lay-up would absorb moisture at the same rate. In order to track the moisture content throughout the series of tests they were weighed on a precision balance.

The first stage of the impact testing was the trial indentation tests. The Air Force standard for impact damage tolerance states that the composite panel must withstand an impact which produces a 0.1 inch deep dent, up to a maximum impact energy of 100 ft-lbf. It is known from previous experience that 74-ply and thicker laminates are governed by the 100 ft-lbf limit, while the 9 and 27-ply specimens reach the 0.1 inch dent depth limit at impact energies significantly lower than that limit. The 48-ply specimens may be governed by either criterion depending on the particular material and stacking sequence. An added benefit of the trial indentation tests is that they provide a few extra specimens and hence the opportunity to work out any difficulties with the test setup before starting tests on the panels which are used to collect the final test data. They are used solely to find the correct impact energy and are not subjected to non-destructive investigation of damage area or compression after impact strength. To have extra panels was fortunate because several of the 9 and 27-ply trial indentation specimens blistered during heating with the heat gun. These specimens served as lessons in how fast the test panels could be safely heated, and only one (of eight) actual test specimen blistered.

For both lay-ups the 48-ply nominal thickness panels the impact energy was governed by the 100 ft-lbf limit; the dent depths did not exceed 0.1 inch. With the proper impact energies determined, impacting of the actual test specimens began. The first step in a test was to remove the specimen from its foil bag and weigh it on the balance. Then the panel was heated, either in the oven or by the heat gun. When the proper temperature was reached (higher than the test temperature of 350° F due to cooling between the end of the heating and the actual impacting) the specimen was placed in the drop tester and impacted. The panel was then removed from the drop tester and taken out of the test fixture which was placed immediately back in the oven. After the panel cooled enough to be handled with bare hands, it was weighed again to determine how much moisture was lost. All the moisture data was stored in a spreadsheet so the new moisture content was calculated automatically based on data from a similar traveler. Next the indentation depth was

determined using a dial gage. Finally the specimen was resealed in a new foil bag to await the next phase of the experiment.

When the impact tests were finished, the specimens were subjected to non-destructive investigation (NDI) to determine the damage area due to the impact. The particular method used was C-scan, which is an ultrasonic technique. Two tests were performed on each specimen to quantify the size of the delaminated area inside the panel. One was a through-transmission test, which quantifies damage by measuring the attenuation of the ultrasonic signal as it travels through the thickness of the specimen. For a composite laminate, there is little loss of signal intensity in the undamaged region, but negligible transmission through the damaged zone. Thus the delaminated area is very distinct on the results of the C-scan. The second test is a pulse-echo method which measures time of flight of the ultrasonic signal from the source, allowing the depth of the damage to be determined. A hard copy of the results of both tests on each panel were received after NDI and the damage area was measured using a planimeter.

After NDI, the specimens were again weighed with the precision balance and sealed in foil bags. The next, and final phase of the test program will be to determine the post-impact compressive strength of the damaged panels. This test will be performed by other technicians. There are also a series of undamaged moisture-conditioned panels, from the same batch of material as the panels which were impacted, which will be tested in compression to get baseline data on compression strength. Similarly, there are a number of unidirectional specimens which will be tested in order to find basic lamina properties. The tests which will be performed are 0° tension, 90° tension, 0° compression, 90° compression, and 45° shear.

Results and Conclusions

The experimental portion of this research program is still in progress. The tests that were performed under the Summer Graduate Student Research Program represent a small but significant element of a program which has been ongoing for more than two years and will continue next year. At this point there are no final results available to report. Some intermediate findings will be reported at the upcoming Air Force Aircraft Structural Integrity Program conference in San Antonio in December 1994. The data on dent depths and delaminated areas for moisture-conditioned panels will be compared to previously reported results for unconditioned panels impacted at room temperature in order to quantify the effect that hot, humid service conditions have on the impact tolerance of laminated composite aircraft structures.

X-RAY DIFFRACTION STUDY OF SILOXANE/CHOLESTEROL BASED LIQUID CRYSTALS

Edward Peter Socci
Research Assistant
Department of Materials Science & Engineering

University of Virginia
Thornton Hall
Charlottesville, VA 22903-2442

Final Report for:
Graduate Student Research Program
Wright Laboratory

Sponsored by:
Air Force Office of Scientific Research
Bolling Air Force Base, DC

and

Wright Laboratory

September 1994

X-RAY DIFFRACTION STUDY OF SILOXANE/CHOLESTEROL BASED LIQUID CRYSTALS

Edward Peter Socci
Research Assistant
Department of Materials Science & Engineering
University of Virginia

Abstract

Liquid crystalline materials exhibit a state of aggregation that is intermediate between the crystalline solid and the isotropic liquid. A series of liquid crystalline compounds based upon derivatives of cholesterol were studied by X-ray diffraction and molecular modeling. Some of these materials have been processed into ordered, optically clear films which are of potential use as matrices for optical devices. The smectic and chiral nematic phases of four liquid crystalline dimers were examined by X-ray diffraction. Two low energy conformations of these compounds, extended and folded, were examined by molecular mechanics calculations. Models for the packing of each of these molecules in the liquid crystalline phase are proposed.

X-RAY DIFFRACTION STUDY

OF SILOXANE/CHOLESTEROL BASED LIQUID CRYSTALS

Edward Peter Socci

Introduction

Recently, characterization of the liquid crystalline phases of cholesteryl ester substituted cyclosiloxanes has been completed [1,2,3,4,5,6,7,8,9]. This class of compounds exhibit both smectic and cholesteric phases. X-ray diffraction studies of these materials indicate the presence of two distinct types of packing of these molecules in the liquid crystalline phase. Type I packing is observed in materials in which the cholesterol moiety is attached to the cyclosiloxane "backbone" by a short spacer group. In this packing scheme the cholesteryl esters are partially interdigitated. Type II packing occurs in materials with longer spacer groups. Cholesteryl ester molecules are fully interdigitated in the Type II packing scheme. It has been suggested that the Type II structure is a more efficiently packed structure than Type I.

This class of liquid crystalline materials is of interest for use in non-linear optical applications [2]. Optically active chromophores have been covalently attached to the cyclosiloxane backbones (along with the cholesteryl ester substituents). Ordered, optically clear thin films can be produced from these materials. Chromophores can be aligned by an electric field placed across films heated above their glass transition temperatures. These aligned materials are quenched to room temperature, locking in the preferential orientation of the chromophores. Second harmonic generation signals from these films have been realized, however, temporal stability of the output signal is low due to the relaxation of the aligned chromophores. An increase in temporal stability is a long range goal of this research.

The molecular environment in which the aligned chromophore resides is important in determining temporal stability. The Type II structure, in which the cholesteryl esters are fully interdigitated, may provide an ordered matrix for the chromophores in which the rate of relaxation from an aligned to unaligned state is decreased due to the efficiently packed molecules (i.e. a reduction in regions of low molecular density). However, the Type II structure is favored in materials with long spacer groups that inherently have low glass transition temperatures. A low glass transition temperature is a characteristic which inevitably reduces the temporal stability of an aligned thin film. To

circumvent this problem, a new series of cholesterol/siloxane based liquid crystalline materials was synthesized [4]. These compounds are based upon linear backbones (rather than cyclic) and are lower in molecular weight than the cyclic compounds. It was hoped that *fully* interdigitated structures (as a result of fewer steric interactions between cholesterol moieties) would be formed from compounds that had *short* spacer groups attaching the ester to the siloxane backbone. In this way, materials with efficiently packed structures and relatively high glass transition temperatures would be produced. These materials could be substituted with non-linear optical chromophores and processed into optically clear thin films for useful applications. This research report describes the study of the structure(s) of four cholesteryl ester substituted linear dimers. Three of the dimers have a central siloxane core (differing in length). The fourth dimer has a central core composed of Si and C. The structure(s) of each compound were probed by elevated temperature X-ray diffraction.

Methods

Powdered samples were obtained from the Materials Directorate, Wright-Patterson Air Force Base. Samples were packed into 1 mm diameter glass capillaries. The capillaries were vibrated with a small file to facilitate the movement of the powdered sample into the capillary. The capillaries were heated above their clearing temperatures in a Mettler melting point determination device or an electric heater built into the X-ray apparatus. Pre-heating caused the sample to flow to the bottom of the capillary ensuring that a suitable amount of sample was in the path of the X-ray beam.

X-ray diffraction experiments were undertaken with Ni-filtered, Cu Kα radiation (λ_{ave}=1.5418 Å) from a Rigaku Rotaflex RU-300 rotating anode X-ray source operated at 40kV/300mA (12 kW). An evacuated Warhus camera was used to record the diffraction patterns. Pressure inside the Warhus camera was typically between 0.5 and 1.0 Torr. Samples were mounted in a modified sample holder and placed in a micro-heater located inside the Warhus camera. The temperature was monitored by an Omega model 149 temperature controller equipped with a type T thermocouple (copper/constantan). Samples were equilibrated for 10-60 minutes at the temperature of interest prior to obtaining the diffraction patterns. X-ray diffraction patterns were recorded on Kodak DEF-5 direct exposure flat X-ray film with a sample to film distance of 50 mm. Exposure times were typically 10 minutes. Films were

developed with standard techniques. Intensity *versus* 2θ plots were obtained by densitometry of the flat X-ray negatives by a Molecular Dynamics personal densitometer running ImageQuant software.

Materials Studied

The four liquid crystalline materials studied are illustrated in Figure 1. The thermal transitions of each compound are listed in Table 1. Each compound differs only in the chemical nature of the central region of the molecule. Cholesteryl-4-allyloxybenzoate (C4AB) mesogens are substituted at each end of the central moiety.

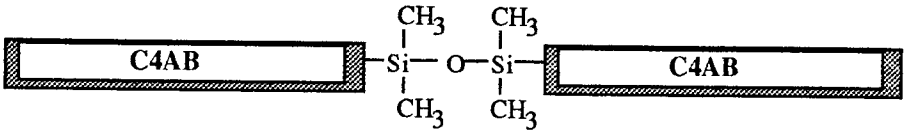
X-ray Diffraction from the Liquid Crystalline Phase

Smectic Phase

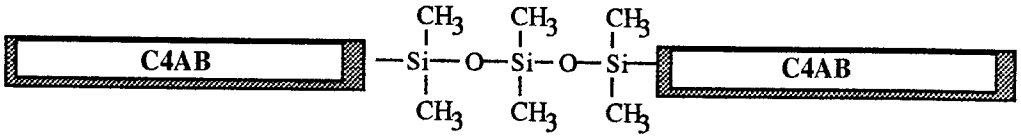
In general, a smectic phase consists of layers of molecules that are on average perpendicular to the plane of the layer [10]. The X-ray diffraction pattern of such an assembly generally consists of one or two Bragg reflections due to the layered structure, and a diffuse wide angle reflection from the average intermolecular spacing of molecules within a layer [10].

Nematic Phase

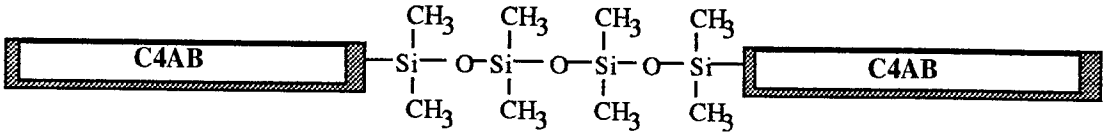
The molecules in a nematic or chiral nematic phase have only short-range orientational order. Information from X-ray diffraction patterns of these materials is therefore limited [10]. In most cases a small angle reflection which corresponds approximately to the length of the molecule is observed. Smectic-like fluctuations often occur, resulting in a pseudo-layered structure. This can also give rise to a small angle reflection analogous to the smectic phase Bragg peak. A diffuse ring due to the average lateral intermolecular spacing of molecules is observed at wider angles.



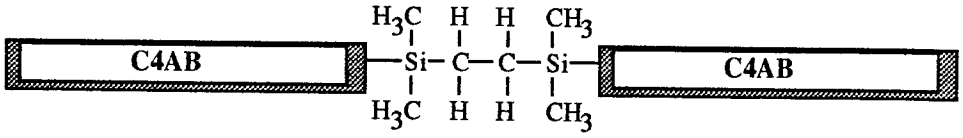
H48



H39



H115



H116

Figure 1: Liquid crystalline compounds examined.

Table 1. Thermal transitions of cholesterol/siloxane based compounds [4].

Compound	Thermal Transitions /°C
H48	k 41 S_A 212 i
H39	k 80 S_A 225 i
H115	k 32 S_C* 58 S_A 204 i
H116	k 192 S_A 220 i

k=crystalline, S_A=smectic A, S_C*=chiral smectic C, n*=chiral nematic, i=isotropic

Results and Discussion

This section describe the results of the X-ray diffraction study of the liquid crystalline compounds illustrated in Figure 1. Possible models for the structure of the liquid crystalline phases are given based upon two proposed conformations. Molecular mechanics calculations are undertaken to examine the energy of each conformation.

H48

Compound H48 exhibits a S_A phase. Two diffraction patterns were obtained from this sample: (1) an elevated temperature pattern at 80° C and (2) a room temperature pattern. The sample was first heated above the clearing temperature (212° C) into the isotropic liquid phase, cooled to 80° C (into the S_A phase) and equilibrated for 60 minutes at 80° C prior to recording a diffraction pattern. Two reflections are observed: (1) a small angle reflection corresponding to a d-spacing of 31.0 Å and (2): a wide angle reflection corresponding to an average spacing of 5.42 Å. No additional reflections were observed in this compound.

The room temperature diffraction pattern of H48 was also obtained. This pattern was taken after the sample was cleared and then cooled to 22° C at a cooling rate of approximately 3°/min. The two observed reflections (31.5 Å and 5.39 Å) correspond to the d-spacings observed in the diffraction pattern taken at 80° C. This indicates that the structure of the S_A phase was retained upon cooling to room temperature.

H39

Compound H39 also exhibits a S_A liquid crystalline phase. H39 was first heated above the clearing temperature (225° C) and then cooled to 159° C (S_A phase). The sample was equilibrated at 159° C for 60 minutes prior to recording the diffraction pattern. The observed small angle reflection corresponds to a d-spacing of 32.5 Å. The wide angle reflection corresponds to a d-spacing of 5.29 Å.

The room temperature diffraction pattern of H39 is similar to the diffraction pattern taken at 159° C. The small angle reflection corresponds to a d-spacing of 33.2 Å. The wide angle reflection corresponds to a d-spacing of 5.19 Å. These results indicate that the S_A structure present at 159° C is retained at room temperature.

H115

H115 exhibits a chiral smectic C (S_C*) and S_A phase. X-ray diffraction experiments were undertaken as a function of temperature in order to probe the structural transition on cooling from the S_A to the S_C*. A sample of H115 was heated above the clearing temperature (204° C) and cooled into the S_A phase. The first diffraction pattern

was recorded at 184° C. A small angle reflection is observed which corresponds to d-spacing of 33.9 Å. The wide angle reflection corresponds to a d-spacing of 5.69 Å. Additional diffraction patterns were made as a function of temperature to examine the S_A to S_C* phase transition. The sample was cooled to the desired temperature, equilibrated for 10 minutes, and exposed to X-rays for 10 minutes. The experiment temperature and wide and small angle d-spacings are listed in Table 2.

Table 2. Experimental data from H115†.

Temperature /°C	Small Angle d-Spacing /Å	Wide Angle d-Spacing /Å
184	33.9(3)	5.69(4)
151	33.6(3)	5.68(4)
125	33.6(3)	5.54(4)
100	34.0(3)	5.48(4)
91	33.7(3)	5.46(4)
81	33.9(3)	5.40(4)
71	34.0(3)	5.27(4)
65	33.7(3)	5.38(4)
60	33.7(3)	5.35(4)
55	32.9(2)	5.29(4)
50	32.6(2)	5.34(4)
45	32.6(2)	5.29(4)
40	32.1(2)	5.29(4)

†The number in parentheses is the standard deviation in the last digit.

The variation of the small angle spacing as a function of temperature is illustrated in Figure 2. Error bars of 0.75% of the measured d-spacing are a result of multiple measurements of the same reflection. The S_A to S_C* transition is observed at approximately 58° C, which is equivalent to the transition temperature observed in D.S.C. measurements. As the S_A to S_C* transition is approached the d-spacing decreases. This is a result of a structural change within the lamellae, as the molecular orientation changes from a non-tilted to a tilted structure. The relatively gradual change of d-spacing as a function of temperature has been observed in other S_C-S_A transitions [5]. The molecular tilt angle within lamellae of the S_C* phase at 40° C was calculated to be 19°. This value was calculated assuming an extended length of the molecule to be 34.0 Å. A variation in the wide angle d-spacing as a function of temperature was also observed in this compound (Figure 3). As the temperature is decreased, the average lateral spacing of molecules also decreases.

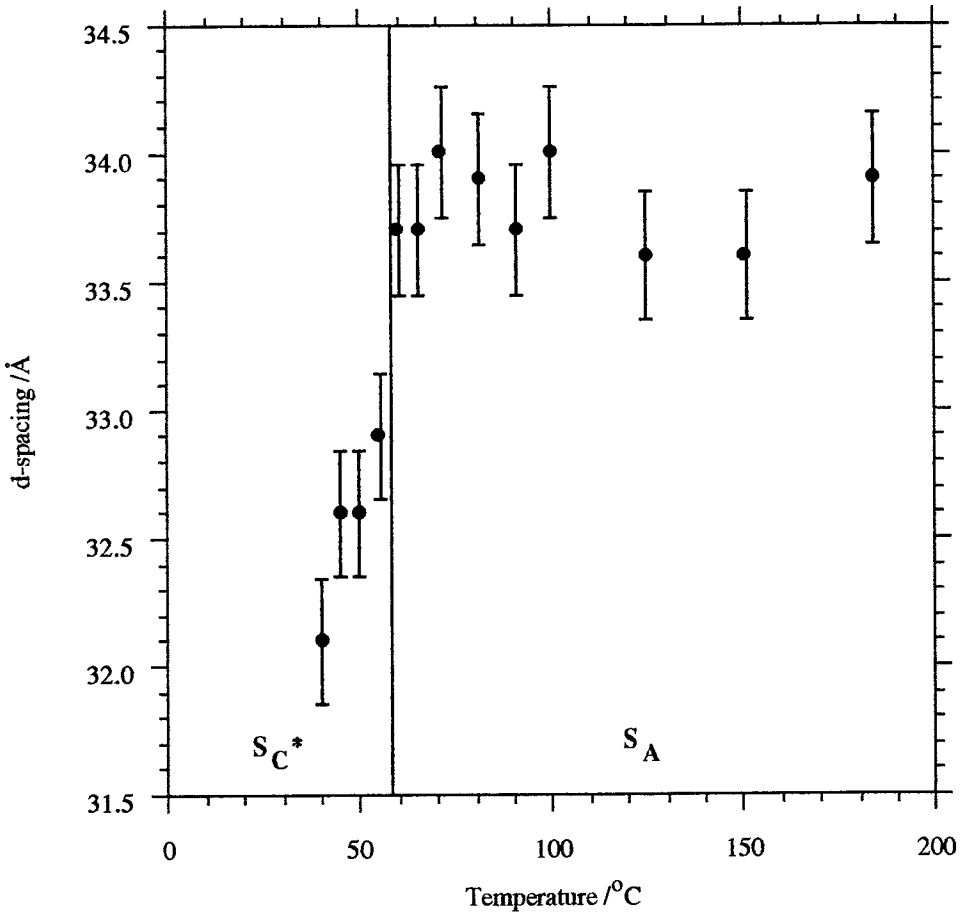


Figure 2: A plot of the small angle d-spacing as a function of temperature. As the S_A -> S_C* transition temperature is approached, the d-spacing decreases. The calculated molecular tilt angle within the lamellae of the S_C* phase is approximately 19°. Error bars are from multiple measurements.

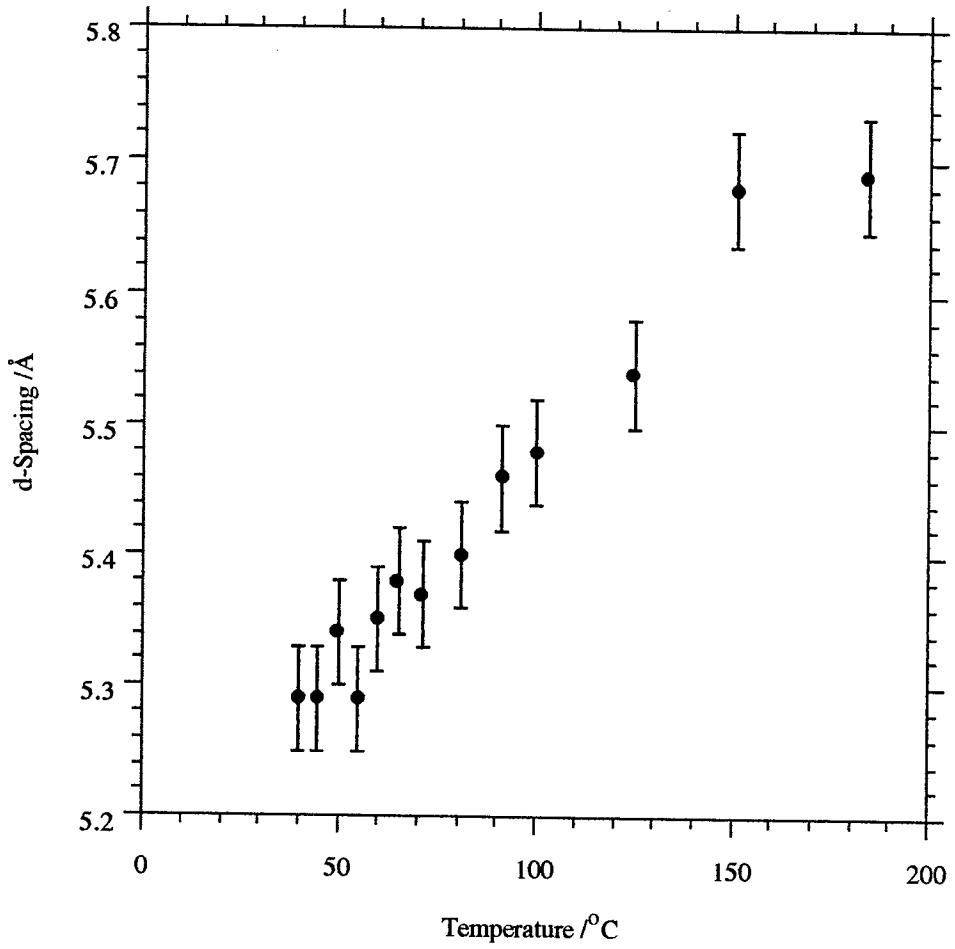


Figure 3: A plot of the wide angle d-spacing as a function of temperature for H115. A decrease in the intermolecular separation is observed as the temperature is reduced. Error bars are from multiple measurements.

H116

H116 exhibits a S_A phase. Previous polarizing optical microscopy and differential scanning calorimetry results [4] also indicated the possible presence of a S_B phase between 172° C-192° C. The detection of a S_B phase by polarizing optical microscopy is difficult. Therefore the presence of the S_B phase was examined by X-ray diffraction.

A sample of H116 was heated above the clearing temperature (220° C) and cooled into the S_A phase. The sample was equilibrated at 205° C prior to recording a diffraction pattern. Six additional diffraction patterns were obtained at lower temperatures (with an equilibration of 10 minutes at each temperature). The observed small angle d-spacing was approximately constant (30 Å) at each temperature. A plot of the small angle d-spacing versus temperature is given in Figure 4. An increase in the wide angle d-spacing as a function of increasing temperature was observed in H116. A plot of the wide angle d-spacing versus temperature is given in Figure 5.

The presence of a S_B phase could not be verified with X-ray diffraction. The wide angle reflection should sharpen as a result of the regular lateral spacing of molecules within lamellae in a S_B phase [10]. No such sharpening was observed. Upon further analysis of the differential scanning calorimetry and polarizing optical microscopy data the S_B phase was determined to be a second crystalline form of H116.

The observed diffraction patterns from each of the compounds studied have been used to develop models for the structure of the liquid crystalline phase of these molecules . The calculated length of each compound in two low energy conformations was compared with the observed d-spacing of the small angle reflection.

Two low energy geometries, referred to as the extended and folded conformations, were examined. The SYBYL 6.0 molecular modeling program [11] was used to construct and energy minimize (by steepest descents and Powell methods) extended and folded conformations from each of the four compounds studied. The relative energies of each of the conformations was compared. In each case the potential energy of the *folded* conformation was lower than that of the extended. The van der Waals energy was significantly lower for the folded conformations. Further, the bonded atom energy (i.e., bond length deformation energy, bond angle deformation energy, etc.) was lower in the folded conformation in all compounds but H116. Computational data are given in Table 3.

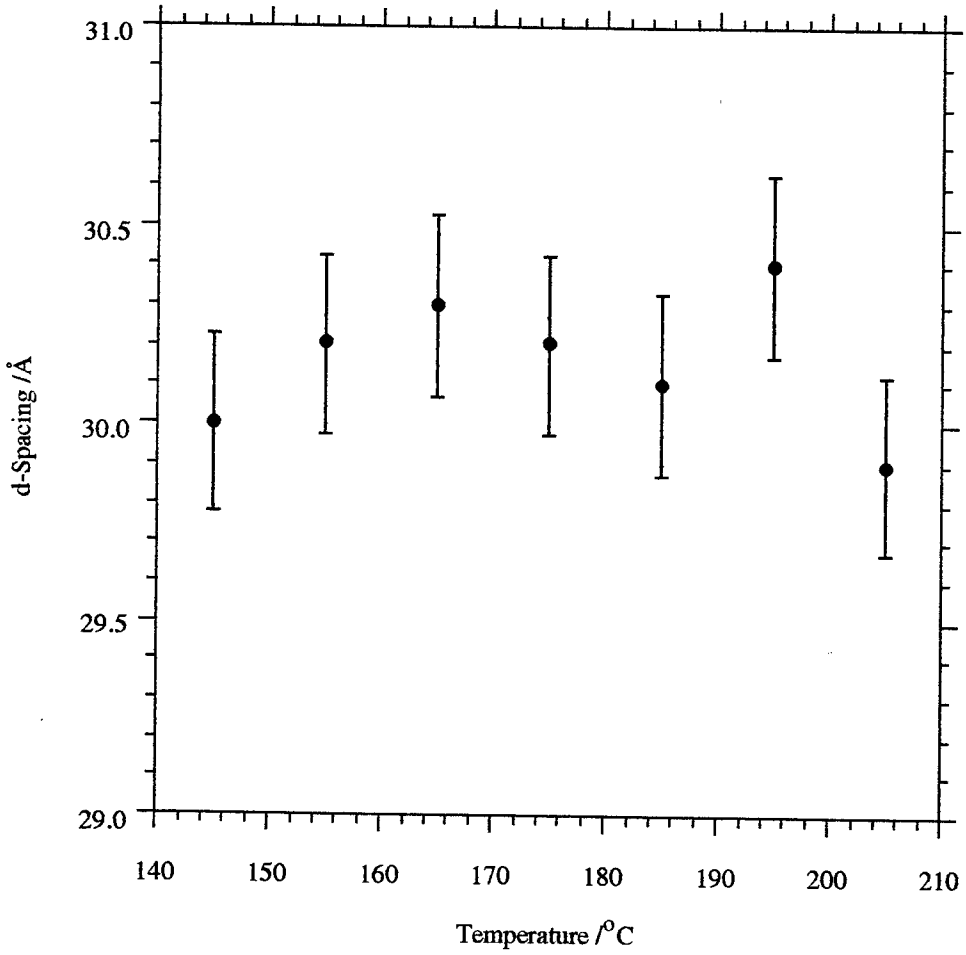


Figure 4: A plot of the small angle d-spacing as a function of temperature for H116.

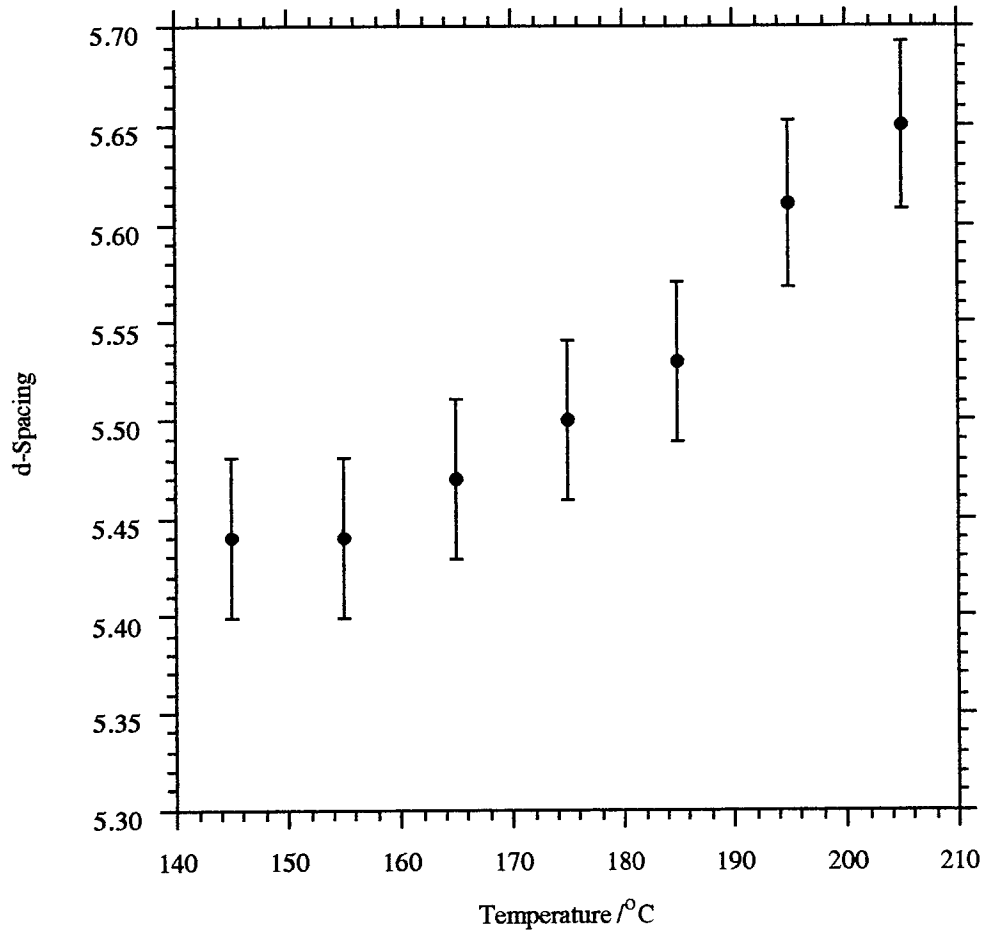


Figure 5: A plot of the wide angle d-spacing as a function of temperature for H116. An decrease in the intermolecular separation is observed as the temperature is decreased.

Table 3. Energies of extended and folded conformations of siloxane-based dimers.

Compound	Conformation	Bonded atom Energy /kcal/mol	van der Waals Energy /kcal/mol	Total Energy /kcal/mol
H48	Extended	70.9	-5.2	65.7
H48	Folded	69.5	-17.8	51.7
H39	Extended	73.4	-6.8	66.6
H39	Folded	71.4	-16.4	55.0
H115	Extended	69.6	-11.4	58.2
H115	Folded	64.7	-21.2	43.5
H116	Extended	72.9	-2.7	70.2
H116	Folded	76.4	-10.5	65.9

Packing schemes based upon these conformations (extended and folded) are illustrated in Figures 6-7. The repeat distance in the two packing schemes are compared to the experimentally observed d-spacings. The observed d-spacings from the siloxane dimers correspond closely to the calculated length of the C4AB unit and the siloxane backbone. Listed in Table 4 are the observed small angle spacings and the calculated lengths of the cholesteryl unit plus the siloxane backbone. The calculated lengths of the extended conformations was an average of all possible end-to-end lengths between terminal H atoms. The calculated lengths of the folded conformations was an average of the end-to-end lengths between the terminal H atom of the C4AB units and the center-most H atoms in the linear backbone. Similar analyses have been made in other siloxane-based liquid crystalline systems [1,3,5,12].

Table 4. Calculated lengths for extended and folded conformations and observed layer thickness.

Compound	$d_{calculated}$ / Å Extended	$d_{calculated}$ / Å Folded	$d_{observed}$ / Å
H48	32	32	30
H39	34	30	33
H115	34	32	34
H116	32	30	30

In each compound there is good agreement between the measured d-spacing and the calculated length of the C4AB and siloxane backbone. A distinction between an extended and a folded conformation cannot be made based upon the single reflection (due to layers) in the X-ray diffraction pattern of these materials.

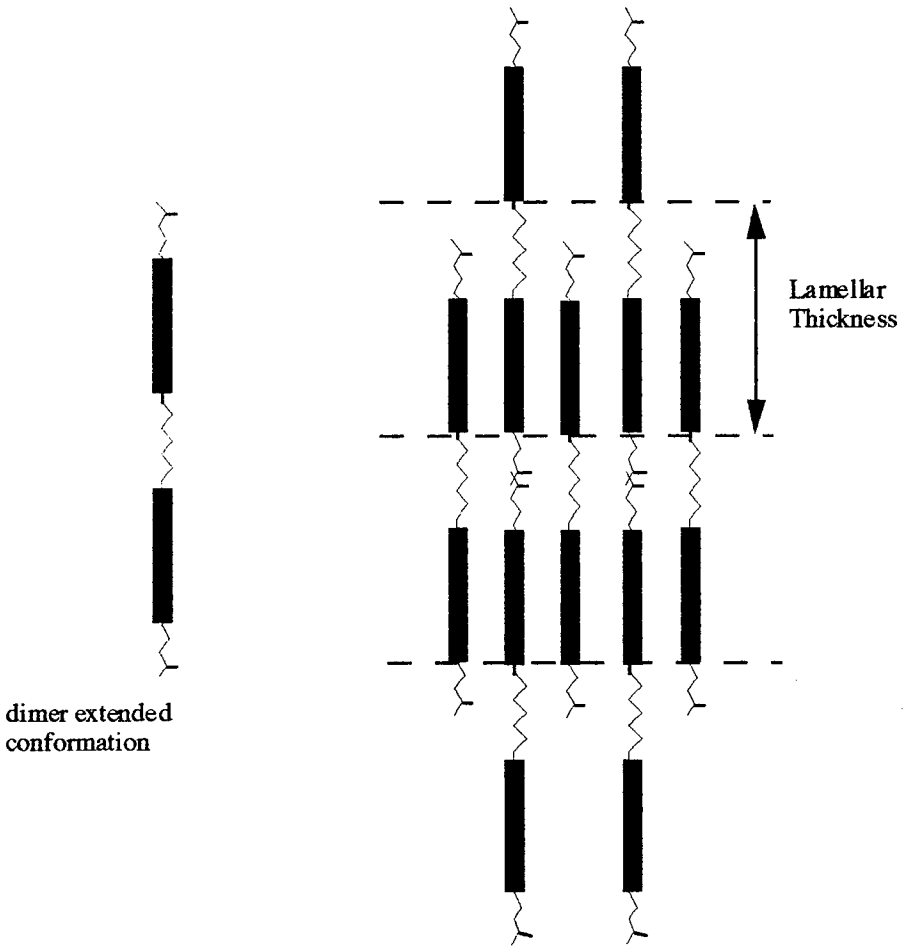


Figure 6: Model of the S_A phase of extended siloxane based dimers. The molecules are interdigitated, consistent with the observed small angle X-ray reflection.

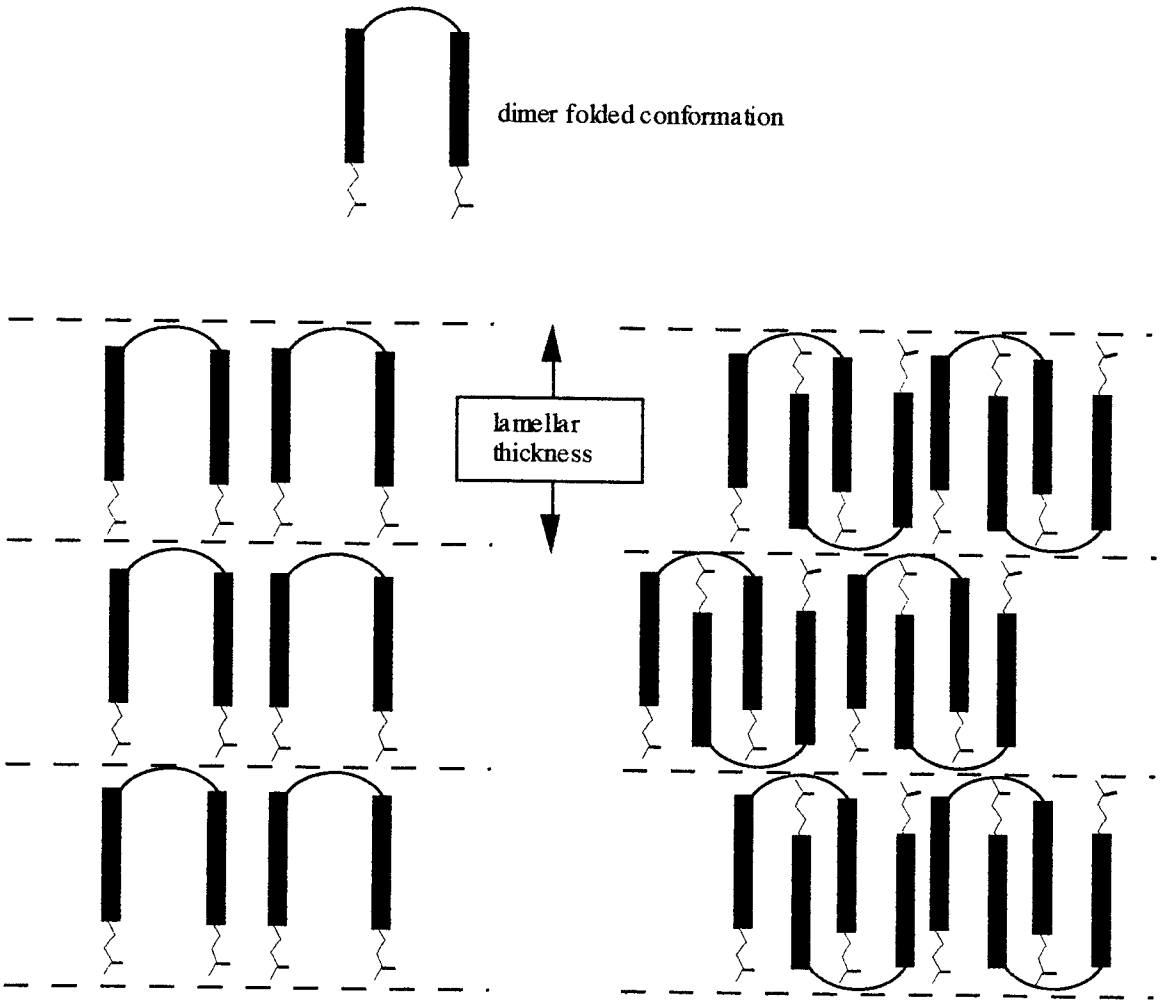


Figure 7: Models of the S_A phase of folded siloxane-based dimers. The molecules are packed in two possible arrangements.

Conclusions

The structures of the liquid crystalline phases of four liquid crystalline dimers were studied by X-ray diffraction. Molecules are interdigitated (Type II packing) and arranged in layers. The molecules exhibited no observable Type I packing. The width of a layer is approximately equal to the length of the linear core and one cholesteryl ester. The lowest energy conformation of a dimer is folded. Two possible models for the packing of the molecules were given based upon extended and folded conformations. However based upon the limited data in the X-ray diffraction patterns, the conformation of the molecule cannot be absolutely ascertained.

References

1. Bunning, T. J., Ph.D. Dissertation (1992) University of Connecticut.

2. Bunning, T. J., Klei, H. E., Samulski, E. T., Crane, R. L., Linville, R. J., *Liquid Crystals* (1992), **10**, 445.

3. Bunning, T. J., Klei, H. E., Samulski, E. T., Adams, W. W., Crane, R. L., *Mol. Cryst. Liq. Cryst.* (1993) **231**, 163.

4. Gresham, K. D., McHugh, C. M., Bunning, T. J., Klei, H. E., Samulski, E. T., Crane, R. L., *Am. Chem. Soc., Div. Polym.Chem., Polym. Prepr.* (1993), **34**, 594.

5. Bunning, T. J., Campbell, A., Adams, W. W., Socci, E. P., Farmer, B. L., manuscript in preparation.

6. Pachter, R. , Bunning, T. J., Adams, W. W., *Comp. Polym. Sci.* (1991) **1**, 179.

7. Socci, E. P., Farmer, B. L., Bunning, T. J., Pachter, R., Adams, W. W., *Liquid Crystals* (1993), **6**, 811.

8. Pachter, R., Bunning, T. J., Crane, R. L., Adams,. W. W., Socci, E. P., Farmer, B. L., *Makromol. Chem., Theory and Simul.* (1993), **2**, 337.

9. Socci, E. P., Farmer, B. L., Bunning, T. J., Pachter, R., Adams, W. W., *U. S. Air Force Technical Report #WL-TR-91-4137* (1992).

10. Davidson, P., Levelut, A. M., *Liquid Crystals* (1992), **2**, 469.

11. SYBYL program and manual, version 6.0.1., Tripos Associates (1991).

12. Kreuzer, F. H., Maurer, R., Spes, P., *Makromol. Chem., Macromol. Symp.* (1991), **50**, 215.

ANNEALED FUZZY CONTROL FOR A SELF-TUNING PIEZOELECTRIC VIBRATION ABSORBER

Edward A. Thompson
Doctoral Student
Department of Aerospace Engineering
& Engineering Mechanics

University of Cincinnati
Cincinnati, OH 45221-0070

Final Report for:
Graduate Student Research Program
Wright Laboratory

Sponsored by:
Air Force Office of Scientific Research
Bolling Air Force Base, DC

and

Wright Laboratory

August 1994

ANNEALED FUZZY CONTROL FOR A SELF-TUNING PIEZOELECTRIC VIBRATION ABSORBER

Edward A. Thompson
Doctoral Student
Department of Aerospace Engineering
& Engineering Mechanics
University of Cincinnati

Abstract

Two annealed fuzzy controllers for a self-tuning piezoelectric vibration absorber are presented. Similar to a mechanical damped vibration absorber, the piezoelectric absorber must be tuned to a particular mode of vibration. A self-tuning piezoelectric absorber must be able to find and track that mode if it varies in frequency due to changes in system parameters or in the environment. The controllers presented are experimentally demonstrated on a cantilevered beam. The experiments include an examination of the controllers' performance during an abrupt change in system parameters. Both controllers are able to find and track a particular mode faster and more accurately than fixed frequency increment controllers. Also, the annealed fuzzy controllers exhibit a dramatic decrease in oscillatory behavior after the mode is found. Once tuned, reductions of up to 18 dB are observed in the magnitude of the system/disturbance frequency response function. The absorber is shown to remove approximately 80% of the vibration energy from the system.

ANNEALED FUZZY CONTROL FOR A SELF-TUNING PIEZOELECTRIC VIBRATION ABSORBER

Edward A. Thompson

Introduction

Piezoelectric materials have the unique ability to produce an electrical voltage when strained and strain when an electrical voltage is applied. Thus, these materials transform electrical energy into mechanical energy and vice versa. Also, these materials can be used as both sensors and actuators in a wide variety of applications. In recent years, researchers have explored the potential of piezoelectric devices for structural vibration suppression. Examples of these may be found in Hagood and Crawley {3}, Hagood and von Flotow {4}, and Hollkamp and Starchville {5}. Vibration absorbers using piezoelectric material are constructed by creating an LRC electrical network. Because the piezoelectric has associated with it an inherent capacitance, all that is required to form the circuit is the connection of a simple inductor-resistor network. By transforming electrical energy into mechanical energy and vice versa, the electrical mode of the absorber becomes a tunable, mechanical mode of the system. When properly tuned to a particular mode of vibration, the resulting LRC network produces a damped electrical resonance which absorbs energy from the structure.

A self-tuning absorber is able to find and track a particular structural vibration mode. These modes may vary in frequency due to abrupt or gradual changes in the structure. These modes may also drift due to surrounding environmental changes in temperature and pressure. In the latter case, a self-tuning piezoelectric absorber would be a more effective absorber than the traditional viscoelastic treatment which is designed for only small temperature/pressure ranges.

In this paper, Hollkamp's self-tuning piezoelectric vibration absorber is presented as well as the development of a new fuzzy logic control algorithm called *annealed fuzzy control.* Finally, the absorber implementing annealed fuzzy control is demonstrated experimentally on a cantilevered beam. Its performance is then compared to Hollkamp's fixed frequency increment controllers.

Hollkamp's Self-Tuning Piezoelectric Absorber

Hollkamp explains that the design of a vibration absorber is straightforward if the frequency of the structural vibration mode is known. Optimal values of resistance and inductance can be determined for tuning the absorber. Figure 1 illustrates the modal suppression by an optimally tuned absorber as compared to a baseline mistuned structure. For near optimal values of the resistance and inductance, the modal suppression is not flat as will be seen later. If the frequency is not known, however, an adaptive control scheme must be utilized to tune the electrical resonance (i.e. by adjusting the shunt inductance and resistance).

In constructing such an absorber, Hollkamp uses Chen's {2} two operational amplifiers, grounded design for a synthetic inductor. Figure 2 displays the schematic for this design. The effective inductance is linearly proportional to the value of an adjustable resistor. As seen in the figure, a motorized potentiometer is used for the

adjustable resistance. There is an equivalent resistance associated with the design in Figure 2 due to losses in the capacitor. Unfortunately, this resistance may be larger than the optimal design resistance. For more information on the design of the piezoelectric absorber, consult Hollkamp {5} and Chen {2}.

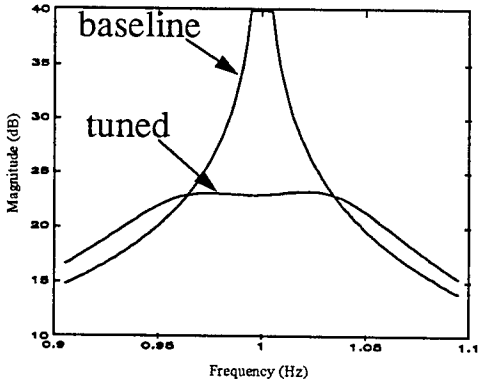


Figure 1. Modal suppression by an optimally tuned absorber.

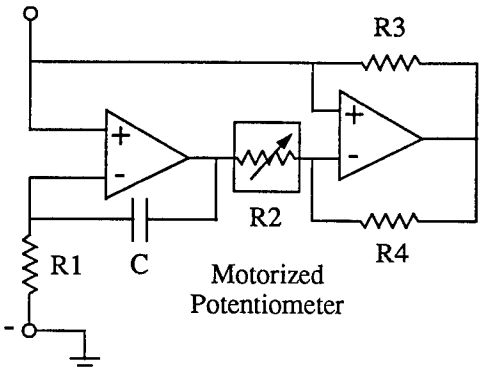


Figure 2. A two-operational amplifier design for a synthetic inductor.

In order for the absorber to find and track a particular mode of vibration, an adaptive control scheme must be implemented. Accordingly, an appropriate performance criterion must be selected. The obvious choice is to minimize the RMS of the structure considered. However, this is only valid if the magnitude of the disturbance is consistent. An alternate approach which eliminates the need for a consistent disturbance is taken by Smith, Maly, and Johnson {6} in their design of a mechanical absorber. They selected as the performance criterion to maximize the ratio of the RMS response of the absorber to the RMS response of the structure. Figure 3 shows an analytical prediction of both the RMS ratio of the absorber to the structure and the RMS response of the structure as the tuning ratio (absorber frequency/structure frequency) varies. As seen, the RMS ratio must be maximized or the RMS of the structure must be minimized to tune the absorber. Hollkamp developed a simple gradient control law based on the RMS ratio performance criterion. It may be stated as: if the estimation of the slope of the RMS ratio is positive, increase the absorber frequency, otherwise decrease it by a set amount.

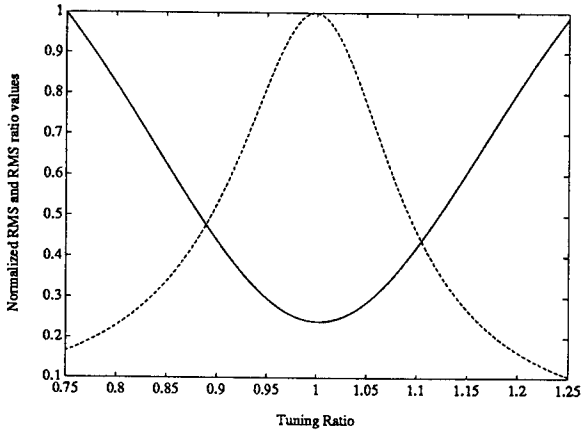


Figure 3. RMS response of the system (solid) and the ratio of the absorber RMS response to the system RMS response (dashed).

Hollkamp published experimental results for a variety of set/fixed controllers. These include both coarse and fine increments as well as a combination of the two. In all cases, the absorber finds and tracks the mode of vibration during abrupt system changes. However, once the absorber finds the correct frequency, it exhibits a large amount of oscillatory behavior about that frequency. Clearly, smaller fixed increments are needed to reduce the amount of dither about the tuned frequency. The combination of coarse and fine increments and the need for smaller increments to reduce the amount of dither motivate the current investigation of a fuzzy logic controller for this problem.

Fuzzy Logic Control

The first step in developing a fuzzy controller is to determine the main control parameters of the system to be controlled. These parameters are often the states of the system and in fuzzy terms are called *linguistic variables*. For the present problem, the structure/system response, the absorber response, the ratio of the two, etc. may be considered as possible choices for the linguistic variables. The next step is to determine a term set which is at the right level of granularity for describing each linguistic variable {1}. An example of a term set is describing the linguistic variable X as being {small, medium, large}. For increased granularity, one might use the *linguistic values* {very small, small, medium, large, very large}. Again, it is important that the right level of granularity be used to describe the linguistic variables. A three-term set may not be sufficient for the proper control of the system. Intermediate linguistic values may be needed to allow more time for the fuzzy controller to correctly respond to system changes.

The process of encoding the linguistic variables into linguistic values is called *fuzzification*. Essential to the success of fuzzy logic is that the linguistic values overlap. For example, in a three-term set, it must be possible for a linguistic variable X to be both small and medium or both medium and large. Overlapping is more easily seen when examining the *membership functions* for the linguistic values. A popular rule of thumb is to have two membership functions overlap by 25 percent. Figure 4 shows a three-term set and how it is possible for a linguistic variable X to be a member of Medium to some degree and also be a member of Large to some degree.

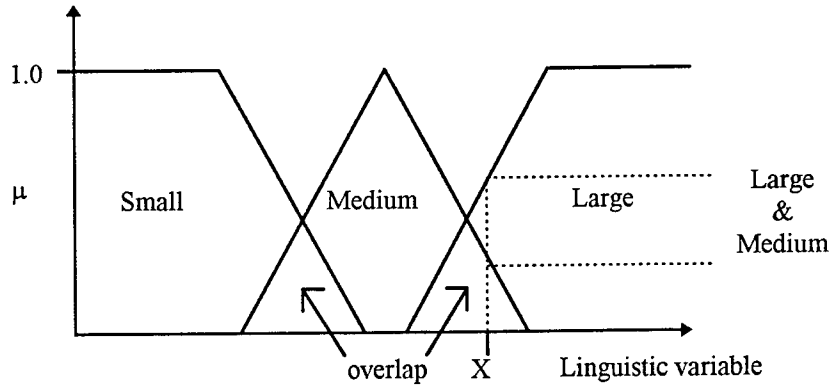


Figure 4. An example of a three-term set and corresponding membership functions.

Fuzzy logic control is a rule-based technology in which the rules are usually written down by human expert operators. A fuzzy control rule may take the form

IF X is Big AND Y is Small THEN Force is Medium. (1)

The above form of a fuzzy rule is particularly easy for human expert operators to express the control knowledge they use to control a system. Look-up tables are often constructed for rules in this form.

Because membership functions overlap, it is possible for more than one rule to fire. The process that determines what control action should be taken when several rules fire is referred to as *conflict resolution.* Consider the rules:

RULE 1: IF X is A_1 AND Y is B_1 THEN Z is C_1 (2)

RULE 2: IF X is A_2 AND Y is B_2 THEN Z is C_2.

Each rule recognizes a state of the system and then prescribes an output action. If the sensor readings for the fuzzy variables X and Y are x_0 and y_0, then the degree to which each fuzzy variable belongs to its corresponding fuzzy value for Rule 1 is $\mu_{A_1}(x_0)$ and $\mu_{B_1}(y_0)$. Similarly, for Rule 2 there are $\mu_{A_2}(x_0)$ and $\mu_{B_2}(y_0)$. These numbers are commonly called *truth values.* Only the minimum of the truth values is used to compute the corresponding output action for each rule. The *strength* of Rule 1 and Rule 2 may be calculated by:

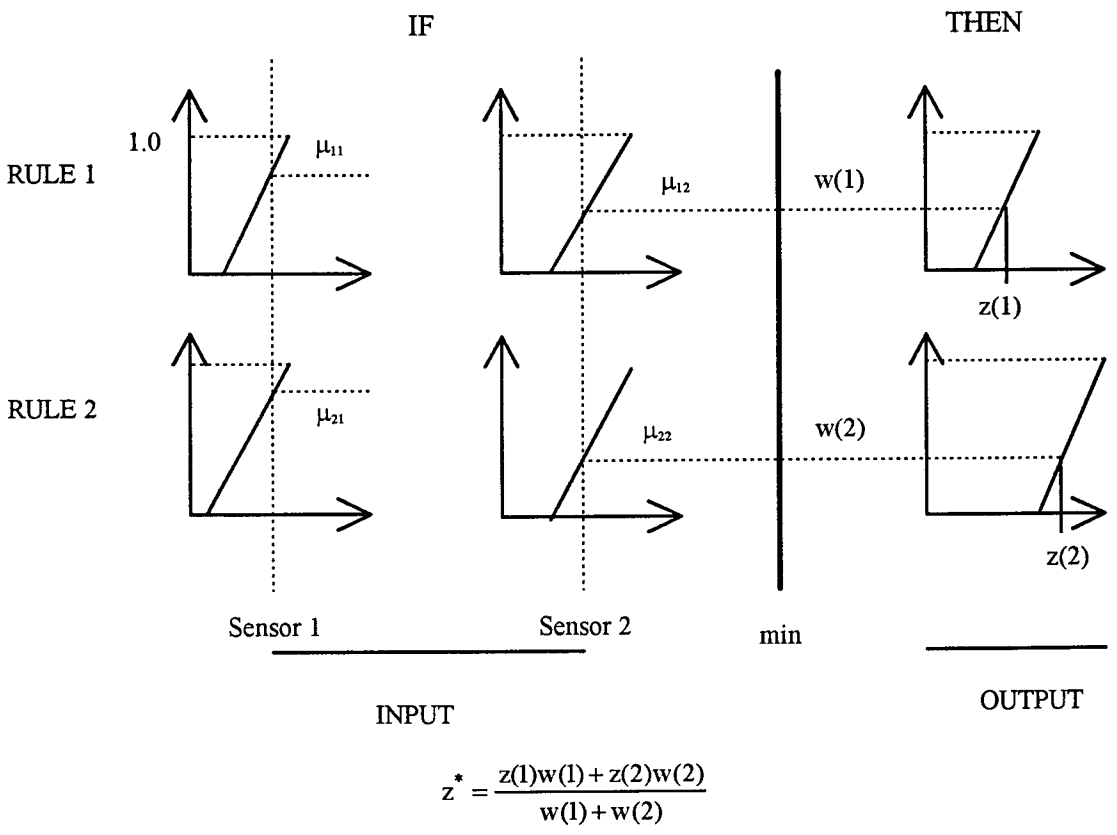
$$w(1) = \min\left\{\mu_{A_1}(x_0), \mu_{B_1}(y_0)\right\} \qquad w(2) = \min\left\{\mu_{A_2}(x_0), \mu_{B_2}(y_0)\right\}. \tag{3}$$

The corresponding output action recommended by each rule, z(1) and z(2), is found by applying the strengths above to the membership function for the control action linguistic value of each rule. The final nonfuzzy control action is a combination of the recommended output actions which is calculated using Tsukamoto's defuzzification method:

$$z^* = \frac{\sum_{i=1}^{n} w(i)z(i)}{\sum_{i=1}^{n} w(i)} \tag{4}$$

where n is the number of rules fired with strength w(i) and z(i) is the amount of control action recommended by rule i.

The process of *defuzzification* is graphically depicted in Figure 5, taken from Berenji {1}. Sensor measurements are fuzzified. The degree to which these measurements belong to a particular linguistic value, μ, is determined by examining the corresponding membership function. Only the smallest μ (which is equal to the strength w(i) of rule i) for each rule is considered when determining the output action or the THEN part of the rule. The output action, z(i), for rule i is computed in just the opposite manner of computing μ as seen in the figure. The overall output of the fuzzy controller is determined from equation (4) above.



$$z^* = \frac{z(1)w(1) + z(2)w(2)}{w(1) + w(2)}$$

Figure 5. Defuzzification of two fired rules using Tsukamoto's monotonic membership functions.

Annealed Fuzzy Control

Recall Hollkamp's fixed controller. By taking fixed step sizes in frequency, Hollkamp's absorber is able to find and track a particular mode of vibration. However, the controller is slow and/or exhibits large oscillations about the tuned frequency. The goal of a fuzzy controller is to recommend appropriate step sizes given the values of the linguistic variables which result in faster convergence and smaller amplitude oscillations about the tuned frequency. Two special fuzzy logic controllers are developed in this section for use in Hollkamp's self-tuning piezoelectric vibration absorber. These controllers implement an annealed fuzzy control algorithm. The first design uses only the ratio of the absorber RMS response to the structure RMS response as the linguistic variable. The second controller implements the RMS response of the structure as the linguistic variable. Since the two controllers are similar, only the design of the first will be discussed in detail. Modifications to the first controller needed to obtain the second are then presented.

As mentioned above, the first controller uses the ratio of the RMS response of the absorber to that of the structure as the only linguistic variable. A six-term set {Small, Medium Small, Medium, Medium Large, Large, and Very Large} is used to fuzzify the linguistic variable. Figure 6 shows the membership functions selected for each of the linguistic values. Note that the membership functions are defined in terms of the maximum value of the linguistic variable. For example, Small ranges from 0 to 15 percent of the maximum value. This is important

for the annealing process discussed later. Also note that when the ratio is greater than 80 percent of the maximum value, it belongs to the linguistic value Very Large with degree one. A special output action is designed for this linguistic value which helps reduce the dither observed when implementing a fixed step size control law.

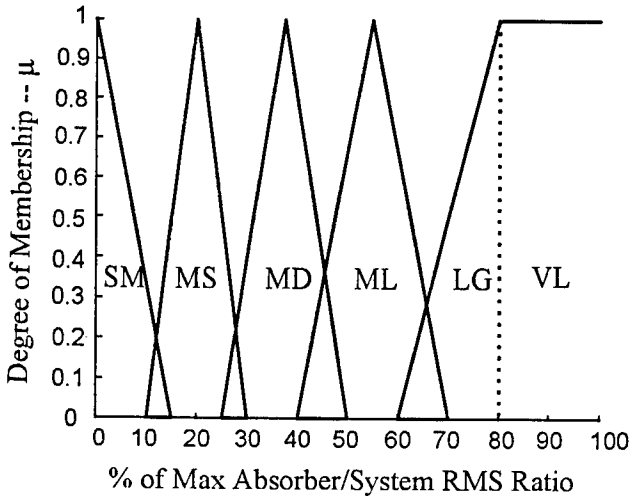


Figure 6. Fuzzy membership functions and corresponding linguistic values.

The function of the fuzzy controller is to recommend frequency step sizes to be taken with the ultimate goal of tuning the absorber. Therefore, when the ratio falls within a particular membership function (or two) an output action or step size must be recommended. The step size is also assigned a six-term set for fuzzification. The term set is {exponentially decreasing Small, Small, Medium Small, Medium, Medium Large, and Large}. The membership functions for the increment size, like those for the ratio, are defined in terms of the percentage of the maximum increment. In fact, the first five membership functions are exactly the same as those for the ratio, only inverted; i.e. Large becomes Small, Medium Large becomes Medium Small, etc. In addition, the membership function for the linguistic value Small yields a step size from a predetermined minimum frequency increment to 15% of the maximum increment, not 0 to 15% of the maximum increment as expected. The step size associated with the ratio being Very Large is exponentially decreased to zero from the minimum increment. The exponential decrease in step size reduces the magnitude of the oscillations about the tuned frequency. Table 1 lists the rules for the fuzzy controller. Figures 7 and 8 illustrate rules 4 and 6.

Table 1. A list of all rules used in the fuzzy controller design 1.

1.	IF RMS Ratio is Small THEN Step Size is Large
2.	IF RMS Ratio is Medium Small THEN Step Size is Medium Large
3.	IF RMS Ratio is Medium THEN Step Size is Medium
4.	IF RMS Ratio is Medium Large THEN Step Size is Medium Small
5.	IF RMS Ratio is Large THEN Step Size is Small
6.	IF RMS Ratio is Very Large THEN Step Size is exp. dec. Small

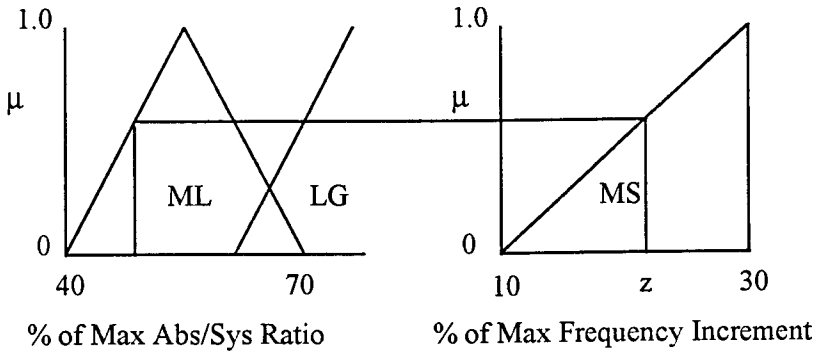


Figure 7. Illustration of Rule 4 from Table 1.

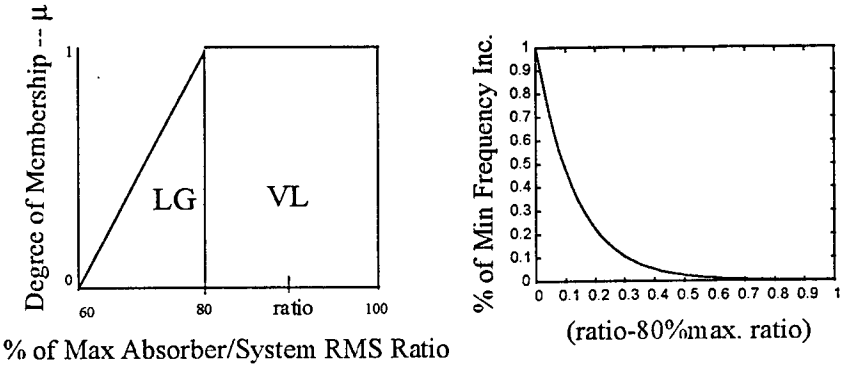


Figure 8. When the ratio is greater than 80% of the maximum, the increment exponentially decreases.

Like Hollkamp's fixed step size controller, the fuzzy controller uses an approximation of the slope of the RMS ratio curve to determine which direction to take a step. In order for the fuzzy controller to work, however, the maximum ratio of RMS responses must be computed. This can be done in several ways. A simple calibration in which the frequency is swept over a certain range containing the tuned value will approximate the maximum ratio. A bisection or golden section search can also be implemented. These searches require less time than a fine sweep over the frequency range of the absorber.

For a constant set of system parameters the fuzzy controller defined above works well. It is quick to find the tuned frequency and the oscillations about that frequency are small. Unfortunately, when there is a change in the system parameters, the controller fails to perform better than the fixed step size controller. The reason being that the maximum RMS ratio changes for the new set of parameters. The change in the maximum ratio is not large, but it is enough to adversely effect the performance of the fuzzy controller.

Instead of computing an approximation for the maximum RMS ratio every time the system parameters change, a controller is designed which slowly anneals through a range of maximum RMS ratio values. The concept of annealing is borrowed from *simulated annealing*. The first annealed fuzzy controller starts with an upper bound value of the maximum RMS ratio that is larger than the true value. This ratio is slowly decreased according to the schedule in equation (5) to a lower bound value which is less than the actual value. The annealing rocess occurs over a number of sampling periods which is not too large and not too small. At some point during

the annealing process the true value of the maximum RMS ratio is reached. At this point the controller is 'tuned' to the current set of system parameters and quickly converges to the desired mode of vibration. The annealing must be slow enough to allow the controller to capture the tuned frequency while annealed through the actual maximum RMS ratio value. When the value of the maximum ratio is greater than the actual value, frequency step sizes are large. This allows for a fast rise time. When the value of the maximum RMS ratio falls below the actual value, frequency step sizes approach zero. Thus, virtually all oscillations about the tuned frequency previously observed are eliminated. It should be noted that when the ratio is annealed far below the actual value, the measured RMS ratios will be greater than the annealed value. When this happens, the step size is set to a value near zero. If the step size is set to zero, there is no way to estimate the slope of the RMS ratio curve using a two-point approximation. Figure 9 shows what the membership functions observe during the annealing process.

$$\text{New Max. RMS Ratio} = \text{Upper Bound} - \frac{(\text{Upper Bound} - \text{Lower Bound})}{\text{Total Annealed Sampling Periods}} \times \text{Sampling Period Index} \qquad (5)$$

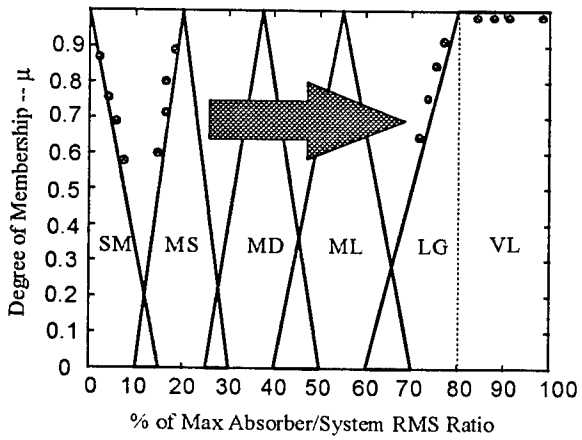


Figure 9. As the maximum RMS ratio is annealed, measured RMS ratios move from Small and Medium Small to Large and Very Large linguistic values.

The second annealed fuzzy controller uses the RMS response of the structure as the linguistic variable to be controlled. A five term set {Small, Medium Small, Medium, Medium Large, Large} is used to describe the linguistic variable. Figure 10 reveals the corresponding membership functions. Again, the membership functions are defined in terms of the maximum value of the linguistic variable for annealing. Since the RMS response of the system needs to be minimized, large values of the system RMS generate large freqency step sizes and small values generate small step sizes. In fact, the membership functions for the output action, i.e. frequency step sizes, are identical to those in Figure 10 with the maximum step size being predetermined by the user. The rules for the fuzzy controller are simply IF System RMS is Large THEN Step Size is Large, IF System RMS is Medium Large THEN Step Size is Medium Large, ..., and IF System RMS is Small THEN step size is Small.

The annealing for this controller is slightly different than the previous controller. Instead of estimating a maximum value, it is assumed that the absorber will reduce the initial observed system RMS response. Therefore,

the initial system RMS response that the absorber sees is defined as the maximum. This value is then slowly increased, forcing the lower membership functions to be activated. Eventually, all measured system RMS responses lie within the Small membership function and all step sizes approach zero. Figure 10 depicts the effect of upward annealing of the maximum system RMS response. If annealed slowly, the controller converges to the tuned frequency with virtually no dither. A sample annealing schedule is given in equation (6) below;

$$\text{Max.Sys.RMS} = \text{Init.Sys.RMS} \times K^{i} \qquad (6)$$

where K is a constant greater than one and i corresponds to the ith sampling period.

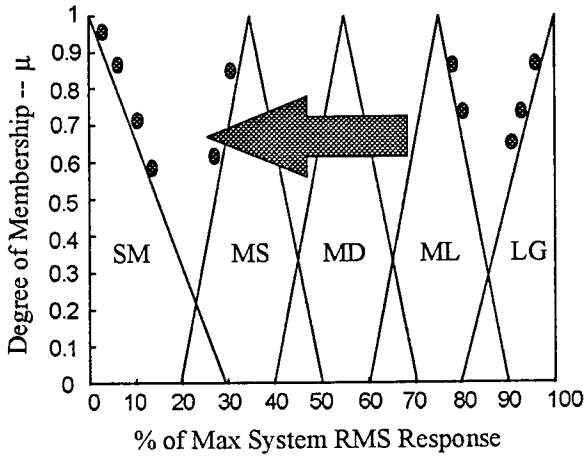


Figure 10. Membership functions and effect of annealing for system RMS response linguistic variable.

Experimental Results

In an attempt to duplicate Hollkamp's results, the same cantilevered beam setup is used. Figure 11 shows the experimental cantilevered beam. Six pairs of 1.5" by 1.5" PZT (G-1195) are attached to the beam. The first pair is used as the absorber. The forth pair measures the system response. One side of the fifth pair is driven as the disturbance (0-100 Hz gaussian random signal). An additional tip mass may be attached to the beam simulating an abrupt change in system parameters. A Hewlett Packard Paragon system provides the random disturbance signal, calculates absorber and system RMS responses, and computes transfer function information. The second bending mode (30.625 Hz) is selected as the mode to be suppressed. The filters pass data in the 10 to 70 Hz frequency range. Software developed for the personal computer commands the motorized potentiometer according to various control laws.

A preliminary experiment was conducted to validate the performance criteria. A simple calibration of the absorber was performed by incrementing the absorber frequency at constant step sizes. Figure 12 shows the experimental curves for the RMS ratio and the system RMS response when the tip mass is not attached. Obviously, these curves are noisier than those in Figure 3 In fact, the measurement accuracy decreases as the sampling period for data acquisition decreases. Figure 13 contains similar curves for a half second sampling period.

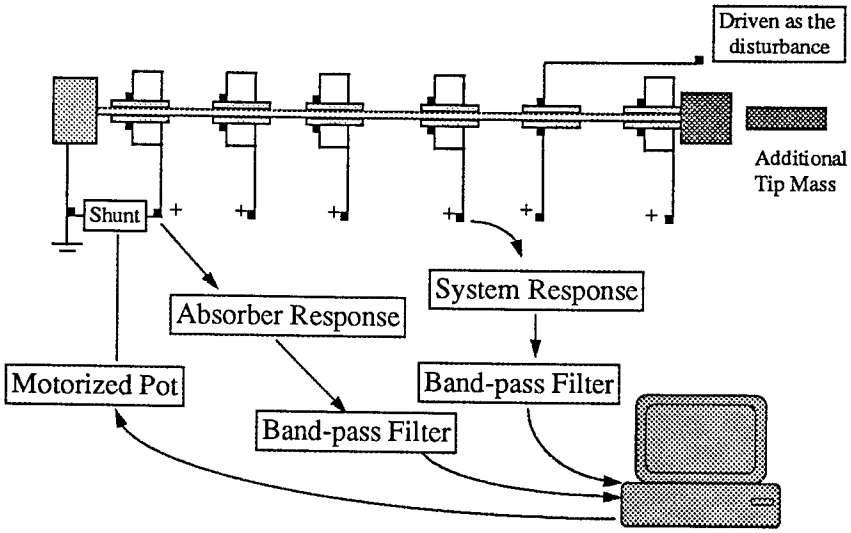


Figure 11. A diagram of the cantilevered beam experimental setup.

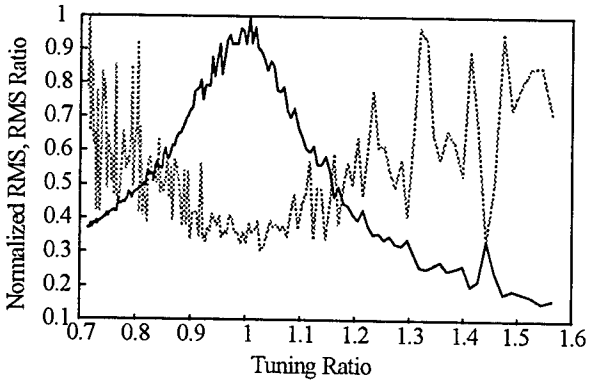


Figure 12. Normalized system RMS (dotted) and RMS ratio (solid) as tuning ratio is varied for a 4 second sampling period. Tip mass not attached.

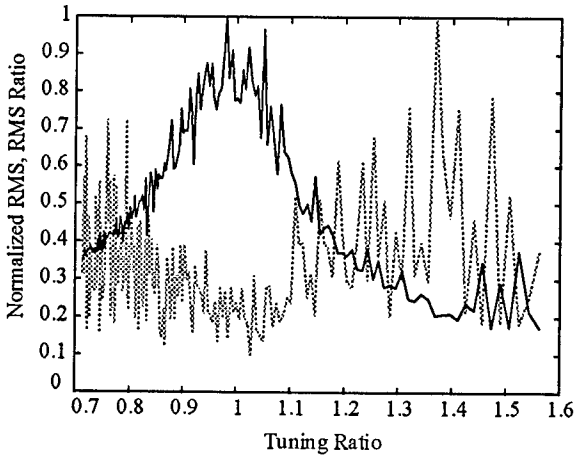


Figure 13. Normalized system RMS (dotted) and RMS ratio (solid) as tuning ratio is varied for a 1/2 second sampling period. Tip mass not attached.

Several experiments implementing both fixed increment and annealed fuzzy control laws were performed. Each experiment began with the motorized potentiometer initialized at the lowest setting and the tip mass attached. The tip mass was removed halfway through the experiment providing an abrupt change in system parameters. Removing the tip mass increased the frequency of the second mode to 40.75 Hz. Different sampling periods were used to test each controller's ability to find and track the mode of vibration through less accurate measurements.

Several methods for determining when a change in system parameters occurs were implemented in the annealed fuzzy controllers. When the absorber is tuned, the RMS ratio is at its maximum. When it is mistuned, the RMS ratio decreases dramatically. The second controller recognizes a change in the modal frequency when the RMS ratio changes by more than 25-45%, depending on the sampling period. A change may also be recognized when the RMS ratio falls below a certain value. This value may be selected from a calibration curve obtained

using a sampling period identical to that implemented during control. Recall that the noise in the measurements are functions of the sampling period. The first controller acknowledges a change in modal frequency if its lower membership functions are activated, i.e. when the RMS ratio is low. In each of the above methods, the controller restarts the annealing process when it believes there has been a change in modal frequency.

The first experiments implemented fixed increment control. The results for coarse and fine increments in frequency and a half second sampling period are given in Figures 14 and 15. For coarse tuning, the rise time is small (about 5 seconds), but the dither about the tuned frequency is large. The controller drifts away from the tuned frequency by up to 6 Hz in one instance. Fine tuning reduces the amount of dither to about ±2 Hz, but the controller has a much slower rise time (about 20 seconds). Both fast rise time and small dither can be obtained by implementing coarse tuning initially and then fine tuning later. However, the combined controller will only be as good as its components.

It should be noted that the fixed increment controllers are less likely to drift away from the tuned frequency when larger sampling periods are used. Recall that for large sampling periods more accurate estimations for the system and absorber RMS response are obtained. Thus, a more accurate estimation of the slope of the RMS ratio curve is obtained and the controller is more likely to take steps in the right direction.

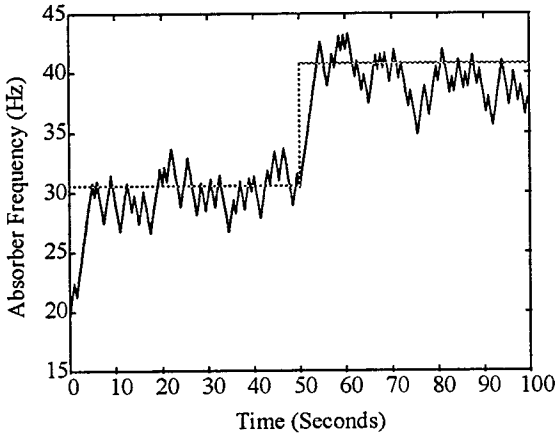


Figure 14. Experimental results for coarse tuning using 1/2 sec sampling period. Tuned frequency is also shown (dotted).

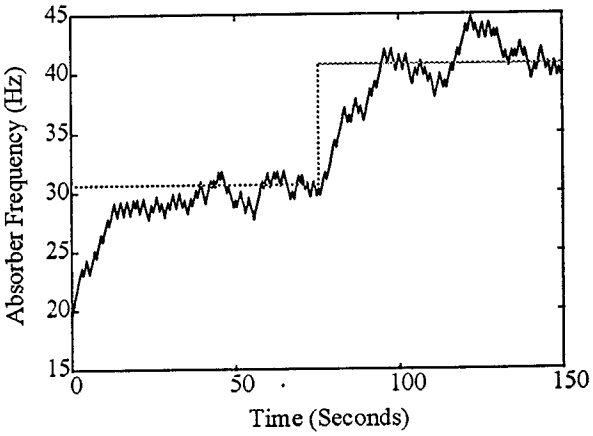


Figure 15. Experimental results for fine tuning. using 1/2 sec sampling period. Tuned frequency is also shown (dotted).

The next set of experiments were conducted using the annealed fuzzy controllers. A golden section search was implemented in the first controller to estimate the maximum RMS ratio. For a four second sampling period, only nine samples were needed to compute this value. However, as the sampling period was decreased, the ability of the golden section search algorithm to approximate the maximum RMS ratio deteriorated due to the increased noise. For a half second sampling period, the search rarely found a good approximation for the maximum RMS response ratio causing the controller to fail.

Figure 16 provides the experimental results using a four second sampling period. Figure 17 shows a successful performance of the controller for a half second sampling period. Note that the first nine sampling

periods are used to approximate the maximum value of the RMS ratio. The controller is activated on the tenth sampling period. In both figures, the controller quickly converges to the tuned frequency. In Figure 16, the controller finds the tuned frequency without dither. It recognizes a system change at 240 seconds and restarts the annealing process to again quickly find the new tuned frequency without dither. Figure 17 demonstrates the robustness of the annealed fuzzy controller. An inaccurate measurement at about 30 seconds misleads the controller into thinking that a change in system parameters has occurred. The controller restarts the annealing schedule and again quickly finds the tuned frequency. The controller also tracks the tuned frequency when the tip mass is removed.

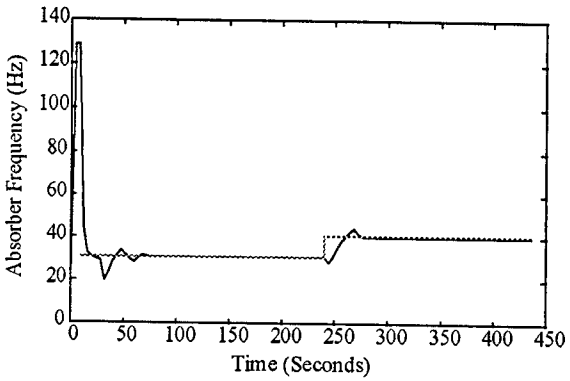


Figure 16. Annealed fuzzy control implementing the golden section search algorithm. A 4 second sampling period is used. Tuned frequency (dotted).

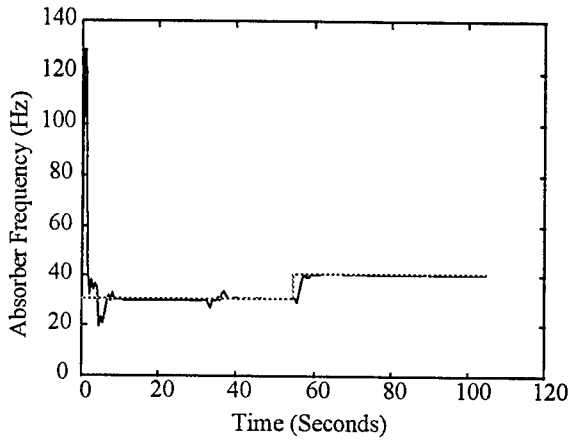


Figure 17. Annealed fuzzy control implementing the golden section search algorithm. A 1/2 second sampling period is used. Tuned frequency (dotted).

It is interesting to examine calibration curves for the RMS ratio with and without the tip mass attached to the beam. Figures 18 and 19 illustrate the effect of the sampling period length on measurement accuracy. These figures also point out that even if a good estimation can be obtained for the maximum RMS ratio, the first controller design will be slow to converge. In order to eliminate dither, the fuzzy controller anneals slowly through the noisy measurements. As seen in Figure 18, in order for the controller to perform successfully, the maximum RMS ratio must be annealed from 7 to 5.5, approximately. For the half second sampling period, the RMS ratio must be annealed from 7.5 to 3.5, approximately, to clear the noise. Otherwise, the controller will experience the bad measurement and restart the annealing process thinking that a change in modal frequency occurred (as was the case in Figure 17). A longer annealing time means slower convergence.

The second fuzzy controller design is perhaps more practical than the first in that it does not require a calibration or a search algorithm to find the maximum RMS ratio. Recall that the second controller was designed with the system RMS response as the linguistic variable. It uses the initial measurement of the system RMS as the maximum and anneals upward. Again, the inductance (absorber frequency) step sizes are taken in a direction dictated by an estimation of the slope of the RMS ratio curve.

Figures 20 and 21 give the experimental results for the second annealed fuzzy controller design. The rise time for each sampling period is much faster than exhibited by the first controller. Only a few sampling periods are needed to reach the tuned frequency. As the maximum system RMS is annealed, the controller converges to the tuned frequency eliminating any oscillations about that frequency. The second controller is also able to find and track the second modal frequency during an abrupt change in the cantilevered beam's parameters. The performance of the controller in Figure 21 is similar to that in Figure 17. The robustness of this controller is also demonstrated by a noisy measurement. At approximately 12 seconds, an inaccurate system RMS measurement resets the annealing process allowing the controller to converge more closely to the actual tuned frequency.

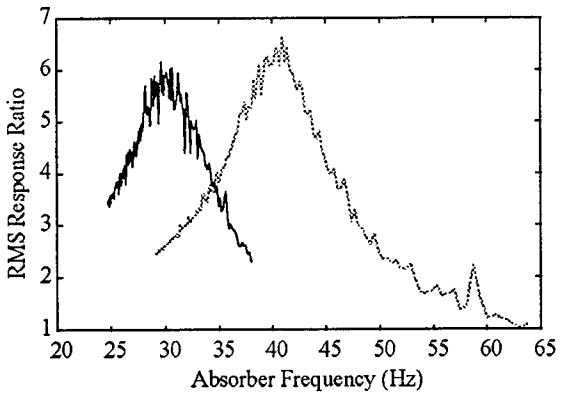


Figure 18. Calibration curves for the RMS ratio with (solid) and without (dotted) the tip mass for a 4 second sampling period.

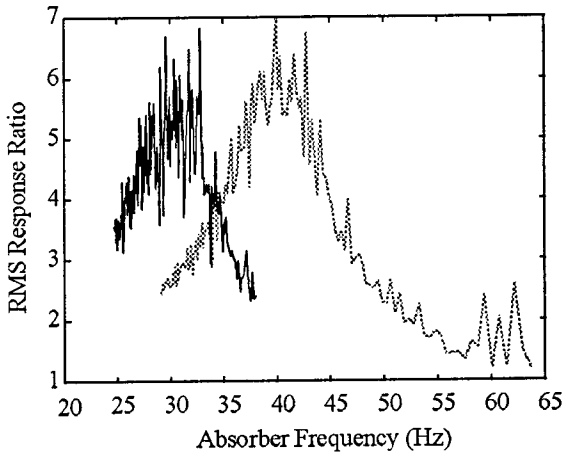


Figure 19. Calibration curves for the RMS ratio with (solid) and without (dotted) the tip mass for a 1/2 second sampling period.

Table 2 gives the final converged values of frequency that were obtained in Figures 16, 17, 20, and 21 for both annealed fuzzy controllers. Both controllers were able find and track the second mode of vibration to within 1.0 Hz. Of all the experiments, the most either of the controllers missed the tuned frequency by was about 0.75 Hz. This occurred in Figure 21 when the tip mass was removed.

Next, consider the effect of the tuned absorber on the power of the system. Figure 22 presents a frequency response function of the system with and without the mass. The figure also shows the corresponding responses when the absorber is tuned to the second modal frequency. With the tip mass attached, the tuned absorber reduced the peak value of the second mode from 10.2 dB to -3.6 dB (a 13.8 dB reduction). Without the tip mass, the tuned absorber reduced the peak value from 12.6 dB to -5.2 dB (an 18 dB reduction). Using the power of the system without the absorber as a baseline for comparison, Table 3 shows up to an 82.26% reduction in the vibration energy when the absorber is tuned. Even when the controller misses the tuned frequency by 0.8 Hz, the power is reduced by 81.58%. The frequency response function for the nearly tuned case is given in Figure 23. Notice that the nearly tuned response is not as flat as the tuned responses given in Figure 22. Power was calculated by the

following equation:

$$\text{Power} = \int_{2\pi 10}^{2\pi 70} |H(j\omega)|^2 \, d\omega \qquad (7)$$

where $H(j\omega)$ is an experimental FRF.

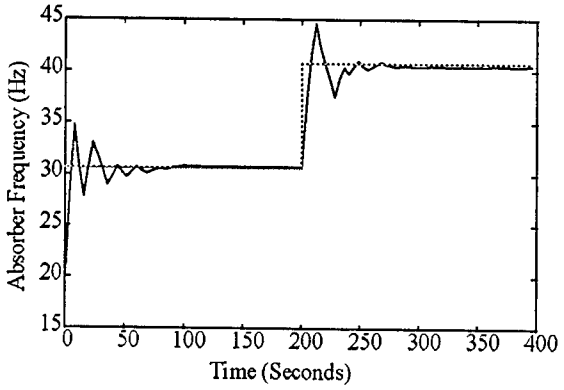


Figure 20. Results for the second annealed fuzzy controller design for a 4 second sampling period. Tuned frequency shown (dotted).

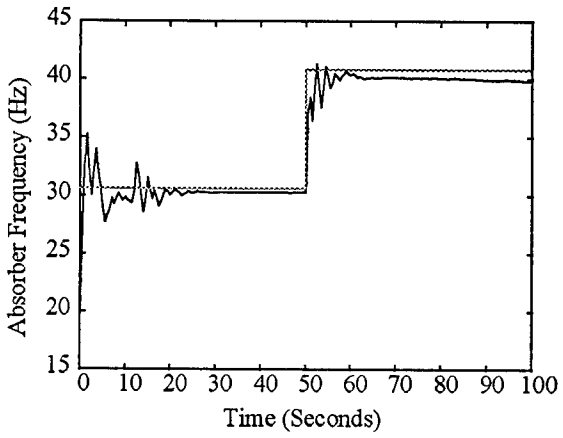


Figure 21. Results for the second annealed fuzzy controller design for a 1/2 second sampling period. Tuned frequency shown (dotted).

Table 2. Tuned absorber results from Figures 14, 15, 18, and 19.

Sampling Period (Seconds)		Actual Tuned Frequency (Hz)	Annealed Fuzzy Controller & Frequency 1	2
4	With Tip Mass	30.625	30.7	30.75
	Without Tip Mass	40.75	40.2	40.5
1/2	With Tip Mass	30.625	30.1	30.25
	Without Tip Mass	40.75	40.7	40.0

Table 3. Comparison of experimentally tuned power with baseline (no absorber) power.

	Normalized Power (%)	
Baseline (No Absorber)	100	
With Tip Mass	25.2	
Without Tip Mass	17.74	
Nearly Tuned Absorber	18.42	(Worst Case, No Tip Mass, Figure 21 & 23)

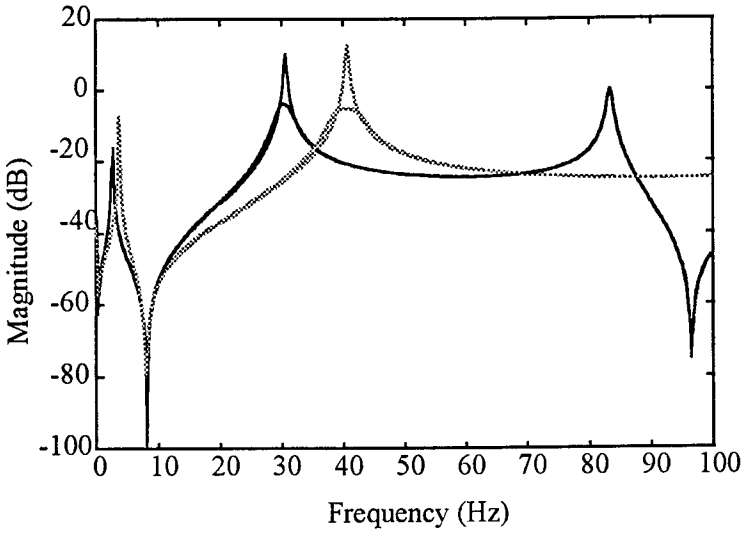


Figure 22. Measured frequency response with (solid) and without (dotted) tip mass attached. Both tuned and untuned frequency response curves are shown.

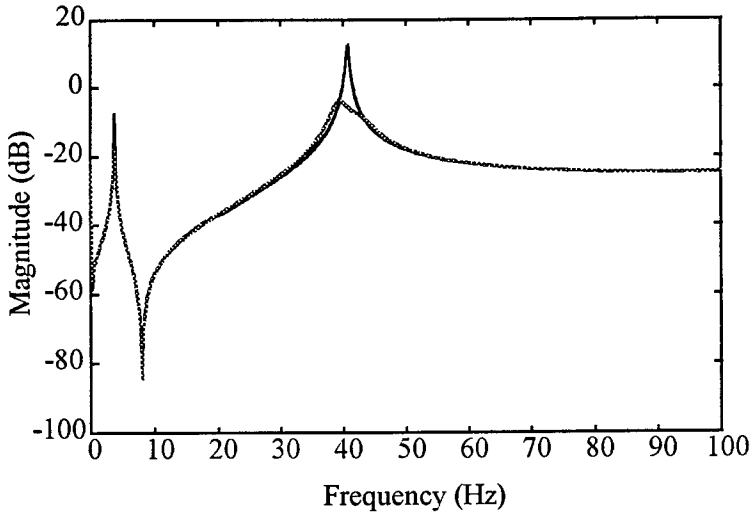


Figure 23. Measured frequency responses for nearly tuned (dotted) and untuned (solid) cases. Tip mass not attached.

Conclusions

Two designs of an annealed fuzzy controller for a self-tuning piezoelectric vibration absorber have been presented. These controllers have experimentally demonstrated the ability to find a particular mode of vibration. Compared to Hollkamp's fixed increment controller, the annealed fuzzy controllers have a faster rise time and practically eliminate any oscillation about the tuned frequency once it is discovered. By successfully suppressing the second mode of vibration of the cantilevered beam using only a half second sampling period, the annealed fuzzy controller exhibited the ability to perform with highly uncertain measurements. In fact, there were some

instances when an uncertain measurement reset the annealing process causing the controller to settle on a more accurate tuned frequency. This phenomenon can be compared to *reannealing* in simulated annealing.

Even when the tip mass was removed from the cantilevered beam, changing the modal frequency, both annealed fuzzy absorbers were able to recognize the change and find the new tuned frequency. However, in order to recognize the change in system parameters, the second fuzzy controller needed an additional RMS ratio monitor. The first design could realize modal frequency changes by observing the activation of its membership functions. The second design could be modified to perform similarly by annealing through a small range of maximum system RMS responses instead of annealing upward indefinitely.

In each of the controllers discussed, two measurements are required; the system RMS response and the absorber RMS response. It would be more practical to devise a controller which is based on only one measurement. This would reduce the number of sensors and the computational effort needed for successful control.

Acknowledgments

This work was sponsored by the Air Force Office of Scientific Research and the Graduate Student Research Program. The author would like to thank Dr. Joseph J. Hollkamp and Wright Laboratory/FIBGC for their complete cooperation and expertise in the field of piezoelectric materials and vibration suppression.

References

1. H. R. Berenji and P. Khedar, 1992, "Learning and Tuning Fuzzy Logic Controllers Through Reinforcements," *IEEE Transactions on Neural Networks*, Vol. 3, No. 5, pp.724-740.

2. W. K. Chen, 1986, *Passive and Active Filters*, John Wiley and Sons, Inc., New York.

3. N. W. Hagood and E. F. Crawley, 1989, "Experimental Investigation into Passive Damping Enhancement for Space Structures," *Proc. of the 30th AIAA/ASME/ASC/AHS/ Structures Structural Dynamics and Materials Conference,* Mobile, Alabama, AIAA Paper 89-3436, pp. 97-109.

4. N. W. Hagood and A. von Flotow, 1991, "Damping of Structural Vibrations with Piezoelectric Materials and Resonant Shunts," *Journal of Sound and Vibration*, Vol. 146, No. 2, pp. 243-268.

5. J. J. Hollkamp and T. F. Starchville, Jr., 1994, "A Self-Tuning Piezoelectric Vibration Absorber," *The 35th AIAA/ASME/ASCE/AHS/ACS Structures, Structural Dynamics and Materials Conference Adaptive Structures Forum*, AIAA Paper 94-1790.

6. K. E. Smith, J. R. Maly, and C. D. Johnson, 1991, "Smart Tuned-Mass Dampers," *Proceedings of the ADPA/AIAA/ASME/SPIE Conference on Active Materials and Adaptive Structures*, Alexandria, VA, pp.19-22.

PIXEL PLANE DESIGN FOR A SIMD GRAPHIC PROCESSOR

Brent A. Veltkamp
Graduate Student
Department of Electrical Engineering

Michigan State University
East Lansing, MI 48825

Final Report for:
Summer Graduate Student Research Program
Wright Patterson Laboratory

Sponsored by:
Air Force Office of Scientific Research
Bolling Air Force Base, DC

and

Wright Patterson Laboratory

August 1994

PIXEL PLANE DESIGN FOR A SIMD GRAPHIC PROCESSOR

Brent A. Veltkamp
Graduate Student
Department of Electrical Engineering
Michigan State University

Abstract

This paper presents the design and layout of a high performance graphics processing unit. The operation of the unit is in parallel, which helps to give it high performance and allows it to take advantage of parallelism inherit inside of code and instructions. The system will run at 100MHz to handle the graphic processing, enhance the I/O capabilities of the frame buffer, and free up the CPU for more useful system operations.

PIXEL PLANE DESIGN FOR A SIMD GRAPHIC PROCESSOR

Brent A. Veltkamp

Introduction

Every computer graphics system has a frame buffer, computation engine and an interconnection between these. This interconnection is responsible for determining how fast and flexible the system is and to some degree how much the system will cost. Most personal computers use the most flexible and cost efficient graphics system, shown in Figure 1. This configuration, while being easy to build and program, is limited in speed by two factors; the CPU and the bus.

The CPU, in this setup, is forced to perform all graphical computations as well as run the rest of the system. While the CPU does graphic computations the rest of the system is forced to wait. For graphic intensive jobs this lose of processing time can be substantial. All interactions between the CPU and frame buffer has to take place on the system bus. The speed, of this interaction, is thereby limited to the bus size or bandwidth. In this basic configuration, the only way to increase graphic performance would be to increase the bandwidth or get a faster CPU.

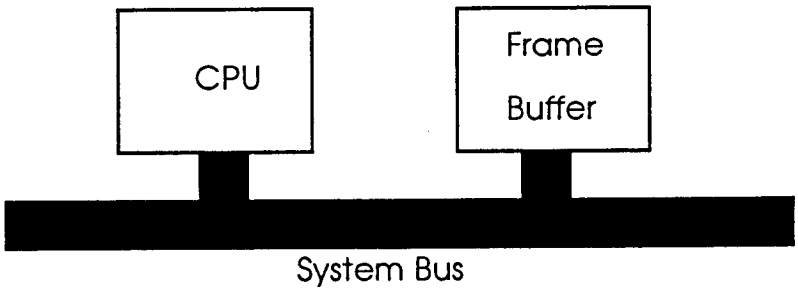


Figure 1

The goal is to design a graphics computation chip that is fast, 100 MHz, and reasonably cost efficient. Figure 2 shows an outline of the proposed graphic subsystem. The system contains a linear tree, alu and memory component for each pixel. The system will handle 4096 pixels at a time, this number was found to be a good compromise between speed and size. The graphic system will therefore handle a

64 by 64 area on the screen and process the graphical information in parallel. The main computations will be done using the alu for each pixel, thereby freeing up the host CPU so it can continue to process other instructions.

The proposed system can greatly enhance graphic processing, largely due to its parallelism. It breaks your screen up into 64 by 64 chunks that will be processed, with each chunk being done in parallel. The I/O processing of the graphics system with the frame buffer will still be limited by the bandwidth but it has some enhanced features that will be discussed.

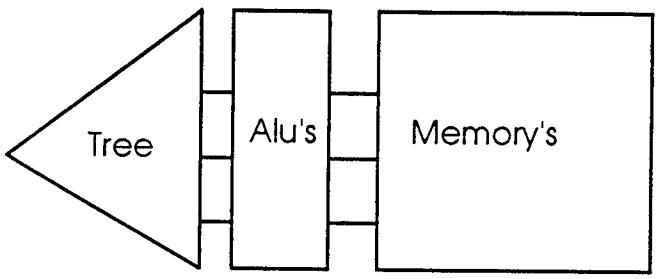


Figure 2

The overall tree is 12 stages deep, with six stages for x oriented calculations and six stages for y oriented calculations. This means that each chip represents a 64x64 pixel area on the video display. Thus, there is a total of 4096 pixel memory locations, attached to 4096 ALU's, receiving input from 4096 outputs of the 12 stage linear tree. However, for optimal space utilization, this arrangement is broken up into 32 pieces called planes. Each plane has 128 pixel memory locations, 128 ALU's and 128 tree outputs[1, pp 12]. It is the design and layout of this plane that is the topic of this research project.

Methodology

The design of the graphic system depends on the construction of a generic plane and the interconnection of 32 planes to form the system. The overview of a plane is shown in Figure 3. The plane has tree, alu and memory stages as well as an I/O and crossbar stage. The crossbar stage is used to interconnect the memory and alu and will be discussed later on.

Although relatively simple, the bit-serial ALU's form the heart of each plane. It is the job of the ALU to process data coming in from the linear tree subsystem, to read from and write to the memory

subsystem, and to control which memory locations will be overwritten with new values[1, pp 23]. The layout and design of the ALU are shown in Figures 4 and 5 respectively. The ALU is responsible for controlling data flow, reading from the linear tree and reading and writing to memory. The design uses three flip-flops which are used to store the previous sum, carry and any changes that need to be made to the enable register. The enable register controls who and when you can read or write to memory, thereby giving each ALU control over its own memory.

The data used by each ALU comes from the linear tree subsystem. The linear tree is basically just a bit serial multiplier that operates in parallel. It takes in three inputs, A, B and C and outputs the function: Ax + By + C, where x and y are the pixel location on the display. Figures 6 and 7 show the layout and design of a tree stage. The initial problem with this design is that it requires 4096 tree stages, therefore it requires 4096 multipliers, which would require a large chip area. This is where the linear tree idea came about, instead of building 4096 multipliers in parallel, if you analyze the bit multiplication's you would see that each stage either gives an output of a one or a zero. From that analysis it becomes clear that building the tree as a binary tree would be effective, since each stage only has two outputs. Using this idea we achieved a logarithmic improvement in the chips area, dropping the required number of multipliers down to 127 per plane. This new linear tree is seven stages deep, thereby causing it to run slower than if we used 4096 parallel multipliers but the saving of die area, uses 1/32 the area of the parallel area, makes this a practical compromise. The bit multiplier is constructed from a full adder and the tree stage uses three flip-flops to store values. Two of the flip-flops are used to store the stages potential values, which depend on whether the input is a one or a zero.

The memory is the largest component of the plane. It is composed to 128 bits of static RAM, basic six cell SRAM. The memory was made static for low power consumption, especially when the chip is in an idle state. The use of static RAM also allows us to store the value without having to add an external dynamic refresh circuitry. The 128 bits of RAM for each pixel will be to store the red, green and blue values , each double buffered, along with room for z buffer data or alpha blending data[1, pp 41]. The memory system stores the changes that the ALU makes to each pixel until it is read out to the frame buffer. The memory system is made of two rows of 64 bits each to try to limit the width of the plane and to match its layout size with that of the ALU and the other components. The memory is accessible by both the ALU and the I/O which is controlled by the crossbar.

The memory is connected to the ALU and I/O by way of a crossbar. The layout and design, of the crossbar, are shown in Figures 8 and 9. The crossbar is responsible for allowing interaction to occur between memory and either the ALU or I/O port. It handles reading as well as writing to memory and its main requirement is to allow fast access to memory. The crossbar also has to allow concurrent access from both the ALU and I/O, by this I mean that they can both read from memory at the same time, or while one writes to memory the other one can read the value. The ALU and I/O are not allowed to both write at the same time, due to the fact that they are accessing the same bit of memory.

The I/O circuitry has really two functions: to preload the memory and to read out to the frame buffer. The graphic system is setup with 32 output pins, thereby allowing only one bit per plane to be written out at a time. When reading from the I/O the same bit location in all planes will be read out in parallel, one bit per plane.

Each bitslice, the connection of one tree, ALU, I/O and memory, will have a different pixel associated with it. Since the I/O only reads from one pixel location at a time, this lead to the need to hardwire the address of each bitslice. This hardwiring is acceptable since each plane is the same and the I/O reads from the same pixel location in all planes in parallel.

The operating procedures and component sizes had to be varied to find the optimal configuration to achieve the 100Mhz goal. This requires that all reads and writes be completed within 5ns, for 50% duty cycle. The completed design size turns out at 1.5mm by 1.9mm per plane.

Procedure

Since the 100Mhz requirement placed the largest responsibility on the crossbar, it thereby became the first component to be constructed. The crossbar allows us to write to memory in 4.1ns from either the ALU or the I/O, which meets our writing requirement. Reading to the ALU is quite fast, a minor 3.6ns and as one would expect the reading to the I/O is slower at 4.3ns. These times will allow us to have 100Mhz operation with a 50% duty cycle and also gives us a 15% error margin. The height of the crossbar came out as 14.68 microns. This lead to the need to match its height with that of the tree, ALU and memory. The height of the crossbar is what allows us to create a double height memory, two rows of 64 bits each.

The ALU and memory were basic layouts but the tree proved to be a challenge. The key to the linear tree is that it has seven levels but only 127 multipliers. The trick was trying to wire it flat so we had 127 tree stages on top of each other, this became necessary to minimize the width of each bitslice.

Once a bitslice was constructed then we need to array 128 of them to create the plane. Each bitslice ended up being 1.5mm by 14.68microns, which leads to our plane size of 1.5mm by 1.9mm.

Testing

Testing was done at all phases of design, except for the plane itself since it had too many inputs and too many components to easily test. Each components design and layout was tested using HSpice to make sure it was operating correctly and within the 100Mhz guidelines. A bitslice was then formed and it was tested as well, it had to be left running over night due to the number of components in the bitslice. The outputs were checked for glitches or potential glitches as well as faulty outputs and slow read times. The bitslice performed correctly and most importantly it met the 100Mhz requirement. The testing brought about the chose of the optimal reading and writing procedures, which are as follows:

Writing from the ALU:

1:	Assert PchL	For precharging memory lines, a 1ns precharge time.
2:	Assert WrDat	Occurs at same time as Asserting PchL
3:	Assert WrEnL	Happens once WrDat is stable.
4:	Assert Row and Word	Choose the correct row and word location, occurs after precharge.
5:	Assert SaEn	A 2ns signal to use the Sense Amplifier to force the data into memory.
6:	Data now stored in memory	

Reading to the ALU:

1:	Assert PchL	For removing previous value from Sense Amplifier, 1ns signal.
2:	Assert Row and Word	Choose the correct row and word location, done after 1 finishes.
3:	Assert SaEn	A 2ns signal to use the Sense Amplifier to force the data into memory.
4:	Data available at ALU	

Reading and writing from I/O is done the same way except there is an extra signal, IOread, that is used. Also while the ALU and I/O can both read or one can read while the other writes, at the same time which can enhance the I/O capabilities.

Conclusion

A different type of graphic processor has been developed here. It runs at 100Mhz and has the added speed of using parallelism to handle a 64 by 64 block of the display at a time. It has a rather simplistic design, built from the interconnection of 32 planes which are built from the interconnection of 128 bitslices. It increases system performance by handling graphic routines that the CPU, in general, would be forced to do itself. Each bitslice has its own memory and all the memory, in each plane, can be accessed in parallel. Also each ALU in the plane has complete control over its own memory. I/O to the frame buffer is handled by a 32 bit I/O port on the chip. I/O is enhanced since it is done in parallel, one bit being read from each plane as well as easy preloading of the memory through the I/O port. The plane has been designed, laid out and tested error free completing this part of the graphic processor.

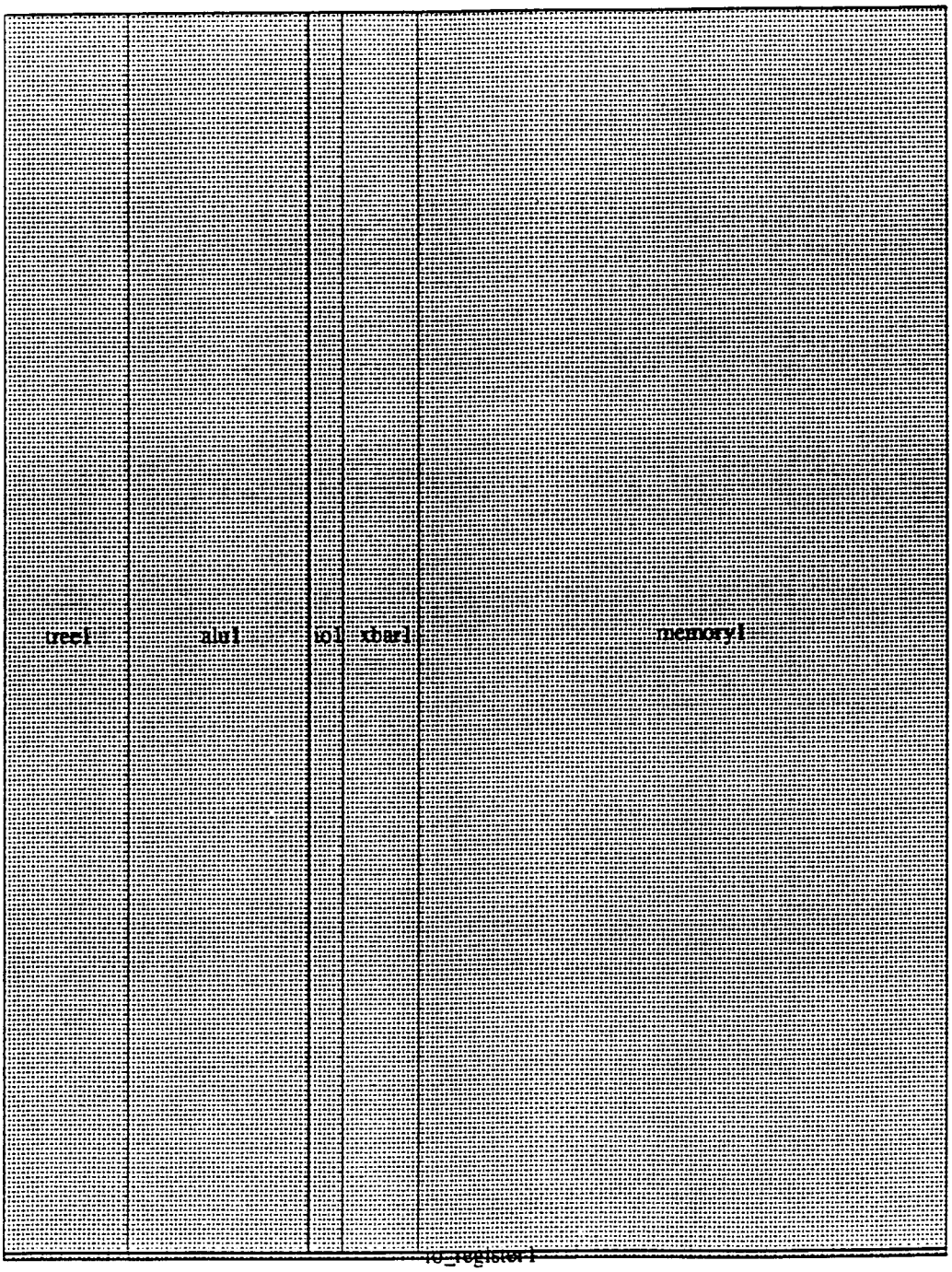


Figure 3

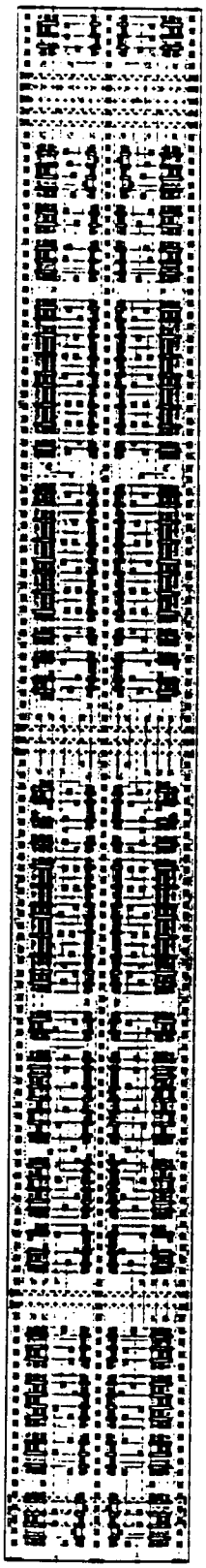


Figure 4

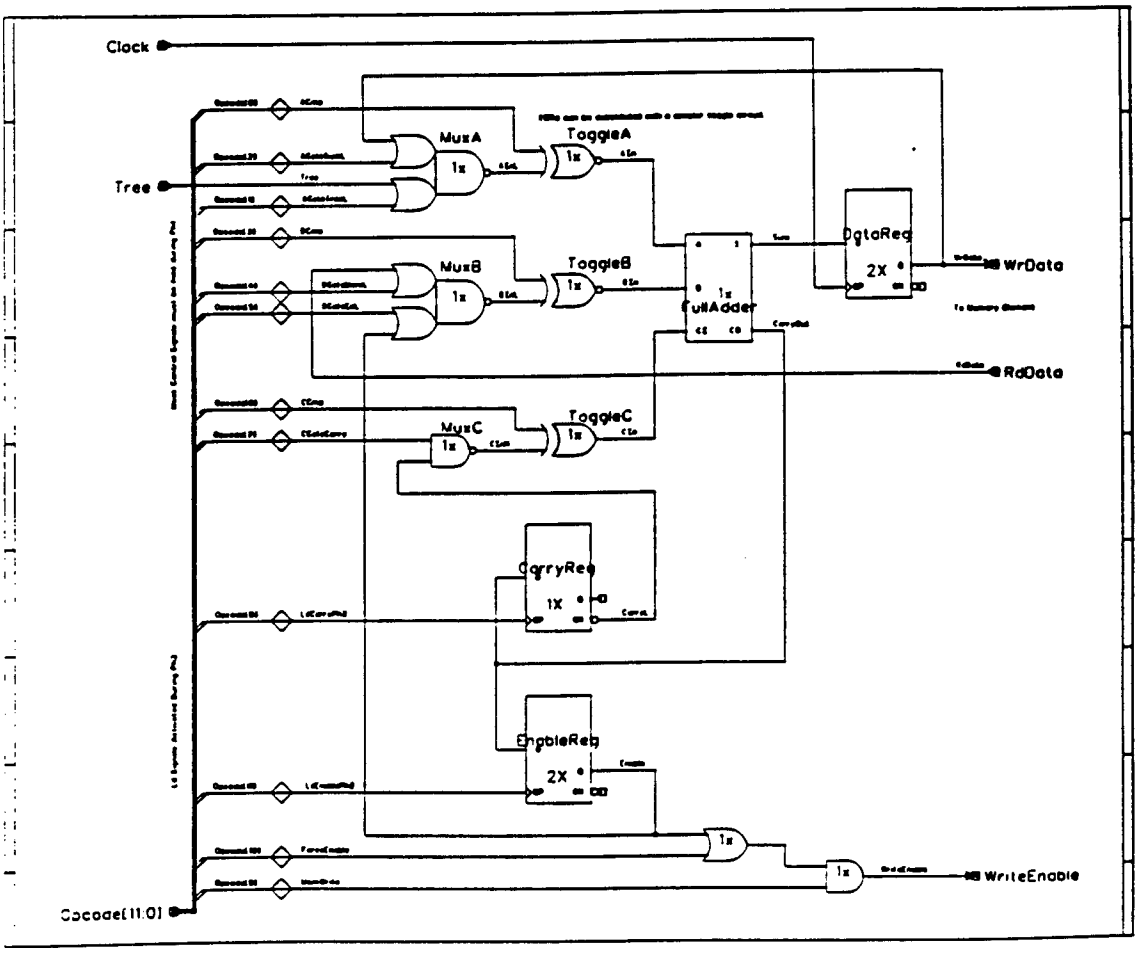

Clock
Tree
Opcode[11:0]
MuxA
MuxB
MuxC
ToggleA
ToggleB
ToggleC
FullAdder
DataReg
2X
WrData
RdData
CarryReg
1X
EnableReg
2X
WriteEnable

Figure 5

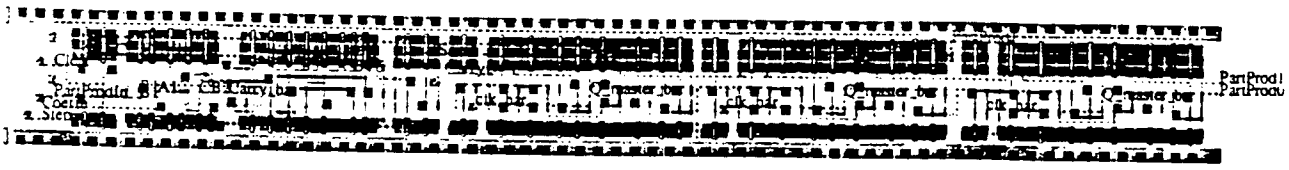


Figure 6

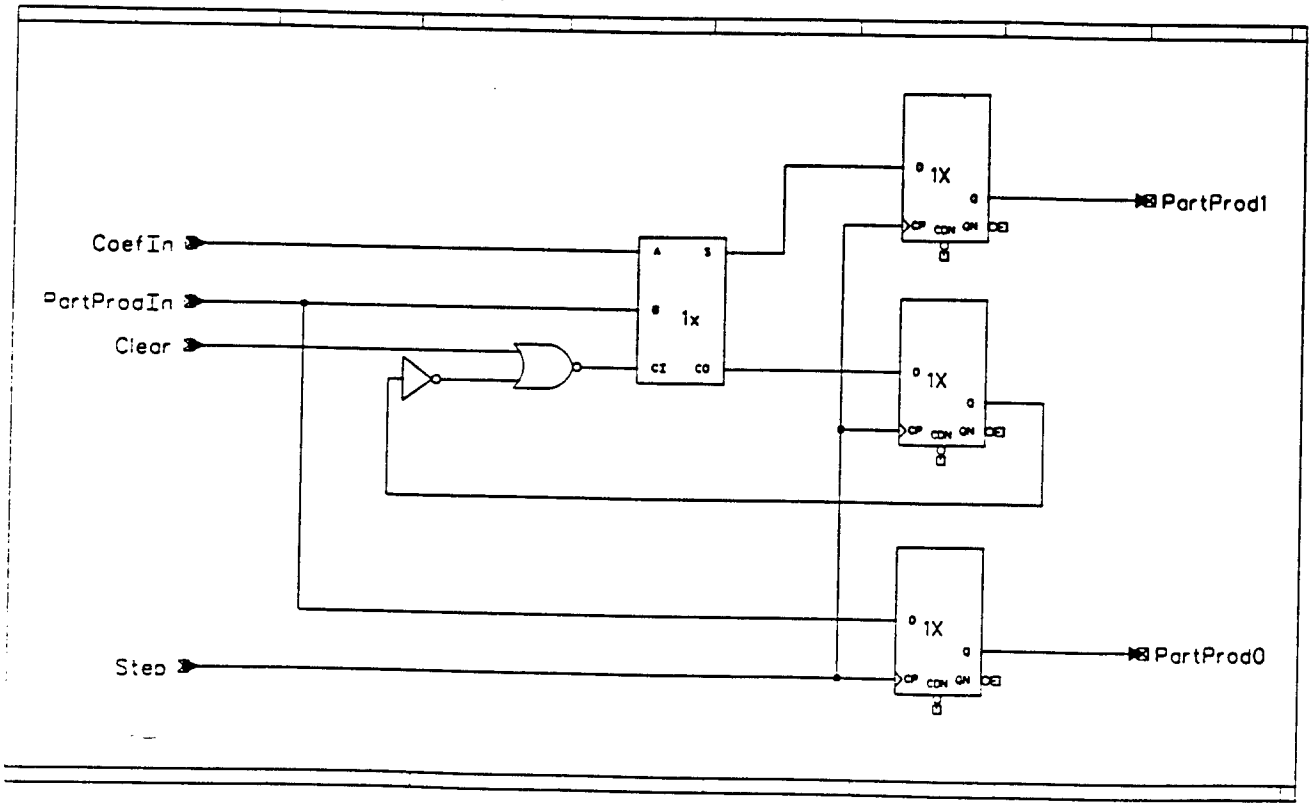


Figure 7

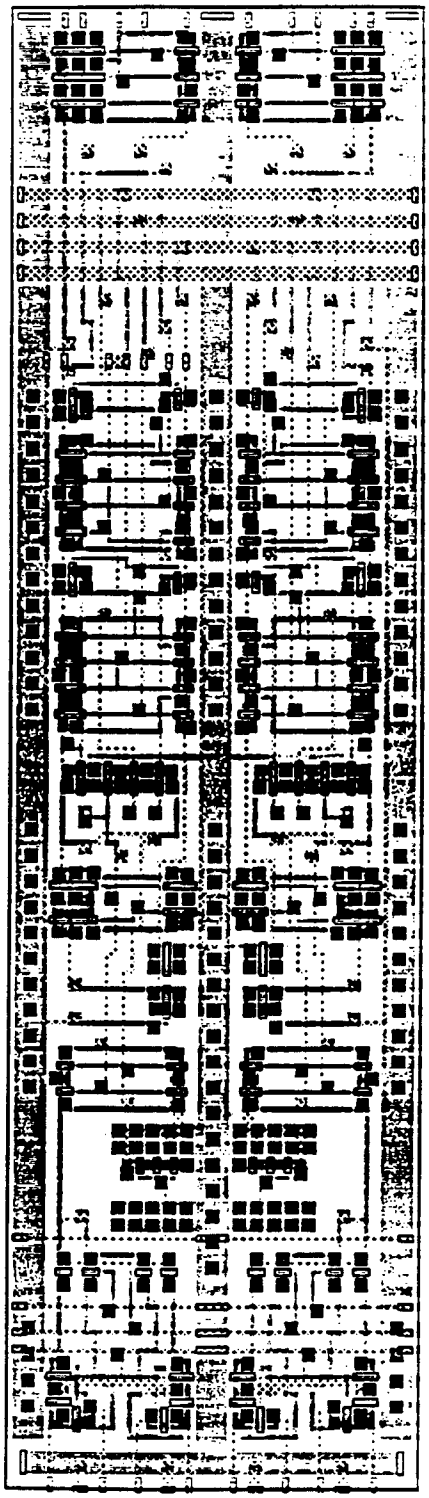


Figure 8

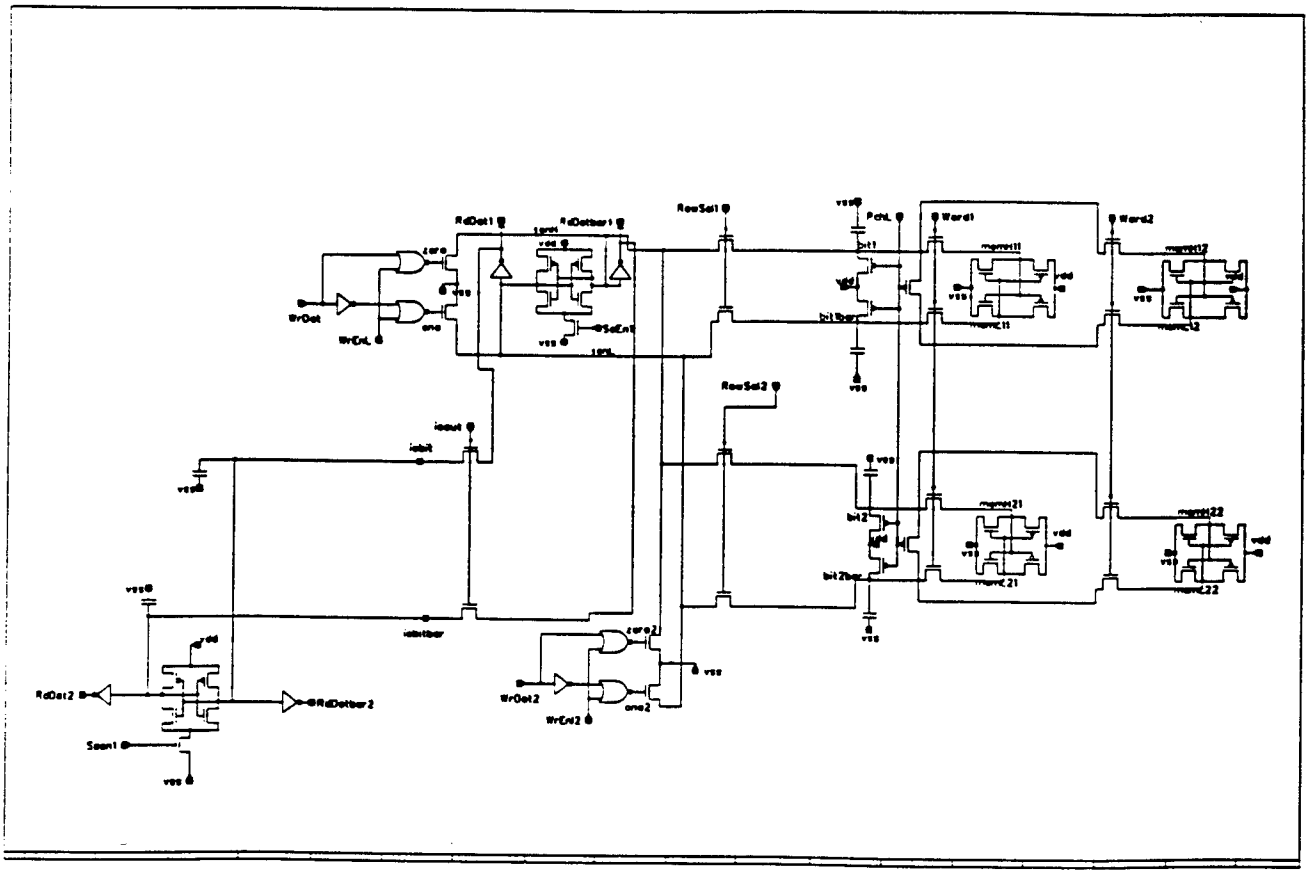


Figure 9

References:

[1] Capt. Scott E. Bilik, *The Modeling and Simulation of a SIMD Graphics Engine in VHDL*, M.S. Thesis, Wright State University, 1993.

THE COMBINATORICS OF FUNCTION DECOMPOSITION AND APPLICATIONS OF LEARNING THEORY

Christopher C. Vogt
Ph.D. Graduate Student
Department of Computer Science and Engineering

University of California, San Diego
0114
La Jolla, CA 92037
vogt@cs.ucsd.edu

Final Report for:
Graduate Student Research Program
Wright Laboratory

Sponsored by:
Air Force Office of Scientific Research
Bolling Air Force Base, DC

and

Wright Laboratory

August 1994

THE COMBINATORICS OF FUNCTION DECOMPOSITION AND APPLICATIONS OF LEARNING THEORY

Christopher C. Vogt
Ph.D. Graduate Student
Computer Science and Engineering, 0114
UC San Diego
La Jolla, CA 92037
vogt@cs.ucsd.edu

Abstract

The use of function decomposition as a Machine Learning technique is explored combinatorially. Results from Computational Learning Theory are applied to get an upper bound on the minimum number of samples that function decomposition requires to accurately learn any function. This bound is exponential in the size of the function, but linear in the complexity of the function as measured by Decomposed Function Cardinality. In the process of exploration, two other discoveries are made. First, the greedy method of searching for a function decomposition currently in use by the Pattern Theory research team cannot find decompositions for a significant number of functions. Second, the assumption of a Solomonoff-Levin distribution on functions from the real world may not be as reasonable as it is believed to be, since it could lead to the conclusion that the real world is random.

THE COMBINATORICS OF FUNCTION DECOMPOSITION AND APPLICATIONS OF LEARNING THEORY

Christopher C. Vogt

1 Introduction

Pattern Theory represents a new approach to algorithm development at the crossroads of Logic Minimization and Machine Learning. When viewed in the latter framework, it makes sense to apply the results from Computational Learning Theory (COLT) to analyze the behavior of the algorithms used to implement Pattern Theory. One such algorithm, Basic Greedy Decomposition (BGD), uses a top-down recursive approach to attempt to find a minimally sized representation of a partially specified function. In this paper, BGD is analyzed combinatorially to allow application of the COLT framework with two goals in mind. First, a meaningful bound on the minimum number of samples needed to accurately learn a function is sought. Second, by carefully analyzing the search space of BGD, it is hoped that useful heuristics for limiting the size of that space can be found.

2 Background

Pattern Theory [1] approaches the problem of classification learning from a functional perspective. The problem it attempts to solve can be stated as follows: given a partially specified function $f^m(x_1, .., x_n)$ on n variables with m outputs specified, find a total function f consistent with f^m which extrapolates well. In other words, Pattern Theory attempts to fill in the missing values of f^m with values which seem likely based on the patterns in the specified values. Central to Pattern Theory are the concepts of Function Decomposition and Decomposed Function Cardinality. Function Decomposition is simply the inverse of the mathematical concept of composition, which states that it is possible to specify some functions as the composition of others. For example, the function $f(x, y, z, w)$ might be specified as $f(x, y, z, w) = g(h_1(x, y), h_2(z, w))$. This can be seen graphically in Figure 1.

Decomposed Function Cardinality (DFC) is a measure of the complexity of a function. It is based on the sum of the function cardinalities in the representation of the decomposition of the function. In the above example, if f, g, h_1, and h_2 are all functions on binary variables, then the size of f is $2^4 = 16$ since it has 4 inputs, whereas the sizes of g, h_1, and h_2 are all $2^2 = 4$ since they each have only 2 inputs. The overall size of the first representation of f (a lookup table) is 16, whereas the second, decomposed representation has a size of $4 + 4 + 4 = 12$. One can imagine that there may be a number of ways of decomposing a function. The DFC of a function is the *smallest* (in terms of the sum of function cardinalities) way of representing that function as a decomposition. Because of this bias to DFC, Pattern Theory can be viewed as embracing the concept of Occam's Razor. It has been shown [7] that DFC is a robust measure of the "patternedness" of a function over a wide variety of domains. It has also been shown that functions with a low DFC can be learned with fewer samples than ones with higher DFC, and that randomly generated functions tend to have a high DFC whereas functions taken from "the real world" mostly have low DFC.

BGD is an algorithm for finding a decomposition of a function with minimal DFC. It attempts to search the space of all decompositions of a function with smaller size than a lookup table. It uses a top-down recursive approach. Given a function $f(x_1, .., x_n)$ on n variables, it checks to see if there is a partition of the input variables (V_1, V_2, V_3) which allows the function to be represented as the composition $F(\phi_1(V_1, V_3), ..., \phi_k(V_1, V_3), V_2, V_3)$. This can be seen graphically in Figure 2.

[1] For a more complete background on Pattern Theory, see [7]

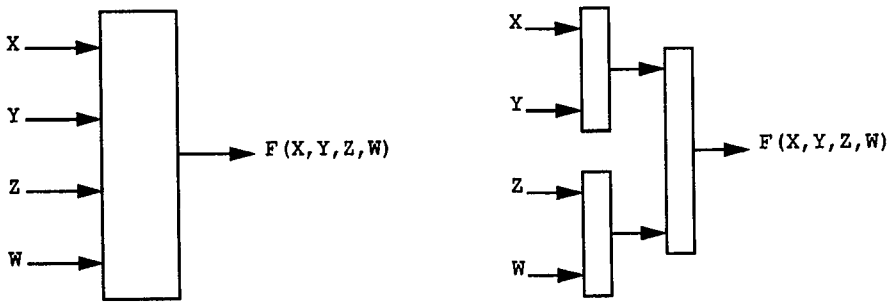


Figure 1: $f(x, y, z, w)$ and $g(h_1(x, y), h_2(z, w))$

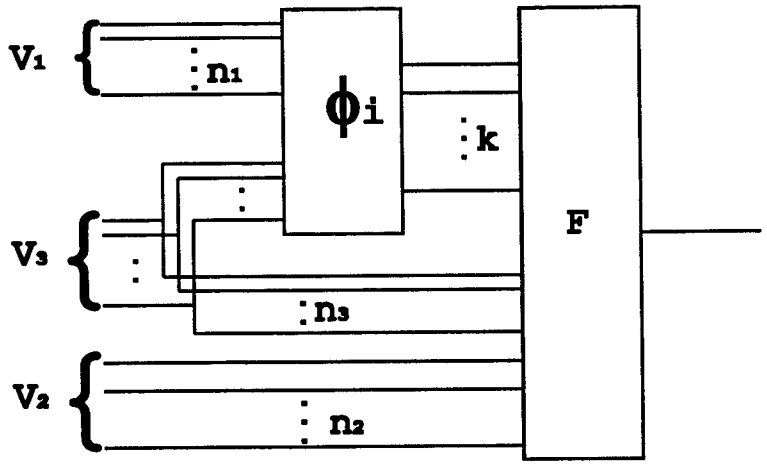


Figure 2: A Basic First Level Decomposition

BGD then recursively attempts to decompose $\phi_1, ..., \phi_k$ and F. BGD keeps track of the smallest sized decomposition seen thus far, and after exploring all possibilities, reports this decomposition as the one which has minimal DFC. As is shown later in this paper, the size of the search space for BGD is doubly exponential in the number of inputs n. For this reason, implementations of BGD, such as FLASH [6], must always use some kind of heuristic to limit the search. Thus, it is possible that the actual decomposition with minimal DFC may not be found. Furthermore, it has not been proven that this algorithm will always find the minimal decomposition even if the space is searched exhaustively. Despite these limitations, FLASH has been able to find the minimal decomposition for most functions, given enough time.

BGD can be viewed as a learning algorithm in the following sense. If the function to be decomposed is only partially specified, BGD can still decompose it. If a lookup table is then computed from the decomposition, previously unspecified outputs will then be assigned values. In this way, the originally specified outputs are viewed as *samples* of the function. They are also known as *cares*, whereas unspecified values are *don't cares*. Because BGD never changes the value of a *care*, it is a *consistent* learning algorithm. As an example, assume the partially specified binary function to be learned is $f^2(0,1) = 0$, $f^2(1,1) = 1$ [Note: the superscript 2 indicates that the function has 2 samples, namely for the input vectors (0,1) and (1,1)]. BGD would find the minimal decomposition which was consistent with the samples seen, namely $f(x,y) = x$. Now the previously unspecified outputs of (0,0) and (1,0) have values (0 and 1 respectively). This example also illustrates another important concept used in this paper, the idea of a *vacuous* variable. In this example, y is a vacuous variable because the value of the function does not depend on it in any way.

Currently, the theory and implementation of BGD are only developed for functions with binary inputs and a single binary output. Extensions to multi-valued and continuous functions are currently under development [3][5]. This paper only addresses the binary case, but in most cases results could be easily extended to the more general models.

3 BGD as a PAC Learning Algorithm

Computational learning theory (see [1], p. 30) tells us that the minimum number of samples m_0 needed by a Probably Approximately Correct (PAC) learning algorithm in order to be $(1-\delta)$ certain that a function is learned to within ϵ accuracy is given by the bound:

$$m_0 \geq \frac{1}{\epsilon} \ln \frac{|H|}{\delta} \tag{1}$$

where H is the set of all hypotheses (i.e., the set of all candidate functions). The following theorem will allow us to apply this result to BGD:
Theorem: BGD is a PAC learning algorithm.
Proof:

- The hypothesis space searched by BGD (H) is finite (see below).
- BGD is consistent (by design).

Then by Theorems 4.1.1 and 4.2.1 of [1], BGD is PAC.

Thus, if the size of H can be found, we will be able to find a meaningful bound on the minimum number of samples for PAC learning.

3.1 m_0 versus m

It is important to note that within the COLT framework, m_0 is the number of samples drawn with replacement. For BGD, we are more interested in the case where samples are taken *without* replacement,

which is exactly m. The relationship between m_0 and m can be found using probabilistic arguments as follows. View the selection of a sample as selecting a ball from an urn of N numbered balls. Suppose this is done a total of m_0 times. How many different balls can one expect to see? This is exactly m. Clearly for small m_0, $m \approx m_0$. However, as $m_0 \to \infty$, $m \to N$. In our case, $N = 2^n$, the number of samples in an n variable function. Because no closed form solution could be found to this problem, a program was written to simulate the experiment, assuming a uniform distribution of the balls in the urn. Given m_0 and N, it simulated the above experiment 100 times and output the average m. Its results were consistent with the preceding analysis. Throughout this paper, this method was used to convert m_0 bounds provided by COLT into real bounds on m for BGD.

4 Calculating $|H|$ and Bounding m

Given a partial function f^m on n non-vacuous variables with m cares, the hypothesis space that BGD considers is:

$$H = \Gamma = \{f | DFC(f) < 2^n\}$$

Where Γ is the set of all total functions on n variables with DFC less than the maximum (2^n). As noted previously, it cannot be proven that BGD considers all decompositions, but rather some subset $D \subseteq \Gamma$. D can be characterized by analyzing the behavior of BGD. Specifically, let (V_1, V_2, V_3) be a partition of the inputs of f^m, with $|V_1| = n_1$, $|V_2| = n_2$ and $|V_3| = n_3$. Furthermore, consider the first-level decomposition which consists of k functions $(\phi_1, ..., \phi_k)$ on $V_1 \cup V_3$ (with $k \geq 1$) and one function (F) on the outputs of $(\phi_1, ..., \phi_k)$ and the inputs $V_2 \cup V_3$ (see Figure 2).

Definition: A *basic first-level decomposition* is a first-level decomposition which satisfies the following constraint:

$$k2^{n_1+n_3} + 2^{k+n_2+n_3} < 2^n \tag{2}$$

Then the set $H = D = \{f | f$ has a basic first-level decomposition $\}$ includes all first level decompositions with DFC less then 2^n, and is more precisely the space of functions that BGD considers.

4.1 Bounding $|D|$

For a given n, $|D|$ can be bounded by applying the following algorithm:

For each choice of $n_1 \in [2..n-1]$:

- Choose n_1 variables to be in V_1 $\left[\begin{pmatrix} n \\ n_1 \end{pmatrix}\right]$
- For each choice of $n_3 \in [0..n-n_1]$:
  - Choose n_3 of the remaining variables to be in V_3 $\left[\begin{pmatrix} n-n_1 \\ n_3 \end{pmatrix}\right]$
  - Find the maximum[2] k which satisfies (2)
  - If such a k exists,
    - Count the total number of ways of choosing each ϕ_i $[2^{k2^{n_1+n_3}}]$
    - Count the total number of ways of choosing F $[2^{2^{k+n_1+n_3}}]$

[2] Only the maximum k need be considered, since any function that can be represented with less than k functions (ϕ_i) can also be represented with k such functions.

n	$\log_{10}\|D\|$	$\log_{10} 2^{2^n}$
4	5	5
5	9	10
6	17	19
7	35	39
8	70	77
9	138	154
10	273	308
11	544	617
12	1159	1233
13	2316	2466
14	4628	4930

Table 1: Number of BGD Decomposable Functions

The worst-case number of ways to do each step is shown in brackets after the step. Thus, the size of D is:

$$|D| \leq \sum_{n_1} \sum_{n_3} \binom{n}{n_1} \binom{n-n_1}{n_3} 2^{k2^{n_1+n_3}} \cdot 2^{2^{k+n_1+n_3}} \tag{3}$$

This is an upper bound on $|D|$ because it overcounts in the following sense. It is possible for the same function to be realizable by two different decompositions. This would happen if, by chance, all of the ϕ_i and F are associative with respect to composition.

Definition Two functions f and g are *associative* with respect to composition iff:

$$\forall X, Y \subset V : f(g(X), Y) = g(f(X), Y)$$

For example, the function "or" on two variables is associative with itself, because $(x_1 + x_2) + x_3 = x_1 + (x_2 + x_3)$.

However, since it seems likely that associativity with respect to composition is a rare occurrence, we will henceforth use the upper bound (3) as our measure of the size of D. Table 1 shows approximate values of $|D|$ for $n \in [4..14]$, with 2^{2^n} (the total number of binary functions on n variables) included as a reference.

The results from this section seem to be in conflict with Lupanov. According to Ross, et. al. [7], Lupanov's results show that for $n > 16$, most functions decompose at least a little. When $|D|$ is calculated using (3), the fraction of decomposable functions to the total number of functions $\left(\frac{|D|}{2^{2^n}}\right)$ is exponentially decreasing - clearly not "most!" This implies that the top-down approach of BGD misses a significant number of decompositions, especially for functions with a large number of variables. Thus, for some functions BGD cannot find the decomposition with the actual DFC of f^m. This will be important later on in this paper, when BGD is examined as an Occam algorithm.

4.2 Finding Minimum m Based on $|D|$

Substituting $|D|$ into (1) yields:

$$m_0 \geq \frac{1}{\epsilon} \ln \frac{|D|}{\delta} \tag{4}$$

Values for m_0 are shown in Table 2 for $\epsilon = \delta = 0.1$. Again, for comparison, m_0 is also shown for the worst case, when all functions on n variables are considered as hypotheses. In this case, $|H| = 2^{2^n}$, and

n	m_0 for D	m_0 worst	m for D	m worst	Max # samples
4	130	134	16	16	16
5	229	245	32	32	32
6	409	467	64	64	64
7	835	911	128	128	128
8	1634	1798	256	256	256
9	3202	3572	511	512	512
10	6320	7121	1022	1023	1024
11	12543	14219	2044	2046	2048
12	26702	28415	4090	4092	4096
13	53345	56806	8181	8184	8192
14	106598	113589	16360	16368	16384

Table 2: Bounds on m_0 and m for D and worst case, with $\epsilon = \delta = 0.1$

ϵ	δ	Actual m	Theory m	Theory m_0
.3	.3	125	225	541
.2	.2	175	246	814
.1	.1	225	256	1634
.1	.3	225	256	1623
0	0	256	256	∞

Table 3: Experimental versus Theoretical m for *pal-outp*

(1) becomes:

$$m \geq \frac{2^n \ln 2 - \ln \delta}{\epsilon}$$

Also for comparison, the maximum number of samples possible is shown. What this table tells us is that even though using D as our hypothesis space improves the bound on m_0, the bound itself is virtually useless, since in all cases it tells us we have to see more samples than is possible! However, when m is estimated from m_0 using the technique described in section 3.1, we find that it closely tracks the maximum number of samples. As n increases, m is no longer maximum due to the values of ϵ and δ. Furthermore, the difference between the worst case and that for BGD becomes larger with increasing n.

4.3 Comparing Theoretical m to Experimental Values

Table 3 compares the bound provided by (4) with experimental values of m. A number of 8-variable functions were decomposed using FLASH with various values for ϵ and δ (see [8]). The highest value for m was taken from among these functions. This happened to always be for the function *pal-outp*, a function whose output is a palindrome with the first half randomly generated. This table compares these values to the ones from (4), and verifies the equation as an upper bound. (NOTE: experimental values for m were only tested at multiples of 25, so the actual m might be smaller).

A close examination of the other functions tested in [8] shows that ones with lower DFC consistently have lower bounds on m. Perhaps a better formulation of the bound would also be in terms of the DFC of f^m.

5 BGD as an Occam Algorithm

Occam learning algorithms are roughly ones which embrace Occam's Razor: the simplest hypothesis which takes into account all examples is the best one. Intuitively, BGD should be Occam, since its goal is to minimize complexity in terms of DFC. If we can prove BGD Occam, then some basic COLT results will allow us to say something about the minimum sample size as a function of DFC. Before formally defining what it means to be Occam, we must first cover a few other definitions (taken from Anthony and Biggs [1]).

Definition: A *representation* is a surjective mapping from some set Ω to the hypothesis space H. For example, for BGD, Ω={all decompositions found by BGD}. The mapping takes a decomposition and maps it to the function it represents. This is clearly a surjection, since many decompositions may map to the same function, and only those functions with a BGD decomposition are considered as hypotheses.

Definition: A hypothesis space H is *graded by representation size* if $H = \cup H_r$, and $H_r = \{h|h$ has a minimal representation of size $r\}$. For BGD, the hypothesis space D can be graded by DFC, so that $D_d = \{f|DFC(f) = d\}$. Furthermore, any hypothesis $h \in H$ is usually specified by its minimal representation in Ω and denoted h_ω.

Definition: An algorithm L is *Occam* with respect to a representation $\Omega \rightarrow H$ if:

- L is consistent
- given a training set of length m for a target $t \in H_r$, the output hypothesis h_ω is such that $||\omega|| \leq m^\alpha r^\beta$ where $0 < \alpha < 1$ and $\beta \geq 1$ are constants.

One of the most important results for Occam algorithms states that, if an algorithm is Occam, we can bound m_0 as:

$$m_0 \geq \left(\frac{r^\beta \ln 2 + \ln \frac{2}{\delta}}{\epsilon} \right)^{\frac{1}{(1-\alpha)}} \tag{5}$$

In other words, the number of samples is $O(r^{\frac{\beta}{1-\alpha}})$ for given ϵ and δ.

Imagine for now a new algorithm similar to BGD, but which always finds the best DFC. Call this algorithm BGD'. BGD' is Occam, since it is consistent and $||\omega|| = r = DFC(f^m)$. This last statement can be made because BGD' always finds a representation of size $DFC(f^m)$. Note that in this case, we take $\beta = 1$ and $\alpha \rightarrow 0$, and (5) becomes:

$$m_0 \geq \frac{DFC(f^m) \ln 2 + \ln \frac{2}{\delta}}{\epsilon} \tag{6}$$

Unfortunately, BGD does not have the property that it always finds the smallest representation. However, if we could somehow bound the actual representation size that BGD does find as a polynomial in $DFC(f^m)$, we could state that the minimum number of samples was also a polynomial of the same order.

In practice, without any restrictions on the search space of decompositions, BGD almost always finds a decomposition of size $DFC(f^m)$, or one which is very close. Thus it seems likely that BGD *is* Occam, and that $\beta \rightarrow 1$ and $\alpha \rightarrow 0$. Thus, (6) will most probably apply to BGD. Table 4 shows values for m_0 if we make these assumptions.

Of course, in order to make these numbers make sense, we have to convert them to a value of m using section 3.1. This means we must assume some value of n. Table 5 shows m for various n and DFC. It verifies that for a fixed n, m is roughly linear in DFC, as predicted by (6). It also shows that for fixed DFC, m appears to approach a limit as n increases.

We can now compare these theoretical bounds to experimental ones from [8]. Table 6 shows these comparisons and verifies the theoretical values as (poor) upper bounds.

DFC	m_0
4	58
8	86
16	141
32	252
64	474
128	918
256	1805
512	3579
1024	7128
2048	14226
4096	28422

Table 4: m_0 for any function based on DFC ($\epsilon = \delta = 0.1$)

$n \rightarrow$	4	5	6	7	8	9	10	11	12	13	14
$DFC \downarrow, 2^n \rightarrow$	16	32	64	128	256	512	1024	2048	4096	8192	16384
4	16	27	38	47	52	55	56	57	57	58	58
8	16	30	47	63	73	79	82	84	85	86	86
16	-	32	57	86	108	123	132	136	139	140	140
32	-	-	63	111	161	198	223	237	245	248	250
64	-	-	-	125	216	308	381	424	448	460	467
128	-	-	-	-	249	427	607	739	823	869	893
256	-	-	-	-	-	497	850	1200	1462	1620	1710
512	-	-	-	-	-	-	993	1692	2386	2901	3214
1024	-	-	-	-	-	-	-	1985	3376	4757	5777
2048	-	-	-	-	-	-	-	-	3968	6746	9510
4096	-	-	-	-	-	-	-	-	-	7936	13487

Table 5: m as a function of n and $DFC(f^m)$ ($\epsilon = \delta = 0.1$)

Function	DFC	Exp m	Theory m
kdd1	8	25	73
kdd3	16	50	108
add0	48	75	$\approx$187
mux8	64	100	216
pal-dbl	128	175	249

Table 6: Experimental and Theoretical m for various functions

6 Characterizing the Space of DFC, Δ

Given that the learnability of a function is based on its DFC, an interesting question is: How are DFC's distributed in the real world? First, we define DFC as a random variable which maps a function onto its DFC. Thus, if the space of all functions is $\mathcal{F}$ and the space of all DFC is Δ, we have $DFC : \mathcal{F} \mapsto \Delta$. By definition, the probability of a particular DFC, d is:

$$P[DFC = d] = \sum_{f \in \mathcal{F}: DFC(f) = d} P[f]$$

In order to calculate this value, we need to be able to do two things: count the number of all functions with a particular DFC, D_d, and estimate the probability of choosing a function from the real world.

In order to characterize $|D_d|$ for any d, let $d_{max} = 2^n - 4$ be the maximum DFC less than 2^n, since DFC is always a multiple of 4 [7]. Then from Table 1 we note that:

$$|D| \leq 2^{d_{max}}$$

Furthermore, since:

$$|D| = |D_{d_{max}}| + \ldots + |D_{4(n-1)}|$$

and we know from experiments that $|D_d|$ is exponential in d, we can say that

$$|D| \approx |D_{d_{max}}|$$

Thus,

$$|D_{d_{max}}| \leq 2^{d_{max}}$$

Furthermore, it can be shown that

$$B_n = |D_{d_{min}}| \geq 2^{d_{min}}.$$

Where B_n is the number of disjunctive functions on n variables. A disjunctive function is defined by Butler [2] as: each input used only once, all subfunctions have two inputs. It can be shown that the set of all disjunctive functions is precisely $D_{4(n-1)}$ - the set of all functions with the minimal possible DFC (assuming no vacuous variables).

Thus, a reasonable guess is that:

$$|D_d| \approx 2^d \tag{7}$$

It is noted that this approximation is consistent with the experimental data from [7].

For the probability of a function, one seemingly reasonable assumption is that $P[f^m] = 2^{-L(e(f^m))}$, inspired by the Solomonoff-Levin distribution [4], where e is an encoding of the function, and L is the length of that encoding. This states that simpler functions are much more likely as candidates for a learning algorithm than complex ones, and this relationship is exponentially decreasing. When applying this to Pattern Theory, it is reasonable to assume that $L(e(f)) \approx DFC(f)$, so $P[DFC(f^m) = d] = 2^{-d}$.

Therefore, the probability of getting a particular DFC when choosing a function from the "real world" is:

$$P[DFC = d] = \frac{2^d}{2^d} = 1 \tag{8}$$

Of course, this is impossible, and probably reflects the fact that we are using many assumptions and approximations. However, it still seems to imply that the probability is independent of d. This means that the space of DFC, Δ, is uniformly distributed, and we can calculate its expected value as:

$$E[DFC] = \frac{2^n}{2} = 2^{n-1} \tag{9}$$

The implications of (8) and (9) are important to consider. They state that DFC's are uniformly distributed amongst real world problems. In other words, given a function from "the real world," the

chances of it having high DFC are equal to those of it having low DFC. This means that the real world is basically random! This conclusion is certainly counter-intuitive and deserves further investigation. Perhaps the assumption of a Solomonoff-Levin distribution is not as reasonable as it seems. Or, perhaps (8) is actually a function of n and/or d, in which case the conclusion that Δ is uniform would not be valid.

7 Characterizing the Search Space

The preceding analysis is interesting and gives meaningful bounds, but can we do better? We can use a similar analysis to carefully characterize the size of the actual search space of decompositions that BGD explores, S_{fm}. This is an upper bound on the size of the hypothesis space, since the number of functions that BGD considers cannot be more than the number of distinct decompositions. We count $|S_{fm}|$ by mimicking the behavior of BGD as follows [3]:

For each choice of $n_1 \in [2..n-1]$:

- Choose n_1 variables to be in V_1 $\left[\left(\begin{array}{c} n \\ n_1 \end{array}\right)\right]$
- For each choice of $n_3 \in [0..n-n_1]$:
  - Choose n_3 of the remaining variables to be in V_3 $\left[\left(\begin{array}{c} n-n_1 \\ n_3 \end{array}\right)\right]$
  - Find the maximum k which satisfies (2)
  - If such a k exists,
    - Create the partition matrix
    - Decide which columns in the partition matrix to combine (the graph-coloring problem) [$\gamma(2^{n_1+n_3})$, see below]
    - Count the total number of ways of encoding the labels for the columns [$\sigma(k, 2^k)$, see below]
    - Possibly decompose each ϕ_i and F [$\sum |S_{\phi_i}|$ and $|S_F|$]

Thus, the size of S_{fm} is bounded as follows:

$$|S_{fm}| \leq \sum_{n_1} \sum_{n_3} \left(\begin{array}{c} n \\ n_1 \end{array}\right) \left(\begin{array}{c} n-n_1 \\ n_3 \end{array}\right) \gamma(2^{n_1+n_3}) \cdot \sigma(k, 2^k) \cdot |S_F| \cdot \sum_{i=1}^{k} |S_{\phi_i}|$$

or, if we assume the size of the search space is the same for all ϕ_i, we have:

$$|S_{fm}| \leq \sum_{n_1} \sum_{n_3} \left(\begin{array}{c} n \\ n_1 \end{array}\right) \left(\begin{array}{c} n-n_1 \\ n_3 \end{array}\right) \gamma(2^{n_1+n_3}) \cdot \sigma(k, 2^k) \cdot |S_F| \cdot k|S_\phi| \qquad (10)$$

7.1 Counting Graph Colorings

To count the number of different ways a graph with V vertices can be colored, we first restrict ourselves to looking at the case where we know the chromatic number of the graph, κ. With this fixed, we must then decide how many ways we can partition the nodes so that each one gets one of the κ colors. This is equivalent to determining the number of sets of size κ of natural numbers less than V whose elements sum to V. For example, when $V = 7$ and $\kappa = 4$, we have:

[3] The following arguments assume some familiarity with the details of BGD. See [7] for these details.

$$\{1,1,1,4\}$$
$$\{1,1,2,3\}$$
$$\{1,2,2,2\}$$

Call this set of sets $P_{V,\kappa}$. For each $p \in P_{V,\kappa}$, we must choose nodes to be in each of the sets. Counting the number of ways to do this is simple, and for the above example, the answers are:

$$\binom{7}{4}$$
$$\binom{7}{3} \cdot \binom{4}{2}$$
$$\binom{7}{2} \cdot \binom{5}{2} \cdot \binom{3}{2}$$

respectively. If we represent each of these numbers as $C(p)$, then the number of ways of coloring a graph is:

$$\gamma(V) \leq \sum_{\kappa=1}^{V} \sum_{p \in P_{V,\kappa}} C(p) \tag{11}$$

This is certainly a worst-case upper bound because it basically assumes that there are no edges in the graph (i.e., all columns are compatible), which only happens when the column variables are vacuous or when there are mostly don't cares.

7.2 Counting Encodings

The encoding problem can be phrased as follows: Given a $y \times x$ matrix, fill it with 0's and 1's in such a way that the columns are unique. We wish to know how many ways this is possible. We proceed recursively:

1. Choose a number of elements (i) in the first row to be ones, and make the rest zeroes $\left[\binom{x}{i}\right]$
2. Create two submatrices from the remaining rows in the matrix, one consisting of all columns where the first row has a one, and one of columns where the first row has a zero
3. Recursively solve the problem on the remaining submatrices of size $(y-1) \times (x-i)$ and $(y-1) \times i$

In this way, we obtain a formula for $\sigma(y, x)$:

$$\sigma(y,x) = \sum_{i=1}^{x-1} \binom{x}{i} \sigma(y-1, x-i) \cdot \sigma(y-1, i) \tag{12}$$

And in our particular case, $x = \nu = 2^k$ (the maximum column multiplicity) and $y = k$ (the number of new functions ϕ_i).

It can be shown[4] that a closed form of (12) exists, and is actually

$$\sigma(y,x) = (x)_y = \frac{x!}{(x-y)!} \tag{13}$$

[4] This result due to Mark Axtell

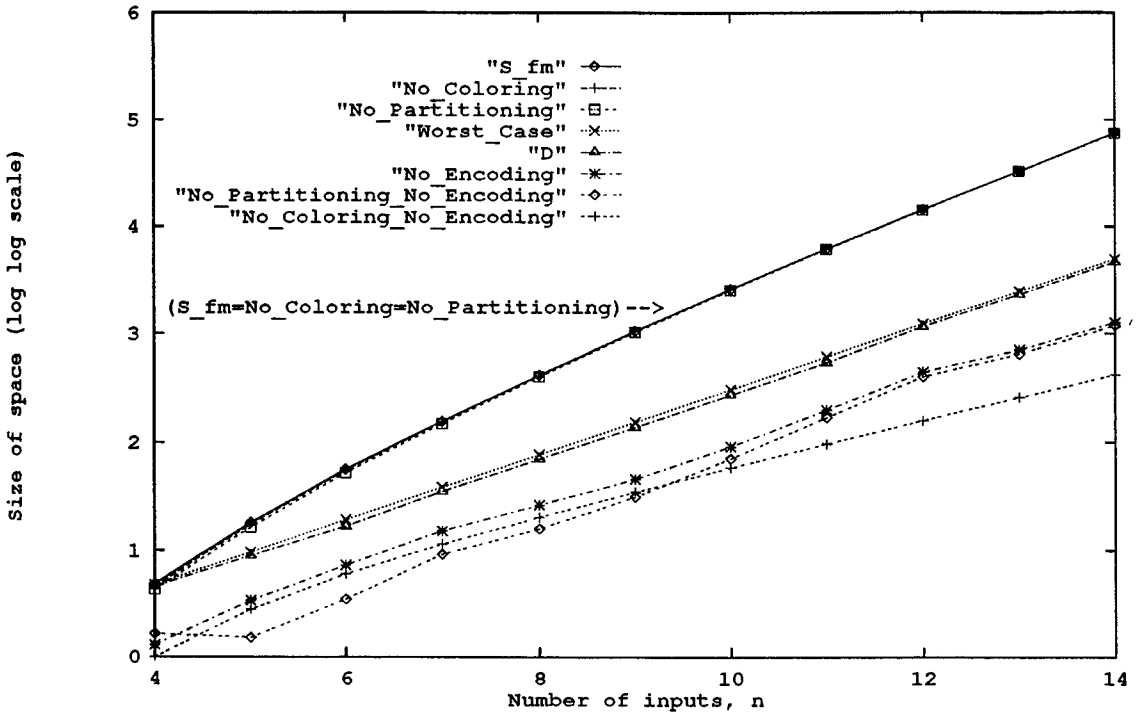


Figure 3: Size of BGD Search Space as a function of n

7.3 Calculating $|S_{fm}|$ and the Contributions of Subproblems

A program was written to calculate $|S_{fm}|$ for $n \in [4..14]$ using (10). Figure 3 shows its value on a doubly logarithmic scale as a function of n. As reference lines, 2^{2^n} and $|D|$ are shown. These represent worst-case values - namely, when all functions on n variables are considered as hypotheses and when all decomposable functions are considered, respectively. The graph shows that the bound provided by (10) is not very useful since it is much greater than both worst cases!

The three non-recursive parts of equation (10) correspond to a different parts of the BGD algorithm, namely partitioning, coloring, and encoding. By holding each factor constant, the effect of having a constant time algorithm for solving that part of the algorithm can be examined. To determine the contributions of each factor of (10), the program was modified to hold each one constant. The results are also plotted in Figure 3. The only change which significantly affects the shape of the $|S_{fm}|$ curve is when $\sigma(k, 2^k)$ is constant, i.e., when the encoding problem is solved in constant time.

These results suggest that it is imperative that the encoding algorithm be extremely efficient if BGD is to be implemented. Furthermore, close examination of the partition selection problem (assuming that encoding is solved) shows that as n grows, selecting a partition contributes less to the overall size of S_{fm}. It therefore seems that partition selection is not of critical importance. The current implementation of BGD, FLASH, is so successful in part due to its greedy selection of an encoding and coloring. It must be noted, however, that this analysis is based on *worst case upper bounds*. The entire dynamics of (10) could change dramatically if more realistic functions were used for γ and σ.

V	m	d	ν
max=2^{n-1}	max=2^n	variable	Assume average case is linear in d
max=2^{n-1}	variable	max=2^n	For $m < 2^{n_1+n_2+2n_3-1}$, linear in m, else V
variable	max=2^n	max=2^n	$\min(2^{2^{n_2+n_3}}, 2^{n_1+n_3})$

Table 7: ν as a function of V, m, and $DFC(f^m)$

7.4 Tightening the Bound on $|S_{f^m}|$

When we calculate $|S_{f^m}|$, we find it to be much larger than the total number of functions on n variables, 2^{2^n}. Clearly, we are either overcounting, or BGD considers the same function as a hypothesis multiple times. Assuming the former, one way to tighten the bound is to take into account the function being decomposed. This will affect the size of both $\gamma(x)$ and $\sigma(y, x)$, but not the number of partitions.

The easiest way to limit $\gamma(x)$ is to realize that in actuality, it is a function of the graph to be colored, which in turn is a function of the partition and f^m. Since we are attempting this analysis for the general case, we need to be able to characterize this in terms of some aspects of the graph which we can compute. The most likely candidates are V, E, and κ – the number of vertices, edges, and the chromatic number. If we limit ourselves to the first and last, we already know the answer, it is just a simplification of (11), namely:

$$\gamma(V, \kappa) \leq \sum_{p \in P_{V,\kappa}} C(p) \tag{14}$$

Furthermore, we note that κ is in actuality the column multiplicity of the partition matrix, ν. It is actually a function of V and E, and E is a function of V, m, and $DFC(f^m)$. So, κ is a function: $\kappa = \nu(V, m, d)$. Upon close inspection, one notes that if any one of the inputs to ν is small, so is ν. In fact, we can expect it to be 1 or 2. Table 7 shows a guess at what happens if we hold each possible pair of variables fixed at its maximum and vary the remaining variable.

Each of these cases provides an upper bound on ν, so if we take the maximum of these, we have a worst-case estimate for ν, namely:

$$\nu(V, m, d) = \max \begin{cases} \frac{V-2}{2^n-4} d + 2 - \frac{4(V-2)}{2^n-4} \\ \min(V, \frac{m(V-1)}{2^{n_1+n_2+2n_3-1}} + 1) \\ \min(2^{2^{n_2+n_3}}, 2^{n_1+n_3}) \end{cases}$$

To bound $\sigma(y, x)$ more tightly, all we need to do is note that the second parameter to σ is actually κ, and not 2^k.

Therefore, assuming these revisions to γ and σ, (10) becomes:

$$|S_{f^m,d}| \leq \sum_{n_1} \sum_{n_3} \binom{n}{n_1} \binom{n-n_1}{n_3} \gamma(2^{n_1+n_3}, \kappa) \cdot \sigma(k, \kappa) \cdot |S_{F^{\hat{m}}, d_F}| \cdot k |S_{\phi_i^{2^{n_1+n_3}}, d_{\phi_i}}| \tag{15}$$

where

$$\kappa = \nu(2^{n_1+n_3}, m, d)$$

This revision introduces an explicit dependence on both m and d. If we wish to continue in this vein, we must be able to estimate $\hat{m}$, the number of cares in F, and d_F, d_{ϕ_i}, the DFC's of the component functions. If $\nu = 2^k$, then the only cares will come from the partition matrix, and there can be at most $\nu 2^{n_2+n_3}$ of these. If $\nu < 2^k$, though, there will be $2^{n_2+n_3}$ don't cares (one for each row in the partition

matrix) added for each of the "missing" $2^k - \nu$ columns. Thus, there will be $2^{n_2+n_3} - (2^k - \nu)2^{n_2+n_3}$ cares. Thus, the number of cares in F will be

$$\hat{m} \leq 2^{n_2+n_3} \cdot (1 + \nu - 2^k) + \nu 2^{n_2+n_3}$$

The worst case values for each DFC would be when all other DFC's were minimal, which gives us:

$$d_F \leq d - 4k(n_1 + n_3 - 1)$$

and

$$d_{\phi_i} \leq d - 4(k + n_2 + n_3 - 1) + 4(k-1)(n_1 + n_3 - 1))$$

Unfortunately, in practice, the equation for ν given above always yields a $\nu > 2^k$, due to its worst-case assumptions. This means that this value should not be used when computing σ or γ because if it were the case that $\nu > 2^k$, BGD would not even consider the decomposition. Thus, equations (10) and (15) differ only in their recursive terms.

Also, unfortunately, values of $|S_{fm}|$ could not be recomputed using (15) due to the time constraints of this project.

8 Conclusions and Future Work

The main conclusions of this paper can be summarized as follows:

- The hypothesis space of BGD, D, is significantly smaller than the set of all functions. Furthermore, since for $n > 16$, almost all functions decompose, it must be that BGD misses a large number of these functions.
- The minimum number of samples that BGD requires to learn a function is exponential in the number of inputs (see Table 2), and only slightly better than the worst case.
- The minimum number of samples that BGD requires to learn a function depends heavily on the DFC of that function. For a given DFC, the number of samples needed appears to approach a limit as the number of inputs increases. For a given number of inputs, the number of samples is roughly linear in the DFC. (See Table 5)
- The previous two results are consistent with experimental results, but only provide loose upper bounds on the number of samples. (Tables 3 and 6)
- The space of DFC appears to be uniformly distributed amongst real world problems, assuming a Solomonoff-Levin distribution.
- In the worst case, the order of importance (from most to least) of the different subproblems solved by BGD is: encoding, coloring, partitioning.

Of all of these conclusions, the last two are most suspect. Future work could focus on more rigorously proving (or disproving) the uniformity of Δ. Also, a lot more can be done in terms of combinatorially exploring S_{fm}.

9 Acknowledgements

The author wishes to thank the entire Pattern Theory team at WL/AART-2, especially Tim Ross and David Gadd, for their insight and suggestions. He also wishes to thank the Air Force Office of Scientific Research for providing the opportunity and support to do this research.

References

[1] Martin Anthony and Norman Biggs. *Computational Learning Theory.* Cambridge University Press, Cambridge, England, 1992. WL Lib, Q325.5 .A58 1992.

[2] Jon T. Butler. On the number of functions realized by cascades and disjunctive networks. *IEEE Transactions on Computers*, C-24(7):681–690, July 1975.

[3] K. Y. Fang and A. S. Wojcik. Modular decomposition of combinational multiple-valued circuits. *IEEE Transactions on Computers*, 37, 1988.

[4] Ming Li and Paul M. B. Vitányi. Kolmogorov complexity and its applications. In Jan Van Leeuwen, editor, *Handbook of Theoretical Computer Science*, volume A, chapter 4, pages 189–254. The MIT Press, Cambridge, Massachusetts, 1990.

[5] Timothy D. Ross, Jeffrey A. Goldman, David A. Gadd, Michael J. Noviskey, and Mark L. Axtell. On the decomposition of real-valued functions. In *Third International Workshop on Post-Binary ULSI Systems in affiliation with the Twenty-Fourth International Symposium on Multiple-Valued Logic*, 1994.

[6] Timothy D. Ross, Michael J. Noviskey, Mark L. Axtell, and David A. Gadd. FLASH software description. Technical report, Wright Laboratory, USAF, WL/AART, WPAFB, OH 45433-6543, 1994.

[7] Timothy D. Ross, Michael J. Noviskey, Timothy N. Taylor, and David A. Gadd. Pattern theory: An engineering paradigm for algorithm design. Final Technical Report WL-TR-91-1060, Wright Laboratory, USAF, WL/AART, WPAFB, OH 45433-6543, August 1991.

[8] Scott E. Sadowski. PAC versus area methods of determining learnability. Final report, AFOSR High School Apprenticeship Program, August 1994.

DOCUMENTATION OF BOUNDARY LAYER CHARACTERISTICS FOR LOW CHORD-REYNOLDS-NUMBER FLOW ON THE SUCTION SURFACE OF A LOW-PRESSURE TURBINE AIRFOIL

Terry W. Simon
Professor
and
Ralph Volino
Graduate Student
Department of Mechanical Engineering

University of Minnesota
111 Church St. S. E.
Minneapolis, MN 55455

Final Report for:
Summer Faculty Research Program
Graduate Student Research Program
Wright Laboratory
Wright-Patterson AFB

Sponsored by:
Air Force Office of Scientific Research
Bolling Air Force Base, DC

and

Wright Laboratory

September 1994

DOCUMENTATION OF BOUNDARY LAYER CHARACTERISTICS FOR LOW CHORD-REYNOLDS-NUMBER FLOW ON THE SUCTION SURFACE OF A LOW-PRESSURE TURBINE AIRFOIL

Terry W. Simon, Professor
Ralph Volino, Graduate Student
Department of Mechanical Engineering
University of Minnesota

Abstract

It is recognized that the low-pressure turbine has, because of its low chord Reynolds number, regions of strong acceleration and diffusion effects. Consequently, there are extended regions of transition from laminar to turbulent flow and there is a strong likelihood of having regions of flow separation. To investigate this low-Reynolds number flow, a program was initiated where a representative low-pressure turbine airfoil configuration is installed in a wind tunnel facility and run at chord Reynolds numbers of 40,000 and 80,000. High background turbulence and disturbances from passing wakes are imposed upon the flow to simulate the turbine environment. The boundary layer state, laminar-like or turbulent, separated or attached, is characterized for representative operating conditions. Instrumentation includes hot-wire anemometry and surface-mounted thin film sensors. When without wake passing disturbances, surface static pressure taps are used to document surface static pressure coefficient, Cp, distributions. With background turbulence present but without wakes, cases are run for TI levels of 1.0 and 20 % for chord Reynolds numbers of 40,000 and 80,000. These cases are repeated with wake generation at representative blade velocities. For documenting the approach flow, turbulence spectra and turbulence intensities are taken for the various TI levels and Re_c values with and without wake generation. From this, the integral length scales are computed. Measurements within the cascade include, on the suction surface, the transition location, the separation location, and the point of reattachment. Instruments for locating these regions are surface-mounted thin-film gages and a hot-wire sensor positioned very near the wall at various streamwise locations. To document the statistical quantities when operating with wake generation, rms fluctuation levels of an ensemble of records are taken behind the wakes and between the airfoils. They are encoded off the translation device and plotted versus t/τ (the dimensionless time within the wake passing period). These data are used to characterize the unsteadiness.

List of Symbols

Symbol	Definition (units)
Lower-case symbols:	
f	Wake passing frequency (Hz).
s	Streamwise distance.
t	Time (sec).
u'	Fluctuation component of streamwise velocity (m/sec).
w'	Fluctuation component of cross-span velocity (m/sec).
Upper-case symbols:	
C	Chord length of the airfoil (m).
C_p	Static pressure coefficients, $(P - P_{static,1})/(P_{tot} - P_{static,1})$.
K	Acceleration parameter, $\nu/U_\infty^2 \, dU_\infty/ds$.
P	Pressure (kPa).
Re_c	Chord Reynolds number, $V_2 C/\nu$.
S	Dimensionless wake passing frequency, Strouhal number, $2\pi fC/V_1$.
TI	Turbulence intensity, $\sqrt{\overline{(u')^2}}/U$, $\sqrt{\dfrac{\overline{(u')^2 + 2(v')^2}}{3}}\Big/U$, or $\sqrt{\dfrac{\overline{(u')^2 + (v')^2 + (w')^2}}{3}}\Big/U$.
U	Mean streamwise velocity (m/sec).
V	Flow velocity (m/sec).
Lower-case Greek symbols:	
τ	The wake-passing period (sec).
ν	Kinetic viscosity (m^2/sec).
Subscripts	
∞	at the edge of the boundary layer
static	static, or thermodynamic, value
tot	total, of stagnation, value
1	in the plenum upstream of the airfoil row
2	in the plenum downstream of the airfoil row

DOCUMENTATION OF BOUNDARY LAYER CHARACTERISTICS FOR LOW CHORD-REYNOLDS-NUMBER FLOW ON THE SUCTION SURFACE OF A LOW-PRESSURE TURBINE AIRFOIL

Terry W. Simon
Ralph Volino

Introduction

Compressor and turbine design models have been moderately successful in predicting losses and heat transfer rates in the high-pressure components of the gas turbine where chord Reynolds numbers are large and separation and transition regions are small. When applied to low chord Reynolds number flows, these models fail to match experimental data and often fail to converge. Being able to predict transition at low Reynolds number operation is important for the design of some components of the gas turbine engine. For instance, in the low pressure turbine where designs are aft-loaded, 90% of the blade suction surface can be covered with transitional boundary layer flow (Mayle, 1991). When the chord Reynolds number on an airfoil is decreased, the flow acceleration effect on the boundary layer rises in magnitude and the boundary layer is more likely to separate. An approximate onset of separation Re_c value is 400,000, as given on Fig. 1 which was taken from Sharma, Ni, and Tanrikut (1994). Elevated free-stream turbulence, would reduce the separation Reynolds number. The effects of disturbances due to wakes generated by upstream airfoil rows on this separation Reynolds are more uncertain. Wakes tend to increase the turbulence level (not always, but in general) and they change the momentary angle of attack to off-design angles, favoring increased separation on the suction surface, if the flow were behaving in a quasi static manner. Under high-frequency oscillation of the flow due to passing wakes, the effects are not certain. Needed are transient measurements of the boundary layer flow over the downstream portions of the suction surface, ensemble-averaged on the wake passage event. Such measurements provide information about the state of the boundary layer and the receptivity of the boundary layer to external disturbances, including those from the passing wakes. Possible wake generators may be cylinders, representing wake turbulence with large-scale turbulence, thin plates oriented parallel to the flow so that the wake is decaying boundary layer turbulence which consists of mostly small-scale turbulence, or actual airfoils. Comparisons of measurements in cascades and rotating rigs indicate that losses and heat loads are higher in the unsteady flow than in steady flow (Sharma et al., 1994, Hodson, 1983, Blair et al., 1988, Doorley et al., and Sharma et al. 1990). Sharma et al., 1994 proposed scaling on a relative time scale to capture this effect. The appropriate ratio is the wake passage period divided by the transit period for fluid

flow through the airfoil row. Cases of similar values of this ratio display similar augmentation due to unsteadiness. Such scaling is applied in the present study. Operation at low Reynolds numbers would create separation zones allowing a study of the effect of the wakes on the incipience to the separation process, on the free-shear layer transition length, and on the separation bubble length. Under low-Reynolds-number conditions, upstream wakes can result in smaller separation zones and lower losses relative to steady slow. Presently, no model has been developed to capture this effect (Sharma et al., 1994). Thus, wake effects on the separated flow must be included for a low-Reynolds number study to be accurate and complete. Hot-wire anemometry measurements can be made in the free-shear layers over the separation bubbles without affecting the flow. Measurements within the separated flow zone are difficult, but possible, and needed. With these measurements, one could assess whether the change in incidence angle during the wake passing event is of importance or whether the main wake-related effect is the turbulence washing over the boundary layer and free-shear-layer flows. Thus, careful documentation of the turbulence and wake disturbance effects is needed in support of design model development.

Objectives

The objectives of this program are to determine the transition and separation zone locations for a particular low-pressure airfoil under representative conditions, including an assessment of the effects of free-stream turbulence and of wake passings on the locations of these zones. A secondary objective is to document the pre-separation boundary layer receptivity to external disturbances and the instability of the free-shear layer over the separation zone. In doing so, the cases of Table 1 are investigated, the transition and separation zones for each are located, and measurements are taken in the pre-separation boundary layer and in the separation zone. For cases with wakes, this documentation is given for various times within the wake passing period.

Method

First, the wake generator and the turbulence generation equipment are taken out of the flow and the entry flow is documented for Cases 1 and 3. Documentation is by measuring the transverse uniformity of mean velocity and turbulence intensity (based upon the streamwise component of velocity only) then characterizing the turbulence with single-velocity-component power spectral density distributions and the isotropy of the flow with measurements of the streamwise and cross-span components of turbulence intensity on a streamline which passes though the center of the cascade. Once the turbulence is characterized, the static pressure coefficient distribution on the surface of the blade is documented and the locations of critical points related

to transition and separation are found for the two cases. Next, the turbulence generator is activated and the above measurements are repeated (Cases 2 and 4). When this is complete, the wake generator is activated and Cases 5 through 8 are documented. These cases require a somewhat different measurement program. The single-component power spectral density distribution is taken downstream of the wake generator and within the center of the cascade channel. Single-component turbulence intensity measurements are time resolved according to the fraction of the wake-passing period; values of RMS fluctuation values from an ensemble of 50 records are taken. Time resolution for these readings is 1/100 of a passing period. Next, the unsteady locations of critical points regarding transition and separation are located for various times within a wake-passing period, again with the 1/100 period resolution and with a spatial resolution of about 2.5 mm (0.10 inch). This test program is outlined in Table 2. The separate effects of Reynolds number, turbulence intensity, and wake passage disturbances are assessed by comparing these 8 data sets.

Experimental Apparatus

Cascade Facility

The experiments are conducted in the AFIT cascade facility. This wind tunnel is driven with a Buffalo Forge Model No. BL-365 centrifugal blower operating in the suction mode. Flow velocity control is with an Allen-Bradley Model No. 1336S motor controller, with inlet dampers on the fan, and with a bypass vent on the ductwork between the test section and the fan. A schematic of the wind tunnel layout is given at Fig. 2. The cascade consists of four geometrically identical blades of chord length 11.4 cm (4.5 inches).

Turbulence Generator

Upstream of the cascade is a turbulence generation device which consists of a passive square grid of 13 mm by 13 mm (0.5 inch by 0.5 inch) square bars arranged with a 25.4 mm (1.0 inch) center-to-center spacing. This resides 1.5 m (57 inches) upstream of the cascade row. A distance of 0.6 m (24 inches) downstream of the passive grid is an active jet grid with 3 tubes with 6 blowing holes each distributed and oriented as shown in Fig. 3. The passive grid/jet grid arrangement is a replica of one described by Sahm and Moffat, 1992.

Wake Generator

At a distance of 7.6 cm upstream of the leading edge of the cascade row is a series of 6 cylinders which are traversed across the tunnel cross-section in the transverse direction. These cylinders simulate the wakes that are generated by the airfoil row which resides just upstream of the airfoil row of interest in an actual turbine. The cylinders which simulate the wakes in

the facility are 9.5 mm (0.375 inch) in diameter and are separated by the same transverse spacing as that of the airfoils, 91.7 mm (3.611 inches). These cylinders are driven by a device which is capable of translating them at selected velocities from 0.5 m/sec to as high as 5.5 m/sec. The total translation distance is 43 cm (17 inches) and it is estimated that about 6.5 cm (2.5 inches) each is required for acceleration and deceleration phases of the translation. Early tests with the translation driver, alone, indicate that over the central 30 cm (12 inches) of travel, the velocity is uniform to within 6% of the nominal velocity at the low end of the velocity range and within 1.5% at the high end of the range. The translation is powered by a spring, to aid with the initial acceleration, and with a 1 hp, DC electric motor to continue the acceleration and sustain the velocity by driving a push bar with a 78 mm (3 inch) diameter friction wheel. This drive motor is model number DC-1 of the Reliance Electric Co. Maximum rotational speed is 1725 RPM. The drive device is shown on Fig. 4. The translation slide is sketched in Fig. 5. The wake generating tubes are inserted in holes in the runner and the drive bar is driven by the drive device. Attached to the drive mechanism is a photo-diode sensor which indicates when the translation runner has moved a distance of 10 cm (4 inches). The signal from this sensor is used to activate the data acquisition trigger. The sensor's voltage rises from 0 to ~ 2 v as a fin on the drive bar of the slide mechanism interrupts a light beam. This signal is input to a Hewlett-Packard 8012B Pulse Generator which converts this to a stronger signal which is adjustable but is usually set to give a 0 to 3 v rise when the fin interrupts the light beam. This signal is available to the data acquisition system. The duration of the measurement portion of the translation is from one to five wake passings, which ranged from 16 ms to 0.2 sec for the cases tested.

Hot Wire Anemometer

Instantaneous local velocities are measured using a TSI Model 100 (IFA-100) Intelligent Flow Analyzer, constant-temperature anemometer with a TSI Model No. 1210-T1.5 Tungsten single-wire, hot-wire probe or a TSI Model No. 1243-20 platinum cross-sensor, hot-film probe. The cross-sensor probe is used to document the isotropy of turbulence of the flow ahead of the cascade. It has two 51 μm (2 mil) diameter sensors, mounted perpendicular to one another, parallel to the airfoil axes, and 45° to the cascade endwall and to the flow. The single-wire is used for streamwise velocity measurements and for indicating the state of the boundary layer on the suction surface of the airfoil by traversing it to very near the surface and measuring the fluctuation intensity and interrogating the waveform to detect signs of flow reversal. The probe can be traversed to near the surface with an optical rotator device with a precision of one second of rotation which results in a precision of translation of 4 μm (16 μinch). The single-wire probe has one 3.8 μm (150 μinch) diameter wire, mounted perpendicular to the flow and to

the cascade endwall. Each hot-wire output signal, an analog voltage, is amplified and filtered using the TSI Model No. 158 signal conditioner. Each is read with the data acquisition unit.

Surface-Mounted Thin-Film Gages

The surface-mounted, thin-film gages are small, hot-film elements vapor-deposited on a thin sheet of polymeric substrate and sandwiched between another such sheet. The sensor resistance is approximately 2 ohms. The resistance changes with temperature similarly to that of the wire of the hot-wire anemometer sensor discussed above. The surface-mounted sensor is driven with the same anemometer bridge as used for the hot-wire sensor, the IFA-100. The sensor streamwise separation distance is 2.5 mm (0.1 inch). The sheet employed in the present study contains 30 sensors aligned along the streamwise distance. This sensor is wrapped around an airfoil so that it covers, approximately, the downstream 70% of the suction surface and the downstream 15% of the pressure surface.

Surface Static Pressure

The surface static pressures are read using 22 static pressure ports installed on a blade surface. They are connected to steel tubing which extends through the endwall of the facility connecting to tygon tubing outside which, in turn, lead to a 36-port Scanivalve selector. The Scanivalve is programmed to bring the ports, one at a time, into communication with the diaphragm of a Validyne, 860 Pa- (3.5 inch)- maximum-pressure-difference, variable-reluctance, pressure transducer driven by a Validyne model CD-15 Carrier Demodulator. The pressure transducer provides an analog voltage signal which is read with the data acquisition unit. Ten seconds is allowed between each reading for the pressure to equalize with the diaphragm.

Temperatures

Flow temperature is measured with an iron-constantan (Type J) thermocouple. The digitizer is used to acquire the thermocouple signal and convert it to temperature. Additionally, a combination of a single Type J thermocouple and an Omega Digicator displays a readout of the flow temperatures for visual reference by the operator.

Data Acquisition

All the data acquisition is with a Hewlett-Packard High Speed Data Acquisition System, Model No. HP3852A. This unit has a 13-bit (sign plus 12 digits) A/D converter driven by a High-Speed FET Multiplexer, allowing multiple channels of high speed acquisition with nearly simultaneous sampling. For X-wire measurements, two channels are sampled; for all other measurements, a

single channel is sampled. Sampling rates of as high as 100,000 samples/sec can be achieved and record lengths of up to 8192 readings can be acquired (for X-wire measurements 50,000 samples/sec can be acquired and 4096 points per channel can be stored). The data acquisition unit also has a 16 bit integrating digital voltmeter which is used for acquisition of pressure readings from the pressure transducer and thermocouple readings of the air temperature in the wind tunnel. Temperature readings are stored along with all hot-wire readings for correction of the hot-wire voltages to the calibration temperature. A relay actuator on the HP3852A controlled the Scanivalve drive motor. Data are transferred to a Unisys model PW^2 386-based PC computer via a National Instruments IEEE-488 interface board. Data acquisition is controlled with the PC using software written in QuickBASIC. Data processing is done on the PC using software written in QuickBASIC or on a Sun workstation in Minnesota as explained below.

Data for spectral measurements are acquired with the single-wire probe located 5.4 cm (2 inches) upstream of the blades in the center of the channel. Data for the analysis are acquired in three sections. The first section is acquired with a 100 kHz sampling rate and low-pass filtered at 10 kHz. The second section is acquired with a 10 kHz sampling rate and low-pass filtered at 1 kHz. The third section is acquired at 1 kHz with low-pass filtering at 100 Hz. For each section, 10 traces of 8192 points are digitized. Raw voltage data from the IFA-100 as well as calibration constants and the ambient temperature are stored to disc. These data are then transferred to a Sun workstation at the University of Minnesota for processing. A program written in C is used to perform a Fast Fourier Transform (FFT) and compute the power spectral density of each half-trace of data (i.e. 20 records of 4096 points each are processed with the FFT for each of the three sampling rates). The 20 spectra at each sampling rate are then averaged to create a composite spectrum. The three sections of the spectrum are then pieced together for presentation. Acquiring the spectra in sections allows better resolution of both high and low frequencies, maximizing the quality of the spectrum, given the limited amount of data that can be acquired and stored in the digitizer for each record.

The uniformity of the flow in the wind tunnel is checked with both the single-wire probe and the X-wire probe. With the single-wire, the probe is moved to various positions in the flow, were 4000 data points are digitized at a 100 Hz sampling rate. The instantaneous data are converted to velocities and averaged to give U and u'. These two values are then stored. The procedure for the X-wire is similar. A total of 250 data points are acquired in 60 seconds. The values of U, V, u' and v' are calculated and stored. All hot-wire data are low-pass filtered at 5 kHz, with the exception of the spectral data described above.

For unsteady measurements with the traversing wakes in use, raw voltage traces from the IFA-100 are digitized and stored for later ensemble averaging. Traces could be acquired from the single-wire probe or from one of the hot-film sensors mounted on an airfoil. The sampling rate and record length of each trace are adjusted so that 100 samples are acquired between each wake passing event. Fifty traces, corresponding to 50 traverses of the slider mechanism are acquired at each position of interest for later conversion to velocities and for ensemble averaging.

Static pressure measurements are taken at 22 positions around the airfoil and from a pitot tube located 5.4 cm (2 inches) upstream of the airfoil. Total pressure is also measured with the pitot tube. From these measurements, the pressure coefficient distribution around the airfoil is calculated and stored.

Status of the Program

The entire test facility has been modified to accept the new airfoils, the new wake generator, and the new turbulence generator. Four new airfoils have been constructed, two without instrumentation, one with the surface-mounted thin-film sensors, and a fourth with the static pressure taps. The thin-film sensor sheet of 30 hot-film elements has been attached to bus wires. The slider mechanism and the device which drives it has been designed, constructed, and qualified. A photo-diode device to create a trigger signal for the data acquisition has been constructed and checked out. All data acquisition methodology has been developed (including modification of the software) and checked. The tunnel modification is essentially complete. The facility now stands essentially ready for the beginning of data acquisition. Unfortunately, a few small but necessary machining operations remain that have prevented the actual data-taking portion of the program from beginning during the Summer period allotted for the program. Thus, arrangements have been made for continuation.

ACKNOWLEDGMENTS

We wish to express our gratitude to the Aero Thermal research team of the Wright Propulsion Laboratory for their aid and support; Richard Rivir, Task Manager, and, within the Laboratory, Greg Cala, David Pestian, Shichuan Ou, and Chris Murawski. We especially appreciate the sound technical advice and encouragement of our host Dick Rivir. We also thank Professor Paul King of the Air Force Institute of Technology for the use of the AFIT facilities and for his technical help. The fabrication of the new airfoil blades and modification work on the wind tunnel were done by Dave Driscoll at the AFIT shop. We thank him for his steady and careful efforts, especially for the cast airfoils which are truly works of art. We also appreciate the skill and patience of James Higgins, Shop Foreman, and Tim Klopfenstein at the Dayton Research Institute Shop at the University of Dayton. Finally we thank AFOSR for their financial support and RDL for their fine management of the program.

References

Blair, M. F., Dring, R. P., and Joslyn, H. D., 1988, "The Effects of Turbulence and Stator-Rotor Interactions on Turbine Heat Transfer, Part I, Design Operating Conditions," ASME Paper #88-GT-125.

Doorley, D. J., Oldfield, M. L. G., and Scrivener, C. T. J., "Wake Passing in a Turbine Rotor Cascade," AGARD CP-390, Paper No. 7, Bergen, Norway.

Hodson, H. P., 1983, "The Development of Unsteady Boundary Layers in the rotor of an Axial-Flow Turbine," AGARD Proceedings No. 351, *Viscous Effects in Turbomachines.*

Mayle, R.E., 1991, "The Role of Laminar-Turbulent Transition in Gas Turbine Engines, ASME Paper No. 91-GT-261.

Sahm, M. K., and Moffat, R. J., "Turbulent Boundary Layers with High Turbulence: Experimental Heat Transfer and Structure on Flat and Convex Walls," Report No. HMT-45, Thermosciences Division, Mechanical Engineering Department, Stanford University, 1992

Sharma, O. P., Pickett, G. F., and Ni, R. H., 1990, "Assessment of Unsteady Flows in Turbines," ASME Paper #90-GT-150.

Sharma, O. P., Ni, R. H. and Tanrikut, S., "Unsteady Flows in turbines - Impact on Design Procedure," from *Turbomachinery Design Using CFD*, AGARD Lecture Series No. 195, given at the Ohio Aerospace Institute, May 1994.

Table 1

Cases of the study

Case number	Re_c	TI (%)	Case number	Re_c	TI (%)
without wake generation			with wake generation		
1	40,000	1	5	40,000	1
2	40,000	20	6	40,000	20
3	80,000	1	7	80,000	1
4	80,000	20	8	80,000	20

Table 2 Outline of the Test Program

I. No Wake Generator
   A. For Re_c = 40,000 and 80,000
      1. For no turbulence generator and an active turbulence generator
         a. Transverse distributions
            - U
            - $\sqrt{\overline{(u')^2}}/U$
         b. For the centerspan and mid-passage streamline
            - 1-D PSD
            - $\sqrt{\overline{(u')^2}}/U$, $\sqrt{\overline{(w')^2}}/U$
         c. For the airfoil surfaces
            - C_p
            - Locations of laminar & turbulent, attached & separated flows

II. With the Wake Generator
   A. For Re_c = 40,000 and 80,000
      1. For no turbulence generator and active turbulence generator
         a. For the centerspan and mid -passage streamline
            - 1-D PSD
            - Time-resolved:
               > $\sqrt{\overline{(u')^2}}/U$
               > Locations of laminar & turbulent, attached & separated flows

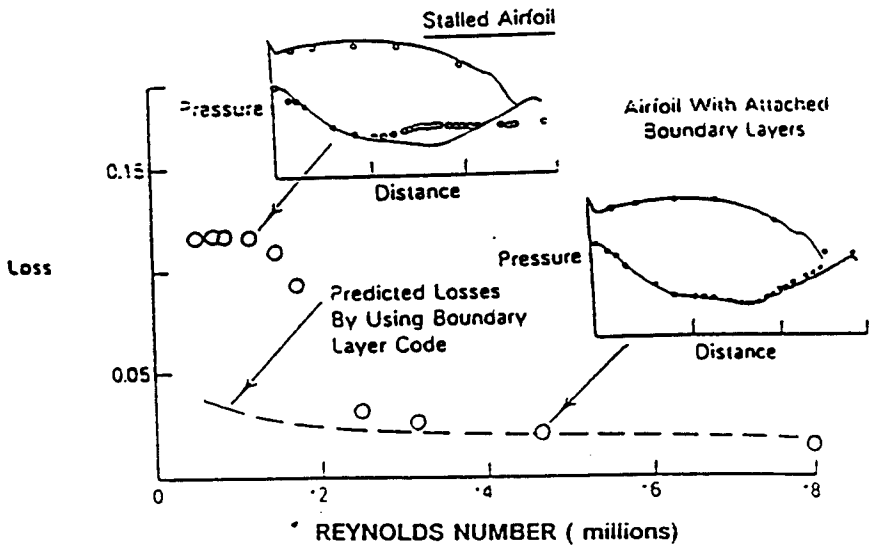


Fig. 1 High loss levels measured for airfoils at low Reynolds number. Boundary layer flow separation evident on airfoil suction surfaces. Taken from Sharma, Ni, and Tanrikut, 1994.

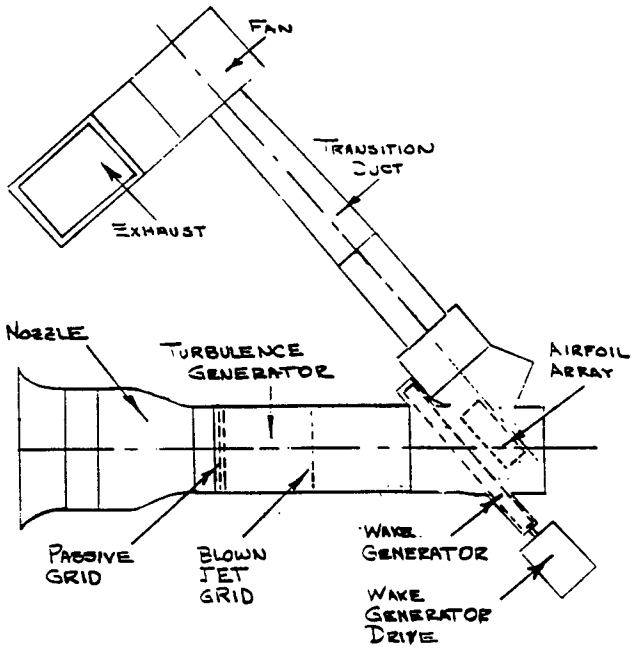


Fig. 2 Layout of the wind tunnel facility.

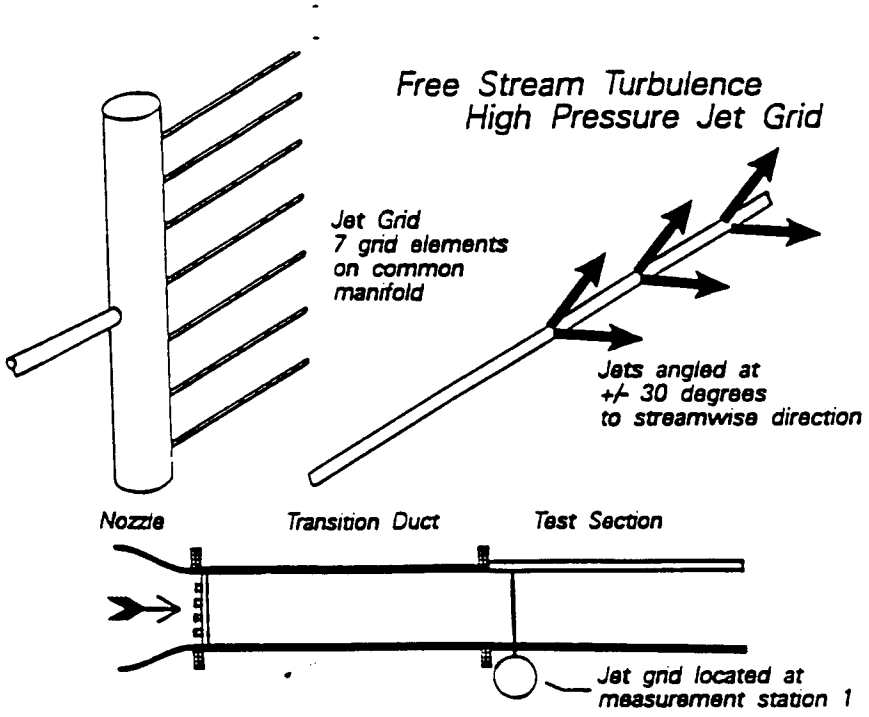


Fig. 3 Schematic of the jet grid. From Sahm and Moffat, 1992.

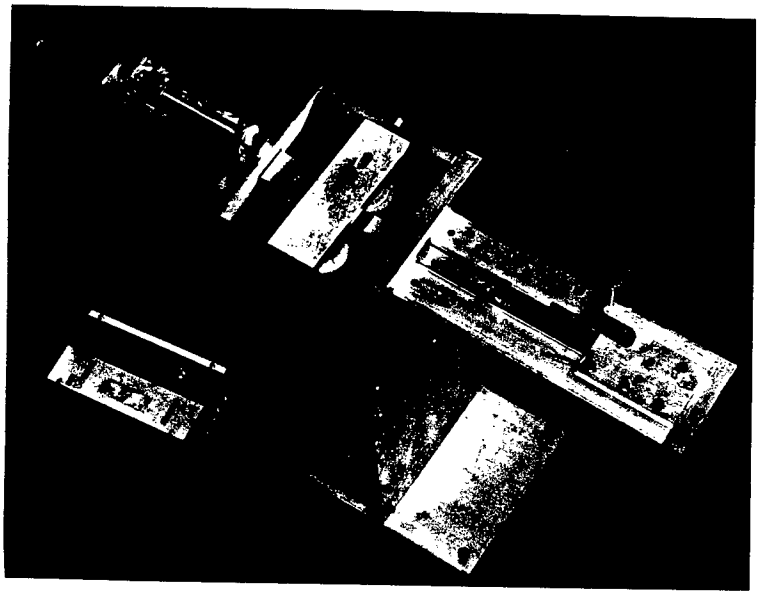


Fig. 4 A photograph of the wake generator driving mechanism.

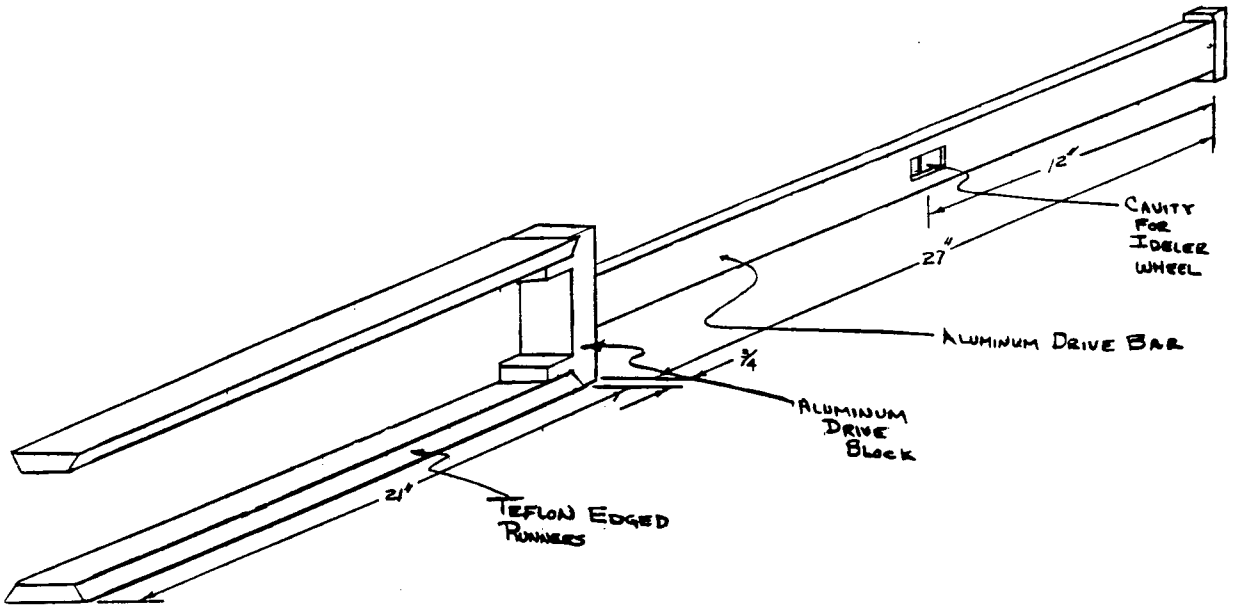


Fig. 5 A sketch of the traverse slider and the push bar

INTEGRATION OF CHAMP FIRM MACRO LIBRARY WITH DSS SYNTHESIS SYSTEM

Jeffrey A. Walrath
Graduate Student
Department of Electrical and Computer Engineering

University of Cincinnati
814 Rhodes Hall
Cincinnati, Ohio 45221

Final Report for:
Graduate Student Research Program
Wright Laboratories
WL/AAAT

Sponsored by:
Air Force Office of Scientific Research
Bolling Air Force Base, DC

and

Wright Laboratories
WL/AAAT

September 1994

INTEGRATION OF CHAMP FIRM MACRO LIBRARY WITH DSS SYNTHESIS SYSTEM

Jeffrey A. Walrath
Graduate Student
Department of Electrical and Computer Engineering
University of Cincinnati

Abstract

With the current development of high-level synthesis tools such as MSS[1], there has been a significant reduction in design times for application-specific integrated circuits. Another recent development has been the introduction of FPGA (Field Programmable Gate Array) technology which is used for rapid-prototyping of processor designs. Since most high-level synthesis tools target an ASIC architecture, this summer's research project addressed the issue of using high-level synthesis tools to generate register level designs suitable for use on FPGA architectures.

INTEGRATION OF CHAMP FIRM MACRO LIBRARY
WITH DSS SYNTHESIS SYSTEM

Jeffrey A. Walrath

Introduction

Under sponsorship of Wright Laboratories, the University of Cincinnati's Laboratory for Digital Design Environments has developed a Multicomponent Synthesis System (MSS)[1]. MSS is capable of generating multi-chip designs from large behavioral specifications of application specific electronic systems. The MSS system contains a variety of synthesis, partitioning and test tools. Of these tools, DSS (Distributed VHDL Synthesis System) was the focus of the research during the summer intern-ship.

DSS is a high-level synthesis system which accepts behavioral specifications in VHDL and generates register level designs also in VHDL. A register level design contains a *data path* and a *controller*. Whereas the controller is a collection of communicating state machines, the data path is a net-list of register level components selected from a parameterized register level component library called the Synthesis Library (SL). In the usual synthesis process which generates custom layouts, each register level component is further refined into gate level components that are eventually bound to primitive cells from a standard cell library.

Lockheed Sanders has been engaged in the CHAMP project sponsored by the US Air Force. As part of the project, Lockheed Sanders is involved in the development of high-performance application specific processors based on the FPGA (Field Programmable Gate Array) technology. To facilitate rapid development of the processors, Lockheed Sanders developed a Firm Macro Library (FML)[2]. Each module within the library is a composition of combinational logic blocks supported by the FPGA technology.

To further facilitate rapid development of CHAMP designs, the DSS Synthesis Library was rewritten in terms of components from the Lockheed Sander's Firm Macro Library. This entailed writing new VHDL models for each component in the Synthesis Library. Thus, a data path generated by DSS when elaborated would contain a net-list of FML components which could be bound to combinational logic blocks on an FPGA.

Methodology

Originally, the components in the DSS Synthesis Library were VHDL behavioral models which described the functionality of each component. Each behavioral model also contained a description of the input and output ports. Thus, the DSS system expects the input and output ports to be in the predefined order described by the VHDL model. Results derived with the original DSS library flatten to a net-list of components from the Synthesis Library (e.g. adders, registers, etc.). For further refinement of the net-list (e.g. each component is a net-list of Firm Macro Library modules), the new DSS component must also maintain the same input and output port list and perform the same functionality as the original behavioral model.

Research began by first comparing the Firm Macro Library (FML) components with the components in the DSS library. This comparison produced three categories of DSS components: common, specific, and unmappable. A common component is one that is in both the FML and the DSS library. A specific component is one that does not correspond to any component in the FML, but the component can be constructed from several different components in the FML. And an unmappable component is one that can not be constructed

Common	Specific	Unmappable
Adder	Bus Selector	And
Subtractor	Signal	Or
Multiplier	Shift Register	Xor
Divider	Bus Concatenate	Nand
Multiplexer	Constant Register	Nor
Comparator		Xnor
Latch		Not

Figure 1: Three categories of DSS components

with any component from FML. Figure 1 shows the categorized listing of all 19 components from the DSS Synthesis Library.

The first DSS component to be rewritten was the divider. Since the FML had a single 26-bit divider, developing a new DSS component was a straight forward task. Inputs and outputs to the DSS component were aligned with the inputs and outputs to the FML divider. In the case where the DSS input size was smaller than 26 bits, the unconnected bits of the FML divider were connected to the most significant bit of the respective input. Thus, all inputs to the FML divider were sign extended to ensure proper results and functionality. Figure 2 shows the actual VHDL code written for the new DSS divider.

Creating a new DSS component for the multiplier was similar to the divider with the difference that the FML contained both an 11-bit and 16-bit multiplier. In this case, the DSS component was created so that it checks the input size and instantiates the smallest FML multiplier necessary to obtain the correct functionality. Again, the inputs and outputs are aligned and the unused input bits to the FML multiplier are sign extended.

Next on the list of components to be rewritten was the DSS latch component. The FML contained a single 16-bit clock enabled register which performed the same operation as the DSS latch. When the input to the DSS latch is 16 bits or less, only a single FML register is instantiated and connected. If, however, the input is greater than 16 bits, the DSS component instantiates 2 FML registers and correctly aligns the inputs. For this DSS component, nothing had to be done to the unconnected bits of the FML register when the input size was something other than 16 or 32.

Rewriting the DSS adder was more complicated than the divider, multiplier, and latch. Various sized DSS adders were constructed using 7 different fixed sized FML adder components. Input to the DSS component is compared against the sizes of the various FML adders and the appropriate FML adder is instantiated. Once instantiated, the inputs and outputs to the DSS component are aligned with the inputs and outputs of the FML adder. If the input size to the DSS component is smaller than the input to the FML component, the unconnected bits of FML adder are connected to ground. Also, if the output size of the DSS component is smaller than the instantiated adder, the DSS carry-out is connected to the appropriate output line from the FML adder which may not necessarily be the designated carry-out. For example, if the input is 8 bits wide, then the output is also 8 bits wide and the carry-out is connected to the 9th bit of the adder and not the designated carry-out of the 12-bit FML adder.

```
entity C_divider is
 generic (width : INTEGER := 4; delay : TIME := 0 ns);
 port (Input1, Input2 : in Bit_Vector((width - 1) downto 0);
     Output : out Bit_Vector((width - 1) downto 0));
end C_divider;

architecture Behavior of C_divider is
 component DIVXXT1
   generic (delay : time := 0 ns);
   port (Input1, Input2 : in Bit_Vector(25 downto 0);
     Output : out Bit_Vector(12 downto 0));
 end component;
 for all : DIVXXT1 use entity Lib.DIVXXT1(BEHAVIORAL);

 signal inp1  : bit_vector(31 downto 0);
 signal inp2  : bit_vector(31 downto 0);
 signal outp  : bit_vector(31 downto 0);
 signal bout  : bit_vector(1 downto 0);
 signal empty : bit;

begin
 inp1(31 downto width) <= (others => Input1(width-1));
 inp1(width-1 downto 0) <= Input1;
 inp2(31 downto width) <= (others => Input2(width-1));
 inp2(width-1 downto 0) <= Input2;

 outp(31 downto 13) <= (others => outp(12));
 Output <= outp(width-1 downto 0);

 G1:if(width <= 26) generate
   Div26 : DIVXXT1
     generic map (delay)
     port map (Input1 => inp1(25 downto 0),
               Input2 => inp2(25 downto 0),
               Output => outp(12 downto 0));
 end generate G1;

 G2:if(width > 26) generate
   Assert false
     report "No divider component for inputs greater than 26 bits!!!"
     severity failure;
 end generate G2;
end Behavior;
```

Figure 2: VHDL code for the new DSS divider

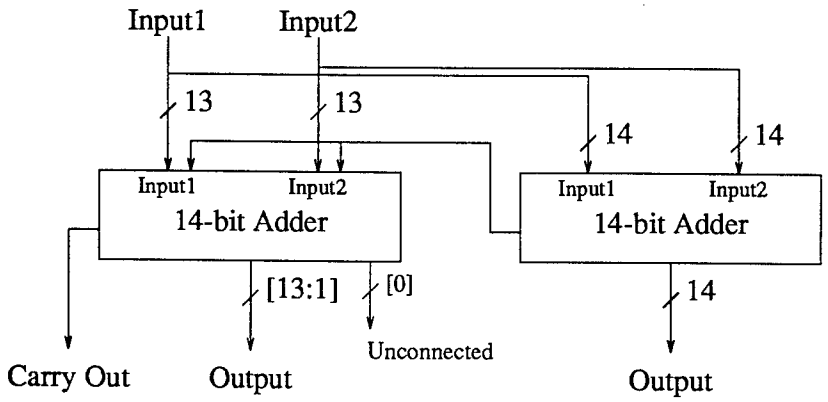


Figure 3: Construction of the 27-bit adder

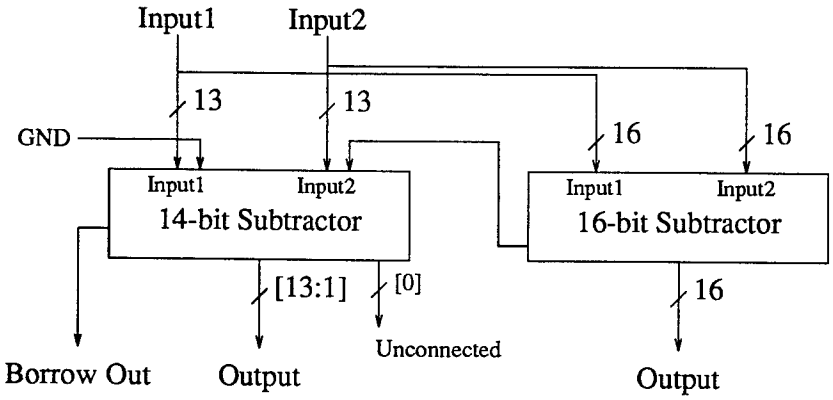


Figure 4: Construction of the 29-bit subtracter

Since the largest FML adder is 26 bits, inputs greater than 26 bits cause the DSS adder to instantiate 2 FML adders. But because the FML adders have no carry-in line, the DSS component was written so that it uses the least significant bit of the second adder as a carry-in line. Thus, the output of the least significant bit of the second adder is not connected to any outputs of the DSS component. Figure 3 shows how the DSS adder component is connected to generate a 27-bit adder.

Development of the DSS subtracter was similar to the adder. The subtracter selects one of 3 possible FML subtracters to instantiate based on the input size. All inputs and outputs are correctly aligned and the borrow-out is connected to the appropriate output line depending on the input size and the size of the FML component. However, the difference between the adder and subtracter occurs with the connection of borrow-in when 2 FML subtracters are connected together. Figure 4 shows the connectivity of 2 FML subtracters to create a 29-bit subtracter. Notice that one of the least significant bits of the second subtracter is not connected to borrow-in but instead to ground.

Another complicated component to rewrite was the DSS comparator. Where the DSS comparator generates three output signals, the FML comparator only generates one. Output signals from the DSS comparator indicate when $A > B$, $A < B$ and $A = B$. However, the FML comparator simply indicates when $A > B$. Creating the DSS comparator meant using 2 FML comparators and wiring them such that one DSS input connects to the A input of the first comparator and to B of the second comparator. Similarly, the second

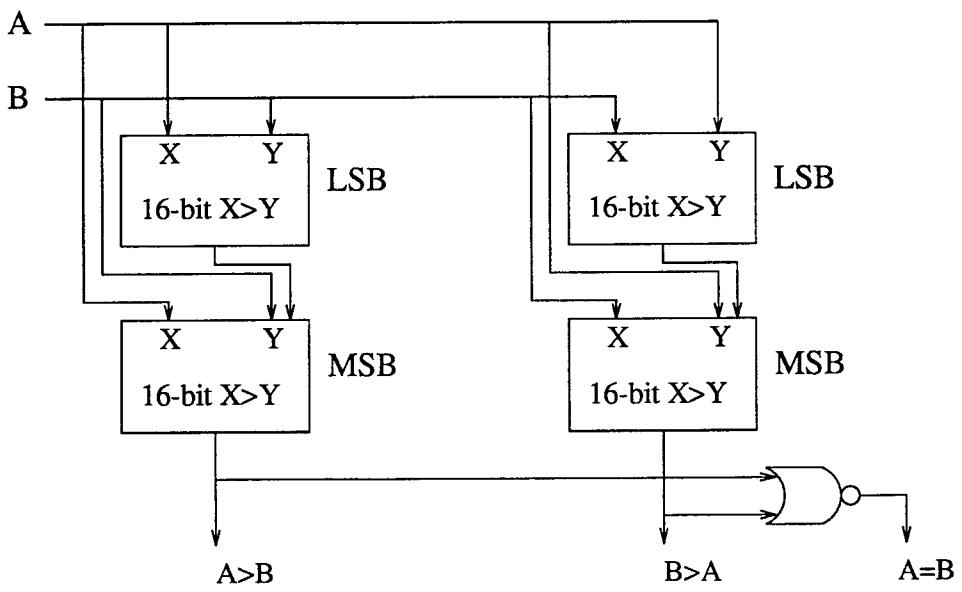


Figure 5: Construction of the 16-bit comparator

DSS input connects to the B input of the first comparator and the A input of the second. This connectivity generated only 2 of the 3 required output signals. Generating the $A = B$ signal was accomplished by connecting the the outputs of the two FML comparators to a NOR gate. For inputs sizes greater than 16 bits, two comparators were connected together to generate a 31-bit comparator. Two of these 31-bit comparators were then wired in a similar fashion as the 16-bit configuration to produce the 3 output signals. Figure 5 shows the construction of the 31-bit comparator.

Of the common DSS components, the last one to be rewritten was the multiplexer. A 16-bit 2-to-1 multiplexer was the only FML component that could be used to build the DSS multiplexer. Depending upon the number of inputs, the DSS multiplexer had to connect one or more of the FML multiplexers together to produce the necessary result. For example, a 5-to-1 multiplexer uses four of the FML multiplexers connected in a binary tree configuration to correctly implement the required functionality. Figure 6 shows the construction of the 4 FML multiplexers to produce a 16-bit 5-to-1 multiplexer.

Construction of DSS bus selector was similar to the multiplexer. However, the control logic to the bus selector is not encoded as it is with a multiplexer. Whereas an 8-to-1 multiplexer has 3 select lines, the 8-to-1 bus selector has 8 select lines. Thus, the construction of a bus selector was simply to add a 2-to-1 FML multiplexer for each input over the first. For example a 5-to-1 bus selector will instantiate 4 FML multiplexers. Figure 7 shows the construction of the 4 FML multiplexers to produce a 16-bit 5-to-1 bus selector.

Constructing the DSS shift register required using three different components from the FML. Behaviorally, the shift register is a master-slave register with the ability to load new data, shift the current data to the right or left by one bit. Thus, the FML components necessary to implement the DSS shift register were a clock enabled register, a standard falling-edge register, and two 2-to-1 multiplexers. Together the clock enabled register and the standard register compose the master-slave configuration of the shift register. With the two multiplexers, a 3-to-1 multiplexer was constructed that selects from three possible inputs: the new

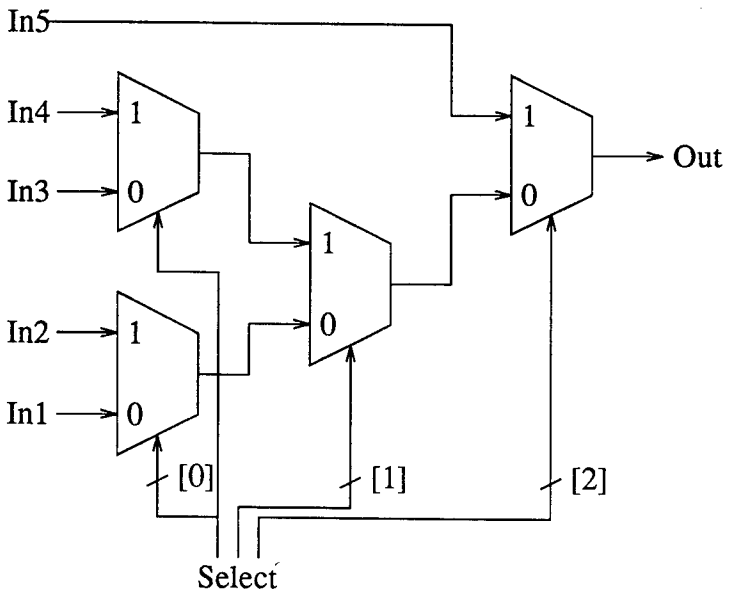


Figure 6: Construction of the 16-bit 5-to-1 multiplexer

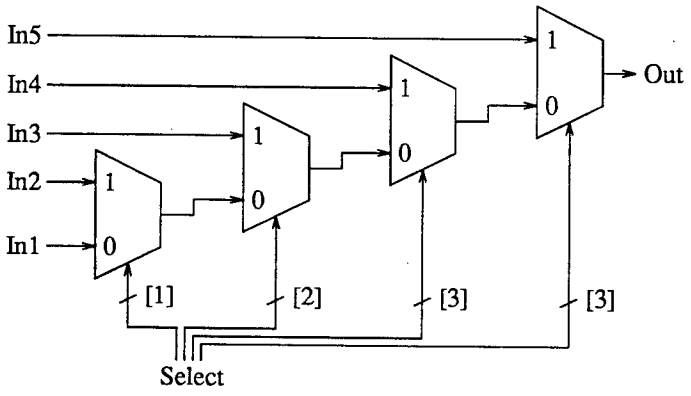


Figure 7: Construction of the 16-bit 5-to-1 bus selector

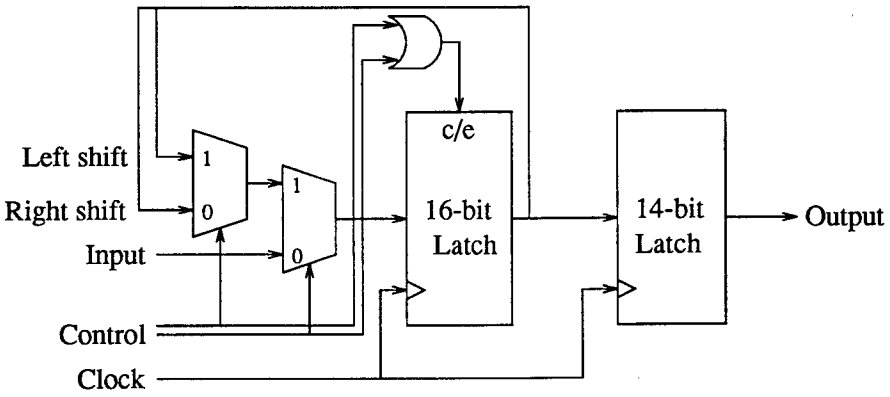


Figure 8: Construction of the 14-bit shift register

value to be loaded, the current value shifted right, or the current value shifted left.

Because the FML contained only one clock enabled register, all master registers in the DSS shift register component are 16 bits. However, there were 5 possible choices of FML registers for the slave register in the shift register. In order to minimize the size of the slave register, the DSS component was constructed with smallest register that would still maintain correct functionality. Figure 8 shows the construction of a 14-bit shift register.

Of all the components that were rewritten, the DSS signal register component was the most complicated to design with components from the FML. Behaviorally, the signal register is a master-slave register with that has two load signals and generates two extra outputs signals in addition to the actual output data. One load signal controls the master register while the second controls the slave section. The two extra output signals are status information about what is occuring in the register. A QUIET signal is generated to indicate when data has been loaded into the master register, and a STABLE signal indicates when the data in the mast matches the data in the slave.

In order to construct the signal register, two clock enabled registers, three single bit flip-flops, and two $A > B$ comparators were used from the FML. Combination of the two clock enabled registers formed the master-slave register with the two separate load lines. Generation of the STABLE output signal was accomplished by combining the two comparators to form an $A = B$ comparator which compared the data in the master register to the data in the slave register. All the single bit flip-flops were used to generate the QUIET signal. Figure 9 shows the construction of a 16-bit signal register. A 32-bit signal register is two 16-bit configurations with a slightly different comparator connection.

Both the bus concatenate and constant register components did not have to be rewritten. Neither component is an actual component in the sense that it does not perform some functional operation on inputs to produce outputs. A constant register component has no inputs and simply connects output bits to power or ground to generate a constant binary value. The bus concatenate component has as inputs two buses and concatenates them to produce a third bus.

With all the DSS components rewritten as net-lists of FML components, the next step was testing of each new component to verify that it performed that same functionality as the original behavioral model. In order test the DSS components, behavioral VHDL models were created for the various FML components that were used in the construction of the DSS components. With these FML models, simulation could be

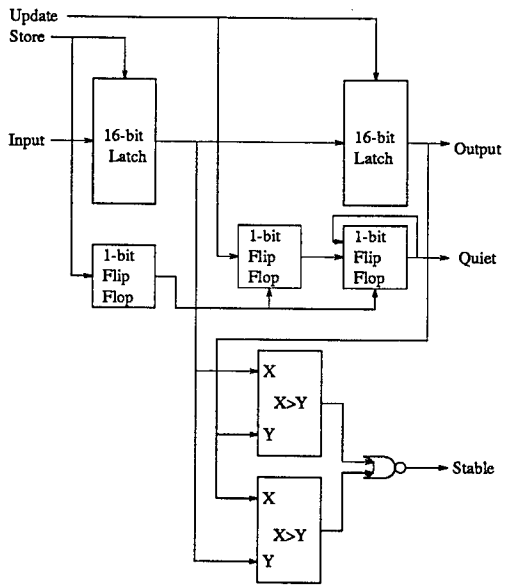


Figure 9: Construction of the 16-bit signal register

done on the new DSS components to verify correct functionality and connectivity.

Testing of the new DSS components was accomplished by writing VHDL test benches for each component. A test bench instantiated all sizes of the DSS component being tested, applied the test vectors to each instantiation, and displayed observed results along with expected results to the screen. For example, the test bench for the new DSS adder instantiated 32 adders (one for each input size from 1 to 32 bits), then applied 8 test vectors and printed the results to the screen. All the new components were tested an any errors corrected. Thus, the new DSS Synthesis Library components achieved the same functionality outline in the original behavioral models. Appendix A is an example test bench for the DSS adder component.

However, the new DSS Synthesis Library was not complete without a component information file. This file contains the speed and area data for every component in the synthesis library. Thus, for each new DSS component, the number of combinational logic blocks (CLB) used for a given input size along with the associated clock delay was calculated. Once calculated, all the data was entered into the component information file to be used whenever the new DSS components were used for high-level synthesis.

Results

Once the new DSS Synthesis Library was completed and verified, it was tested on a design example provided by Lockheed Sanders called the Spectral Filter. One of current Lockheed Sanders projects involves implementing several different signal processing filters in a system with the Spectral Filter being one of the more difficult filters to develop. Use of the Spectral Filter served as a good test for comparison between the DSS generated design and the Lockheed Sanders design. Appendix B contains the VHDL behavioral code of the Spectral Filter used as input to DSS.

DSS generated a data path and controller for the Spectral Filter in approximately 4 minutes. In the data path, 90 DSS components were used with the longest path delay through the data path being 20 clock

cycles. The data path required 128 individual control signals to perform the functionality described by the behavioral VHDL code. In terms of the FPGA architecture, the 90 DSS components in the data path require roughly 3000 combinational logic blocks (CLB). Of these 3000 CLBs, only 2200 are actually used by the data path to perform the specified functionality.

Analysis of Results

Unused CLBs can be are attributed to the limited selection of fixed size components in the Firm Macro Library from which all the DSS components were built. For example, the construction of a 17-bit DSS latch requires two 16-bit FML registers which leaves 15 input bits unconnected resulting in 7 unused CLBs. After closer inspection, two areas were found to contain the largest number of unused CLBs. Of all the CLBs used to implement mutliplexers in the design, roughly 400 of them are unused. So many CLBs go unused because there are several 1-bit multiplexers in the data path that can only be implmented with 16-bit FML multiplexers. Another area where a large number of CLBs are unused is the divider. Because the Firm Macro Library contained only one divider that was extremely large, any divider in the data path smaller than the FML divider would not use all the CLBs. For the Spectral Filter, roughly 200 CLBs are unused in the divider.

Further analysis showed that improvements could be made to the macro library to improve the various CLB counts. If the current Firm macro Library were extended to a parameterized library and the construction of the DSS components remained the same, the CLB count for the Spectral Filter would drop from 3000 to 2200 CLBs. Furthermore, if a macro library of strictly DSS components was developed , the CLB count would drop to around 2000 CLBs.

Future Work

1. Although much work was done with synthesizing designs for an FPGA architecture, further work needs to be done to complete the design process. Specifically, the controller generated by DSS needs to be integrated with an FPGA architecture in order to work with the synthesized data path. Integrating the the controller is a task more involved than simply rewriting library components as was done for the data path. Since the DSS generated controller is a PLA-based state machine which is not suitable to an FPGA architecture, a mapping is required to produce a controller that is sutiable to the FPGA environment.

2. Another topic of interest that needs further research is methods for reducing the CLB counts of the data path. A simple solution is to develop a macro library which is solely based on the DSS components. A better library would completely eliminate the unused CLBs in the data path. Another solution for reducing CLB counts would be to develop new DSS optimization algorithms to target an FPGA architecture instead of an ASIC architecture. By creating new algorithms to account for CLB usage, the overall design would again contain fewer CLBs. A less involved solution would be to modify the existing optimization algorithms to account for an FPGA architecture.

3. A final topic for future work would be to integrate the high-level DSS synthesis system with other lower-level synthesis systems that partition, place and route the CLBs on the FPGA. Work is currently being

done at the University of Cincinnati to take a net-list of CLB as input and produce the necessary files to program an FPGA. Integration of the DSS tool with these other tools would require development a translator from the current net-list of Firm Macro Library components to a net-list of CLB components.

References

[1] R. Vemuri, "A Multicomponent Synthesis System for Multi-chip Modules", Computer, April 1993.
[2] Lockheed Sanders, "Firm Macro Library Tables", private communication, March 1994.

Appendix A - Example of VHDL Test Bench

```
Library lib;
use lib.all;

Library std;
use std.textio.all;

entity TB is
end TB;

architecture test of TB is
  function bits_to_int (input : Bit_Vector )return INTEGER is
    variable ret_val : integer := 0;
    variable bit_chk : bit     := '1';
    variable negate  : integer := 1;
    variable incr    : integer := 0;
  begin
    if(input(input'HIGH) = '1') then
      bit_chk := '0';
      negate := -1;
      incr := 1;
    end if;

    for i in input'RANGE loop
      if(input(i) = bit_chk) then
     ret_val := 2**i + ret_val;
      end if;
    end loop;

    return negate*(ret_val+incr);
  end bits_to_int;

 component C_adder
   generic (width : INTEGER := 4; delay : TIME := 0 ns);
   port (Input1, Input2 : in Bit_Vector((width - 1) downto 0);
     Output : out Bit_Vector(width downto 0));
 end component;
 for all : C_Adder use entity Lib.C_Adder(Behavior);

 type bv_arr is array (32 downto 1) of bit_vector(32 downto 0);
 signal inp1 : bit_vector(31 downto 0);
 signal inp2 : bit_vector(31 downto 0);
 signal outp : bv_arr;
 constant adder_delay : time := 0 ns;
begin
  -- create all adders
 G1:for ctr in 1 to 33 generate
   Adder : C_Adder
     generic map (ctr, adder_delay)
     port map (Input1 => inp1(ctr-1 downto 0),
```

```
            Input2 => inp2(ctr-1 downto 0),
            Output => outp(ctr)(ctr downto 0));
end generate G1;

 -- test all the adders
Test_Adders : process
  variable io   : line;
  variable str  : string (1 to 255);
  variable str2 : string (1 to 255);
  variable str3 : string (255 downto 1);
  variable in1 : integer;
  variable in2 : integer;
begin
  str(1 to 7) := " bit - ";
  str2(1 to 18) := "adder should be - ";

   -- apply test inputs
  for tloop in 1 to 8 loop
    if(tloop = 1) then
      inp1 <= X"00000000";
      inp2 <= X"00000000";
      str(8 to 16) := "test 1 - ";
      str3(33 downto 1) := "000000000000000000000000000000000";
    elsif(tloop = 2) then
      inp1 <= X"FFFFFFFF";
      inp2 <= X"00000000";
      str(8 to 16) := "test 2 - ";
      str3(33 downto 1) := "011111111111111111111111111111111";
    elsif(tloop = 3) then
      inp1 <= X"00000000";
      inp2 <= X"FFFFFFFF";
      str(8 to 16) := "test 3 - ";
      str3(33 downto 1) := "011111111111111111111111111111111";
    elsif(tloop = 4) then
      inp1 <= X"FFFFFFFF";
      inp2 <= X"00000001";
      str(8 to 16) := "test 4 - ";
      str3(33 downto 1) := "100000000000000000000000000000000";
    elsif(tloop = 5) then
      inp1 <= X"00000001";
      inp2 <= X"FFFFFFFF";
      str(8 to 16) := "test 5 - ";
      str3(33 downto 1) := "100000000000000000000000000000000";
    elsif(tloop = 6) then
      inp1 <= X"FFFFFFFF";
      inp2 <= X"FFFFFFFF";
      str(8 to 16) := "test 6 - ";
      str3(33 downto 1) := "111111111111111111111111111111110";
    elsif(tloop = 7) then
      inp1 <= X"55555555";
      inp2 <= X"55555555";
```

```
      str(8 to 16) := "test 7 - ";
      str3(33 downto 1) := "010101010101010101010101010101010";
    elsif(tloop = 8) then
      inp1 <= X"CCCCCCCC";
      inp2 <= X"CCCCCCCC";
      str(8 to 16) := "test 8 - ";
      str3(33 downto 1) := "110011001100110011001100110011000";
    end if;
    wait for 1 ns;

    wait for adder_delay;
    write(io, str2);
    write(io, str3);
    writeline(output, io);
    for ctr in 1 to 32 loop
      write(io, ctr, left, 2);
      write(io, str);
      write(io, outp(ctr)(ctr downto 0), right, 33);
      write(io, ' ');
      write(io, '(');
      write(io, bits_to_int(inp1(ctr-1 downto 0)));
      write(io, ')');
      write(io, '+');
      write(io, '(');
      write(io, bits_to_int(inp2(ctr-1 downto 0)));
      write(io, ')');
      write(io, '=');
      write(io, '(');
      write(io, bits_to_int(outp(ctr)(ctr-1 downto 0)));
      write(io, ')');
      writeline(output, io);
    end loop;
    writeline(output, io);
  end loop;

  -- stop the test
  wait;
end process Test_Adders;
end test;

-- configuration of test bench
configuration CONFIG of TB is
 for TEST
 end for;
end CONFIG;
```

Appendix B - VHDL Behavioral Description of Spectral Filter

```
entity FILTER is
 port(Start_Sim : in bit;
      P1 : in integer;  P1_Addr : out integer;
      P2 : in integer;  P2_Addr : out integer;
      S1 : in integer;  S1_Addr : out integer;
      S2 : in integer;  S2_Addr : out integer;
      W0 : out integer; W0_Addr : out integer);
end FILTER;

architecture SPECTRAL of FILTER is
begin
 P1 : process
   variable CP1P2 : integer;
   variable CP1P1 : integer;
   variable ALPHA : integer;
   variable i     : integer;
   variable j     : integer;
   variable k     : integer;
   variable l     : integer;
   variable mem   : integer;
   variable mem1  : integer;
   variable mem2  : integer;
 begin
    -- loops for filter calculation
   i := 2;
   while( i < 126) loop
     j := 2;
     while(j < 126) loop
        -- initialize local variables
       CP1P2 := 0;
       CP1P1 := 0;
       ALPHA := 0;

        -- take 5x5 matrix of local pixels
       k := 0;
       while(k < 5) loop
         l := 0;
         while(l < 5) loop
            -- calculate memory for fetch
           mem1 := i+k-2;
           mem2 := j+l-2;
           mem := mem1*128+mem2;

            -- fetch data from memory
           P1_Addr <= mem;
           P2_Addr <= mem;
           wait on P1, P2 until not (P1'stable and P2'stable);

            -- calculate with read data
```

```
        CP1P2 := CP1P2 + P1*P2;
        CP1P1 := CP1P1 + P1*P1;

         -- increment l;
        l := l+1;
      end loop;

       -- increment k
      k := k+1;
    end loop;

     -- fetch one more point
    mem1 := i*128;
    mem := mem1+j;
    P1_Addr <= mem;
    P2_Addr <= mem;
    S1_Addr <= mem;
    S2_Addr <= mem;
    wait on P1, P2, S1, S2 until not (P1'stable and P2'stable and
      S1'stable and S2'stable);

     -- setup output data address
    W0_Addr <= mem;

     -- do filter calculations
    CP1P1 := CP1P1 - P1*P1;
    if (CP1P1 = 0) then
      W0 <= 0;
    else
      CP1P2 := CP1P2 - P1*P2;
      ALPHA := CP1P2/CP1P1;
      W0 <=  S2 - ALPHA*S1;
    end if;

     -- increment j;
    j := j+1;
  end loop;

   -- increment i;
  i := i+1;
 end loop;
end process;
end SPECTRAL;
```